

Comprehensive Model of Jupiter's Polar Aurora

©2019

Stephen Jeffrey Houston

B.S. Physics, Kansas State University, 2015

Submitted to the graduate degree program in Department of Physics and Astronomy and the Graduate Faculty of the University of Kansas in partial fulfillment of the requirements for the degree of Doctor of Philosophy.

Prof. Thomas E. Cravens, Chair

Prof. Bruce A. Twarog

Committee members

Prof. David Z. Besson

Asst. Prof. Ian M. Lewis

Assoc. Prof. Brian Ackley

Date defended: May 16, 2019

The Dissertation Committee for Stephen Jeffrey Houston certifies
that this is the approved version of the following dissertation:

Comprehensive Model of Jupiter's Polar Aurora

Committee:

Prof. Thomas E. Cravens, Chair

Date approved: May 16, 2019

Abstract

The source of auroral X-ray emission from the Jovian polar caps, whether from electron bremsstrahlung or heavy ion precipitation, has been a topic of debate for the past 40 years, beginning with the Einstein Observatory's first measurement of X-ray emission in 1979. Since then the Röntgen satellite, Chandra X-ray Observatory, and XMM-Newton have distinguished heavy ion (oxygen and sulfur) line emission in the X-ray spectrum and measure a total power of about 1 GW. There have been many attempts to model both bremsstrahlung and ion precipitation with the goal of reproducing what is being seen; however, both have encountered push back. Electron bremsstrahlung modeling has fallen short of producing the total overall power output being observed by our earth-orbiting X-ray observatories. Whereas heavy ion precipitation has been able to reproduce strong X-ray fluxes, but the proposed incident ion energies seemed to likely be much higher (>1 MeV/nucleon) than what was thought to be present above Jupiter's polar caps. Now with the National Aeronautics and Space Administration's (NASA's) Juno spacecraft arriving at Jupiter, there have been many measurements of heavy ion populations above the polar cap with energies up to 300-400 keV/nucleon (keV/u), well below predictions the of previous models. Meanwhile, Schultz et al. (2019) have provided a new outlook on how ion-neutral collisions in the Jovian atmosphere are occurring, providing an entirely new set of impact cross-sections and a total of 35 collision processes (prior models only account for 9). A model is described for the transport of magnetospheric oxygen and sulfur ions with low charge state and energies up to several MeV/nucleon (MeV/u) as they precipitate into Jupiter's polar atmosphere. A revised and updated hybrid Monte Carlo

model originally developed by Ozak et al. (2010) is used to model the Jovian X-ray aurora. The current model uses a wide range of incident oxygen ion energies (10 keV/u - 5 MeV/u) and the most up-to-date collision cross-sections. In addition, the effects of the secondary electrons generated from the heavy ion precipitation are included using a two-stream transport model that computes the secondary electron fluxes and their escape from the atmosphere. The model also determines H₂ Lyman-Werner band emission intensities, including a predicted spectrum and the associated color ratio. I predict X-ray fluxes, efficiencies, and synthetic spectra for various initial ion energies considering opacity effects from two different atmospheres. The data is made available for quick X-ray calculations given an input ion flux. A calculation is given that demonstrates an *in situ* measured heavy ion flux above Jupiter's polar cap is capable of producing over 1 GW of X-ray emission. Implications of the new model results for interpretation of data from NASA's Juno mission are discussed.

Contents

1	Introduction	1
1.1	Dynamos	2
1.2	Magnetospheres	3
1.3	Ionospheres	5
1.4	Auroras	6
1.4.1	Earth	8
1.4.2	Jupiter	9
1.5	Magnetosphere-Ionosphere Coupling	12
1.5.1	Magnetohydrodynamic Theory	14
1.5.2	Pedersen and Hall Conductivities	17
1.5.3	Field-Aligned Currents	19
1.5.4	Parallel Electric Fields	20
1.5.5	Magnetosphere-Ionosphere Coupling at Jupiter	22
1.6	Juno	24
2	Physical Processes Related to the Jovian Aurora	29
2.1	Ion Impact Cross-Section Overview	29
2.2	Energy Loss	37
2.2.1	Ejected Electron Energy Transformations	38
2.3	Neutral Atmospheres	41
2.3.1	Jupiter	42
3	Electron Precipitation	46

3.1	Introduction	46
3.2	Two-Stream Model	47
3.2.1	Physical Process	48
3.2.2	Electron Impact Cross-Sections	48
3.2.3	Results	49
3.2.4	Synthetic Ultraviolet Spectrum	53
3.2.5	Color Ratios	54
3.2.6	Field-Aligned Currents	58
3.2.7	Ionospheric Dynamics	60
3.3	Ionospheric Model	62
3.3.1	Chemical Model Atmosphere	63
3.3.2	Physical Processes	67
3.3.3	Results	68
4	Ion Precipitation Model	71
4.1	Introduction	71
4.2	Monte Carlo Model	72
4.2.1	Collision Processes	73
4.2.2	Energy Loss	74
4.2.2.1	Secondary Electron Production	75
4.2.3	Charge State Distribution	76
4.2.4	Depth Effects	79
4.2.5	Ion Production Rates	82
4.2.6	Synthetic X-ray Spectra	82
4.2.7	Juno Data	85
5	Ion Precipitation Results - Field-Aligned Currents and Ultraviolet Emission	88
5.1	Primary Effects	88

5.2	Secondary Electron Effects	96
5.3	Field-Aligned Currents	109
5.4	Airglow Emissions	112
5.5	Color Ratios and Predicted UV Spectra	118
6	Ion Precipitation Results - X-ray Production	125
6.1	Ion Production Rates	126
6.2	X-ray Production	129
6.3	X-ray Efficiencies	132
6.3.1	X-ray Spectra	137
7	Ion Precipitation Results - Juno Model-Data Comparisons	140
7.1	X-ray Results	140
7.2	Secondary Electrons - Two-Stream Results	144
7.3	Ionosphere for the Juno Case	152
7.3.1	Pedersen and Hall Conductivities	156
7.4	Discussion on Data Usage	158
8	Summary and Conclusions	161
8.1	Conclusion	161
8.2	Final Discussion	163
A	Tables of Oxygen NSIM and SIM Cross-Sections and Average Energy Loss Values	181
B	Tables of Sulfur NSIM and SIM Cross-Sections and Average Energy Loss Values	200
C	Tables of Chemical Reactions	232
D	Additional Oxygen Tables	242
E	Additional Sulfur Tables	248

List of Figures

1.1	Model of Jupiter’s (left) and Saturn’s (right) magnetic field at the surface of each planet. For Jupiter’s magnetic field a VIP4 model was used along with data taken from Juno’s Perijove 1 pass (shown as a black line) from Moore et al. (2017). Saturn’s magnetic field was modeled using the Hammer-Aitoff projection from Jones (2011)	3
1.2	A schematic of Jupiter’s magnetosphere and its interaction with the solar wind and the IMF. (Credit: Fran Bagenal and Steve Bartlett)	4
1.3	A.) The solar wind is the primary source of ions that generate Earth’s aurora. Although Earth’s magnetosphere deflects much of the solar wind, some particles are able to penetrate it and contribute to the aurora. B.) Charged particles follow a helical trajectory, bouncing between mirror points. The mirror points are determined by the particles pitch angle, or the angle of the particles velocity vector with respect to the magnetic field. C.) The process that causes ionization, heating, and emission due to collisions between incoming particles and the stationary atmosphere.	7
1.4	Jupiter’s northern aurora viewed in the UV wavelength by HST. Visible are satellite footprints, the main auroral oval, and the polar aurora, where heavy ion precipitation occurs.	9
1.5	An image from the Chandra X-ray Observatory taken on 18 December 2000 presented by Gladstone et al. (2002). An average X-ray emission of about 4 R is shown to emit from the polar caps.	11

1.6	Northern polar auroral zone spectrum presented by Dunn et al. (2016) measured by the Chandra X-ray Observatory. The cross-hairs represent the data measured by the observatory, while the solid line is a combination of lines that have been fitted to the data with half-widths fixed at 20 eV.	12
1.7	A schematic (not to scale) of Jupiter's current system showing the connection of the ionosphere to the outer magnetosphere. The region labeled "Inner Hill current system" is responsible for corotation of outward flowing magnetospheric plasma with the planet from sporadic current flow. The "Outer Hill current system" extends from ~ 20 to $\sim 60 R_j$. (See Stallard et al. (2001))	13
1.8	An equivalent simple electric circuit to illustrate the current system associated with auroral generation. The source, labeled " ϵ ", is the current generated through force imbalances when the magnetosphere lags behind corotation of the planet. The ionospheric resistance, labeled as " R_{iono} ", is due to ion-neutral collisions in the atmosphere. The aurora produced is then the resultant light source in this analogy. .	15
1.9	Illustration of the equipotential lines in the Jovian auroral region from Hill (2004). Shown are the parallel and Pedersen current densities, J_{\parallel} and J_P , respectively. . . .	21

1.10 Sketch of the Jovian magnetosphere and the connection to the ionosphere. The magnetic field lines are indicated by the arrowed solid lines, coming out of the northern hemisphere into the southern. The magnetic field lines are extended outwards by azimuthal currents in the middle magnetosphere current sheet. Io is the main generator of the plasma that makes up the current sheet. The dotted region represents the plasma, beginning as a torus produced by Io and diffusing outwards to form a plasma sheet. The plasma rotates with the Jovian magnetic field due to MI coupling. Indicated in the figure are three separate angular velocities. ω is the angular velocity of the planetary magnetic field, Ω_J is Jupiter's angular velocity, and Ω_j^* is the angular velocity of the neutral atmosphere in the Pedersen layer of the ionosphere. Ω_j^* is expected to have a value between ω and Ω_J due to the torque produced by ion-neutral collisional friction. The arrowed dashed lines represent the Pedersen current system that closes through Birkeland currents in the plasma sheet, where there is a radial outward current system. Shown is the case of subcorotation of the plasma (i.e., $\omega \leq \Omega_J$). Because the magnetic field lags behind corotation of the planet, the field lines are bent out of the meridian plane. The Birkeland current system is responsible for this "lagging" configuration associated with the azimuthal field components B_ϕ shown. (From Cowley et al. (2003).) . . . 23

1.11 Schematic of Juno with a description of each instrument onboard. 25

1.12 Orthographic projections of Jupiter's northern and southern aurora at the 1 bar level in the UV wavelength. The yellow line is the spacecraft trajectory marked with hourly tic marks. In the left column are UV intensities summed between 60 and 180 nm and in the right column are color ratios that have been given as the ratio between 155 to 162 nm and 123 to 130 nm (Connerney et al., 2017). 27

1.13	Oxygen and sulfur ion spectrogram measured by JEDI on the 7th perijove pass over the main auroral oval. The top figure shows the pitch angle distribution, where it is evident that energetic heavy ion precipitation is occurring when looking at the loss cone (pitch angles approaching 0° or 180°). The bottom figure is the energy spectrogram during the same time period. There are inverted-V distributions in the ion energy associated with ion acceleration.	28
2.1	Comparison of Schultz et al. (2017) NSIM cross-section calculations of electronic plus nuclear stopping power for oxygen ion transport through H_2 gas (squares) with Schultz et al. (2019) SIM cross-section calculations (circles). Also plotted are the accepted values from SRIM 2013 (Ziegler et al., 2013) (solid line).	31
2.2	SIM single ionization cross-section as a function of energy for collisions of O^{q+} in H_2 . Each curve corresponds to a different charge state, $q = 0 - 8$. Note the dominance of the single ionization cross-section at high oxygen ion energies. Data taken from Schultz et al. (2019).	35
2.3	SIM double capture + single stripping cross-section as a function of energy for collisions of O^{q+} in H_2 . Each curve corresponds to a different charge state, $q = 2 - 7$. Data taken from Schultz et al. (2019).	35
2.4	SIM double ionization cross-section as a function of energy for collisions of S^{q+} in H_2 . Each curve corresponds to a different charge state, $q = 0 - 16$. Data taken from Schultz et al. (2019).	36
2.5	SIM transfer ionization cross-section as a function of energy for collisions of S^{q+} in H_2 . Each curve corresponds to a different charge state, $q = 1 - 16$. Data taken from Schultz et al. (2019).	36
2.6	Comparison of the stopping power produced by my oxygen precipitation model and the accepted electronic+nuclear stopping power values from SRIM 2013 (Ziegler et al., 2013).	38

2.7	Comparison of the stopping power produced by my sulfur precipitation model and the accepted electronic+nuclear stopping power values from SRIM 2013 (Ziegler et al., 2013).	39
2.8	Atmospheric density profiles of H ₂ , He, CH ₄ , and H based on data shown in Mau-rellis & Cravens (2001) and Sinclair et al. (2018), referred to as atmosphere 1. Also shown is the neutral temperature profile as a function of altitude and pressure.	43
2.9	Atmospheric density profiles of H ₂ , He, and CH ₄ in my well-mixed atmosphere, referred to as atmosphere 2. Also shown is the neutral temperature profile as a function of altitude and pressure.	45
3.1	Lyman band (B ¹ Σ _u ⁺) excitation cross-sections in H ₂ from electron impact. Com-pared here are the cross-sections produced by Yoon et al. (2008) and the two-stream code. The vertical bars associated with the Y08 data represent an experi-mental error of 20%. This figure has been taken directly from Ozak Munoz (2012).	50
3.2	Volume emission rate of various monoenergetic electron beams of 1 mW/m ² into the top of Jupiter’s atmosphere (atmosphere 1). The emission rate includes H ₂ Lyman and Werner band emission and Lyman alpha line emission from H, which contributes a very small amount to the overall emission rate.	51
3.3	Vertical distribution of methane number density vs. pressure for the model used in the current paper (red solid line) compared to those used by Gérard et al. (2014) (dashed-dotted lines). The model numbers are the same as those used by Gérard et al. (2014), where more information can be found on the atmospheric models. . .	52
3.4	Predicted Lyman-Werner spectrum from a 20 keV monoenergetic electron beam with an input of 1 mW/m ² . The red line is calculated with a θ of 60° and the green line with a θ of 80°, while the black line is what is expected when no opacity effects are considered. The Ly-α line at 121.6 nm has been withheld from these predictions.	54

3.5 Initial monoenergetic electron beam energy vs. color ratio for three viewing angles of 0° , 60° , and 80° . The solid blue and red lines are color ratio measurements with an electron input using my two-stream model and the methane distribution from atmosphere 1 (Fig. 2.8). The solid maroon and dark blue lines are color ratio measurements with an electron input using my two-stream model and the methane distribution from atmosphere 2 (Fig. 2.9). The dashed-dotted lines are my two-stream model with the methane distributions presented in Gérard et al. (2014), at a viewing angle of 60° . The dashed lines are results from Gérard et al. (2014) using their electron transport model with their different atmosphere models. The green lines correspond to their model 1, pink to their model 2, and black to their model 3. The unattenuated color ratio is 1.32 for my precipitation model and 1.1 for theirs. Overlaid are two lines that represent the CR upper limit values of the polar cap and main oval associated with Figure 1.12. 57

3.6 Predicted electron escape flux vs. electron energy for precipitating monoenergetic electron beams with energies of 5, 10, 20, 50, 100, and 200 keV. A step plot has been used to show the size of the corresponding energy bins that are output by the two-stream code. Here I have assumed an incident input power of 1 mW/m^2 59

3.7 Ion production rate profiles vs. H_2 density for a 1 mW/m^2 monoenergetic, 20 keV electron beam. This is solely production from precipitating and secondary electrons, no photoionization has been included, i.e. a night side case. These electrons precipitated into atmosphere 1. 61

3.8 Atmospheric profile used by the chemical model. Additional hydrocarbons have been added because they become important to chemical reaction rates at low altitudes. This is an extension of atmosphere 1. 63

3.9 A second atmospheric profile used by the chemical model. Additional hydrocarbons have been added because they become important to chemical reaction rates. This is an extension of atmosphere 2, where I have considered an upper limit well-mixed atmosphere. 64

3.10 8 of the resulting 27 steady state ion densities (plus electrons) calculated by the chemical reactions model from a 20 keV monoenergetic electron beam with an input power of 1 mW/m² into atmosphere 1. No other ionization mechanisms have been considered (i.e., no photoionization or primary ionization from heavy ion precipitation). 69

3.11 8 of the resulting 27 steady state ion densities (plus electrons) calculated by the chemical reactions model from a 20 keV monoenergetic electron beam with an input power of 1 mW/m² into atmosphere 2. No other ionization mechanisms have been considered (i.e., no photoionization or primary ionization from heavy ion precipitation). 70

4.1 Oxygen charge state distribution as a function of ion energy. The high charge state peaks have dramatically shifted to lower energies than previous models produced. Houston et al. (2018) and Ozak et al. (2010) had the peak of O⁶⁺ at ~900 keV/u; however, due to the use of newly developed SIM cross-sections, the peak has now shifted down to an energy of ~350 keV/u. 78

4.2 Sulfur charge state distribution as a function of ion energy. The high charge state peaks have dramatically shifted to lower energies than previous models produced. Ozak et al. (2010) had the peaks of S⁶⁺ and S¹⁴⁺ at ~500 keV/u and ~2.2 MeV/u, respectively. Due to the use of newly developed SIM cross-sections, the peaks have now shifted down to energies of ~275 keV/u and ~900 keV/u, respectively. 78

4.3 Photoabsorption cross-sections of H, He, and C as a function of photon energy. From Cravens et al. (1995). 80

4.4	Illustration of an ion precipitating through the atmosphere. Included is secondary electron production, photoemission, and potential photoabsorption from atmospheric CH ₄ . In the top left of the figure is an inset of the trajectory of a charged particle in a magnetic field, describing the pitch angle of the particle and indicating a helical trajectory. This would be the motion seen if one was to zoom out from the collision processes.	81
4.5	Oxygen and sulfur flux measurements from JEDI on the Juno spacecraft during Perijove 7. The points marked with a diamond are the actual JEDI measurements. The lines represents the interpolation of the data that I applied to the measurements.	86
5.1	Oxygen ion production rate vs. density for initial oxygen ion energies of 0.05, 0.3, 2, and 5 MeV/u and an initial input of 1 ion/cm ² /s from charge exchange collisions.	89
5.2	Sulfur ion production rate vs. density for initial oxygen ion energies of 0.05, 0.3, 1, and 2 MeV/u and an initial input of 1 ion/cm ² /s from charge exchange collisions.	90
5.3	H ₂ ⁺ production rate profiles vs. H ₂ density for oxygen ions with initial energy of 0.05, 0.3, 2, and 5 MeV/u. This includes primary H ₂ ⁺ production from the Jovian precipitation code (dot-dashed lines) and secondary H ₂ ⁺ production from the two-stream code (dotted lines) with an initial input of 1 ion/cm ² /s.	92
5.4	H ₂ ⁺ production rate profiles vs. H ₂ density for sulfur ions with initial energy of 0.05, 0.3, 1, and 2 MeV/u. This includes primary H ₂ ⁺ production from the Jovian precipitation code (dot-dashed lines) and secondary H ₂ ⁺ production from the two-stream code (dotted lines) with an initial input of 1 ion/cm ² /s.	93
5.5	H ⁺ production rate profiles vs. H ₂ density for oxygen ions with initial energy of 0.05, 0.3, 2, and 5 MeV/u. This includes primary H ⁺ production from the Jovian precipitation code (dot-dashed lines) and secondary H ⁺ production from the two-stream code (dotted lines) with an initial input of 1 ion/cm ² /s.	94

5.6	H ⁺ production rate profiles vs. H ₂ density for sulfur ions with initial energy of 0.05, 0.3, 1, and 2 MeV/u. This includes primary H ⁺ production from the Jovian precipitation code (dot-dashed lines) and secondary H ⁺ production from the two-stream code (dotted lines) with an initial input of 1 ion/cm ² /s.	95
5.7	Forward secondary electron production rates for various altitudes from the ion precipitation and two-stream model for an incident ion energy of 0.05 MeV/u (energy flux of 0.8 MeV). These production rates are due to a single oxygen ion/cm ² /s input into the top of the atmosphere. Ionizing collisions are the dominant process that produces low energy electrons, while stripping collisions are what produce the tails (higher energy) of the electron distributions.	97
5.8	Forward secondary electron production rates for various altitudes from the ion precipitation and two-stream model for an incident ion energy of 0.3 MeV/u (energy flux of 4.8 MeV). These production rates are due to a single oxygen ion/cm ² /s input into the top of the atmosphere. Ionizing collisions are the dominant process that produces low energy electrons, while stripping collisions are what produce the tails (higher energy) of the electron distributions.	98
5.9	Forward secondary electron production rates for various altitudes from the ion precipitation and two-stream model for an incident ion energy of 2 MeV/u (energy flux of 32 MeV). These production rates are due to a single oxygen ion/cm ² /s input into the top of the atmosphere. Ionizing collisions are the dominant process that produces low energy electrons, while stripping collisions are what produce the tails (higher energy) of the electron distributions.	99

5.10 Forward secondary electron production rates for various altitudes from the ion precipitation and two-stream model for an incident ion energy of 5 MeV/u (energy flux of 80 MeV). These production rates are due to a single oxygen ion/cm²/s input into the top of the atmosphere. Ionizing collisions are the dominant process that produces low energy electrons, while stripping collisions are what produce the tails (higher energy) of the electron distributions. 100

5.11 Forward secondary electron production rates for various altitudes from the ion precipitation and two-stream model for an incident ion energy of 0.05 MeV/u (energy flux of 1.6 MeV). These production rates are due to a single sulfur ion/cm²/s input into the top of the atmosphere. Ionizing collisions are the dominant process that produces low energy electrons, while stripping collisions are what produce the tails (higher energy) of the electron distributions. 101

5.12 Forward secondary electron production rates for various altitudes from the ion precipitation and two-stream model for an incident ion energy of 0.3 MeV/u (energy flux of 9.6 MeV). These production rates are due to a single sulfur ion/cm²/s input into the top of the atmosphere. Ionizing collisions are the dominant process that produces low energy electrons, while stripping collisions are what produce the tails (higher energy) of the electron distributions. 102

5.13 Forward secondary electron production rates for various altitudes from the ion precipitation and two-stream model for an incident ion energy of 1 MeV/u (energy flux of 32 MeV). These production rates are due to a single sulfur ion/cm²/s input into the top of the atmosphere. Ionizing collisions are the dominant process that produces low energy electrons, while stripping collisions are what produce the tails (higher energy) of the electron distributions. 103

5.14 Forward secondary electron production rates for various altitudes from the ion precipitation and two-stream model for an incident ion energy of 2 MeV/u (energy flux of 64 MeV). These production rates are due to a single sulfur ion/cm²/s input into the top of the atmosphere. Ionizing collisions are the dominant process that produces low energy electrons, while stripping collisions are what produce the tails (higher energy) of the electron distributions. 104

5.15 Predicted electron escape flux vs. electron energy for precipitating oxygen ion energies of 0.05, 0.3, 2, and 5 MeV/u. A step plot has been used to show the size of the corresponding energy bins that are output by the ion precipitation model to be used by the two-stream code. This figure is with an incident input of 1 ions/cm²/s. 105

5.16 Predicted electron escape flux vs. electron energy for precipitating sulfur ion energies of 0.05, 0.3, 1, and 2 MeV/u. A step plot has been used to show the size of the corresponding energy bins that are output by the ion precipitation model to be used by the two-stream code. This figure is with an incident input of 1 ions/cm²/s. . 106

5.17 Upward electron flux for a single ion/cm²/s vs. altitude for electron energies of 10, 20, 50, 100, and 1000 eV and initial oxygen ion energies of 0.05, 0.3, 2, and 5 MeV/u. 107

5.18 Upward electron flux for a single ion/cm²/s vs. altitude for electron energies of 10, 20, 50, 100, and 1000 eV and initial sulfur ion energies of 0.05, 0.3, 1, and 2 MeV/u. 108

5.19 Airglow emission production from secondary electrons produced from a single incident oxygen ion/cm²/s. 117

5.20 Airglow emission production from secondary electrons produced from a single incident sulfur ion/cm²/s. 117

5.21 Predicted Lyman-Werner spectrum from an input of 1 oxygen ion/cm²/s at 0.05 MeV/u. The red line is calculated with a θ of 60° and the green line with a θ of 80° , while the black line is what is expected when no opacity effects are considered. The Ly- α line at 121.6 nm has been withheld from these predictions. 118

5.22 Predicted Lyman-Werner spectrum from an input of 1 oxygen ion/cm²/s at 0.3 MeV/u. The red line is calculated with a θ of 60° and the green line with a θ of 80° , while the black line is what is expected when no opacity effects are considered. The Ly- α line at 121.6 nm has been withheld from these predictions. 119

5.23 Predicted Lyman-Werner spectrum from an input of 1 oxygen ion/cm²/s at 2 MeV/u. The red line is calculated with a θ of 60° and the green line with a θ of 80° , while the black line is what is expected when no opacity effects are considered. The Ly- α line at 121.6 nm has been withheld from these predictions. 119

5.24 Predicted Lyman-Werner spectrum from an input of 1 oxygen ion/cm²/s at 5 MeV/u. The red line is calculated with a θ of 60° and the green line with a θ of 80° , while the black line is what is expected when no opacity effects are considered. The Ly- α line at 121.6 nm has been withheld from these predictions. 120

5.25 Predicted Lyman-Werner spectrum from an input of 1 sulfur ion/cm²/s at 0.05 MeV/u. The red line is calculated with a θ of 60° and the green line with a θ of 80° , while the black line is what is expected when no opacity effects are considered. The Ly- α line at 121.6 nm has been withheld from these predictions. 120

5.26 Predicted Lyman-Werner spectrum from an input of 1 sulfur ion/cm²/s at 0.3 MeV/u. The red line is calculated with a θ of 60° and the green line with a θ of 80° , while the black line is what is expected when no opacity effects are considered. The Ly- α line at 121.6 nm has been withheld from these predictions. 121

5.27 Predicted Lyman-Werner spectrum from an input of 1 sulfur ion/cm²/s at 1 MeV/u. The red line is calculated with a θ of 60° and the green line with a θ of 80° , while the black line is what is expected when no opacity effects are considered. The Ly- α line at 121.6 nm has been withheld from these predictions. 121

5.28	Predicted Lyman-Werner spectrum from an input of 1 sulfur ion/cm ² /s at 2 MeV/u. The red line is calculated with a θ of 60° and the green line with a θ of 80° , while the black line is what is expected when no opacity effects are considered. The Ly- α line at 121.6 nm has been withheld from these predictions.	122
5.29	Initial ion energy vs. color ratio for two viewing angles of 60° (solid lines) and 80° (dash-dotted lines) for both oxygen and sulfur precipitation into atmosphere 1 and atmosphere 2. Oxygen precipitation into atmosphere 1 is indicated by the black lines, oxygen into atmosphere 2 by the black lines, sulfur into atmosphere 1 by the red lines, and sulfur into atmosphere 2 by the pink lines.	124
6.1	The O ⁶⁺ and O ⁷⁺ production rates from TI, SC, and SC+SS vs. H ₂ density and altitude for various incident ion energies (E=0.2, 0.3, 0.5, 1.0, 2.0, 5.0, 10.0, and 25.0 MeV/u). The production rates have been normalized to a single incident ion/cm ² /s.	127
6.2	The S ⁷⁺ and S ⁸⁺ production rates from TI, SC, and SC+SS vs. H ₂ density and altitude for various incident ion energies (E=0.2, 0.3, 0.5, 1.0, and 2.0 MeV/u). The production rates have been normalized to a single incident ion/cm ² /s.	128
6.3	The entire outgoing X-ray flux efficiency for all X-ray producing oxygen charge states as a function of initial ion energy from a single incident ion/cm ² /s with an isotropic downward distribution of pitch angles. The condition of no opacity is shown by the solid line, an exit angle of 0° is represented by the dashed line, an exit angle of 80° by the dotted line, and an exit angle of 90° by the dash-dot line. Atmosphere 1 consideration is in black and atmosphere 2 is in gray. Every exit angle is with respect to the Jovian spin axis. The figure on the right is a magnified portion of the figure on the left (represented by the black rectangle), used to emphasize the efficiencies of ions in the energy range of JEDI measurements.	133

6.4 The entire outgoing X-ray flux efficiency for all X-ray producing sulfur charge states as a function of initial ion energy from a single incident ion/cm²/s with an isotropic downward distribution of pitch angles. The condition of no opacity is shown by the solid line, an exit angle of 0° is represented by the dashed line, an exit angle of 80° by the dotted line, and an exit angle of 90° by the dash-dot line. Atmosphere 1 consideration is in black and atmosphere 2 is in gray. Every exit angle is with respect to the Jovian spin axis. The figure on the right is a magnified portion of the figure on the left (represented by the black rectangle), used to emphasize the efficiencies of ions in the energy range of JEDI measurements. 135

6.5 Synthetic X-ray spectra showing the contribution from each charge state. This spectra includes emission from both charge exchange and direct excitation collisions considering no opacity effects from an incident ion beam of 500 keV/u with an input is 1 ion/cm²/s for both species. Not shown is the emission from S¹⁴⁺ which peaks at ~2450 eV with an intensity several orders of magnitude lower than the more prominent emission lines. 138

6.6 Synthetic X-ray spectra with opacity effects at three viewing angles through an atmosphere with a deep, originally considered homopause (atmosphere 1) and an atmosphere that is well-mixed through the top of the atmosphere (atmosphere 2), what I consider an upper-limit to opacity effects. Initial ion energies are 500 keV/u for both oxygen and sulfur precipitation and the input is 1 ion/cm²/s for both species. Photon energies below about 400 eV are shown to be much more affected by the opacity than higher photon energies. 139

7.1 Ion production rate from X-ray producing charge exchange collisions combined with X-ray producing direct excitation collisions of each ion charge state vs. H₂ density and altitude from Juno’s PJ 7 pass. Also included is the altitude integrated production rate of each charge state displayed. It is evident from the charge states obtained that X-rays will be produced. 141

7.2	Predicted X-ray spectra from JEDI's ion flux measurements during the PJ 7 polar cap pass in 2017. These spectra assume no opacity effects (black line), an opacity effect with an exit angle of 80° through atmosphere 1 (blue line), and the same exit angle through atmosphere 2 (red line). It appears emission from oxygen is the most prominent source of X-rays associated with this flux measurement, which may have been anticipated from the JEDI data taken at this time, but is likely not always the case.	143
7.3	H ⁺ and H ₂ ⁺ production rates vs. H ₂ density as a result of ion precipitation and the associated secondary electrons. The ion flux input into the model was from the PJ 7 polar cap pass in 2017, displayed in Figure 4.5.	145
7.4	Forward secondary electron production rates for various altitudes from the ion precipitation and two-stream model for an incident ion flux from Juno's PJ 7 pass. Ionizing collisions are the dominant process that produces low energy electrons, while stripping collisions are what produce the tails (higher energy) of the electron distributions.	146
7.5	Predicted electron escape flux vs. electron energy for precipitating ions measured by Juno during the PJ 7 polar cap pass. A step plot has been used to show the size of the corresponding energy bins that are output by the ion precipitation model to be used by the two-stream code.	147
7.6	Upward electron flux vs. altitude for electron energies of 10, 20, 50, 100, and 1000 eV and initial oxygen ion input flux from the PJ 7 polar cap pass measured by Juno in 2017.	148
7.7	Airglow emission production from secondary electrons produced from oxygen and sulfur ions measured by Juno during the PJ 7 polar cap pass in 2017.	150

7.8	Lyman-Werner spectra in both atmospheres from oxygen and sulfur ions measured by Juno during the PJ 7 polar cap pass in 2017. The red and pink lines are calculated with a θ of 60° (pink line is behind the green line) and the green and blue lines with a θ of 80° , while the black line is what is expected when no opacity effects are considered. The Ly- α line at 121.6 nm has been withheld from these predictions.	151
7.9	Ion production rate profiles vs. H ₂ density from oxygen and sulfur ions measured by Juno during the PJ 7 polar cap pass in 2017. This production is solely that from secondary electrons, primary ionization has been excluded and no photoionization is considered, i.e. a night side case.	153
7.10	8 of the resulting 27 steady state ion densities (plus electrons) calculated by the chemical reactions model from precipitating ions measured by Juno during the PJ 7 polar cap pass. Photoionization has not been considered, but primary ionization from precipitating oxygen and sulfur is included, along with ionization from secondary electrons.	154
7.11	Ionospheric profiles calculated by the chemical reactions model from precipitating ions measured by Juno during the PJ 7 polar cap pass. Photoionization has not been considered, but primary ionization from precipitating oxygen and sulfur is included, along with ionization from secondary electrons. I emphasize hydrocarbon production by focusing on the lower altitudes with H ⁺ and e ⁻ included for reference.	155
7.12	Ionospheric conductivities versus altitude associated with the ionospheric densities calculated by using a measured Juno ion flux from Perijove 7 as an input.	157
7.13	Ionospheric conductivities versus altitude associated with ionospheric densities calculated by inputting a 1 mW/m ² electron beam at a monoenergetic energy of 20 keV. This is an energy commonly seen by the JADE instrument on Juno (Ebert et al., 2019).	157

List of Tables

2.1	The energy loss model for each process considered as given in Schultz et al. (2019). For the SIM processes (e.g., DI+SS), the energy loss is the sum of the energy loss of the target and projectile process. $IP_{1,2}(H_2)$ is the first or second ionization potential of hydrogen and $IP_{1,2}(q)$ is the first or second ionization potential of O^{q+} or S^{q+}	40
3.1	Monoenergetic electron beam primary input current density, energy flux, electron flux, and secondary current density per 1 mW/m^2	58
3.2	Altitude integrated ion production rates for monoenergetic electron beams with an input power of 1 mW/m^2 . Production rates emanate from both primary electron precipitation and resulting secondary electrons.	62
4.1	Ionization potentials in eV of every oxygen and sulfur charge state used by the ion precipitation model.	75
5.1	Monoenergetic oxygen ion beam escape energy flux, electron flux, and secondary current density per $1 \text{ net ion/cm}^2/\text{s}$	110
5.2	Monoenergetic sulfur ion beam escape energy flux, electron flux, and secondary current density per $1 \text{ net ion/cm}^2/\text{s}$	111
5.3	Column-integrated ion-production rates for a primary input power of 1 mW/m^2 oxygen ions in units of $\text{cm}^{-2}\text{s}^{-1}$	113
5.4	Column-integrated ion-production rates for a primary input power of 1 mW/m^2 sulfur ions in units of $\text{cm}^{-2}\text{s}^{-1}$	114
5.5	Column-integrated ultraviolet airglow emission rates for a primary input power of 1 mW/m^2 oxygen ions in units of $\text{cm}^{-2}\text{s}^{-1}$	115

5.6	Column-integrated ultraviolet airglow emission rates for a primary input power of 1 mW/m ² sulfur ions in units of cm ⁻² s ⁻¹	116
6.1	Altitude integrated X-ray production [photons/cm ² /s] from both charge exchange and direct excitation collisions as a function of charge state and initial ion energy from an input of 1 ion/cm ² /s with an isotropic downward distribution of pitch angles. 130	
6.2	Altitude integrated X-ray production [photons/cm ² /s] from both charge exchange and direct excitation collisions as a function of charge state and initial ion energy from an input of 1 ion/cm ² /s with an isotropic downward distribution of pitch angles. 131	
6.3	The X-ray efficiency ([cm ² sec] ⁻¹ [keV/u] ⁻¹) of outgoing photons as a function of initial ion energy including opacity effects from a single incident ion/cm ² /s with an isotropic downward distribution of pitch angles. The viewing angles of 0° and 90° are displayed for both atmosphere 1 and 2. The efficiencies shown here includes X-ray production from both charge exchange and direct excitation collisions. . . .	134
7.1	Tabulated JEDI oxygen ion measurements discussed in Section 4.2.7 and shown in Figure 4.5.	160
A.1	The integral cross-section and associated average energy loss for single and double stripping for O ^{q+} + H ₂ (q=0,1,... 8) collisions with impact energies between 1 and 25000 keV/u. (From Schultz et al. (2019))	182
A.2	The integral cross section and associated average energy loss for single and double projectile excitation for O ^{q+} + H ₂ (q=0,1,... 8) collisions with impact energies between 1 and 25000 keV/u. (From Schultz et al. (2019))	183
A.3	The integral cross section and associated average energy loss for NSIM and SIM processes in O + H ₂ collisions with impact energies between 1 and 25000 keV/u. (From Schultz et al. (2019))	184

A.4	The integral cross section and associated average energy loss for NSIM and SIM processes in $O^+ + H_2$ collisions with impact energies between 1 and 25000 keV/u. (From Schultz et al. (2019))	185
A.5	The integral cross section and associated average energy loss for NSIM and SIM processes in $O^{2+} + H_2$ collisions with impact energies between 1 and 25000 keV/u. (From Schultz et al. (2019))	187
A.6	The integral cross section and associated average energy loss for NSIM and SIM processes in $O^{3+} + H_2$ collisions with impact energies between 1 and 25000 keV/u. (From Schultz et al. (2019))	189
A.7	The integral cross section and associated average energy loss for NSIM and SIM processes in $O^{4+} + H_2$ collisions with impact energies between 1 and 25000 keV/u. (From Schultz et al. (2019))	191
A.8	The integral cross section and associated average energy loss for NSIM and SIM processes in $O^{5+} + H_2$ collisions with impact energies between 1 and 25000 keV/u. (From Schultz et al. (2019))	193
A.9	The integral cross section and associated average energy loss for NSIM and SIM processes in $O^{6+} + H_2$ collisions with impact energies between 1 and 25000 keV/u. (From Schultz et al. (2019))	195
A.10	The integral cross section and associated average energy loss for NSIM and SIM processes in $O^{7+} + H_2$ collisions with impact energies between 1 and 25000 keV/u. (From Schultz et al. (2019))	197
A.11	The integral cross section and associated average energy loss for NSIM and SIM processes in $O^{8+} + H_2$ collisions with impact energies between 1 and 25000 keV/u. (From Schultz et al. (2019))	199
B.1	The integral cross section and associated average energy loss for SIM and NSIM processes in $S + H_2$ collisions with impact energies between 1 and 2000 keV/u. (From Gharibnejad et al. (2019))	201

B.2	The integral cross section and associated average energy loss for SIM and NSIM processes in $S^+ + H_2$ collisions with impact energies between 1 and 2000 keV/u. (From Gharibnejad et al. (2019))	202
B.3	The integral cross section and associated average energy loss for SIM and NSIM processes in $S^{2+} + H_2$ collisions with impact energies between 1 and 2000 keV/u. (From Gharibnejad et al. (2019))	203
B.4	The integral cross section and associated average energy loss for SIM and NSIM processes in $S^{3+} + H_2$ collisions with impact energies between 1 and 2000 keV/u. (From Gharibnejad et al. (2019))	205
B.5	The integral cross section and associated average energy loss for SIM and NSIM processes in $S^{4+} + H_2$ collisions with impact energies between 1 and 2000 keV/u. (From Gharibnejad et al. (2019))	207
B.6	The integral cross section and associated average energy loss for SIM and NSIM processes in $S^{5+} + H_2$ collisions with impact energies between 1 and 2000 keV/u. (From Gharibnejad et al. (2019))	209
B.7	The integral cross section and associated average energy loss for SIM and NSIM processes in $S^{6+} + H_2$ collisions with impact energies between 1 and 2000 keV/u. (From Gharibnejad et al. (2019))	211
B.8	The integral cross section and associated average energy loss for SIM and NSIM processes in $S^{7+} + H_2$ collisions with impact energies between 1 and 2000 keV/u. (From Gharibnejad et al. (2019))	213
B.9	The integral cross section and associated average energy loss for SIM and NSIM processes in $S^{8+} + H_2$ collisions with impact energies between 1 and 2000 keV/u. (From Gharibnejad et al. (2019))	215
B.10	The integral cross section and associated average energy loss for SIM and NSIM processes in $S^{9+} + H_2$ collisions with impact energies between 1 and 2000 keV/u. (From Gharibnejad et al. (2019))	217

B.11	The integral cross section and associated average energy loss for SIM and NSIM processes in $S^{10+} + H_2$ collisions with impact energies between 1 and 2000 keV/u. (From Gharibnejad et al. (2019))	219
B.12	The integral cross section and associated average energy loss for SIM and NSIM processes in $S^{11+} + H_2$ collisions with impact energies between 1 and 2000 keV/u. (From Gharibnejad et al. (2019))	221
B.13	The integral cross section and associated average energy loss for SIM and NSIM processes in $S^{12+} + H_2$ collisions with impact energies between 1 and 2000 keV/u. (From Gharibnejad et al. (2019))	223
B.14	The integral cross section and associated average energy loss for SIM and NSIM processes in $S^{13+} + H_2$ collisions with impact energies between 1 and 2000 keV/u. (From Gharibnejad et al. (2019))	225
B.15	The integral cross section and associated average energy loss for SIM and NSIM processes in $S^{14+} + H_2$ collisions with impact energies between 1 and 2000 keV/u. (From Gharibnejad et al. (2019))	227
B.16	The integral cross section and associated average energy loss for SIM and NSIM processes in $S^{15+} + H_2$ collisions with impact energies between 1 and 2000 keV/u. (From Gharibnejad et al. (2019))	229
B.17	The integral cross section and associated average energy loss for SIM and NSIM processes in $S^{16+} + H_2$ collisions with impact energies between 1 and 2000 keV/u. (From Gharibnejad et al. (2019))	231
C.1	Electron Dissociative Recombination (continued)	233
C.2	Ion-Molecule Reactions (continued)	235
C.2	Ion-Molecule Reactions (continued)	236
C.2	Ion-Molecule Reactions (continued)	237
C.2	Ion-Molecule Reactions (continued)	238
C.2	Ion-Molecule Reactions (continued)	239

C.2	Ion-Molecule Reactions (continued)	240
D.1	Altitude integrated ion production [$\text{cm}^{-2} \text{s}^{-1}$] from charge exchange collisions (i.e. TI, SC, SC+SS) for oxygen with incident ion energies between 10 and 25000 keV/u with no opacity effects considered. Everything has been normalized to a single incident ion/cm ² /s.	242
D.2	Altitude integrated ion production [$\text{cm}^{-2} \text{s}^{-1}$] from direct excitation collisions (i.e. SI+SPEX, DI+SPEX, TEX+SPEX) for oxygen with incident ion energies between 10 and 25000 keV/u with no opacity effects considered. Everything has been normalized to a single incident ion/cm ² /s.	243
D.3	The X-ray efficiency ($[\text{cm}^2\text{sec}]^{-1}[\text{keV/u}]^{-1}$) of outgoing photons as a function of initial ion energy including opacity effects from a single incident ion/cm ² /s with an isotropic downward distribution of pitch angles. No opacity effects and the viewing angles of 0°, 80°, and 90° are displayed for atmosphere 1. The efficiency shown here is that solely from charge exchange collisions for oxygen. I also include the X-ray efficiencies that correspond to the JEDI energy bins at the time of writing.	244
D.4	The X-ray efficiency ($[\text{cm}^2\text{sec}]^{-1}[\text{keV/u}]^{-1}$) of outgoing photons as a function of initial ion energy including opacity effects from a single incident ion/cm ² /s with an isotropic downward distribution of pitch angles. No opacity effects and the viewing angles of 0°, 80°, and 90° are displayed for atmosphere 2. The efficiency shown here is that solely from charge exchange collisions for oxygen. I also include the X-ray efficiencies that correspond to the JEDI energy bins at the time of writing.	245
D.5	The X-ray efficiency ($[\text{cm}^2\text{sec}]^{-1}[\text{keV/u}]^{-1}$) of outgoing photons as a function of initial ion energy including opacity effects from a single incident ion/cm ² /s with an isotropic downward distribution of pitch angles. No opacity effects and the viewing angles of 0°, 80°, and 90° are displayed for atmosphere 1. The efficiency shown here is that solely from direct excitation collisions for oxygen. I also include the X-ray efficiencies that correspond to the JEDI energy bins at the time of writing.	246

D.6 The X-ray efficiency ($[\text{cm}^2\text{sec}]^{-1}[\text{keV/u}]^{-1}$) of outgoing photons as a function of initial ion energy including opacity effects from a single incident ion/cm²/s with an isotropic downward distribution of pitch angles. No opacity effects and the viewing angles of 0°, 80°, and 90° are displayed for atmosphere 2. The efficiency shown here is that solely from direct excitation collisions for oxygen. I also include the X-ray efficiencies that correspond to the JEDI energy bins at the time of writing. 247

E.1 Altitude integrated ion production [$\text{cm}^{-2} \text{s}^{-1}$] from charge exchange collisions (i.e. TI, SC, SC+SS) for sulfur with incident ion energies between 10 and 2000 keV/u with no opacity effects considered. Everything has been normalized to a single incident ion/cm²/s. 249

E.2 Altitude integrated ion production [$\text{cm}^{-2} \text{s}^{-1}$] from direct excitation collisions (i.e. SI+SPEX, DI+SPEX, TEX+SPEX) for sulfur with incident ion energies between 10 and 2000 keV/u with no opacity effects considered. Everything has been normalized to a single incident ion/cm²/s. 250

E.3 The X-ray efficiency ($[\text{cm}^2\text{sec}]^{-1}[\text{keV/u}]^{-1}$) of outgoing photons as a function of initial ion energy excluding opacity effects from a single incident ion/cm²/s with an isotropic downward distribution of pitch angles. No opacity effects is displayed for atmosphere 1. The efficiency shown here is that solely from charge exchange collisions for sulfur. 251

E.4 The X-ray efficiency ($[\text{cm}^2\text{sec}]^{-1}[\text{keV/u}]^{-1}$) of outgoing photons as a function of initial ion energy including opacity effects from a single incident ion/cm²/s with an isotropic downward distribution of pitch angles. The viewing angle of 0° is displayed for atmosphere 1. The efficiency shown here is that solely from charge exchange collisions for sulfur. 252

E.5 The X-ray efficiency ($[\text{cm}^2\text{sec}]^{-1}[\text{keV/u}]^{-1}$) of outgoing photons as a function of initial ion energy including opacity effects from a single incident ion/cm²/s with an isotropic downward distribution of pitch angles. The viewing angle of 80° is displayed for atmosphere 1. The efficiency shown here is that solely from charge exchange collisions for sulfur. 253

E.6 The X-ray efficiency ($[\text{cm}^2\text{sec}]^{-1}[\text{keV/u}]^{-1}$) of outgoing photons as a function of initial ion energy including opacity effects from a single incident ion/cm²/s with an isotropic downward distribution of pitch angles. The viewing angle of 90° is displayed for atmosphere 1. The efficiency shown here is that solely from charge exchange collisions for sulfur. 254

E.7 The X-ray efficiency ($[\text{cm}^2\text{sec}]^{-1}[\text{keV/u}]^{-1}$) of outgoing photons as a function of initial ion energy excluding opacity effects from a single incident ion/cm²/s with an isotropic downward distribution of pitch angles. No opacity effects is displayed for atmosphere 2. The efficiency shown here is that solely from charge exchange collisions for sulfur. 255

E.8 The X-ray efficiency ($[\text{cm}^2\text{sec}]^{-1}[\text{keV/u}]^{-1}$) of outgoing photons as a function of initial ion energy including opacity effects from a single incident ion/cm²/s with an isotropic downward distribution of pitch angles. The viewing angle of 0° is displayed for atmosphere 2. The efficiency shown here is that solely from charge exchange collisions for sulfur. 256

E.9 The X-ray efficiency ($[\text{cm}^2\text{sec}]^{-1}[\text{keV/u}]^{-1}$) of outgoing photons as a function of initial ion energy including opacity effects from a single incident ion/cm²/s with an isotropic downward distribution of pitch angles. The viewing angle of 80° is displayed for atmosphere 2. The efficiency shown here is that solely from charge exchange collisions for sulfur. 257

E.10 The X-ray efficiency ($[\text{cm}^2\text{sec}]^{-1}[\text{keV/u}]^{-1}$) of outgoing photons as a function of initial ion energy including opacity effects from a single incident ion/cm²/s with an isotropic downward distribution of pitch angles. The viewing angle of 90° is displayed for atmosphere 2. The efficiency shown here is that solely from charge exchange collisions for sulfur. 258

E.11 The X-ray efficiency ($[\text{cm}^2\text{sec}]^{-1}[\text{keV/u}]^{-1}$) of outgoing photons as a function of initial ion energy excluding opacity effects from a single incident ion/cm²/s with an isotropic downward distribution of pitch angles. No opacity effects is displayed for atmosphere 1. The efficiency shown here is that solely from direct excitation collisions for sulfur. 259

E.12 The X-ray efficiency ($[\text{cm}^2\text{sec}]^{-1}[\text{keV/u}]^{-1}$) of outgoing photons as a function of initial ion energy including opacity effects from a single incident ion/cm²/s with an isotropic downward distribution of pitch angles. The viewing angle of 0° is displayed for atmosphere 1. The efficiency shown here is that solely from direct excitation collisions for sulfur. 260

E.13 The X-ray efficiency ($[\text{cm}^2\text{sec}]^{-1}[\text{keV/u}]^{-1}$) of outgoing photons as a function of initial ion energy including opacity effects from a single incident ion/cm²/s with an isotropic downward distribution of pitch angles. The viewing angle of 80° is displayed for atmosphere 1. The efficiency shown here is that solely from direct excitation collisions for sulfur. 261

E.14 The X-ray efficiency ($[\text{cm}^2\text{sec}]^{-1}[\text{keV/u}]^{-1}$) of outgoing photons as a function of initial ion energy including opacity effects from a single incident ion/cm²/s with an isotropic downward distribution of pitch angles. The viewing angle of 90° is displayed for atmosphere 1. The efficiency shown here is that solely from direct excitation collisions for sulfur. 262

E.15 The X-ray efficiency ($[\text{cm}^2\text{sec}]^{-1}[\text{keV/u}]^{-1}$) of outgoing photons as a function of initial ion energy excluding opacity effects from a single incident ion/cm²/s with an isotropic downward distribution of pitch angles. No opacity effects is displayed for atmosphere 2. The efficiency shown here is that solely from direct excitation collisions for sulfur. 263

E.16 The X-ray efficiency ($[\text{cm}^2\text{sec}]^{-1}[\text{keV/u}]^{-1}$) of outgoing photons as a function of initial ion energy including opacity effects from a single incident ion/cm²/s with an isotropic downward distribution of pitch angles. The viewing angle of 0° is displayed for atmosphere 2. The efficiency shown here is that solely from direct excitation collisions for sulfur. 264

E.17 The X-ray efficiency ($[\text{cm}^2\text{sec}]^{-1}[\text{keV/u}]^{-1}$) of outgoing photons as a function of initial ion energy including opacity effects from a single incident ion/cm²/s with an isotropic downward distribution of pitch angles. The viewing angle of 80° is displayed for atmosphere 2. The efficiency shown here is that solely from direct excitation collisions for sulfur. 265

E.18 The X-ray efficiency ($[\text{cm}^2\text{sec}]^{-1}[\text{keV/u}]^{-1}$) of outgoing photons as a function of initial ion energy including opacity effects from a single incident ion/cm²/s with an isotropic downward distribution of pitch angles. The viewing angle of 90° is displayed for atmosphere 2. The efficiency shown here is that solely from direct excitation collisions for sulfur. 266

Chapter 1

Introduction

In the work presented here I am interested in the auroral processes at Jupiter, including magnetosphere-ionosphere coupling, photoemission, and ionization of the atmosphere. In particular, I aim to present a heavy ion precipitation model that is able to input *in situ* Juno measurements and predict the associated X-ray production, which has hitherto been inconclusive, and predict associated field-aligned current systems, ionization of the atmosphere, and color ratios in UV emission. The goals of this work can be summarized as follows:

- Model energetic sulfur, oxygen, and electron precipitation into the Jovian atmosphere using a Monte Carlo simulation.
- Generate charge state fraction equilibria as a function of atmospheric H₂ density for sulfur and oxygen ions.
- Simulate Juno ion and electron measurements above the polar cap and auroral oval.
- Predict X-ray and ultraviolet spectra given input ion and electron fluxes, including atmospheric absorption effects.
- Explain Earth-orbit-based observations of intense X-ray emission emitting from the Jovian polar caps using the results of the heavy ion precipitation model.
- Calculate ionization production from ion and electron precipitation in the atmosphere of Jupiter.

- Investigate the affects of secondary electron production in the atmosphere and their escape-ment.
- Calculate field-aligned currents and airglow emission associated with secondary electron production and input ion fluxes.

The complex nature of this subject requires an introductory chapter with several sections dedi-cated to building up the necessary physics background. Thus, in Chapter 1, I begin with planetary dynamos and their importance to large scale magnetic fields. This is followed by a number of sections concerning magnetospheres, ionospheres, aurorae at Earth and Jupiter, magnetosphere-ionosphere coupling and the physics involved, and finally I introduce the Juno spacecraft. Subse-quently, in Chapter 2 I delve into the physical processes associated with aurorae; then my electron and ion precipitation models are introduced in Chapters 3 and 4, respectively. I discuss the results associated with field-aligned currents and ultraviolet emission in Chapter 5, and Chapter 6 consists of X-ray results. Finally, I put the results into the context of Juno measurements in Chapter 7, summarizing and concluding with a final discussion in Chapter 8.

1.1 Dynamos

Dynamo theory is proposed to be the driving mechanism in celestial bodies that produce and main-tain internal magnetic fields for astronomically long time scales. Although there are several known types of dynamos, they all share the same underlying principle: fluid motion converts kinetic en-ergy into magnetic energy. For this conversion, and the production of the dynamo, to take place there are three necessities: 1) there must be an electrically conducting fluid (metallic hydrogen in Jovian-like planets), 2) the fluid must be in motion (generally convection), and 3) $R_m \gg 1$, where R_m is the magnetic Reynolds number, since too much Ohmic diffusion will destroy a dynamo. Dy-namos create a highly ordered spherically harmonic magnetic field that approaches the $l=1, m=0$ harmonic (dipole) as $r \rightarrow \infty$. This is the case at Jupiter (although it has a higher-order multipole at the surface than expected) and Saturn, which is remarkably axisymmetric, shown in Figure 1.1.

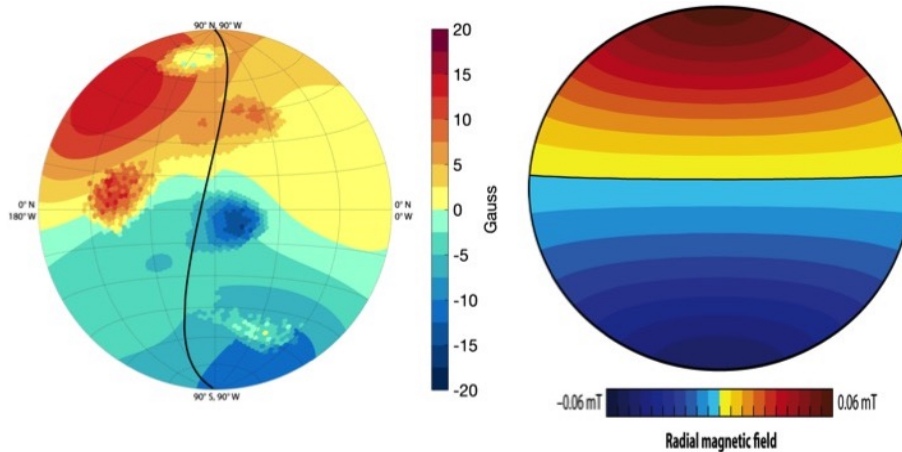


Figure 1.1: Model of Jupiter’s (left) and Saturn’s (right) magnetic field at the surface of each planet. For Jupiter’s magnetic field a VIP4 model was used along with data taken from Juno’s Perijove 1 pass (shown as a black line) from Moore et al. (2017). Saturn’s magnetic field was modeled using the Hammer-Aitoff projection from Jones (2011)

Dynamos are the source of magnetospheres for every planet in our solar system that has an internal magnetic field (Mercury, Earth, Jupiter, Saturn, Uranus, and Neptune).

1.2 Magnetospheres

The magnetosphere is defined by the region of space where the magnetic field of the object is the dominant magnetic field, in contrast to that of the interplanetary magnetic field (IMF) produced by the sun. Figure 1.2 illustrates the magnetosphere and some of the key features that define the magnetosphere, including the solar wind, or the charged particles flowing from the sun. Also shown is the bow shock, which is a shock wave formed at the boundary between the solar wind and the magnetosphere; the magnetopause, described as the boundary between the plasma within the magnetosphere and the interplanetary plasma; the magnetosheath, defined as the space between the bow shock and the magnetopause; and the magnetotail, which is the portion of the magnetosphere that is opposite the compressed magnetic field on the solar side and extends beyond the planet. The magnetosphere itself is defined where the motion of charged particles is controlled by the magnetic field of the planet. As shown in Figure 1.2, the magnetosphere deflects external charged particles (i.e., the solar wind) around itself as charged particles find it particularly difficult to move

perpendicular to and across magnetic field lines. This deflection of the solar wind forms a cavity of low density plasma inside the magnetosphere.

At Earth the magnetospheric shield brings protection from highly energetic particles that are troublesome for electronics onboard satellites and it also prevents the solar wind from stripping away Earth's atmosphere (as seen on Mars, which no longer has a dynamo and consequently no global magnetic field).

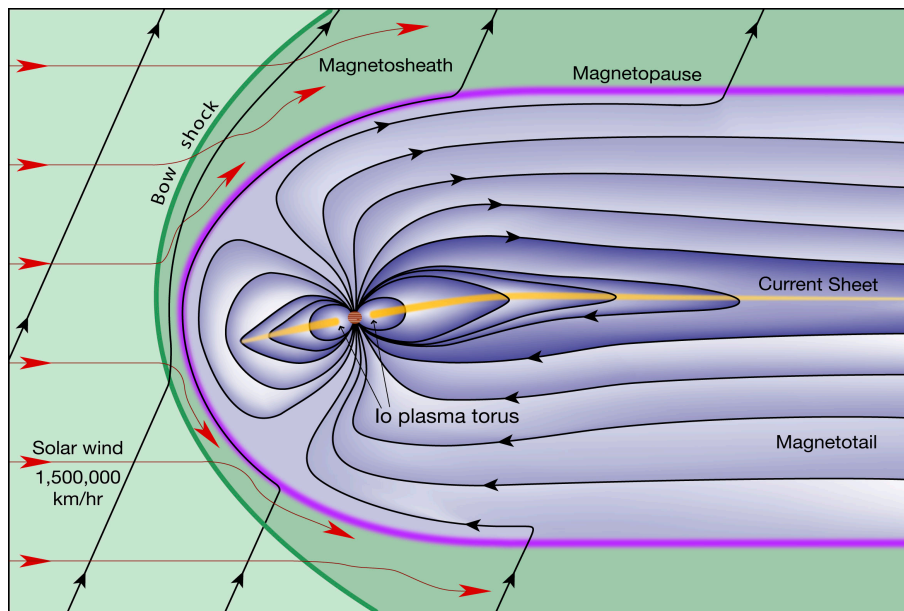


Figure 1.2: A schematic of Jupiter's magnetosphere and its interaction with the solar wind and the IMF. (Credit: Fran Bagenal and Steve Bartlett)

The most interesting magnetospheres are those with a source of plasma. At Earth, the solar wind is an external source of plasma that populates the magnetosphere with charged particles creating the Van Allen Belts and the aurora borealis. Jupiter has an internal plasma source of sulfur and oxygen ions from the sulfur dioxide volcanoes on its satellite, Io, creating a plasma torus following Io's orbit at about $6 R_J$ ($R_J = 1$ Jovian radii = 71,492 km). These heavy ions will follow magnetic field-aligned currents, precipitate into the upper atmosphere, and are thought to be responsible for X-ray emission from the polar caps of Jupiter. Saturn has a source of plasma that is a median between Earth and Jupiter. The solar wind provides a source of particles but Saturn's moon Enceladus has geysers that blast a water vapor plume into the magnetosphere, becoming a

contributor to the plasma with water group ions. Magnetosphere extend toward the planet, where they touch the ionosphere.

1.3 Ionospheres

The ionosphere is the uppermost portion of a planet's atmosphere; it is a spherical shell that is composed of electrons, electrically charged atoms and molecules, and neutral particles. The creation of the ionosphere is due to neutral atoms and molecules in a planet's upper atmosphere that are ionized by solar and cosmic radiation and by highly energetic particle precipitation that result in ionizing collisions. At Earth, the ionosphere is largely composed of electrons, O^+ , H^+ , He^+ , N^+ , NO^+ , N_2^+ , and O_2^+ because these particles make up the major neutral constituents in our atmosphere. H_2 and H have the largest population in Jupiter's upper atmosphere, with He becoming more prevalent than H beneath the homopause. Thus, the Jovian ionosphere is largely composed of various ionized hydrogen isotopes.

Ionosphere population densities vary depending on the temperature of the planet, neutral composition, and whether it is the day-side or night-side case. Density variations have been seen with respect to local time and latitude, corresponding with ultraviolet radiation input. The ions produced in the ionosphere may undergo electron recombination processes or ion-neutral chemical reactions. At Jupiter, H_2^+ , H_3^+ , and H^+ are the most dense constituents in the ionosphere. H^+ is an important proxy for the electron density in the upper ionosphere, while H_3^+ and H^+ are useful in the mid ionosphere, and the ionized hydrocarbon density in the lower atmosphere. H_3^+ can be measured using infrared emission signatures and is helpful in determining atmospheric temperatures.

Ionospheres have dynamic current systems that play an important role in how surrounding plasmas (i.e., the magnetosphere) interact with the atmosphere, and how atmospheric ion and electron loss can occur. At high latitudes, where the intrinsic planetary magnetic field maps further out into the magnetosphere, energetic charged particles may follow magnetic field lines and be lost into deep space, particularly if the field lines are open. There are also current systems that extend through the ionosphere down into the thermosphere, as is the case with Jupiter. Because the iono-

sphere lags behind the corotation of the planet, there are collisions between ions and neutrals in the upper atmosphere. These ion-neutral collisions are partially responsible for the phenomenon of magnetospheric plasma corotation with planetary rotation. Field-aligned ("Birkeland") currents are created to maintain the transmission of the torque (produced by collisional friction) through the ionosphere into the magnetosphere. These currents couple the ionosphere to the magnetosphere by supplying angular momentum from the ionosphere (high density plasma) to the magnetospheric (lower density) plasma. This has been a major topic of research when trying to understand the interaction between a planets magnetosphere and ionosphere, known as magnetosphere-ionosphere (MI) coupling.

1.4 Auroras

Speaking generally, the auroral process consists of an electric generator, a current system, and a resultant light source, supplied by the generator. The generator of an aurora is anything that supplies the magnetosphere with ionized particles that ultimately bombard the atmosphere, this is often times the solar wind or a satellite (Figure 1.3a). When the magnetosphere is supplied with energetic charged particles, the particles precipitate along the magnetic field lines, creating current systems (Figure 1.3b). Precipitating particles follow the magnetic field line until they are either reflected by the increasing magnetic field strength (known as "magnetic mirroring") or interact with the atmosphere, which produces the aurora. If the atmosphere is dense enough to be collisional, then the interactions between the electrons, protons, or charged particles with the neutral atmosphere result in ionization, heating, and electromagnetic emission (Figure 1.3c).

Aurorae are comprised of two main components, diffuse and discrete aurora. If diffuse, the aurora is generated by charged particles that are trapped within the magnetosphere (see drift particles in Figure 1.3b) creating an aurora that is equatorward of the auroral oval. Trapped particle precipitation occurs when the drifting particles are scattered into their loss cones, ultimately finding the upper atmosphere. This creates low intensity emission which makes it difficult to observe any discrete, internal structure in the aurora.

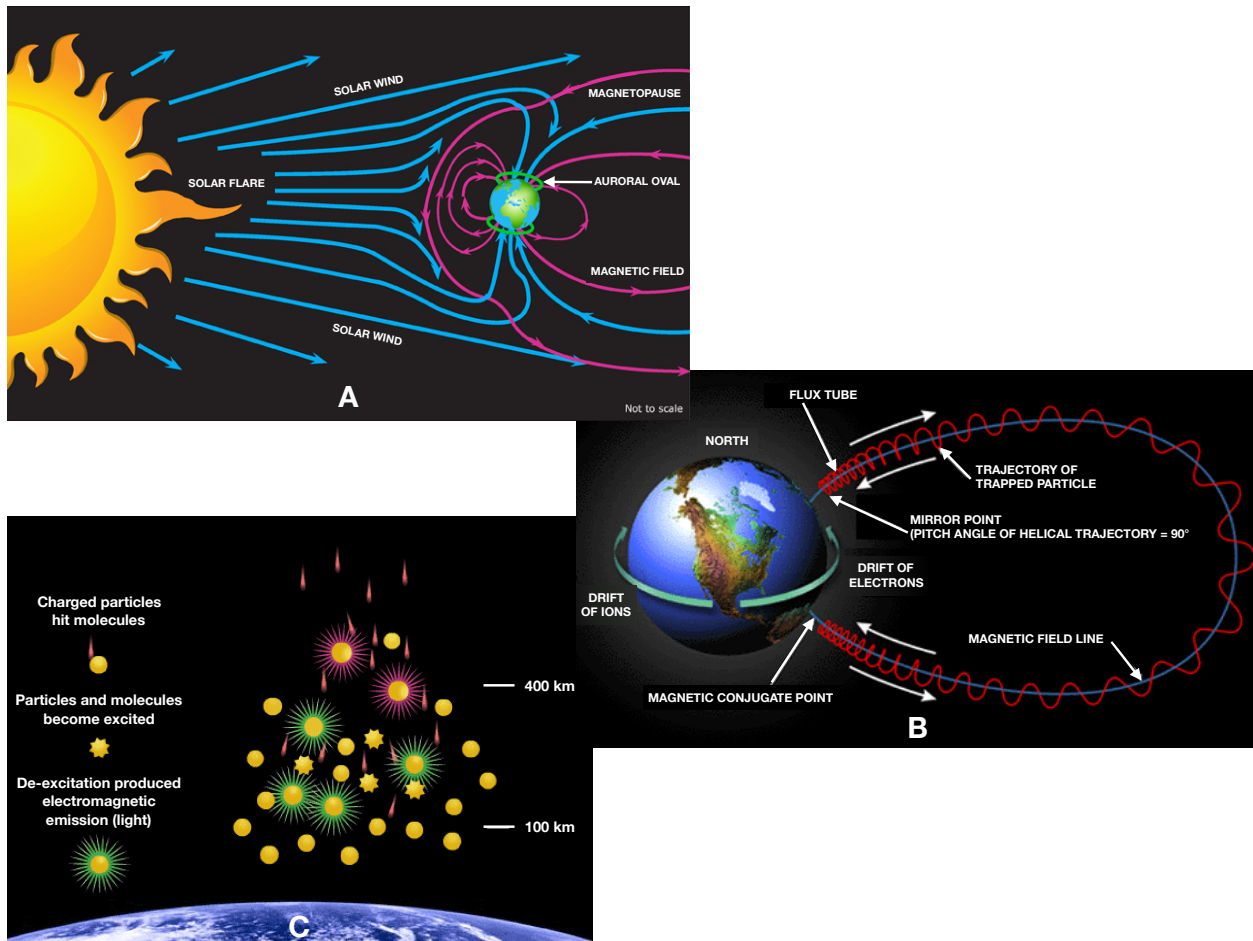


Figure 1.3: A.) The solar wind is the primary source of ions that generate Earth’s aurora. Although Earth’s magnetosphere deflects much of the solar wind, some particles are able to penetrate it and contribute to the aurora. B.) Charged particles follow a helical trajectory, bouncing between mirror points. The mirror points are determined by the particles pitch angle, or the angle of the particles velocity vector with respect to the magnetic field. C.) The process that causes ionization, heating, and emission due to collisions between incoming particles and the stationary atmosphere.

The other component of aurorae is the discrete portion. Discrete aurorae are much more intense as they are created from particle acceleration along field-aligned currents resulting in highly energized interactions between precipitating particles and the neutral atmosphere. These aurorae occur at higher latitudes, around the magnetic poles, and have much more structure and coherency. Due to the high energy nature of discrete aurorae, it is not uncommon to see extreme ultraviolet (EUV) and X-ray emission, particularly at planets with very strong magnetic fields, such as Jupiter.

High latitude aurorae map out to magnetic field lines that either extend into the tail of the magnetosphere (magnetotail) if it is on the night side or into the IMF-magnetosphere boundary

(magnetopause, see Figure 1.3a) on the day side. At the magnetopause the magnetic field lines from the planet and the IMF can connect and disconnect, creating open field lines that extend from the planet out into the heliosphere, outside of the magnetosphere. This creates an opening for solar wind particles to enter into the system while also allowing a route of escapement for particles to leave the magnetosphere and be picked up by the solar wind.

1.4.1 Earth

Earth has a generic aurora that encapsulates various auroral features. Firstly, at Earth there are two primary generators that drive the aurora, the plasma sheet and the solar wind. The plasma sheet, is just that, a sheet of plasma that divides the magnetosphere along the magnetic equator into two lobes. This plasma contains trapped electrons and protons that are drifting around the planet (due to magnetospheric corotation), populated by both the solar wind and auroral backscattered particles from the polar caps. When these particles are scattered into their loss cones from the inner portion of the plasma sheet, they follow along the magnetic field lines until they find the upper atmosphere, producing Earth's diffuse aurora. The solar wind is able to enter the magnetosphere at the magnetopause boundary due to reconnection occurring between the IMF and the magnetosphere, topologically connecting the sun's magnetic field to Earth's. This creates a path for the solar wind to travel to the magnetotail and into the outer plasma sheet, where the plasma flows sunward (so on the night side, toward the planet). The plasma in the middle and outer plasma sheet can undergo field-aligned acceleration, where particles form "inverted-V"¹ precipitation. This precipitation is much more energetic than that from the inner plasma sheet and creates the discrete nighttime aurora.

¹"Inverted-V" refers to the shape of the particle energy distribution seen in an energy spectrogram and is a strong indicator of field-aligned acceleration. Examples of this will be given in more detail later.

1.4.2 Jupiter

Past ultraviolet (UV) observations of Jupiter's aurora (e.g. Clarke et al. (1998); Grodent et al. (2003b,a)) revealed that the Jovian aurora consists of three separate regions that vary in space and time independently, suggesting different driving processes in each region. The three regions are: (1) the footprint emissions from Jupiter's satellites, primarily Io, Europa, and Ganymede (Bonfond, 2010; Bonfond et al., 2013; Grodent et al., 2009), (2) the emissions from the main oval (or main emission), and (3) the more poleward emissions, referred to as the polar emission. These three regions can be seen in Figure 1.4. Unlike the main oval, the polar auroral morphology is highly spatially and temporally variable (Dunn et al., 2017; Gladstone et al., 2002; Jackman et al., 2018). Note that the current systems associated with MI coupling linked to polar emissions are still not well understood.

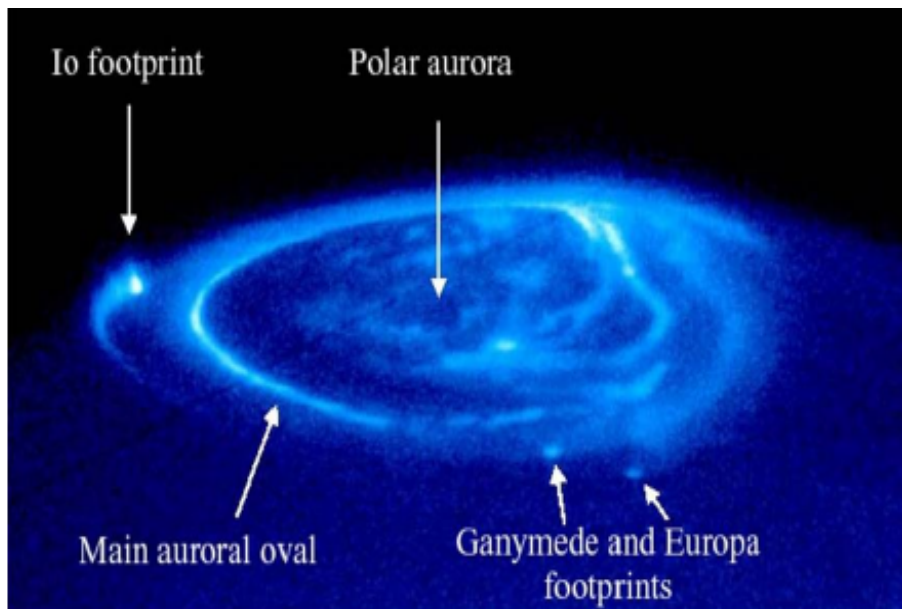


Figure 1.4: Jupiter's northern aurora viewed in the UV wavelength by HST. Visible are satellite footprints, the main auroral oval, and the polar aurora, where heavy ion precipitation occurs.

Like Earth, Jupiter has a plasma sheet that is responsible for auroral emission. Unlike Earth, Jupiter's aurora is almost entirely self-contained, meaning there is little particle input from the sun. Where Earth has the solar wind as a prominent generator of magnetospheric plasma, Jupiter has the Galilean moons (Io, Europa, Ganymede, and Callisto) that populate the magnetosphere with

plasma, including heavy ions (i.e. sulfur and oxygen).

Ultraviolet observations suggest a total input power flux of $10^{13} - 10^{14}$ W for the main auroral oval emission from each hemisphere. In addition to UV emission, X-ray emissions have also been observed in the polar cap by XMM-Newton, the Röntgen satellite (ROSAT), and Chandra X-ray Observatory (CXO) with a total X-ray power of about 1 GW and an output flux of about 2-6 R (Rayleigh (R) = 10^6 photons/cm²/s), demonstrated in Figure 1.5 (e.g. Branduardi-Raymont et al. (2007); Elsner et al. (2005); Gladstone et al. (2002); Waite et al. (1994)). Observations by CXO overlaid on HST-FUV (Hubble Space Telescope-Far Ultraviolet) observations (Branduardi-Raymont et al., 2008) showed a soft X-ray ($E < 2$ keV) component due to line emission, which appears to be collocated in the active region of the polar cap. The X-ray aurora morphology is also highly variable; for example, ~ 45 -minute pulsation period in the X-ray emissions was detected by CXO (Gladstone et al., 2002), but was absent in other observations. The observed X-ray spectra in the polar cap show line emission due to heavy ion excitation followed by K-shell X-ray emission. The excitation is due to charge exchange and excitation of precipitating oxygen and sulfur ions resulting from collisions with atmospheric molecular hydrogen (cf. Cravens et al. (1995); Ozak et al. (2010); Houston et al. (2018)) indicating an internal source of plasma. Figure 1.6 shows an X-ray spectrum emitted from the northern Jovian polar cap from Dunn et al. (2016) where the lower photon energies are associated with sulfur line emission and the higher energies with oxygen line emission.

X-ray production associated with heavy ion precipitation has been modeled over many years (Cravens et al., 1995; Horanyi et al., 1988; Hui et al., 2010; Ozak et al., 2010, 2013; Houston et al., 2018) with the goal of reproducing the X-ray data. Cravens et al. (1995) suggested that charge transfer and electron removal collisions could explain the X-ray aurora using an ~ 1 MeV per nucleon (1 MeV/u) incident oxygen ion energy. O^{7+} and O^{8+} charge exchange collisions with atmospheric H_2 produce excited O^{6+} and O^{7+} ions that emit X-rays. The high charge state ions are created via electron removal collisions of low charge state (e.g., O^+) ions with H_2 . More recent models require that the incident sulfur and oxygen ions be very energetic (1 - 2 MeV/u) to produce

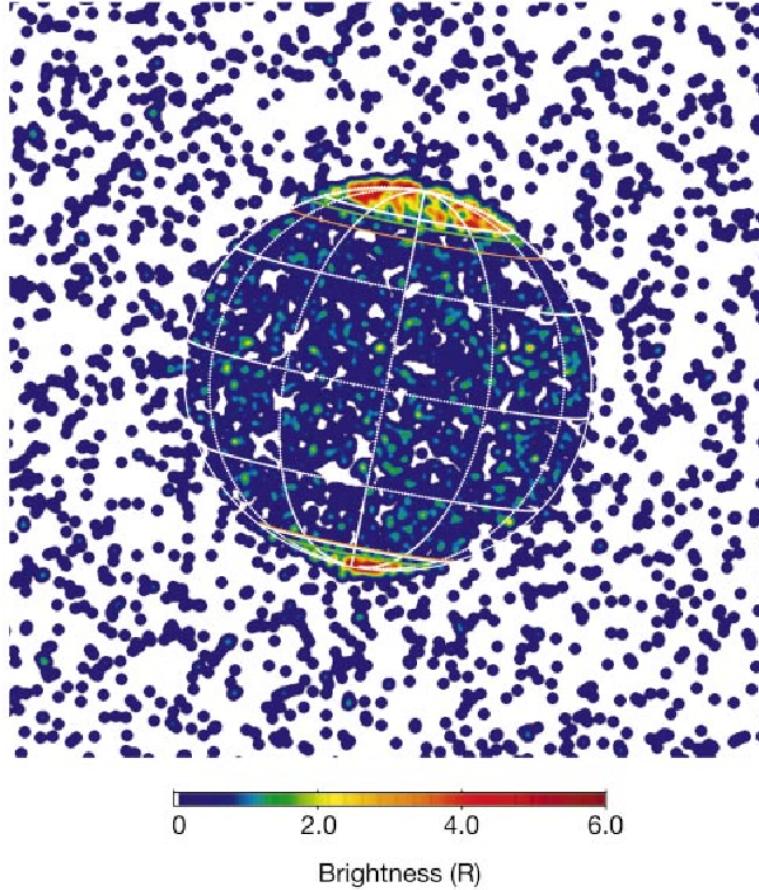


Figure 1.5: An image from the Chandra X-ray Observatory taken on 18 December 2000 presented by Gladstone et al. (2002). An average X-ray emission of about 4 R is shown to emit from the polar caps.

the X-rays observed (Hui et al., 2010; Ozak et al., 2010; Houston et al., 2018).

The location of the X-ray emission on the polar cap appears to be magnetically connected to the outer magnetosphere or to the magnetopause region, perhaps influenced by the Dungey cycle (Bunce et al., 2004; Cowley et al., 2003). However, fluxes of MeV heavy ions in the outer magnetosphere (Mauk et al., 2004) are too low to produce X-rays as predicted by the previous models. Consequently, ion acceleration by a field-aligned potential or another mechanism is required (Cravens et al., 2003). In this paper I show the observed X-ray intensities can be explained with heavy ion precipitation at energies as low as 0.3 MeV/u.

Recently, Dunn et al. (2016) analyzed the consequences for the X-ray aurora due to an interplanetary coronal mass ejection (ICME) at Jupiter. They mapped the observed emissions from the

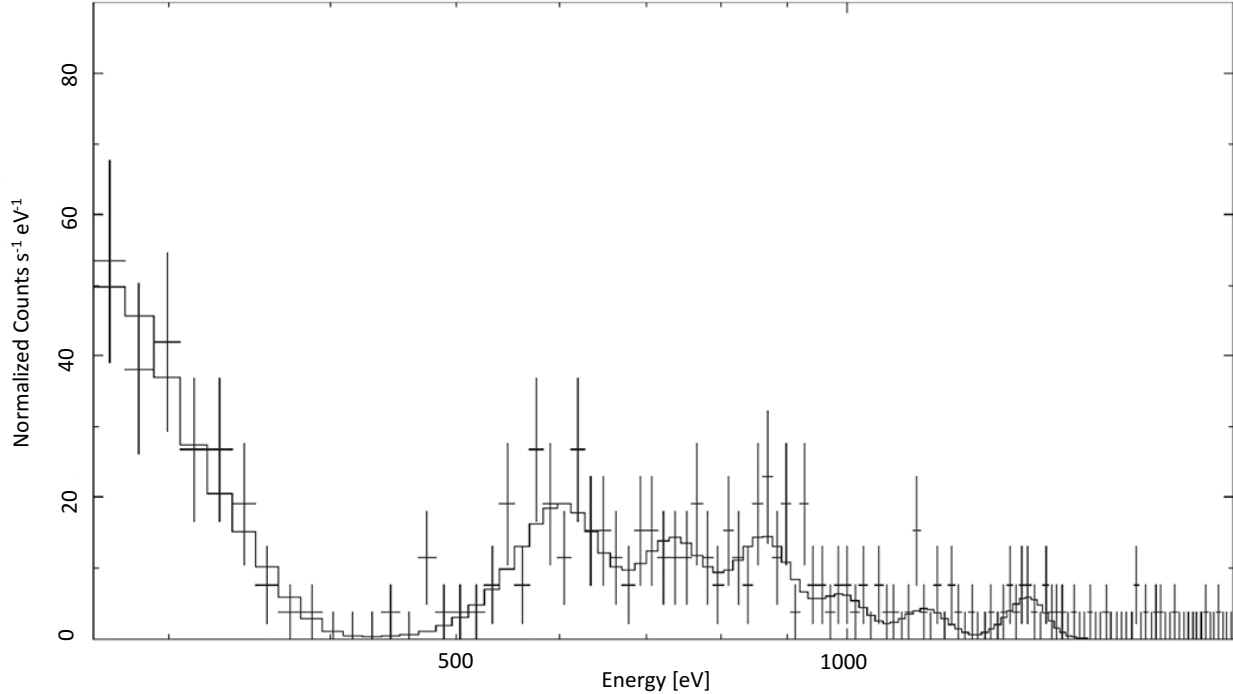


Figure 1.6: Northern polar auroral zone spectrum presented by Dunn et al. (2016) measured by the Chandra X-ray Observatory. The cross-hairs represent the data measured by the observatory, while the solid line is a combination of lines that have been fitted to the data with half-widths fixed at 20 eV.

outer magnetosphere to the polar ionosphere using the Vogt et al. (2011) field. Their analysis indicated that precipitating magnetospheric sulfur ions are important than oxygen ions for the region 50 - 90 R_J . On the other hand, emissions mapping to closed field lines at distances even further in the outer magnetosphere (70 - 120 R_J) or on open field lines appear to be due to a mixture between precipitating oxygen and carbon or sulfur ions. The observations also exhibited distinct periodicities, with periods of 26 minutes from the sulfur ions and 12 minutes from the sulfur/carbon and oxygen ions in the hotspot region. This difference seems to also indicate a different origin of the emissions from different species.

1.5 Magnetosphere-Ionosphere Coupling

MI coupling involves the exchange of energy and momentum between different plasma regions, including the linkage and coupling of colder, denser ionospheric plasmas with more energetic mag-

netospheric plasmas. Current systems are created in the magnetosphere to prevent electrodynamic force imbalances that can close in the ionosphere. These Birkeland currents from the magnetosphere into or out of the ionosphere aid in the transfer of energy and momentum from ionospheric corotation with the planet to the outer magnetosphere; see Figure 1.7 for the Jovian example. Often times auroral emission accompanies field-aligned currents and can be used as an important diagnostic tool for unveiling the structure of the current systems.

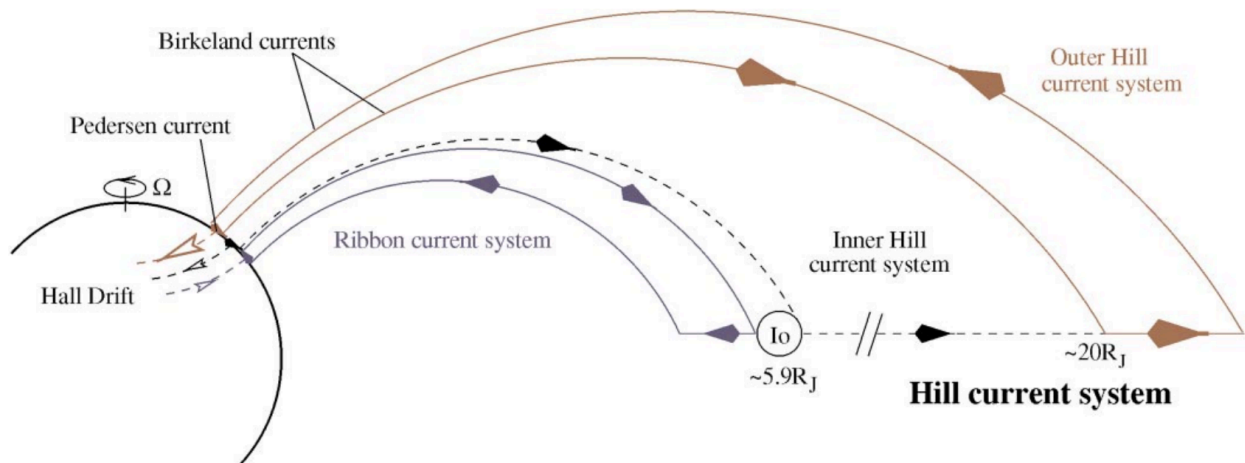


Figure 1.7: A schematic (not to scale) of Jupiter's current system showing the connection of the ionosphere to the outer magnetosphere. The region labeled "Inner Hill current system" is responsible for corotation of outward flowing magnetospheric plasma with the planet from sporadic current flow. The "Outer Hill current system" extends from ~ 20 to $\sim 60 R_J$. (See Stallard et al. (2001))

Figure 1.7 illustrates many different characteristics of the current systems in Jupiter's magnetosphere that maintain the magnetospheric corotation with the planet through mechanisms posed by Hill (1979). Initially, the "Inner Hill current system" is generated by a slippage in the magnetic field that interacts with the satellite Io, and the associated plasma torus. As the plasma emitted from the sulfur dioxide volcanoes on Io diffuses outward, away from the planet and from Io at about $6 R_J$, an equatorial plasmashet is created that is pulled into corotation by the passage of this current system. The plasma initially lags behind the magnetic field, but is almost instantaneously brought into corotation, switching the current off again. Neutral-ion collisions between the thermosphere (in corotation with the planet) and the ionosphere (lags behind corotation because the magnetic field lines attached to the lagging equatorial plasmashet are also attached to the ionosphere) sup-

ply angular momentum to the equatorial plasmashield, where corotation is reestablished. Around 20 R_J the magnetic field becomes too weak and the required velocity too great for this mechanism to maintain corotation, thus it begins to breakdown.

The "Outer Hill current system" takes over where the Inner Hill current system breaks down. It begins with "Birkeland" currents generated at the top of the auroral ionosphere at the 20 R_J footprint where they flow out, along magnetic field lines (called Field-Aligned Currents, or FAC), to the equatorial plasmashield. They flow through the plasmashield out to around 50 or 60 R_J where corotation completely breaks down and rotation of the magnetosphere almost entirely ceases. From here, the currents flow back along the magnetic field into the top of the ionosphere and the circuit is finally complete through Pedersen and Hall currents that flow through the auroral ionosphere at locations associated with the 20 R_J and 50 or 60 R_J footprints. It is important to note that these inexact locations suggested by Hill (1979) are likely to have considerable temporal variations, but are possibly inner (20 R_J) and outer (60 R_J) limits.

A good analogy for this is to think of a simple circuit with a resistor and a light bulb, shown in Figure 1.8. The initial current is generated through force imbalances when the magnetosphere lags behind corotation of the planet, thus current systems are produced to supply energy and angular momentum to the plasma in the magnetosphere. The current flows into the ionosphere where there is resistance in the form of ion-neutral collisions and energy is lost as heat. Then, just as a light bulb emits light through photoemission of a gas, an aurora is created in the atmosphere, which is the light source shown in Figure 1.8.

1.5.1 Magnetohydrodynamic Theory

There are several ways in which the magnetosphere and ionosphere can be linked and are described by fluid dynamics and Maxwell's equations. This leads to a set of self-consistent magnetohydrodynamic² (MHD) equations that relate the plasma mass density, velocity, pressure, and external

²Here I present a very brief overview of the 4 MHD equations. For a more detailed description see Nicholson (1983); Cravens (1997) and references therein.

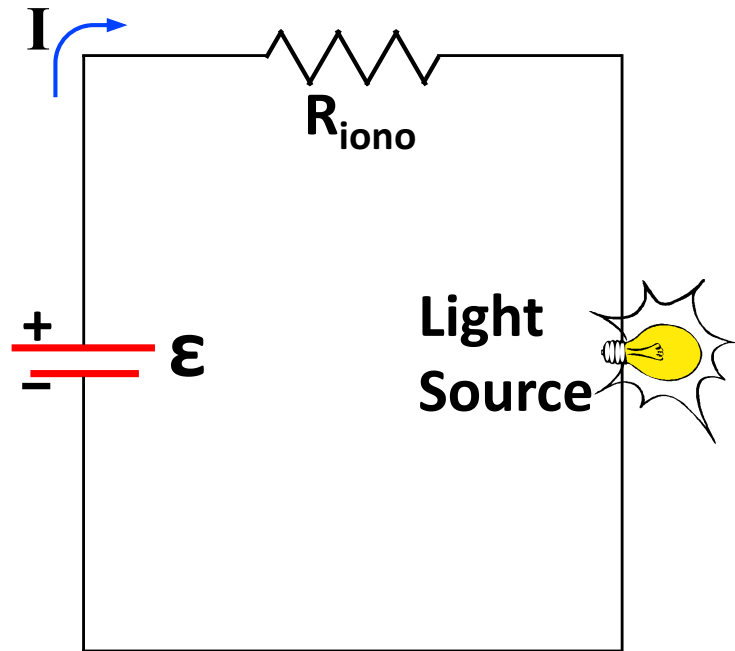


Figure 1.8: An equivalent simple electric circuit to illustrate the current system associated with auroral generation. The source, labeled " ϵ ", is the current generated through force imbalances when the magnetosphere lags behind corotation of the planet. The ionospheric resistance, labeled as " R_{iono} ", is due to ion-neutral collisions in the atmosphere. The aurora produced is then the resultant light source in this analogy.

magnetic field, making it useful for a magnetized plasma. The MHD equations are derived from the (collisional) Navier-Stokes equation, making a couple assumptions and converting the two-fluid model (both electron and ion flow) into a single-fluid model, where the motion of electrons is neglected and only that of heavy ions is considered. Thus, the following mechanisms can be used to explain the linkage between the magnetosphere and ionosphere: 1) through the mass of particles by a fluid (or mass) continuity equation

$$\frac{\partial \rho_M}{\partial t} + \nabla \cdot (\rho_M \mathbf{u}) = 0 \quad (1.1)$$

where ρ_M is the mass density of the plasma and \mathbf{u} is the plasma bulk velocity. Or simply, Equation 1.1 states that, within the system, matter is neither created nor destroyed. 2) Through momentum transfer with the momentum equation

$$\rho_M \left(\frac{\partial}{\partial t} + \mathbf{u} \cdot \nabla \right) \mathbf{u} = \mathbf{J} \times \mathbf{B} - \nabla (p_i + p_e) + \rho_M \mathbf{g} - \rho_M \nu_{in} (\mathbf{u} - \mathbf{u}_n) \quad (1.2)$$

where \mathbf{J} is the current density, \mathbf{B} is the magnetic field, p_i and p_e are the ion and electron pressures, respectively, ν_{in} is the ion-neutral collision frequency, and \mathbf{u}_n is the neutral flow velocity. Here, it is important to remember that the mass density, ρ_M , multiplied by the plasma bulk velocity, \mathbf{u} , is the momentum of the plasma. In Equation 1.2, $\mathbf{J} \times \mathbf{B}$ is the magnetic (Lorentz) force term and can be written as

$$\mathbf{J} \times \mathbf{B} = \frac{(\mathbf{B} \cdot \nabla) \mathbf{B}}{\mu_0} - \nabla \left(\frac{B^2}{2\mu_0} \right). \quad (1.3)$$

where μ_0 is the permeability of free space. The first term on the right hand side of Equation 1.3 is the magnetic tension force and the second term is the gradient of the magnetic pressure ($p_B = B^2/2\mu_0$). Eq. 1.3 is found when the Lorentz force term is expanded using Ampere's law without Maxwell's correction. And finally, 3) through the energy equation

$$\frac{d}{dt} \left(\frac{p}{\rho_M^\gamma} \right) = 0 \quad (1.4)$$

where γ is the ratio of the specific heats, C_p/C_v , and is typically taken as the adiabatic index for a monatomic gas, $5/3$. MHD assumes that the plasma has quasi-neutrality and high electrical conductivity allowing it to easily induce magnetic fields. The EM fields obey Maxwell's equations along with being subject to the condition $\nabla \cdot \mathbf{B} = 0$.

The magnetic field time evolution can be defined by using the generalized Ohm's law (idealized to $\mathbf{E} \approx \mathbf{J}/\sigma - \mathbf{u} \times \mathbf{B}$) with Faraday's law ($\nabla \times \mathbf{E} = -\frac{\partial \mathbf{B}}{\partial t}$), which yields the magnetic induction, and 4th MHD, equation

$$\frac{\partial \mathbf{B}}{\partial t} = \nabla \times (\mathbf{u} \times \mathbf{B}) - \nabla \times (D_m \nabla \times \mathbf{B}). \quad (1.5)$$

$D_m = \eta/\mu_0$ is the magnetic diffusion equation with η being the resistivity (or inverse of conductivity, $\eta = 1/\sigma$). When a plasma has very high electrical conductivity ($\sigma \rightarrow \infty$, $\eta \rightarrow 0$), the magnetic diffusion equation is approximated as $D_m \approx 0$ and the last term of Equation 1.5 can be neglected,

allowing the first term to dominate. Now described is a magnetic field with a temporal evolution dependent on the spatial evolution of the plasma bulk flow velocity, \mathbf{u} , crossed with the magnetic field. This is the case of ideal MHD and it allows for advantageous thinking of the magnetic field lines as "frozen into" the plasma flow. This describes how a magnetic field of sufficient strength can cause magnetospheric plasma to corotate with planets such as Earth, Jupiter, or Saturn and is the underlying basis for everything presented in this work.

1.5.2 Pedersen and Hall Conductivities

The current density throughout the entire ionosphere is

$$\mathbf{J} = J_{\parallel} \hat{\mathbf{b}} + J_{\perp} \hat{\perp} + J_H \hat{\mathbf{n}} \quad (1.6)$$

where J_{\parallel} , J_{\perp} , and J_H are the parallel, Pedersen, and Hall current densities. I have defined a coordinate system here such that one axis, $\hat{\mathbf{b}}$, is aligned with the magnetic field and is the unit vector in the magnetic field direction, $\hat{\mathbf{b}} = \mathbf{B}/|\mathbf{B}|$. $\hat{\perp}$ is the axis perpendicular to the magnetic field unit vector that points toward the magnetic pole. Thus, $\hat{\mathbf{n}}$ is perpendicular to $\hat{\mathbf{b}}$ and points along the magnetic field lines of latitude, or $\hat{\perp} \times \hat{\mathbf{b}} = \hat{\mathbf{n}}$ (and $\hat{\mathbf{n}} \times \hat{\mathbf{b}} = -\hat{\perp}$). An electric field geometry can be constructed such that $\mathbf{E}' = \mathbf{E}'_{\parallel} + \mathbf{E}'_{\perp} = E'_{\parallel} \hat{\mathbf{b}} + E'_{\perp} \hat{\perp}$. Here \mathbf{E}' is the electric field in the reference frame of the neutral gas (moving at velocity \mathbf{u}_n) such that $\mathbf{E}' = \mathbf{E} + \mathbf{u}_n \times \mathbf{B}$.

The current density can be found by starting with its definition

$$\mathbf{J} = \sum_k n_k q_k \mathbf{u}_k \quad (1.7)$$

where the density (n_k), charge (q_k), and bulk flow velocity (\mathbf{u}_k) are summed over all plasma species, k , including electrons. The ion densities n_k are a known quantity, but the current density must be related to the electric field to find the velocities \mathbf{u}_k . I introduced the momentum equation with Equation 1.2; however, I no longer wish to consider the ions and electrons as a single fluid. Instead it is necessary to present more general forms of the momentum equation for each plasma species

which will be simplified. The moment equation used for electrons is

$$n_e m_e \left[\frac{\partial}{\partial t} + \mathbf{u}_e \cdot \nabla \right] \mathbf{u}_e = -n_e e [\mathbf{E} + \mathbf{u}_e \times \mathbf{B}] - \nabla p_e + n_e m_e \mathbf{g} - \sum_{t \neq e} n_e m_e \nu_{et} (\mathbf{u}_e - \mathbf{u}_t) \quad (1.8)$$

and for ions

$$n_i m_i \left[\frac{\partial}{\partial t} + \mathbf{u}_i \cdot \nabla \right] \mathbf{u}_i = +n_i e [\mathbf{E} + \mathbf{u}_i \times \mathbf{B}] - \nabla p_i + n_i m_i \mathbf{g} - \sum_{t \neq i} n_i m_i \nu_{it} (\mathbf{u}_i - \mathbf{u}_t) - P_i (m_i \mathbf{u}_i - m_n \mathbf{u}_n) \quad (1.9)$$

where t is the every species present, including electrons, ions, and neutrals. The terms on the left hand side of the equations are inertial terms which can be neglected because the particle dynamics are going to be dominated by the horizontal currents. This also implies that the terms associated with gravity, \mathbf{g} , can ignored. The pressure gradients in the horizontal direction are small due to stratification of the atmosphere, especially relative to the horizontal component of current, so all of the pressure terms can be ignored, i.e. $\nabla p_k \sim 0$. To further simplify these equations I only consider collisions between species k and the neutrals, i.e. the only collisional friction term remaining is ν_{kn} . I have reasonably disregarded ion-ion collisions and for further simplicity ignored electron-ion collisions, which is a less reasonable assumption, and any additional ion production P_i is neglected. I am left with an approximate momentum equation for species k such that

$$0 = q_k \{ \mathbf{E}' + (\mathbf{u}_k - \mathbf{u}_n) \times \mathbf{B} \} - m_k \nu_{kn} (\mathbf{u}_k - \mathbf{u}_n). \quad (1.10)$$

where m_k and \mathbf{u}_k are the mass and the bulk velocity of the plasma species, and \mathbf{u}_n is the neutral atmosphere bulk velocity.

Solving Equation 1.10 for \mathbf{u}_k and using the definition of current density, \mathbf{J} , in Equation 1.7, Ohm's law can be generalized to

$$\mathbf{J} = \sigma_0 \mathbf{E}'_{\parallel} + \sigma_{\perp} \mathbf{E}'_{\perp} + \sigma_H \mathbf{E}'_{\perp} \times \hat{\mathbf{b}} \quad (1.11)$$

where σ_0 , σ_\perp , and σ_H , are the parallel, Pedersen, and Hall conductivities, respectively. The parallel, Pedersen, and Hall currents are then given by

$$J_\parallel = \sigma_0 E_\parallel, \quad J_H = \sigma_H E_\perp, \quad \text{and} \quad J_\perp = \sigma_\perp E_\perp. \quad (1.12)$$

The parallel conductivity is

$$\sigma_0 = \sum_k \sigma_{0k} \quad \text{with} \quad \sigma_{0k} = \frac{n_k q_k^2}{m_k \nu_{kn}} \quad (1.13)$$

where ν_{kn} is the collision frequency between plasma species k and the atmospheric neutrals, for all ion species and electrons. The Pedersen conductivity is then

$$\sigma_\perp = \sum_k \sigma_{0k} \frac{\nu_{kn}^2}{\nu_{kn}^2 + \Omega_k^2} \quad (1.14)$$

and the Hall conductivity is

$$\sigma_H = - \sum_k \sigma_{0k} \frac{\nu_{kn} \Omega_k}{\nu_{kn}^2 + \Omega_k^2} \quad (1.15)$$

where $\Omega_k = q_k B / m_k$ and is the gyrofrequency for plasma species k . Thus, the contribution from electrons to the Hall current is positive because Ω_k is negative for electrons. For a detailed discussion and derivation of the momentum equation and the various conductivities, I refer to Cravens (1997).

1.5.3 Field-Aligned Currents

An issue evolves with the MHD approach when a large intrinsic magnetic field is present (e.g. considering an area of space too close to the planet) because the induced field in the plasma is insignificant when compared to the total magnetic field. So, when considering the ionosphere it is more useful to calculate the electrical current from the numerous ion species and electrons in the ionosphere, then use the steady-state charge continuity equation, $\nabla \cdot \mathbf{J} = 0$. Therefore, the

ionosphere is often analyzed separately from the magnetosphere.

Rather than MHD the field-aligned electrical currents from magnetosphere dynamics that flow into the top of the ionosphere are used as boundary conditions to determine the current density in the ionosphere. If J_{\parallel} is the MI boundary current density, the charge continuity law must be satisfied in the ionosphere following:

$$J_{\parallel} = -\nabla \cdot \mathbf{K}_{\perp} \quad (1.16)$$

where \mathbf{K}_{\perp} is the horizontal current integrated vertically over the extent of the ionosphere. Integrating the Pedersen and Hall currents (shown in Figure 1.7 and Equation 1.12) over the height of the ionosphere (\mathbf{K}_P and \mathbf{K}_H , respectively) add together to produce the horizontal current densities:

$$\mathbf{K}_{\perp} = \mathbf{K}_P + \mathbf{K}_H, \quad \mathbf{K}_P = \Sigma_P \mathbf{E}'_{\perp}, \quad \mathbf{K}_H = \Sigma_H \mathbf{E}'_{\perp} \times \hat{\mathbf{b}} \quad (1.17)$$

where Σ_P and Σ_H are the ionospheric height integrated Pedersen and Hall electrical conductivities

$$\begin{aligned} \Sigma_P &= \int_{\text{bottom}}^{\text{top}} \sigma_{\perp} dz \\ \Sigma_H &= \int_{\text{bottom}}^{\text{top}} \sigma_H dz. \end{aligned} \quad (1.18)$$

Once the parallel currents are determined, the different regions can be linked through dynamics and force balance equations.

1.5.4 Parallel Electric Fields

A reasonable question when thinking about aurorae generation is: how are particles accelerated into the top of the atmosphere, especially when highly intensive emission is observed? There are two processes that I want to briefly discuss that could possibly lead to magnetic field-aligned electric potentials which in turn accelerate particles into the atmosphere. However, the processes associated with the MeV potential drops observed at Jupiter (Clark et al., 2017a) are still debated, and there has not been a clear consensus on what generates them.

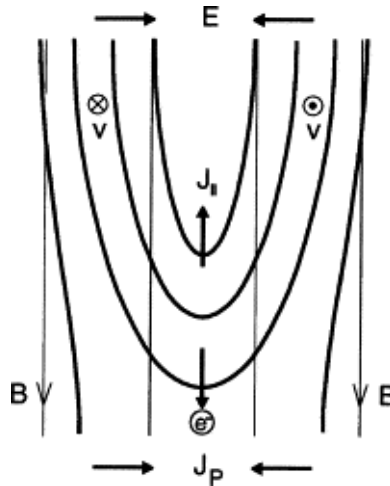


Figure 1.9: Illustration of the equipotential lines in the Jovian auroral region from Hill (2004). Shown are the parallel and Pedersen current densities, J_{\parallel} and J_P , respectively.

One hypothesis is through a basic acceleration mechanism also seen at Earth, illustrated in Figure 1.9. In this scenario, charge separation along with a magnetospheric $\mathbf{E} \times \mathbf{B}$ drift causes a layer of charge density (J_{\parallel} in Fig. 1.9) to form between two electric field regions (discussed fully in Hill (2004)). Charges build up in the magnetosphere above the atmosphere from the FAC, much like a capacitor in a simple current system, only now some particles are reflecting off of the increased magnetic field. As the magnetosphere continues to attempt corotation with the planet, more charged particles will gather above the atmosphere and charge separation occurs. Eventually, when the charge separation is great enough, a large parallel electric field is generated to close the Birkeland current system through the ionosphere, allowing the ions or electrons to flow. Where the electric field converges from the $\mathbf{E} \times \mathbf{B}$ drift, a Pedersen current is generated in the atmosphere and an upward Birkeland current is produced. This type of acceleration mechanism will create "inverted-V" signatures in the particle energy distribution spectra, seen in the *in situ* data and shown later in Figure 1.13.

A second, less intuitive, electric field generator is through what are known as Alfvénic waves. This is a type of MHD wave in which the ion flux tubes along a magnetic field line oscillate in response to a restoring force, much like a wave moving along a plucked guitar string. This mechanism generates many different electric fields that flip polarity on a very small spatial scale,

creating a stochastic energy distribution, such as those observed by Juno and presented by Clark et al. (2018) and Ebert et al. (2019). I am less concerned with how the particles get to energies seen by Juno, or even the energy gained between Juno and the atmosphere, instead I take Juno data at face value and input it at energies directly observed. Thus, I will not expand on this any further and instead will refer the reader to Khurana & Kivelson (1989) and Manners et al. (2018).

1.5.5 Magnetosphere-Ionosphere Coupling at Jupiter

Jupiter has a measured magnetic field strength of ~ 7.8 Gauss (Connerney et al., 2017), over 20 times greater than Earth's surface field, and rotates with a period of about 10 hours. Jupiter is unique in the sense that it has a large internal plasma source from Io's sulfur dioxide volcanoes. All of the plasma created by Io must eventually be removed from the magnetosphere, either escaping down the magnetotail, being carried out to the magnetopause, or lost into the atmosphere of Jupiter, lest too much mass-loading occurs.

The great field strength and rapid rotation create a large angular momentum with which the magnetospheric plasma attempts to corotate. For corotation to be accomplished, MI current systems are created. The SO_2 from Io is dissociated and ionized, creating sulfur and oxygen ions with an equal number of electrons forming a plasma torus at Io's orbital distance ($\sim 6 R_J$). The plasma torus is largely confined to the equatorial toroidal plasma sheet created by the torus, as seen in Figure 1.10.

The recently created heavy ions are now subject to the magnetic field and begin following corotation. As more mass enters the magnetospheric system, $\mathbf{J} \times \mathbf{B}$ forces are required to conserve angular momentum. These newly acquired forces are associated with the field-aligned currents linking the magnetosphere and ionosphere. Because angular momentum increases with radial distance, the $\mathbf{J} \times \mathbf{B}$ force term and field-aligned currents must also increase. This occurs out to about $30 R_J$ where coupling can no longer supply the required force to maintain corotation and the magnetic field begins lagging.

The plasma that populates the Jovian magnetosphere is in the presence of large magnetic fields

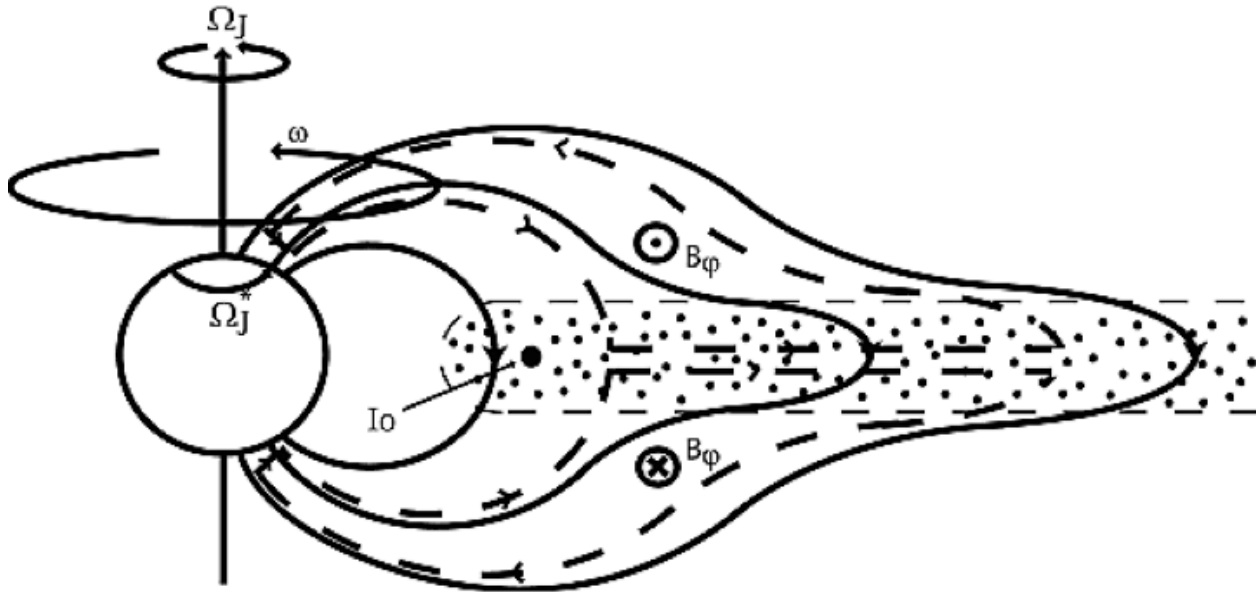


Figure 1.10: Sketch of the Jovian magnetosphere and the connection to the ionosphere. The magnetic field lines are indicated by the arrowed solid lines, coming out of the northern hemisphere into the southern. The magnetic field lines are extended outwards by azimuthal currents in the middle magnetosphere current sheet. Io is the main generator of the plasma that makes up the current sheet. The dotted region represents the plasma, beginning as a torus produced by Io and diffusing outwards to form a plasma sheet. The plasma rotates with the Jovian magnetic field due to MI coupling. Indicated in the figure are three separate angular velocities. ω is the angular velocity of the planetary magnetic field, Ω_J is Jupiter's angular velocity, and Ω_J^* is the angular velocity of the neutral atmosphere in the Pedersen layer of the ionosphere. Ω_J^* is expected to have a value between ω and Ω_J due to the torque produced by ion-neutral collisional friction. The arrowed dashed lines represent the Pedersen current system that closes through Birkeland currents in the plasma sheet, where there is a radial outward current system. Shown is the case of sub-corotation of the plasma (i.e., $\omega \leq \Omega_J$). Because the magnetic field lags behind corotation of the planet, the field lines are bent out of the meridional plane. The Birkeland current system is responsible for this "lagging" configuration associated with the azimuthal field components B_ϕ shown. (From Cowley et al. (2003).)

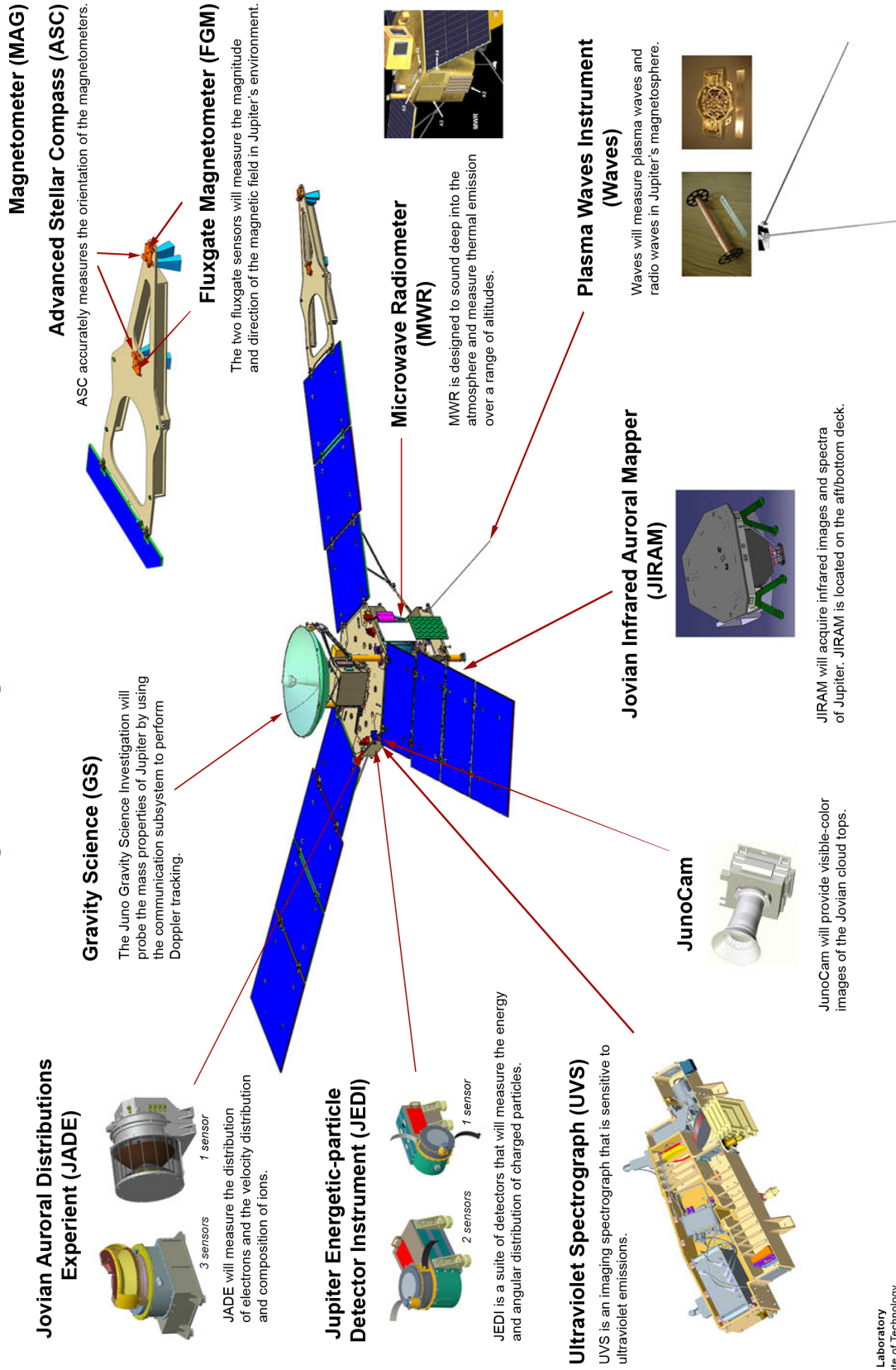
and field-aligned currents that are trying to maintain corotation. The ions and electrons follow the Birkeland currents from the outer magnetosphere and flow through the ionosphere. As the charged particles reach the planetary polar caps following magnetic field lines they precipitate into the upper atmosphere where brilliant auroral displays occur. The total auroral power is approximated to be 10^{13} - 10^{14} W, 100 times greater than the power input from solar EUV at Jupiter. There is about 1 MA of current associated with the Io auroral footprint and about 100 MA accompanying the main auroral oval (see Fig. 1.4) that maps out to the middle magnetosphere where energetic electrons are responsible for the aurora.

The MI coupling and corotation current systems are probably not the same driver for the X-ray emission from the polar caps. That is likely associated with magnetic reconnection processes taking place in the magnetopause or magnetotail regions where large electric potentials can be imposed across the magnetosphere, accelerating heavy ions to energies required for X-ray production. Dayside magnetopause magnetic reconnection is a possible driver for the downward field-aligned currents that map to the polar caps, as suggested by Bunce et al. (2004). Magnetic reconnection is not easily described using fluid theory and is not explored further in this paper.

1.6 Juno

Juno is a solar powered, atmosphere-skimming, NASA funded spacecraft that arrived to Jupiter on July 4th, 2016 where it began a 53.4 day polar orbit. This orbit includes an apoJove that takes Juno far beyond the orbit of Callisto, going as far out as $113 R_J$, and brings Juno in to about $1.06 R_J$ during periJove, $\sim 4,200$ km above the cloud tops. Onboard Juno are eight science instruments that measure Jupiter's gravitational and magnetic fields, count and calculate electron and ion species in the magnetosphere, and observe Jupiter in every wavelength from ultraviolet (UV) to radio. The complete set of Juno instruments is shown in Figure 1.11, but two of the instruments that are most relevant to this research include the Jovian Auroral Distribution Experiment (JADE) detector (McComas et al., 2017) and the Jovian Energetic-particle Distribution Instrument (JEDI) (Mauk et al., 2017a).

Juno Payload System Overview



Jet Propulsion Laboratory
California Institute of Technology
Pasadena, California
www.nasa.gov

Figure 1.1.1: Schematic of Juno with a description of each instrument onboard.

JADE is a particle detector that is comprised of three electron sensors (JADE-Es) and a single low energy ion sensor (JADE-I). The JADE-Es are capable of measuring electrons fluxes between ~ 100 eV and 100 keV, while JADE-I measures ions from ~ 5 eV to ~ 50 keV and provides ion composition measurements from 1 to 50 amu. The ion composition measurements have fine enough resolution ($m/\Delta m \sim 2.5$) to separate heavy and light ions, along with distinguishing between O^+ and S^+ . The *in situ* measurements of electrons and ions made by JADE are critical to understanding the processes that produce the strong Jovian aurora seen in the main auroral oval.

Figure 1.12 has been taken from Connerney et al. (2017) and displays complete polar maps of UV emission from Jupiter's northern and southern aurora measured by Juno during the spacecraft's first polar pass. Panels A and C present the total UV emission measured in kiloRayleigh where the main auroral oval is distinguishable and is associated with the electron measurements made by JADE. Panels B and C show the color ratio during the same time. The color ratio is a measurement of methane absorption and a proxy for the electron precipitation energy, which is discussed in greater detail in Section 3.2.5.

JEDI is a high energy particle detector that consists of three particle sensors that measure the energy, angle, and ion composition distributions of ions ranging in energy from H:20 keV and O,S:50 keV to > 1 MeV, and the energy and angle distribution of electrons from < 40 to > 500 keV. The measurements of high energy, heavy ions is pivotal to the explanation I propose of observed X-rays coming from Jupiter's polar caps.

Precipitating energetic ions have been measured during each perijove at a broad spectrum of energies. Figure 1.13 presents a JEDI heavy ion flux measurement during a northern polar pass over the polar caps and main auroral oval. The top panel shows an angle spectrogram which presents the oxygen ion pitch angle with respect to time, or location of the spacecraft as it orbits Jupiter. Up to a time of about 2:33, there is a high intensity of trapped ions (ions with a pitch angle between $\sim 10^\circ$ and $\sim 170^\circ$) that are unable to precipitate into the atmosphere, and instead get reflected back into the magnetosphere due to the increase in magnetic field strength. Contrary to the trapped or magnetically reflected particles, the time between 2:33-2:35 illustrates a precipitation

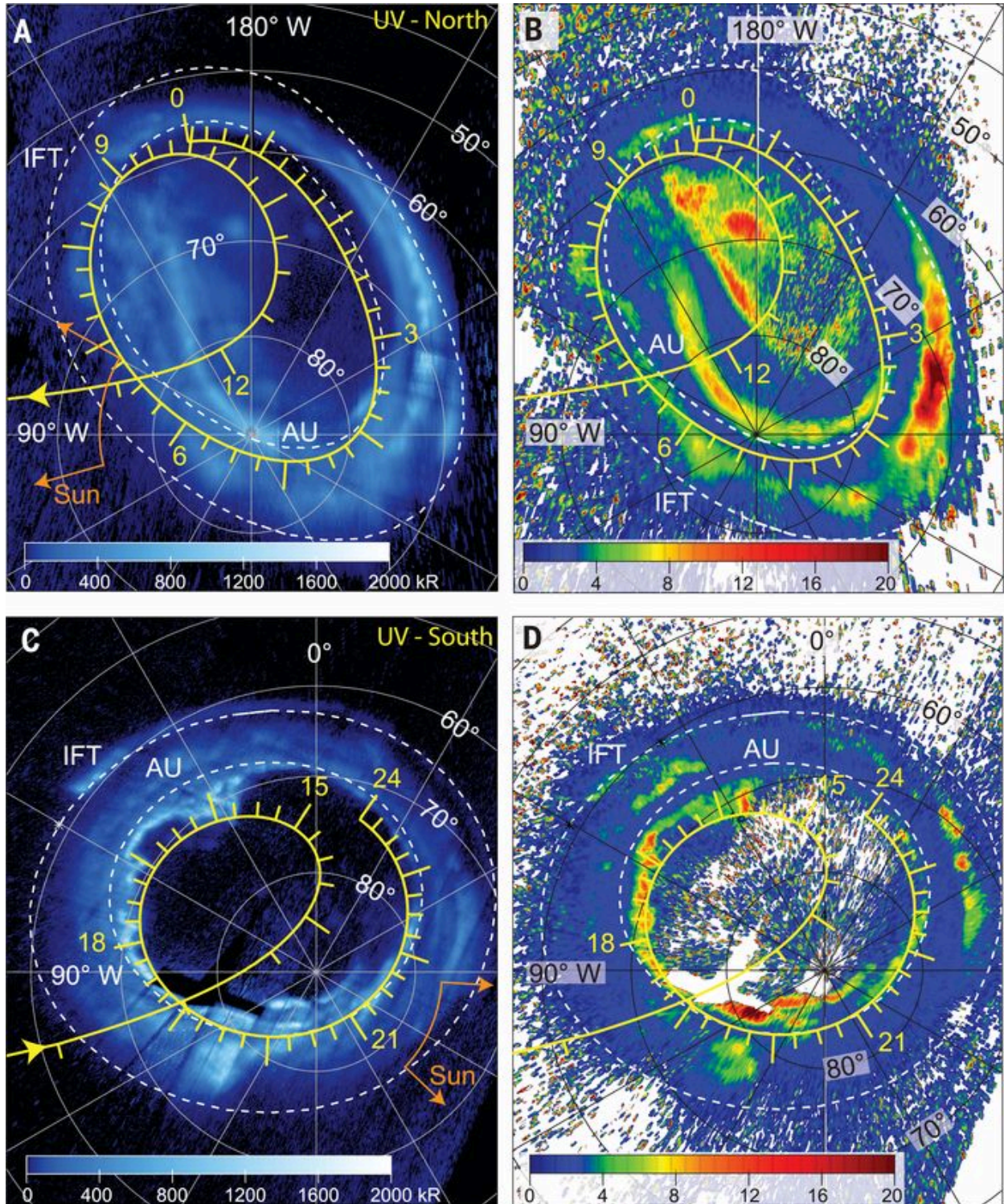


Figure 1.12: Orthographic projections of Jupiter's northern and southern aurora at the 1 bar level in the UV wavelength. The yellow line is the spacecraft trajectory marked with hourly tic marks. In the left column are UV intensities summed between 60 and 180 nm and in the right column are color ratios that have been given as the ratio between 155 to 162 nm and 123 to 130 nm (Connerney et al., 2017).

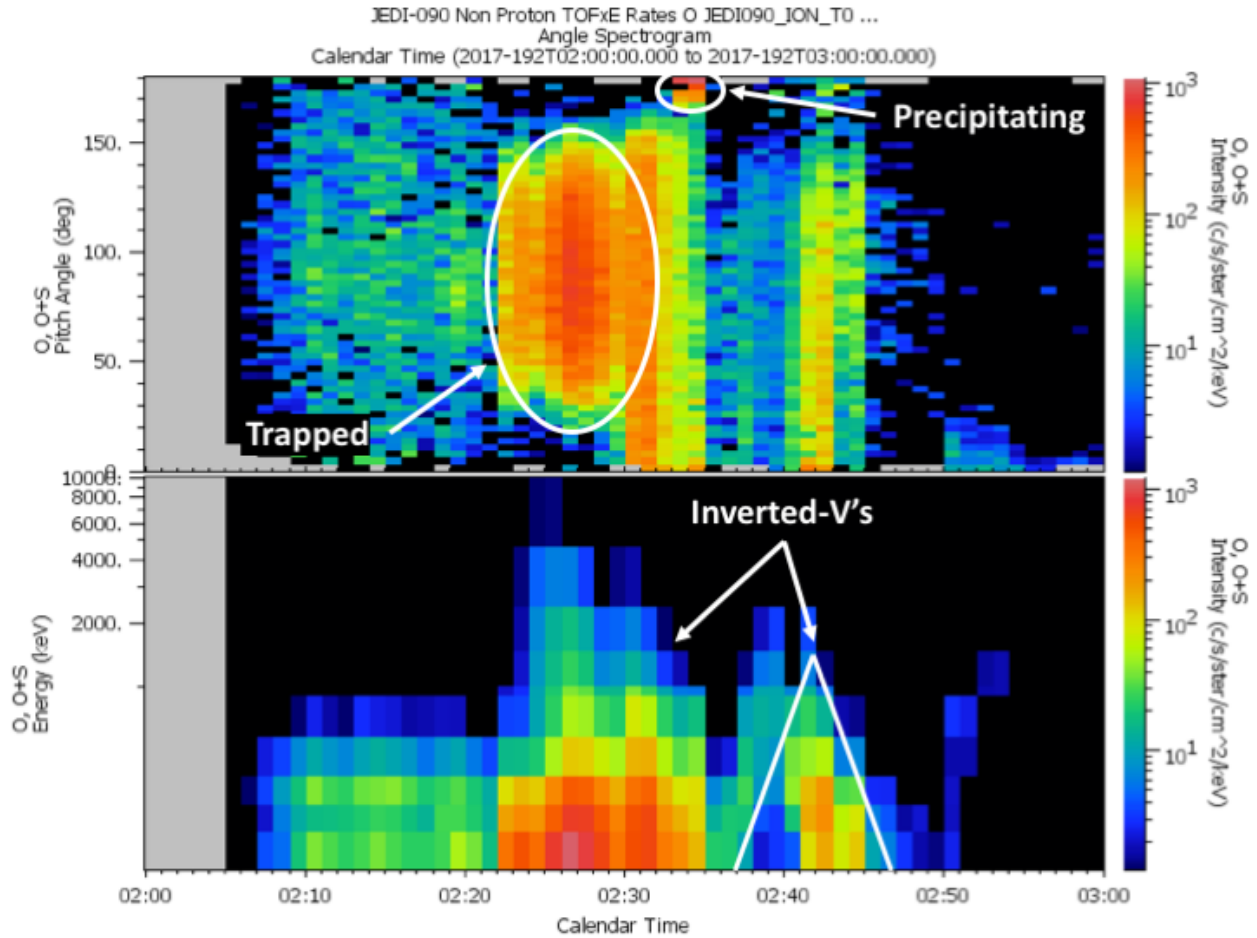


Figure 1.13: Oxygen and sulfur ion spectrogram measured by JEDI on the 7th perijove pass over the main auroral oval. The top figure shows the pitch angle distribution, where it is evident that energetic heavy ion precipitation is occurring when looking at the loss cone (pitch angles approaching 0° or 180°). The bottom figure is the energy spectrogram during the same time period. There are inverted-V distributions in the ion energy associated with ion acceleration.

signature designated by a high intensity flux with a pitch angle $>170^\circ$, where 180° is down, toward the planet. The precipitating particles are said to be in a "loss cone" and are able to reach the atmosphere and help in the production of the aurora. The bottom panel displays ion energy as a function of time, called an energy spectrogram. An important aspect of the energy spectrogram is the inverted-V signatures seen, indicating ion acceleration from field-aligned potentials.

Chapter 2

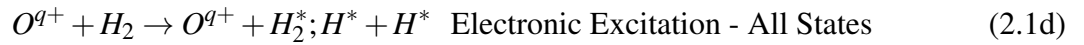
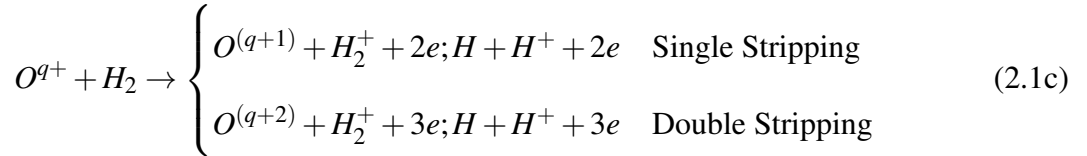
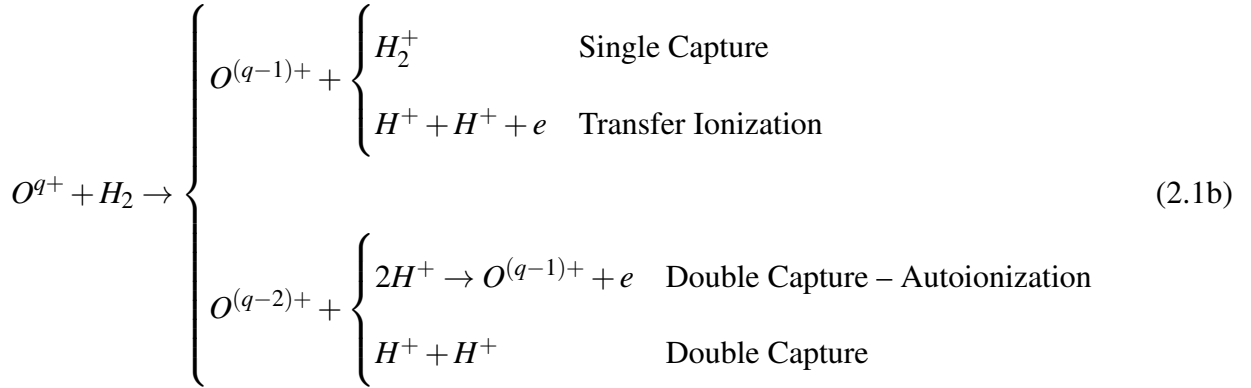
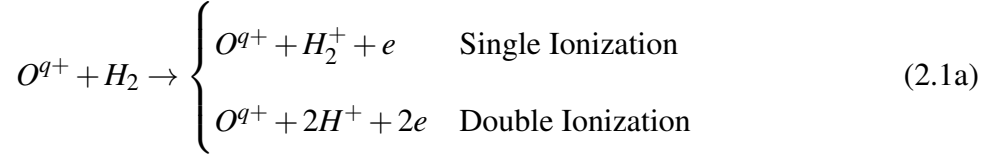
Physical Processes Related to the Jovian Aurora

The ion precipitation model begins with injecting oxygen (O) and sulfur (S) ions into the top of the atmosphere with some initial energy. The incident pitch angle is assumed to have an isotropic downward distribution and is randomly chosen for each individual ion and scaled as the cosine of the pitch angle. Penetration depth and energy loss are affected by the initial energy, incident pitch angle, and orientation of the magnetic field lines, which are assumed to be perpendicular to the top of the atmosphere at the poles. As the ions precipitate through the atmosphere, they undergo collisional interactions with the atmospheric constituents. To determine how far each ion precipitates before a collision and what type of collision will occur, I use the most up to date ion impact cross-sections available from Schultz et al. (2019); Gharibnejad et al. (2019). These integral cross-sections include oxygen (Schultz et al., 2017, 2019) and sulfur (Gharibnejad et al., 2019) collisions with H₂, the primary constituent in the Jovian atmosphere (Seiff et al., 1996, 1997; Maurellis & Cravens, 2001).

2.1 Ion Impact Cross-Section Overview

Over the past couple of years there have been significant improvements to existing cross-section data relevant to ion precipitation at Jupiter. Initially, when Ozak et al. (2010) was modeling Jovian ion precipitation, they only considered five possible collisions; electron stripping of the projectile, target to projectile charge transfer, projectile excitation, target ionization, and target excitation, which was relevant for both oxygen and sulfur. Then, Ozak et al. (2013) extended the possible collisions to include double target ionization, transfer ionization, double capture-autoionization, and

double stripping of projectile ions. Houston et al. (2018), with updated oxygen cross-section data from Schultz et al. (2017), subsequently modeled additional projectile processes, single capture and double capture of electrons from the target molecule, accounting in totality for the following processes:



Although the extended list of collisional possibilities was more comprehensive than anything that had come before it, Schultz et al. (2019) noticed that while the oxygen stopping power¹ was in good agreement with recommended values at both low (10-100 keV/u) and high (>2000 keV/u) collision energies, Schultz et al. (2017) underestimated the recommended stopping power in the intermediate (100 - 2000 keV/u) energy range by up to a factor of nearly two (Fig. 2.1). Originally, Schultz et al. (2017) were considering target processes (e.g., single and double ionization)

¹Stopping power is a measurement of the energy deposition of projectile ions into a gaseous medium, taking into account every process that can occur, often times calculated using benchmarked experimental values without concern for the details of specific projectile-target collisions.

to happen independently, and non-simultaneously (NSIM), from projectile processes (e.g., single and double stripping). Schultz et al. (2019) proposed that target and projectile processes could occur simultaneously (SIM) and the cross-sections should reflect this, ultimately providing the cross-sections for 35 processes that are used in my model and provided in Appendix A.

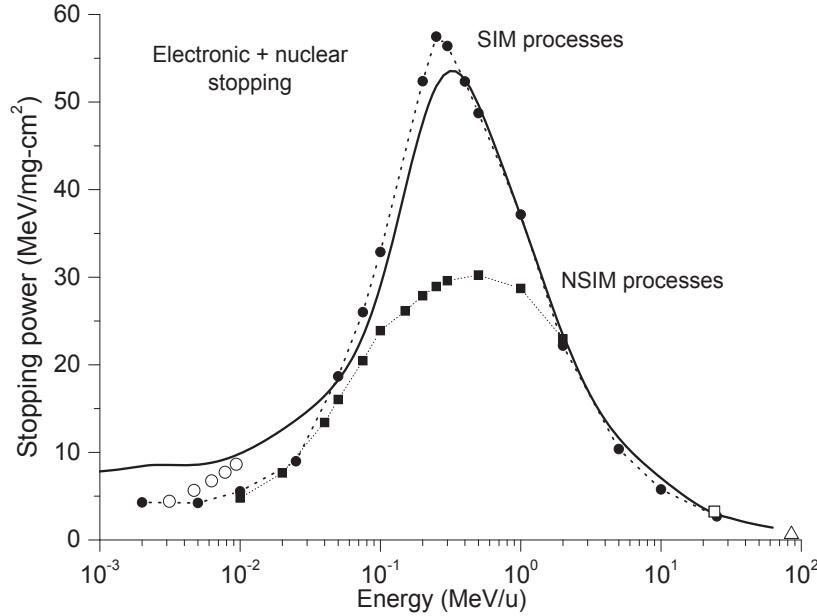
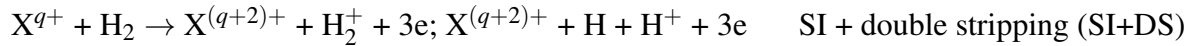
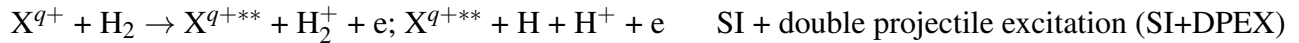
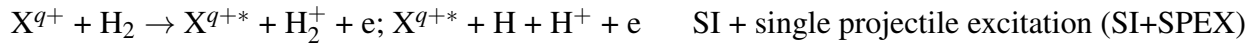
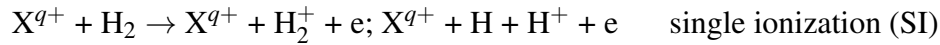


Figure 2.1: Comparison of Schultz et al. (2017) NSIM cross-section calculations of electronic plus nuclear stopping power for oxygen ion transport through H₂ gas (squares) with Schultz et al. (2019) SIM cross-section calculations (circles). Also plotted are the accepted values from SRIM 2013 (Ziegler et al., 2013) (solid line).

The 35 NSIM and SIM projectile and target processes used are the following:



$X^{q+} + H_2 \rightarrow X^{q+*} + H^+ + H^+ + 2e$	DI+SPEX
$X^{q+} + H_2 \rightarrow X^{q+**} + H^+ + H^+ + 2e$	DI+DPEX
$X^{q+} + H_2 \rightarrow X^{(q+1)+} + H^+ + H^+ + 3e$	DI+SS
$X^{q+} + H_2 \rightarrow X^{(q+2)+} + H^+ + H^+ + 4e$	DI+DS
$X^{q+} + H_2 \rightarrow X^{(q-1)+} + H^+ + H^+ + e$	transfer ionization (TI)
$X^{q+} + H_2 \rightarrow X^{(q-1)+*} + H^+ + H^+ + e$	TI+SPEX
$X^{q+} + H_2 \rightarrow X^{(q-1)+**} + H^+ + H^+ + e$	TI+DPEX
$X^{q+} + H_2 \rightarrow X^{q+} + H^+ + H^+ + 2e$	TI+SS
$X^{q+} + H_2 \rightarrow X^{(q+1)+} + H^+ + H^+ + 3e$	TI+DS
$X^{q+} + H_2 \rightarrow X^{(q-2)+**} + H^+ + H^+ \rightarrow X^{(q-1)+} + e$	double capture autionization (DCAI)
$X^{q+} + H_2 \rightarrow X^{(q-2)+***} + H^+ + H^+ \rightarrow X^{(q-1)+*} + e$	DCAI+SPEX
$X^{q+} + H_2 \rightarrow X^{(q-2)+****} + H^+ + H^+ \rightarrow X^{(q-1)+**} + e$	DCAI+DPEX
$X^{q+} + H_2 \rightarrow X^{(q-2)+**} + H^+ + H^+ \rightarrow X^{q+} + 2e$	DCAI+SS
$X^{q+} + H_2 \rightarrow X^{(q-2)+**} + H^+ + H^+ \rightarrow X^{(q+1)+} + 3e$	DCAI+DS
$X^{q+} + H_2 \rightarrow X^{(q-1)+} + H_2^+; X^{(q-1)+} + H + H^+$	single electron capture (SC)
$X^{q+} + H_2 \rightarrow X^{(q-1)+*} + H_2^+; X^{(q-1)+*} + H + H^+$	SC+SPEX
$X^{q+} + H_2 \rightarrow X^{(q-1)+**} + H_2^+; X^{(q-1)+**} + H + H^+$	SC+DPEX
$X^{q+} + H_2 \rightarrow X^{q+} + H_2^+ + e; X^{q+} + H + H^+ + e$	SC+SS
$X^{q+} + H_2 \rightarrow X^{(q+1)+} + H_2^+ + 2e; X^{(q+1)+} + H + H^+ + 2e$	SC+DS
$X^{q+} + H_2 \rightarrow X^{(q-2)+} + H^+ + H^+$	double electron capture (DC)
$X^{q+} + H_2 \rightarrow X^{(q-2)+*} + H^+ + H^+$	DC+SPEX
$X^{q+} + H_2 \rightarrow X^{(q-2)+**} + H^+ + H^+$	DC+DPEX
$X^{q+} + H_2 \rightarrow X^{(q-1)+} + H^+ + H^+ + e$	DC+SS

$X^{q+} + H_2 \rightarrow X^{q+} + H^+ + H^+ + 2e$	DC+DS
$X^{q+} + H_2 \rightarrow X^{q+} + H_2^*$	target excitation (TEX)
$X^{q+} + H_2 \rightarrow X^{q+*} + H_2^*$	TEX+SPEX
$X^{q+} + H_2 \rightarrow X^{q+**} + H_2^*$	TEX+DPEX
$X^{q+} + H_2 \rightarrow X^{(q+1)+} + H_2^* + e$	TEX+SS
$X^{q+} + H_2 \rightarrow X^{(q+2)+} + H_2^* + 2e$	TEX+DS

where X stands for the projectile, either O or S. q is the charge state and depends on the number of electrons bound to the ion; q runs from 0 to 8 for O and from 0 to 16 for S. Some processes are not possible for neutral or singly ionized atoms or, similarly, for fully stripped or O^{7+} and S^{15+} ions (e.g., for neutral O and S, SC and DC are not possible, or for O^{8+} and S^{16+} , SS and DS are not considered).

Because the calculation of the cross-sections is not my work, nor the emphasis of this project, I will not go into great detail of the procedure necessary to provide these cross-sections. Rather, I will briefly explain the methodology and motivation behind their calculations and leave the finer details to the references therein.

Very few experimental cross-section measurements exists for oxygen and sulfur collisions with a molecular hydrogen gas and such a comprehensive experiment is currently too large of an undertaking; therefore, Schultz et al. (2019) and Gharibnejad et al. (2019) generate their cross-section data computationally, using the classical trajectory Monte Carlo (CTMC) method. Collisions are simulated with the CTMC method by an iterative solution of Hamilton's equations of motion for the motions of the particles and sampling electron trajectories from a large ensemble of configurations of initial electronic orbits. Using this method, the energy and angle of secondary electrons² are able to be recorded and are described by a data set of singly differential cross-sections (discussed further in the following section). After several million iterations, at various initial ion energies and every ion charge state, the likelihood of each NSIM process can be determined by the integral

²Electrons that have been removed from the projectile or target particle

cross-section produced. The CTMC model has been tested against other collisional systems where more experimental data exists to assess the accuracy of the results, including the comparison of stopping powers, shown in Figure 2.1 (Schultz et al., 2017).

In calculating the NSIM cross-sections, the CTMC method is only able to analyze either projectile electrons or target electrons at one time, not both at the same time, lest the destabilization of the classical model occurs. Therefore, when treating target processes the projectile electrons were considered inactive, and similarly, in the treatment of the projectile processes the target electrons were considered inactive and a multi-electron CTMC model was used. Therefore, calculation of the simultaneous (SIM) cross-sections has to be done independently (Schultz et al., 2017, 2019; Gharibnejad et al., 2019).

The model developed by Schultz et al. (2019) is to partition the NSIM integral cross-sections with respect to all possible SIM processes. The NSIM target processes are calculated without any regard to what is happening to the projectile; that is to say, the target process is achieved without knowing which fraction of collisions also result in a projectile process occurring. The NSIM integral cross-sections for the target processes are therefore partitioned into fractions that describe what happens to the projectile process as well. For example, double ionization (DI) can be split into fractions where it can occur with single projectile excitation (DI+SPEX), with double projectile excitation (DI+DPEX), with single stripping of a projectile electron (DI+SS), with double stripping of a projectile electron (DI+DS), or with nothing happening to the projectile (DI). Ultimately, the fraction of each SIM process is determined by the overlap of probability between the NSIM target processes and projectile processes as a function of impact parameter. The details of these calculations can be found in Schultz et al. (2017, 2019); Gharibnejad et al. (2019) and the references therein. Examples of the oxygen SIM cross-sections for SI and DC+SS are shown in Figures 2.2 and 2.3, and sulfur cross-sections associated with DI and TI are displayed in Figures 2.4 and 2.5.

Figure 2.1 demonstrates the agreement in oxygen stopping power between Schultz et al. (2019) and Ziegler et al. (2013). I also produce a stopping power for both oxygen and sulfur with my

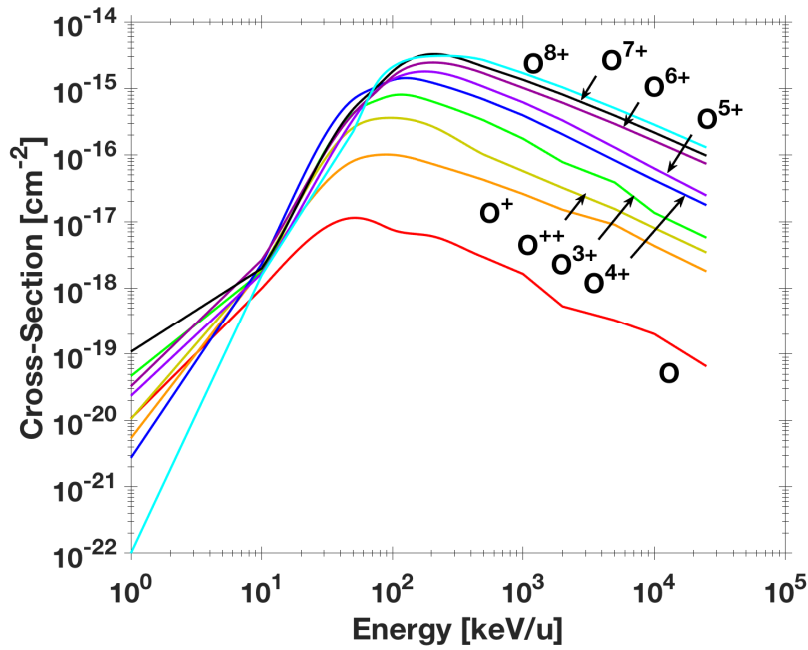


Figure 2.2: SIM single ionization cross-section as a function of energy for collisions of O^{q+} in H_2 . Each curve corresponds to a different charge state, $q = 0 - 8$. Note the dominance of the single ionization cross-section at high oxygen ion energies. Data taken from Schultz et al. (2019).

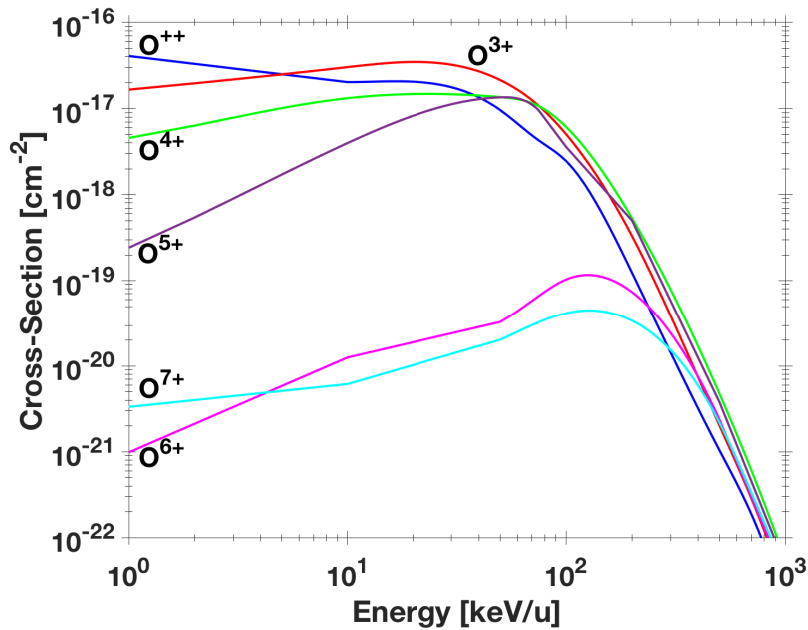


Figure 2.3: SIM double capture + single stripping cross-section as a function of energy for collisions of O^{q+} in H_2 . Each curve corresponds to a different charge state, $q = 2 - 7$. Data taken from Schultz et al. (2019).

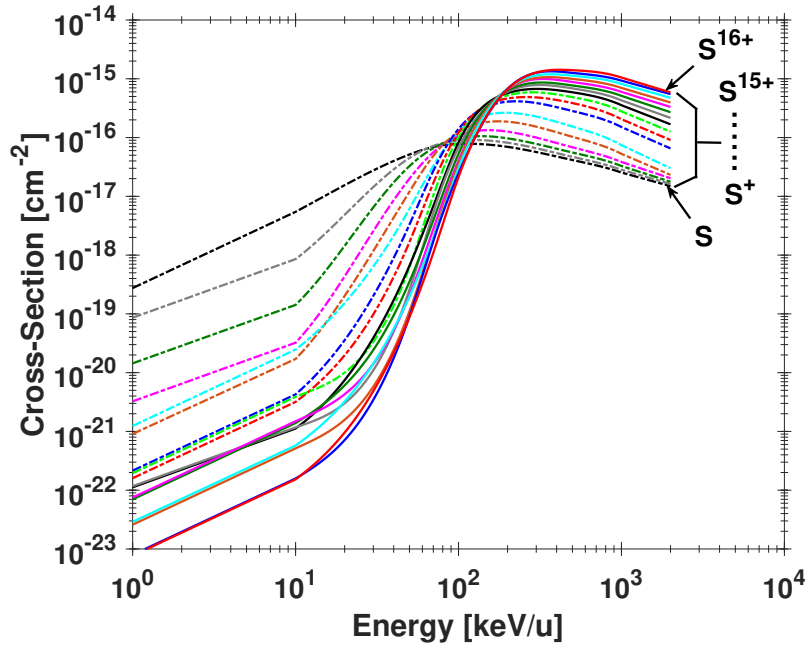


Figure 2.4: SIM double ionization cross-section as a function of energy for collisions of S^{q+} in H_2 . Each curve corresponds to a different charge state, $q = 0 - 16$. Data taken from Schultz et al. (2019).

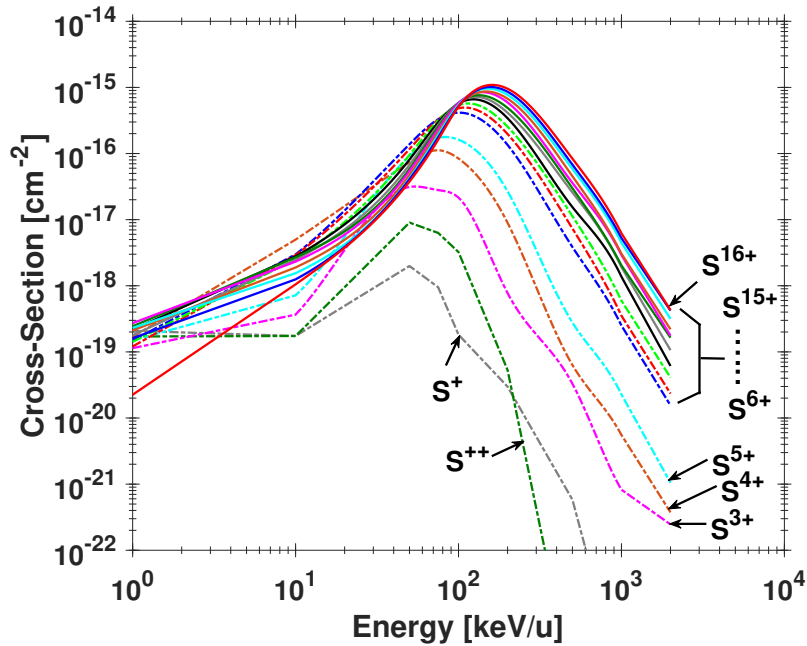


Figure 2.5: SIM transfer ionization cross-section as a function of energy for collisions of S^{q+} in H_2 . Each curve corresponds to a different charge state, $q = 1 - 16$. Data taken from Schultz et al. (2019).

model that I compare with Ziegler et al. (2013) in Figures 2.6 and 2.7. It is evident that the stopping power of oxygen with the references are in fair agreement, especially at high ion energies. However, my stopping power for sulfur does not agree nearly as well as oxygen. The upper energy tail of my precipitation model shows a larger stopping power than what SRIM predicts, and there is a drastic turn to lower stopping power at the middle energy range. This discrepancy is largely because of the error in the sulfur cross-section data at high energies. When sulfur ions become highly ionized, it is harder for Gharibnejad et al. (2019) to model them accurately because of the low cross-sections and the fewer counts their model produces. The poor quality of the stopping power will ultimately be reflected in the charge state distributions, discussed in Chapter 4.

2.2 Energy Loss

After an ion collides with an H_2 molecule there is a certain amount of energy lost (or gained) depending on the type of collision that occurred and the secondary electron energy and angle. The energy change is determined by an energy loss model as described by Schultz et al. (2019) and is shown in Table 2.1. $IP_{1,2}(H_2)$ is the first or second ionization potential (15.43 eV and 16.43 eV, respectively) of hydrogen and $IP_{1,2}(q)$ is the first or second ionization potential of O^{q+} or S^{q+} , shown in Table 4.1. $\langle \Delta e^i(E) \rangle$ is the average energy loss for process i (SC, DC, TI, SPEX, and DPEX) at ion impact energy E and is given in Appendix A for oxygen and Appendix B for sulfur.

$\langle E_e^i(E) \rangle$ is the average ejected electron energy from process i (SI, DI, TI, and DCAI) at a given ion impact energy, E , and can be determined by sampling the singly differential cross-section (SDXS) data. On average, the sampling of the SDXSs will return the average ejected electron energy. The same sampling is also true for ejected electron angle, which is important for the SS and DS processes.

$\langle \tilde{E}_e^{SS,DS}(E) \rangle$ is the average ejected electron energy transformed from the target frame into the projectile frame, since the energy loss of the projectile comes from the electron energy in the projectile frame. The cross-section data for SS and DS are in the target frame, so a straightforward transformation must be done to calculate the correct energy loss (given in Appendix B of Schultz

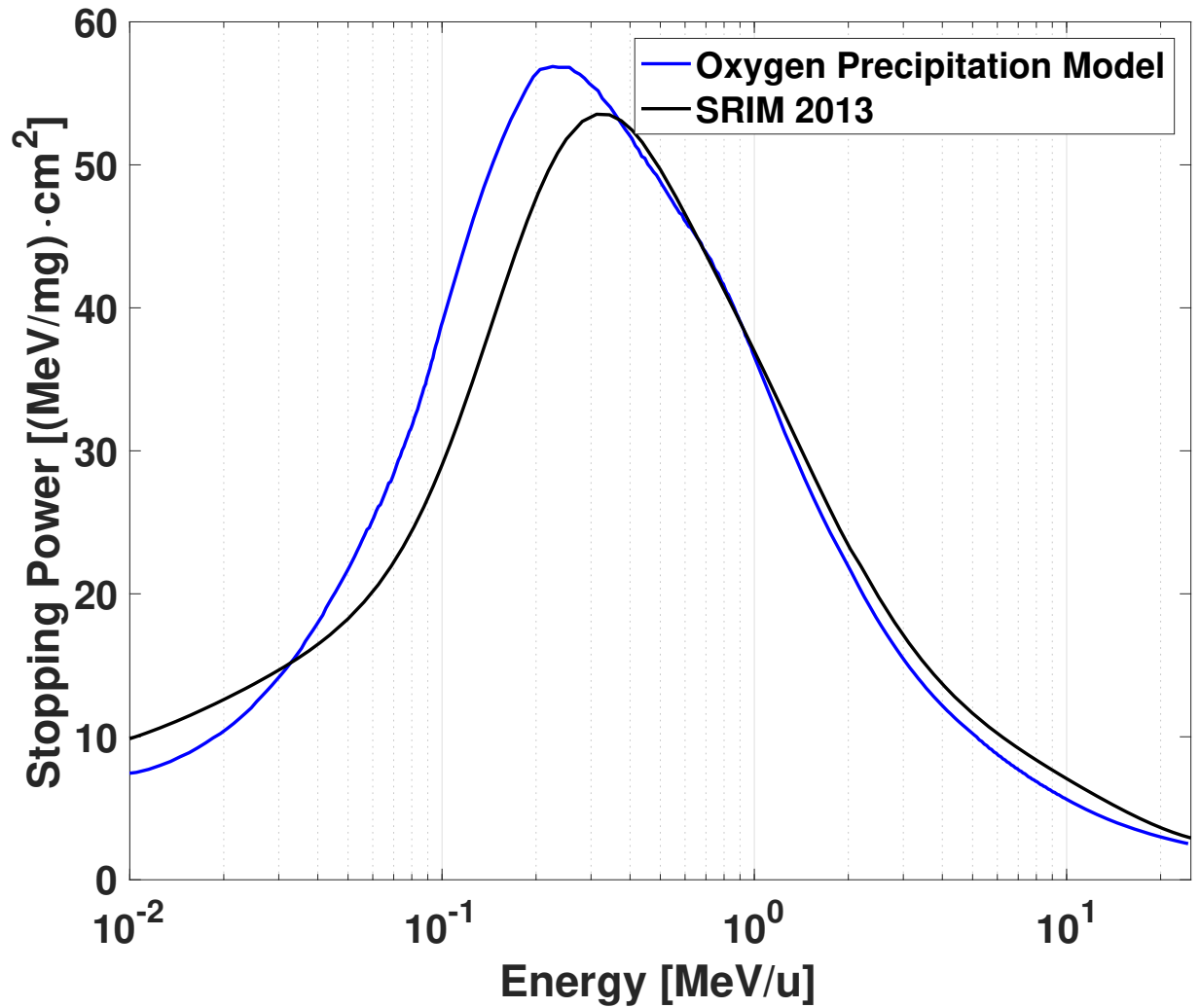


Figure 2.6: Comparison of the stopping power produced by my oxygen precipitation model and the accepted electronic+nuclear stopping power values from SRIM 2013 (Ziegler et al., 2013).

et al. (2019)).

2.2.1 Ejected Electron Energy Transformations

Firstly, let the electron energy in the target frame (i.e., the electron energy sampled with SDXSs) be denoted as E'_e and the electron's velocity in the projectile frame as $\vec{v}=(v_x, v_y, v_z)$, given by

$$E'_e = \frac{1}{2}[v_x^2 + v_y^2 + (v_z + v_{proj})^2] \quad (2.2)$$

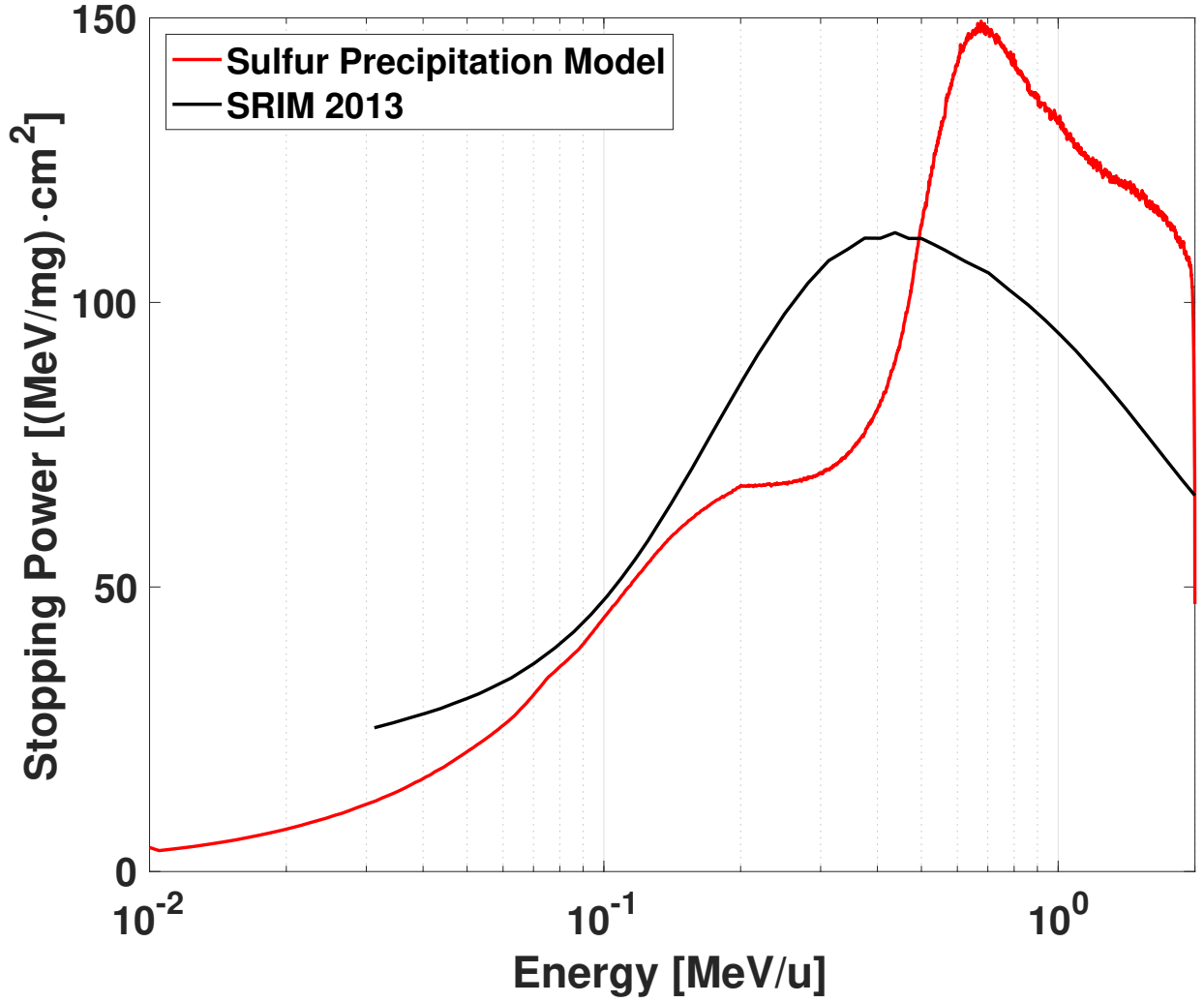


Figure 2.7: Comparison of the stopping power produced by my sulfur precipitation model and the accepted electronic+nuclear stopping power values from SRIM 2013 (Ziegler et al., 2013).

where v_{proj} is the velocity of the projectile. The angle the electron is ejected in the target frame (i.e., the electron angle sampled with SDXSs), θ'_e , is given by

$$\theta'_e = \cos^{-1} \frac{v_z + v_{proj}}{[v_x^2 + v_y^2 + (v_z + v_{proj})^2]^{\frac{1}{2}}} . \quad (2.3)$$

Next, if we solve both Equation 2.2 and 2.3 for the square of the velocity of the ejected electron, $v^2 (= v_x^2 + v_y^2 + v_z^2)$, we obtain

Table 2.1: The energy loss model for each process considered as given in Schultz et al. (2019). For the SIM processes (e.g., DI+SS), the energy loss is the sum of the energy loss of the target and projectile process. $IP_{1,2}(H_2)$ is the first or second ionization potential of hydrogen and $IP_{1,2}(q)$ is the first or second ionization potential of O^{q+} or S^{q+} .

Reaction	Energy loss
TEX	$\Delta e^{EX} = 7.7 \text{ eV}$
SI	$\Delta e^{SI} = IP_1(H_2) + \langle E_e^{SI}(E) \rangle$
DI	$\Delta e^{DI} = IP_1(H_2) + IP_2(H_2) + \langle E_e^{DI}(E) \rangle$
SC	$\Delta e^{SC} = \langle \Delta e^{SC}(E) \rangle$
DC	$\Delta e^{DC} = \langle \Delta e^{DC}(E) \rangle$
TI	$\Delta e^{TI} = IP_1(H_2) + \langle E_e^{TI}(E) \rangle + \langle \Delta e^{TI}(E) \rangle$
DCAI	$\Delta e^{DCAI} = \langle E_e^{DCAI}(E) \rangle$
SS	$\Delta e^{SS} = IP_1(q) + \langle \tilde{E}_e^{SS}(E) \rangle$
DS	$\Delta e^{DS} = IP_1(q) + IP_2(q) + \langle \tilde{E}_e^{DS}(E) \rangle$
SPEX	$\Delta e^{SPEX} = \langle \Delta e^{SPEX} \rangle$
DPEX	$\Delta e^{DPEX} = \langle \Delta e^{DPEX} \rangle$

$$v^2 = 2E'_e - 2v_z v_{proj} - v_{proj}^2 \quad (2.4)$$

$$v^2 = \frac{(v_z + v_{proj})^2}{\cos^2 \theta'_e} - 2v_z v_{proj} - v_{proj}^2 \quad (2.5)$$

Equating these two equations leaves us with the following

$$2E'_e = \frac{(v_z + v_{proj})^2}{\cos^2 \theta'_e} \quad (2.6)$$

We are now left with an expression with all but one known variable, v_z . Solving for v_z yields

$$v_z = \sqrt{2E'_e \cos^2 \theta'_e} - v_{proj} \quad (2.7)$$

Because we are able to derive v_z with all known variables, we obtain the electron ejection energy; and although not needed in my ion precipitation model, for completeness we now also have the angle in the projectile frame

$$E_e = \frac{1}{2}m_e v^2 \quad (2.8)$$

$$\theta_e = \cos^{-1} \left(\frac{v_z}{\sqrt{v^2}} \right) \quad (2.9)$$

where v^2 can be calculated from Equation 2.4. Thus, the transformation of electrons from the target frame into the projectile frame by sampling E'_e and θ'_e is accomplished and SS and DS energy loss values can be calculated.

2.3 Neutral Atmospheres

All of the planets in the solar system, along with some satellites, have an atmosphere that is considered to be in hydrostatic equilibrium or hydrostatic balance. That is to say, the force of gravity on the atmosphere is balanced by the pressure gradient force, or

$$\nabla p = \rho \mathbf{g} \quad (2.10)$$

where ∇p is the gradient of the atmospheric pressure, ρ is the atmospheric density, and \mathbf{g} is the acceleration due to gravity and can be written as $\mathbf{g} = -g\hat{\mathbf{z}}$. Now, with all quantities as a function of altitude, z , and with the equation of state ($\rho = mp/k_B T$), Equation 2.10 can be written as

$$\frac{\partial p}{\partial z} = -\rho g = -\frac{mg}{k_B T} p \quad (2.11)$$

where k_B is the Boltzmann constant, m is the appropriate mean mass of the molecules that make up the given fluid under consideration, and T is the temperature. Equation 2.11 can easily be solved such that

$$p(z) = p_0 \exp \left\{ - \int_{z_0}^z \frac{mg dz'}{k_B T(z')} \right\} \quad (2.12)$$

where p_0 and z_0 are reference points for a given pressure and altitude, respectively. When considering a limited altitude range, one can assume an isothermal atmosphere, where $T = \text{constant}$, and

that gravity is constant. Thus, Equation 2.12 becomes

$$p(z) = p_0 e^{-(z-z_0)/H} \quad (2.13)$$

where H is the scale height,

$$H \equiv \frac{k_B T}{mg}. \quad (2.14)$$

The scale height is the e -folding length and describes the increase in height with which the pressure decreases exponentially. It is a useful tool for the upper atmosphere, where one can approximate atmospheric isothermality on the order of multiple scale heights. (Note: The scale heights for Earth and Jupiter are roughly 8 km and 30 km, respectively.)

An important consideration for the model is the atmospheric profile. The density of atmospheric constituents and the scale height determine how far an ion will move before undergoing a collision and the column density dictates the amount of photoemission escapes the atmosphere. The more atmosphere an ion or photon travels through, the higher probability of a collision or photoabsorption.

Because all of the ion impact cross-sections I use are ion-neutral collisions with molecular hydrogen, the primary constituent in the atmosphere of Jupiter, I often show figures that are with respect to H_2 density, with altitude as a secondary axis. This negates the necessity of having to know the exact H_2 distribution in the Jovian atmosphere, the exact altitude can be adjusted when there are better measurements of the polar atmosphere. However, this becomes more difficult when considering alternate species that need to be adjusted based on how they react chemically in the atmosphere, especially above the homopause. I resolve this by proposing two atmospheres, discussed in the following section.

2.3.1 Jupiter

Houston et al. (2018) used a neutral atmosphere originally presented by Maurellis & Cravens (2001) based on Galileo probe data (Seiff et al., 1996, 1997) and remote observations (Sada et al.,

1998). The same atmosphere is used here, only I have extended the depth from 200 km to -88 km, where 0 km is set to where the pressure is equal to 1 bar (Fig. 2.8). The atmosphere below 200 km has been generated using temperature-pressure profiles retrieved from NASA's Infrared Telescope Facility and the Texas Echelon Cross Echelle Spectrograph Instrument (IRTF-TEXES) (Sinclair et al., 2018). Using the temperature and pressure, the ideal gas law is then solved to obtain the total number density. Because this is below the homopause, where a well-mixed atmosphere is present, the mixing ratios from 200 km are extended down to -88 km to calculate the number density of each species.

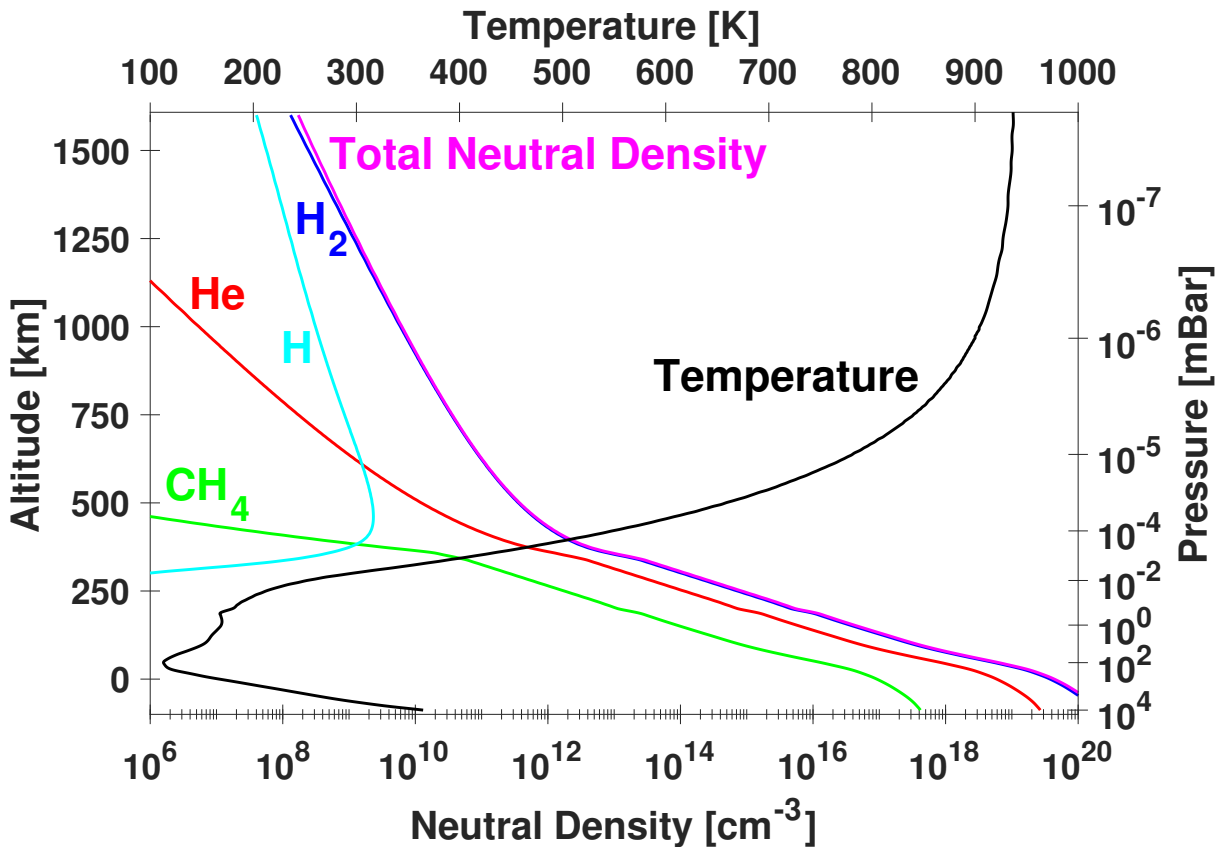


Figure 2.8: Atmospheric density profiles of H₂, He, CH₄, and H based on data shown in Maurellis & Cravens (2001) and Sinclair et al. (2018), referred to as atmosphere 1. Also shown is the neutral temperature profile as a function of altitude and pressure.

The *in situ* measurements of the Galileo probe were taken when it plummeted into the equatorial atmosphere, not the polar atmosphere. Thus, there has been much speculation about the composition of the atmosphere over the polar caps (see Section 5.2 of Clark et al. (2018), Gérard

et al. (2014), and Parkinson et al. (2006)). To help combat this, I generate a second atmospheric profile (Figure 2.9) by taking the mixing ratio of molecular hydrogen to helium and methane at the bottom of the density profile in Figure 2.8 and then redistribute the helium and methane from the top of the atmosphere with that same mixing ratio. This allows for a completely well-mixed atmosphere that ignores a defined homopause; rather, the entire atmosphere is homogeneous. The H_2 distribution of this atmosphere remains the same as that in Fig 2.8, thus ion precipitation will not be effected because only ion collisions in a hydrogen gas are considered. However, when photoemission is discussed, the well-mixed atmosphere will have greater photoabsorption effects. Atomic hydrogen is ignored in the well-mixed atmosphere because of how chemically active it tends to be (as can be seen in the original atmosphere, below the homopause) and it is not unreasonable to think the column density of H will have negligible effects on the opacity of X-ray emission, as it does in the original atmosphere. I will refer to the atmosphere displayed in Figure 2.8 as “atmosphere 1” and the well-mixed atmosphere in Figure 2.9 as “atmosphere 2”.

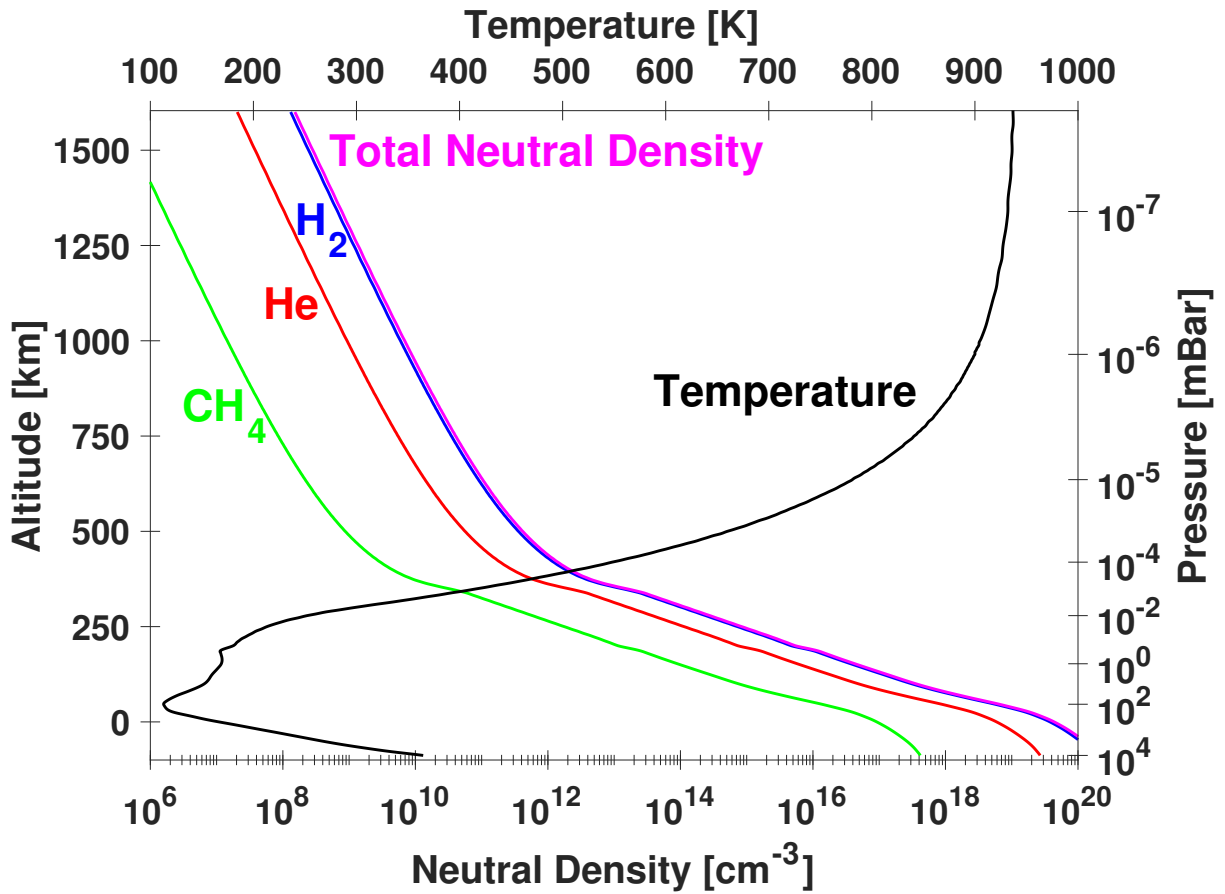


Figure 2.9: Atmospheric density profiles of H_2 , He, and CH_4 in my well-mixed atmosphere, referred to as atmosphere 2. Also shown is the neutral temperature profile as a function of altitude and pressure.

Chapter 3

Electron Precipitation

3.1 Introduction

Several types of precipitating particles and atoms play key roles in the Jovian auroral atmosphere. For example, ion precipitation is the major contributor to X-ray emission coming from high altitudes over the polar caps. However, electrons are the dominant species in the Jovian magnetosphere and are responsible (along with protons) for the main auroral oval. They also contribute to soft X-ray production through electron bremsstrahlung, but, more importantly, electrons are the primary current carriers into the top of the atmosphere and in the ionosphere.

There are several mechanisms for electron generation in the auroral atmosphere. First, electrons are produced through photoionization of atmospheric constituents. This is the main contributor to the ionosphere at Earth; however, at Jupiter this plays much less of a role due to the large number of electrons produced by particle precipitation and the relatively low solar photon flux at 5.2 AU. There are photoionized electrons in the Jovian ionosphere, but due to their low density compared to other sources, I do not consider them in this model.

A second method of electron production in the atmosphere is from precipitating magnetospheric electrons, referred to as electron precipitation. This mechanism is responsible for the extremely intense UV aurora shown in Figure 1.4 and also produces soft X-rays from electron bremsstrahlung. The X-rays emitted from electron precipitation are very different than those generated by heavy ion precipitation. The X-ray spectrum due to bremsstrahlung is a continuum rather than discrete line emission, and it is primarily associated with the main auroral oval, not the polar caps.

A third method of electron generation is secondary electron production from the precipitation of either electrons or ions into the atmosphere. Many of the ion-neutral collisions listed in Section 2.1 produce one or multiple electrons. These are the resulting electrons referred to as secondary electrons and I book-keep every one produced, including the energy and angle of said electrons. To simulate the consequences of both electron precipitation and secondary electron production, I use a two-stream model.

3.2 Two-Stream Model

Ion precipitation produces secondary electrons from ionization or stripping collisions and this is included in the ion Monte Carlo simulation. The heavy ion model tracks secondary electrons, recording their energy, the altitude where they were produced, and the direction in which they were ejected (downward deeper into the atmosphere or upward escaping it). The secondary electrons, some of them rather energetic, also interact with the neutral atmosphere. I model the electron fluxes with a two-stream approach adapted to include the appropriate cross-sections for the Jovian atmospheric composition. The two-stream model yields electron fluxes, ion production rates, Lyman and Werner band emission rates, and escape-electron energy and power spectra. Originally, the two-stream model was used for photoelectron interactions at Earth (Banks & Nagy, 1970; Nagy & Banks, 1970). Since then it has been further developed for modeling of electron transport for various comets, Saturn's moon Titan (Cravens et al., 2008; Gan & Cravens, 1992; Gan et al., 1993; Robertson et al., 2009), and Enceladus (Ozak et al., 2012). I use a modified two-stream code that was directly adapted for Jupiter's polar region (Ozak Munoz, 2012; Ozak et al., 2013).

In this research, I primarily use the two-stream model for analysis of secondary electron production from heavy ion precipitation. However, it can be used for low (non-relativistic) electron precipitation, which I will show results for here. Electron precipitation of course includes the production of secondary electrons, which are taken into account by the two-stream model. The secondary electron production associated with heavy ion precipitations is discussed later in Chapter 4.

3.2.1 Physical Process

For the two-stream method electrons are considered to move only up (with flux Φ^+) or down (flux Φ^-) the magnetic field line, as a function of energy, ϵ , and path length, s . The equations used are as follows (Banks & Nagy, 1970; Nagy & Banks, 1970):

$$\frac{d\Phi^\mp}{ds} = - \sum_k n_k(s) (\sigma_{inel}^k + p_s^k \sigma_s^k) \Phi^\mp(\epsilon, s) + \sum_k n_k(s) p_e^k \sigma_e^k \Phi^\pm(\epsilon, s) + q_{prec}(\epsilon, s) + q^\mp(\epsilon, s) \quad (3.1)$$

where n_k is the neutral density of the atmospheric species, k , σ_{inel}^k is the total inelastic cross-section for a neutral species, and p_s^k and σ_s^k are the electron backscatter probability and cross-section, respectively. The first term of the equation calculates the loss of electrons from the flux in each direction due to absorption or backscatter. The second term, p_e^k and σ_e^k , are the elastic probability and cross-section. The third term, $q_{prec}(\epsilon, s)$, is the secondary electron production rate provided by the ion precipitation model. The final term, $q^\mp(\epsilon, s)$, is the electron production rate due to cascading from higher energies by inelastic collisions, which involves keeping track of every electron as they move from one energy bin to another. Variable energy bins are used with widths ranging from 0.5 eV for low electron energies below 10 eV and increasing to 200 eV wide bins for energies near 10 keV.

3.2.2 Electron Impact Cross-Sections

The electron impact cross-section data has been compiled from multiple sources by Ozak Munoz (2012). I have largely taken the work done by her, and reused it in the two-stream model. Although not my work, I will discuss her motivation here. The cross-sections for electron impact with molecular hydrogen have been adapted from a compilation done by Yoon et al. (2008) (Y08), who recommend the best available experimental values at the time the paper was written. Whenever available, Ozak Munoz (2012) prioritized the use of experimental data over theoretical data. However, to have the cross-section information in a form compatible with the code and to have the cross-section values where experimental data was missing, she fitted the available data with analyt-

ical functions commonly used for the computation of cross-sections. For the electron-H₂ inelastic collisions she fitted the data with the analytical function adapted from Green & Dutta (1967); Miles et al. (1972); Garvey et al. (1977). For the ionization cross-sections, she used the approximation given by Green & Sawada (1972) to fit the Y08 data. For the electron impact excitation cross-sections for the singlet states, B¹Σ_u⁺ and C¹Π_u, she based computation on the measurements done by Liu et al. (1998). For the E,F¹Σ_g⁺ state she used the data obtained by Liu et al. (2003). For the remaining singlet excitation states, she adapted the values given by Dalgarno et al. (1999). Cross-sections for H Ly-α emission by dissociation have been obtained from data reported by Ajello et al. (1995) and fitted by an analytical function given by Shemansky et al. (1985). The electron ionization cross-section for H₂ was fitted to the recommended values measured by Straub et al. (1996).

Electron impact cross-sections for He were obtained by Jackman et al. (1977), electron-H cross-sections for electron energies below 3 keV were taken from Olivero et al. (1973) and from Stone & Kim (2002) for energies higher than 3 keV. Total ionization cross-sections for electron impact with atomic H were fitted to data from Shah et al. (1987). Finally, electron-CH₄ impact cross-sections were adapted from Gan & Cravens (1992) and Gan et al. (1992). An example from Ozak Munoz (2012) of the impact cross-sections can be seen in Figure 3.1 which shows the cross-section for the excited singlet state B¹Σ_u⁺ in H₂, the state responsible for the Lyman excitation band. For the finer details on the fitting parameters for the analytical functions to all the cross-sections computed I refer the reader to Ozak Munoz (2012).

3.2.3 Results

Juno has measured electrons with energies up to 1 MeV in the polar aurora region (Connerney et al., 2017; Clark et al., 2018). An electron with energy of 100 keV travels at about $0.2c$. As noted above, the two-stream model is inadequate at modeling electron precipitation at high energies because it does not take into account relativistic effects. This is perfectly suitable for secondary electron production, because they are not produced at relativistic energies and certainly not above

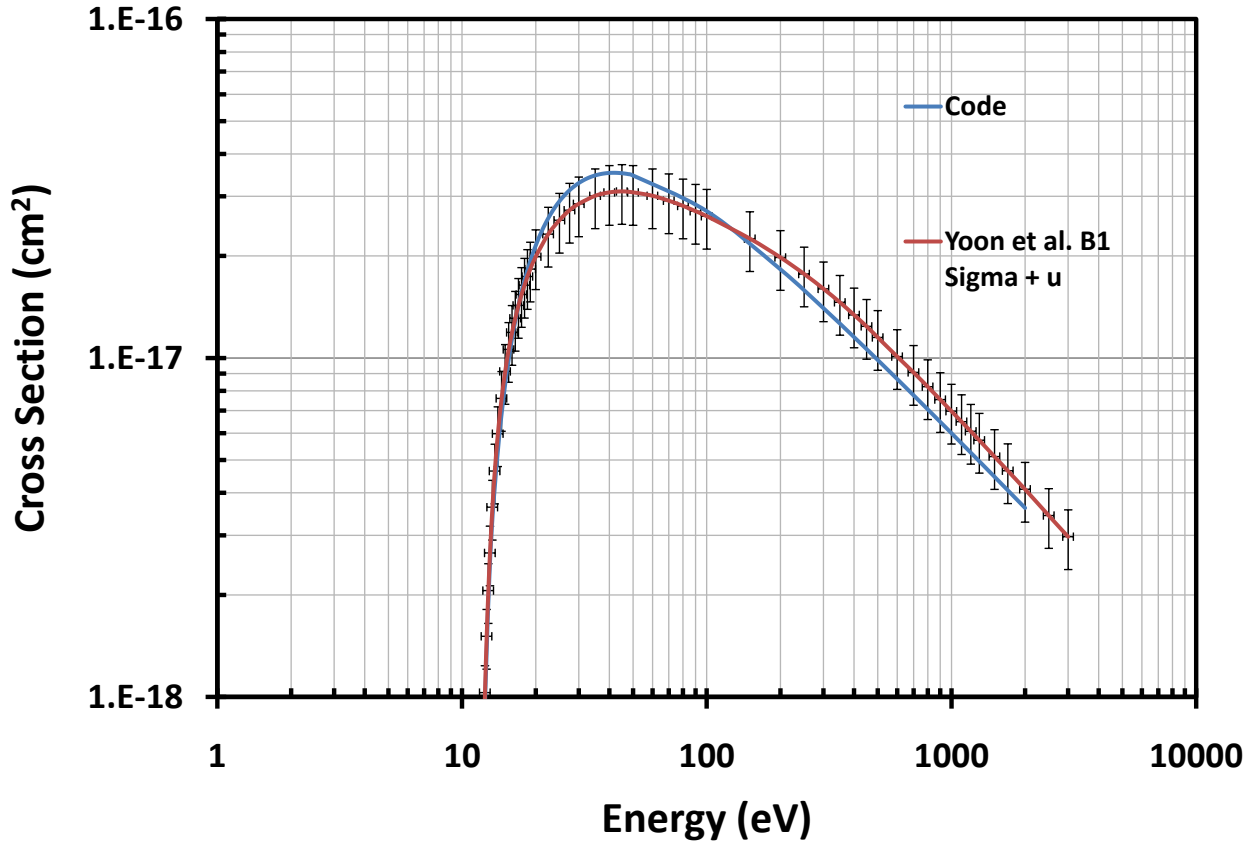


Figure 3.1: Lyman band ($B^1\Sigma_u^+$) excitation cross-sections in H_2 from electron impact. Compared here are the cross-sections produced by Yoon et al. (2008) and the two-stream code. The vertical bars associated with the Y08 data represent an experimental error of 20%. This figure has been taken directly from Ozak Munoz (2012).

100 keV. Thus, to see a comprehensive electron precipitation model of the main auroral oval, I refer the reader to Gérard et al. (2014), but here I present results associated with low energy electron precipitation to provide an idea of the implications. I input monoenergetic electron beams at energies of 5, 10, 20, 50, 100, and 200 keV with an input power of 1 mW/m^2 and an isotropic distribution of incident pitch angles. Every run through the two-stream model is through atmosphere 1, rather than the well-mixed atmosphere, atmosphere 2, unless explicitly stated.

The B+C volume emission rate for each electron beam is displayed in Figure 3.2, which also shows the location in the atmosphere of the energy deposition. When comparing this to Figure 6 of Gérard et al. (2014) one sees a difference of $\sim 50\%$ and $\sim 30\%$ in volume emission rate and penetration depth, respectively, for electron beams over 20 keV, with my electron beams produc-

ing less emission and penetrating deeper into the atmosphere, particularly as the electron beams increase in energy. However, for the lower energy electron beams, i.e. 5, 10, and 20 keV, the two-stream volume emission rate is only about 10% less than that reported by Gérard et al. (2014). I attribute the discrepancy to a difference in cross-sections used and my use of about half an order of magnitude higher CH_4 number density below pressures of 10^{-4} mBar, shown in Figure 3.3. It is important to keep in mind that this two-stream model does not account for relativistic electron energies, as well.

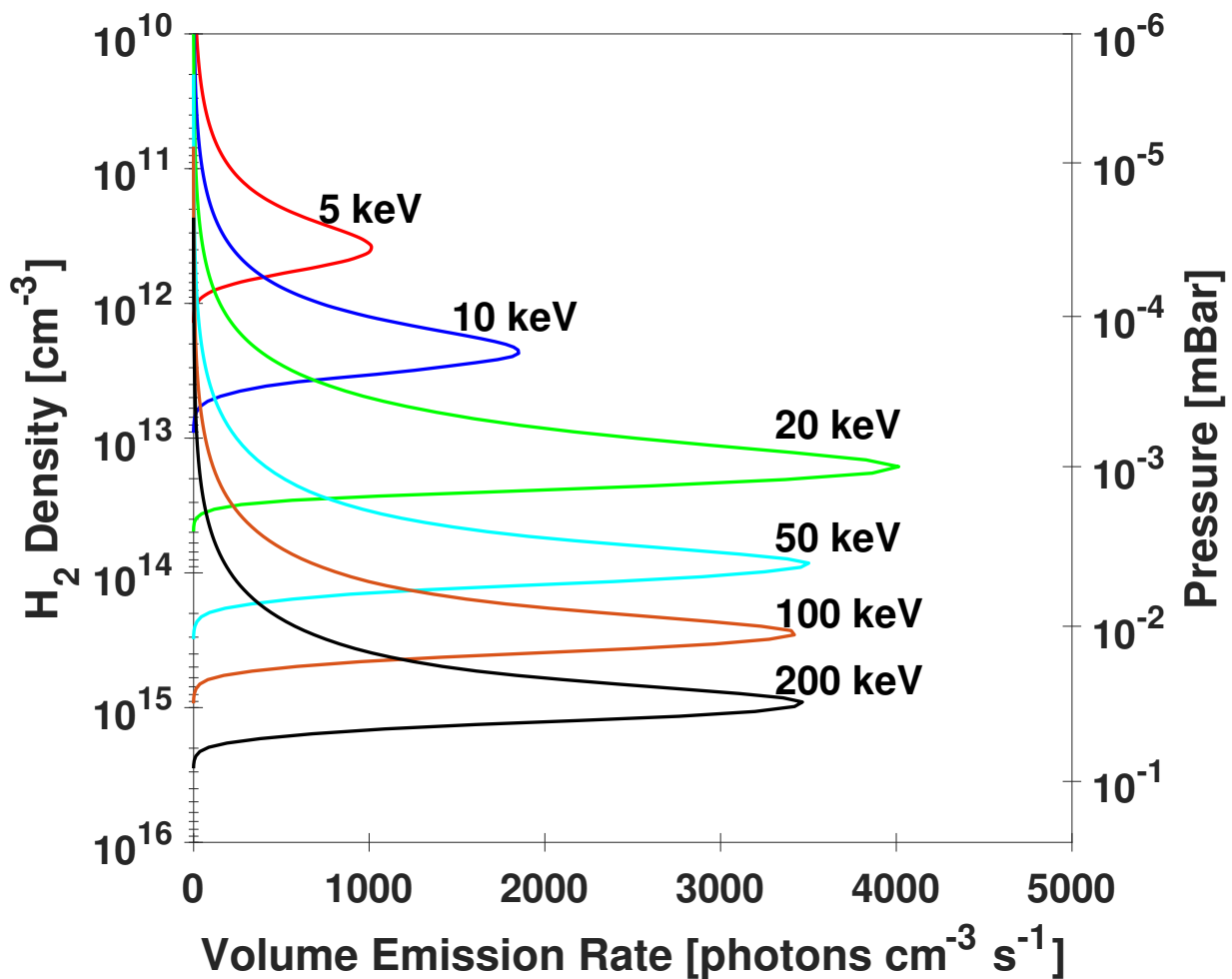


Figure 3.2: Volume emission rate of various monoenergetic electron beams of 1 mW/m^2 into the top of Jupiter's atmosphere (atmosphere 1). The emission rate includes H_2 Lyman and Werner band emission and Lyman alpha line emission from H, which contributes a very small amount to the overall emission rate.

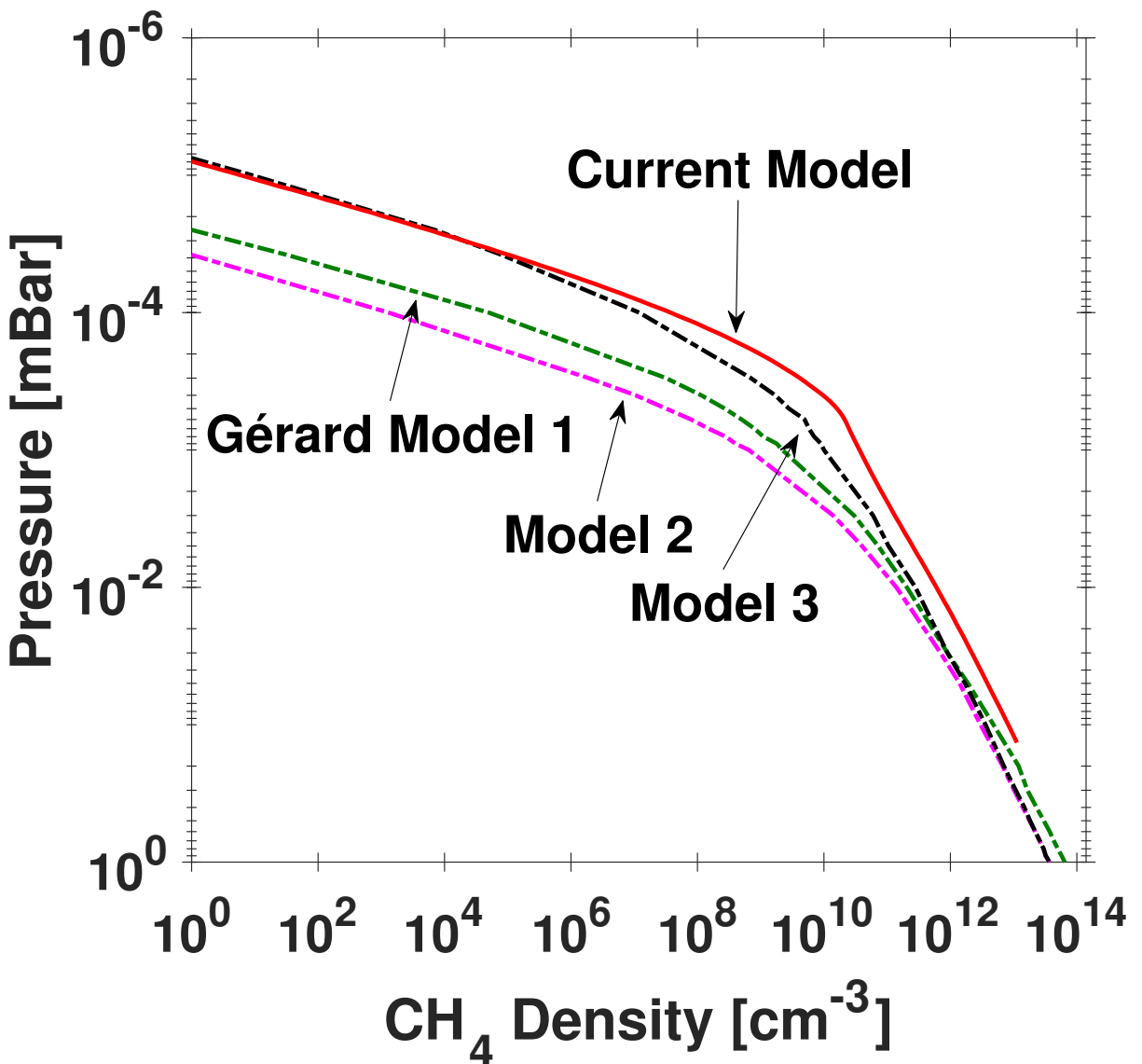


Figure 3.3: Vertical distribution of methane number density vs. pressure for the model used in the current paper (red solid line) compared to those used by Gérard et al. (2014) (dashed-dotted lines). The model numbers are the same as those used by Gérard et al. (2014), where more information can be found on the atmospheric models.

Figure 3.3 compares the atmospheric methane distribution used in the present research to that used by Gérard et al. (2014). They consider three different atmospheric models (numbered the same in Figure 3.3) obtained from Moses et al. (2005) and Grodent et al. (2001). When comparing my results to theirs, it is important to remember there is also a difference in the H₂ density relative to the CH₄ density. When I use their atmospheric model for my results, I only use their methane distribution for results produced by my model with my H₂ column density.

3.2.4 Synthetic Ultraviolet Spectrum

Any energetic particle, electron or ion, will both ionize and electronically excite atmospheric species, particularly H₂. For example, the excitation of the B¹Σ_u⁺ and C¹Π_u states of H₂ leads to UV airglow in the Lyman and Werner bands. Excitation of atomic hydrogen either directly with H or from dissociative excitation collisions with H₂ produces Ly-α photons. Cascading processes from higher electronic states can also produce Lyman and Werner band emission (~10% of the Lyman band emission).

To simulate the UV spectrum, I assume the laboratory spectrum results of e⁻ + H₂ from Dziczek et al. (2000) where 20 eV electrons were used for electron impact with H₂ and UV resonance transitions determined by both direct excitation and cascade processes are considered. The dominant 121.6 nm Lyman-α band has been ignored due to the difficulties in calculating opacity effects that are different from Lyman-Werner emission. I reproduce the same laboratory spectrum with Lyman-Werner emission generated from precipitating electrons in Figure 3.4. To do this, I normalize the UV spectrum to a total intensity of 1 and then multiply the Lyman-Werner production from my electron precipitation and the two-stream model by the normalized spectrum to get production as a function of wavelength. Photoabsorption cross-sections of methane from Kameta et al. (2002) are used for 90-120 nm, Chen & Wu (2004) for 120-160 nm, and Hudson (1971) for 160-170 nm.

The spectrum intensity, $I(\lambda)$, along line of sight is calculated as

$$4\pi I(\lambda) = \int P(\lambda, z) e^{-\tau(\lambda, z)} dz \quad (3.2)$$

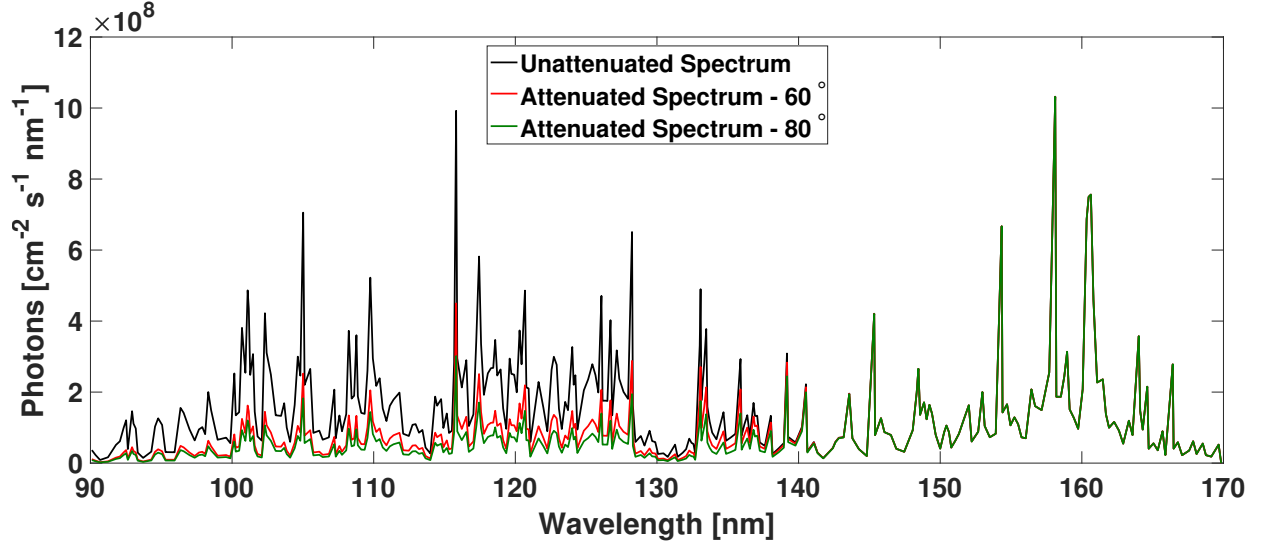


Figure 3.4: Predicted Lyman-Werner spectrum from a 20 keV monoenergetic electron beam with an input of 1 mW/m^2 . The red line is calculated with a θ of 60° and the green line with a θ of 80° , while the black line is what is expected when no opacity effects are considered. The Ly- α line at 121.6 nm has been withheld from these predictions.

where $P(\lambda, z)$ is the production rate of Lyman-Werner band emission as a function of both wavelength, λ , and altitude, z . $\tau(\lambda, z_0)$ is the optical depth due to photoabsorption of methane at altitude z_0 and is denoted as

$$\tau(\lambda, z_0) = \sigma_{CH_4}(\lambda) \int_{z_0}^{\infty} n_{CH_4}(z) \sec\theta dz \quad (3.3)$$

where $\sigma_{CH_4}(\lambda)$ is the photoabsorption cross-section of methane for a given λ , $n_{CH_4}(z)$ is the density of methane for a given altitude, and $\sec\theta dz$ is the path length along the line of sight. For my results, I use a viewing angle, θ , of both 60° and 80° with respect to the axis of rotation. Also presented in Figure 3.4, along with an unabsorbed spectrum, is a predicted UV spectrum with an attenuation that is dependent upon the depth of electron penetration, the location of Lyman-Werner band production in the atmosphere, and consequently the initial electron energy input.

3.2.5 Color Ratios

The so-called color ratio in the UV spectral region has been useful for estimating the depth of penetration of precipitating electrons at Jupiter and Saturn. Basically, hydrocarbon species (e.g.,

CH₄) concentrated below the homopause absorb more at some wavelengths than others, which modifies the emergent UV spectrum (e.g., Gustin et al. (2012, 2016)). The color ratio (CR) has been defined as

$$CR = \frac{\int_{155}^{162} I(\lambda) d\lambda}{\int_{123}^{130} I(\lambda) d\lambda} \quad (3.4)$$

where $I(\lambda)$ is the intensity at a given wavelength (in units of nm). The CR is simply the ratio of photons between 155-162 nm (largely unabsorbed by hydrocarbons) and 123-130 nm (more readily absorbed by hydrocarbons).

Color ratio is a good indicator for hydrocarbon column densities penetrated by precipitating electrons. A higher value of CR is indicative of a higher hydrocarbon density and, in the case of Jupiter, UV rays being produced deeper in the atmosphere. This is due to hydrocarbons having a high photoabsorption cross-section for wavelengths shorter than 140 nm. In my color ratio calculation, I only consider methane as the photoabsorber of UV photons. For me, an unabsorbed spectrum has a CR equal to 1.32.

Observations made by the Hubble Space Telescope were interpreted using color ratio, which allowed incident electron energies to be estimated (Gérard et al., 2014). This has been followed by color ratio measurements made by the UV spectrometer onboard the Juno spacecraft (Gladstone et al., 2017a; Bonfond et al., 2017; Connerney et al., 2017). Both Gérard et al. (2014) and Bonfond et al. (2017) have shown color ratios between 1 and 20 for the Juno UV observations. In the current paper, I include color ratio, as well as overall airglow intensity, for both ion and electron precipitation models. Note, however, that color ratio is sensitive to the distribution of methane in the neutral atmosphere model.

Figure 3.5 demonstrates that color ratio goes up, as expected, as the initial monoenergetic electron energy increases and penetrates deeper into the atmosphere where there are higher levels of methane. Depending on the atmosphere, the color ratio begins deviating from 1.32 for energies higher than 20 keV in atmosphere 1 and 10 keV in atmosphere 2. Gérard et al. (2014) have an electron CR with an unabsorbed value of 1.1. They discuss 3 different atmosphere models (Fig. 3.3) in their calculation, and each model stays close to a CR value of 1.1 until the electron beam

is ~ 50 keV. With 100 keV electrons, Gérard et al. (2014) have color ratios between 1 and 2. This differs greatly from my calculations at 100 keV, which correspond to a CR of ~ 76 in atmosphere 1. All of their calculations are done with a viewing angle of 60° . The higher column density of CH_4 in my atmospheric model can once again partially explain this difference, since CH_4 is the main absorber of UV emission and my electrons are penetrating deeper into the atmosphere (perhaps due to a difference in H_2 column density and/or a difference in electron impact cross-sections used by the two different electron transport models).

I also overlay two lines onto Figure 3.5 that correspond to an upper limit color ratio for the polar cap and main auroral oval region for the northern hemisphere in Figure 1.12. The highest CR associated with the main auroral oval is about 6. This correlates to an electron beam of 30 keV in atmosphere 1 at a viewing angle of 0° (i.e., if the Juno spacecraft is directly above the pole when it makes the UV color ratio measurement), or a 8 keV electron beam if the well-mixed atmosphere 2 is considered and the observation is from an angle of 80° with respect to the spin axis. The polar cap has a max color ratio of 20 in Figure 1.12. This CR corresponds to an electron beam with an initial energy of about 50 keV in atmosphere 1, with an exit angle of 0° .

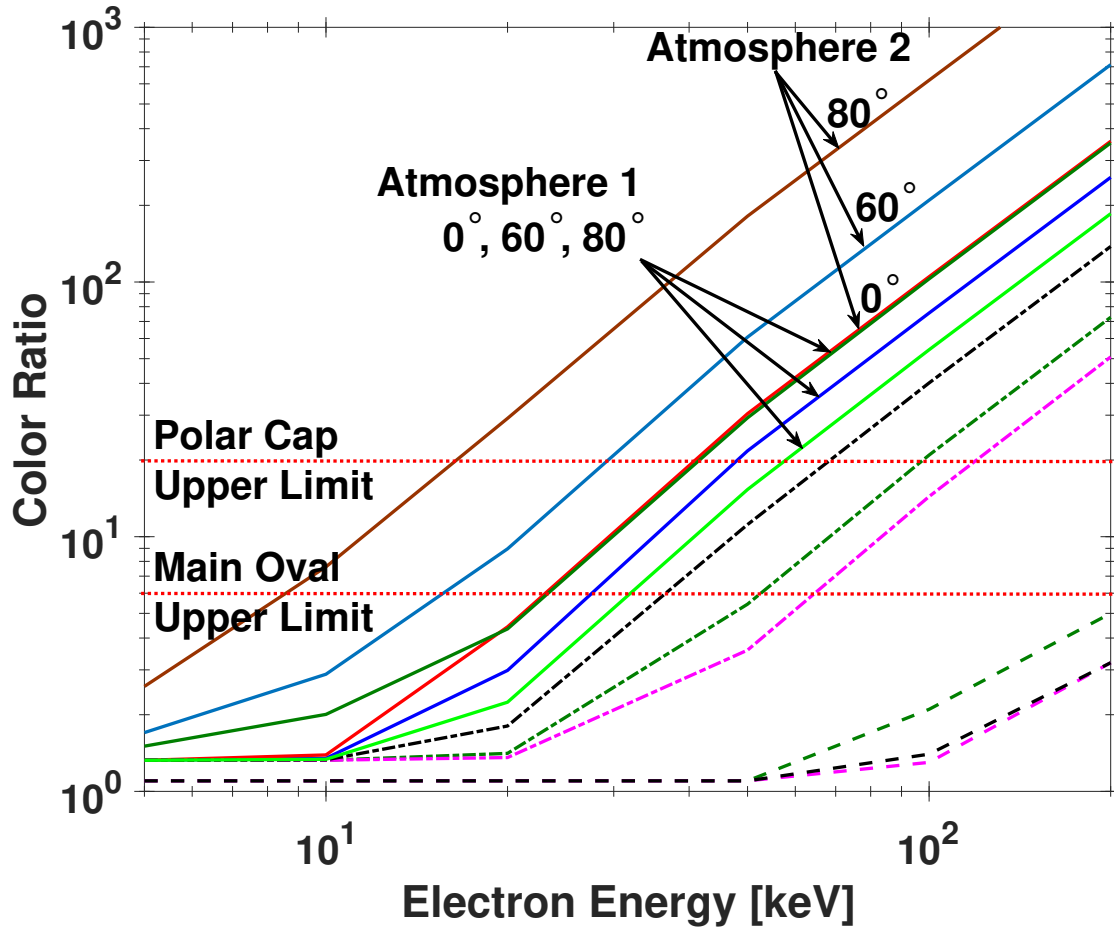


Figure 3.5: Initial monoenergetic electron beam energy vs. color ratio for three viewing angles of 0°, 60°, and 80°. The solid blue and red lines are color ratio measurements with an electron input using my two-stream model and the methane distribution from atmosphere 1 (Fig. 2.8). The solid maroon and dark blue lines are color ratio measurements with an electron input using my two-stream model and the methane distribution from atmosphere 2 (Fig. 2.9). The dashed-dotted lines are my two-stream model with the methane distributions presented in Gérard et al. (2014), at a viewing angle of 60°. The dashed lines are results from Gérard et al. (2014) using their electron transport model with their different atmosphere models. The green lines correspond to their model 1, pink to their model 2, and black to their model 3. The unattenuated color ratio is 1.32 for my precipitation model and 1.1 for theirs. Overlaid are two lines that represent the CR upper limit values of the polar cap and main oval associated with Figure 1.12.

3.2.6 Field-Aligned Currents

Generally, field-aligned currents (FAC) that go into the top of the ionosphere are carried by cold, upmoving electrons and FAC that are directed out of the ionosphere are created by precipitating electrons. Thus, the electron precipitation from the two-stream code will produce upward (out of the atmosphere) and downward (into the atmosphere) currents from the fast moving ("hot") electrons precipitating and the secondary backscattered ("cold") electrons, respectively. Although, as I have discussed, the two-stream code is better suited for secondary electrons than electron precipitation, I think it is important to discuss the affects on the FAC due to precipitating electrons. These type of electron beams would likely be seen over Jupiter's main auroral oval, rather than the polar caps.

Figure 3.6 shows the upward secondary electron flux that I predict will leave the atmosphere (at 3000 km) from monoenergetic electron beams with an initial input power of 1 mW/m². Each of these escaping electron fluxes have a stark cut off at the input energy of the electron beam, this is because energy is conserved and the precipitating electrons will not be able to produce secondary electrons with energies greater than they carry. The plot uses "stairs" for the lines so that the size of the 2-stream electron energy bins can be seen by the width of each step. The upward electron fluxes represent a downward field-aligned current which should be offset with the upward current carried by downwardly moving electrons, shown in Table 3.1.

Table 3.1: Monoenergetic electron beam primary input current density, energy flux, electron flux, and secondary current density per 1 mW/m².

Energy [keV]	Primary Current Density [A/m ²]	Escape Energy Flux [eV/cm ² /s]	Escape Electron Flux [electrons/cm ² /s]	Secondary Current Density [A/m ²]
5	2.04E-09	2.04E+10	1.35E+07	2.17E-12
10	1.01E-09	1.91E+10	5.69E+06	9.12E-13
20	1.03E-10	1.28E+10	2.10E+06	3.36E-13
50	7.77E-12	1.07E+10	6.26E+05	1.00E-13
100	2.02E-12	9.63E+09	2.86E+05	4.58E-14
200	1.06E-12	8.71E+09	1.34E+05	2.15E-14

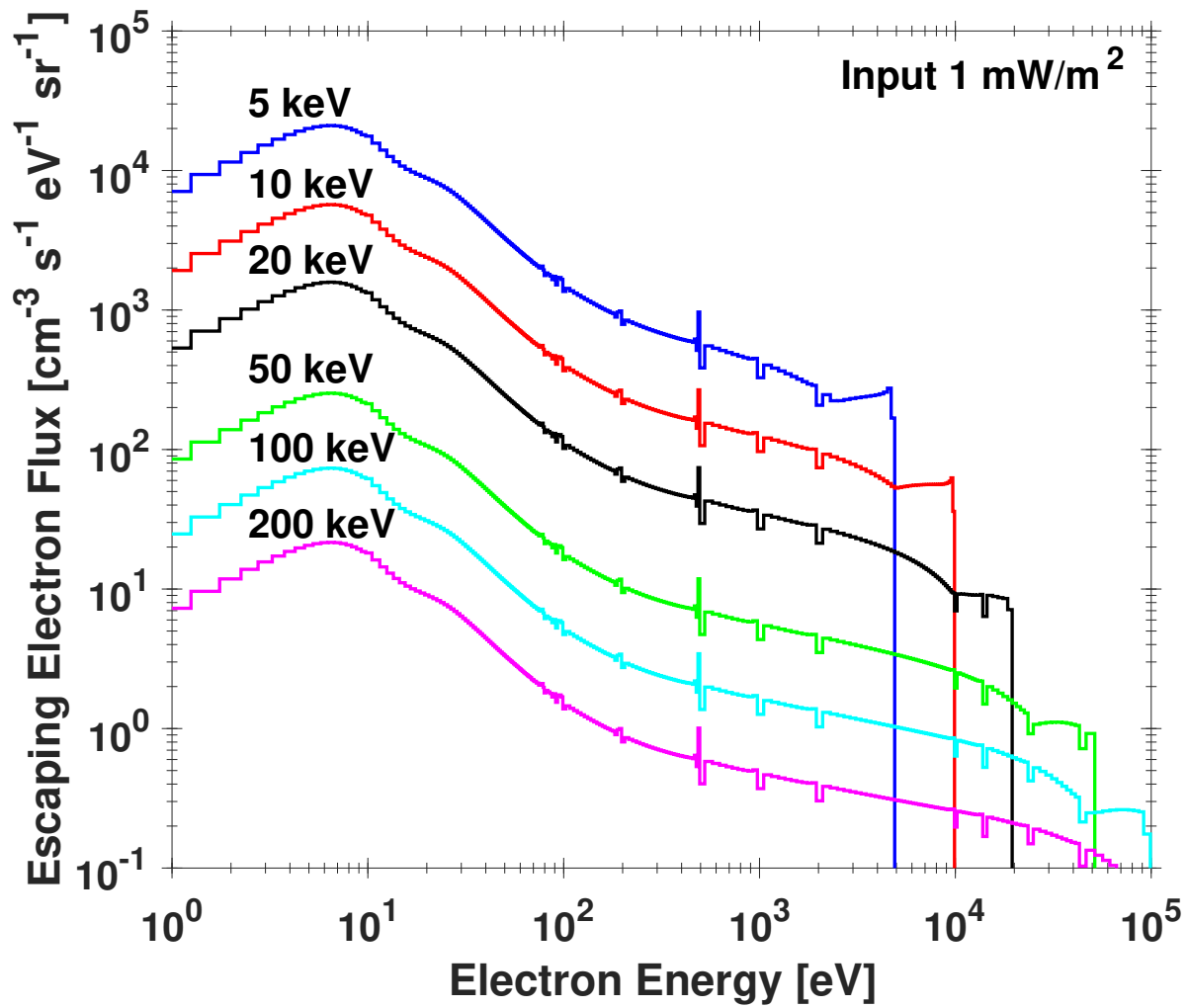


Figure 3.6: Predicted electron escape flux vs. electron energy for precipitating monoenergetic electron beams with energies of 5, 10, 20, 50, 100, and 200 keV. A step plot has been used to show the size of the corresponding energy bins that are output by the two-stream code. Here I have assumed an incident input power of 1 mW/m^2 .

It is evident that as electrons precipitate with higher energy, more energetic secondary electrons are produced but the secondary electrons have difficulty escaping the atmosphere because they are produced deeper in the atmosphere. However, lower energy electron beams create electrons high in the atmosphere, giving these secondary electrons an opportunity to escape the upper atmosphere.

3.2.7 Ionospheric Dynamics

As the electrons precipitate through the atmosphere, not only will currents be generated, but the atmosphere will become ionized. The two-stream code calculates the ionization rate of each atmospheric constituent caused by precipitating and secondary electrons the following way:

$$P^{n_k}(z) = \sum_E \sigma_{ion}^{n_k}(\Phi^+(z) + \Phi^-(z))\Delta E \quad (3.5)$$

where $\sigma_{ion}^{n_k}$ denotes the ionization cross-section for ion species n_k , at electron energy E . Φ^\pm is the upward/downward electron flux along the field line at altitude s and ΔE is the width of the electron energy bin. An example of the ion production rate is shown in Figure 3.7 for a monoenergetic electron beam of 20 keV with an initial input of 1 mW/m² into atmosphere 1.

It is evident the peak ionization rate, and consequently the peak of the energy deposition, occurs at the same H₂ density as the peak of photon emission rate shown in Figure 3.2. Just as photoemission indicates, as the energy of the electron beam increases the bulk of the energy deposition will occur deeper in the atmosphere. This same behavior is expected to occur with heavy ion precipitation in the next chapter.

The 20 keV electron beam is penetrating deep enough in the atmosphere to go past the homopause. Hydrocarbon ion production does not begin occurring until an altitude of about 450 km. In a case where the electron beam stops above the homopause (e.g. a 5 keV electron beam deposits most of its energy around 700 km) there is very little ionization of the hydrocarbon species. This can be seen column integrated ion production rates of each atmospheric species, summarized for an input power of 1 mW/m² in Table 3.2.

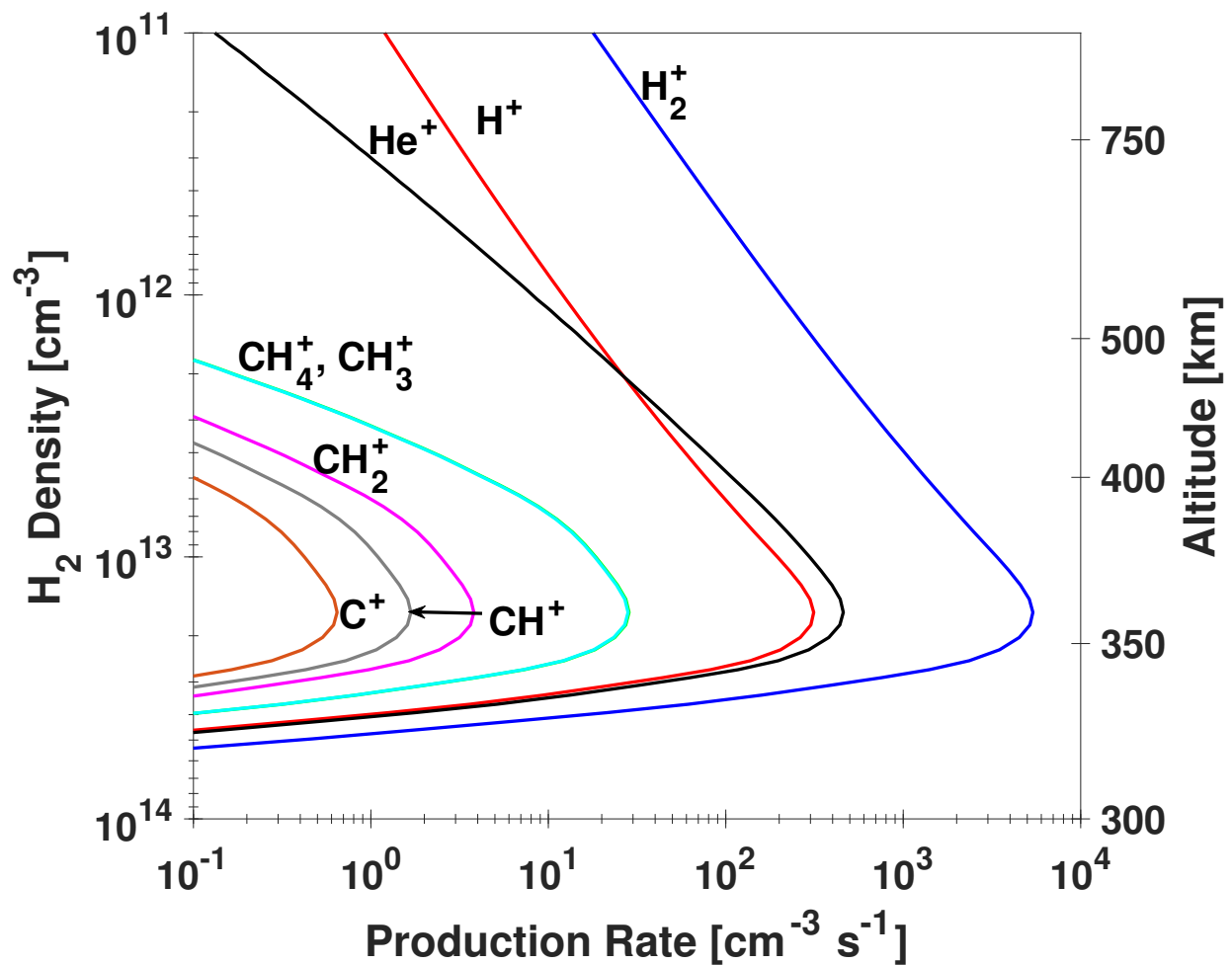


Figure 3.7: Ion production rate profiles vs. H_2 density for a 1 mW/m^2 monoenergetic, 20 keV electron beam. This is solely production from precipitating and secondary electrons, no photoionization has been included, i.e. a night side case. These electrons precipitated into atmosphere 1.

Table 3.2: Altitude integrated ion production rates for monoenergetic electron beams with an input power of 1 mW/m². Production rates emanate from both primary electron precipitation and resulting secondary electrons.

Ion Produced	Column Production Rate [cm ⁻² s ⁻¹]					
	5 keV	10 keV	20 keV	50 keV	100 keV	200 keV
H ₂ ⁺	1.69E+10	1.62E+10	1.54E+10	1.47E+10	1.44E+10	1.43E+10
H ⁺	1.10E+09	9.81E+08	9.04E+08	8.52E+08	8.38E+08	8.33E+08
He ⁺	2.35E+08	6.63E+08	1.16E+09	1.30E+09	1.32E+09	1.34E+09
CH ₄ ⁺	1.18E+04	5.15E+06	5.95E+07	7.90E+07	8.18E+07	8.34E+07
CH ₃ ⁺	1.17E+04	5.09E+06	5.88E+07	7.80E+07	8.08E+07	8.25E+07
CH ₂ ⁺	1.57E+03	6.87E+05	7.95E+06	1.06E+07	1.09E+07	1.12E+07
CH ⁺	6.82E+02	3.01E+05	3.52E+06	4.71E+06	4.89E+06	5.01E+06
C ⁺	2.58E+02	1.15E+05	1.35E+06	1.82E+06	1.90E+06	1.94E+06

The hydrocarbon ion production rate for 5 keV is significantly lower than that of the higher energy electron beams, and CH₄⁺ production is six orders of magnitude lower than H₂⁺ for that beam. This beam does not penetrate deep enough into the atmosphere to reach high levels of CH₄ densities, thus unable to produce large numbers of ionized hydrocarbons. However, after 10 or 20 keV, the electron beams produce a very similar amount of hydrocarbon ionization.

3.3 Ionospheric Model

As demonstrated, one of the products from the two-stream code is the ionization of atmospheric constituents. However, not yet considered are the effects these newly introduced ions have on ionospheric densities. There are two mechanisms to consider to find a steady state ionosphere. The first is the recombination of electrons (both precipitating and secondary) with the ions that make up the ionosphere. The second is the chemical reactions between ions and neutrals. However, before introducing these processes, more robust atmosphere profiles need to be created to account for supplementary hydrocarbon species.

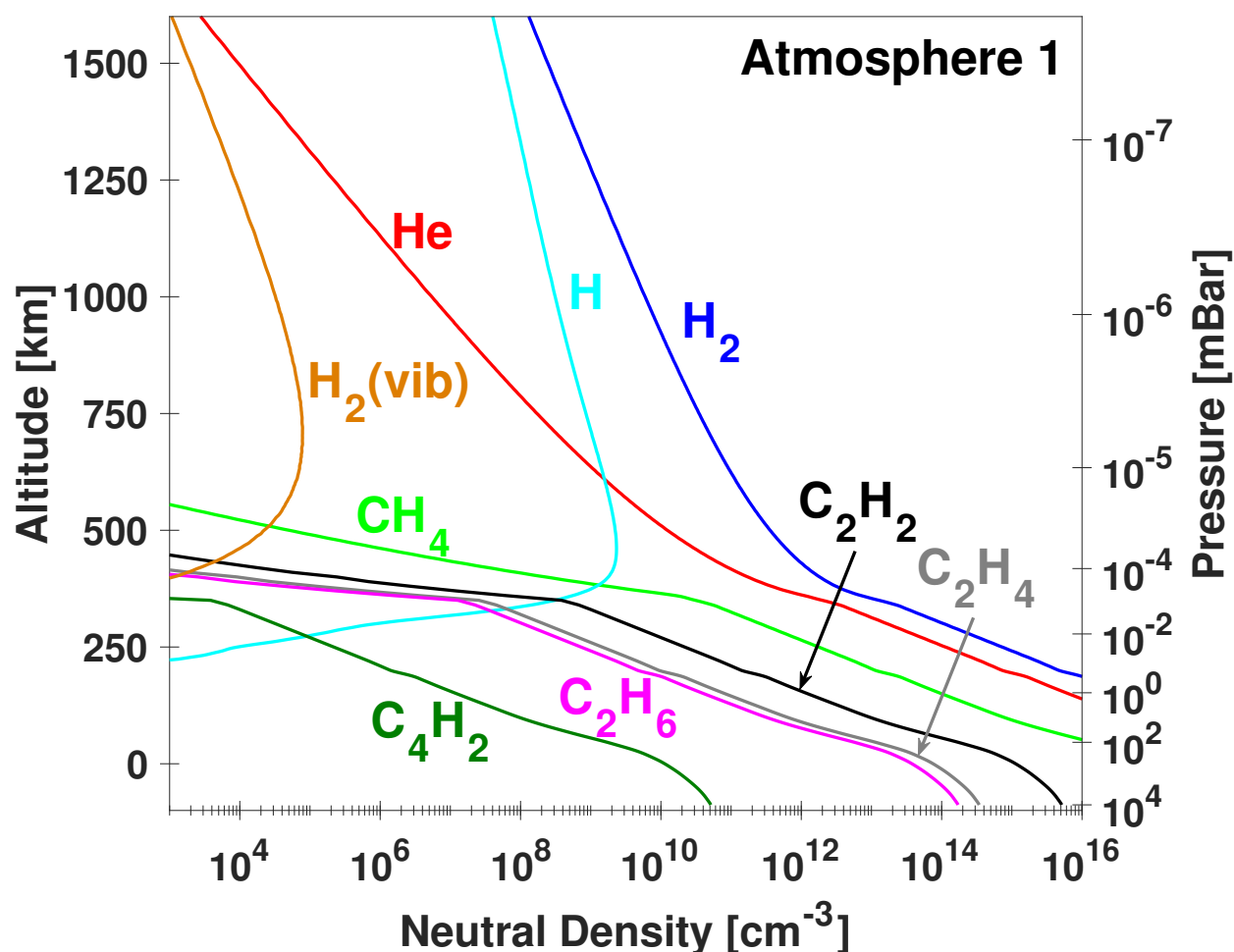


Figure 3.8: Atmospheric profile used by the chemical model. Additional hydrocarbons have been added because they become important to chemical reaction rates at low altitudes. This is an extension of atmosphere 1.

3.3.1 Chemical Model Atmosphere

A more in-depth atmosphere needs to be considered because there are additional hydrocarbon species that are important for ion-neutral reactions at low altitudes. To accomplish this, I introduce C_2H_2 , C_2H_4 , C_2H_6 , C_4H_6 , and $H_2(vib)$ into the atmosphere profiles displayed in Figures 2.8 and 2.9. I am still using an atmosphere with a distinct homopause (Atmosphere 1, Fig. 3.8) and one that is assumed to be well mixed throughout (Atmosphere 2, Fig. 3.9).

For atmosphere 1 at low altitudes (below the homopause, $z < 350$ km) and the entirety of atmosphere 2, the additional hydrocarbons were calculated using simple mixing ratios vs. H_2 density.

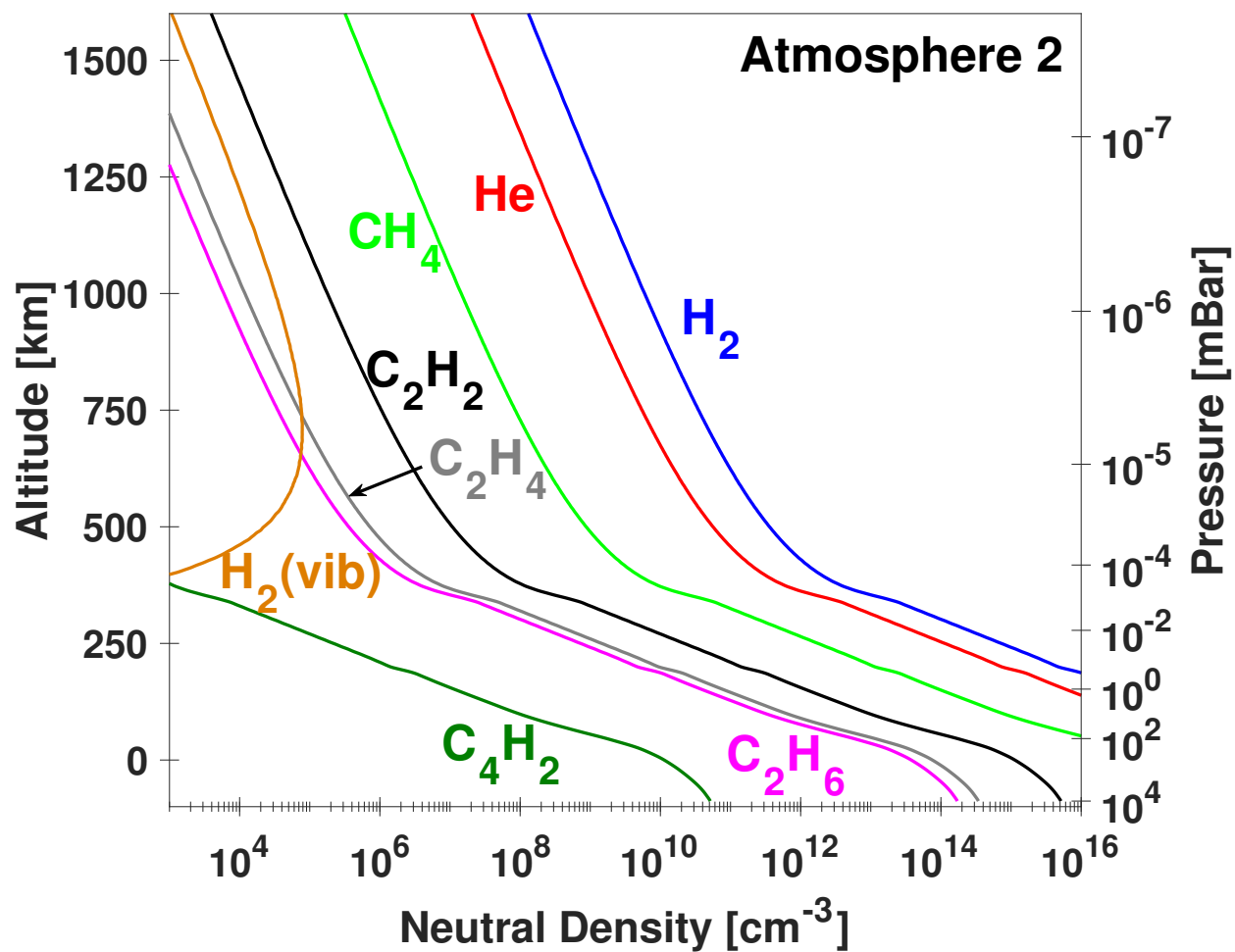


Figure 3.9: A second atmospheric profile used by the chemical model. Additional hydrocarbons have been added because they become important to chemical reaction rates. This is an extension of atmosphere 2, where I have considered an upper limit well-mixed atmosphere.

Perry et al. (1999) present mixing ratios of 3×10^{-5} and 2×10^{-6} with respect to H_2 for C_2H_2 and C_2H_4 , respectively. Gladstone et al. (1996) report a mixing ratio of 1×10^{-6} for C_2H_6 and Atreya (1986) show a mixing ratio of 3×10^{-10} for C_4H_2 . To produce the upper portion of atmosphere 1 (above the homopause, $z > 350$ km), I assume hydrostatic equilibrium and use that static atmosphere law

$$n_k(z) = n_k(z = 350) e^{-z/H(z)} \quad (3.6)$$

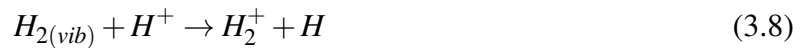
where $n_k(z)$ is the species density at altitude $z > 350$ km and $n_k(z = 350)$ is the species density at $z = 350$ km. $H(z) = k_B T(z) / m_k g$ and is the scale height for each species, k .

Finally, the last constituent I consider is the vibrationally excited states of H_2 with a vibrational quantum number greater than or equal to four, i.e. $H_{2(vib \geq 4)}$, which I refer to as $H_{2(vib)}$. This is because H^+ only reacts with H_2 when the vibrational levels are equal to or greater than four, but not the lower levels. $H_{2(vib)}$ is dependent on the vibrational temperature (T_{vib}) in the following way

$$n_{H_{2(vib)}}(z) = n_{H_2}(z) e^{-21960/T_{vib}}. \quad (3.7)$$

$T_{(vib)}$ increases or decreases with the number of electron-neutral collisions in the auroral regions. I have not completed an extensive study of the correct vibrational temperature to use, but Ozak Munoz (2012) presented results where she varied T_{vib} in the chemical model and compared the resulting electron densities to other models and observations. She concluded that $T_{vib} = 2T(z)$ produced the most appropriate match to expected results, where $T(z)$ is the temperature in the atmospheric model (Fig. 2.8). Therefore, I use that relation in my calculation of $H_{2(vib)}$.

The vibrational states of H_2 are important because they are a loss mechanism for H^+ in a reaction that produces H_2^+ (the last reaction in Table C.2); that is,

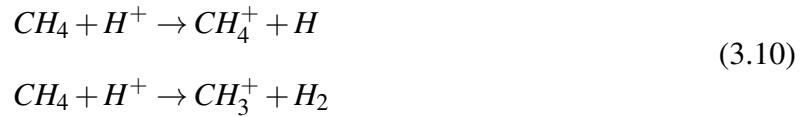


with a large rate coefficient of $1.00 \times 10^{-9} \text{ cm}^3 \text{ s}^{-1}$. Therefore, if $n_{H_{2(vib)}}$ increases there will be

an associated increase in H_2^+ with a simultaneous efficient sink mechanism for H^+ . Prevalent production sources for H^+ and H_2^+ include the electron-neutral collision reactions



As H^+ increases, the reactions



adequately produce ionized hydrocarbons in the ionosphere with rate coefficients of $2.30 \times 10^{-9} \text{ cm}^3 \text{ s}^{-1}$ and $1.50 \times 10^{-9} \text{ cm}^3 \text{ s}^{-1}$, respectively. With a source of CH_4^+



is able to produce further hydrocarbon species (rate coefficient of $1.50 \times 10^{-9} \text{ cm}^3 \text{ s}^{-1}$). Meanwhile, due to Equations 3.8 and 3.9, as H_2^+ increases the reaction



will greatly produce H_3^+ , an important species in the ionosphere and thermosphere, and at times the most abundant ion species. This is one of the most dominant chemical reactions in the Jovian atmosphere having a rate coefficient of $2.08 \times 10^{-9} \text{ cm}^3 \text{ s}^{-1}$ and considering H_2 has the highest atmospheric density. Finally, through the electron recombination reactions



H_3^+ is effectively lost, converting back to H and H_2 .

3.3.2 Physical Processes

There are now a total of nine neutral species that make up atmosphere 1, and eight in atmosphere 2. The chemical code simulates these neutral species, and the electrons, interacting with 27 different ion species: H^+ , He^+ , H_2^+ , H_3^+ , HeH^+ , CH_5^+ , CH_4^+ , CH_3^+ , CH_2^+ , CH^+ , C^+ , $C_2H_7^+$, $C_2H_6^+$, $C_2H_5^+$, $C_2H_4^+$, $C_2H_3^+$, $C_2H_2^+$, C_2H^+ , $C_3H_7^+$, $C_3H_6^+$, $C_3H_5^+$, $C_3H_4^+$, $C_3H_3^+$, $C_3H_2^+$, C_3H^+ , $C_nH_m^+$, and $H_2C_3H^+$, ultimately resulting in 35 electron recombination processes shown in Table C.1 and 163 ion-neutral reactions shown in Table C.2.

The chemical code simulates all of these reactions in an attempt to calculate the steady state ionosphere. To do this, the model solves the continuity equations

$$\frac{\partial n_k}{\partial t} + \frac{\partial \phi_k}{\partial z} = P_k - L_k n_k \quad (3.14)$$

where k denotes electrons or the species of ion. Due to quasi-neutrality, the model assumes $n_e = \sum_i n_i$, where i is each ion species. The first term in the continuity equation, $\partial n_k / \partial t$, is the change in density of a species with respect to change in time, where the ultimate goal of the simulation is to solve for $\partial n / \partial t = 0$. $\partial \phi_k / \partial z$ is the change in flux of species k over an altitude z and describes the vertical transport by molecular diffusion. The chemical model assumes hydrostatic equilibrium, effectively ignoring this second term. P_k is the production of species k , and is the result of electron recombination or a chemical reaction. Finally, L_k is the loss function of a species. Electrons only have a single form of loss, which is governed the ion-electron recombination coefficient, α , shown in Table C.1. However, for ions, both ion-electron recombination and ion-neutral reactions must be taken into account. Ion-neutral reactions are determined by reaction rates, β_i shown in Table C.2. Both the recombination rate coefficients and reaction rate coefficients are used to find the characteristic time constant for a given reaction by $\tau = (\alpha n_e)^{-1}$ and $\tau = (\beta_i n_i)^{-1}$, respectively.

3.3.3 Results

The ionospheric model is important to magnetosphere-ionosphere coupling, the structure of the ionosphere, and determining currents in the ionosphere. However, as electron precipitation is not the main focus of this research, I present a couple of results from the 20 keV monoenergetic electron beam here as a proof of concept and use conductivities generated from electron precipitation for a comparison mechanism in Chapter 7.

First, I consider the resulting ion production rates from the 20 keV electron beam with a power input of 1 mW/m^2 (Fig. 3.7) into atmosphere 1. This produces the steady state ionosphere shown in Figure 3.10. It is evident from this ionospheric density profile that ionized hydrogen is the major constituent until the homopause is reached, then the electrons precipitate deep enough to produce ionized hydrocarbons in abundance.

Next, I input the two-stream ion production rates from the 20 keV electron beam from atmosphere 2, into the chemical code also initialized with atmosphere 2 and present the results in Figure 3.11. The y-axis has been extended to include much of the ion density from the supplementary hydrocarbon profile at high altitudes. Atmosphere 2 constrains the density of many ion species which ultimately produce CH_5^+ , as can be seen by the steady increase of CH_5^+ . In particular, the H_3^+ density is significantly lower than what Figure 3.10 suggests throughout the entirety of the ionosphere. The ion density of H_3^+ is one that can be remotely measured with infrared observations and atmosphere 2 likely produces too little H_3^+ . This poses a problem with the use of a completely well-mixed atmosphere and it seems that the true polar atmosphere is between atmosphere 1 and 2. However, this does not entirely rule out a well-mixed atmosphere, but more work certainly needs to be done to resolve this. It is important to note that I have not included any photoionization effects and this would greatly influence the ion populations in the upper atmosphere.

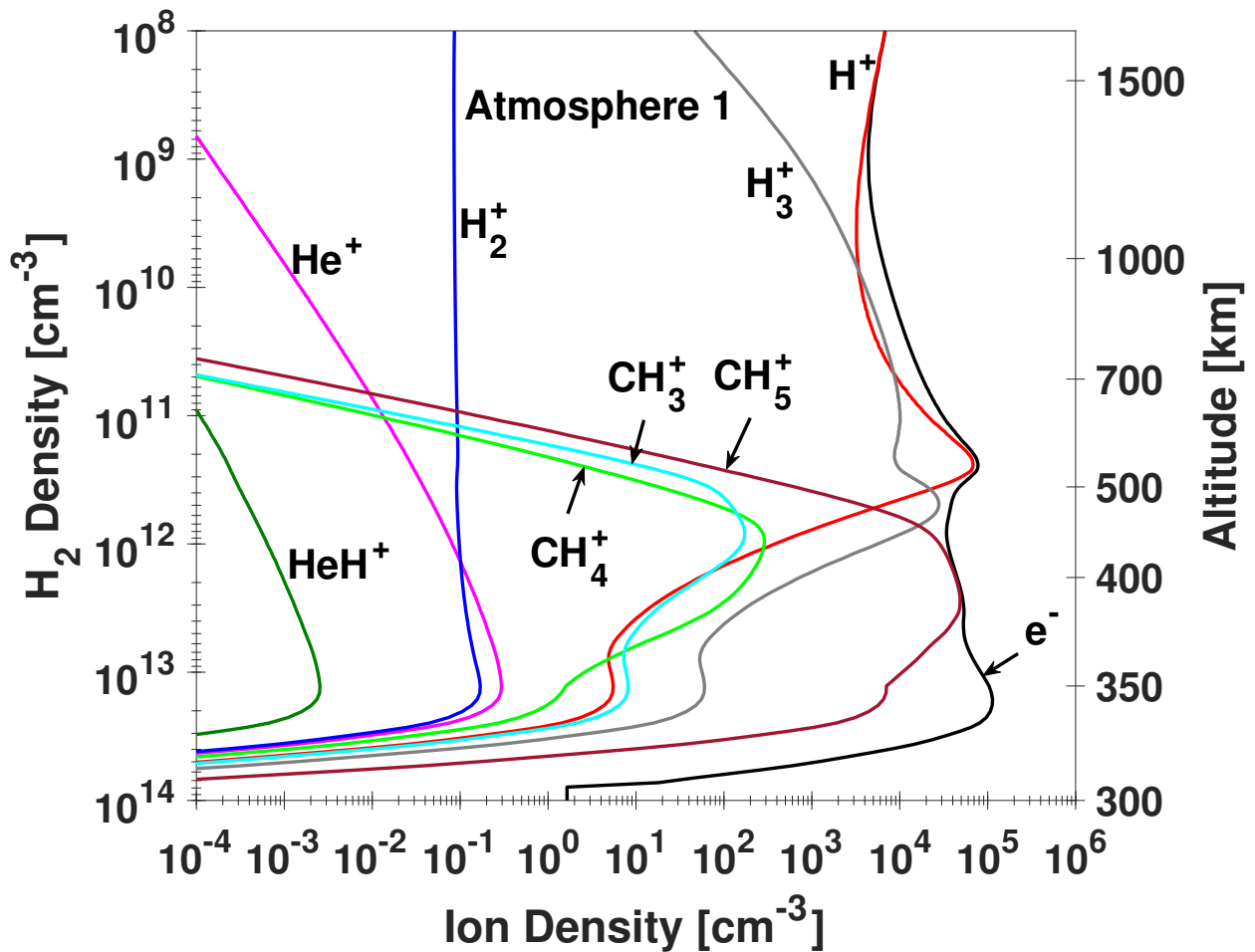


Figure 3.10: 8 of the resulting 27 steady state ion densities (plus electrons) calculated by the chemical reactions model from a 20 keV monoenergetic electron beam with an input power of 1 mW/m² into atmosphere 1. No other ionization mechanisms have been considered (i.e., no photoionization or primary ionization from heavy ion precipitation).

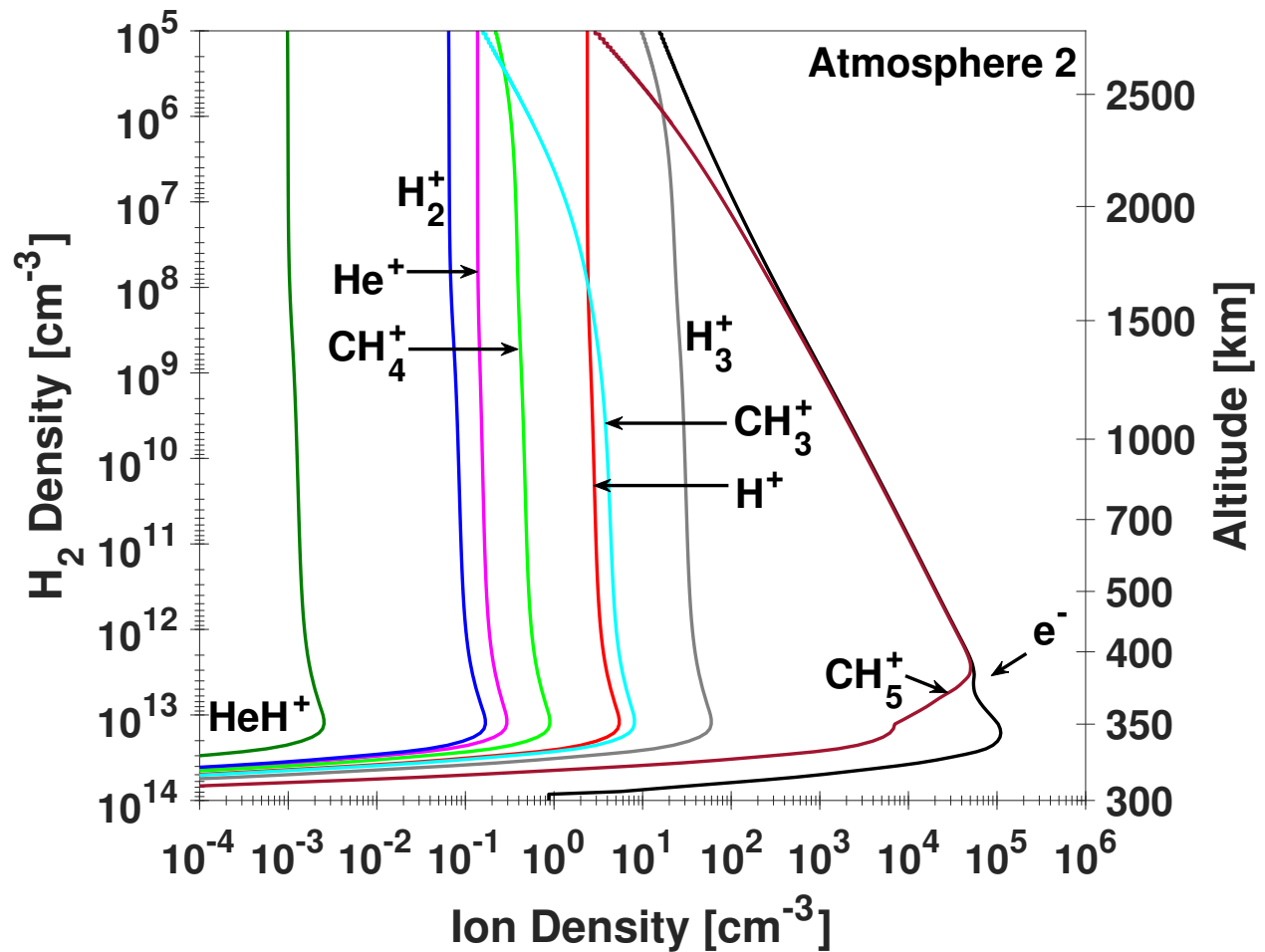


Figure 3.11: 8 of the resulting 27 steady state ion densities (plus electrons) calculated by the chemical reactions model from a 20 keV monoenergetic electron beam with an input power of 1 mW/m² into atmosphere 2. No other ionization mechanisms have been considered (i.e., no photoionization or primary ionization from heavy ion precipitation).

Chapter 4

Ion Precipitation Model

4.1 Introduction

X-ray production associated with heavy ion precipitation has been modeled over many years (Cravens et al., 1995; Horanyi et al., 1988; Houston et al., 2018; Hui et al., 2009; Hui et al., 2010; Kharchenko et al., 1998, 2006, 2008; Liu & Schultz, 1999; Ozak et al., 2010, 2013) with the goal of reproducing the observed X-ray measurements. Cravens et al. (1995) suggested that charge transfer and electron removal collisions could explain the X-ray aurora using a ≈ 1 MeV per nucleon (1 MeV/u) incident oxygen ion energy. O^{7+} and O^{8+} charge exchange collisions with atmospheric H_2 produce excited O^{6+} and O^{7+} ions that emit X-rays. The high charge state ions are created via electron removal collisions of low charge state (e.g., O^+) ions with H_2 . The current models require that the incident sulfur and oxygen ions be very energetic (1 – 2 MeV/u) to produce the X-rays observed (Hui et al., 2009; Hui et al., 2010; Ozak et al., 2010). The location of the X-ray emission on the polar cap appears to be magnetically connected to the outer magnetosphere or to the magnetopause region perhaps influenced by the Dungey cycle (Bunce et al., 2004; Cowley et al., 2003). However, fluxes of MeV heavy ions in the outer magnetosphere (Mauk et al., 2004) are too low to produce X-rays and, consequently, ion acceleration by a field-aligned potential or another mechanism is required (Cravens et al., 2003).

Recently, Dunn et al. (2016) analyzed the consequences for the X-ray aurora due to an interplanetary coronal mass ejection (ICME) at Jupiter. They mapped the observed emissions from the outer magnetosphere to the polar ionosphere using the Vogt et al. (2011) field. Their analysis indicated that precipitating magnetospheric sulfur ions were more important than oxygen ions for

the region $50 - 90 R_J$. On the other hand, emissions mapping to closed field lines at distances even further in the outer magnetosphere ($70 - 120 R_J$) or on open field lines appear to be due to a mixture between precipitating oxygen and carbon or sulfur ions. The observations also exhibited distinct periodicities, with periods of 26 minutes from the sulfur ions and 12 minutes from the sulfur/carbon and oxygen ions in the hotspot region. This difference seems to also indicate a different origin of the emissions from different species.

In this paper I present an updated, more robust model that follows from previous models developed by Houston et al. (2018); Ozak et al. (2010, 2013). Ozak et al. (2010) developed a Monte Carlo model (MCM) that was inspired by previous models (Hui et al., 2009; Hui et al., 2010; Kharchenko et al., 1998, 2006, 2008) to compare results with a Continuous Slow-Down model (CSDM). The primary goal of the updated MCM at the time was to include the altitude dependence of the X-ray spectra by including a neutral atmosphere to better understand the opacity effects in the emission. Ozak et al. (2013) then developed this model further to include secondary electron production, and Houston et al. (2018) primarily focused on FAC and ultraviolet (UV) emission from oxygen.

In the current model, I use the same neutral atmosphere (see Figure 2.8) that was used by my predecessors, although it is now extended deeper, and introduce another, fully mixed atmosphere (Figure 2.9). I include ion-neutral cross-section improvements for both oxygen and sulfur in H_2 , now using SIM collisions rather than NSIM (Section 2.1). Juno data (both oxygen and sulfur flux measurements) are adapted and input into a heavy ion precipitation model for the first time ever. Although X-ray production has been the major topic of previous papers, here I include all auroral effects from ion precipitation.

4.2 Monte Carlo Model

To model the ion precipitation, I inject 20,000 ions (there is very little statistical difference after $\approx 3,000$ ions) into the upper atmosphere, one-by-one, all with the same initial energy and initial charge state. The incident pitch angle is assumed to have an isotropic downward distribution and,

thus, is randomly chosen for each individual ion and scaled as the cosine of the pitch angle. Penetration depth and energy loss are affected by the initial energy. The ions are given an initial charge state of O^+ and S^{++} , as these are charge states with the highest abundance in the Jovian magnetosphere (Delamere et al., 2005; Dougherty et al., 2017; Kim et al., 2019), although they keep no memory of their initial charge state as they precipitate through the atmosphere (Kharchenko et al., 2008). Penetration of the ions into the atmosphere is determined probabilistically with a Monte Carlo simulation, where the probability of having a collision is

$$P = 1 - e^{-\sigma_{tot}\Delta N}. \quad (4.1)$$

σ_{tot} is the sum of all possible ion impact cross-sections for a given energy and charge state and ΔN is the change in column density that each ion undergoes before colliding with another H_2 molecule. Equation 4.1 can be rearranged to solve for ΔN such that

$$\Delta N = \frac{-\ln(P)}{\sigma_{tot}} \quad (4.2)$$

where P is a random number between zero and one. Once determining there will be a collision after a penetration distance of ΔN , the next step is to produce a collision.

4.2.1 Collision Processes

The type of collision process that occurs is decided randomly based on the allowed collisions for the given charge state (e.g. an O^{8+} ion cannot undergo a single or double stripping collision, as it has already been stripped of all its electrons) and the cross-section of the possible collisions (The full list of every collision process considered can be found in Section 2.1 and the associated integral cross-sections in Appendices A and B.). The probability of a given process occurring is

$$P_{proc} = \frac{\sigma_{proc}}{\sigma_{tot}} \quad (4.3)$$

where P_{proc} is the probability for a given collision process and σ_{proc} is the cross-section of said process. Calculating the probability with Equation 4.3 naturally normalizes P_{proc} such that

$$\sum_{proc=1}^{35} P_{proc} = 1. \quad (4.4)$$

The process is then decided randomly by allowing a random number generator to output a number between zero and one.

There are a number of things that can occur to the ion with each collision. It can (1) gain an electron thereby lowering the charge state and emitting a photon, (2) lose an electron (referred to as a secondary electron), increasing its charge state, (3) it can become excited, leading to photon emission when it de-excites, or (4) it can excite, ionize, and/or dissociate the target H₂ molecule. Each of these possibilities can occur independently or as a combination of two or more. Depending on what exactly happens to the ion and target molecule a certain amount of energy will be lost by the ion determined by the energy loss model displayed in Table 2.1.

4.2.2 Energy Loss

Each collision yields a loss of energy for the precipitating ion. The amount of energy lost depends on the type of collision, the energy transferred to secondary electrons (if applicable), the ionization potential of hydrogen (if applicable), and the ionization potential of oxygen or sulfur (if applicable). I use energy loss models adapted from Table A of Schultz et al. (2019) (shown in Table 2.1), along with the energy of the ejected electrons from collisions, to calculate the energy loss in the system. This represents another improvement to the Ozak et al. (2010) and Ozak et al. (2013) models, which calculated the energy loss using an empirical stopping power and did not consider the type of collision in this calculation.

There are a number of processes that determine the energy lost by the ion that can be broadly categorized in the following way; (1) H₂ can be excited, where the ion loses 7.7 eV if it is oxygen, and between 4-8 eV for sulfur. (2) H₂ can lose one or two electrons where the ion loses the amount

Table 4.1: Ionization potentials in eV of every oxygen and sulfur charge state used by the ion precipitation model.

Charge State	Ionization Potential [eV]	Charge State	Ionization Potential [eV]	Charge State	Ionization Potential [eV]
O	13.62	S	10.36	S ⁸⁺	379.8
O ⁺	35.12	S ⁺	23.34	S ⁹⁺	447.7
O ²⁺	54.94	S ²⁺	34.86	S ¹⁰⁺	504.6
O ³⁺	77.41	S ³⁺	47.22	S ¹¹⁺	564.4
O ⁴⁺	113.9	S ⁴⁺	72.59	S ¹²⁺	652.0
O ⁵⁺	138.1	S ⁵⁺	88.05	S ¹³⁺	707.0
O ⁶⁺	739.3	S ⁶⁺	281.0	S ¹⁴⁺	3228
O ⁷⁺	871.4	S ⁷⁺	328.8	S ¹⁵⁺	3494

of energy corresponding to the first, and possibly second, ionization potentials of H₂ (IP₁(H₂) = 15.43 eV, IP₂(H₂) = 16.43 eV). (3) The ion can become excited where the energy loss is associated with the ion energy and charge state. (4) The ion can lose one or more electrons and the energy loss is equal to the energy of the ejected electron(s) plus the ionization potential(s) of the ion at the given charge state, shown in Table 4.1. If the ion loses multiple electrons, the ionization potential of the initial charge state plus the ionization potential of the next charge state is used.

The first and third energy loss possibilities are calculated by the model in a straight-forward way, i.e., Schultz et al. (2019) and Gharibnejad et al. (2019) give energy loss values for the excitation of H₂ and all O and S charge states. However, the calculation of the energy loss associated with secondary electrons is not nearly as simple. Every electron ejected from an ion or H₂ has an associated energy and angle that is governed by singly differential cross-sections.

4.2.2.1 Secondary Electron Production

The present model uses singly differential cross-sections (abbreviated as “sdxs”) as a function of energy and angle to calculate the probability that a secondary electron will be ejected with a secondary energy greater than or equal to E_s and with an angle of ejection between 0° - 90°.

Random numbers are used to determine what happens according to:

$$f = 1 - \frac{\int_0^{E_s} (d\sigma/dE)dE}{\int_0^{\infty} (d\sigma/dE)dE} \quad (4.5)$$

where f is the probability of an ejected electron having energy equal to or greater than E_s , $d\sigma/dE$ is the sdxs for the given collision process, and the denominator is the total cross-section. A similar probability distribution function is applied to calculating the angle with which the electron is ejected, but now using the singly differential cross-section as a function of angle, $d\sigma/d\theta$. I integrate the sdxs as a function of angle over all forward angles (between 0° and 90°) for each charge state and for each initial ion energy, and divide by the total cross-section, i.e., the integral over all angles (0° to 180°). This gives the fraction of electrons that will scatter forward. I assume all angles between 0° and 90° to be forward scattering, and the rest to be backward scattering. The pitch angle of the ion influences whether the ejected electron is truly forward or backward and a forward scattered (between 0° and 90°) electron can be transformed into a backward scattered electron for a given pitch angle. For stripping collisions, all the secondary electrons are forward scattering due to the high cross-section for the forward scattering angles in this collision type, since the ejected electron comes from the fast-moving oxygen ion.

Now that all of the energy loss mechanisms have been discussed, the final step is to remove the energy from the precipitating ion. This process is repeated until the ion energy is less than 1 keV/u. The trajectory of the ion is followed through the atmosphere through all these events and is kept track of via the column density displacement, which can later be converted into altitude, H_2 density, or pressure.

4.2.3 Charge State Distribution

Each type of interaction is governed by the energy of the precipitating ion; that is, a more energetic ion will generally be stripped of more electrons than one precipitating with less energy. By knowledge of the stripping and charge transfer cross-sections it is possible to calculate the equi-

librium fractions of each charge state versus the ion energy. This can be done by using transition probabilities, P_{ij}^k :

$$\phi_q^k(E)P_{q,q+1}^k = \phi_{q+1}^k(E)P_{q+1,q}^k \quad (4.6)$$

where $\phi_q^k(E)$ is the fraction of ions in charge state q , at energy E , for species k , either oxygen or sulfur. $P_{q,q+1}^k$ denotes the sum of the stripping cross-sections and $P_{q+1,q}^k$, the sum of the charge transfer cross-sections, for species k . A normalization is given by the condition of each energy

$$\sum_{q=q_0}^{q=Z} \phi_q^k(E) = 1 \quad (4.7)$$

where q_0 denotes the lowest charge state for species k , $q_0=-1$ for O and $q_0=0$ for S, $Z=8,16$ are the nuclear charges for O and S, and $\phi_q^k(E)$ is the charge state fraction. In the model, the charge state distribution is not calculated in this way, instead the charge state history is tracked for each individual ion. This allows the charge state distribution as a function of ion energy to be recorded. The charge state distributions for oxygen and sulfur are shown in Figures 4.1 and 4.2.

The charge state equilibrium fractions demonstrate at what energy the ion will reach a given charge state regardless of the collision processes undergone or the initial ion energy; the ion history is immediately forgotten. From these fractions one can quickly see what energies are required for an ion to begin producing X-rays. For both oxygen and sulfur the sixth charge state must be reached to begin producing X-rays (O^{6+} and S^{6+} with projectile excitation, or O^{7+} and S^{7+} with consequent charge exchange). These charge states are sufficiently reached for both species at an energy between 200-300 keV/u, where they become the most probable charge state for the given energy (a total energy of ~ 3.2 MeV and ~ 6.4 MeV for oxygen and sulfur, respectively). These newly developed equilibrium fractions are no longer in agreement with previous models presented by Ozak et al. (2010) and Houston et al. (2018) where they showed an O^{6+} peak at nearly 1 MeV/u and an S^{6+} peak at 600 keV/u.

Not only does it now require less energy to produce charge states capable of emitting X-rays, but the ions are not penetrating the atmosphere as deeply as was previously modeled because more

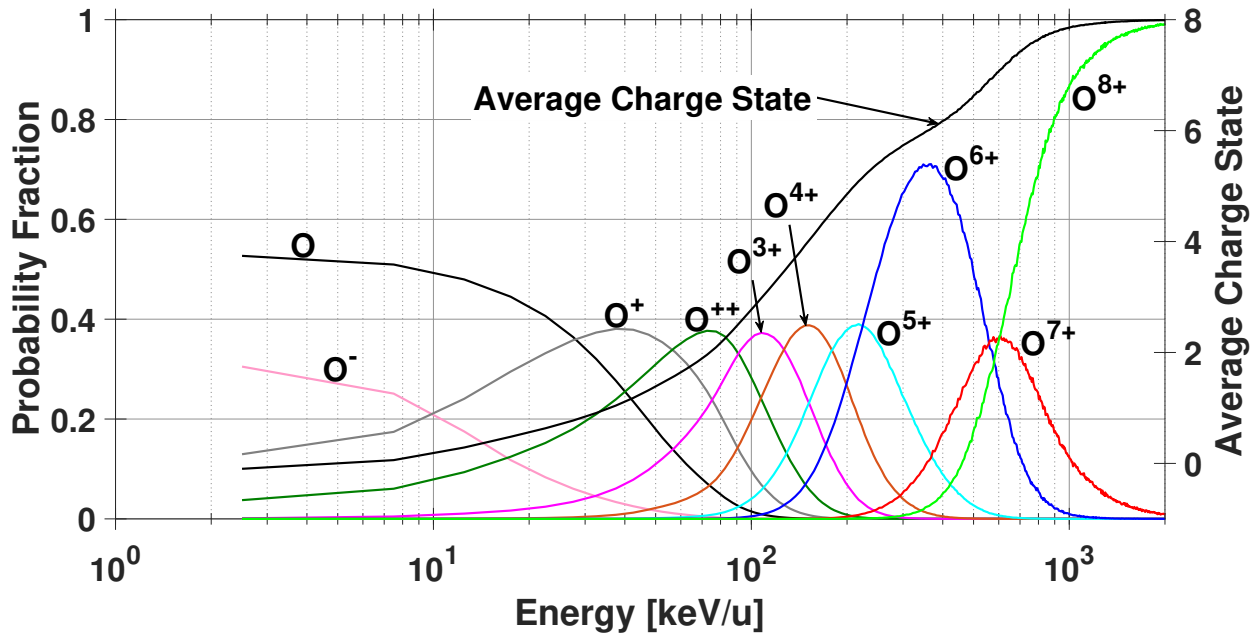


Figure 4.1: Oxygen charge state distribution as a function of ion energy. The high charge state peaks have dramatically shifted to lower energies than previous models produced. Houston et al. (2018) and Ozak et al. (2010) had the peak of O^{6+} at ~ 900 keV/u; however, due to the use of newly developed SIM cross-sections, the peak has now shifted down to an energy of ~ 350 keV/u.

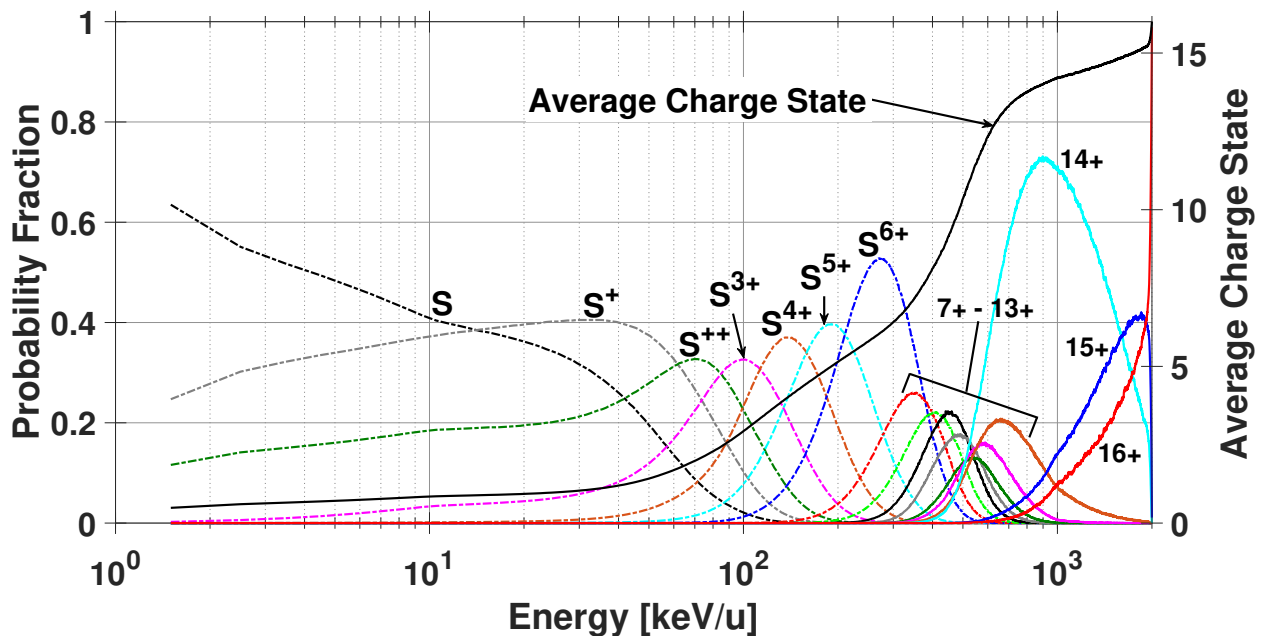


Figure 4.2: Sulfur charge state distribution as a function of ion energy. The high charge state peaks have dramatically shifted to lower energies than previous models produced. Ozak et al. (2010) had the peaks of S^{6+} and S^{14+} at ~ 500 keV/u and ~ 2.2 MeV/u, respectively. Due to the use of newly developed SIM cross-sections, the peaks have now shifted down to energies of ~ 275 keV/u and ~ 900 keV/u, respectively.

energy is being lost in the middle energy range¹, affecting the depth effects and predicted X-ray spectra.

4.2.4 Depth Effects

The opacity of the Jovian atmosphere for UV emission was described in Section 3.2.4; however, to incorporate the optical depth of outgoing X-rays the Chapman function and photoabsorption from additional species are introduced. For X-ray emission, I consider three different path angles, 0° , 80° , and 90° (where the angle is measured with respect to the axis of rotation), and two atmospheric profiles; the density profile shown in Figure 2.8 and a well-mixed atmosphere displayed in Figure 2.9. Similar to Equation 3.3, the optical depth is given by

$$\tau(\lambda, z_0) = Ch(\theta, z_0) \sum_k \sigma_k^{abs}(\lambda) \int_{z_0}^{\infty} n_k(z) dz \quad (4.8)$$

where $\tau(\lambda, z_0)$ is the optical depth as a function of emitted photon wavelength, λ , and the altitude at which the emission occurred, z_0 . $Ch(\theta, z_0)$ is the Chapman function, dependent upon the photon path angle, θ , and the altitude. $\sigma_k^{abs}(\lambda)$ is the absorption cross-section summed over each atmospheric species, k (H_2 , He, and CH_4), and is a function of wavelength. $n_k(z)$ is the neutral density of each atmospheric constituent as a function of altitude, integrated from the point of emission out through the top of the atmosphere.

The Chapman function has been approximated to $Ch(0^\circ \leq \theta \leq 80^\circ, z_0) \approx \sec(\theta)$ for the first two exit angles and

$$Ch\left(\frac{\pi}{2}, z_0\right) = \sqrt{\frac{R_J}{H(z_0)} \frac{\pi}{2}} \quad (4.9)$$

for $\theta=90^\circ$, where R_J is the Jovian radii of 71,492 km and $H(z_0)$ is the scale height at altitude z_0 .

¹See the stopping power discussion given at the end Section 2.1 and in more detail by Schultz et al. (2019).

The spectrum intensity, $4\pi I(\lambda)$ can then be calculated as

$$4\pi I(\lambda) = \int_{z_0}^{\infty} P(\lambda, z) e^{-\tau(\lambda, z_0)} dz \quad (4.10)$$

where $P(\lambda, z)$ is the production rate of X-ray emission as a function of wavelength, λ and altitude, z . z_0 is the deepest altitude that is reached by the ion beam before all of its energy is deposited into the atmosphere and $\tau(\lambda, z_0)$ is the aforementioned optical depth. $P(\lambda, z)$ integrated over every value of λ is equal to the ion production rate $P(z)$ and can be calculated for a given ion charge state.

The absorption cross-sections for these processes depend on the photon wavelength (or energy). They are obtained from Cravens et al. (1995) and shown in Figure 4.3. These cross-sections include photoabsorption from H, He, and C. The H_2 and CH_4 cross-sections were assumed to be the sum of the cross-sections of their elements. The entire collision process is illustrated in Figure 4.4.

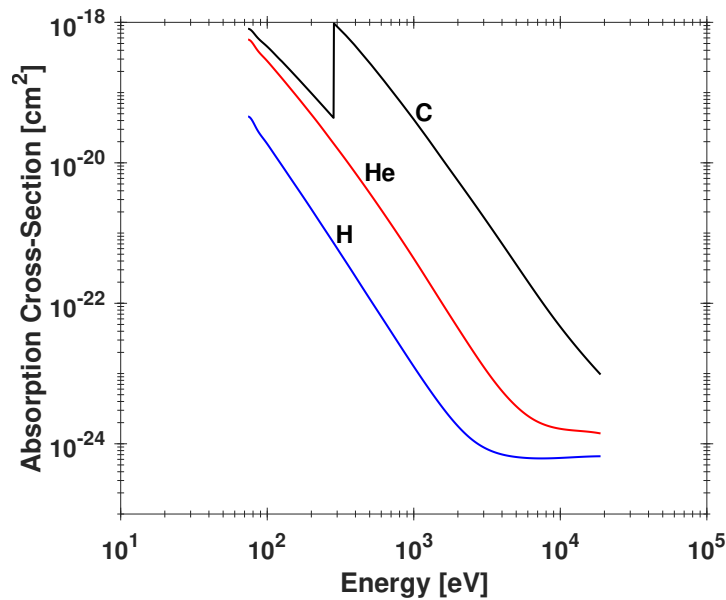


Figure 4.3: Photoabsorption cross-sections of H, He, and C as a function of photon energy. From Cravens et al. (1995).

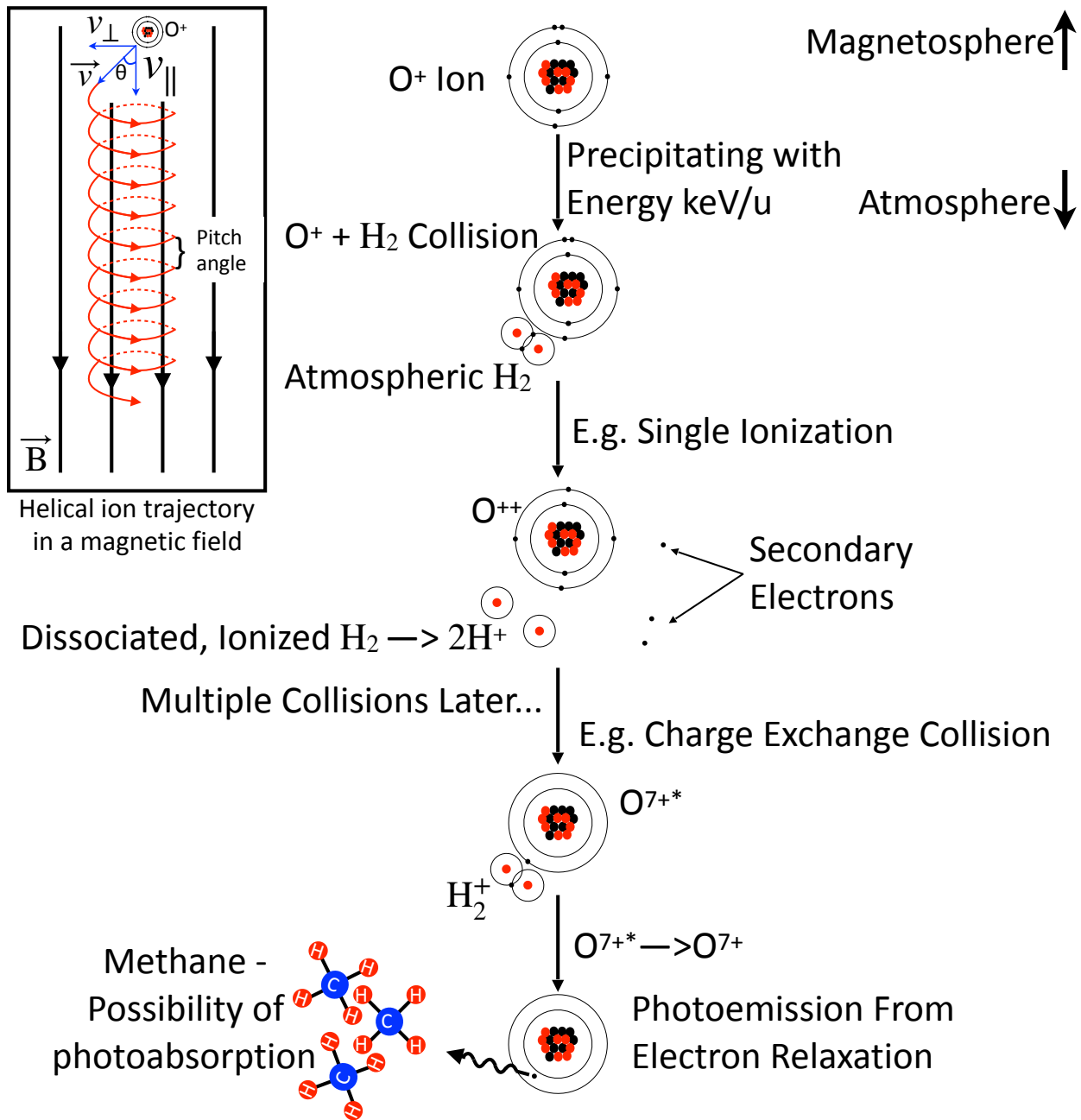


Figure 4.4: Illustration of an ion precipitating through the atmosphere. Included is secondary electron production, photoemission, and potential photoabsorption from atmospheric CH_4 . In the top left of the figure is an inset of the trajectory of a charged particle in a magnetic field, describing the pitch angle of the particle and indicating a helical trajectory. This would be the motion seen if one was to zoom out from the collision processes.

4.2.5 Ion Production Rates

When referring to ion production rates here I am only referencing production from charge transfer collisions, i.e. $X^q \rightarrow X^{q-1}$, and not stripping collisions ($q \rightarrow q+1$), which changes the charge state in the opposite direction. The ion production rate as a function of altitude, $P(z)$, can be calculated outright for a product ion species, k , (e.g. O^{7+} or S^{8+}) as follows:

$$P(z) = n(z)[\sigma_{q,q-1}^k(E(z))]\phi_q^k\Phi^k \quad (4.11)$$

where $n(z)$ is the neutral atmosphere density of H_2 , $\sigma_{q,q-1}^k(E(z))$ denotes the charge transfer cross-sections for species k with energy E at altitude z , ϕ_q^k is the equilibrium fraction given in Equations 4.6 and 4.7, and Φ^k represents the total flux of the initial ion beam. However, the model uses a Monte Carlo method that tracks each ion individually and counts each charge exchange collision that occurs for a given charge state. These collisions are tracked through a set of altitude bins with a given input of $\sim 20,000$ incident ions and then the production rate is normalized to an input of 1 ion/cm²/s.

4.2.6 Synthetic X-ray Spectra

An X-ray can be emitted through either the ion gaining an electron (what I refer to as a charge transfer or charge exchange collision) or the excitation of the ion (called direct excitation). Both of these scenarios result in one or more electrons in an excited state followed by emission of a photon as the electron(s) cascade down to a lower energy state. Although there are many charge transfer and projectile excitation processes I only allow three of each type to ultimately result in the emission of a photon: TI, SC, and SC+SS for charge exchange and SI+SPEX, DI+SPEX, and TEX+SPEX for direct excitation. Any collisions that result in more than one electron being in an excited state at a given time, whether it be through charge exchange, projectile excitation, or a combination of the two (e.g. DC or SC+SPEX collisions), I consider it much more likely for the Auger effect to take place than the emission of a photon.

Hui et al. (2010) created synthetic, charge exchange, X-ray emission lines for photon energies above 200 eV. The emission lines include O^{6+} and O^{7+} with initial ion energies of 1.2 MeV/u and 2.0 MeV/u, and S^{8+} - S^{14+} at 1.86 MeV/u. Although these energies are slightly higher than what I expect to be precipitating, these emission lines are the most comprehensive set available, thus I have taken the 1.2 MeV/u emission lines for oxygen and 1.86 MeV/u lines for sulfur and integrated them into the ion precipitation model. (Note: S^{6+} , S^{7+} , and S^{15+} are not included in this study because Hui et al. (2010) did not include them in their data, although they are X-ray producing charge states.) Hui et al. (2010) were able to produce spectra vs. number of photons/ion which I have re-normalized for each charge state to the total number of photons/charge state. I then multiplied the ion production from charge exchange produced by my model, $P(z)$, by the normalized emission lines to generate $P(\lambda, z)$.

Unfortunately, I do not have any state-selective excitation emission spectra of oxygen and sulfur for direct excitation; instead I apply an approximation to the charge exchange emission lines that are available. Because charge transfer collisions are pulling an electron into the particle from outside of the ionization potential the electron will cascade from very high energy states until it has energetically relaxed. This allows for high energy X-rays to be emitted and many cascading possibilities. However, direct excitation excites an electron from the highest occupied electronic energy level, likely resulting in a change in principal quantum number of only one or two. Once the electron is in a particular energy level it is unaware of whether it has been excited or picked up from outside of the ion; thus, at that point, the cascading probabilities should not differ between charge exchange or excitation. That is to say, electrons relaxing from charge transfer collisions will always be capable of following the same cascade path as an electron excited by direct excitation, but the reverse is not true. Energy levels reached by excitation of the projectile ion will be predominantly to lower levels than produced by charge transfer. Charge transfer produces predominantly to state principal quantum number $n \approx q^{3/4}$, with a distribution below and above this, falling off at high quantum number as $1/n^3$. In contrast, excitation proceeds dominantly to the next highest n-level and rapidly falls off for higher n. So an approximation for excited electrons to start at a lower

n-level is needed. (Note: A second thing to consider would be forbidden excitation transitions for each charge state; however, that requires a much more in-depth study of the situation beyond the scope of this research.)

I first approximate O^{7+} as H, O^{6+} as He, S^{14+} as Li, S^{13+} as Li^+ , S^{12+} as Li^+ or Be, S^{11+} as Be^+ , S^{10+} as Be^{++} , and S^{9+} as Be^{3+} , and assume S^{8+} will follow the same pattern shown by the higher charge states. I then reviewed a number of articles concerning electron-impact excitation of lithium (Griffin et al., 2001), beryllium (Bartschat et al., 1996), lithium-like (Bely, 1966), and beryllium-like (Ballance et al., 2003) particles to understand the relative cross-sections between excitation to various electronic energy levels. The cross-sections for all of these cases were dominated by a change in principal quantum number of one, i.e. when an electron is excited it will typically ($\sim 80\%$ - 85% of the time) only be excited to the next highest energy level. Occasionally, $\sim 15\%$ - 20% of the time, it will be excited to an even higher energy state.

Therefore, I take the two or three most common emission lines, at lower photon energies, from the charge exchange synthetic spectra provided by Hui et al. (2010) and distribute the direct excitation emission in the following way

$$\sum_{i=1}^{2,3} \frac{hc}{\lambda_i} f_i = E \quad (4.12)$$

where h is Planck's constant, c is the speed of light, and λ_i is the wavelength of the most likely emission line, or group of emission lines. If there is a group of emission lines with similar wavelengths ($\Delta\lambda \approx 10$ eV), the emission is distributed evenly among each wavelength because in this simple approximation I do not know the exact state-selective excitation transitions, and forbidden excitation states have not been considered. f_i is the distribution of X-ray production given to each wavelength. If only two lines, or groups of lines, are considered then $f_1=0.85$ and $f_2=0.15$; for three, $f_1=0.80$, $f_2=0.15$, and $f_3=0.05$. E is the total photon energy from emission.

To ensure this approximation is not violating conservation of energy, if the emitted photon energy is greater than the energy loss for single projectile excitation (SPEX), $E > \Delta E$, where ΔE is

the energy loss for SPEX at a given ion energy and charge state shown in Schultz et al. (2019) and Gharibnejad et al. (2019), then the emission given in Equation 4.12 is re-normalized to conserve energy,

$$\sum_{n=1}^{2,3} \frac{hc}{\lambda_n} f_n \varepsilon = E \quad (4.13)$$

where $\varepsilon = \Delta E/E$. If $E < \Delta E$ then I keep the distribution as is and assume the energy difference is due to emission from lower energy photons not considered in the X-ray spectrum and X-ray inefficiencies in emission from the way the electrons cascade through the electron orbitals.

To produce a more realistic observation than perfect line emission that an X-ray observatory would detect I apply a normalized Gaussian distribution to each data point to simulate instrumental response functions, recovering a new intensity:

$$4\pi I'(\lambda) = \sum_{\lambda_\mu} \frac{1}{\sqrt{2\pi\sigma^2}} I(\lambda) e^{-\frac{(\lambda-\lambda_\mu)^2}{2\sigma^2}} \quad (4.14)$$

where λ is now the full spectrum (in eV) which I allow to range from 100 eV to 3500 eV. λ_μ is the wavelength of each emission line and σ^2 is the variance and $\sigma=20$ eV.

4.2.7 Juno Data

With recent measurements from JEDI (Mauk et al., 2017a) on the Juno spacecraft, I have obtained heavy ion flux measurements above Jupiter's polar caps indicating both oxygen and sulfur precipitation (Haggerty et al., 2017; Clark et al., 2017a,b). I input these measurements into the model and produce expected observables for a given flux. For this study, I use heavy ion measurements from a northern auroral pass during Perijove (PJ) 7 on July 11, 2017, displayed in Figure 4.5.

Re-normalization and interpolation of all of the data is necessary to make the flux compatible with the ion precipitation model. The re-normalization requires multiplying the measured intensity by the JEDI energy bin widths (Mauk et al., 2017a) and 2π to obtain a flux in ions/cm²/s. The first three energy bins (170.7, 240.2, and 323.6 keV) on the JEDI instrument are unable to distinguish between oxygen and sulfur; therefore, we assume a distribution of 2/3 oxygen and 1/3 sulfur,

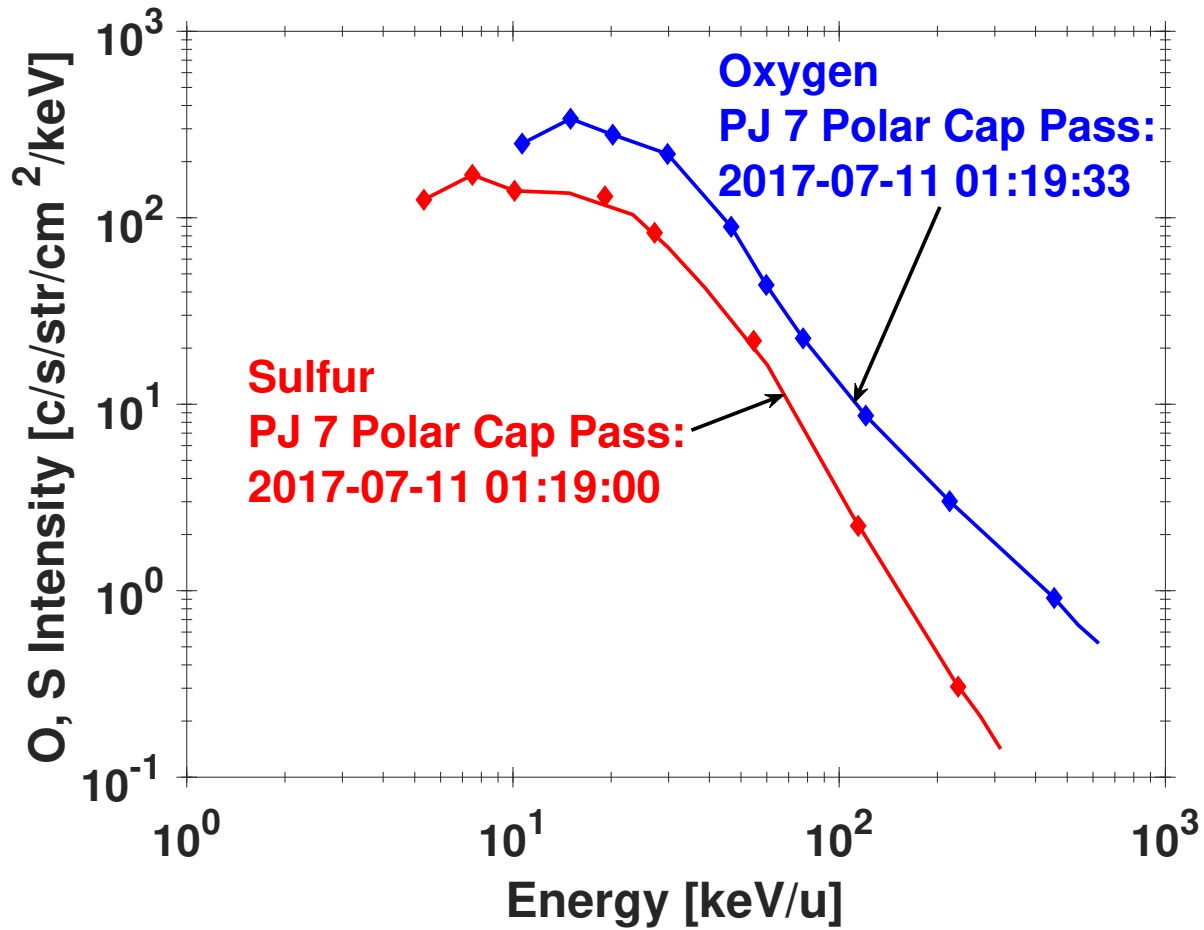


Figure 4.5: Oxygen and sulfur flux measurements from JEDI on the Juno spacecraft during Perijove 7. The points marked with a diamond are the actual JEDI measurements. The lines represents the interpolation of the data that I applied to the measurements.

because the ions likely originate from the sulfur dioxide, SO_2 , volcanoes on Io. However, data have shown various oxygen to sulfur ratios in Jupiter's magnetosphere (Delamere et al., 2005; Dougherty et al., 2017; Kim et al., 2019), but fortunately these low energy bins will not contribute to X-ray production. I then apply a simple linear interpolation to give the data finer resolution so the results are smoother, although it has no effect on the total X-ray production. These flux measurements are an input ion flux into the model, or more simply, one can multiply the output from various monoenergetic runs (which are normalized to an input of $1 \text{ ion/cm}^2/\text{s}$) by the re-normalized flux given by JEDI.

It is important to note that although the low energy bins are unable to distinguish between

oxygen and sulfur, the higher energy bins of JEDI make separate oxygen and sulfur measurements, and in the case presented, oxygen happens to be more abundant. This is not necessarily a typical measurement and, as suggested by X-ray observation, we generally expect sulfur to produce higher concentrations of X-ray emission. Data have indicated that the sulfur to oxygen (S:O) ratio varies between measurements (Delamere et al., 2005; Dougherty et al., 2017; Kim et al., 2019) which needs to be considered when comparing synthetic X-ray spectra with that from observation. Figure 4.5 has an S:O ratio of about 0.3 which is the lowest ratio presented by Radioti et al. (2005, 2006), where the S:O ratio is shown to vary between 0.3-1.2.

Jupiter's X-ray aurora is known to be highly time variable. The X-ray aurora pulses/flares on timescales of a few minutes, while the power output from the aurora can vary by a factor of a few from rotation to rotation (0.5 - 2 GW) and the spectrum is known to change significantly on similar timescales (e.g. Branduardi-Raymont et al. (2007); Elsner et al. (2005); Hui et al. (2010)). The spatial location of the emission may also vary across the auroral zone (Dunn et al., 2017; Gladstone et al., 2002; Jackman et al., 2018), with some suggestion that sulfur X-ray lines may be brighter at lower auroral latitudes (Dunn et al., 2016).

Chapter 5

Ion Precipitation Results - Field-Aligned Currents and Ultraviolet Emission

Past UV observations of Jupiter's aurora suggest a total input power flux of 10^{13} - 10^{14} W for the main auroral oval emission from each hemisphere. A model has been described for the transport of magnetospheric oxygen and sulfur ions with low charge state and energies up to several MeV/nucleon (MeV/u) as they precipitate into Jupiter's polar atmosphere. A revised and updated hybrid Monte Carlo model originally developed by Ozak et al. (2010) is used to model the Jovian aurora. The current model uses a wide range of incident oxygen and sulfur ion energies (10 keV/u - 25 MeV/u for oxygen and 10 keV/u - 2 MeV/u for sulfur) and the most up-to-date ion-impact cross-sections. In addition, the effects of the secondary electrons generated from the heavy ion precipitation are included using the two-stream transport model described in Section 3.2 that computes the secondary electron fluxes and their escape from the atmosphere. The model also determines H₂ Lyman-Werner band emission intensities, including a predicted spectrum and the associated color ratio.

5.1 Primary Effects

X-ray emission is produced by higher charge state ions (O^{8+} , O^{7+} , O^{6+} , and S^{7+} - S^{16+}) colliding with atmospheric H₂ in charge exchange and direct excitation that results in excited O^{7+*} , O^{6+*} , O^{5+*} , and S^{7+*} - S^{16+*} for which the de-excitation results in the emission of EUV and X-ray photons. The approximate emitted photon energies are given by the ionization potentials (e.g., 871 eV for O^{7+} , 739 eV for O^{6+} , and 138 eV for O^{5+}). Note that O^{5+*} produces EUV photons rather

than X-rays, although the ionization potential is large enough to produce soft X-rays. This same mechanism may also account for a small portion of the ultraviolet spectrum seen by ROSAT from the lower oxygen and sulfur charge states, with lower ionization potentials and consequently lower energy photons. Figures 5.1 and 5.2 shows the oxygen and sulfur ion production rate profiles for initial input energies of 0.05, 0.3, 2, and 5 MeV/u for oxygen and 0.05, 0.3, 1, and 2 MeV/u for sulfur.

For both oxygen and sulfur the altitude of peak production rate depends on the initial ion energy, with more energetic ions reaching deeper in the atmosphere. As the initial ion energy increases, the peak production rate of each oxygen charge state begins to converge. This is due to higher energy ions penetrating deeper into the atmosphere where there is a higher density of H_2 ; but as they lose energy they undergo collisions that return their electrons to them (i.e., charge transfer collisions).

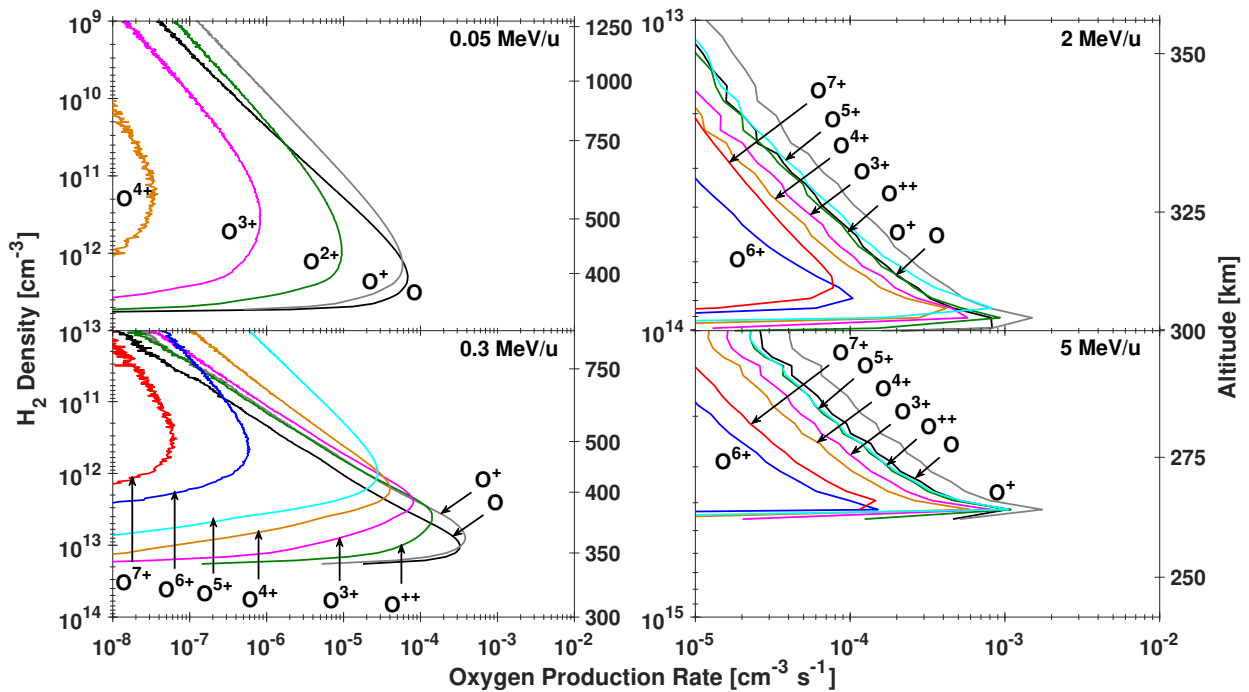


Figure 5.1: Oxygen ion production rate vs. density for initial oxygen ion energies of 0.05, 0.3, 2, and 5 MeV/u and an initial input of 1 ion/cm²/s from charge exchange collisions.

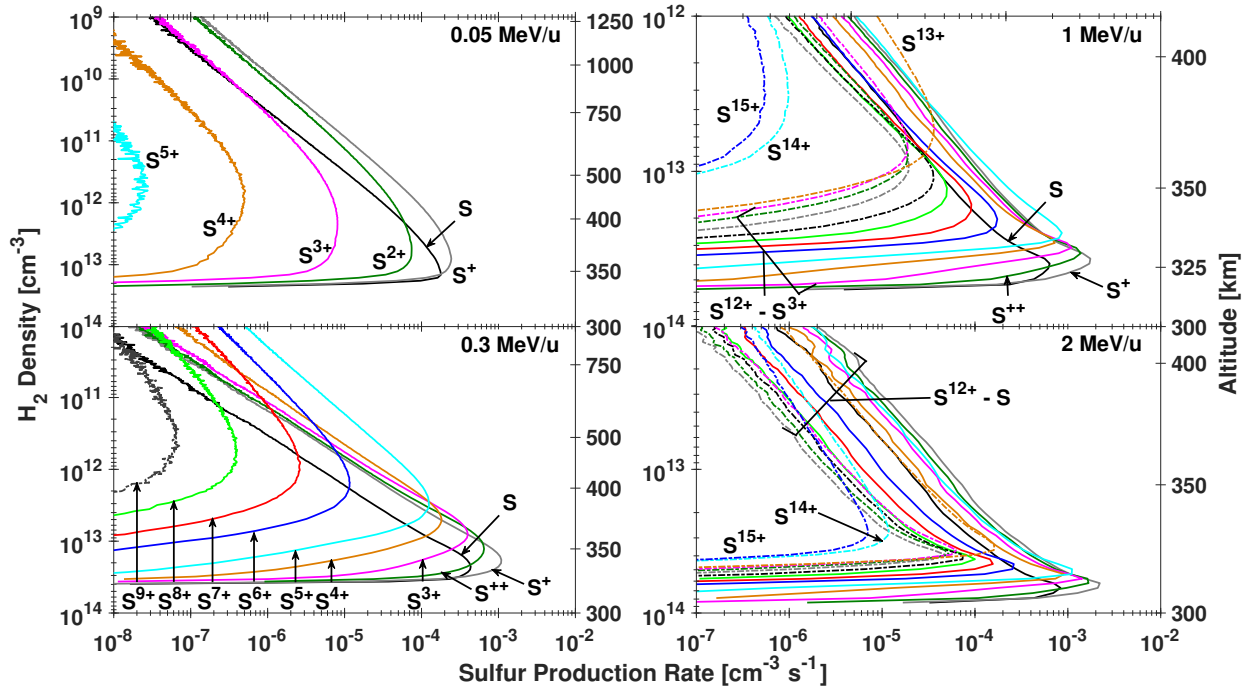


Figure 5.2: Sulfur ion production rate vs. density for initial oxygen ion energies of 0.05, 0.3, 1, and 2 MeV/u and an initial input of 1 ion/cm²/s from charge exchange collisions.

H_2^+ and H^+ production are essential to magnetosphere-ionosphere coupling, as they are largely responsible for the formation and the conductivity of the auroral ionosphere. They also represent most of the energy deposition in the atmosphere. Of similar importance is the excitation of H_2 and H , resulting in airglow emission. Anytime H_2 is ionized there is an electron ejected (apart from the single/double capture processes). The electrons collide with additional neutral particles in the atmosphere, further ionizing and creating more electrons. This motivated me to follow the history of ionized H_2 molecules as shown in Figures 5.3 and 5.4. H_2^+ production can be a product of the ion precipitation model (primary ionization), where heavy ions of various energies collide with neutral H_2 producing H_2^+ . Alternatively, H_2^+ production can come from secondary electrons as tracked by the two-stream model, resulting in additional ionization and excitation of H_2 and H (see Figures 5.3, 5.4, 5.5, and 5.6). Primary ionization plays a larger role than secondary ionization in H_2^+ production and it plays a much more dominant part in H^+ production, as secondary ionization is one to two orders of magnitude smaller. Much like heavy ion production presented in Figures

5.1 and 5.2 the location of the peak H^+ and H_2^+ production rates converge to the same atmospheric density when the initial ion energy increases.

Additionally, excitation of neutral hydrogen is possible (see TEX collisions), rather than ionization. This occurs when H or H_2 molecules do not receive enough energy from the incident oxygen ion to reach the first ionization potential, but are still excited above the ground state. The de-excitation of H_2 can lead to Lyman or Werner band (airglow) emission. For my model, I assume that the excitation process leads to Lyman and Werner band production equally. The de-excitation of H largely leads to Lyman alpha production. The airglow effects of excitation due to electron-neutral collisions are discussed further in the following section.

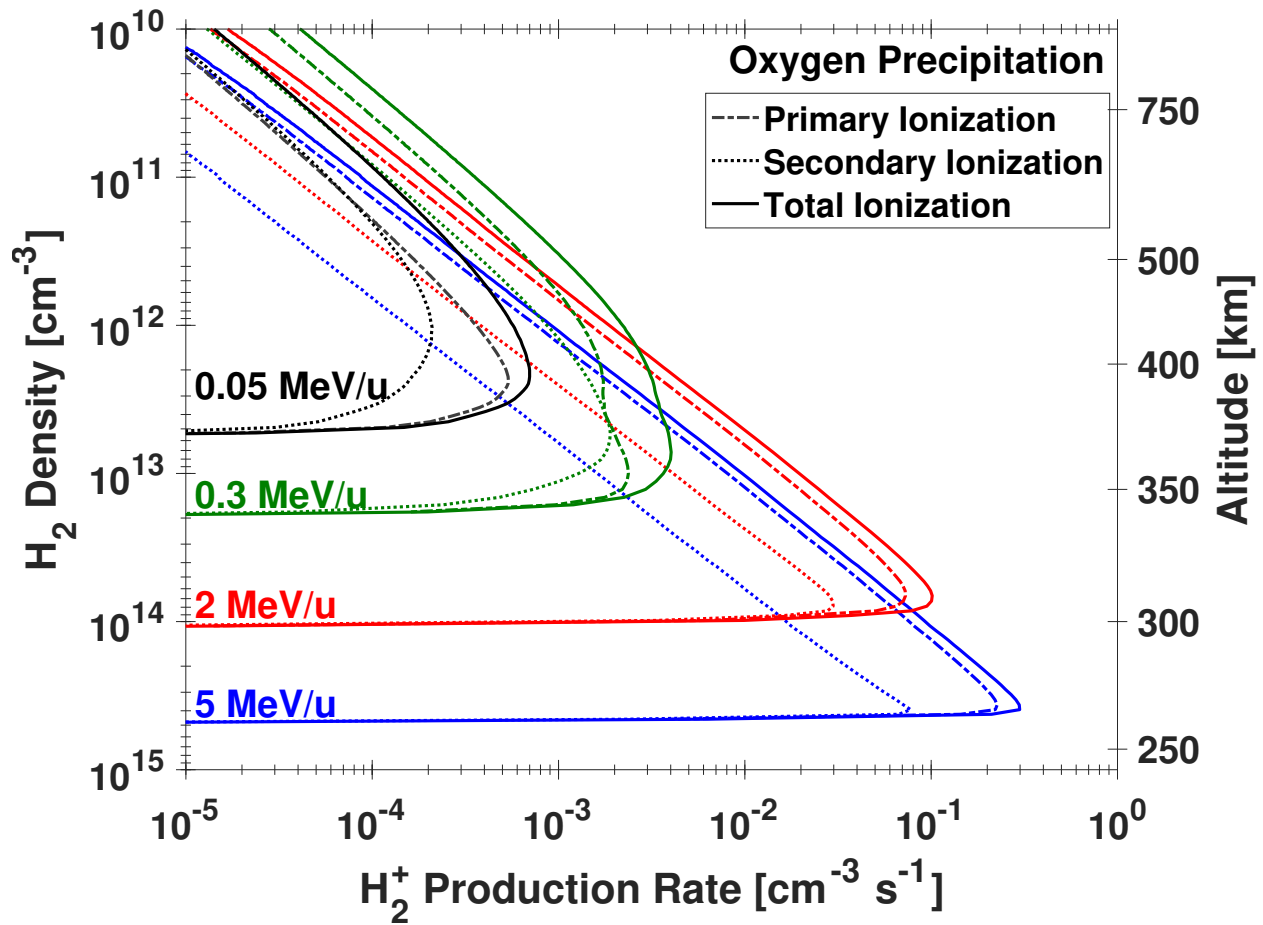


Figure 5.3: H₂⁺ production rate profiles vs. H₂ density for oxygen ions with initial energy of 0.05, 0.3, 2, and 5 MeV/u. This includes primary H₂⁺ production from the Jovian precipitation code (dot-dashed lines) and secondary H₂⁺ production from the two-stream code (dotted lines) with an initial input of 1 ion/cm²/s.

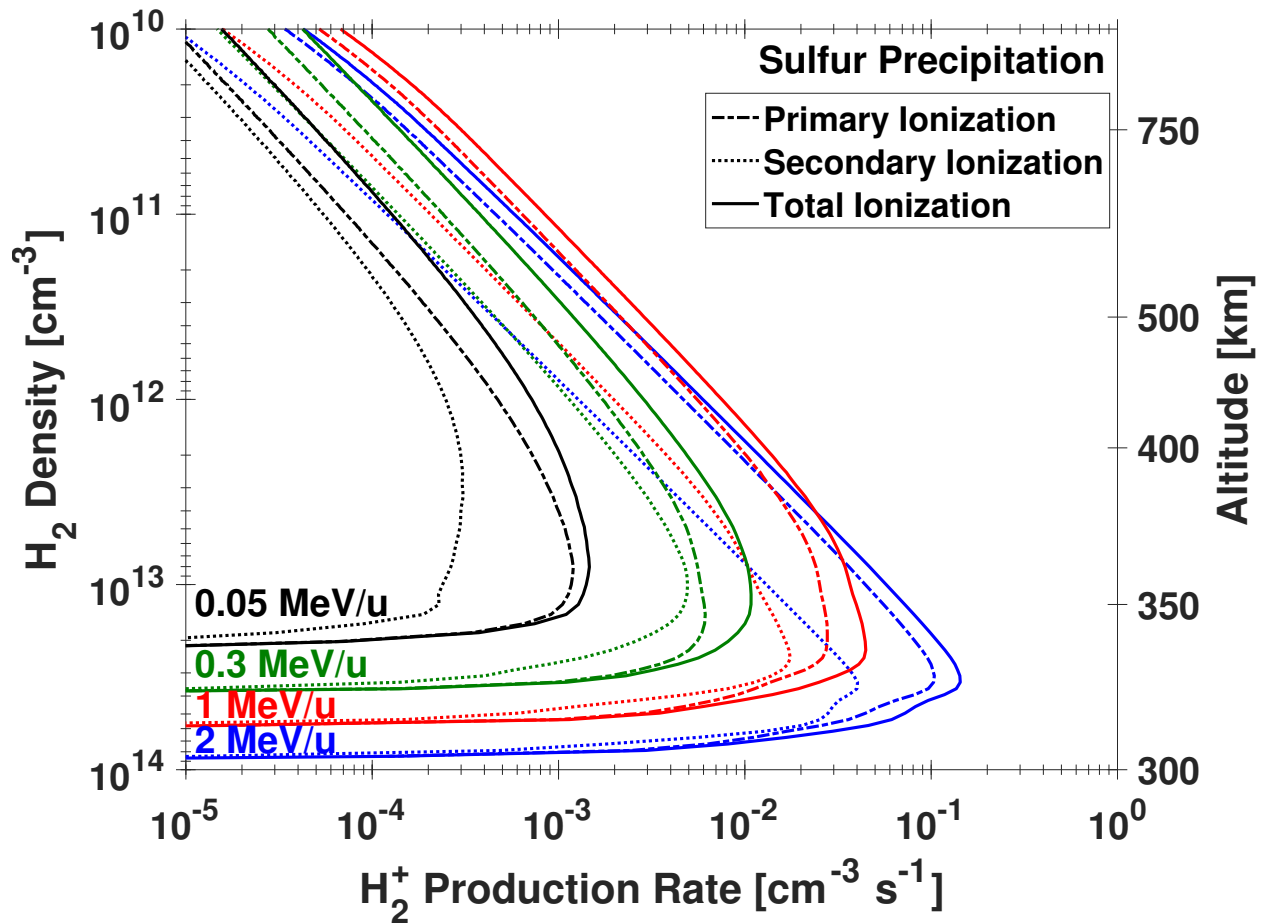


Figure 5.4: H_2^+ production rate profiles vs. H_2 density for sulfur ions with initial energy of 0.05, 0.3, 1, and 2 MeV/u. This includes primary H_2^+ production from the Jovian precipitation code (dot-dashed lines) and secondary H_2^+ production from the two-stream code (dotted lines) with an initial input of 1 ion/cm²/s.

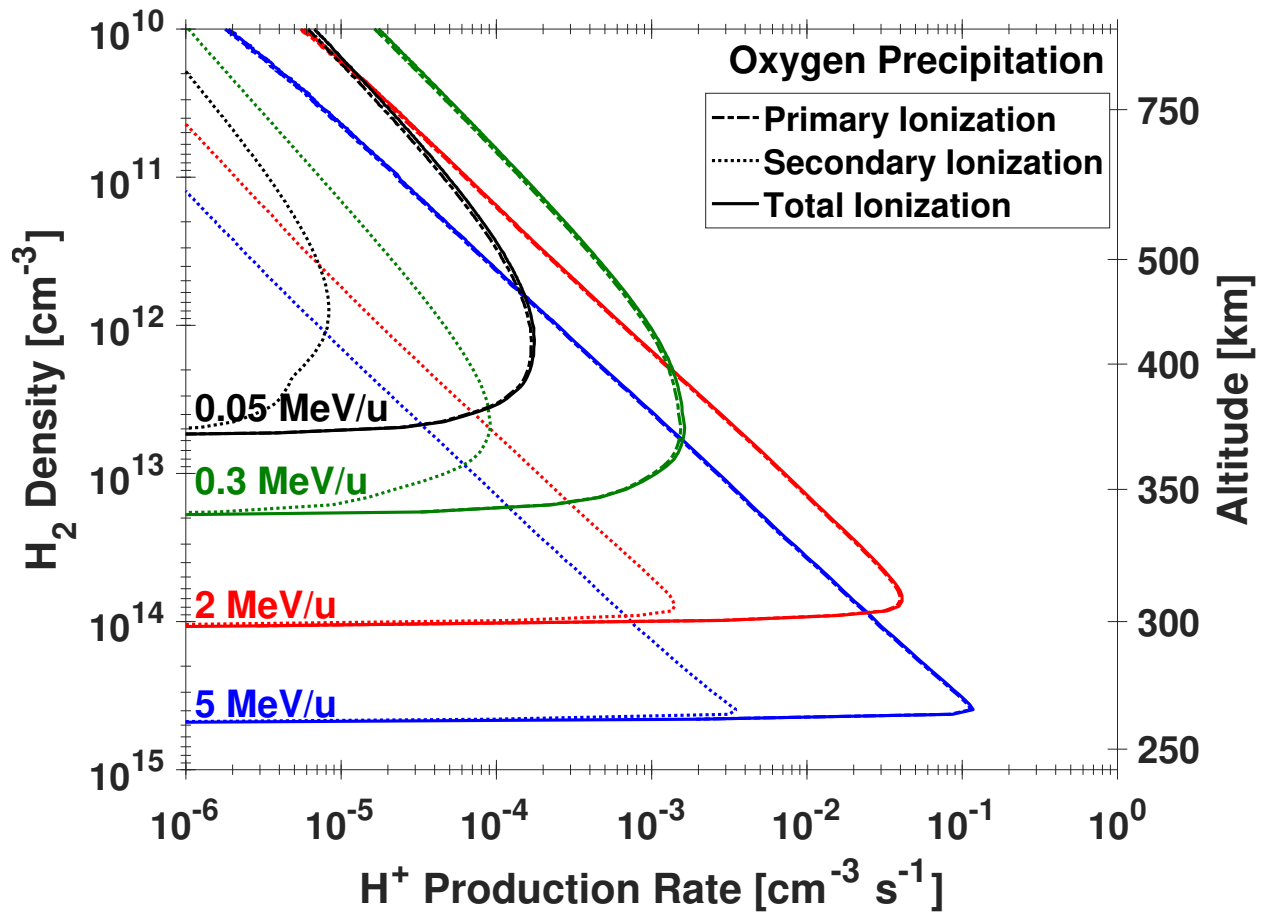


Figure 5.5: H⁺ production rate profiles vs. H₂ density for oxygen ions with initial energy of 0.05, 0.3, 2, and 5 MeV/u. This includes primary H⁺ production from the Jovian precipitation code (dot-dashed lines) and secondary H⁺ production from the two-stream code (dotted lines) with an initial input of 1 ion/cm²/s.

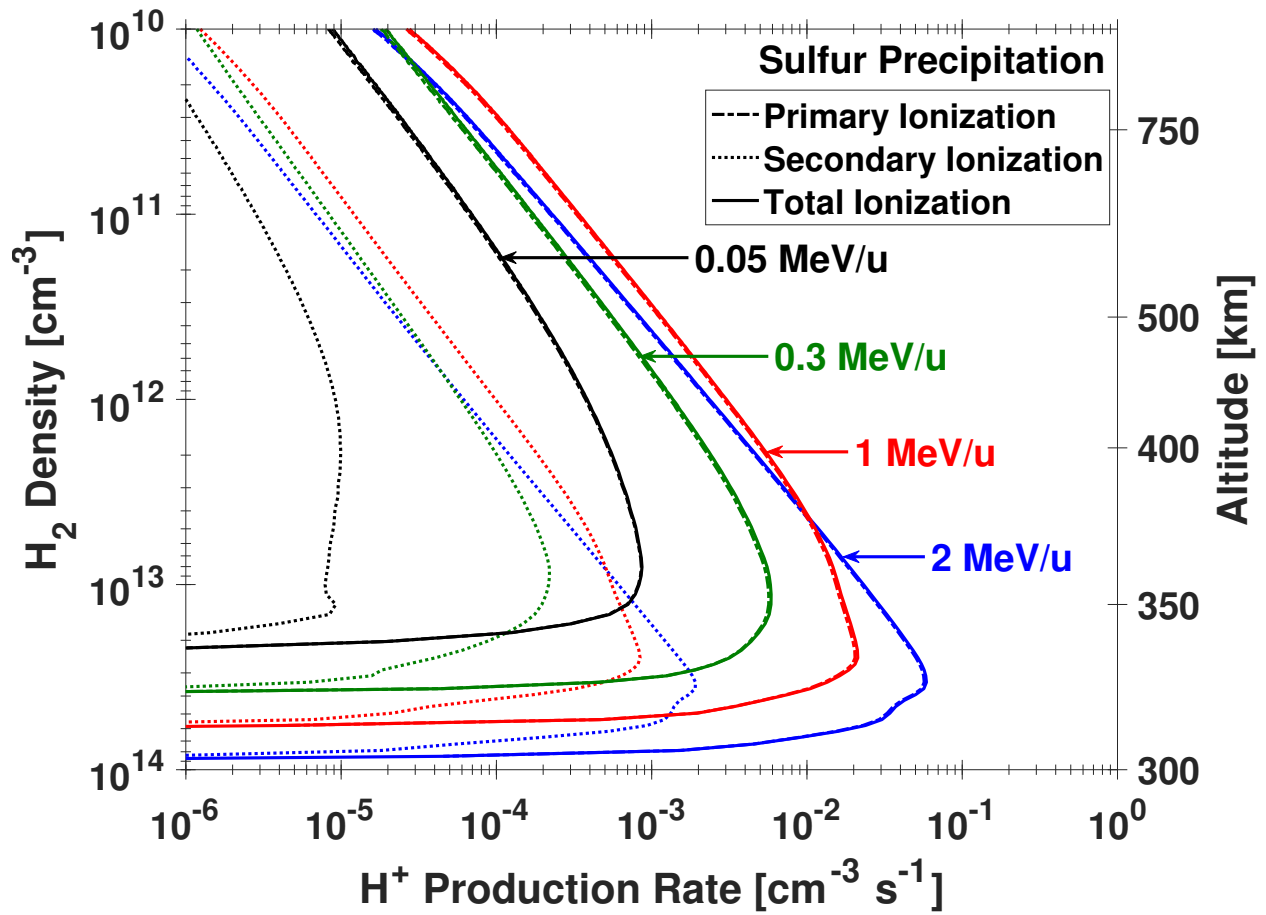


Figure 5.6: H^+ production rate profiles vs. H_2 density for sulfur ions with initial energy of 0.05, 0.3, 1, and 2 MeV/u. This includes primary H^+ production from the Jovian precipitation code (dot-dashed lines) and secondary H^+ production from the two-stream code (dotted lines) with an initial input of 1 ion/ cm^2/s .

5.2 Secondary Electron Effects

As discussed in Section 3.2, ions produce an abundance of secondary electrons as they precipitate through the atmosphere. The ion model tracks every secondary electron produced while the two-stream model makes use of this information. An example of the downward (or forward) secondary electron production spectra for different altitudes is shown in Figures 5.7 - 5.14. The figures include secondary electron production from oxygen precipitation at energies of 0.05, 0.3, 2, and 5 MeV/u and sulfur at 0.05, 0.3, 1, and 2 MeV/u, with an input of 1 ion/cm²/s. Forward electron production helps indicate how a particular incident ion energy will interact with the neutral atmosphere through secondary means, and how deep in the atmosphere there will be currents produced.

One of the instruments on NASA's Juno spacecraft is the Jovian Auroral Distribution Experiment (JADE) detector that can identify electron fluxes between ~ 100 eV and 100 keV (McComas et al., 2017). Thus, I compute the electron fluxes up the magnetic field lines due to primary ion precipitation, for future comparative purposes. Figures 5.15 and 5.16 shows the predictions for the escaping electron flux (i.e., upward flux at and above the top of the atmosphere, 3000 km) as a function of electron energy for precipitating ions with initial energies of 0.05, 0.3, 1, 2, and 5 MeV/u (it is worth noting that the bulk of these predictions fall below the lower limit of the JADE detector). The upward electron fluxes represent an upward field-aligned current which should be combined with the current from downwardly moving ions. With further analysis, Juno measurements should allow me to adjust my estimates of the incoming ion flux needed to account for the observed electron fluxes. There is also the possibility that the escaping electrons will enter an acceleration region located a few R_J above the polar region, which will further accelerate them, perhaps up to relativistic energies (cf. Cravens et al. (2003)). The Ulysses spacecraft detected localized MeV electrons in the high-latitude outer magnetosphere, although these are not permanent features of the planet (Karanikola et al., 2004; McKibben et al., 1993; Zhang et al., 1995). MacDowall et al. (1993) asserted that these MeV accelerated electrons might be responsible for QP-40 radio emissions above the Jovian poles.

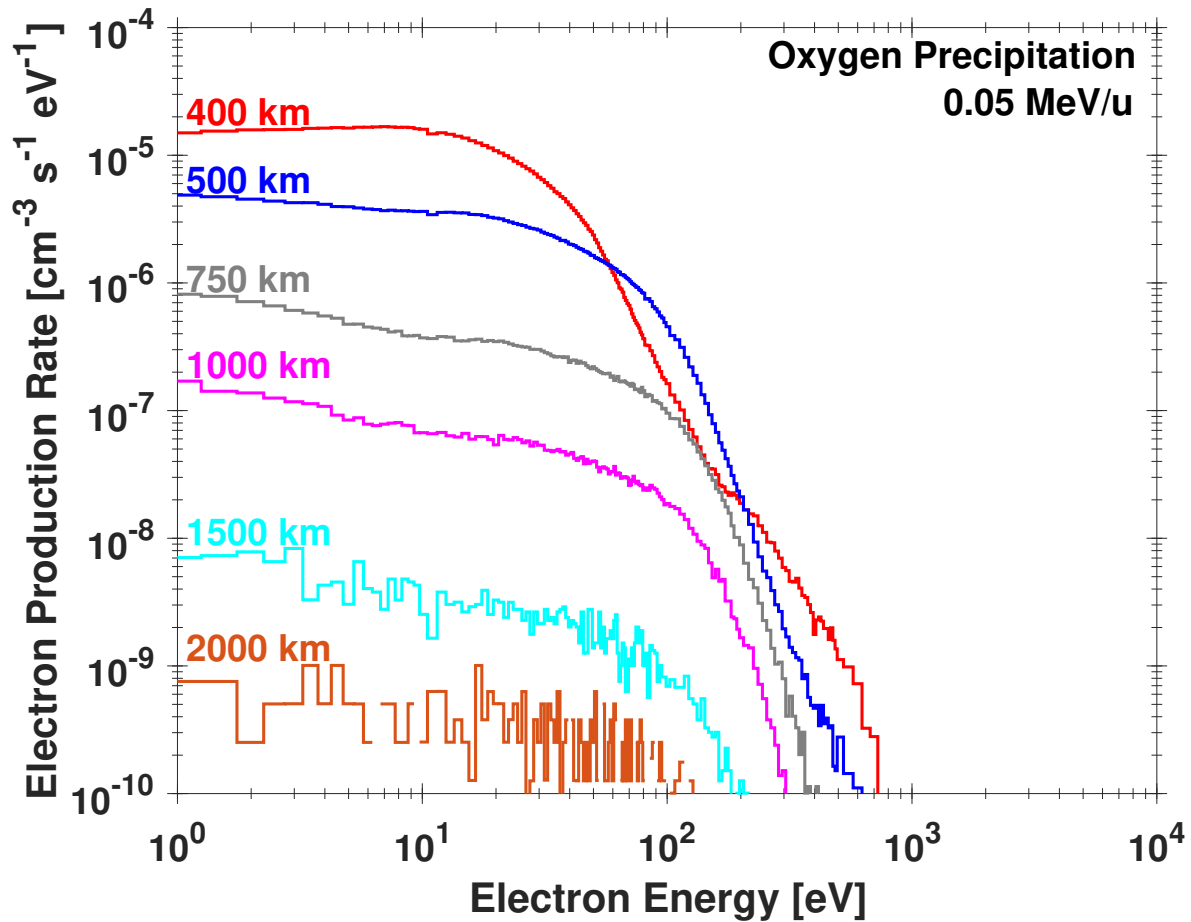


Figure 5.7: Forward secondary electron production rates for various altitudes from the ion precipitation and two-stream model for an incident ion energy of 0.05 MeV/u (energy flux of 0.8 MeV). These production rates are due to a single oxygen ion/cm²/s input into the top of the atmosphere. Ionizing collisions are the dominant process that produces low energy electrons, while stripping collisions are what produce the tails (higher energy) of the electron distributions.

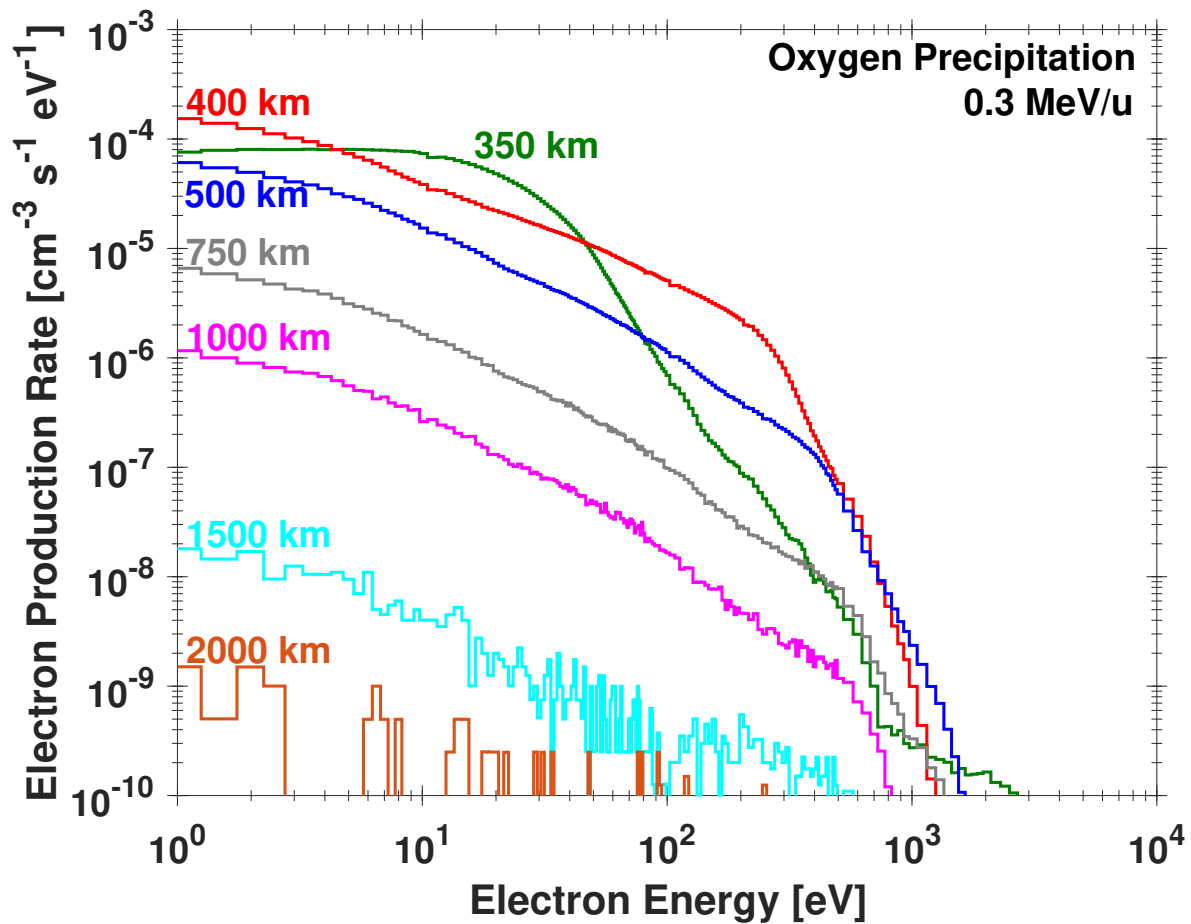


Figure 5.8: Forward secondary electron production rates for various altitudes from the ion precipitation and two-stream model for an incident ion energy of 0.3 MeV/u (energy flux of 4.8 MeV). These production rates are due to a single oxygen ion/cm²/s input into the top of the atmosphere. Ionizing collisions are the dominant process that produces low energy electrons, while stripping collisions are what produce the tails (higher energy) of the electron distributions.

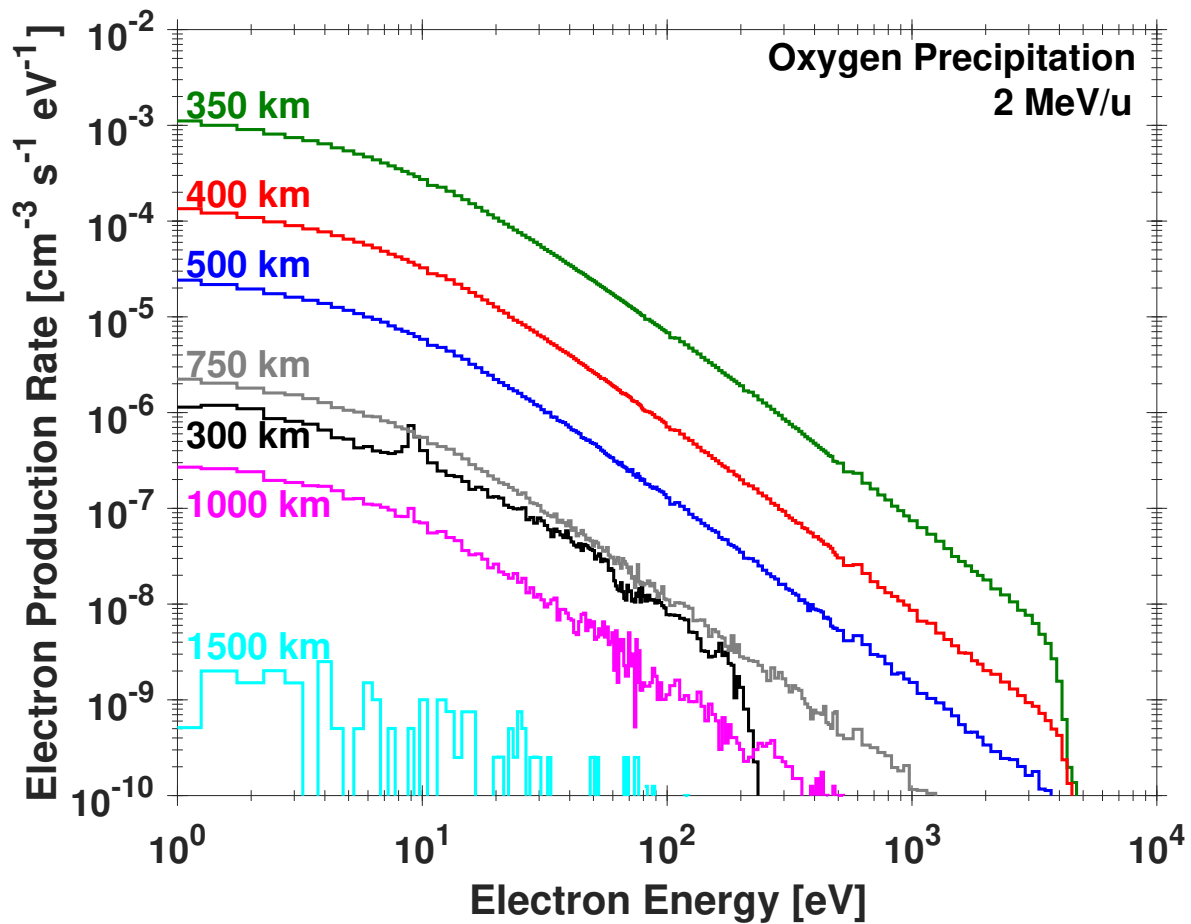


Figure 5.9: Forward secondary electron production rates for various altitudes from the ion precipitation and two-stream model for an incident ion energy of 2 MeV/u (energy flux of 32 MeV). These production rates are due to a single oxygen ion/cm²/s input into the top of the atmosphere. Ionizing collisions are the dominant process that produces low energy electrons, while stripping collisions are what produce the tails (higher energy) of the electron distributions.

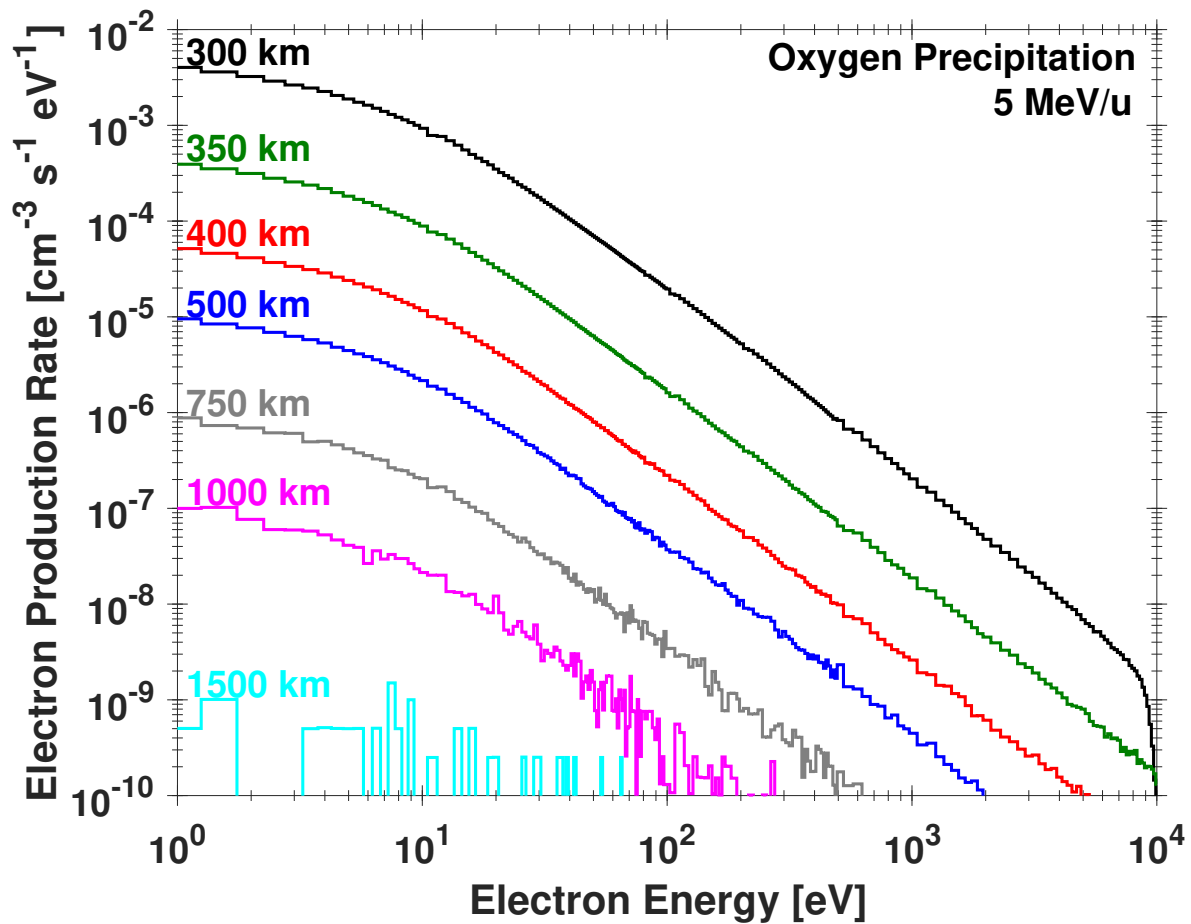


Figure 5.10: Forward secondary electron production rates for various altitudes from the ion precipitation and two-stream model for an incident ion energy of 5 MeV/u (energy flux of 80 MeV). These production rates are due to a single oxygen ion/cm²/s input into the top of the atmosphere. Ionizing collisions are the dominant process that produces low energy electrons, while stripping collisions are what produce the tails (higher energy) of the electron distributions.

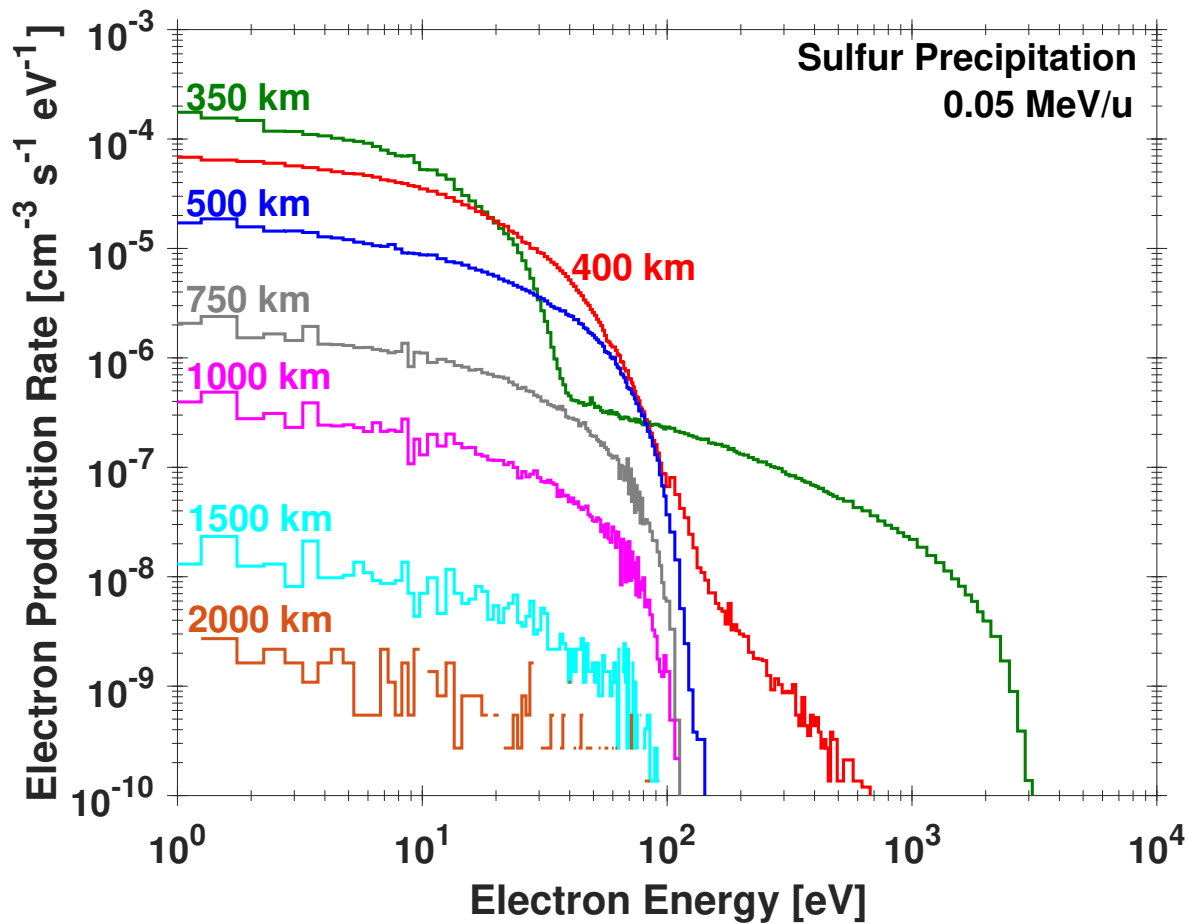


Figure 5.11: Forward secondary electron production rates for various altitudes from the ion precipitation and two-stream model for an incident ion energy of 0.05 MeV/u (energy flux of 1.6 MeV). These production rates are due to a single sulfur ion/cm²/s input into the top of the atmosphere. Ionizing collisions are the dominant process that produces low energy electrons, while stripping collisions are what produce the tails (higher energy) of the electron distributions.

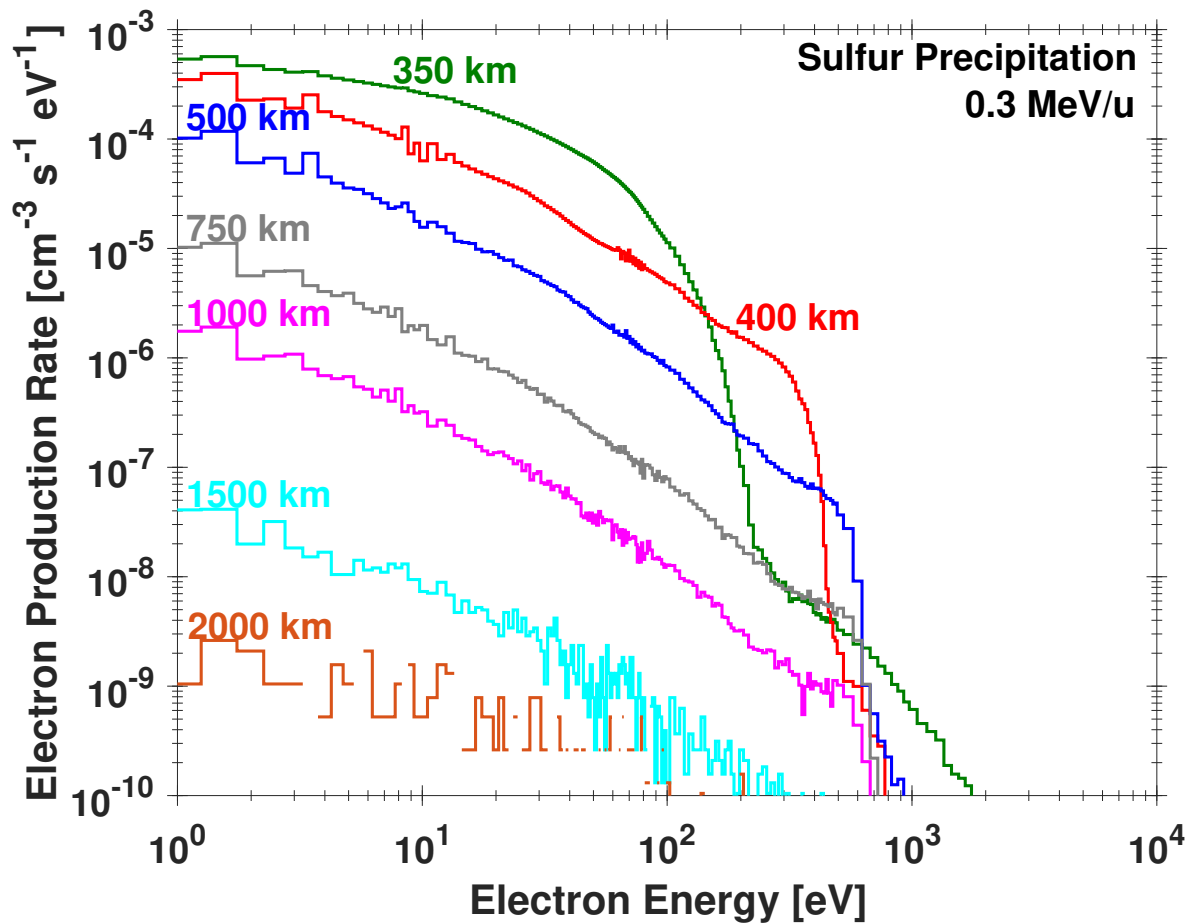


Figure 5.12: Forward secondary electron production rates for various altitudes from the ion precipitation and two-stream model for an incident ion energy of 0.3 MeV/u (energy flux of 9.6 MeV). These production rates are due to a single sulfur ion/cm²/s input into the top of the atmosphere. Ionizing collisions are the dominant process that produces low energy electrons, while stripping collisions are what produce the tails (higher energy) of the electron distributions.

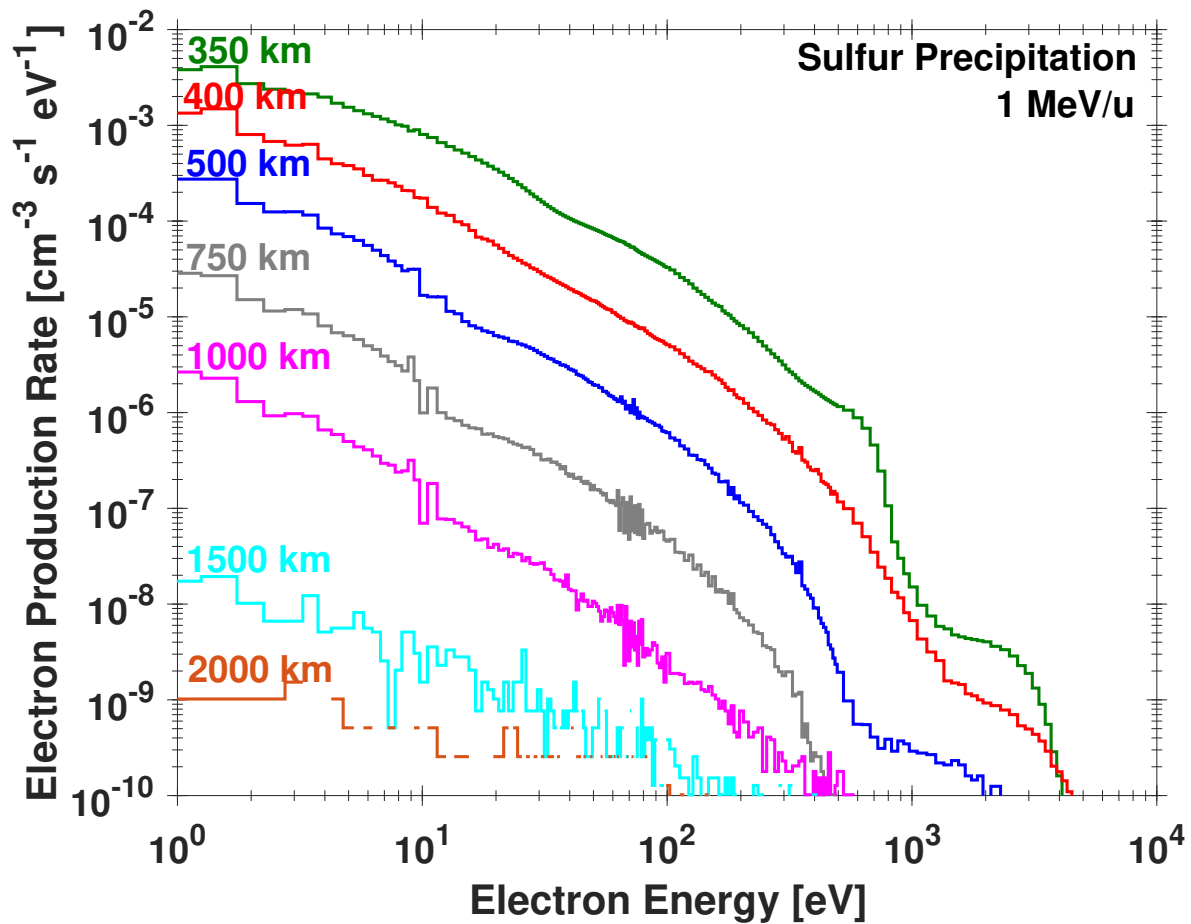


Figure 5.13: Forward secondary electron production rates for various altitudes from the ion precipitation and two-stream model for an incident ion energy of 1 MeV/u (energy flux of 32 MeV). These production rates are due to a single sulfur ion/cm²/s input into the top of the atmosphere. Ionizing collisions are the dominant process that produces low energy electrons, while stripping collisions are what produce the tails (higher energy) of the electron distributions.

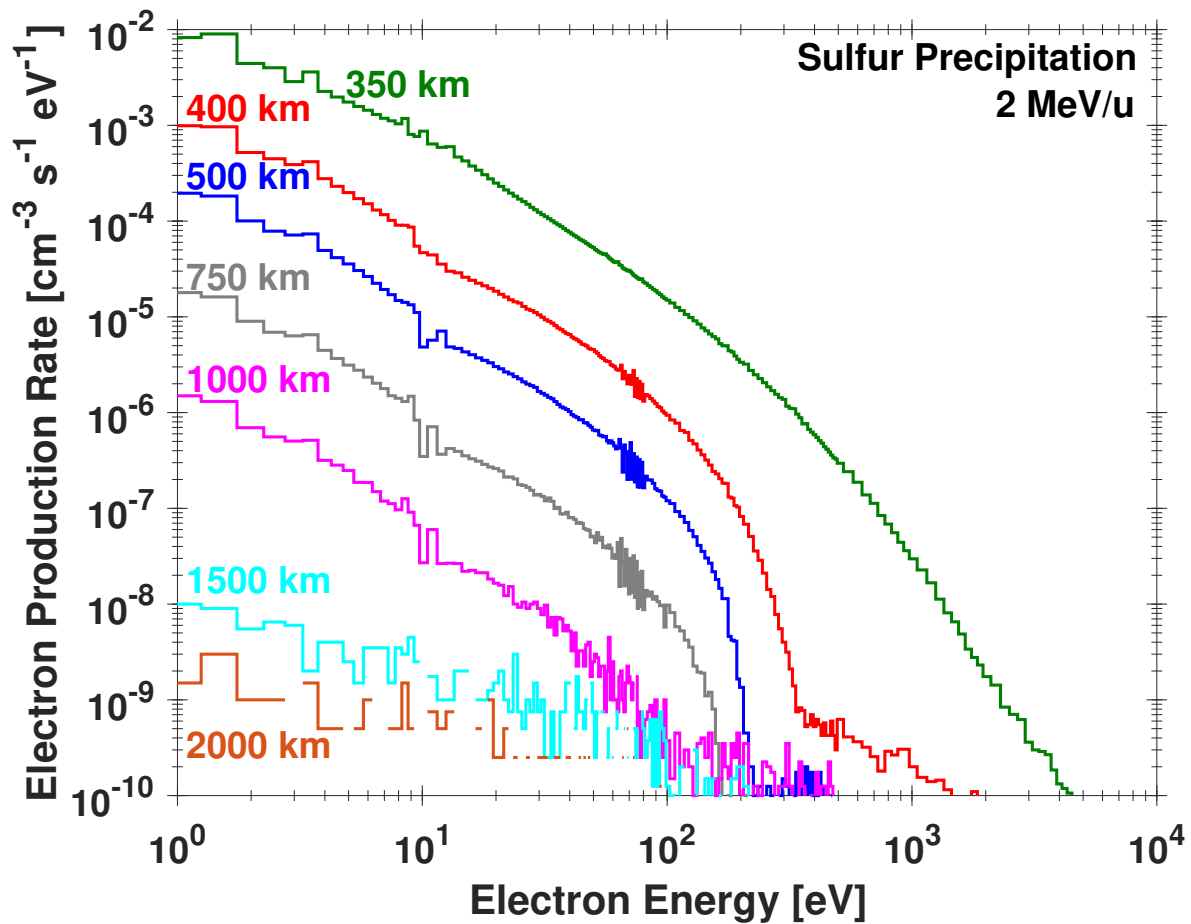


Figure 5.14: Forward secondary electron production rates for various altitudes from the ion precipitation and two-stream model for an incident ion energy of 2 MeV/u (energy flux of 64 MeV). These production rates are due to a single sulfur ion/cm²/s input into the top of the atmosphere. Ionizing collisions are the dominant process that produces low energy electrons, while stripping collisions are what produce the tails (higher energy) of the electron distributions.

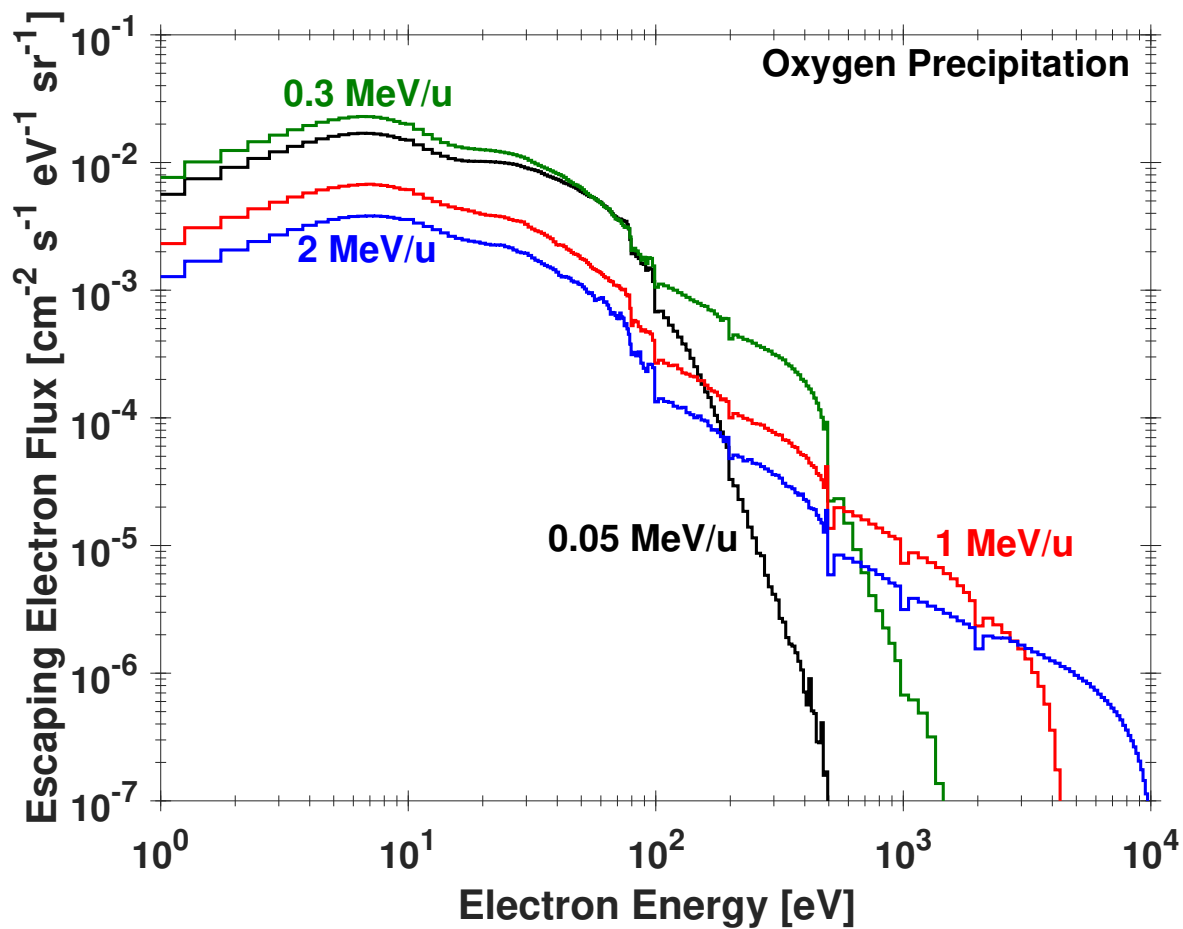


Figure 5.15: Predicted electron escape flux vs. electron energy for precipitating oxygen ion energies of 0.05, 0.3, 2, and 5 MeV/u. A step plot has been used to show the size of the corresponding energy bins that are output by the ion precipitation model to be used by the two-stream code. This figure is with an incident input of 1 ions/cm²/s.

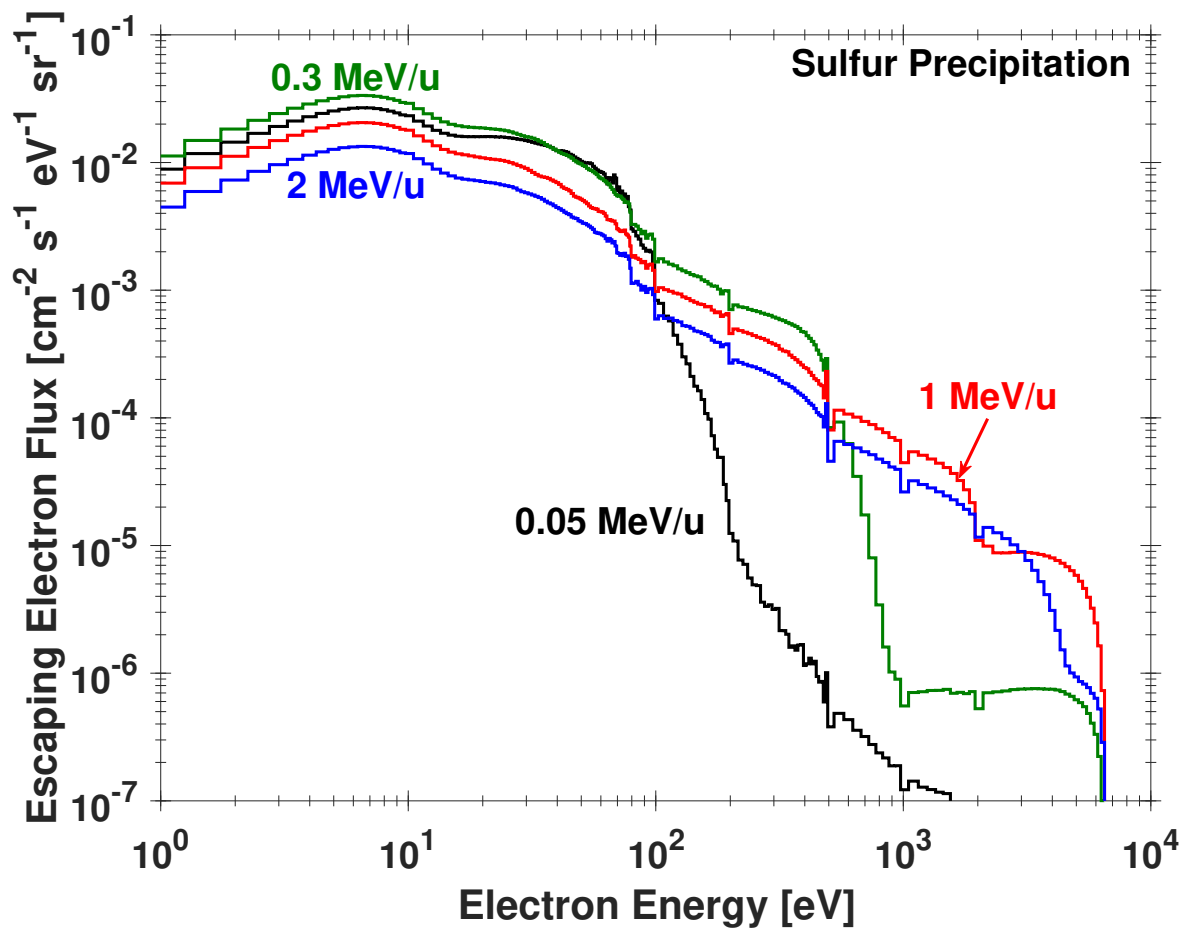


Figure 5.16: Predicted electron escape flux vs. electron energy for precipitating sulfur ion energies of 0.05, 0.3, 1, and 2 MeV/u. A step plot has been used to show the size of the corresponding energy bins that are output by the ion precipitation model to be used by the two-stream code. This figure is with an incident input of 1 ions/cm²/s.

Allegrini et al. (2017) show electron measurements from the JADE detector during the first Perijove pass. Their primary focus is the electron distribution over the main auroral oval, not the X-ray emission regions. They indicate upward (out of the planet) electron beams that reach relativistic energies beyond the scope of the instrument, unlike the lower energies predicted by ion precipitation, which also cannot be seen by JADE. Mauk et al. (2017b) use the JEDI instrument to analyze higher energy electron beams (25-800 keV) for the same Perijove pass, showing electron counts up to the energy limit of the instrument. Figures 5.17 and 5.18 show the upward electron fluxes for a single ion as a function of altitude (below 3000 km) for specific electron energies (i.e., 10, 20, 50, 100, and 1000 eV) and incident ion energies of 0.05, 0.3, 2, and 5 MeV/u for oxygen and 0.05, 0.3, 1, and 2 MeV/u for sulfur. These fluxes, along with the downward precipitation of ions, greatly contribute to the downward field-aligned currents.

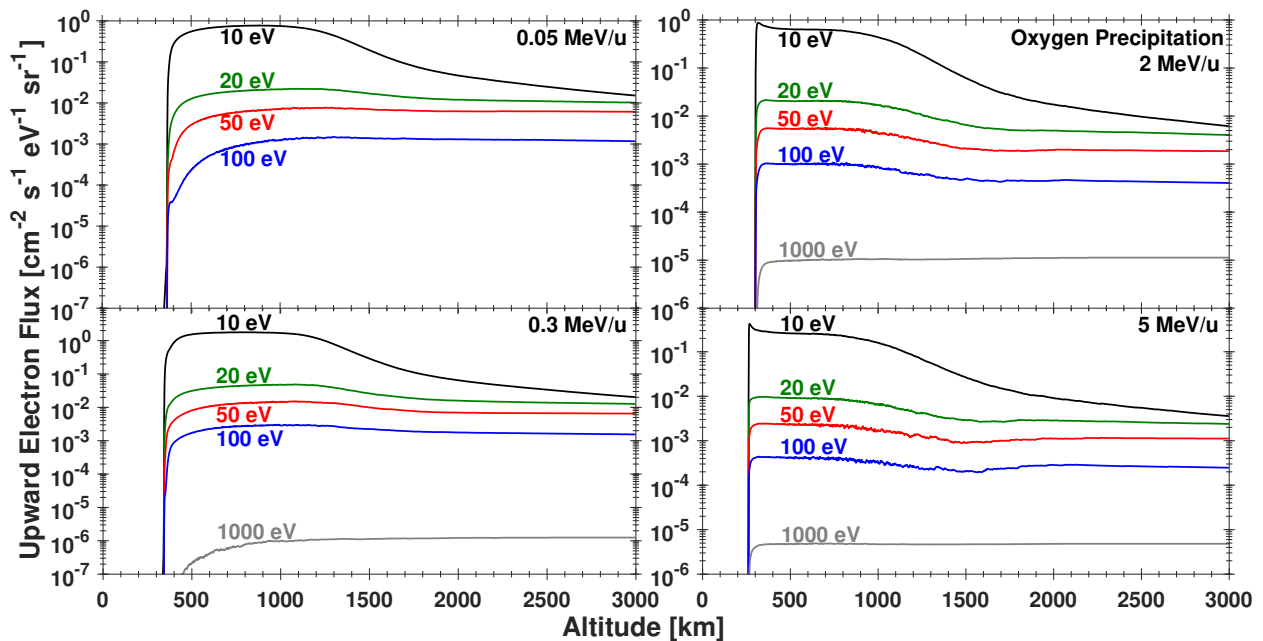


Figure 5.17: Upward electron flux for a single ion/cm²/s vs. altitude for electron energies of 10, 20, 50, 100, and 1000 eV and initial oxygen ion energies of 0.05, 0.3, 2, and 5 MeV/u.

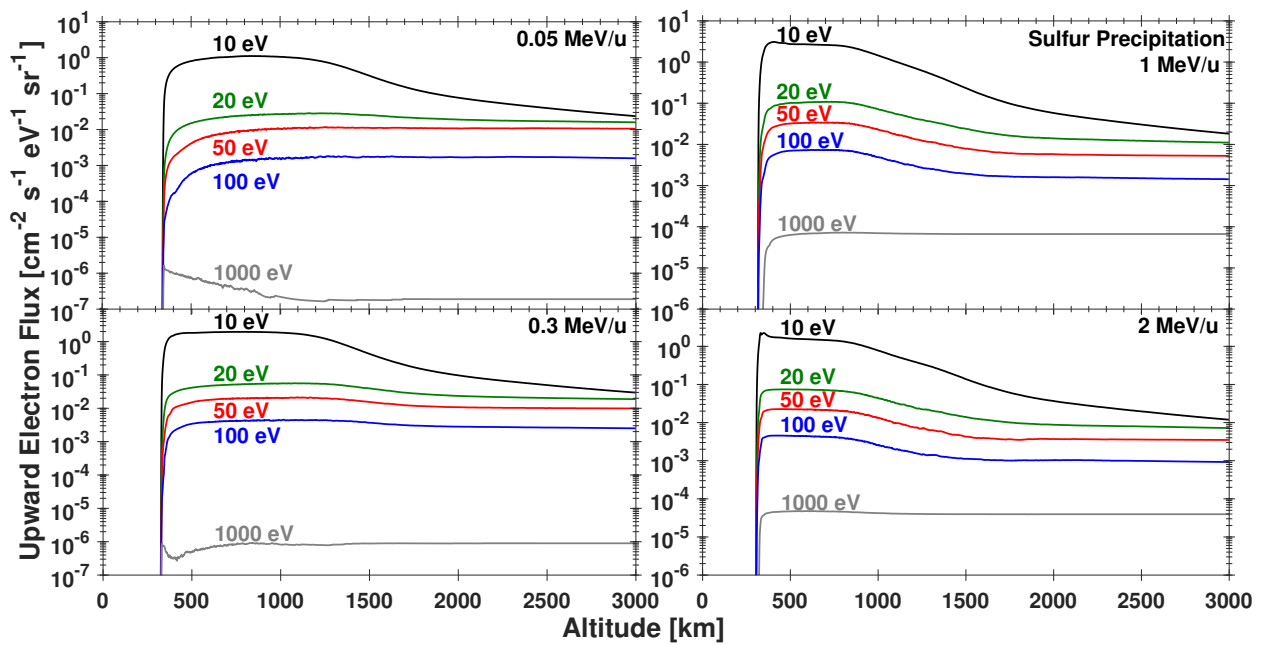


Figure 5.18: Upward electron flux for a single ion/cm²/s vs. altitude for electron energies of 10, 20, 50, 100, and 1000 eV and initial sulfur ion energies of 0.05, 0.3, 1, and 2 MeV/u.

5.3 Field-Aligned Currents

Positively charged ions precipitating into Jupiter's upper atmosphere and electrons flowing out create a downward field-aligned current that should be taken into account for magnetosphere-ionosphere coupling. The magnitude of the current is determined by the flux of ions, their charge state, and the flux of electrons. Integrating over the escape flux of electrons (Figures 5.15 and 5.16) I have determined, per ion, the total energy flux escaping from Jupiter's atmosphere in the form of electrons, along with the total number of electrons escaping, and the current density this escapement creates given an initial ion energy (Tables 5.1 and 5.2). The primary current from 1 net singly ionized oxygen atom/cm²/s will create a current density of 1.6×10^{-15} A/m² and from 1 net doubly ionized sulfur atom/cm²/s will create 3.2×10^{-15} A/m² (both of these are the initial charge state used in the model). These current densities then need to be added to the electron current densities shown in Tables 5.1 and 5.2 for the total current density produced by 1 net ion/cm²/s. It is evident that as ions precipitate with higher energy, more energetic electrons are produced but the electrons have more difficulty escaping from the atmosphere since they are produced deeper. However, lower energy ions create electrons high in the atmosphere, giving these secondary electrons an opportunity to escape the upper atmosphere. Consequently, the current density produced by secondary electrons peaks for initial ion energies of 200-300 keV/u for both oxygen and sulfur.

Table 5.1: Monoenergetic oxygen ion beam escape energy flux, electron flux, and secondary current density per 1 net ion/cm²/s.

Energy [keV]	Escape Energy Flux [eV/cm ² /s]	Escape Electron Flux [electrons/cm ² /s]	Secondary Current Density [A/m ²]
10	4.10E+01	1.67E+00	2.68E-15
25	1.08E+02	3.46E+00	5.54E-15
50	1.66E+02	4.33E+00	6.93E-15
75	2.15E+02	4.65E+00	7.45E-15
100	2.58E+02	4.88E+00	7.82E-15
125	2.98E+02	5.29E+00	8.48E-15
150	3.30E+02	5.60E+00	8.97E-15
175	3.59E+02	5.76E+00	9.23E-15
200	3.95E+02	6.01E+00	9.63E-15
250	3.95E+02	5.85E+00	9.37E-15
300	4.01E+02	5.92E+00	9.49E-15
350	3.74E+02	5.35E+00	8.58E-15
400	3.65E+02	5.11E+00	8.19E-15
450	3.72E+02	4.97E+00	7.96E-15
500	3.56E+02	4.45E+00	7.12E-15
600	3.27E+02	3.84E+00	6.16E-15
700	3.12E+02	3.53E+00	5.66E-15
800	3.06E+02	3.34E+00	5.35E-15
900	2.93E+02	2.98E+00	4.78E-15
1000	2.90E+02	2.87E+00	4.60E-15
1250	2.66E+02	2.45E+00	3.92E-15
1500	2.47E+02	2.09E+00	3.34E-15
1750	2.53E+02	2.01E+00	3.23E-15
2000	2.54E+02	1.82E+00	2.92E-15
5000	2.94E+02	1.06E+00	1.70E-15

Table 5.2: Monoenergetic sulfur ion beam escape energy flux, electron flux, and secondary current density per 1 net ion/cm²/s.

Energy [keV]	Escape Energy Flux [eV/cm ² /s]	Escape Electron Flux [electrons/cm ² /s]	Secondary Current Density [A/m ²]
10	1.22E+02	1.18E+00	1.89E-15
25	1.08E+02	3.31E+00	5.30E-15
50	2.54E+02	6.88E+00	1.10E-14
75	3.53E+02	8.08E+00	1.29E-14
100	4.36E+02	8.69E+00	1.39E-14
125	4.84E+02	8.95E+00	1.43E-14
150	5.14E+02	8.91E+00	1.43E-14
175	6.57E+02	9.59E+00	1.54E-14
200	7.99E+02	1.01E+01	1.61E-14
250	8.32E+02	9.80E+00	1.57E-14
300	8.16E+02	9.28E+00	1.49E-14
350	8.78E+02	8.71E+00	1.40E-14
400	1.11E+03	8.80E+00	1.41E-14
450	1.35E+03	8.57E+00	1.37E-14
500	1.67E+03	8.51E+00	1.36E-14
600	2.26E+03	8.06E+00	1.29E-14
700	2.43E+03	7.56E+00	1.21E-14
800	2.26E+03	7.16E+00	1.15E-14
900	2.00E+03	6.70E+00	1.07E-14
1000	1.70E+03	6.08E+00	9.74E-15
1250	1.23E+03	5.13E+00	8.21E-15
1500	1.02E+03	4.45E+00	7.13E-15
1750	9.93E+02	4.13E+00	6.62E-15
2000	1.00E+03	3.88E+00	6.21E-15

5.4 Airglow Emissions

As discussed in the context of electron precipitation in Section 3.2.4, particle precipitation through the atmosphere ionizes and excites the neutral atmospheric species. The excitation of H_2 and H produces Lyman and Werner band UV emission. The altitude-integrated ion production rates from heavy ion precipitation and secondary electrons are shown in Tables 5.3 and 5.4 for oxygen and sulfur, respectively. Tables 5.5 and 5.6 display the altitude-integrated UV airglow emission rates for oxygen and sulfur. Each table presented here is for a primary input power of 1 mW/m^2 .

Figures 5.19 and 5.20 show airglow production rates for a single oxygen and sulfur ion precipitating into the atmosphere with various initial energies. The curves show the emission due to the secondary electrons from the ion precipitation. No photoelectrons are considered (i.e., this is a night-side case, as are all my results). The Lyman bands have the largest production rate in an atmospheric column. As the initial ion energy increases it can penetrate deeper in the atmosphere where the H_2 density is greater. This produces an increase in the Lyman and Werner band production rates associated with H_2 . On the other hand, deeper in the atmosphere the H density decreases, causing a significant decrease in the H Ly- α production rate calculated for higher initial ion energies. The figures show the peak airglow production at altitudes between 300 (H_2 density of $\sim 1.1 \times 10^{14}$) and 400 km (H_2 density of $\sim 1.8 \times 10^{12}$) for most initial energies, which may be above or at the homopause, allowing the emissions to escape the atmosphere with some attenuation. In the current section, optical depth effects have not been considered, but are accounted for in the following section concerning color ratio.

Table 5.3: Column-integrated ion-production rates for a primary input power of 1 mW/m² oxygen ions in units of cm⁻²s⁻¹.

Ion Energy [keV/u]	Secondary Ion Production				Primary Ion Production	
	H ₂ ⁺	H ⁺	He ⁺	CH ₄ ⁺	H ₂ ⁺	H ⁺
10	3.92E+09	1.76E+08	1.81E+07	7.86E+03	1.46E+10	3.72E+09
25	5.55E+09	2.51E+08	3.54E+07	1.48E+05	1.27E+10	4.65E+09
50	6.66E+09	3.29E+08	6.01E+07	6.86E+05	1.01E+10	5.34E+09
75	6.68E+09	3.44E+08	7.48E+07	1.31E+06	8.66E+09	5.40E+09
100	6.35E+09	3.36E+08	8.16E+07	1.84E+06	7.82E+09	5.26E+09
125	6.07E+09	3.26E+08	8.65E+07	2.33E+06	7.47E+09	5.18E+09
150	5.84E+09	3.15E+08	9.01E+07	2.79E+06	7.34E+09	5.13E+09
175	5.64E+09	3.04E+08	9.24E+07	3.20E+06	7.30E+09	5.09E+09
200	5.45E+09	2.95E+08	9.40E+07	3.56E+06	7.31E+09	5.06E+09
250	5.28E+09	2.83E+08	1.01E+08	4.53E+06	7.59E+09	5.12E+09
300	5.12E+09	2.72E+08	1.06E+08	5.41E+06	7.82E+09	5.15E+09
350	5.02E+09	2.63E+08	1.12E+08	6.46E+06	8.11E+09	5.22E+09
400	4.95E+09	2.56E+08	1.19E+08	7.65E+06	8.38E+09	5.30E+09
450	4.83E+09	2.47E+08	1.24E+08	8.76E+06	8.55E+09	5.33E+09
500	4.74E+09	2.40E+08	1.28E+08	9.89E+06	8.73E+09	5.36E+09
600	4.59E+09	2.28E+08	1.35E+08	1.21E+07	9.06E+09	5.43E+09
700	4.44E+09	2.18E+08	1.38E+08	1.36E+07	9.31E+09	5.47E+09
800	4.37E+09	2.13E+08	1.40E+08	1.47E+07	9.56E+09	5.52E+09
900	4.29E+09	2.07E+08	1.42E+08	1.56E+07	9.79E+09	5.56E+09
1000	4.21E+09	2.02E+08	1.43E+08	1.62E+07	9.98E+09	5.58E+09
1250	4.04E+09	1.91E+08	1.42E+08	1.72E+07	1.04E+10	5.61E+09
1500	3.93E+09	1.83E+08	1.41E+08	1.78E+07	1.07E+10	5.63E+09
1750	3.81E+09	1.76E+08	1.39E+08	1.79E+07	1.09E+10	5.58E+09
2000	3.72E+09	1.71E+08	1.37E+08	1.79E+07	1.11E+10	5.55E+09
5000	3.15E+09	1.40E+08	1.17E+08	1.62E+07	1.22E+10	4.96E+09

Table 5.4: Column-integrated ion-production rates for a primary input power of 1 mW/m² sulfur ions in units of cm⁻²s⁻¹.

Ion Energy [keV/u]	Secondary Ion Production				Primary Ion Production	
	H ₂ ⁺	H ⁺	He ⁺	CH ₄ ⁺	H ₂ ⁺	H ⁺
10	1.56E+09	9.19E+07	1.13E+07	9.42E+03	8.26E+09	4.48E+09
25	4.94E+09	1.93E+08	6.01E+07	2.53E+06	1.82E+10	1.29E+10
50	8.72E+09	3.66E+08	1.07E+08	5.93E+06	1.86E+10	1.46E+10
75	1.02E+10	4.58E+08	1.42E+08	8.10E+06	1.70E+10	1.44E+10
100	1.06E+10	4.92E+08	1.64E+08	9.75E+06	1.57E+10	1.38E+10
125	1.05E+10	4.98E+08	1.77E+08	1.11E+07	1.50E+10	1.32E+10
150	1.03E+10	4.93E+08	1.87E+08	1.23E+07	1.46E+10	1.26E+10
175	1.00E+10	4.86E+08	1.95E+08	1.34E+07	1.43E+10	1.22E+10
200	9.82E+09	4.79E+08	2.02E+08	1.46E+07	1.40E+10	1.19E+10
250	9.50E+09	4.67E+08	2.15E+08	1.69E+07	1.38E+10	1.14E+10
300	9.25E+09	4.54E+08	2.27E+08	1.91E+07	1.39E+10	1.11E+10
350	9.03E+09	4.42E+08	2.36E+08	2.10E+07	1.41E+10	1.09E+10
400	8.83E+09	4.31E+08	2.40E+08	2.24E+07	1.43E+10	1.07E+10
450	8.64E+09	4.21E+08	2.41E+08	2.32E+07	1.46E+10	1.06E+10
500	8.43E+09	4.11E+08	2.39E+08	2.34E+07	1.47E+10	1.05E+10
600	8.09E+09	3.97E+08	2.31E+08	2.30E+07	1.51E+10	1.02E+10
700	7.86E+09	3.86E+08	2.25E+08	2.25E+07	1.54E+10	1.01E+10
800	7.70E+09	3.78E+08	2.24E+08	2.23E+07	1.58E+10	1.00E+10
900	7.55E+09	3.69E+08	2.25E+08	2.25E+07	1.62E+10	1.00E+10
1000	7.38E+09	3.59E+08	2.27E+08	2.32E+07	1.65E+10	9.99E+09
1250	6.97E+09	3.35E+08	2.30E+08	2.53E+07	1.69E+10	9.85E+09
1500	6.61E+09	3.16E+08	2.27E+08	2.62E+07	1.70E+10	9.65E+09
1750	6.29E+09	2.99E+08	2.21E+08	2.64E+07	1.70E+10	9.43E+09
2000	6.01E+09	2.84E+08	2.15E+08	2.63E+07	1.69E+10	9.24E+09

Table 5.5: Column-integrated ultraviolet airglow emission rates for a primary input power of 1 mW/m² oxygen ions in units of cm⁻²s⁻¹.

Ion Energy [keV/u]	Lyman Bands			Werner Bands		Lyman Alpha	
	Direct Ex.	Cascade	Primary Ions	Direct Ex.	Primary Ions	H ₂	H
10	2.06E+09	2.91E+08	2.71E+09	1.68E+09	2.71E+09	4.36E+08	1.48E+08
25	2.77E+09	3.91E+08	2.57E+09	2.30E+09	2.57E+09	6.03E+08	1.30E+08
50	3.12E+09	4.35E+08	1.92E+09	2.63E+09	1.92E+09	7.01E+08	1.04E+08
75	3.03E+09	4.20E+08	1.59E+09	2.57E+09	1.59E+09	6.92E+08	8.29E+07
100	2.84E+09	3.90E+08	1.41E+09	2.41E+09	1.41E+09	6.51E+08	6.94E+07
125	2.69E+09	3.68E+08	1.34E+09	2.29E+09	1.34E+09	6.18E+08	6.18E+07
150	2.57E+09	3.51E+08	1.32E+09	2.19E+09	1.32E+09	5.92E+08	5.66E+07
175	2.48E+09	3.37E+08	1.31E+09	2.11E+09	1.31E+09	5.70E+08	5.29E+07
200	2.39E+09	3.26E+08	1.32E+09	2.04E+09	1.32E+09	5.50E+08	4.98E+07
250	2.32E+09	3.15E+08	1.39E+09	1.98E+09	1.39E+09	5.32E+08	4.44E+07
300	2.25E+09	3.06E+08	1.47E+09	1.92E+09	1.47E+09	5.16E+08	3.96E+07
350	2.22E+09	3.01E+08	1.57E+09	1.89E+09	1.57E+09	5.07E+08	3.45E+07
400	2.19E+09	2.98E+08	1.67E+09	1.86E+09	1.67E+09	5.00E+08	2.98E+07
450	2.15E+09	2.92E+08	1.77E+09	1.83E+09	1.77E+09	4.89E+08	2.57E+07
500	2.11E+09	2.87E+08	1.87E+09	1.79E+09	1.87E+09	4.80E+08	2.22E+07
600	2.06E+09	2.80E+08	2.07E+09	1.74E+09	2.07E+09	4.66E+08	1.74E+07
700	2.00E+09	2.72E+08	2.26E+09	1.69E+09	2.26E+09	4.52E+08	1.41E+07
800	1.98E+09	2.69E+08	2.44E+09	1.67E+09	2.44E+09	4.45E+08	1.17E+07
900	1.95E+09	2.65E+08	2.61E+09	1.64E+09	2.61E+09	4.38E+08	9.73E+06
1000	1.92E+09	2.61E+08	2.77E+09	1.62E+09	2.77E+09	4.31E+08	8.10E+06
1250	1.85E+09	2.52E+08	3.13E+09	1.56E+09	3.13E+09	4.14E+08	5.43E+06
1500	1.81E+09	2.47E+08	3.46E+09	1.52E+09	3.46E+09	4.04E+08	3.84E+06
1750	1.76E+09	2.40E+08	3.70E+09	1.48E+09	3.70E+09	3.92E+08	2.86E+06
2000	1.72E+09	2.35E+08	3.93E+09	1.45E+09	3.93E+09	3.84E+08	2.18E+06
5000	1.48E+09	2.03E+08	5.33E+09	1.24E+09	5.33E+09	3.27E+08	3.45E+05

Table 5.6: Column-integrated ultraviolet airglow emission rates for a primary input power of 1 mW/m² sulfur ions in units of cm⁻²s⁻¹.

Ion Energy [keV/u]	Lyman Bands			Werner Bands		Lyman Alpha	
	Direct Ex.	Cascade	Primary Ions	Direct Ex.	Primary Ions	H ₂	H
10	7.51E+08	9.62E+07	2.38E+09	6.15E+08	2.38E+09	1.54E+08	5.58E+07
25	2.72E+09	3.75E+08	4.94E+09	2.18E+09	4.94E+09	5.52E+08	1.01E+08
50	4.44E+09	6.18E+08	4.22E+09	3.64E+09	4.22E+09	9.48E+08	1.26E+08
75	4.99E+09	6.94E+08	3.55E+09	4.15E+09	3.55E+09	1.09E+09	1.17E+08
100	5.04E+09	6.98E+08	3.13E+09	4.21E+09	3.13E+09	1.12E+09	1.03E+08
125	4.93E+09	6.80E+08	2.89E+09	4.13E+09	2.89E+09	1.10E+09	9.05E+07
150	4.77E+09	6.58E+08	2.76E+09	4.01E+09	2.76E+09	1.07E+09	8.04E+07
175	4.63E+09	6.37E+08	2.71E+09	3.90E+09	2.71E+09	1.04E+09	7.25E+07
200	4.51E+09	6.19E+08	2.69E+09	3.80E+09	2.69E+09	1.02E+09	6.54E+07
250	4.33E+09	5.92E+08	2.74E+09	3.65E+09	2.74E+09	9.76E+08	5.52E+07
300	4.20E+09	5.74E+08	2.85E+09	3.55E+09	2.85E+09	9.48E+08	4.74E+07
350	4.10E+09	5.59E+08	2.97E+09	3.46E+09	2.97E+09	9.24E+08	4.15E+07
400	4.00E+09	5.46E+08	3.09E+09	3.38E+09	3.09E+09	9.03E+08	3.77E+07
450	3.92E+09	5.34E+08	3.18E+09	3.31E+09	3.18E+09	8.83E+08	3.52E+07
500	3.82E+09	5.21E+08	3.23E+09	3.23E+09	3.23E+09	8.61E+08	3.35E+07
600	3.66E+09	4.98E+08	3.29E+09	3.09E+09	3.29E+09	8.25E+08	3.24E+07
700	3.55E+09	4.83E+08	3.35E+09	3.00E+09	3.35E+09	8.01E+08	3.10E+07
800	3.47E+09	4.73E+08	3.45E+09	2.94E+09	3.45E+09	7.84E+08	2.82E+07
900	3.40E+09	4.63E+08	3.57E+09	2.88E+09	3.57E+09	7.68E+08	2.42E+07
1000	3.33E+09	4.53E+08	3.70E+09	2.82E+09	3.70E+09	7.51E+08	2.02E+07
1250	3.14E+09	4.29E+08	3.99E+09	2.66E+09	3.99E+09	7.10E+08	1.41E+07
1500	2.98E+09	4.08E+08	4.22E+09	2.53E+09	4.22E+09	6.74E+08	1.06E+07
1750	2.84E+09	3.89E+08	4.42E+09	2.41E+09	4.42E+09	6.42E+08	7.99E+06
2000	2.72E+09	3.72E+08	4.61E+09	2.30E+09	4.61E+09	6.14E+08	6.14E+06

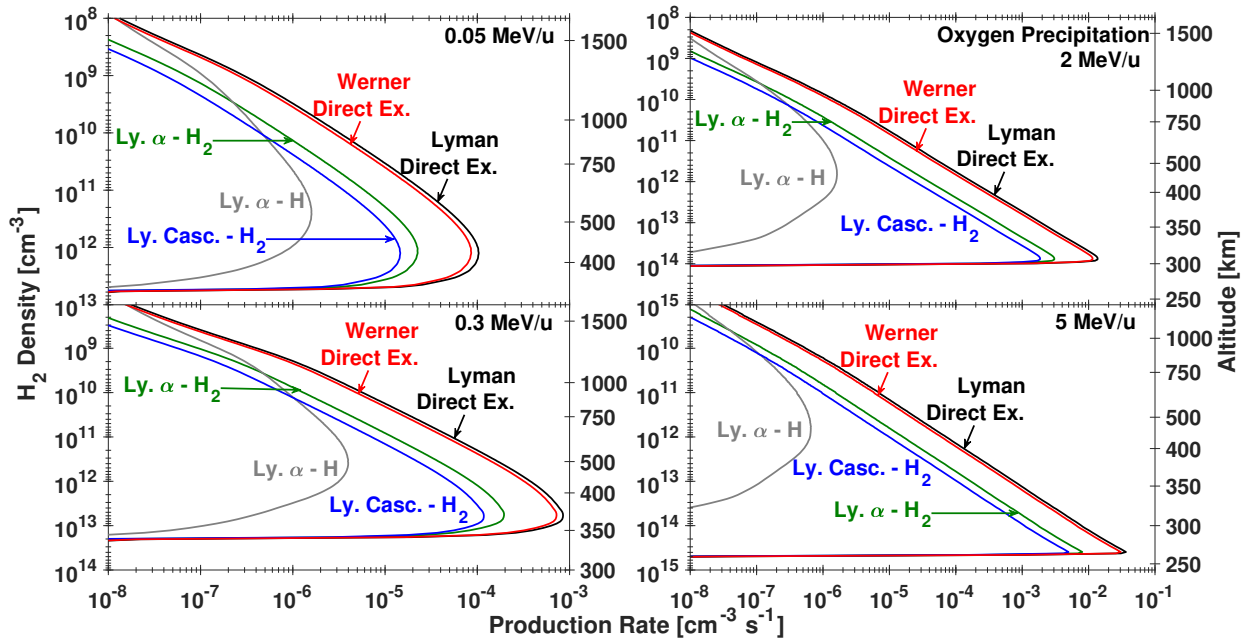


Figure 5.19: Airglow emission production from secondary electrons produced from a single incident oxygen ion/cm²/s.

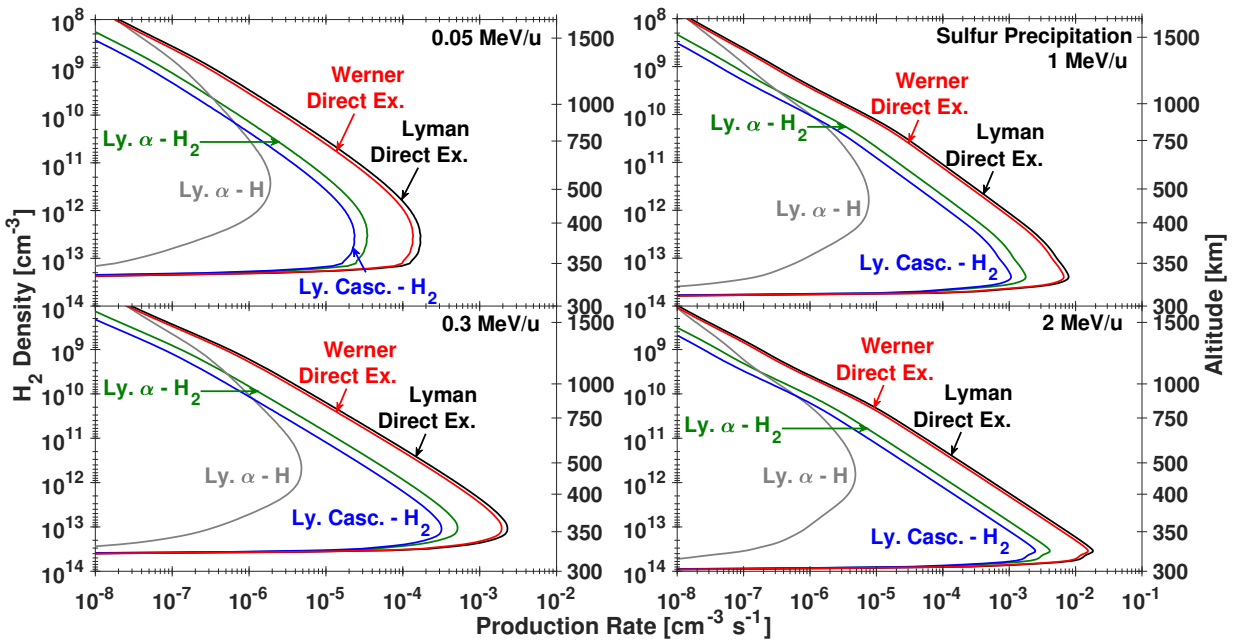


Figure 5.20: Airglow emission production from secondary electrons produced from a single incident sulfur ion/cm²/s.

5.5 Color Ratios and Predicted UV Spectra

Following the same processes I presented in Section 3.2.4, where a predicted UV spectrum from monoenergetic precipitating electrons is displayed, I produce UV spectra for different initial ion energies in Figures 5.21-5.28. Each of these spectra have omitted the Lyman- α line and also include opacity effects from CH₄ at exit angles of 60° and 80° through atmosphere 1. It is clear from these spectra that low energy oxygen ions (50 and 300 keV/u) are not penetrating as deeply as sulfur ions of the same energy/nucleon, as can be seen by the amount of absorption by CH₄; however, when higher initial ion energies are considered, the oxygen ions penetrate deeper than sulfur ions of the same energy/nucleon. This is more readily seen in the color ratio comparison, shown in Figure 5.29, where an unabsorbed spectrum has a color ratio of 1.32.

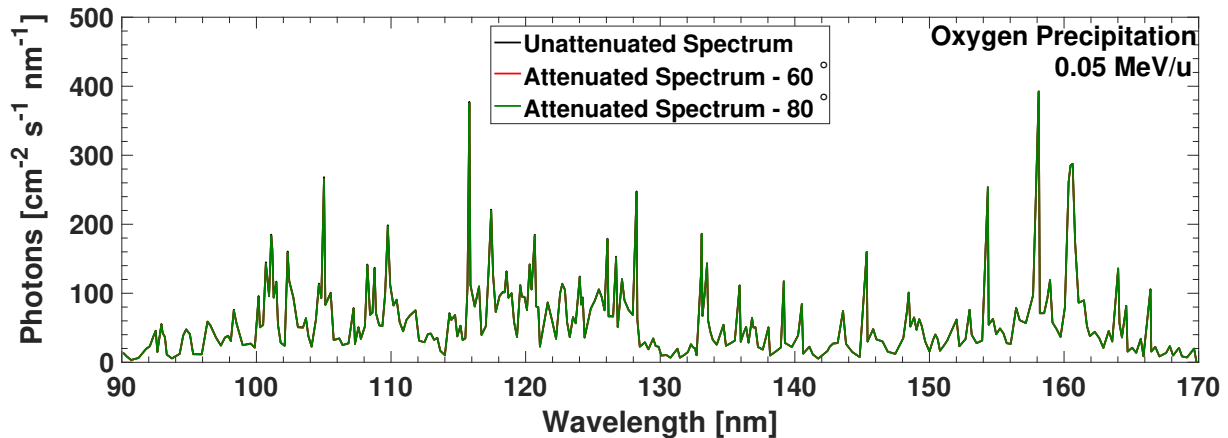


Figure 5.21: Predicted Lyman-Werner spectrum from an input of 1 oxygen ion/cm²/s at 0.05 MeV/u. The red line is calculated with a θ of 60° and the green line with a θ of 80° , while the black line is what is expected when no opacity effects are considered. The Ly- α line at 121.6 nm has been withheld from these predictions.

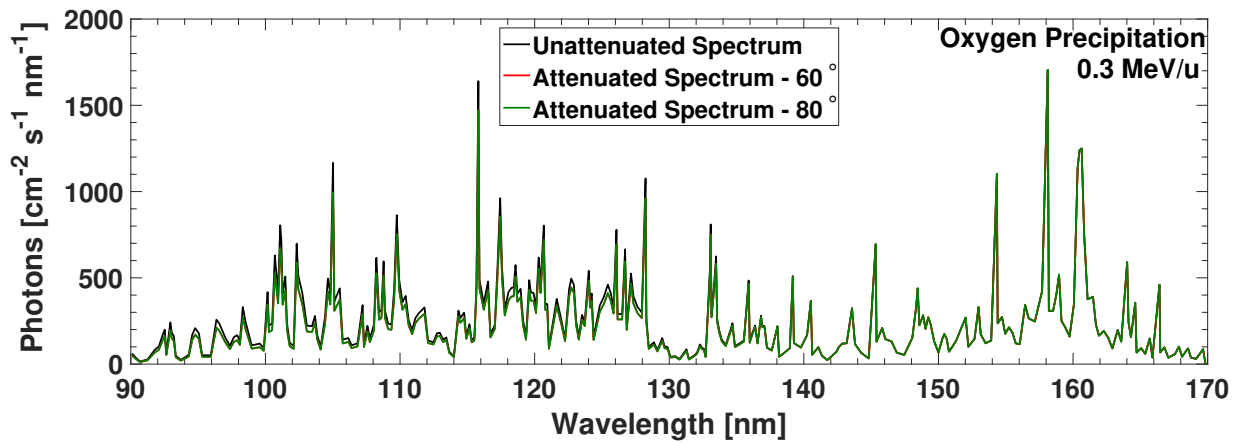


Figure 5.22: Predicted Lyman-Werner spectrum from an input of 1 oxygen ion/cm²/s at 0.3 MeV/u. The red line is calculated with a θ of 60° and the green line with a θ of 80°, while the black line is what is expected when no opacity effects are considered. The Ly- α line at 121.6 nm has been withheld from these predictions.

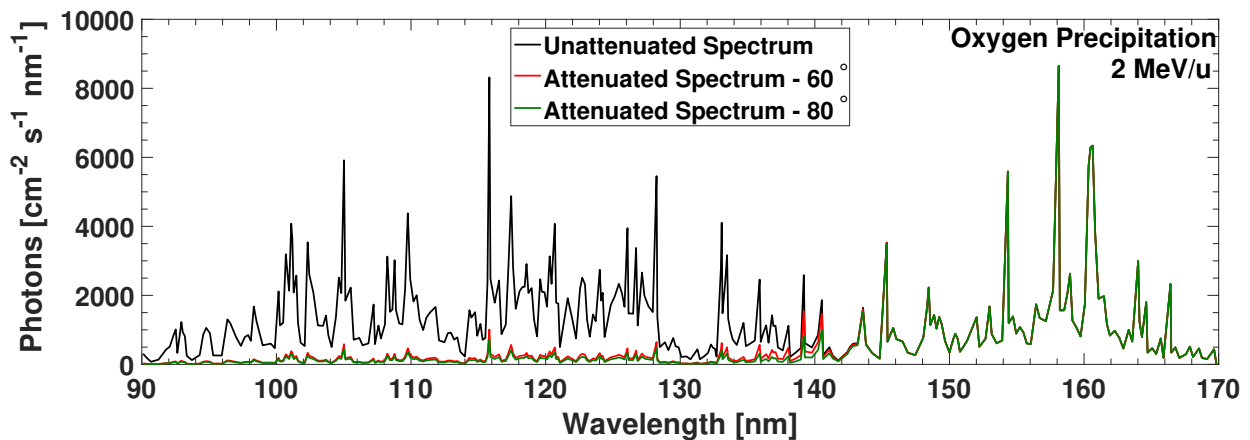


Figure 5.23: Predicted Lyman-Werner spectrum from an input of 1 oxygen ion/cm²/s at 2 MeV/u. The red line is calculated with a θ of 60° and the green line with a θ of 80°, while the black line is what is expected when no opacity effects are considered. The Ly- α line at 121.6 nm has been withheld from these predictions.

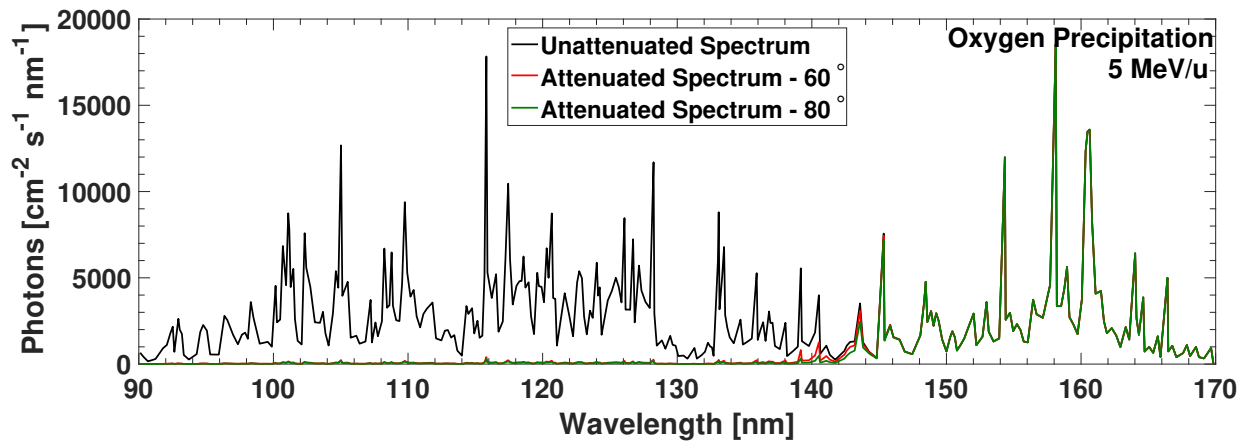


Figure 5.24: Predicted Lyman-Werner spectrum from an input of 1 oxygen ion/cm²/s at 5 MeV/u. The red line is calculated with a θ of 60° and the green line with a θ of 80°, while the black line is what is expected when no opacity effects are considered. The Ly- α line at 121.6 nm has been withheld from these predictions.

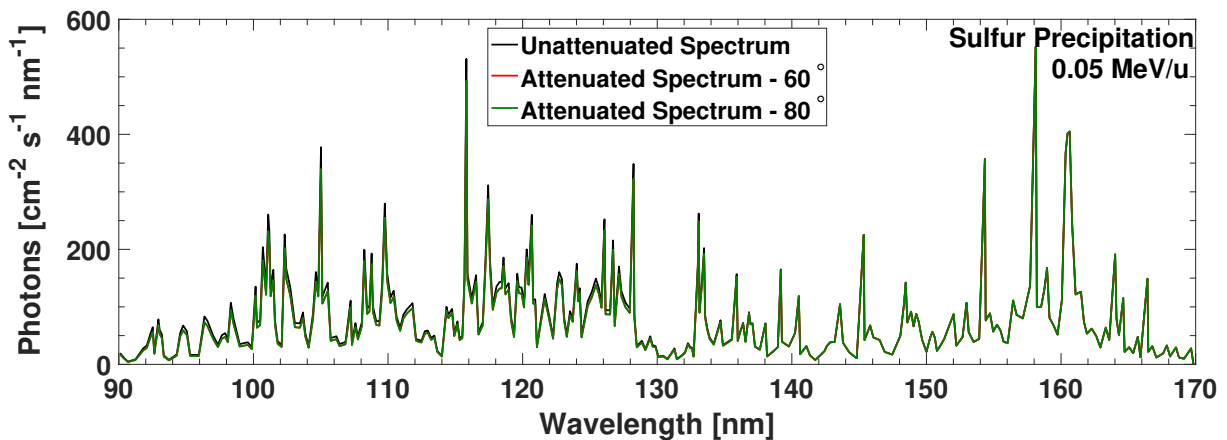


Figure 5.25: Predicted Lyman-Werner spectrum from an input of 1 sulfur ion/cm²/s at 0.05 MeV/u. The red line is calculated with a θ of 60° and the green line with a θ of 80°, while the black line is what is expected when no opacity effects are considered. The Ly- α line at 121.6 nm has been withheld from these predictions.

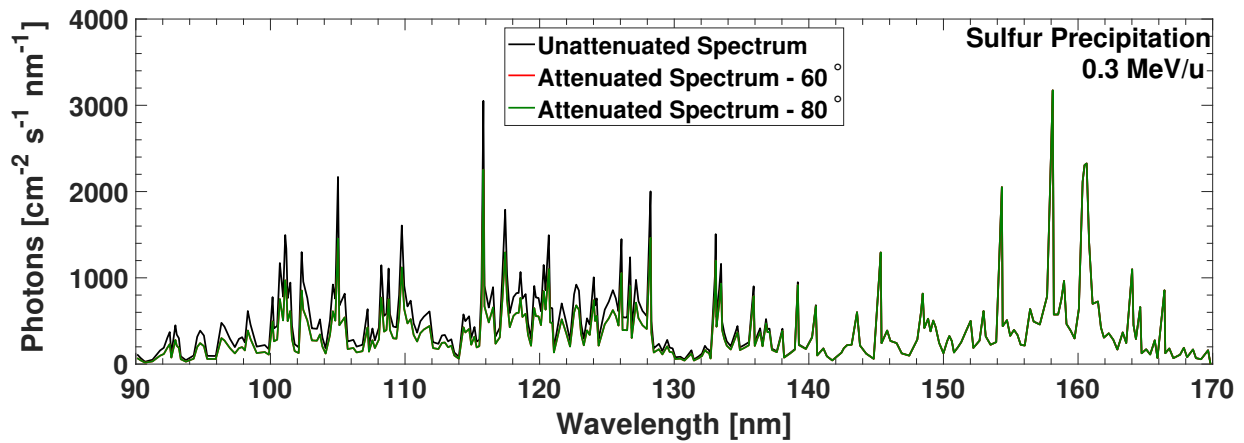


Figure 5.26: Predicted Lyman-Werner spectrum from an input of 1 sulfur ion/cm²/s at 0.3 MeV/u. The red line is calculated with a θ of 60° and the green line with a θ of 80°, while the black line is what is expected when no opacity effects are considered. The Ly- α line at 121.6 nm has been withheld from these predictions.

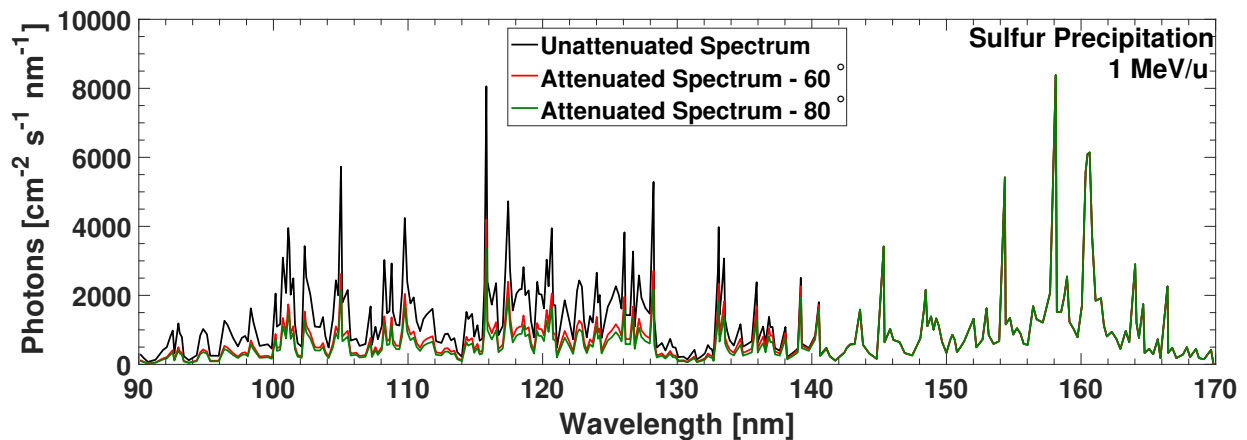


Figure 5.27: Predicted Lyman-Werner spectrum from an input of 1 sulfur ion/cm²/s at 1 MeV/u. The red line is calculated with a θ of 60° and the green line with a θ of 80°, while the black line is what is expected when no opacity effects are considered. The Ly- α line at 121.6 nm has been withheld from these predictions.

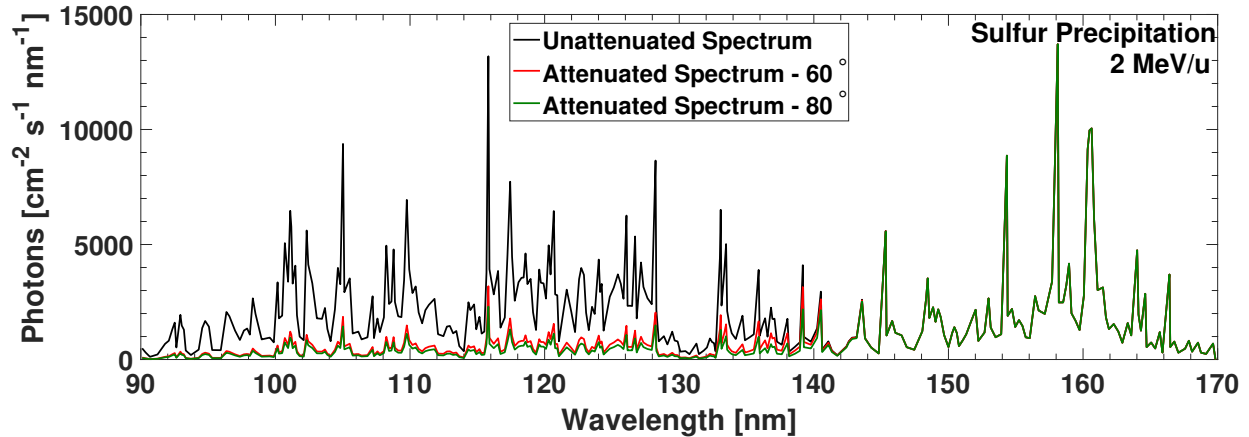


Figure 5.28: Predicted Lyman-Werner spectrum from an input of 1 sulfur ion/cm²/s at 2 MeV/u. The red line is calculated with a θ of 60° and the green line with a θ of 80°, while the black line is what is expected when no opacity effects are considered. The Ly- α line at 121.6 nm has been withheld from these predictions.

For the calculation of CR both atmosphere 1 (Fig. 2.8) and atmosphere 2 (Fig. 2.9) have been considered. In atmosphere 1, sulfur begins deviating from the unattenuated CR almost immediately, with a CR of 1.32 at 10 keV/u and 1.38 at 15 keV/u (60° exit angle case). This differs from oxygen precipitation, which appears to not penetrate deep enough to have a noticeable CR change until about 100 keV/u. The color ratios indicate that at about 500 or 600 keV/u, oxygen ions begin penetrating deeper than sulfur ions do. This coincides with the point in the sulfur stopping power the deviates drastically from the SRIM values (Fig. 2.7). Thus, I begin to lose confidence in the color ratio above an energy of about 400-500 keV/u. Fortunately, those energies are above the upper limit of what JEDI can detect, so there should be less error due to the stopping power discrepancy in sulfur precipitation in the range of JEDI measurements. Atmosphere 2, with a well-mixed atmosphere and consequently a much higher column density of methane, clearly absorbs much more UV than atmosphere 1. This was expected and there is a CR of nearly 100 for 2 MeV/u oxygen ions and an exit angle of 80°.

Figure 1.12 was during the first perijove pass, PJ 1, but a color ratio with an upper limit of 20-25 is pretty typical for the polar cap (see e.g., Gladstone et al. (2017b) - PJ 1 approach, Bonfond et al. (2017) - PJ 1, and Ebert et al. (2019) - PJ 5). When comparing monoenergetic ion precipitation

color ratios to the observed polar cap upper limit of 20 (Fig. 1.12), ion precipitation in atmosphere 1 is unable to reach it. Atmosphere 2 requires an exit angle of 80° and an incident energy of 800 keV/u for oxygen, and over 1 MeV/u for sulfur (which is above the energy of comfortability given the stopping power discrepancy). Of course, this is just the upper limit situation, the actual color ratio ranges between 1-20. At the ion energies measured by Juno (which has an upper limit of 600 keV/u for oxygen and 300 keV/u for sulfur) during PJ 7 my model produces a color ratio of 2-14 for oxygen and 2-7 for sulfur, depending on the atmosphere considered and the observation angle. Although I do not have a CR available for the time and associated atmospheric location that corresponds to the PJ 7 measurement, the conclusion that can be drawn from Figure 5.29 is that the high color ratio observed in the polar cap is likely not solely due to heavy ion precipitation. Proton precipitation is expected, which is able to penetrate deeper into the atmosphere and produce a higher CR in the UV emission, similar to that seen by electrons in Figure 3.5. This type of analysis, with more in-depth study of every precipitating species, can help constrain the atmospheric profile of the Jovian atmosphere. An important point to note when comparing the electron CR and the CR from ion precipitation is that the atmosphere associated with the main auroral oval (where electron precipitation is the primary auroral source) is potentially very different than the atmosphere at the polar cap; remember, they are in two physically different locations. There are different processes occurring at each location that affect the density profiles.

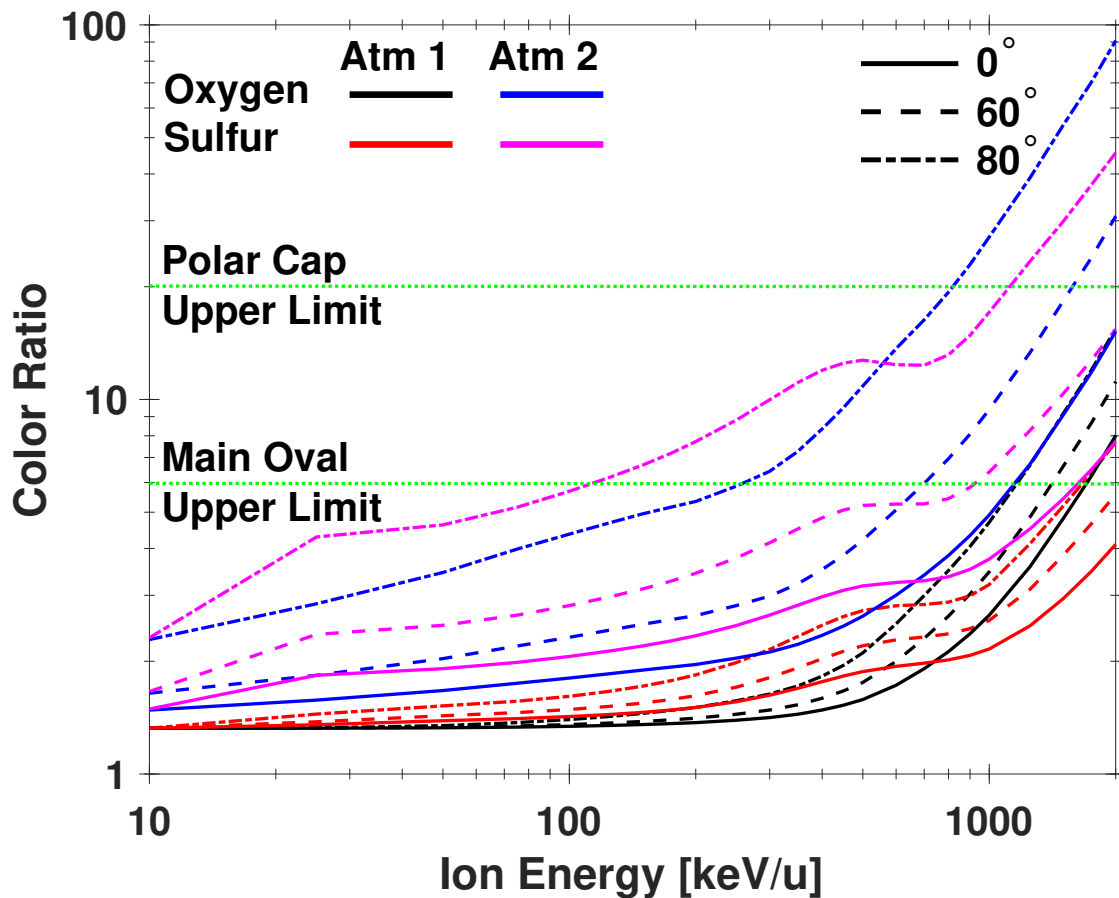


Figure 5.29: Initial ion energy vs. color ratio for two viewing angles of 60° (solid lines) and 80° (dash-dotted lines) for both oxygen and sulfur precipitation into atmosphere 1 and atmosphere 2. Oxygen precipitation into atmosphere 1 is indicated by the black lines, oxygen into atmosphere 2 by the blue lines, sulfur into atmosphere 1 by the red lines, and sulfur into atmosphere 2 by the pink lines.

Chapter 6

Ion Precipitation Results - X-ray Production

X-ray production at Jupiter has been of interest to the space physics community from when it was first observed by the Einstein Observatory in April of 1979 (Metzger et al., 1983). Although Metzger et al. (1983) were unable to distinguish a line spectrum from a continuum due to the limitations of the detector, they proposed that the primary source of X-rays must be coming from heavy ion precipitation, stating, “the shape of the response and the observed X-ray power indicate that the source of this auroral emission is not electron bremsstrahlung as on the Earth, but is most probably line emission from O and S ions with energies between 0.03 and 4.0 MeV/nucleon...”. Now, with the Juno spacecraft orbiting Jupiter, oxygen and sulfur ions have been measured above the polar caps with energies up to 400 keV per nucleon (keV/u) (Haggerty et al., 2017; Clark et al., 2017a,b).

In the past, there have been attempts to reproduce the X-ray emission observed at Jupiter with ion precipitation models (Cravens et al., 1995; Ozak et al., 2010, 2013), but they mostly fell short due to the high energy (>1.2 MeV/u) required to produce X-rays. Although the energies proposed seemed high at the time, this could be overlooked because there were not any *in situ* measurements of the ion energies above the polar cap. However, now with more accurate ion-neutral collision cross-sections from Schultz et al. (2019) and Gharibnejad et al. (2019) that include processes never before considered (i.e., SIM processes), I will show that the necessary ion energy needs to only be about 200 keV/u to begin producing X-rays. This difference largely arises from an increased stopping power at middle energies (see Fig. 2.1) causing a shift in the charge state distribution to lower energies. There is now also X-ray production from direct excitation, as opposed to solely charge exchange collisions modeled by my predecessors.

I expand on the ion precipitation models that have come before (Cravens et al., 1995; Ozak et al., 2010, 2013; Houston et al., 2018), modeling oxygen from 10 keV/u to 25 MeV/u and sulfur between 10 keV/u and 2 MeV/u, in an attempt to explain the X-ray emission from the Jovian polar caps. I consider all charge states of oxygen, including the negative charge state (O^{q+} , $q=-1, 0, \dots, 8$), and all sulfur charge states (S^{q+} , $q=0, \dots, 16$). Ultimately, O^{6+} , O^{7+} , and S^{6+} - S^{15+} are the most important charge states to consider when producing X-rays because their ionization potentials are great enough to emit X-ray photons.

6.1 Ion Production Rates

In Section 4.2.5 I introduced the ion production rate of a given charge state $q-1$ from charge transfer collisions. The production rates as a function of H_2 density and altitude for O^{6+} and O^{7+} are shown in Figure 6.1. For sulfur, Figure 6.2 shows the S^{7+} and S^{8+} charge transfer production rates. It is to be emphasized these production rates only include charge exchange from the three collisions discussed in Section 4.2.5, that is TI, SC, and SC+SS; although other processes can contribute to lowering the overall charge state without emitting a photon (e.g. the Auger process). The altitude integrated production rates for every charge state and various initial ion energies can be found in Appendices D and E, including the production rate of directly excited ions.

It is evident that the production rate of X-ray producing charge states from charge exchange collisions, O^{6+} and S^{7+} , is obtained with as little as 200 keV/u, which is well within the range of ion energies that have been measured by Juno above the polar caps (Haggerty et al., 2017; Clark et al., 2017a,b).

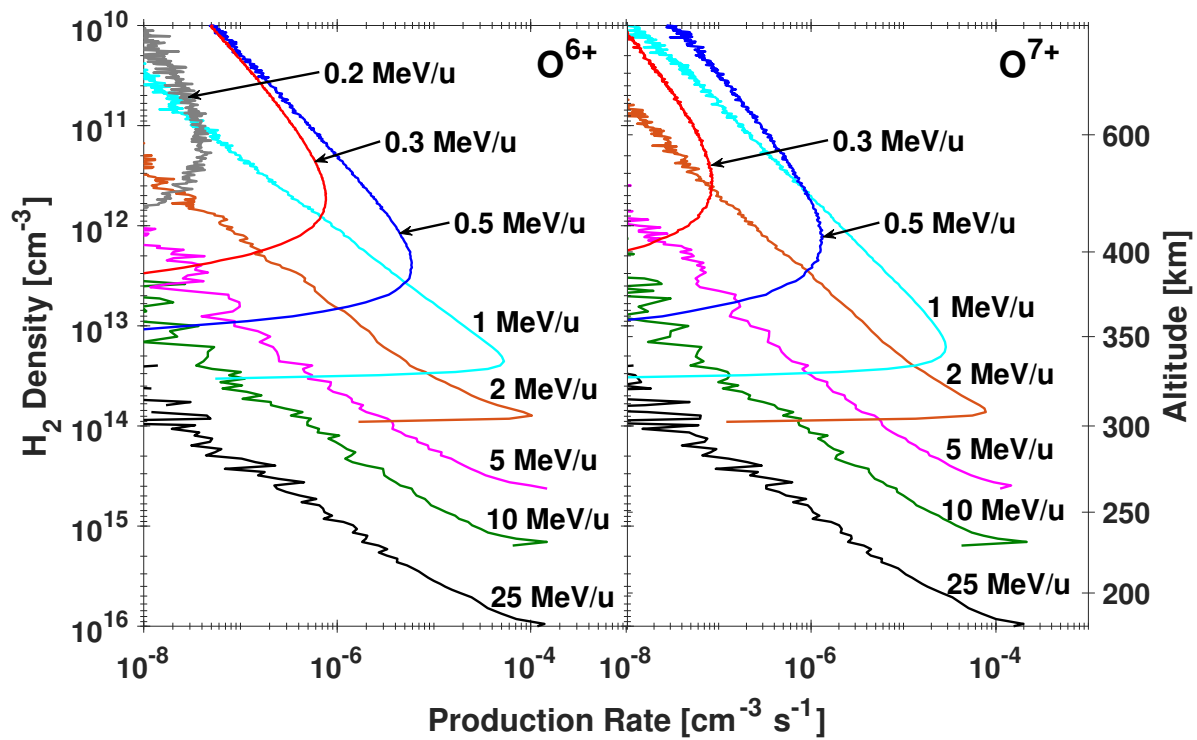


Figure 6.1: The O^{6+} and O^{7+} production rates from TI, SC, and SC+SS vs. H_2 density and altitude for various incident ion energies ($E=0.2, 0.3, 0.5, 1.0, 2.0, 5.0, 10.0,$ and 25.0 MeV/u). The production rates have been normalized to a single incident ion/cm²/s.

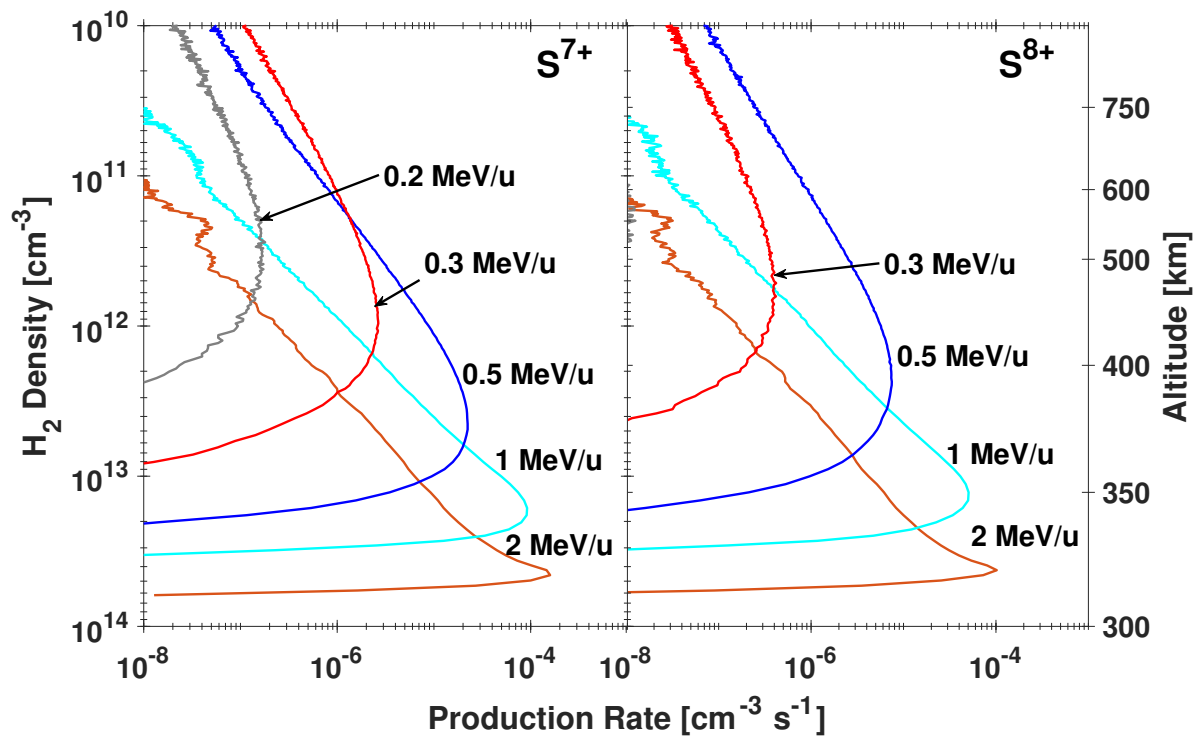


Figure 6.2: The S^{7+} and S^{8+} production rates from TI, SC, and SC+SS vs. H_2 density and altitude for various incident ion energies ($E=0.2, 0.3, 0.5, 1.0,$ and 2.0 MeV/u). The production rates have been normalized to a single incident ion/ cm^2/s .

6.2 X-ray Production

Charge transfer collisions of O^{8+} , O^{7+} , or O^{6+} with H_2 produces O^{7+} , O^{6+} , or O^{5+} ions, respectively, which are energetically able to be highly excited. In general, excited O^{7+} and O^{6+} ions are able to produce photons with X-ray energies (having ionization potentials of 871 eV for O^{7+} and 739 eV for O^{6+}), while O^{5+} is capable of producing photons that can be considered either extreme ultraviolet (EUV) or soft X-ray (ionization potential of 138 eV for O^{5+}). I will not consider O^{5+} photon production to be in the X-ray regime, although this can be ambiguous.

Shown in Tables 6.1 and 6.2 is the total number of X-ray producing collisions for each energy integrated over the entire atmosphere for an input of a single ion/cm²/s. The production has been combined from the two X-ray producing processes, direct excitation and charge exchange. Direct excitation that will likely produce an X-ray occurs for SI+SPEX, DI+SPEX, TEX+SPEX, while the charge exchange processes that will likely produce an X-ray are TI, SC, SC+SS.

Furthermore, Tables 6.1 and 6.2 display the production of the resultant charge state after a collision results in charge exchange or direct excitation. During a charge exchange collision, the ionization state of the atom changes by gaining an electron; I consider the production associated with O^{6+} to be when an electron is transferred to O^{7+} , resulting in O^{6+} . There is no charge state change for direct excitation collisions. These processes of course occur for lower charge states as well; however, the photon emitted from the cascading due to say O^{3+} gaining an electron, which results in O^{2+} , is not nearly energetic enough to be an X-ray.

Table 6.1: Altitude integrated X-ray production [photons/cm²/s] from both charge exchange and direct excitation collisions as a function of charge state and initial ion energy from an input of 1 ion/cm²/s with an isotropic downward distribution of pitch angles.

Ion Energy [keV/u]	Oxygen		Sulfur			
	O ⁶⁺	O ⁷⁺	S ⁷⁺	S ⁸⁺	S ⁹⁺	S ¹⁰⁺
75	1.00E-04	————	6.53E-04	————	————	————
100	5.23E-03	4.98E-05	9.95E-03	1.09E-04	————	————
125	4.89E-02	6.97E-04	1.05E-01	2.07E-03	1.09E-04	————
150	2.88E-01	6.22E-03	5.67E-01	1.96E-02	5.94E-04	————
175	1.09E+00	3.31E-02	2.10E+00	1.04E-01	4.47E-03	1.61E-04
200	2.99E+00	1.07E-01	5.88E+00	4.55E-01	2.77E-02	1.54E-03
250	1.24E+01	6.53E-01	2.68E+01	3.71E+00	3.83E-01	2.90E-02
300	3.04E+01	2.35E+00	7.26E+01	1.55E+01	2.56E+00	2.97E-01
350	5.54E+01	6.16E+00	1.38E+02	4.27E+01	1.05E+01	1.88E+00
400	8.43E+01	1.31E+01	2.05E+02	8.52E+01	2.99E+01	7.71E+00
450	1.13E+02	2.37E+01	2.54E+02	1.32E+02	6.16E+01	2.15E+01
500	1.40E+02	3.81E+01	2.79E+02	1.66E+02	9.51E+01	4.22E+01
600	1.82E+02	7.56E+01	2.91E+02	1.91E+02	1.31E+02	7.56E+01
700	2.06E+02	1.16E+02	2.92E+02	1.95E+02	1.39E+02	8.77E+01
800	2.18E+02	1.52E+02	2.92E+02	1.95E+02	1.40E+02	9.07E+01
900	2.24E+02	1.82E+02	2.92E+02	1.95E+02	1.40E+02	9.14E+01
1000	2.27E+02	2.04E+02	2.91E+02	1.94E+02	1.40E+02	9.12E+01
1250	2.29E+02	2.41E+02	2.91E+02	1.95E+02	1.40E+02	9.11E+01
1500	2.30E+02	2.63E+02	2.91E+02	1.95E+02	1.40E+02	9.11E+01
1750	2.30E+02	2.74E+02	2.91E+02	1.95E+02	1.40E+02	9.11E+01
2000	2.30E+02	2.83E+02	2.91E+02	1.94E+02	1.40E+02	9.10E+01
5000	2.30E+02	3.11E+02	————	————	————	————
10000	2.30E+02	3.13E+02	————	————	————	————
25000	2.30E+02	3.15E+02	————	————	————	————

Table 6.2: Altitude integrated X-ray production [photons/cm²/s] from both charge exchange and direct excitation collisions as a function of charge state and initial ion energy from an input of 1 ion/cm²/s with an isotropic downward distribution of pitch angles.

Ion Energy [keV/u]	S ¹¹⁺	S ¹²⁺	Sulfur S ¹³⁺	S ¹⁴⁺	S ¹⁵⁺
200	1.06E-04	————	————	————	————
250	2.18E-03	4.26E-04	5.32E-05	————	————
300	4.15E-02	8.33E-03	1.10E-03	————	————
350	4.16E-01	1.23E-01	4.67E-02	1.04E-04	5.20E-05
400	2.53E+00	1.03E+00	6.09E-01	1.89E-03	5.12E-04
450	9.88E+00	5.32E+00	4.73E+00	2.32E-02	6.96E-03
500	2.56E+01	1.76E+01	2.18E+01	1.86E-01	1.08E-01
600	6.32E+01	6.05E+01	1.11E+02	1.81E+00	3.04E+00
700	8.46E+01	9.87E+01	2.31E+02	5.32E+00	1.49E+01
800	9.28E+01	1.21E+02	3.38E+02	1.02E+01	4.45E+01
900	9.55E+01	1.33E+02	4.18E+02	1.60E+01	1.04E+02
1000	9.59E+01	1.37E+02	4.70E+02	2.23E+01	2.12E+02
1250	9.62E+01	1.41E+02	5.35E+02	3.74E+01	6.68E+02
1500	9.61E+01	1.41E+02	5.61E+02	5.03E+01	1.31E+03
1750	9.62E+01	1.41E+02	5.71E+02	6.04E+01	2.07E+03
2000	9.64E+01	1.42E+02	5.75E+02	6.75E+01	2.88E+03

6.3 X-ray Efficiencies

The emitted photon flux is determined by using the production rates, shown in Figures 6.1 and 6.2, and Equation 4.10, where 4π is included to convert the intensity units from $\text{cm}^{-2} \text{s}^{-1} \text{sr}^{-1}$ to $\text{cm}^{-2} \text{s}^{-1}$. X-ray emission efficiency is a way of quantifying how many photons are emitted given an incident ion energy and is found by dividing $4\pi I$ by the initial energy of the monoenergetic ion beam. Table 6.3 shows the combined X-ray efficiencies from both charge exchange and direct excitation emission given an incident ion energy, at various viewing angles, using both atmosphere 1 and 2, and with an input of $1 \text{ ion/cm}^2/\text{s}$. The same is also shown in Figures 6.3 and 6.4. The full set of efficiencies for every X-ray emitting charge state at each energy and three different viewing angles plus a no opacity case can be found in Appendices D and E.

The most efficient X-ray emission for O^{6+} is with an incident ion energy of $\sim 600 \text{ keV/u}$ for both atmosphere, $\sim 1 \text{ MeV/u}$ for O^{7+} , $\sim 500 \text{ keV/u}$ S^{8+} , and $\sim 600 \text{ keV/u}$ for S^{9+} . The well-mixed atmosphere has minimal effects on emission from low energy ion precipitation because the ions are not precipitating deeply enough for the large column density to have much of an impact on the X-rays. As one would expect, the viewing angle of 90° greatly reduces emission for high energy ion precipitation when comparing with X-rays that propagate directly up and out of the atmosphere at 0° . This is even more true for X-ray production from sulfur which is the overall most efficient X-ray producer (i.e., S^{8+} at 500 keV/u) with a viewing angle of 0° , but the efficiency is reduced by nearly 60% (for atmosphere 1) when the viewing angle changes to 90° , whereas O^{6+} is only reduced by about 23% (for atmosphere 1) making it the most efficient emitter at 90° . This is an important effect to consider when looking at fluxes from Earth-orbit-based X-ray observations, which are generally taken at a steep viewing angle, especially for the southern aurora.

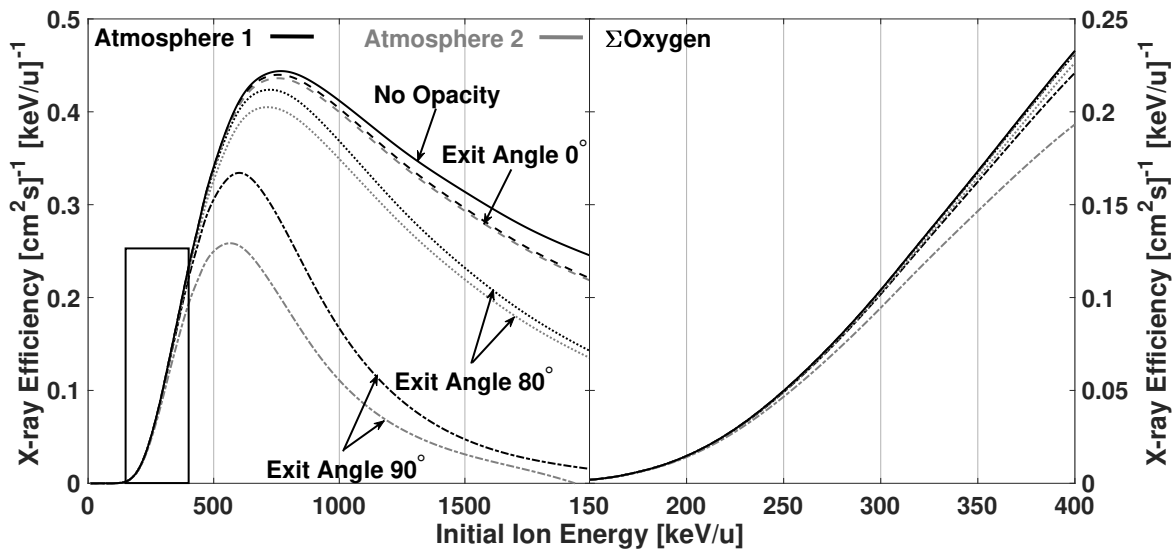


Figure 6.3: The entire outgoing X-ray flux efficiency for all X-ray producing oxygen charge states as a function of initial ion energy from a single incident ion/ cm^2/s with an isotropic downward distribution of pitch angles. The condition of no opacity is shown by the solid line, an exit angle of 0° is represented by the dashed line, an exit angle of 80° by the dotted line, and an exit angle of 90° by the dash-dot line. Atmosphere 1 consideration is in black and atmosphere 2 is in gray. Every exit angle is with respect to the Jovian spin axis. The figure on the right is a magnified portion of the figure on the left (represented by the black rectangle), used to emphasize the efficiencies of ions in the energy range of JEDI measurements.

Atmosphere 1 (Original atmosphere)								
Energy [keV/u]	0°				90°			
	O ⁶⁺	O ⁷⁺	S ⁸⁺	S ⁹⁺	O ⁶⁺	O ⁷⁺	S ⁸⁺	S ⁹⁺
200	0.0141	0.0005	0.0023	0.0001	0.0139	0.0005	0.0019	0.0001
300	0.1195	0.0106	0.0514	0.0085	0.1165	0.0104	0.0365	0.0072
400	0.2008	0.0317	0.2093	0.0745	0.1901	0.0309	0.1195	0.0563
500	0.2669	0.0735	0.3208	0.1882	0.2358	0.0701	0.1327	0.1206
600	0.2884	0.1206	0.3020	0.2145	0.2235	0.1107	0.0772	0.1022
700	0.2787	0.1578	0.2557	0.1924	0.1760	0.1357	0.0370	0.0589
800	0.2573	0.1810	0.2169	0.1663	0.1240	0.1409	0.0185	0.0300
900	0.2333	0.1911	0.1858	0.1443	0.0827	0.1303	0.0106	0.0157
1000	0.2105	0.1918	0.1608	0.1265	0.0551	0.1118	0.0069	0.0093
2000	0.0954	0.1244	0.0527	0.0474	0.0029	0.0128	0.0009	0.0009

Atmosphere 2 (Well-mixed atmosphere)								
Energy [keV/u]	0°				90°			
	O ⁶⁺	O ⁷⁺	S ⁸⁺	S ⁹⁺	O ⁶⁺	O ⁷⁺	S ⁸⁺	S ⁹⁺
200	0.0140	0.0005	0.0022	0.0001	0.0134	0.0005	0.0015	0.0001
300	0.1192	0.0106	0.0507	0.0084	0.1068	0.0100	0.0267	0.0057
400	0.2000	0.0317	0.2048	0.0736	0.1643	0.0289	0.0799	0.0418
500	0.2653	0.0733	0.3113	0.1849	0.1867	0.0633	0.0792	0.0817
600	0.2861	0.1201	0.2904	0.2093	0.1606	0.0954	0.0397	0.0600
700	0.2761	0.1570	0.2441	0.1864	0.1156	0.1111	0.0170	0.0297
800	0.2545	0.1799	0.2060	0.1602	0.0756	0.1096	0.0084	0.0138
900	0.2307	0.1898	0.1760	0.1386	0.0478	0.0967	0.0050	0.0072
1000	0.2080	0.1904	0.1521	0.1212	0.0311	0.0802	0.0033	0.0044
2000	0.0942	0.1234	0.0498	0.0453	0.0017	0.0087	0.0006	0.0006

Table 6.3: The X-ray efficiency ($[\text{cm}^2\text{sec}]^{-1}[\text{keV/u}]^{-1}$) of outgoing photons as a function of initial ion energy including opacity effects from a single incident ion/cm²/s with an isotropic downward distribution of pitch angles. The viewing angles of 0° and 90° are displayed for both atmosphere 1 and 2. The efficiencies shown here includes X-ray production from both charge exchange and direct excitation collisions.

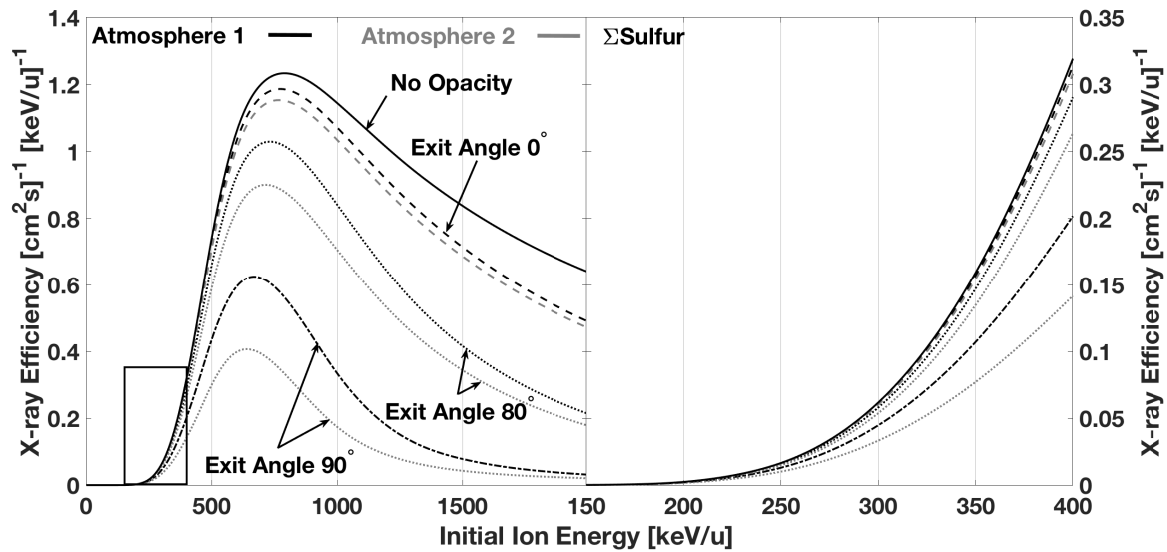


Figure 6.4: The entire outgoing X-ray flux efficiency for all X-ray producing sulfur charge states as a function of initial ion energy from a single incident ion/cm²/s with an isotropic downward distribution of pitch angles. The condition of no opacity is shown by the solid line, an exit angle of 0° is represented by the dashed line, an exit angle of 80° by the dotted line, and an exit angle of 90° by the dash-dot line. Atmosphere 1 consideration is in black and atmosphere 2 is in gray. Every exit angle is with respect to the Jovian spin axis. The figure on the right is a magnified portion of the figure on the left (represented by the black rectangle), used to emphasize the efficiencies of ions in the energy range of JEDI measurements.

Ozak et al. (2010) reported that the most efficient X-ray emission for O^{6+} , O^{7+} , and S^{8+} was for incident ions with energies of 1.5 MeV/u, 2.5 MeV/u, and 1 MeV/u, and efficiency values of ~ 0.009 , ~ 0.003 , and ~ 0.015 , respectively. These required energies are 2-3x higher than what JEDI typically observed. But my revised model with the SIM cross-sections indicate that for O^{6+} , O^{7+} , and S^{8+} the most efficient X-ray emissions occur at energies of 600 keV/u, 1 MeV/u, and 500 keV/u with efficiencies of 0.29, 0.19, and 0.32, respectively (from Tab. 6.3, atmosphere 1, 0° viewing angle). Two major contributions account for such a great difference in X-ray efficiencies. First, with the more complete treatment of the fundamental atomic collision processes, it requires much less energy than inferred in the previous models to strip both oxygen and sulfur ions to a high, X-ray producing charge state, allowing X-rays to be created at much lower energies than previously thought. Second, I am depositing much more energy higher up in the atmosphere due to the increase in stopping power shown by Schultz et al. (2019), ultimately generating X-rays higher in the atmosphere than previously modeled, making them less susceptible to opacity effects even when considering an upper-limit, highly-mixed atmosphere.

There are several useful ways to interpret X-ray efficiencies. Because the efficiencies are calculated with an input of 1 ion/cm²/s, one can view each efficiency as the number of X-ray photons emitted given an initial ion energy. That is to say, if a single oxygen ion with an energy of 300 keV/u is precipitating, then it is expected that $\sim 0.1 \frac{\text{photons}}{\text{cm}^2\text{s}} \frac{1}{\text{keV/u}} \times 300 \text{ keV/u} \approx 30 \text{ photons/cm}^2\text{/s}$ will be emitted. Therefore, 1 oxygen ion/cm²/s at 300 keV/u will produce about 30 photons/cm²/s, or 1 ion/s precipitating results in 30 photons/s. This is an extremely quick estimate that can be made when trying to interpret the emission from a measured JEDI ion flux.

Another practical application of the X-ray efficiencies is to calculate total X-ray power emission for a given initial ion energy. For example; I have just calculated that 1 oxygen ion/s at 300 keV/u will produce 30 photons/s. The average emitted photon energy associated with oxygen is 600 eV (See Section 6.3.1). The power out is then $30 \text{ photons/s} \times 600 \text{ eV} \times 1.6 \times 10^{-9} \frac{\text{Joules}}{\text{eV}} \approx 3 \times 10^{-15} \frac{\text{Joules}}{\text{s}}$ or 3×10^{-15} Watts. Thus, given an ion flux, one can approximate the total power output from the precipitating ions.

Finally, given an ion flux one can estimate the power output from the entirety of the polar cap, or a defined area that Juno has flown over while an X-ray observation has been made simultaneously. If photons/cm²/s is calculated, either through the aforementioned method or as a direct output from my model with a variety of initial ion energies, then finding the power/cm²/s is a matter of combining the two previous methods. That is, (photons/cm²/s) x (average photon energy [eV]) x (1.6x10⁻¹⁹ $\frac{\text{Joules}}{\text{eV}}$) results in W/cm². Now, if the area of the measurement is known, or deduced by geometry, multiplying power/cm² by the area will result in the total power for that area, which can be directly compared to an observed total X-ray power (or luminosity).

6.3.1 X-ray Spectra

When producing a synthetic X-ray spectrum I am able to distinguish between charge states and production type (charge transfer or direct excitation), and consider the effects due to opacity at different viewing angles in atmospheres 1 and 2. Figure 6.5 shows the total X-ray emission for a single oxygen ion plus a single sulfur ion (sulfur to oxygen ratio of 1:1), both with incident energies of 500 keV/u. The emission lines have been distributed with a normalized Gaussian and $\sigma=20$ eV, simulating instrument response functions (discussed in Section 4.2.6). The emission is plotted by charge state to show where in the spectrum each emission line contributes the most, i.e. sulfur dominates at photon energies between 150-500 eV, while oxygen is prominent between 500-900 eV. This particular spectrum accounts for no opacity effects and I have included emission from both charge exchange and direct excitation collisions. The emission from S¹⁴⁺ has two peaks at ~430 eV and ~2450 eV, but the latter is multiple orders of magnitude below the rest of the emission and would be too faint to see in Figure 6.5.

Next, shown in Figure 6.6 is the same total emission from Figure 6.5 (black line) with opacity effects applied from both atmosphere 1 and 2 at three different viewing angles. It is apparent that X-ray emission from sulfur is much more affected by opacity than that from oxygen, which was indicated by the X-ray efficiencies in Table 6.3. This is due to the relatively large photoabsorption cross-sections at longer wavelengths, shown by Cravens et al. (2006) and in Figure 4.3.

It is also important to note how little X-ray absorption occurs at this energy of 500 keV/u, even for atmosphere 2. A 500 keV/u oxygen ion (total energy of 8 MeV) is nearing the upper energy limit of the JEDI instrument of 10 MeV (Mauk et al., 2017a) and a 500 keV/u sulfur ion (16 MeV) is above that limit. This suggests that precipitation of ions with energies within the JEDI limits will have X-ray emission that will escape without undergoing large opacity effects and should be detectable, even if a very well-mixed atmosphere is present. This is due to the new SIM cross-sections no longer allowing the ions to precipitate deep into the atmosphere. These results are much different than those presented by Ozak et al. (2010), which show a reduction in sulfur emission by nearly two orders of magnitude when considering a 90° viewing angle.

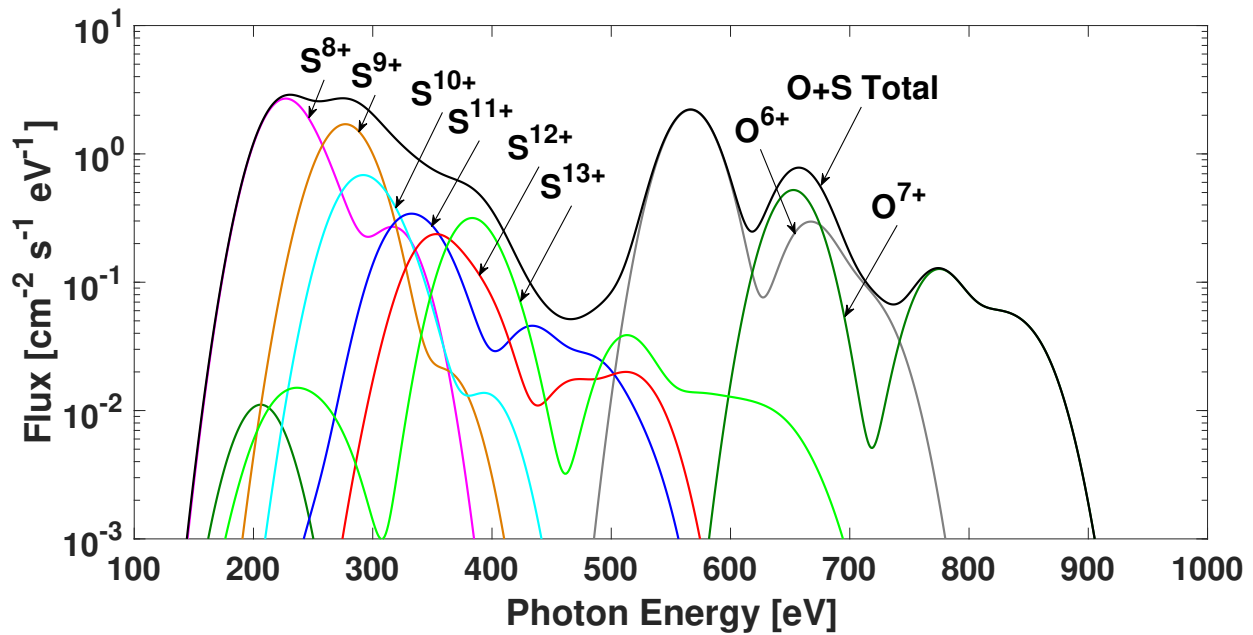


Figure 6.5: Synthetic X-ray spectra showing the contribution from each charge state. This spectra includes emission from both charge exchange and direct excitation collisions considering no opacity effects from an incident ion beam of 500 keV/u with an input is 1 ion/cm²/s for both species. Not shown is the emission from S¹⁴⁺ which peaks at ~2450 eV with an intensity several orders of magnitude lower than the more prominent emission lines.

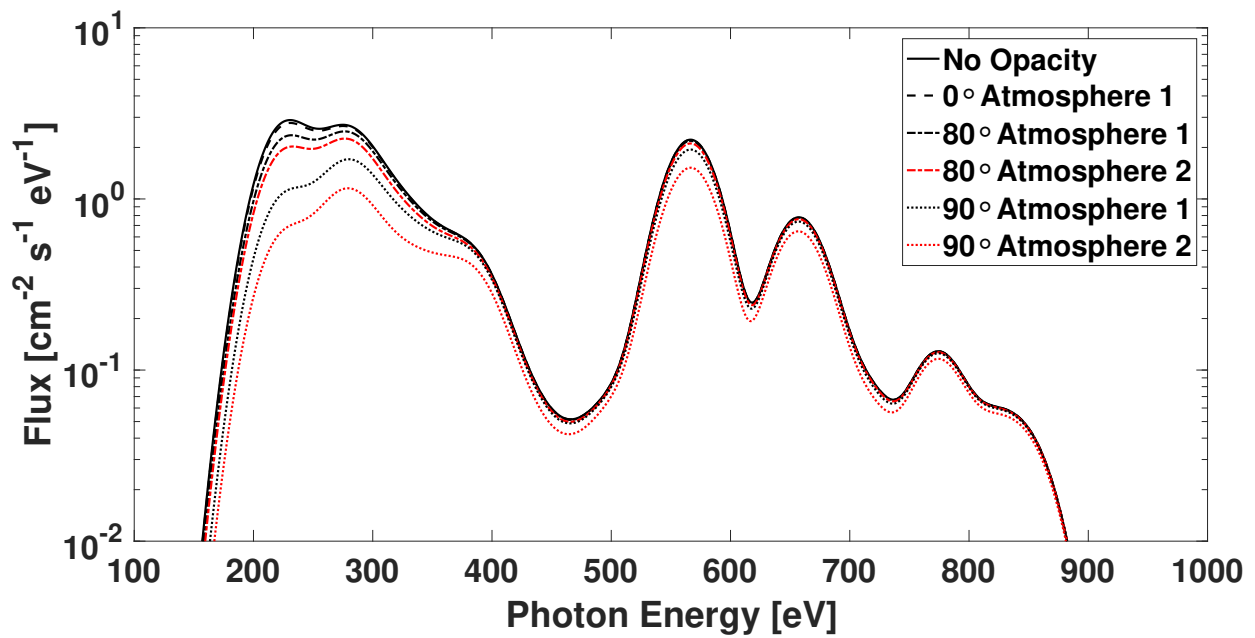


Figure 6.6: Synthetic X-ray spectra with opacity effects at three viewing angles through an atmosphere with a deep, originally considered homopause (atmosphere 1) and an atmosphere that is well-mixed through the top of the atmosphere (atmosphere 2), what I consider an upper-limit to opacity effects. Initial ion energies are 500 keV/u for both oxygen and sulfur precipitation and the input is 1 ion/cm²/s for both species. Photon energies below about 400 eV are shown to be much more affected by the opacity than higher photon energies.

Chapter 7

Ion Precipitation Results - Juno Model-Data Comparisons

The X-ray aurora has shown a strange complexity during observations. For example, at times there seems to be a ~ 45 minute period hot spot as reported by Gladstone et al. (2002); however, during other observations this pulsation does not appear to exist (Elsner et al., 2005; Branduardi-Raymont et al., 2007). Therefore, when analyzing heavy ion measurements made by JEDI, a certain level of awareness needs to be present. It is important to remember that every energy spectrum and flux intensity of oxygen and sulfur is unique. Sometimes oxygen ions are measured with a higher intensity while at other times sulfur measurements are more prevalent. Each collection of data greatly depends on the time and location of where it is made. Thus, when using the JEDI flux measurements, they need to be fine tuned for every case.

7.1 X-ray Results

Finally, I input the JEDI flux measurements, displayed in Figure 4.5, into my model and to determine ion production rates, direct excitation rates, and an expected X-ray spectrum. Displayed in Figure 7.1 are the ion production rates and the altitude integrated production rates from X-ray producing charge exchange collisions (TI, SC, SC+SS) combined with the production rates from X-ray producing direct excitation collisions (SI+SPEX, DI+SPEX, and TEX+SPEX) associated with the PJ 7 ion flux measurements. This demonstrates that the ions seen during this pass are of sufficient energy to reach X-ray producing charge states. It is also evident that the ions do not precipitate deeply enough to go much below the homopause, indicating that absorption will have minimal effects in Atmosphere 1.

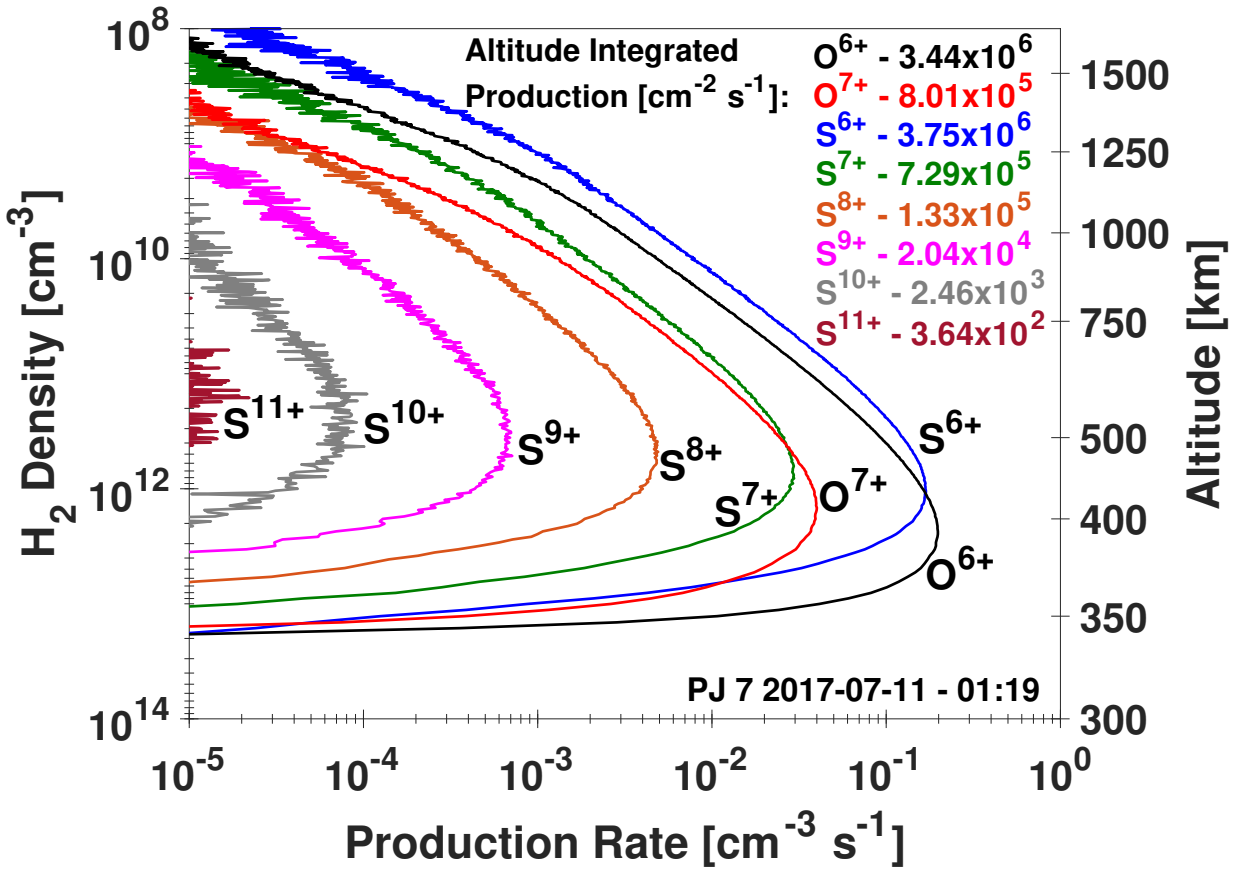


Figure 7.1: Ion production rate from X-ray producing charge exchange collisions combined with X-ray producing direct excitation collisions of each ion charge state vs. H₂ density and altitude from Juno's PJ 7 pass. Also included is the altitude integrated production rate of each charge state displayed. It is evident from the charge states obtained that X-rays will be produced.

Displayed in Figure 7.2 are the X-ray spectra I predict was emitted from JEDI's measured ion flux measurements during PJ 7 (Fig. 4.5), which accounts for X-ray production from both charge exchange and direct excitation collisions. These particular spectra also consider opacity effects with a photon exit angle of 80° through both atmosphere 1 and 2, which I assume to be a common viewing angle for Earth-orbit-based observations; although, opacity effects make little difference on the X-ray emission from ions with this low of initial energy¹. This is evident when comparing the no opacity case to emission through atmosphere 1 and 2, where there is a slight reduction in sulfur emission and no noticeable difference in emission from oxygen. The total X-ray output from this particular JEDI input is on the order of 4 R (1 Rayleigh (R) = 10^6 photons/cm²/s), regardless of opacity and viewing angle. This falls into the exact range that has been measured by the Chandra X-ray Observatory reported by Gladstone et al. (2002) and shown in Figure 1.5 (2-6 R). It is also important to note the general spectral shape when comparing Figure 7.2 to Figure 1.6. It is evident that my model produces a similar shape which can particularly be seen in the three "bumps" produced by the oxygen emission lines between 500 and 1000 eV. One difference is the relative emission between sulfur and oxygen. Figure 1.6 indicates that there is about twice as much sulfur emission as oxygen, whereas Figure 7.2 shows significantly more oxygen emission. This is due to the incident ion flux I input into my model (Fig. 4.5) where a higher abundance of oxygen was measured. This is generally not the case, as indicated by CXO and XMM-Newton observations (Dunn et al., 2016; Elsner et al., 2005) and *in situ* Juno data (Clark et al., 2017b; Haggerty et al., 2017).

¹When comparing an 80° exit angle to a 90° exit angle, the total emitted flux from oxygen emission was only reduced by 5.4% for the 90° case, while emission from sulfur was diminished by 15%.

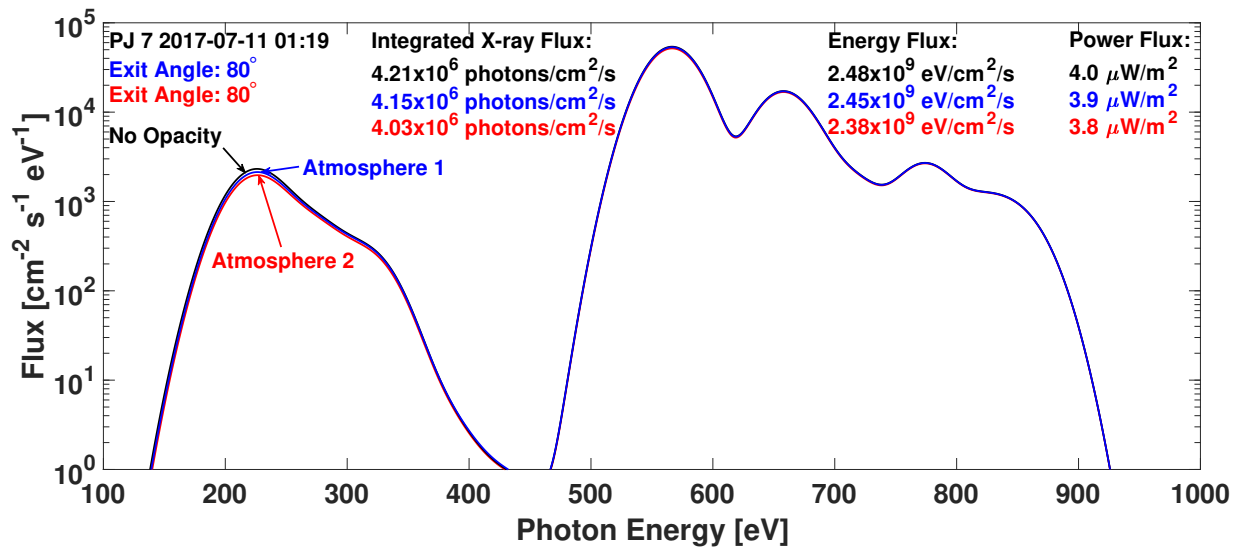


Figure 7.2: Predicted X-ray spectra from JEDI’s ion flux measurements during the PJ 7 polar cap pass in 2017. These spectra assume no opacity effects (black line), an opacity effect with an exit angle of 80° through atmosphere 1 (blue line), and the same exit angle through atmosphere 2 (red line). It appears emission from oxygen is the most prominent source of X-rays associated with this flux measurement, which may have been anticipated from the JEDI data taken at this time, but is likely not always the case.

7.2 Secondary Electrons - Two-Stream Results

The input into the ion precipitation model includes both oxygen and sulfur precipitation simultaneously, as does the input into the two-stream model. Figure 7.3 presents the H^+ and H_2^+ production rates from the JEDI ion flux measurements during PJ 7 as a function of H_2 density and altitude. Both ionization from ion precipitation and the resulting secondary electrons are included. Primary ionization (ionization resulting directly from ion-neutral collisions) is the dominant ionization method for H_2^+ and even more-so for H^+ . Both production rates peak at an altitude between 350 - 400 km, indicating the precipitating ions are reaching the very top of the homopause of atmosphere 1 (Fig. 2.8).

Shown in Figure 7.4 is the forward (downward, deeper into the atmosphere) electron production rates for various altitudes vs. electron energy. The forward electron production is a result output by the two-stream model, where the secondary electrons precipitation through the atmosphere is taken into account. For this particular perijove pass, there is a high energy flux (the tail of the distribution) that showers down to 350 km, presumably from the precipitating sulfur ions.

Figure 7.5 presents the total escape electron flux out of the top of the atmosphere as a function of electron energy. The majority of these electron energies fall below the limits of the JADE detector, 100 eV to 100 keV (McComas et al., 2017). The total energy from the escaping electrons is 3.51×10^8 eV/cm²/s, the total number of electrons is 7.77×10^6 electrons/cm²/s, and the total current density is 1.25×10^{-8} A/m². To find the total current density associated with the PJ 7 polar cap pass, one would need to include the current density from the downward precipitating electrons. To do this, I assume oxygen is in a singly charged state and sulfur is in a doubly charged state for the flux measurement in Figure 4.5. Although this is likely untrue and both oxygen and sulfur ions are in a combination of singly and doubly charged states, the bulk of oxygen is singly charged and sulfur is doubly charged (Delamere et al., 2005; Dougherty et al., 2017; Kim et al., 2019), and I think the fluctuations in charge state of each ion will largely cancel each other out. This leads to an ion current density of 4.93×10^{-9} A/m² for oxygen and 6.20×10^{-9} A/m² for sulfur, or a total current density, from both ions and electrons, of 2.36×10^{-8} A/m².

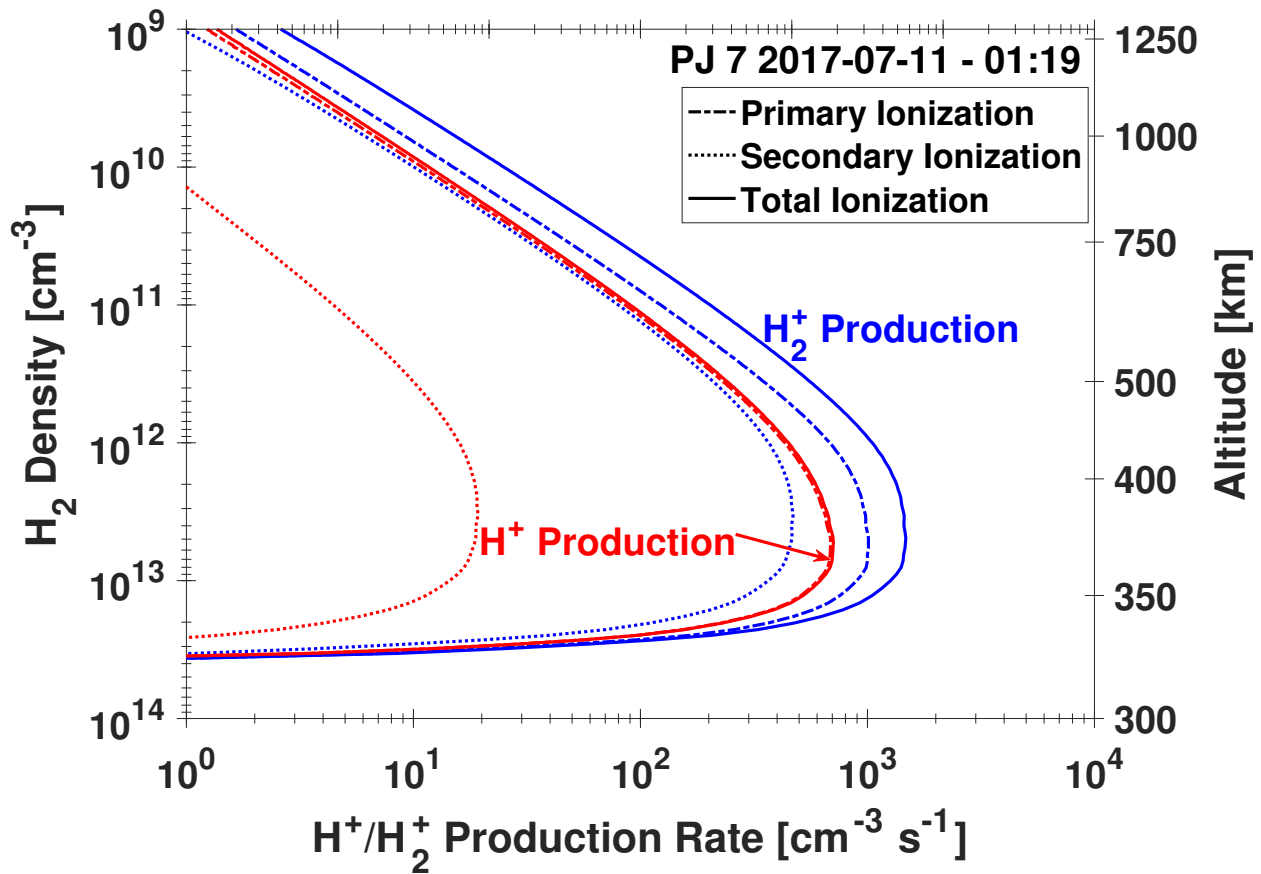


Figure 7.3: H⁺ and H₂⁺ production rates vs. H₂ density as a result of ion precipitation and the associated secondary electrons. The ion flux input into the model was from the PJ 7 polar cap pass in 2017, displayed in Figure 4.5.

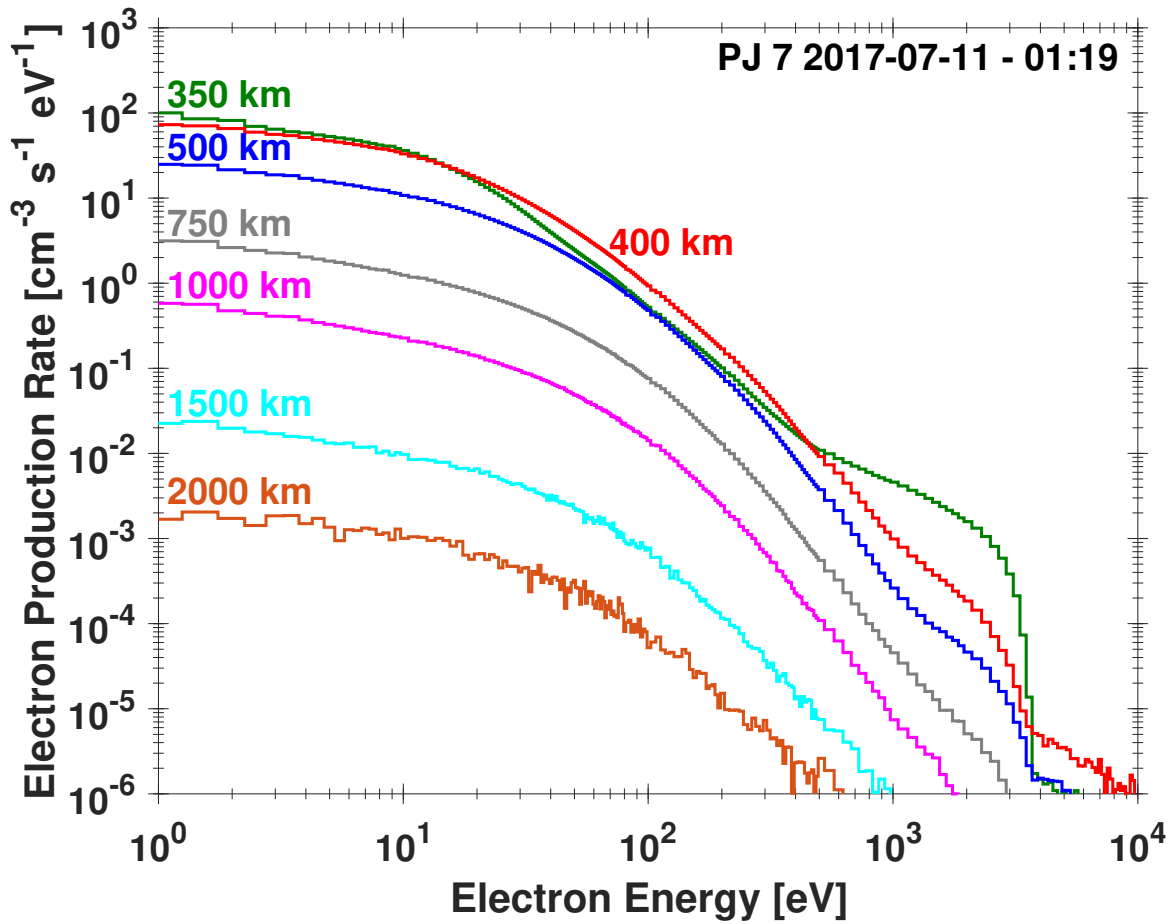


Figure 7.4: Forward secondary electron production rates for various altitudes from the ion precipitation and two-stream model for an incident ion flux from Juno's PJ 7 pass. Ionizing collisions are the dominant process that produces low energy electrons, while stripping collisions are what produce the tails (higher energy) of the electron distributions.

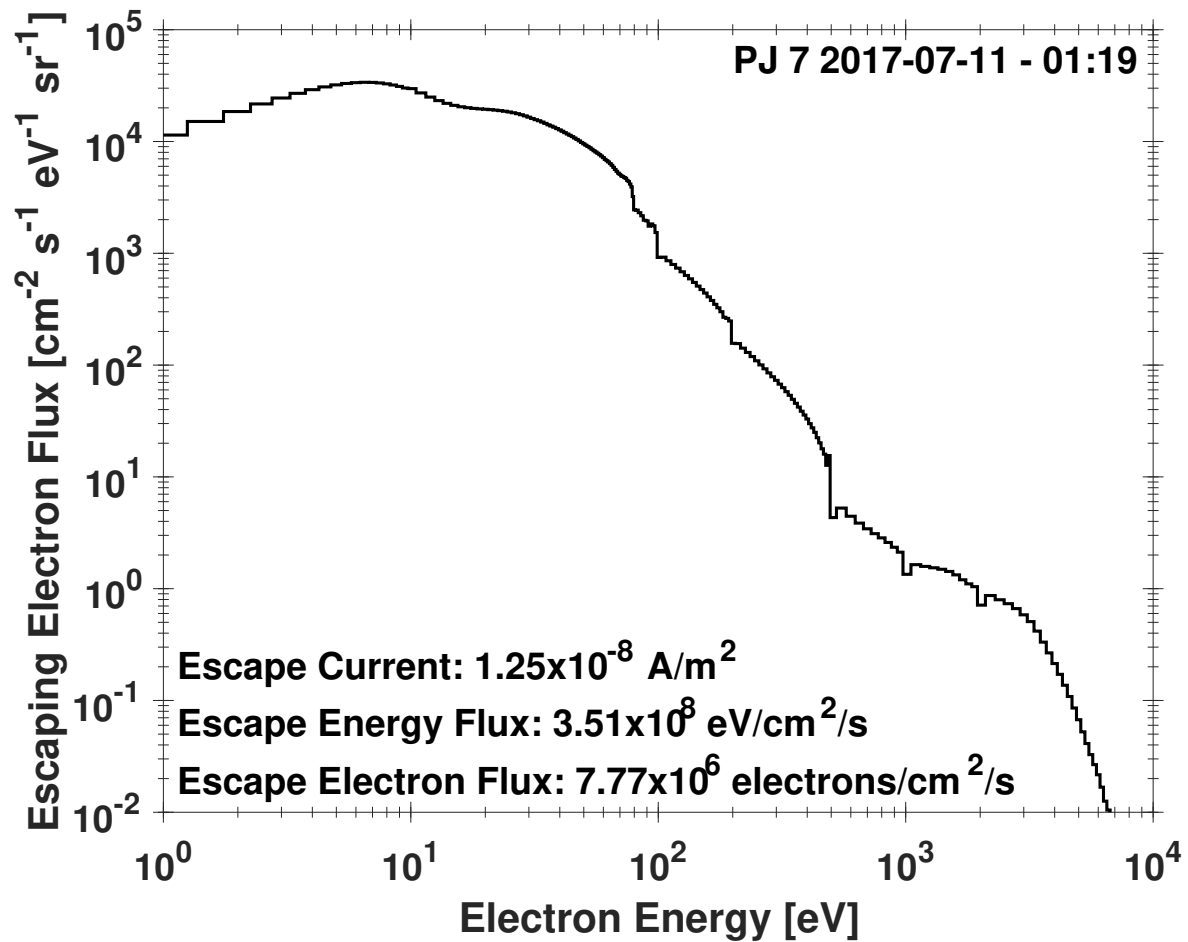


Figure 7.5: Predicted electron escape flux vs. electron energy for precipitating ions measured by Juno during the PJ 7 polar cap pass. A step plot has been used to show the size of the corresponding energy bins that are output by the ion precipitation model to be used by the two-stream code.

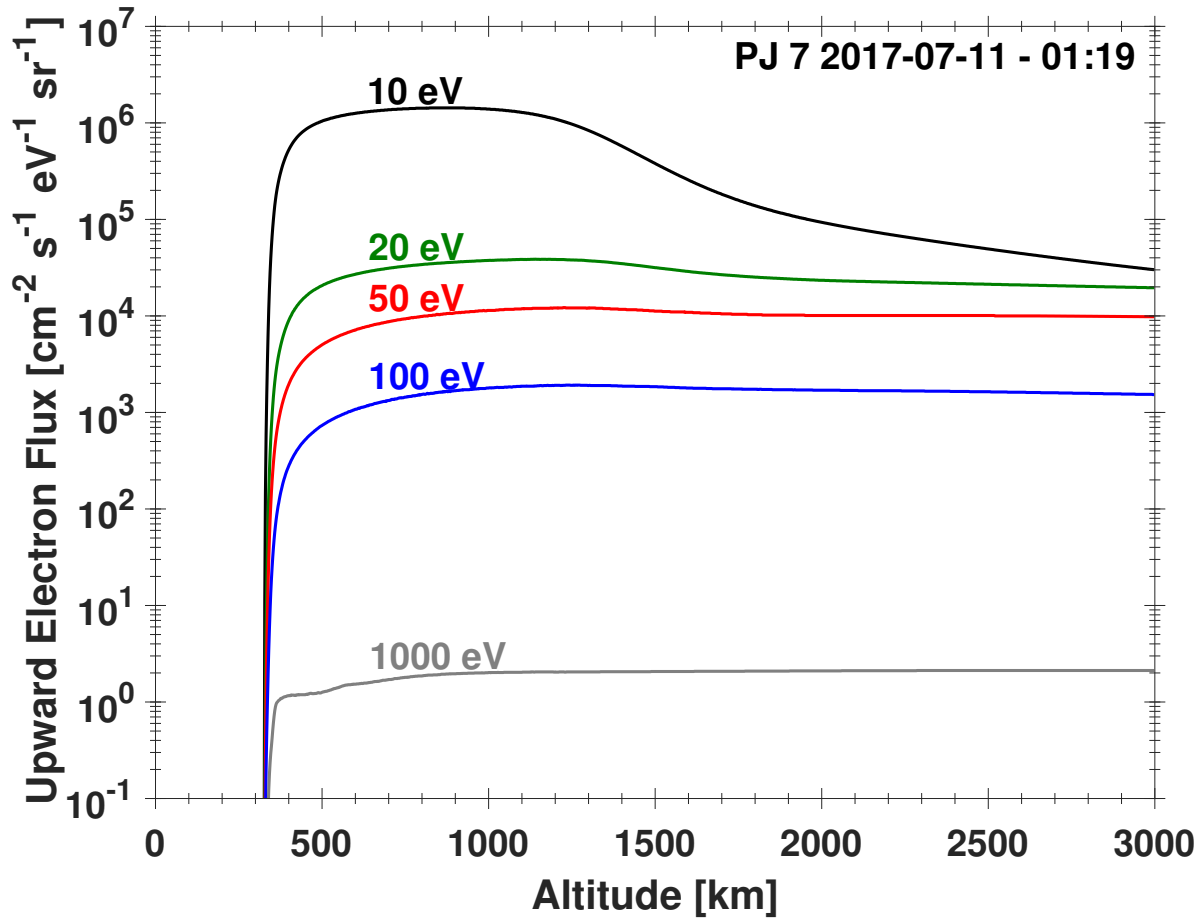


Figure 7.6: Upward electron flux vs. altitude for electron energies of 10, 20, 50, 100, and 1000 eV and initial oxygen ion input flux from the PJ 7 polar cap pass measured by Juno in 2017.

Displayed in Figure 7.6 is the flux of upward moving electrons for various electron energies as a function of altitude. These electrons, along with downward precipitating ions, will generate a current in the ionosphere as they move through it, contributing to an overall field-aligned current. This input ion flux results in a large flux of low energy, upward moving electrons, particularly the 10 eV energy bin. Due to the low energy of most of the incident ions, there is a very small flux of electrons that reach an energy of 1 keV.

Next, Figure 7.7 shows the Lyman and Werner band production rates as a function of H₂ density and altitude. The UV emission associated with this Juno measurement is broadly distributed throughout the depth of the atmosphere, with a large peak that extends for nearly 100 km. The Lyman-alpha band from atomic hydrogen production rate is surprisingly large because of the low

energy distribution of the input ion flux. One would expect the color ratio to be relatively low because the column density of CH_4 the photons travel through will be small, owing to the large amount of UV emission occurring in the upper atmosphere. This is shown in the synthetic UV spectra generated in Figure 7.8. There is little photoabsorption in these spectra for atmosphere 1, regardless of the exit angle considered. The total Lyman and Werner band intensity when no opacity effects are present is 8.83 kR. There is a color ratio of 1.44 for 60° with an output flux of 8.30 kR, and 1.53 for 80° , producing 7.99 kR. However, when the ion precipitation is input into atmosphere 2, the photoabsorption has a larger effect, as one would expect. In atmosphere 2, the unattenuated UV photoemission totals 8.59 kR (not included in the figure), the emission at 60° is 5.64 kR with a CR of 2.52, and at 80° the UV emission is 4.36 kR with a CR of 4.66. Depending on the density profile of the atmosphere, ion precipitation may or may not play a role in the observed CR show in Figure 7.7.

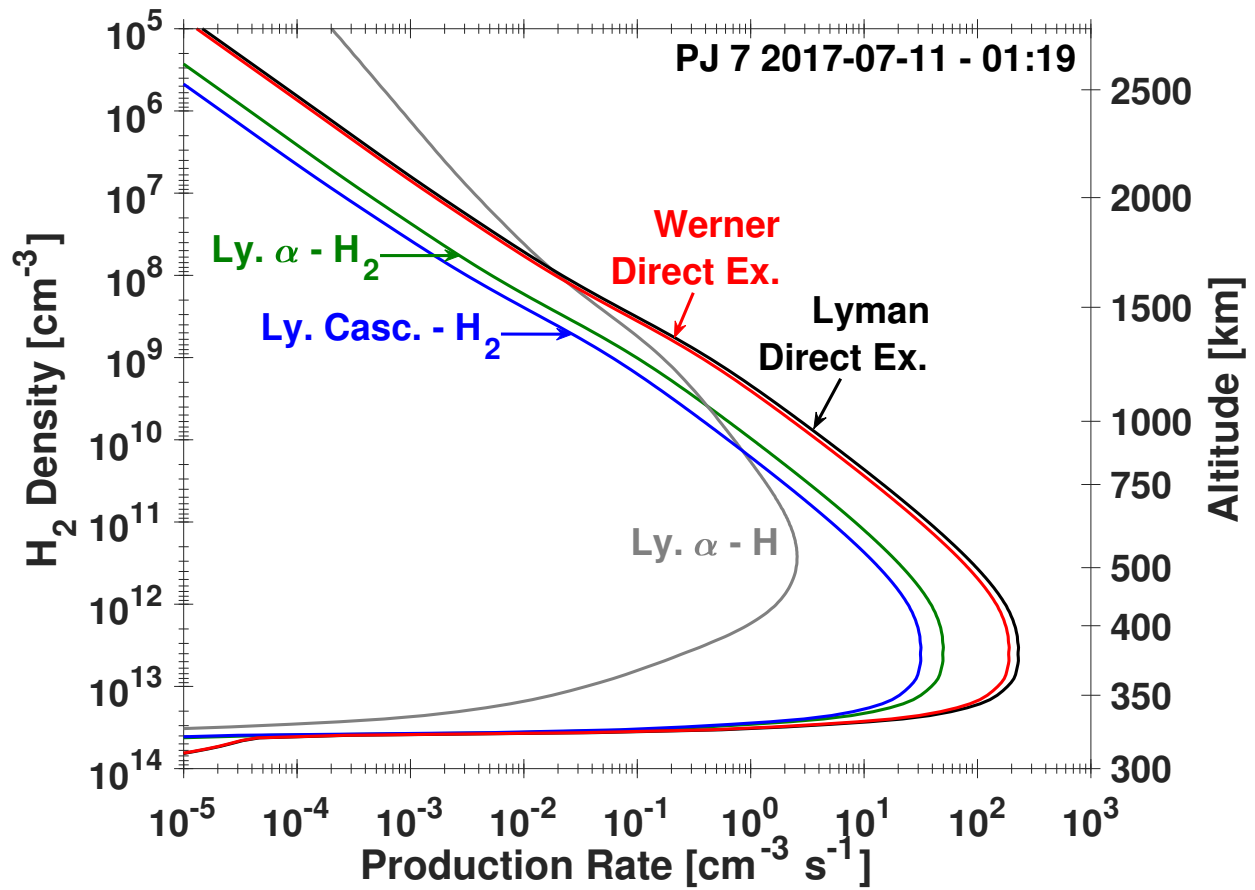


Figure 7.7: Airglow emission production from secondary electrons produced from oxygen and sulfur ions measured by Juno during the PJ 7 polar cap pass in 2017.

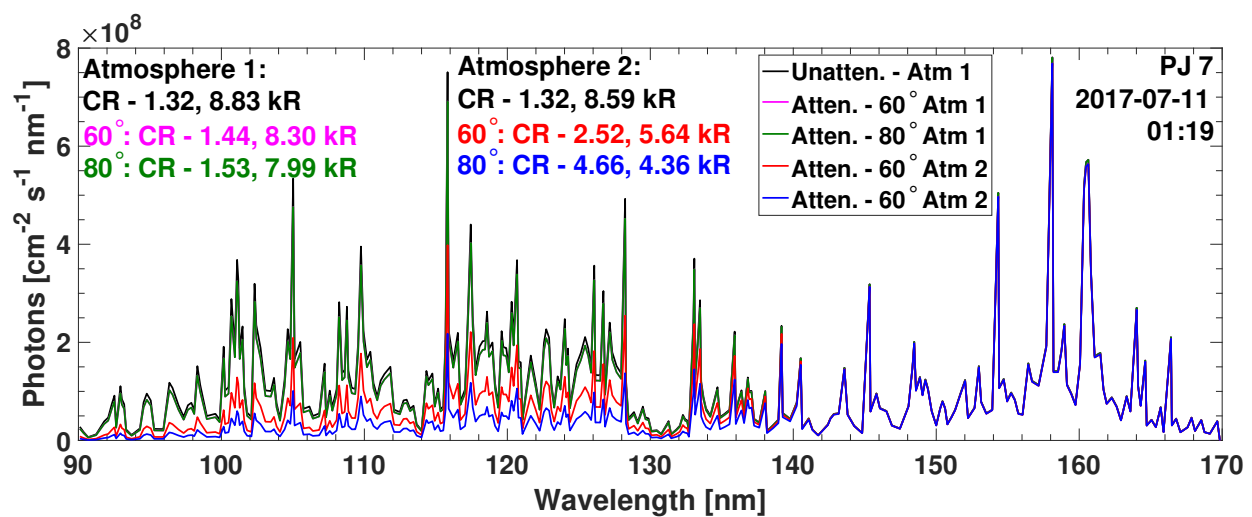


Figure 7.8: Lyman-Werner spectra in both atmospheres from oxygen and sulfur ions measured by Juno during the PJ 7 polar cap pass in 2017. The red and pink lines are calculated with a θ of 60° (pink line is behind the green line) and the green and blue lines with a θ of 80° , while the black line is what is expected when no opacity effects are considered. The Ly- α line at 121.6 nm has been withheld from these predictions.

7.3 Ionosphere for the Juno Case

In addition to H^+ and H_2^+ production rates presented in Figure 7.3, the two-stream model outputs additional ion production rates (Discussed in Section 3.2.7). These ion production rate for the Juno PJ 7 ion flux measurement is displayed in Figure 7.9. This profile is a necessary step in producing the steady state ionosphere from the chemical model presented in Section 3.3. When using the ionospheric/chemical model with this input Juno flux I have assumed $T_{vib}=2T(z)$ (associated with Equation 3.7). The resultant steady state ionosphere is shown in Figure 7.10.

It is interesting to note that although the H^+ production rate from ion precipitation and secondary electron collisions is much smaller than that of H_2^+ , the steady state ionosphere relaxes in such a way that H^+ is more than 5 orders of magnitude greater than H_2^+ above 500 km. This is because there are many reaction processes with large rate coefficients that result in the loss of H_2^+ , whereas the only processes in the upper atmosphere that lower the density of H^+ are $H_2(vib) + H^+$ and the electron recombination process, $H^+ + e^-$. However, below the homopause where CH_4 becomes abundant, H^+ drops significantly as there are multiple hydrocarbon species that will react with H^+ (i.e., CH_4 , C_2H_6 , and C_4H_2). All of the chemical reaction and electron recombination rate coefficients are shown in Appendix C.

H_3^+ , a critical ion used in remotely determining physical processes and temperatures in planetary atmospheres, shows an increase in density until the homopause is reached. Comparing the resultant H_3^+ density with observation is something left for future work but would likely help constrain atmospheric models, especially if all forms of particle precipitation are considered. Following the upper atmosphere, CH_5^+ , the most abundant hydrocarbon species, begins dominating all species below about 450 km largely due to the reaction



CH_4^+ is the most abundant hydrocarbon produced by the two-stream model (along with CH_3^+ , see Fig. 7.9), with H_2 being the major constituent in the neutral atmosphere. The rest of the ionized

hydrocarbon species are displayed in Figure 7.11, where I have emphasized altitudes below the homopause.

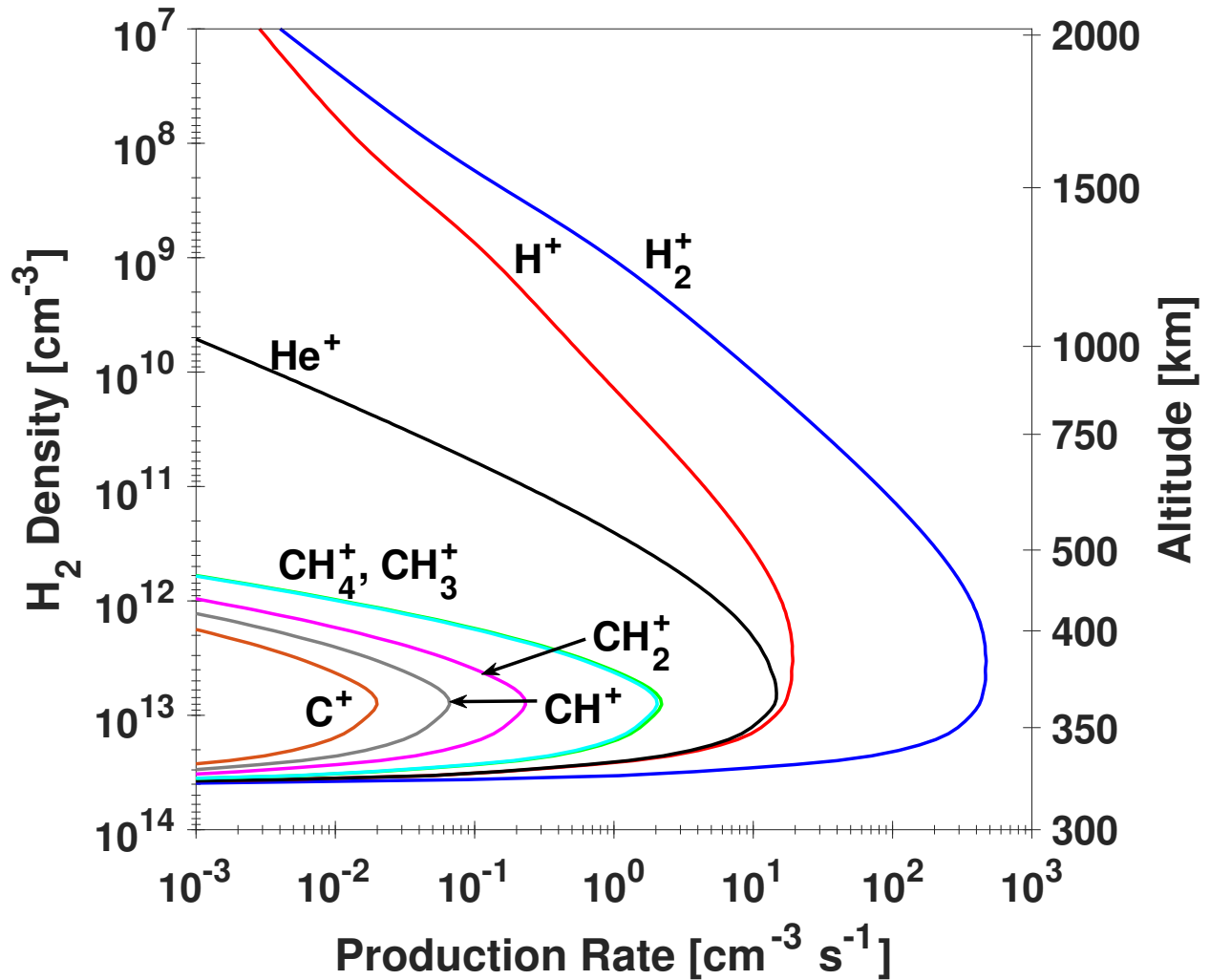


Figure 7.9: Ion production rate profiles vs. H_2 density from oxygen and sulfur ions measured by Juno during the PJ 7 polar cap pass in 2017. This production is solely that from secondary electrons, primary ionization has been excluded and no photoionization is considered, i.e. a night side case.

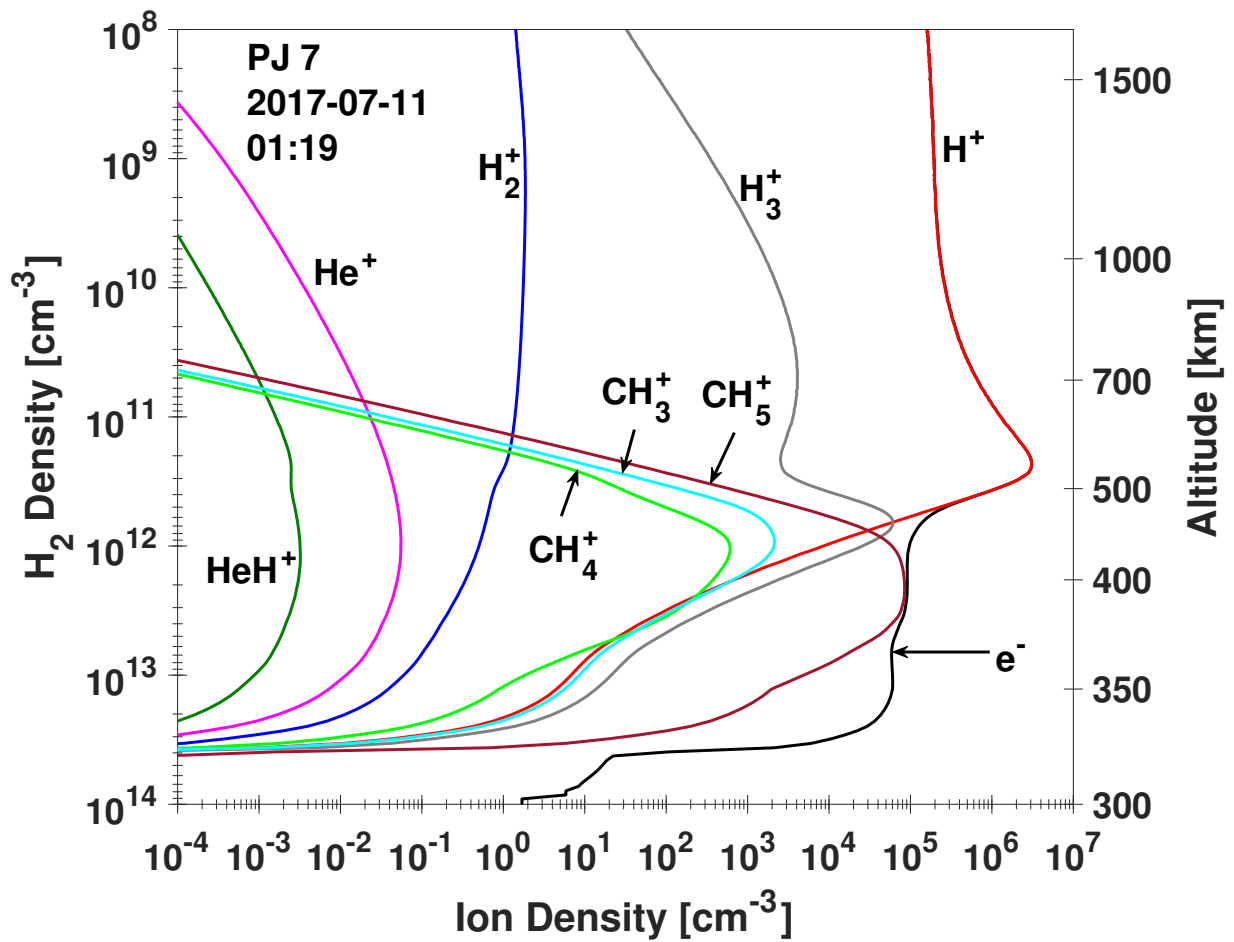


Figure 7.10: 8 of the resulting 27 steady state ion densities (plus electrons) calculated by the chemical reactions model from precipitating ions measured by Juno during the PJ 7 polar cap pass. Photoionization has not been considered, but primary ionization from precipitating oxygen and sulfur is included, along with ionization from secondary electrons.

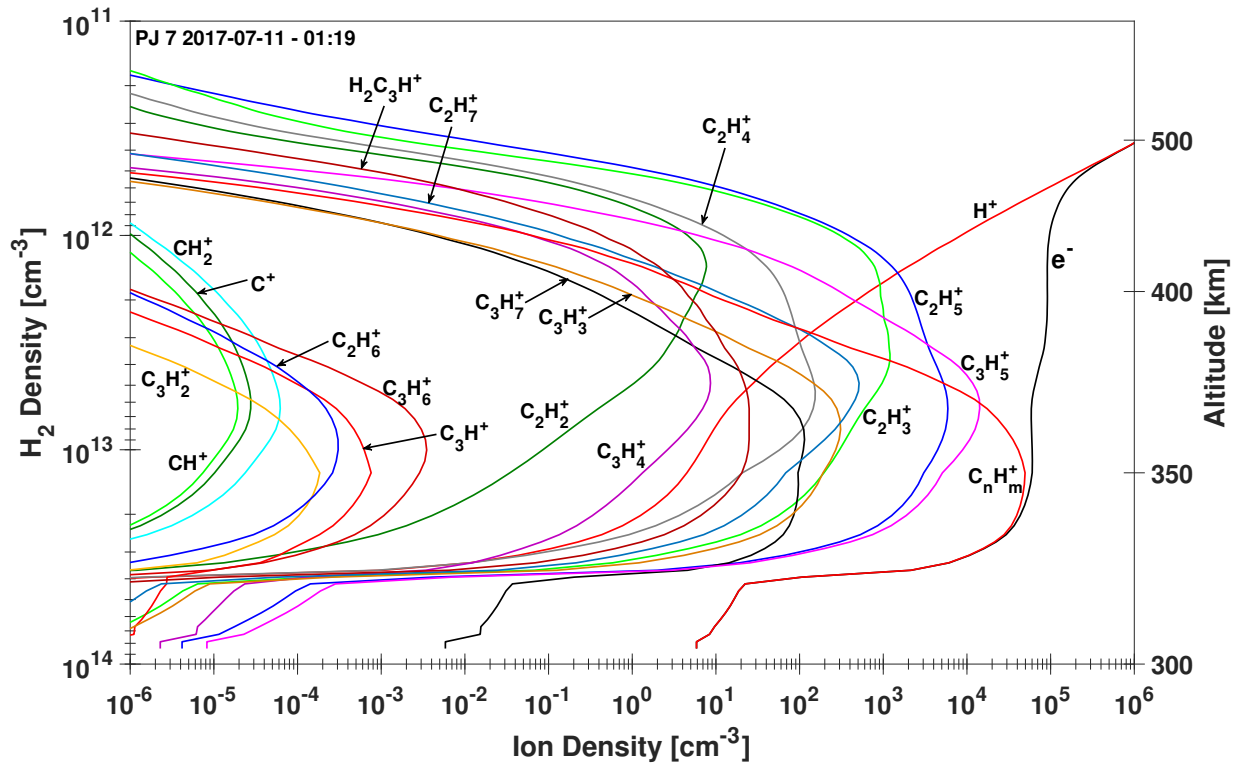


Figure 7.11: Ionospheric profiles calculated by the chemical reactions model from precipitating ions measured by Juno during the PJ 7 polar cap pass. Photoionization has not been considered, but primary ionization from precipitating oxygen and sulfur is included, along with ionization from secondary electrons. I emphasize hydrocarbon production by focusing on the lower altitudes with H⁺ and e⁻ included for reference.

7.3.1 Pedersen and Hall Conductivities

The final results I present are the Pedersen and Hall conductivities associated with ion and electron precipitation into the Jovian atmosphere (discussed in Section 1.5.2). I do not spend a large amount of resources on these calculations, but they are immensely important to the currents in the ionosphere and the magnetospheric current generated through MI coupling and I suggest a more in-depth study needs to be done for future work. For my model, I approximate the electron-neutral collision frequency to be $\nu_{en} = n_{\text{neut}} \times 10^{-8}$ and the ion-neutral collision frequency to be $\nu_{in} = n_{\text{neut}} \times 10^{-9}$, where n_{neut} is the total neutral density (see Equations 1.13, 1.14, and 1.15).

Figure 7.12 presents the ionospheric electrical conductivities as a function of altitude for an input of the ionospheric densities shown in Figures 7.10 and 7.11. Both the Pedersen and Hall conductivities are smallest in the upper atmosphere for the same reason the parallel conductivity is the largest, the ion/electron-neutral collision frequency is small due to the lacking neutral density. This indicates that the upper atmosphere is nearly a perfect conductor for parallel (magnetic field-aligned, or "Birkeland") currents. In the dynamo region (the region with wind-driven currents), between about 300 - 500 km, the Pedersen and Hall currents are the largest, reaching 10^{-5} S/m. The height integrated Pedersen and Hall conductivities are 0.704 and 0.598 Siemens (S).

Figure 7.13 displays Pedersen and Hall conductivities generated by a 20 keV monoenergetic electron beam with an input power of 1 mW/m^2 for comparative purposes. Both sets of conductivities peak at about the same altitude, however the parallel conductivity associated with ion precipitation is about 1-2 orders of magnitude larger than that created by electron precipitation. The height integrated Pedersen conductivity generated by ion precipitation is about twice as large, while the Hall conductivity is more prominent for electron precipitation.

A magnetospheric electric field can be mapped down to the dynamo region, driving both Pedersen and Hall currents; especially at high latitude regions like the polar cap, where magnetic field lines are mapped to the outer magnetosphere. However, even assuming no magnetospheric electric field contribution, i.e. $\mathbf{E} = 0$ in Section 1.5.2, there is still a motional, neutral wind-driven electric field such that $\mathbf{E}' = \mathbf{u}_n \times \mathbf{B}$. At lower altitudes the ion density gets too small while the neutral

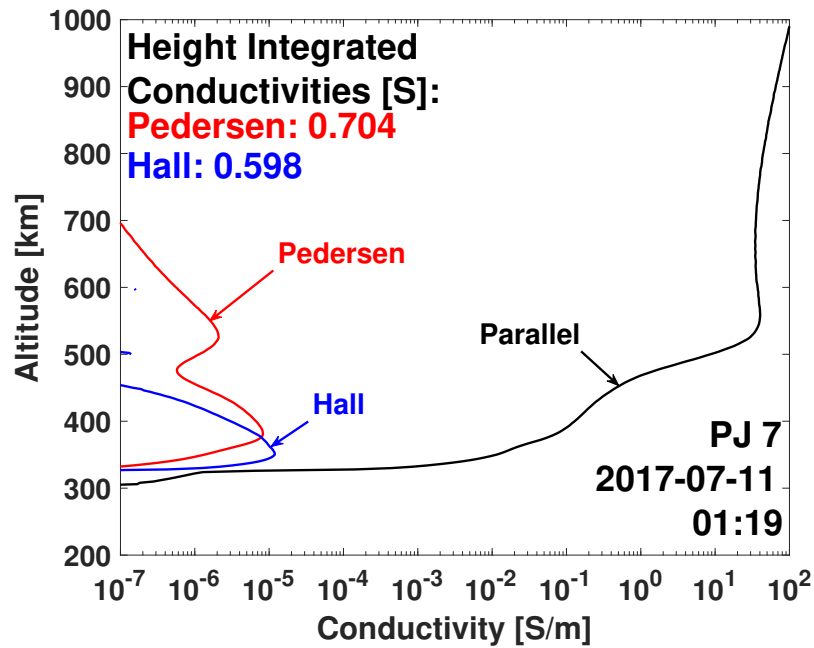


Figure 7.12: Ionospheric conductivities versus altitude associated with the ionospheric densities calculated by using a measured Juno ion flux from Perijove 7 as an input.

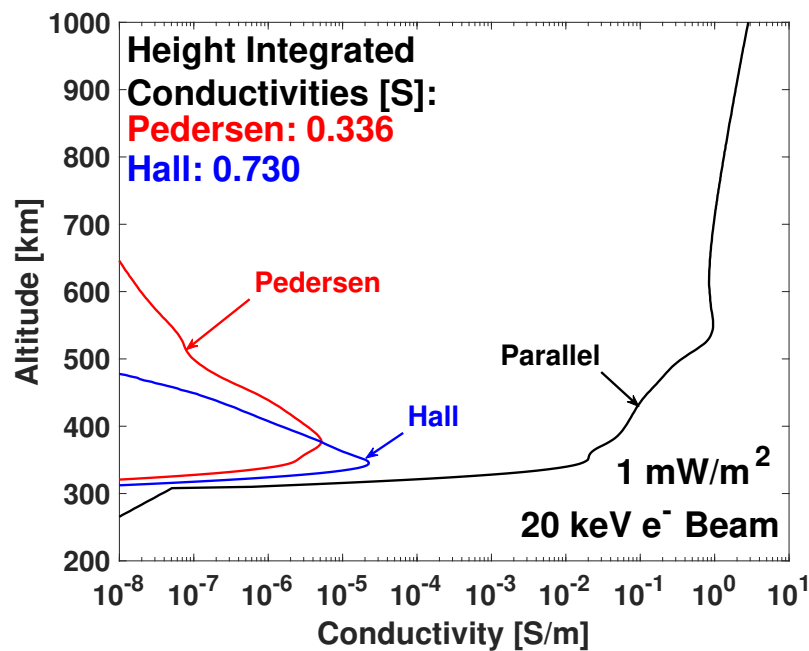


Figure 7.13: Ionospheric conductivities versus altitude associated with ionospheric densities calculated by inputting a 1 mW/m^2 electron beam at a monoenergetic energy of 20 keV. This is an energy commonly seen by the JADE instrument on Juno (Ebert et al., 2019).

density gets substantially larger, effectively shutting off any current generation.

There are a couple of important consequences from the generation of conductivities and currents in the ionosphere (see Figures 1.7 and 1.8), including joule heating and a subsequent raise in the atmospheric temperature of up to a couple hundred Kelvin. The height integrated current densities (from Equation 1.17) in the ionosphere can be used to estimate the electric field-aligned potentials with $\mathbf{K}_{\perp} = \Sigma_{\perp} \mathbf{E}'_{\perp}$. For example, assuming a current density of about 10 MA over a small band across the polar cap, say 10^4 km, or 10^7 m, then $K_{\perp} \approx 10^7 \text{ A} / 10^7 \text{ m} = 1 \text{ A/m}$. With the height integrated Pedersen conductivity calculated to be about 1 S, the electric field can be approximated to $E'_{\perp} \approx \frac{1 \text{ A/m}}{1 \text{ S}} = 1 \text{ V/m}$. This corresponds to a change in the bulk flow velocity (wind), $\Delta u \approx E_{\perp} / B$, of about 1 km/s when approximating Jupiter's magnetic field as $B = 10^{-3} \text{ T}$ (the most recent Juno measured value is $\sim 7.8 \text{ Gauss} = 7.8 \times 10^{-4} \text{ T}$ (Connerney et al., 2017)). This allows for a couple quick estimates of different flow velocities corresponding to different input field-aligned currents; i.e., 1 MA input results in 0.1 km/s, 50 MA in 5 km/s. However, a current between 1-10 MA seems like a fair approximation as it is about the current seen by JEDI with the PJ 7 measurement. There was an input ion flux of about 2×10^6 and an associated escape electron flux of $\sim 8 \times 10^6$ electrons (Fig. 7.5), which sums to a current of approximately $10^7 \text{ e/cm}^2/\text{s}$ or $10^{11} \text{ e/m}^2/\text{s}$. Then, $10^{11} \text{ e/m}^2/\text{s} \times 1.6 \times 10^{-19} \text{ coulombs/e} \approx 2 \times 10^{-8} \text{ coulombs/m}^2/\text{s} = 2 \times 10^{-8} \text{ A/m}^2$. If taking an area of about 10^{14} m^2 (which is the approximate area poleward of 5° latitude), the total current is $\sim 2 \times 10^6 \text{ A}$, or 2 MA. This would correspond to a driven ionospheric density flow of 2 km/s.

7.4 Discussion on Data Usage

In the appendix I have provided as much data as I reasonably can with the goal that anyone can use it to estimate their own X-ray flux as long as they have access to an initial JEDI spectrum. Here I want to layout as clearly as possible how to take an ion flux and produce an X-ray power.

1. The first, and arguably most difficult, part is converting the JEDI energy spectrogram into a usable ion flux. To be done accurately, this requires knowing the width of each energy bin

on JEDI at the time of measurement. I have included the energy bin widths in Table 7.1 that correspond to the data in Figure 4.5. It is likely the energies bins will be changed and resized, if they have not already.

2. Once the bin widths are known, one can convert the intensity from counts/steradian/cm²/s/keV to counts/cm²/sec by multiplying each flux intensity by 2π and the corresponding energy bin width. A second thing to consider is that the first three energy bins cannot distinguish between oxygen and sulfur ions. In this work I used an O:S ratio of 2:1 motivated by the likely source of SO₂ from Io's volcanoes. A different ratio can be used, but those low energies will not affect X-ray production, anyway.
3. Once an intensity of counts/cm²/s vs. ion energy (in keV/u, not total energy) is obtained, one can multiply the intensity by the ion energy (keV/u) and the X-ray efficiency for each charge state of the ion species at a given ion energy in Appendix D or E. To account for all X-rays, charge exchange and direct excitation need to be considered, in which case the X-ray efficiencies can be summed together. This will result in the number of photons/cm²/s produced by each ion charge state and species.
4. Summing the photon production rate for each charge state together will give the total X-ray production rate for a given JEDI pass.
5. Multiplying the photon production rate by the average photon energy, 1.6×10^{-19} J/eV, 10^6 μ W/W, and 10^4 cm²/m² will yield the power in μ W/m². In general, the average photon energy is likely between 500-600 eV. If sulfur emission is higher than oxygen, then 500 eV is more accurate and if oxygen emission is greater, the average photon energy probably tends closer to 600 eV.

As an example, for the JEDI oxygen measurement discussed in this text, the total photon production and power is calculated at each step in Table 7.1.

Oxygen

Energy [keV]	JEDI Flux [c/str/cm ² /s/keV]	Energy Bin Width [keV]	Intensity [c/cm ² /s]	Energy [keV/u]
171	249.9	66	103631	11
240	339.7	71	151542	15
324	279.0	105	184066	20
477	219.8	216	298306	30
746	89.50	346	194571	47
956	43.61	251	68776	60
1240	22.56	300	42525	78
1930	8.687	880	48032	121
3490	3.018	2280	43235	218
7300	0.914	5340	30667	456
Energy [keV/u]	X-Ray Efficiency [†] [cm ² sec] ⁻¹ [keV/u] ⁻¹	X-ray Production photons/cm ² /s		
11	0.0000	0.000		
15	0.0000	0.000		
20	0.0000	0.000		
30	0.0000	0.000		
47	0.0000	0.000		
60	0.0000	0.000		
78	0.0000	0.000		
121	0.0003	1.74x10 ³		
218	0.0246	2.32x10 ⁵		
456	0.2951	4.13x10 ⁶		
Total power flux [μ W/m ²):		4.2		

[†] X-ray efficiency values in Appendix D or E. These values are the sum of O⁶⁺ and O⁷⁺ from both charge exchange and direct excitation for an exit angle of 80° in atmosphere 1.

Table 7.1: Tabulated JEDI oxygen ion measurements discussed in Section 4.2.7 and shown in Figure 4.5.

The total X-ray production shown in Table 7.1 is only about 7% percent higher than what is shown in Figure 7.2, where the power flux was found by integrating over every photon energy. This exact same process can be used for sulfur, where in this example sulfur emission will be much less than oxygen.

Chapter 8

Summary and Conclusions

8.1 Conclusion

The purpose of this work is to extend our understanding of the Jovian aurora through energy deposition, field-aligned currents, UV emission, and X-ray production from ion precipitation for a wide range of incident energies. Previously, Houston et al. (2018); Ozak et al. (2010, 2013) modeled oxygen and sulfur energies emphasizing higher energies (i.e., MeV/u) and X-ray production. I extend the oxygen and sulfur precipitation work to lower energies using updated ion impact cross-sections. The work is intended to aid in the understanding of data from NASA's Juno mission that arrived at Jupiter on July 4, 2016. Initial results from Juno include measurements of oxygen and sulfur ion energies that I have shown are within the realm of the model presented. However, measurements have indicated that the ions present above Jupiter's polar caps are not monoenergetic but cover a distribution of energies. Clark et al. (2017b) present inverted-V signatures in both electron and ion precipitation detected by JEDI during the third auroral pass, hypothesizing that downward parallel potential drops are associated with these signatures. In the southern hemisphere, measurements indicate both oxygen and sulfur exceeding the upper energy limitations of JEDI at the peak of the inverted-V. They cautiously suggest that 10-1000 kV potentials develop to produce the signatures seen.

A careful application of my model to additional Juno data will be required in the future. Juno data suggest that polar emissions are not limited to precipitating oxygen and sulfur ions, but also protons (Haggerty et al., 2017). Thus, one can continue to upgrade the model by considering energetic proton precipitation. Because Juno has measured large proton fluxes one should be motivated

to create a proton precipitation model in the future.

The current work did not address the correlation between X-ray emission and UV emission based on the Juno data that is available to date and the Earth-orbit-based observational data. A reasonable question is: Is there a correlation between UV and X-ray emission, and if so, is it spatial, temporal, or both? Answering this question could lead to further understanding as to whether UV and X-ray emissions are produced by the same source, or if their production is independent from one another. It could be that ions are creating X-ray and UV emission, but most UV emission is coming from an alternative source, i.e., electrons and protons. By measuring X-ray emission, one is able to get diagnostics on the field-aligned currents as I have now proven with the discussion in Section 7.3.1. Higher X-ray flux emission indicates a higher flux of ion precipitation. This, in turn, will lead to a higher escape electron current that contributes to the overall downward currents. As more Juno data is gathered, comparing the measured ion fluxes with the field-aligned current will help to further constrain the model and understand the MI coupling processes taking place at Jupiter.

With electron bremsstrahlung largely proven as unable to produce the totality of X-ray emission observed (Branduardi-Raymont et al., 2004; Elsner et al., 2005), recent heavy ion precipitation models required the precipitating ions to reach energies higher than what was to be expected at Jupiter (Cravens et al., 1995; Ozak et al., 2010, 2013; Houston et al., 2018). Now with *in situ* measurements it is clear the ions are not energetic enough to produce X-rays based on the previous modeling attempts. This forced the rethinking of processes generating X-ray emission from ion precipitation. Schultz et al. (2019) determined not every process was being accounted for in the original precipitation modeling, but simultaneous (both target and ion) processes needed to be considered. This led to a completely new series of processes and cross-sections that I have now utilized for the updated heavy ion precipitation model described in this work. The required initial ion energy to produce X-rays has been reduced dramatically and is now well within the energy range Juno has measured.

I have provided evidence that heavy ion precipitation measured by JEDI can produce X-ray

emission. Thus, another question arises: Can heavy ion precipitation produce *enough* X-ray emission to explain the total observational soft X-ray luminosity of 1-2 GW ((Elsner et al., 2005; Gladstone et al., 2002)? The X-ray emission my model produces when the JEDI ion flux measurement shown in Figure 4.5 are input is $\sim 4 \times 10^6$ photons/cm²/s which is in agreement with an observation presented by Gladstone et al. (2002). This X-ray flux is the sum of all oxygen and sulfur X-ray emission from both charge exchange and direct excitation with an exit angle of 80° from the original atmosphere. Integrating the emission in Figure 7.2, results in an energy flux of $\sim 2.5 \times 10^9$ eV/cm²/s. Converting this to Watts/cm² by multiplying by a factor of 1.6×10^{-19} J/eV yields a power output of 4×10^{-9} W/cm². Now, the total area of X-ray emission on the Jovian polar cap can be assumed to come from within a latitude of $\sim 5^\circ$. This gives an area of $2\pi R_J^2(1-\cos\theta) \approx 10^{18}$ cm² (R_J = Jovian radii = 71,492 km). 4×10^{-9} W/cm² x 10^{18} cm² = 4×10^9 W, or 4 GW. It appears, based on this quick, “back of the envelope” calculation, that we can now account for the entirety of the output power of the X-rays. Of course, the area of emission needs to be greatly constrained, but this exercise shows it is now feasible the ion flux measurements at Jupiter are responsible for the X-ray emission.

8.2 Final Discussion

To summarize the main findings of my work:

- Primary ionization (i.e., ionization due to the primary ion precipitation) leading to H⁺ and H₂⁺ production plus the resulting ionospheric electron and ion densities dominates over secondary ionization (due to the secondary electrons ionizing the atmospheric neutrals), especially in H⁺ production.
- The current density produced by secondary electrons from ions with initial energies between 200 – 300 keV/u seems to dominate for both oxygen and sulfur, compared to the current produced by other initial ion energies. Since these lower-energy ions do not penetrate deep into the atmosphere, it is then easier for the secondary electrons produced to escape and

contribute to the downward current system close to the planet. Although this is a low energy compared to the highest of the model, it is a higher energy than produced by Houston et al. (2018), which indicated 100 - 200 keV/u oxygen ions generated the highest current density, and it is also the upper range of JEDI measurements.

- Airglow emissions produced by ion precipitation are low compared to the main auroral oval emission (only ~ 10 kR), but are still significant enough to contribute some of the observed emission.
- Color ratios computed for ion energies responsible for X-ray emission are between 2 and 10 depending on the atmospheric profile used, which is comparable to recent color ratio observations of the UV aurora by Juno (Bonfond et al., 2017). However, polar atmospheric abundances, particularly CH_4 , need to be investigated further, as there have been attempts from others at modeling this (Gérard et al., 2014; Grodent et al., 2001; Moses et al., 2005).
- New SIM cross-section data has shifted the charge state distribution of both oxygen and sulfur to lower energies than before. The repercussions being, it now requires less energy to strip ions to X-ray producing charge states, resulting in precipitation that does not penetrate as deeply into the atmosphere.
- The aforementioned lack of precipitation depth leads to less absorption of photon emission when opacity effects are considered.
- If an atmosphere of fully mixed constituents is used, the X-ray efficiency is reduced; but, not as drastically as one might expect. The emission from ions at the energies measured by JEDI is only reduced by about 15-20% compared to the original atmosphere.
- X-ray spectra separated into line emission using Gaussian distributions are producible and can be used in coordination with JEDI ion flux measurements and Earth-orbit-based X-ray observations. When comparing the two, opacity effects need to be considered on a case-by-case basis depending on the geometry of the Earth and Jupiter at the time.

- JEDI flux measurements input into the model generate enough X-rays to account for the total X-ray power that has been observed in the past.
- X-rays have demonstrated to be a reliable diagnostic tool of downward currents at Jupiter and the work presented here has increased our understanding of the downward current regions associated with magnetosphere-ionosphere coupling and the aurora. This is another step closer to resolving all the processes necessary in the linkage between the ionosphere and the magnetopause, outer magnetosphere, and the magnetotail.

The future work needed is:

- More JEDI data needs to be put through the model to see if ion flux measurements can consistently produce the observed X-ray fluxes.
- Adding a proton precipitation model is essential to fully simulating the field-aligned currents and the color ratio.
- A comprehensive electron precipitation model would be substantially helpful in modeling the entirety of the processes in the atmosphere, as was seen by the dynamic ionosphere created with an input electron flux.
- The ionospheric model is incomplete and needs to be further understood to shed light on all of the magnetosphere-ionosphere coupling dynamics taking place in the Jovian polar atmosphere.
- The lifetime of each ion species in the steady-state ionosphere needs to be investigated to see the time scale of the currents that are generated.

References

- Ajello, J. M., Kanik, I., Ahmed, S. M., & Clarke, J. T. (1995). Line profile of H Lyman α from dissociative excitation of H₂ with application to Jupiter. *Journal of Geophysical Research: Planets*, 100(E12), 26411–26420.
- Allegrini, F., Bagenal, F., Bolton, S., Connerney, J., Clark, G., Ebert, R. W., Kim, T. K., Kurth, W. S., Levin, S., Louarn, P., Mauk, B., McComas, D. J., Pollock, C., Ranquist, D., Reno, M., Szalay, J. R., Thomsen, M. F., Valek, P., Weidner, S., Wilson, R. J., & Zink, J. L. (2017). Electron beams and loss cones in the auroral regions of Jupiter. *Geophysical Research Letters*, 44(14), 7131–7139.
- Atreya, S. K. (1986). *Atmospheres and Ionospheres of the Outer Planets and Their Satellites*, volume 15. Springer-Verlag Berlin Heidelberg, 1st edition.
- Ballance, C. P., Griffin, D. C., Colgan, J., Loch, S. D., & Pindzola, M. S. (2003). Electron-impact excitation of beryllium and its ions. *Phys. Rev. A*, 68, 062705.
- Banks, P. M. & Nagy, A. F. (1970). Concerning the influence of elastic scattering upon photoelectron transport and escape. *Journal of Geophysical Research*, 75(10), 1902–1910.
- Bartschat, K., Burke, P. G., & Scott, M. P. (1996). Electron impact excitation of beryllium. *Journal of Physics B: Atomic, Molecular and Optical Physics*, 29(20), L769–L772.
- Bely, O. (1966). Excitation of lithium-like ions by electron impacts. *Proceedings of the Physical Society*, 88(3), 587–595.
- Bonfond, B. (2010). The 3-D extent of the Io UV footprint on Jupiter. *Journal of Geophysical Research: Space Physics*, 115(A9). A09217.

- Bonfond, B., Gladstone, G. R., Grodent, D., Greathouse, T. K., Versteeg, M. H., Hue, V., Davis, M. W., Vogt, M. F., Gérard, J.-C., Radioti, A., Bolton, S., Levin, S. M., Connerney, J. E. P., Mauk, B. H., Valek, P., Adriani, A., & Kurth, W. S. (2017). Morphology of the UV aurorae Jupiter during Juno's first perijove observations. *Geophysical Research Letters*, 44(10), 4463–4471.
- Bonfond, B., Hess, S., Bagenal, F., Gérard, J.-C., Grodent, D., Radioti, A., Gustin, J., & Clarke, J. T. (2013). The multiple spots of the Ganymede auroral footprint. *Geophysical Research Letters*, 40(19), 4977–4981.
- Branduardi-Raymont, G., Bhardwaj, A., Elsner, R. F., Gladstone, G. R., Ramsay, G., Rodriguez, P., Soria, R., Waite, J. H., Jr, & Cravens, T. E. (2007). A study of Jupiter's aurorae with XMM-Newton. *A & A*, 463(2), 761–774.
- Branduardi-Raymont, G., Elsner, R. F., Galand, M., Grodent, D., Cravens, T. E., Ford, P., Gladstone, G. R., & Waite, J. H. (2008). Spectral morphology of the X-ray emission from Jupiter's aurorae. *Journal of Geophysical Research: Space Physics*, 113(A2). A02202.
- Branduardi-Raymont, G., Elsner, R. F., Gladstone, G. R., Ramsay, G., Rodriguez, P., Soria, R., & Waite, Jr., J. H. (2004). First observation of Jupiter by XMM-Newton. *Astron. Astrophys.*, 424, 331–337.
- Bunce, E. J., Cowley, S. W. H., & Yeoman, T. K. (2004). Jovian cusp processes: Implications for the polar aurora. *Journal of Geophysical Research: Space Physics*, 109(A9). A09S13.
- Chen, F. Z. & Wu, C. Y. R. (2004). Temperature-dependent photoabsorption cross sections in the VUV-UV region. I. Methane and ethane. *Journal of Quantitative Spectroscopy and Radiative Transfer*, 85, 195–209.
- Clark, G., Mauk, B. H., Haggerty, D., Paranicas, C., Kollmann, P., Rymer, A., Bunce, E. J., Cowley, S. W. H., Mitchell, D. G., Provan, G., Ebert, R. W., Allegrini, F., Bagenal, F., Bolton,

- S., Connerney, J., Kotsiaros, S., Kurth, W. S., Levin, S., McComas, D. J., Saur, J., & Valek, P. (2017a). Energetic particle signatures of magnetic field-aligned potentials over Jupiter's polar regions. *GRL*, 44, 8703–8711.
- Clark, G., Mauk, B. H., Paranicas, C., Haggerty, D., Kollmann, P., Rymer, A., Brown, L., Jaskulek, S., Schlemm, C., Kim, C., Peachey, J., LaVallee, D., Allegrini, F., Bagenal, F., Bolton, S., Connerney, J., Ebert, R. W., Hospodarsky, G., Levin, S., Kurth, W. S., McComas, D. J., Mitchell, D. G., Ranquist, D., & Valek, P. (2017b). Observation and interpretation of energetic ion conics in Jupiter's polar magnetosphere. *GRL*, 44, 4419–4425.
- Clark, G., Tao, C., Mauk, B. H., Nichols, J., Saur, J., Bunce, E. J., Allegrini, F., Gladstone, R., Bagenal, F., Bolton, S., Bonfond, B., Connerney, J., Ebert, R. W., Gershman, D. J., Haggerty, D., Kimura, T., Kollmann, P., Kotsiaros, S., Kurth, W. S., Levin, S., McComas, D. J., Murakami, G., Paranicas, C., Rymer, A., & Valek, P. (2018). Precipitating electron energy flux and characteristic energies in Jupiter's main auroral region as measured by Juno/JEDI. *Journal of Geophysical Research: Space Physics*, 123(9), 7554–7567.
- Clarke, J. T., Ballester, G., Trauger, J., Ajello, J., Pryor, W., Tobiska, K., Connerney, J. E. P., Gladstone, G. R., Waite, J. H., Ben Jaffel, L., & Gérard, J.-C. (1998). Hubble Space Telescope imaging of Jupiter's UV aurora during the Galileo orbiter mission. *Journal of Geophysical Research: Planets*, 103(E9), 20217–20236.
- Connerney, J. E. P., Adriani, A., Allegrini, F., Bagenal, F., Bolton, S. J., Bonfond, B., Cowley, S. W. H., Gérard, J.-C., Gladstone, G. R., Grodent, D., Hospodarsky, G., Jorgensen, J. L., Kurth, W. S., Levin, S. M., Mauk, B., McComas, D. J., Mura, A., Paranicas, C., Smith, E. J., Thorne, R. M., Valek, P., & Waite, J. (2017). Jupiter's magnetosphere and aurorae observed by the Juno spacecraft during its first polar orbits. *Science*, 356(6340), 826–832.
- Cowley, S. W. H., Bunce, E. J., & Nichols, J. D. (2003). Origins of [j]upiter's main oval auroral emissions. *Journal of Geophysical Research: Space Physics*, 108(A4). 8002.

- Cravens, T. E. (1997). *Physics of Solar System Plasmas*. Cambridge University Press.
- Cravens, T. E., Clark, J., Bhardwaj, A., Elsner, R., Waite, J. H., Maurellis, A. N., Gladstone, G. R., & Branduardi-Raymont, G. (2006). X-ray emission from the outer planets: Albedo for scattering and fluorescence of solar X rays. *Journal of Geophysical Research (Space Physics)*, 111, A07308.
- Cravens, T. E., Howell, E., Waite, J. H., & Gladstone, G. R. (1995). Auroral oxygen precipitation at jupiter. *Journal of Geophysical Research: Space Physics*, 100(A9), 17153–17161.
- Cravens, T. E., Robertson, I. P., Ledvina, S. A., Mitchell, D., Krimigis, S. M., & Waite, J. H. (2008). Energetic ion precipitation at Titan. *Geophysical Research Letters*, 35(3), n/a–n/a. L03103.
- Cravens, T. E., Waite, J. H., Gombosi, T. I., Lugaz, N., Gladstone, G. R., Mauk, B. H., & MacDowall, R. J. (2003). Implications of Jovian X-ray emission for magnetosphere-ionosphere coupling. *Journal of Geophysical Research: Space Physics*, 108(A12). 1465.
- Dalgarno, A., Yan, M., & Liu, W. (1999). Electron Energy Deposition in a Gas Mixture of Atomic and Molecular Hydrogen and Helium. *The Astrophysics Journal Supplement Series*, 125, 237–256.
- Delamere, P. A., Bagenal, F., & Steffl, A. (2005). Radial variations in the Io plasma torus during the Cassini era. *Journal of Geophysical Research: Space Physics*, 110(A12).
- Dougherty, L. P., Bodisch, K. M., & Bagenal, F. (2017). Survey of Voyager plasma science ions at Jupiter: 2. Heavy ions. *Journal of Geophysical Research: Space Physics*, 122(8), 8257–8276.
- Dunn, W. R., Branduardi-Raymont, G., Elsner, R. F., Vogt, M. F., Lamy, L., Ford, P. G., Coates, A. J., Gladstone, G. R., Jackman, C. M., Nichols, J. D., Rae, I. J., Varsani, A., Kimura, T., Hansen, K. C., & Jasinski, J. M. (2016). The impact of an icme on the Jovian X-ray aurora. *Journal of Geophysical Research: Space Physics*, 121(3), 2274–2307.

- Dunn, W. R., Branduardi-Raymont, G., Ray, L. C., Jackman, C. M., Kraft, R. P., Elsner, R. F., Rae, I. J., Yao, Z., Vogt, M. F., Jones, G. H., Gladstone, G. R., Orton, G. S., Sinclair, J. A., Ford, P. G., Graham, G. A., Caro-Carretero, R., & Coates, A. J. (2017). The independent pulsations of Jupiter's northern and southern X-ray auroras. *Nature Astronomy*, 1(11), 758–764.
- Dziczek, D., Ajello, J. M., James, G. K., & Hansen, D. L. (2000). Cascade contribution to the H₂ Lyman band system from electron impact. *Phys. Rev. A*, 61(6), 064702.
- Ebert, R. W., Greathouse, T. K., Clark, G., Allegrini, F., Bagenal, F., Bolton, S. J., Connerney, J. E. P., Gladstone, G. R., Imai, M., Hue, V., Kurth, W. S., Levin, S., Louarn, P., Mauk, B. H., McComas, D. J., Paranicas, C., Szalay, J. R., Thomsen, M. F., Valek, P. W., & Wilson, R. J. (2019). Comparing electron energetics and UV brightness in Jupiter's northern polar region during Juno Perijove 5. *Geophysical Research Letters*, 46(1), 19–27.
- Elsner, R. F., Lugaz, N., Waite, J. H., Cravens, T. E., Gladstone, G. R., Ford, P., Grodent, D., Bhardwaj, A., MacDowall, R. J., Desch, M. D., & Majeed, T. (2005). Simultaneous Chandra X-ray, Hubble Space Telescope ultraviolet, and Ulysses radio observations of Jupiter's aurora. *Journal of Geophysical Research: Space Physics*, 110(A1). A01207.
- Gan, L. & Cravens, T. E. (1992). Electron impact cross-sections and cooling rates for methane. *Planetary Space Science*, 40, 1535–1544.
- Gan, L., Cravens, T. E., & Keller, C. N. (1993). A Time-Dependent Model of Suprathermal Electrons at Titan. In T. I. Gombosi (Ed.), *Plasma Environments of Non-Magnetic Planets* (pp. 171).
- Gan, L., Keller, C. N., & Cravens, T. E. (1992). Electrons in the ionosphere of Titan. *Journal of Geophysical Research: Space Physics*, 97(A8), 12137–12151.
- Garvey, R. H., Porter, H. S., & Green, A. E. S. (1977). Relativistic yield spectra for H₂. *Journal of Applied Physics*, 48, 4353–4359.

- Gérard, J.-C., Bonfond, B., Grodent, D., Radioti, A., Clarke, J. T., Gladstone, G. R., Waite, J. H., Bisikalo, D., & Shematovich, V. I. (2014). Mapping the electron energy in Jupiter's aurora: Hubble spectral observations. *Journal of Geophysical Research: Space Physics*, 119(11), 9072–9088. 2014JA020514.
- Gharibnejad, H., Schultz, D., Cravens, T., & Houston, S. (2019). Data for secondary-electron production from ion precipitation at Jupiter IV: Simultaneous and non-simultaneous target and projectile processes in collisions of $S^{q+} + H_2$ ($q=0-16$). In preparation.
- Gladstone, G. R., Allen, M., & Yung, Y. L. (1996). Hydrocarbon Photochemistry in the Upper Atmosphere of Jupiter. *Icarus*, 119, 1–52.
- Gladstone, G. R., Persyn, S. C., Eterno, J. S., Walther, B. C., Slater, D. C., Davis, M. W., Versteeg, M. H., Persson, K. B., Young, M. K., Dirks, G. J., Sawka, A. O., Tumlinson, J., Sykes, H., Beshears, J., Rhoad, C. L., Cravens, J. P., Winters, G. S., Klar, R. A., Lockhart, W., Piepgrass, B. M., Greathouse, T. K., Trantham, B. J., Wilcox, P. M., Jackson, M. W., Siegmund, O. H. W., Vallerga, J. V., Raffanti, R., Martin, A., Gérard, J.-C., Grodent, D. C., Bonfond, B., Marquet, B., & Denis, F. (2017a). The ultraviolet spectrograph on NASA's Juno mission. *Space Science Reviews*, 213(1), 447–473.
- Gladstone, G. R., Versteeg, M. H., Greathouse, T. K., Hue, V., Davis, M. W., Gérard, J.-C., Grodent, D. C., Bonfond, B., Nichols, J. D., Wilson, R. J., Hospodarsky, G. B., Bolton, S. J., Levin, S. M., Connerney, J. E. P., Adriani, A., Kurth, W. S., Mauk, B. H., Valek, P., McComas, D. J., Orton, G. S., & Bagenal, F. (2017b). Juno-UVS approach observations of Jupiter's auroras. *Geophysical Research Letters*, 44(15), 7668–7675.
- Gladstone, G. R., Waite, J. H., Grodent, D., Lewis, W. S., Crary, F. J., Elsner, R. F., Weisskopf, M. C., Majeed, T., Jahn, J. M., Bhardwaj, A., Clarke, J. T., Young, D. T., Dougherty, M. K., Espinosa, S. A., & Cravens, T. E. (2002). A pulsating auroral X-ray hot spot on Jupiter. *Nature*, 415(6875), 1000–1003.

- Green, A. E. S. & Dutta, S. K. (1967). Semi-empirical cross sections for electron impacts. *Journal of Geophysical Research (1896-1977)*, 72(15), 3933–3941.
- Green, A. E. S. & Sawada, T. (1972). Ionization cross sections and secondary electron distributions. *Journal of Atmospheric and Terrestrial Physics*, 34, 1719.
- Griffin, D. C., Mitnik, D. M., Colgan, J., & Pindzola, M. S. (2001). Electron-impact excitation of lithium. *Phys. Rev. A*, 64, 032718.
- Grodent, D., Bonfond, B., Radioti, A., Gérard, J.-C., Jia, X., Nichols, J. D., & Clarke, J. T. (2009). Auroral footprint of Ganymede. *Journal of Geophysical Research: Space Physics*, 114(A7). A07212.
- Grodent, D., Clarke, J. T., Kim, J., Waite, J. H., & Cowley, S. W. H. (2003a). Jupiter's main auroral oval observed with HST-STIS. *Journal of Geophysical Research: Space Physics*, 108(A11). 1389.
- Grodent, D., Clarke, J. T., Waite, J. H., Cowley, S. W. H., Gérard, J.-C., & Kim, J. (2003b). Jupiter's polar auroral emissions. *Journal of Geophysical Research: Space Physics*, 108(A10). 1366.
- Grodent, D., Waite Jr., J. H., & Gérard, J.-C. (2001). A self-consistent model of the Jovian auroral thermal structure. *Journal of Geophysical Research: Space Physics*, 106(A7), 12933–12952.
- Gustin, J., Bonfond, B., Grodent, D., & Gérard, J.-C. (2012). Conversion from HST ACS and STIS auroral counts into brightness, precipitated power, and radiated power for H₂ giant planets. *Journal of Geophysical Research: Space Physics*, 117(A7). A07316.
- Gustin, J., Grodent, D., Ray, L., Bonfond, B., Bunce, E., Nichols, J., & Ozak, N. (2016). Characteristics of north Jovian aurora from STIS FUV spectral images. *Icarus*, 268(Supplement C), 215 – 241.

- Haggerty, D. K., Mauk, B. H., Paranicas, C. P., Clark, G., Kollmann, P., Rymer, A. M., Bolton, S. J., Connerney, J. E. P., & Levin, S. M. (2017). Juno/JEDI observations of 0.01 to >10 MeV energetic ions in the Jovian auroral regions: Anticipating a source for polar X-ray emission. *Geophysical Research Letters*, 44(13), 6476–6482. 2017GL072866.
- Hill, T. W. (1979). Inertial limit on corotation. *J. Geophys. Res.*, 84, 6554–6558.
- Hill, T. W. (2004). Auroral structures at Jupiter and Earth. *Advances in Space Research*, 33, 2021–2029.
- Horanyi, M., Cravens, T. E., & Waite, J. H. (1988). The precipitation of energetic heavy ions into the upper atmosphere of Jupiter. *Journal of Geophysical Research: Space Physics*, 93(A7), 7251–7271.
- Houston, S. J., Ozak, N., Young, J., Cravens, T. E., & Schultz, D. R. (2018). Jovian auroral ion precipitation: Field-aligned currents and ultraviolet emissions. *Journal of Geophysical Research: Space Physics*, 123(3), 2257–2273.
- Hudson, R. D. (1971). Critical review of ultraviolet photoabsorption cross sections for molecules of astrophysical and aeronomic interest. *Reviews of Geophysics*, 9(2), 305–406.
- Hui, Y., Schultz, D. R., Kharchenko, V. A., Bhardwaj, A., Branduardi-Raymont, G., Stancil, P. C., Cravens, T. E., Lisse, C. M., & Dalgarno, A. (2010). Comparative analysis and variability of the Jovian X-ray spectra detected by the Chandra and XMM-Newton observatories. *Journal of Geophysical Research: Space Physics*, 115(A7).
- Hui, Y., Schultz, D. R., Kharchenko, V. A., Stancil, P. C., Cravens, T. E., Lisse, C. M., & Dalgarno, A. (2009). The Ion-induced Charge-exchange X-ray Emission of the Jovian Auroras: Magnetospheric or Solar Wind Origin? *Astrophys. J.*, 702, L158–L162.
- Jackman, C., Knigge, C., Altamirano, D., Gladstone, R., Dunn, W., Elsner, R., Kraft, R., Branduardi-Raymont, G., & Ford, P. (2018). Assessing quasi-periodicities in Jovian X-ray

- emissions: Techniques and heritage survey. *Journal of Geophysical Research: Space Physics*, 123(11), 9204–9221.
- Jackman, C. H., Garvey, R. H., & Green, A. E. S. (1977). Electron impact on atmospheric gases, I. updated cross sections. *Journal of Geophysical Research (1896-1977)*, 82(32), 5081–5090.
- Jones, C. A. (2011). Planetary magnetic fields and fluid dynamos. *Annual Review of Fluid Mechanics*, 43(1), 583–614.
- Kameta, K., Kouchi, N., Ukai, M., & Hatano, Y. (2002). Photoabsorption, photoionization, and neutral-dissociation cross sections of simple hydrocarbons in the vacuum ultraviolet range. *Journal of Electron Spectroscopy and Related Phenomena*, 123(2), 225 – 238. Determination of cross-sections and momentum profiles of atoms, molecules and condensed matter.
- Karanikola, I., Athanasiou, M., Anagnostopoulos, G., Pavlos, G., & Preka-Papadema, P. (2004). Quasi-periodic emissions (15–80min) from the poles of Jupiter as a principal source of the large-scale high-latitude magnetopause boundary layer of energetic particle. *Planetary and Space Science*, 52(5), 543 – 559. Jupiter after Galileo and Cassini.
- Kharchenko, V., Bhardwaj, A., Dalgarno, A., Schultz, D. R., & Stancil, P. C. (2008). Modeling spectra of the north and south Jovian X-ray auroras. *J. Geophys. Res.*, 113, 8229–+.
- Kharchenko, V., Dalgarno, A., Schultz, D. R., & Stancil, P. C. (2006). Ion emission spectra in the Jovian X-ray aurora. *Geophys. Res. Lett.*, 33, 11105–+.
- Kharchenko, V., Liu, W., & Dalgarno, A. (1998). X ray and EUV emission spectra of oxygen ions precipitating into the Jovian atmosphere. *J. Geophys. Res.*, 103, 26687–26698.
- Khurana, K. K. & Kivelson, M. G. (1989). Ultralow frequency MHD waves in Jupiter’s middle magnetosphere. *Journal of Geophysical Research: Space Physics*, 94(A5), 5241–5254.
- Kim, T., Ebert, R., Valek, P., Allegrini, F., McComas, D., Bagenal, F., Chae, K., Livadiotis, G., Loeffler, C., Pollock, C., Ranquist, D., Thomsen, M., Wilson, R., Clark, G., Kollmann, P., Mauk,

- B., Bolton, S., & Levin, S. (2019). Properties of Jupiter's plasma sheet ions observed by Juno JADE including estimates of in-situ abundance for o^+ and s^{2+} . In preparation.
- Kim, Y. H. & Fox, J. L. (1994). The chemistry of hydrocarbon ions in the Jovian ionosphere. *Icarus*, 112, 310–325.
- Liu, W. & Schultz, D. R. (1999). Jovian X-Ray Aurora and Energetic Oxygen Ion Precipitation. *Astrophys. J.*, 526, 538–543.
- Liu, X., Shemansky, D. E., Abgrall, H., Roueff, E., Ahmed, S. M., & Ajello, J. M. (2003). Electron impact excitation of h_2 : resonance excitation of $\text{B}^1\Sigma_u^+(J_j=2, v_j=0)$ and effective excitation function of $\text{EF}^1\Sigma_g^+$. *Journal of Physics B: Atomic, Molecular and Optical Physics*, 36(2), 173–196.
- Liu, X., Shemansky, D. E., Ahmed, S. M., James, G. K., & Ajello, J. M. (1998). Electron-impact excitation and emission cross sections of the H_2 Lyman and Werner Systems. *Journal of Geophysical Research: Space Physics*, 103(A11), 26739–26758.
- MacDowall, R., Kaiser, M., Desch, M., Farrell, W., Hess, R., & Stone, R. (1993). Quasiperiodic Jovian radio bursts: observations from the Ulysses Radio and Plasma Wave Experiment. *Planetary and Space Science*, 41(11), 1059 – 1072. Special Issue: Ulysses Flyby of Jupiter.
- Manners, H., Masters, A., & Yates, J. N. (2018). Standing Alfvén waves in Jupiter's magnetosphere as a source of ~ 10 - to 60-min quasiperiodic pulsations. *Geophysical Research Letters*, 45(17), 8746–8754.
- Mauk, B. H., Haggerty, D. K., Jaskulek, S. E., Schlemm, C. E., Brown, L. E., Cooper, S. A., Gurnee, R. S., Hammock, C. M., Hayes, J. R., Ho, G. C., Hutcheson, J. C., Jacques, A. D., Kerem, S., Kim, C. K., Mitchell, D. G., Nelson, K. S., Paranicas, C. P., Paschalidis, N., Rossano, E., & Stokes, M. R. (2017a). The Jupiter Energetic Particle Detector Instrument (JEDI) investigation for the Juno mission. *Space Science Reviews*, 213(1), 289–346.

- Mauk, B. H., Haggerty, D. K., Paranicas, C., Clark, G., Kollmann, P., Rymer, A. M., Mitchell, D. G., Bolton, S. J., Levin, S. M., Adriani, A., Allegrini, F., Bagenal, F., Connerney, J. E. P., Gladstone, G. R., Kurth, W. S., McComas, D. J., Ranquist, D., Szalay, J. R., & Valek, P. (2017b). Juno observations of energetic charged particles over Jupiter's polar regions: Analysis of monodirectional and bidirectional electron beams. *Geophysical Research Letters*, 44(10), 4410–4418. 2016GL072286.
- Mauk, B. H., Mitchell, D. G., McEntire, R. W., Paranicas, C. P., Roelof, E. C., Williams, D. J., Krimigis, S. M., & Lagg, A. (2004). Energetic ion characteristics and neutral gas interactions in Jupiter's magnetosphere. *Journal of Geophysical Research: Space Physics*, 109(A9).
- Maurellis, A. N. & Cravens, T. E. (2001). Ionospheric effects of comet Shoemaker-Levy 9 impacts with Jupiter. *Icarus*, 154(2), 350 – 371.
- McComas, D. J., Alexander, N., Allegrini, F., Bagenal, F., Beebe, C., Clark, G., Crary, F., Desai, M. I., De Los Santos, A., Demkee, D., Dickinson, J., Everett, D., Finley, T., Gribanova, A., Hill, R., Johnson, J., Kofoed, C., Loeffler, C., Louarn, P., Maple, M., Mills, W., Pollock, C., Reno, M., Rodriguez, B., Rouzaud, J., Santos Costa, D., Valek, P., Weidner, S., Wilson, P., Wilson, R. J., & White, D. (2017). The Jovian Auroral Distributions Experiment (JADE) on the Juno mission to Jupiter. *Space Science Reviews*, 213(1), 547–643.
- McKibben, R., Simpson, J., & Zhang, M. (1993). Impulsive bursts of relativistic electrons discovered during Ulysses' traversal of Jupiter's usk-side magnetosphere. *Planetary and Space Science*, 41(11), 1041 – 1058. Special Issue: Ulysses Flyby of Jupiter.
- Metzger, A. E., Gilman, D. A., Luthey, J. L., Hurley, K. C., Schnopper, H. W., Seward, F. D., & Sullivan, J. D. (1983). The detection of X rays from Jupiter. *J. Geophys. Res.*, 88, 7731–7741.
- Miles, W. T., Thompson, R., & Green, A. E. S. (1972). Electron-impact cross sections and energy deposition in molecular hydrogen. *Journal of Applied Physics*, 43(2), 678–686.

- Moore, K. M., Bloxham, J., Connerney, J. E. P., Jorgensen, J. L., & Merayo, J. M. G. (2017). The analysis of initial Juno magnetometer data using a sparse magnetic field representation. *Geophysical Research Letters*, 44(10), 4687–4693. 2017GL073133.
- Moses, J. I., Fouchet, T., Bézard, B., Gladstone, G. R., Lellouch, E., & Feuchtgruber, H. (2005). Photochemistry and diffusion in Jupiter's stratosphere: Constraints from ISO observations and comparisons with other giant planets. *Journal of Geophysical Research: Planets*, 110(E8).
- Nagy, A. F. & Banks, P. M. (1970). Photoelectron fluxes in the ionosphere. *Journal of Geophysical Research*, 75(31), 6260–6270.
- Nicholson, D. R. (1983). *Introduction to Plasma Theory*. John Wiley & Sons, Inc.
- Olivero, J. J., Bass, J. N., & Green, A. E. S. (1973). Photoelectron excitation of the Jupiter dayglow. *Journal of Geophysical Research (1896-1977)*, 78(16), 2812–2826.
- Ozak, N., Cravens, T. E., Jones, G. H., Coates, A. J., & Robertson, I. P. (2012). Modeling of electron fluxes in the Enceladus plume. *Journal of Geophysical Research: Space Physics*, 117(A6).
- Ozak, N., Cravens, T. E., & Schultz, D. R. (2013). Auroral ion precipitation at Jupiter: Predictions for Juno. *Geophysical Research Letters*, 40(16), 4144–4148.
- Ozak, N., Schultz, D. R., Cravens, T. E., Kharchenko, V., & Hui, Y.-W. (2010). Auroral X-ray emission at Jupiter: Depth effects. *Journal of Geophysical Research: Space Physics*, 115(A11). A11306.
- Ozak Munoz, N. (2012). *Models of Jupiter's Polar Aurora*. PhD thesis, University of Kansas.
- Parkinson, C. D., Stewart, A. I. F., Wong, A. S., Yung, Y. L., & Ajello, J. M. (2006). Enhanced transport in the polar mesosphere of Jupiter: Evidence from Cassini UVIS helium 584 Å airglow. *Journal of Geophysical Research: Planets*, 111(E2).
- Perry, J. J., Kim, Y. H., Fox, J. L., & Porter, H. S. (1999). Chemistry of the Jovian auroral ionosphere. *J. of Geophys. Res.*, 1041, 16541–16566.

- Radioti, A., Krupp, N., Woch, J., Lagg, A., Glassmeier, K.-H., & Waldrop, L. S. (2005). Ion abundance ratios in the Jovian magnetosphere. *Journal of Geophysical Research: Space Physics*, 110(A7).
- Radioti, A., Krupp, N., Woch, J., Lagg, A., Glassmeier, K.-H., & Waldrop, L. S. (2006). Correction to “Ion abundance ratios in the Jovian magnetosphere”. *Journal of Geophysical Research: Space Physics*, 111(A10).
- Robertson, I., Cravens, T., Waite, J., Yelle, R., Vuitton, V., Coates, A., Wahlund, J., gren, K., Mandt, K., Magee, B., Richard, M., & Fattig, E. (2009). Structure of Titan’s ionosphere: Model comparisons with Cassini data. *Planetary and Space Science*, 57(14-15), 1834–1846.
- Sada, P., Bjoraker, G., Jennings, D., McCabe, G., & Romani, P. (1998). Observations of CH₄, C₂H₆, and C₂H₂ in the stratosphere of Jupiter. *Icarus*, 136(2), 192—201.
- Schultz, D., Gharibnejad, H., Cravens, T., & Houston, S. (2019). Data for secondary-electron production from ion precipitation at Jupiter II: Simultaneous and non-simultaneous target and projectile processes in collisions of O^{q+} + H₂ (q=0-8). *Atomic Data and Nuclear Data Tables*, 126, 1 – 69.
- Schultz, D., Ozak, N., Cravens, T., & Gharibnejad, H. (2017). Ionization of molecular hydrogen and stripping of oxygen atoms and ions in collisions of O^{q+} + H₂ (q=0-8): Data for secondary electron production from ion precipitation at Jupiter. *Atomic Data and Nuclear Data Tables*, 113, 1 – 116.
- Seiff, A., Kirk, D. B., Knight, T. C. D., Mihalov, J. D., Blanchard, R. C., Young, R. E., Schubert, G., von Zahn, U., Lehmacher, G., Milos, F. S., & Wang, J. (1996). Structure of the atmosphere of Jupiter: Galileo probe measurements. *Science*, 272(5263), 844–845.
- Seiff, A., Kirk, D. B., Knight, T. C. D., Young, L. A., Milos, F. S., Venkatapathy, E., Mihalov, J. D., Blanchard, R. C., Young, R. E., & Schubert, G. (1997). Thermal structure of Jupiter’s upper atmosphere derived from the Galileo probe. *Science*, 276(5309), 102–104.

- Shah, M. B., Elliott, D. S., & Gilbody, H. B. (1987). Pulsed crossed-beam study of the ionisation of atomic hydrogen by electron impact. *Journal of Physics B: Atomic and Molecular Physics*, 20(14), 3501–3514.
- Shemansky, D. E., Ajello, J. M., & Hall, D. T. (1985). Electron impact excitation of H₂ - Rydberg band systems and the benchmark dissociative cross section for H Lyman-alpha. *The Astrophysical Journal*, 296, 765–773.
- Sinclair, J., Orton, G., Greathouse, T., Fletcher, L., Moses, J., Hue, V., & Irwin, P. (2018). Jupiter's auroral-related stratospheric heating and chemistry II: Analysis of IRTF-TEXES spectra measured in December 2014. *Icarus*, 300, 305 – 326.
- Stallard, T., Miller, S., Millward, G., & Joseph, R. D. (2001). On the dynamics of the Jovian ionosphere and thermosphere: I. The measurement of ion winds. *Icarus*, 154(2), 475 – 491.
- Stone, P. M. & Kim, Y. K. (2002). Electron-impact cross-sections for dipole- and spin-allowed excitations of hydrogen, helium, and lithium. *Journal of Research of National Institute of Standards and Technology*, 107, 327–337.
- Straub, H. C., Renault, P., Lindsay, B. G., Smith, K. A., & Stebbings, R. F. (1996). Absolute partial cross sections for electron-impact ionization of h₂, n₂, and o₂ from threshold to 1000 ev. *Phys. Rev. A*, 54, 2146–2153.
- Vogt, M. F., Kivelson, M. G., Khurana, K. K., Walker, R. J., Bonfond, B., Grodent, D., & Radioti, A. (2011). Improved mapping of Jupiter's auroral features to magnetospheric sources. *Journal of Geophysical Research: Space Physics*, 116(A3).
- Waite, J. H., Bagenal, F., Seward, F., Na, C., Gladstone, G. R., Cravens, T. E., Hurley, K. C., Clarke, J. T., Elsner, R., & Stern, S. A. (1994). ROSAT observations of the Jupiter aurora. *Journal of Geophysical Research: Space Physics*, 99(A8), 14799–14809.

- Woodall, J., Agundez, M., Markwick-Kemper, A. J., & Millar, T. J. (2007). The UMIST Database for Astrochemistry 2006. *A&A*, (pp. 1197 – 1204).
- Yelle, R. V. & Miller, S. (2004). *Jupiter's Thermosphere and Ionosphere*, chapter 9. Planetary Science. Cambridge.
- Yoon, J.-S., Song, M.-Y., Han, J.-M., Hwang, S. H., Chang, W.-S., Lee, B., & Itikawa, Y. (2008). Cross sections for electron collisions with hydrogen molecules. *Journal of Physical and Chemical Reference Data*, 37(2), 913–931.
- Zhang, M., McKibben, R. B., Simpson, J. A., Cowley, S. W. H., Staines, K., Anglin, J. D., Marsden, R. G., Sanderson, T. R., & Wenzel, K.-P. (1995). Impulsive bursts of energetic particles in the high-latitude duskside magnetosphere of Jupiter. *Journal of Geophysical Research: Space Physics*, 100(A10), 19497–19512.
- Ziegler, J. F., Ziegler, M. D., & P., B. J. (2013). *Stopping and Range of Ions in Matter*. Version 2013.00.

Appendix A

Tables of Oxygen NSIM and SIM Cross-Sections and Average Energy Loss Values

Table A.1: The integral cross-section and associated average energy loss for single and double stripping for $O^{q+} + H_2$ ($q=0,1,\dots, 8$) collisions with impact energies between 1 and 25000 keV/u. (From Schultz et al. (2019))

Single Stripping								
E keV/u	O cross section cm ²	Eloss eV	O ⁺ cross section cm ²	Eloss eV	O ²⁺ cross section cm ²	Eloss eV	O ³⁺ cross section cm ²	Eloss eV
1	3.41E-17	21.1	1.91E-18	6.92	2.32E-19	68.4	1.43E-20	92.2
10	1.89E-16	24.0	3.39E-17	46.1	5.62E-18	67.2	7.98E-19	91.6
50	1.79E-16	44.9	7.82E-17	65.2	3.71E-17	82.3	1.29E-17	105.
75	1.64E-16	50.5	7.59E-17	75.0	4.10E-17	93.3	1.86E-17	114.
100	1.52E-16	53.8	7.09E-17	83.0	4.09E-17	102.	2.07E-17	123.
200	1.23E-16	58.8	5.64E-17	100.	3.30E-17	128.	1.85E-17	154.
500	8.48E-17	60.7	3.56E-17	116.	2.02E-17	159.	1.12E-17	199.
1000	5.99E-17	60.5	2.30E-17	126.	1.23E-17	177.	6.66E-18	231.
2000	3.99E-17	59.0	1.41E-17	131.	7.12E-18	189.	3.75E-18	259.
5000	2.14E-17	57.8	6.75E-18	138.	3.24E-18	209.	1.64E-18	286.
10000	1.27E-17	58.6	3.70E-18	143.	1.72E-18	216.	6.74E-19	321.
25000	5.94E-18	58.0	1.61E-18	145.	7.25E-19	245.	3.15E-19	346.
E keV/u	O ⁴⁺ cross section cm ²	Eloss eV	O ⁵⁺ cross section cm ²	Eloss eV	O ⁶⁺ cross section cm ²	Eloss eV	O ⁷⁺ cross section cm ²	Eloss eV
1	2.53E-22	133.	1.76E-24	149.	1.00E-30	829.	1.00E-30	971.
10	4.71E-20	131.	5.54E-21	160.	1.00E-25	839.	5.00E-26	991.
50	2.17E-18	145.	5.19E-19	172.	1.01E-22	858.	2.09E-23	1011.
75	4.35E-18	153.	1.17E-18	179.	5.03E-22	864.	9.54E-23	1019.
100	6.06E-18	159.	1.82E-18	185.	1.26E-21	897.	2.76E-22	1045.
200	7.54E-18	193.	2.87E-18	218.	9.59E-21	915.	2.06E-21	1080.
500	5.02E-18	257.	2.07E-18	293.	9.19E-20	955.	2.58E-20	1103.
1000	3.00E-18	303.	1.23E-18	354.	1.97E-19	1084.	6.83E-20	1227.
2000	1.69E-18	350.	6.65E-19	408.	1.87E-19	1339.	7.48E-20	1490.
5000	7.15E-19	399.	2.85E-19	470.	9.86E-20	1780.	4.09E-20	2018.
10000	3.68E-19	444.	1.45E-19	503.	5.28E-20	2135.	2.19E-20	2377.
25000	1.51E-19	531.	5.93E-20	552.	2.04E-20	2396.	9.00E-21	2698.
Double Stripping								
E keV/u	O cross section cm ²	Eloss eV	O ⁺ cross section cm ²	Eloss eV	O ²⁺ cross section cm ²	Eloss eV	O ³⁺ cross section cm ²	Eloss eV
1	1.23E-20	60.7	8.62E-23	107.	1.00E-24	142.	1.00E-24	201.
10	1.85E-18	75.3	8.37E-20	116.	5.08E-21	161.	1.00E-21	221.
50	5.62E-18	110.	1.56E-18	151.	3.76E-19	192.	5.36E-20	263.
75	6.36E-18	127.	1.95E-18	172.	6.39E-19	213.	1.58E-19	275.
100	6.19E-18	139.	2.12E-18	189.	8.52E-19	228.	2.95E-19	291.
200	5.09E-18	175.	1.80E-18	230.	8.93E-19	284.	4.42E-19	352.
500	2.72E-18	219.	8.97E-19	303.	4.52E-19	380.	2.59E-19	462.
1000	1.36E-18	241.	4.29E-19	335.	2.08E-19	421.	1.25E-19	549.
2000	6.36E-19	244.	1.57E-19	351.	7.92E-20	446.	4.55E-20	617.
5000	1.86E-19	234.	4.34E-20	334.	1.94E-20	452.	1.04E-20	696.
10000	6.91E-20	244.	1.43E-20	349.	6.28E-21	530.	3.28E-21	735.
25000	1.68E-20	243.	3.08E-21	384.	1.22E-21	551.	6.27E-22	864.
E keV/u	O ⁴⁺ cross section cm ²	Eloss eV	O ⁵⁺ cross section cm ²	Eloss eV	O ⁶⁺ cross section cm ²	Eloss eV		
1	1.00E-25	267.	1.00E-29	897.	1.00E-30	1691.		
10	1.00E-22	292.	1.00E-26	942.	1.00E-27	1811.		
50	6.31E-21	334.	2.00E-24	1027.	1.00E-25	2011.		
75	2.22E-20	342.	1.00E-23	1077.	5.00E-25	2061.		
100	4.79E-20	352.	3.30E-23	1111.	1.60E-24	2109.		
200	1.06E-19	413.	2.09E-22	1214.	3.70E-24	2160.		
500	6.75E-20	543.	2.55E-21	1264.	2.37E-22	2134.		
1000	2.92E-20	637.	5.01E-21	1506.	1.34E-21	2318.		
2000	1.07E-20	720.	5.71E-21	1883.	1.77E-21	2894.		
5000	2.29E-21	823.	1.81E-21	2440.	6.24E-22	3481.		
10000	6.99E-22	912.	6.18E-22	2838.	2.17E-22	3972.		
25000	1.34E-22	1280.	1.25E-22	3344.	4.22E-23	5389.		

Table A.2: The integral cross section and associated average energy loss for single and double projectile excitation for $O^{q+} + H_2$ ($q=0,1,\dots, 8$) collisions with impact energies between 1 and 25000 keV/u. (From Schultz et al. (2019))

Single Projectile Excitation								
E keV/u	O cross section cm ²	Eloss eV	O ⁺ cross section cm ²	Eloss eV	O ²⁺ cross section cm ²	Eloss eV	O ³⁺ cross section cm ²	Eloss eV
1	1.78E-17	12.3	2.34E-18	29.2	1.15E-18	41.0	3.47E-19	47.8
10	4.30E-17	12.5	2.73E-17	30.3	2.28E-17	42.5	1.13E-17	52.3
50	2.31E-17	12.5	1.89E-17	30.4	3.14E-17	44.1	2.65E-17	56.7
75	2.15E-17	12.5	1.66E-17	30.4	2.71E-17	43.9	2.43E-17	57.3
100	1.77E-17	12.5	1.53E-17	30.3	2.43E-17	43.8	2.17E-17	57.0
200	1.70E-17	12.5	1.25E-17	30.3	1.93E-17	43.6	1.67E-18	56.4
500	1.27E-17	12.4	8.65E-18	30.3	1.30E-17	43.4	1.08E-17	55.9
1000	9.58E-18	12.4	6.06E-18	30.2	8.91E-18	43.3	7.27E-18	55.6
2000	6.85E-18	12.4	3.97E-18	30.2	5.69E-18	43.2	4.51E-18	55.5
5000	3.94E-18	12.4	2.09E-18	30.1	2.88E-18	43.0	2.21E-18	55.1
10000	2.45E-18	12.4	1.20E-18	30.1	1.61E-18	43.0	1.24E-18	55.0
25000	1.24E-18	12.4	5.58E-19	30.1	7.25E-19	42.9	5.39E-19	54.9
E keV/u	O ⁴⁺ cross section cm ²	Eloss eV	O ⁵⁺ cross section cm ²	Eloss eV	O ⁶⁺ cross section cm ²	Eloss eV	O ⁷⁺ cross section cm ²	Eloss eV
1	3.30E-20	63.1	2.91E-20	63.3	1.00E-25	420.	4.68E-22	586.
10	2.38E-18	70.3	1.19E-18	71.1	8.68E-23	469.	3.20E-22	508.
50	1.10E-17	78.2	6.00E-18	82.8	4.63E-21	479.	1.95E-21	526.
75	1.28E-17	80.5	7.68E-18	86.2	1.56E-20	490.	5.74E-21	533.
100	1.25E-17	81.5	7.88E-18	88.5	3.09E-20	497.	1.17E-20	538.
200	9.25E-18	80.8	5.93E-18	88.5	1.09E-19	515.	4.43E-20	566.
500	5.85E-18	79.9	3.70E-18	86.5	3.48E-19	543.	1.66E-19	601.
1000	3.82E-18	79.2	2.39E-18	85.3	3.18E-19	550.	1.65E-19	620.
2000	2.33E-18	78.9	1.44E-18	84.9	2.20E-19	546.	1.15E-19	617.
5000	1.12E-18	78.3	6.79E-19	84.1	1.16E-19	544.	5.94E-20	608.
10000	6.15E-19	78.1	3.70E-19	83.3	6.54E-20	542.	3.26E-20	606.
25000	2.64E-19	77.9	1.61E-19	83.3	2.78E-20	540.	1.42E-20	603.
Double Projectile Excitation								
E keV/u	O cross section cm ²	Eloss eV	O ⁺ cross section cm ²	Eloss eV	O ²⁺ cross section cm ²	Eloss eV	O ³⁺ cross section cm ²	Eloss eV
1	5.80E-21	48.0	2.97E-19	41.0	1.83E-22	97.0	1.00E-22	120.
10	6.38E-20	54.9	1.41E-18	46.7	5.52E-20	108.	1.48E-20	147.
50	4.91E-20	61.7	1.00E-18	47.4	1.93E-19	111.	2.13E-19	162.
75	3.70E-20	64.2	8.57E-19	47.3	1.74E-19	111.	3.16E-19	164.
100	3.62E-20	64.9	7.53E-19	46.8	1.46E-19	111.	3.36E-19	168.
200	2.70E-20	63.2	6.31E-19	46.6	8.38E-20	110.	2.17E-19	170.
500	1.61E-20	65.9	4.11E-19	46.7	4.21E-20	110.	9.89E-20	169.
1000	1.06E-20	63.7	2.69E-19	46.1	2.38E-20	110.	5.36E-20	170.
2000	5.29E-21	58.5	1.55E-19	45.8	1.06E-20	110.	2.30E-20	169.
5000	1.99E-21	65.1	6.59E-20	45.7	3.49E-21	110.	6.92E-21	167.
10000	8.65E-22	66.1	3.26E-20	45.5	1.28E-21	109.	2.53E-21	169.
25000	2.61E-22	62.3	9.88E-21	44.8	2.91E-22	110.	5.40E-22	171.
E keV/u	O ⁴⁺ cross section cm ²	Eloss eV	O ⁵⁺ cross section cm ²	Eloss eV	O ⁶⁺ cross section cm ²	Eloss eV		
1	1.00E-23	140.	1.00E-30	550.	1.00E-33	800.		
10	3.62E-21	168.	1.00E-25	620.	1.00E-28	900.		
50	1.11E-19	181.	1.10E-22	661.	5.00E-25	1000.		
75	1.92E-19	184.	5.73E-22	662.	5.63E-24	1302.		
100	2.27E-19	186.	1.38E-21	655.	1.41E-23	1115.		
200	1.43E-19	188.	4.75E-21	685.	2.80E-22	1183.		
500	6.15E-20	186.	1.44E-20	758.	2.64E-21	1211.		
1000	1.29E-20	185.	1.05E-20	789.	3.33E-21	1230.		
2000	1.31E-20	184.	5.69E-21	794.	1.93E-21	1242.		
5000	3.89E-21	183.	1.90E-21	779.	6.58E-22	1214.		
10000	1.35E-21	183.	7.31E-22	790.	1.72E-22	1237.		

Table A.3: The integral cross section and associated average energy loss for NSIM and SIM processes in O + H₂ collisions with impact energies between 1 and 25000 keV/u. (From Schultz et al. (2019))

Channel	Energy 1 keV/u	Eloss eV	10	Eloss eV	50	Eloss eV	75	Eloss eV	100	Eloss eV	200	Eloss eV
	cross section cm ²		cross section cm ²		cross section cm ²		cross section cm ²		cross section cm ²		cross section cm ²	
SI	1.07E-17	30.4	9.94E-19	36.0	1.14E-17	60.3	9.67E-18	80.0	7.54E-18	97.8	6.09E-18	145.
SI+SS	6.16E-18	51.4	3.71E-17	60.0	8.44E-17	105.	8.44E-17	131.	8.52E-17	152.	7.12E-17	204.
SI+DS	1.35E-18	91.1	1.50E-17	95.1	4.16E-17	170.	4.22E-17	207.	4.30E-17	237.	3.80E-17	320.
SI+SPEX	6.38E-18	42.7	3.76E-17	48.5	8.50E-17	72.8	8.50E-17	92.5	8.52E-17	110.	7.12E-17	158.
SI+DPEX	2.69E-18	78.4	1.73E-17	90.9	3.26E-17	122.	3.57E-17	144.	2.91E-17	163.	3.06E-17	208.
SI SUM	2.73E-17		1.08E-16		2.55E-16		2.57E-16		2.50E-16		2.17E-16	
DI	1.00E-21	154.	7.14E-21	96.5	8.56E-20	151.	4.61E-20	201.	1.64E-20	246.	1.53E-20	362.
DI+SS	4.61E-19	175.	5.33E-18	121.	2.42E-17	196.	2.62E-17	252.	2.58E-17	300.	1.91E-17	303.
DI+DS	6.52E-20	215.	4.03E-18	156.	2.14E-17	261.	2.30E-17	328.	2.26E-17	385.	1.67E-17	537.
DI+SPEX	4.61E-19	166.	5.35E-18	109.	2.43E-17	164.	2.62E-17	214.	2.58E-17	259.	1.91E-17	375.
DI+DPEX	2.04E-19	202.	4.28E-18	151.	1.99E-17	213.	2.18E-17	265.	1.97E-17	311.	1.54E-17	425.
DI SUM	1.19E-18		1.90E-17		8.99E-17		9.72E-17		9.39E-17		7.03E-17	
TEX	2.41E-20	7.70	5.20E-19	7.70	7.01E-18	7.70	6.88E-18	7.70	6.03E-18	7.70	6.11E-18	7.70
TEX+SS	1.04E-17	34.7	4.16E-17	31.7	4.03E-17	52.6	3.76E-17	58.2	3.76E-17	61.5	3.39E-17	66.5
TEX+DS	4.13E-18	68.4	1.85E-17	66.8	1.76E-17	118.	1.62E-17	134.	1.62E-17	147.	1.46E-17	182.
TEX+SPEX	1.04E-17	20.0	4.19E-17	20.2	4.06E-17	20.2	3.79E-17	20.2	3.76E-17	20.2	3.39E-17	20.2
TEX+DPEX	6.91E-18	55.7	2.14E-17	62.6	1.35E-17	69.4	1.34E-17	71.9	1.06E-17	72.6	1.15E-17	70.9
TEX SUM	3.19E-17		1.24E-16		1.19E-16		1.12E-16		1.08E-16		1.00E-16	
Channel	Energy 500 keV/u	Eloss eV	1000	Eloss eV	2000	Eloss eV	5000	Eloss eV	10000	Eloss eV	25000	Eloss eV
	cross section cm ²		cross section cm ²		cross section cm ²		cross section cm ²		cross section cm ²		cross section cm ²	
SI	2.93E-18	189.	1.64E-18	203.	5.32E-19	205.	3.27E-19	192.	2.02E-19	182.	6.55E-20	168.
SI+SS	5.28E-17	250.	4.09E-17	264.	3.14E-17	264.	2.07E-17	250.	1.43E-17	241.	8.51E-18	226.
SI+DS	3.06E-17	408.	2.51E-17	444.	1.78E-17	449.	1.32E-17	426.	9.15E-18	416.	4.36E-18	411.
SI+SPEX	5.29E-17	201.	4.09E-17	215.	3.13E-17	217.	2.07E-17	204.	1.43E-17	194.	8.50E-18	180.
SI+DPEX	2.77E-17	255.	2.15E-17	267.	1.65E-17	264.	8.22E-18	257.	5.76E-18	248.	3.76E-18	230.
SI SUM	1.67E-16		1.30E-16		9.75E-17		6.31E-17		4.37E-17		2.52E-17	
DI	1.41E-21	466.	7.02E-22	485.	3.00E-22	467.	1.05E-22	420.	4.70E-23	397.	1.70E-23	336.
DI+SS	1.03E-17	527.	6.01E-18	546.	3.35E-18	526.	1.41E-18	478.	6.72E-19	456.	2.38E-19	394.
DI+DS	9.05E-18	685.	5.33E-18	726.	2.81E-18	711.	1.24E-18	654.	5.84E-19	631.	1.62E-19	579.
DI+SPEX	1.03E-17	478.	6.01E-18	497.	3.35E-18	479.	1.41E-18	432.	6.72E-19	409.	2.38E-19	348.
DI+DPEX	8.68E-18	532.	4.96E-18	549.	2.70E-18	526.	9.22E-19	485.	4.31E-19	463.	1.62E-19	398.
DI SUM	3.83E-17		2.23E-17		1.22E-17		4.98E-18		2.36E-18		8.00E-19	
TEX	2.54E-18	7.70	9.90E-19	7.70	1.22E-19	7.70	2.34E-20	7.70	9.66E-21	7.70	9.00E-22	7.70
TEX+SS	2.75E-17	68.4	2.27E-17	68.2	1.85E-17	66.7	1.33E-17	65.5	9.68E-18	66.3	6.27E-18	65.7
TEX+DS	1.25E-17	226.	1.11E-17	248.	8.43E-18	251.	7.48E-18	242.	5.84E-18	242.	3.17E-18	251.
TEX+SPEX	2.77E-17	20.1	2.27E-17	20.1	1.84E-17	20.1	1.33E-17	20.1	9.68E-18	20.1	6.27E-18	20.1
TEX+DPEX	1.11E-17	73.6	9.29E-18	71.4	7.77E-18	66.2	4.45E-18	72.8	3.50E-18	73.8	2.69E-18	70.0
TEX SUM	8.13E-17		6.68E-17		5.32E-17		3.86E-17		2.87E-17		1.84E-17	

Table A.4: The integral cross section and associated average energy loss for NSIM and SIM processes in $O^+ + H_2$ collisions with impact energies between 1 and 25000 keV/u. (From Schultz et al. (2019))

Channel	Energy 1 keV/u	10		50		75		100		200		
		cross section cm ²	Eloss eV									
SI	5.40E-21	21.6	1.94E-18	24.4	8.14E-17	49.0	1.00E-16	65.4	1.01E-16	80.7	7.43E-17	122.
SI+SS	1.59E-19	42.6	9.97E-18	48.4	6.43E-17	93.9	6.44E-17	116.	6.34E-17	135.	5.62E-17	181.
SI+DS	1.08E-20	82.3	4.52E-18	83.5	1.88E-17	159.	2.34E-17	192.	2.63E-17	220.	2.72E-17	297.
SI+SPEX	1.59E-19	50.8	1.05E-17	54.7	6.73E-17	79.4	6.89E-17	95.8	6.34E-17	111.	5.66E-17	152.
SI+DPEX	1.51E-19	62.6	9.20E-18	71.1	3.82E-17	96.4	4.50E-17	113.	4.37E-17	128.	4.17E-17	169.
SI SUM	4.85E-19		3.61E-17		2.70E-16		3.02E-16		2.98E-16		2.56E-16	
DI	5.00E-24	42.5	1.00E-20	55.5	2.33E-18	130.	4.23E-18	178.	4.91E-18	219.	3.38E-18	326.
DI+SS	3.67E-22	89.4	8.10E-19	102.	2.22E-17	195.	2.82E-17	253.	2.87E-17	302.	2.26E-17	426.
DI+DS	1.00E-23	150.	5.93E-19	157.	1.45E-17	282.	2.01E-17	350.	2.16E-17	406.	1.77E-17	556.
DI+SPEX	3.67E-22	71.7	8.12E-19	85.8	2.24E-17	160.	2.86E-17	208.	2.88E-17	249.	2.27E-17	356.
DI+DPEX	3.67E-22	83.5	8.05E-19	102.	1.94E-17	177.	2.57E-17	225.	2.60E-17	266.	2.08E-17	373.
DI SUM	1.12E-21		3.03E-18		8.08E-17		1.07E-16		1.10E-16		8.72E-17	
TI	7.53E-21	14.8	4.15E-19	22.8	3.77E-18	82.0	2.07E-18	122.	1.07E-18	160.	5.55E-20	277.
TI+SS	2.11E-19	61.7	9.16E-18	68.9	2.39E-17	147.	1.55E-17	197.	9.91E-18	243.	2.35E-18	377.
TI+DS	1.65E-20	122.	4.73E-18	124.	1.46E-17	234.	1.14E-17	294.	7.97E-18	347.	2.10E-18	507.
TI+SPEX	2.13E-19	44.0	9.40E-18	53.1	2.42E-17	112.	1.57E-17	152.	9.93E-18	190.	2.35E-18	307.
TI+DPEX	2.05E-19	56.0	8.70E-18	69.5	2.03E-17	129.	1.43E-17	169.	9.23E-18	207.	2.29E-18	324.
TI SUM	6.53E-19		3.24E-17		8.68E-17		5.90E-17		3.81E-17		9.15E-18	
SC	4.86E-16	-7.47	2.81E-16	-2.57	4.81E-17	19.2	1.53E-17	32.8	6.09E-18	46.4	1.68E-19	101.
SC+SS	3.78E-17	39.4	8.28E-17	43.5	3.23E-17	84.4	1.48E-17	108.	8.38E-18	129.	1.83E-18	201.
SC+DS	6.87E-19	99.8	1.50E-17	98.5	7.78E-18	171.	5.56E-18	205.	3.96E-18	233.	1.28E-18	331.
SC+SPEX	4.46E-17	21.7	1.12E-16	27.7	3.41E-17	49.6	1.57E-17	63.2	8.47E-18	76.7	1.83E-18	131.
SC+DPEX	2.58E-17	33.5	6.10E-17	44.1	1.77E-17	66.6	1.05E-17	80.1	6.20E-18	93.2	1.64E-18	148.
SC SUM	5.95E-16		5.52E-16		1.40E-16		6.19E-17		3.31E-17		6.75E-18	
TEX	4.02E-19	7.70	1.10E-17	7.70	5.83E-17	7.70	6.86E-17	7.70	7.84E-17	7.70	7.28E-17	7.70
TEX+SS	4.77E-18	54.6	3.37E-17	53.8	3.01E-17	72.9	2.65E-17	82.7	2.62E-17	91.0	2.57E-17	108.
TEX+DS	5.22E-19	115.	1.18E-17	109.	6.77E-18	159.	7.92E-18	179.	9.28E-18	195.	1.09E-17	238.
TEX+SPEX	4.86E-18	36.9	3.66E-17	38.0	3.21E-17	38.1	2.89E-17	38.1	2.66E-17	38.0	2.59E-17	38.0
TEX+DPEX	4.45E-18	48.7	2.99E-17	54.4	1.57E-17	55.1	1.70E-17	55.0	1.65E-17	54.5	1.77E-17	54.3
TEX SUM	1.50E-17		1.23E-16		1.43E-16		1.49E-16		1.57E-16		1.53E-16	

Channel	Energy 500 keV/u		1000		2000		5000		10000		25000	
	cross section cm ²	Eloss eV										
SI	4.24E-17	165.	2.60E-17	184.	1.51E-17	190.	8.99E-18	184.	4.32E-18	176.	1.79E-18	163.
SI+SS	4.48E-17	226.	3.66E-17	245.	2.76E-17	249.	1.84E-17	322.	1.26E-17	319.	7.73E-18	308.
SI+DS	2.25E-17	384.	1.86E-17	425.	1.56E-17	434.	9.00E-18	518.	6.64E-18	525.	3.01E-18	547.
SI+SPEX	4.53E-17	195.	3.62E-17	215.	2.80E-17	220.	1.83E-17	214.	1.25E-17	206.	7.67E-18	193.
SI+DPEX	3.29E-17	212.	2.57E-17	230.	1.86E-17	236.	1.28E-17	230.	9.52E-18	222.	5.70E-18	208.
SI SUM	1.88E-16		1.43E-16		1.05E-16		6.66E-17		4.56E-17		2.59E-17	
DI	1.34E-18	427.	5.61E-19	452.	2.28E-19	441.	6.78E-20	405.	1.67E-20	367.	1.11E-22	331.
DI+SS	1.24E-17	543.	7.08E-18	578.	3.75E-18	572.	1.52E-18	543.	6.98E-19	510.	2.43E-19	476.
DI+DS	9.49E-18	730.	5.32E-18	787.	2.94E-18	791.	1.06E-18	739.	5.13E-19	716.	1.42E-19	715.
DI+SPEX	1.24E-17	457.	7.06E-18	482.	3.76E-18	471.	1.52E-18	435.	6.97E-19	397.	2.43E-19	361.
DI+DPEX	1.13E-17	474.	6.28E-18	498.	3.23E-18	487.	1.33E-18	451.	6.34E-19	413.	2.20E-19	376.
DI SUM	4.69E-17		2.63E-17		1.39E-17		5.50E-18		2.56E-18		8.48E-19	
TI	1.76E-21	511.	6.34E-23	794.	1.00E-24	1341.	5.00E-27	2933.	9.00E-29	5479.	4.00E-31	13624.
TI+SS	1.65E-19	627.	1.49E-20	920.	1.07E-21	1472.	1.90E-23	3071.	1.10E-24	5622.	2.50E-26	13769.
TI+DS	1.59E-19	814.	1.47E-20	1129.	1.07E-21	1692.	1.90E-23	3267.	1.10E-24	5828.	2.50E-26	14008.
TI+SPEX	1.65E-19	541.	1.49E-20	824.	1.07E-21	1371.	1.90E-23	2963.	1.10E-24	5509.	2.50E-26	13654.
TI+DPEX	1.64E-19	558.	1.48E-20	840.	1.07E-21	1387.	1.90E-23	2979.	1.10E-24	5525.	2.50E-26	13669.
TI SUM	6.55E-19		5.94E-20		4.28E-21		7.60E-23		4.40E-24		1.00E-25	
SC	1.00E-21	264.	1.00E-23	537.	1.00E-25	1081.	2.00E-28	2715.	2.00E-30	5438.	4.00E-33	13607.
SC+SS	1.52E-19	380.	1.86E-20	663.	1.96E-21	1212.	7.20E-23	2853.	2.95E-24	5581.	8.60E-26	13752.
SC+DS	1.38E-19	567.	1.83E-20	872.	1.96E-21	1432.	7.20E-23	3049.	2.95E-24	5787.	8.60E-26	13991.
SC+SPEX	1.52E-19	294.	1.86E-20	567.	1.96E-21	1111.	7.20E-23	2745.	2.95E-24	5468.	8.60E-26	13637.
SC+DPEX	1.50E-19	311.	1.86E-20	583.	1.96E-21	1127.	7.20E-23	2761.	2.95E-24	5484.	8.60E-26	13652.
SC SUM	5.93E-19		7.41E-20		7.84E-21		2.88E-22		1.18E-23		3.44E-25	
TEX	5.12E-17	7.70	3.12E-17	7.70	1.75E-17	7.70	8.13E-18	7.70	3.28E-18	7.70	3.01E-19	7.70
TEX+SS	2.19E-17	124.	1.94E-17	133.	1.54E-17	139.	1.11E-17	146.	9.20E-18	151.	6.53E-18	153.
TEX+DS	9.20E-18	311.	8.33E-18	343.	7.47E-18	359.	5.34E-18	342.	4.31E-18	357.	2.16E-18	392.
TEX+SPEX	2.23E-17	38.0	1.91E-17	37.9	1.58E-17	37.9	1.26E-17	37.8	9.11E-18	37.8	6.30E-18	37.8
TEX+DPEX	1.44E-17	54.4	1.20E-17	53.8	1.04E-17	53.5	7.94E-18	53.4	6.50E-18	53.2	4.61E-18	52.5
TEX SUM	1.19E-16		9.00E-17		6.66E-17		4.51E-17		3.24E-17		1.99E-17	

Table A.5: The integral cross section and associated average energy loss for NSIM and SIM processes in $O^{2+} + H_2$ collisions with impact energies between 1 and 25000 keV/u. (From Schultz et al. (2019))

Channel	Energy 1 keV/u		10		50		75		100		200	
	cross section cm ²	Eloss eV										
SI	1.05E-20	22.7	2.00E-18	23.4	2.57E-16	32.6	3.50E-16	41.0	3.62E-16	48.7	2.73E-16	69.2
SI+SS	4.08E-20	91.1	3.97E-18	90.6	4.97E-17	115.	6.24E-17	134.	7.57E-17	151.	7.00E-17	197.
SI+DS	2.40E-21	165.	4.98E-19	168.	1.60E-17	225.	1.77E-17	254.	2.61E-17	277.	3.24E-17	354.
SI+SPEX	4.30E-20	63.7	5.09E-18	65.9	5.79E-17	76.7	6.98E-17	84.9	8.83E-17	92.5	8.22E-17	113.
SI+DPEX	5.37E-21	120.	1.94E-18	131.	1.75E-17	144.	2.60E-17	152.	2.55E-17	160.	3.61E-17	179.
SI SUM	1.02E-19		1.35E-17		3.98E-16		5.26E-16		5.78E-16		4.94E-16	
DI	1.00E-24	33.7	2.44E-21	54.8	8.91E-18	116.	1.96E-17	157.	2.14E-17	190.	1.71E-17	276.
DI+SS	3.12E-24	102.	1.45E-19	122.	1.47E-17	198.	2.55E-17	250.	3.23E-17	292.	3.00E-17	404.
DI+DS	6.92E-25	176.	2.98E-20	199.	8.89E-18	308.	1.47E-17	370.	2.07E-17	418.	2.15E-17	560.
DI+SPEX	3.12E-24	74.7	1.51E-19	97.3	1.54E-17	160.	2.64E-17	201.	3.41E-17	234.	3.17E-17	320.
DI+DPEX	2.08E-24	131.	1.08E-19	163.	9.32E-18	227.	1.78E-17	268.	2.05E-17	301.	2.27E-17	386.
DI SUM	1.00E-23		4.36E-19		5.72E-17		1.04E-16		1.29E-16		1.23E-16	
TI	1.36E-20	0.85	9.50E-19	15.4	3.10E-17	80.5	2.24E-17	118.	1.01E-17	132.	7.19E-19	242.
TI+SS	8.73E-20	69.3	6.03E-18	82.6	3.66E-17	163.	3.04E-17	211.	2.19E-17	234.	4.67E-18	370.
TI+DS	1.03E-20	143.	9.26E-19	160.	2.02E-17	273.	1.77E-17	331.	1.48E-17	360.	3.79E-18	526.
TI+SPEX	9.62E-20	41.9	7.18E-18	57.9	3.90E-17	125.	3.12E-17	162.	2.28E-17	176.	4.79E-18	286.
TI+DPEX	1.27E-20	97.9	3.32E-18	123.	2.13E-17	192.	2.13E-17	229.	1.47E-17	243.	3.93E-18	352.
TI SUM	2.20E-19		1.84E-17		1.48E-16		1.23E-16		8.43E-17		1.79E-17	
DCAI	1.39E-19	19.4	1.58E-18	41.9	7.10E-18	93.1	1.80E-18	118.	3.71E-19	140.	2.05E-21	222.
DCAI+SS	6.85E-19	87.8	4.42E-18	109.	4.44E-18	175.	1.84E-18	211.	6.84E-19	242.	2.07E-20	350.
DCAI+DS	8.19E-20	162.	8.02E-19	187.	2.14E-18	285.	9.48E-19	331.	4.46E-19	368.	1.71E-20	506.
DCAI+SPEX	7.54E-19	60.4	5.40E-18	84.4	4.83E-18	137.	1.93E-18	162.	7.20E-19	184.	2.13E-20	266.
DCAI+DPEX	9.09E-20	116.	2.60E-18	150.	2.29E-18	204.	1.18E-18	229.	4.41E-19	251.	1.77E-20	332.
DCAI SUM	1.75E-18		1.48E-17		2.08E-17		7.70E-18		2.66E-18		7.89E-20	
SC	7.48E-16	-21.1	6.18E-16	-16.2	2.40E-16	26.2	9.28E-17	39.8	3.50E-17	53.4	1.64E-18	87.3
SC+SS	1.72E-17	47.3	6.63E-17	51.0	3.75E-17	109.	2.34E-17	133.	1.49E-17	156.	2.93E-18	215.
SC+DS	1.78E-18	121.	4.39E-18	128.	9.60E-18	218.	6.19E-18	253.	5.39E-18	281.	1.69E-18	372.
SC+SPEX	2.54E-17	19.9	1.40E-16	26.3	4.50E-17	70.3	2.62E-17	83.7	1.71E-17	97.2	3.20E-18	131.
SC+DPEX	8.73E-19	75.9	2.14E-17	91.8	1.07E-17	137.	9.36E-18	151.	5.29E-18	164.	1.84E-18	197.
SC SUM	7.93E-16		8.50E-16		3.43E-16		1.58E-16		7.77E-17		1.13E-17	
DC	4.86E-16	-20.4	4.56E-17	-10.6	8.23E-18	62.6	1.80E-18	89.8	4.86E-19	117.	2.70E-21	196.
DC+SS	4.08E-17	48.0	2.03E-17	56.6	9.64E-18	145.	4.28E-18	183.	2.46E-18	219.	1.23E-19	324.
DC+DS	3.37E-18	122.	1.71E-18	134.	4.96E-18	255.	2.60E-18	303.	1.83E-18	345.	1.10E-19	480.
DC+SPEX	6.11E-17	20.6	3.71E-17	31.9	1.03E-17	107.	4.41E-18	134.	2.53E-18	161.	1.24E-19	240.
DC+DPEX	2.33E-18	76.6	7.30E-18	97.4	5.24E-18	174.	3.11E-18	201.	1.81E-18	228.	1.13E-19	306.
DC SUM	5.94E-16		1.12E-16		3.84E-17		1.62E-17		9.12E-18		4.73E-19	
TEX	4.88E-19	7.70	1.47E-17	7.70	1.26E-16	7.70	1.55E-16	7.70	1.87E-16	7.70	2.03E-16	7.70
TEX+SS	1.97E-18	76.1	2.63E-17	74.9	1.53E-17	90.0	1.74E-17	101.	2.08E-17	110.	2.27E-17	136.
TEX+DS	1.20E-19	150.	2.41E-18	152.	3.86E-18	200.	3.76E-18	221.	5.73E-18	236.	9.23E-18	292.
TEX+SPEX	2.18E-18	48.7	3.73E-17	50.2	1.83E-17	51.8	2.01E-17	51.6	2.52E-17	51.5	2.76E-17	51.3
TEX+DPEX	3.24E-19	105.	1.00E-17	116.	4.25E-18	119.	6.26E-18	119.	5.55E-18	119.	1.03E-17	118.
TEX SUM	5.08E-18		9.07E-17		1.68E-16		2.03E-16		2.44E-16		2.73E-16	

Channel	Energy 500 keV/u		1000		2000		5000		10000		25000	
	cross section cm ²	Eloss eV										
SI	1.02E-16	131.	5.74E-17	154.	3.22E-17	167.	1.55E-17	170.	8.03E-18	168.	3.44E-18	157.
SI+SS	4.12E-17	290.	3.60E-17	331.	2.76E-17	356.	1.88E-17	379.	1.49E-17	384.	9.34E-18	402.
SI+DS	2.10E-17	511.	1.72E-17	575.	1.50E-17	613.	1.01E-17	622.	4.96E-18	698.	2.35E-18	708.
SI+SPEX	4.54E-17	174.	3.65E-17	197.	2.79E-17	210.	1.88E-17	213.	1.49E-17	211.	9.42E-18	200.
SI+DPEX	2.47E-17	241.	2.09E-17	264.	1.62E-17	277.	8.98E-18	280.	5.45E-18	277.	2.35E-18	267.
SI SUM	2.34E-16		1.68E-16		1.19E-16		7.22E-17		4.82E-17		2.69E-17	
DI	6.98E-18	370.	2.73E-18	401.	1.02E-18	402.	2.70E-19	374.	7.33E-20	355.	1.15E-20	322.
DI+SS	1.59E-17	529.	8.78E-18	578.	4.59E-18	591.	1.82E-18	583.	9.25E-19	571.	3.25E-19	567.
DI+DS	1.15E-17	750.	6.81E-18	822.	3.36E-18	848.	1.30E-18	826.	4.54E-19	885.	1.26E-19	873.
DI+SPEX	1.65E-17	413.	8.83E-18	444.	4.60E-18	445.	1.82E-18	417.	9.25E-19	398.	3.26E-19	365.
DI+DPEX	1.26E-17	480.	6.76E-18	511.	3.53E-18	512.	1.18E-18	484.	4.93E-19	464.	1.26E-19	432.
DI SUM	6.35E-17		3.39E-17		1.17E-17		6.39E-18		2.87E-18		9.15E-19	
TI	1.01E-20	472.	6.50E-22	762.	2.00E-23	1309.	1.50E-25	2803.	4.00E-27	5511.	3.00E-29	13664.
TI+SS	2.54E-19	631.	1.91E-20	939.	1.22E-21	1498.	2.42E-23	3012.	1.54E-24	5727.	3.00E-26	13909.
TI+DS	2.32E-19	852.	1.83E-20	1183.	1.20E-21	1755.	2.42E-23	3355.	1.54E-24	6041.	3.00E-26	14215.
TI+SPEX	2.54E-19	515.	1.91E-20	805.	1.22E-21	1352.	2.42E-23	2846.	1.54E-24	5554.	3.00E-26	13707.
TI+DPEX	2.40E-19	582.	1.88E-20	872.	1.21E-21	1419.	2.42E-23	2913.	1.54E-24	5620.	3.00E-26	13774.
TI SUM	9.90E-19		7.60E-20		4.87E-21		9.70E-23		6.16E-24		1.20E-25	
DCAI	1.00E-24	438.	1.00E-27	650.	1.00E-30	1000.	1.50E-34	1700.	2.00E-37	2600.	3.00E-41	4500.
DCAI+SS	4.43E-23	597.	2.50E-25	827.	1.25E-27	1189.	1.00E-30	1991.	5.00E-33	2816.	3.75E-36	4745.
DCAI+DS	4.43E-23	818.	2.50E-25	1071.	1.25E-27	1446.	1.00E-30	2152.	5.00E-33	3130.	3.75E-36	5051.
DCAI+SPEX	4.43E-23	481.	2.50E-25	693.	1.25E-27	1043.	1.00E-30	1743.	5.00E-33	2643.	3.75E-36	4543.
DCAI+DPEX	4.43E-23	548.	2.50E-25	760.	1.25E-27	1110.	1.00E-30	1810.	5.00E-33	2709.	3.75E-36	4610.
DCAI SUM	1.78E-22		1.00E-24		5.00E-27		4.00E-30		2.00E-32		1.50E-35	
SC	1.56E-21	251.	5.00E-24	523.	5.00E-27	1068.	2.00E-30	2701.	7.00E-33	5425.	2.00E-36	13594.
SC+SS	1.94E-19	410.	2.07E-20	700.	2.20E-21	1257.	6.28E-23	2910.	2.63E-24	5641.	1.00E-25	13839.
SC+DS	1.59E-19	631.	1.95E-20	944.	2.20E-21	1514.	6.28E-23	3153.	2.63E-24	5955.	1.00E-25	14145.
SC+SPEX	1.95E-19	294.	2.07E-20	566.	2.20E-21	1111.	6.28E-23	2744.	2.63E-24	5468.	1.00E-25	13637.
SC+DPEX	1.71E-19	361.	2.03E-20	633.	2.20E-21	1178.	6.28E-23	2811.	2.63E-24	5534.	1.00E-25	13704.
SC SUM	7.21E-19		8.12E-20		8.80E-21		2.51E-22		1.05E-23		4.00E-25	
DC	2.00E-24	523.	1.00E-26	1068.	1.00E-29	2157.	2.00E-33	5425.	3.00E-36	10871.	7.00E-40	27209.
DC+SS	1.04E-21	682.	1.33E-23	1245.	2.50E-27	2346.	5.00E-32	5634.	1.25E-35	11087.	2.50E-40	27454.
DC+DS	1.01E-21	903.	1.31E-23	1489.	2.50E-27	2603.	5.00E-32	5877.	1.25E-35	11401.	2.50E-40	27760.
DC+SPEX	1.04E-21	566.	1.33E-23	1111.	2.50E-27	2200.	5.00E-32	5468.	1.25E-35	10914.	2.50E-40	27252.
DC+DPEX	1.03E-21	633.	1.33E-23	1178.	2.50E-27	2267.	5.00E-32	5535.	1.25E-35	10980.	2.50E-40	27319.
DC SUM	4.12E-21		5.30E-23		1.00E-26		2.02E-31		5.30E-35		1.70E-39	
TEX	1.53E-16	7.70	9.17E-17	7.70	4.93E-17	7.70	1.93E-17	7.70	9.00E-18	7.70	2.49E-18	7.70
TEX+SS	2.01E-17	167.	1.97E-17	185.	1.63E-17	197.	1.35E-17	217.	1.15E-17	224.	8.27E-18	253.
TEX+DS	9.18E-18	388.	8.27E-18	429.	7.92E-18	454.	6.38E-18	460.	3.25E-18	538.	1.74E-18	559.
TEX+SPEX	2.27E-17	51.1	2.02E-17	51.0	1.64E-17	50.9	1.41E-17	50.7	1.15E-17	50.7	8.27E-18	50.6
TEX+DPEX	1.10E-17	118.	1.02E-17	118.	8.61E-18	118.	5.61E-18	118.	3.60E-18	117.	1.74E-18	118.
TEX SUM	2.16E-16		1.50E-16		9.85E-17		5.89E-17		3.89E-17		2.25E-17	

Table A.6: The integral cross section and associated average energy loss for NSIM and SIM processes in $O^{3+} + H_2$ collisions with impact energies between 1 and 25000 keV/u. (From Schultz et al. (2019))

Channel	Energy 1 keV/u	10		50		75		100		200		
		cross section cm ²	Eloss eV									
SI	4.67E-20	20.0	1.76E-18	22.8	4.26E-16	24.5	6.58E-16	32.1	7.88E-16	36.7	6.45E-16	47.7
SI+SS	2.08E-20	112.	1.56E-18	114.	3.80E-17	129.	4.90E-17	146.	6.17E-17	160.	7.05E-17	202.
SI+DS	8.34E-22	221.	1.00E-19	244.	9.39E-18	287.	9.51E-18	308.	1.16E-17	328.	1.91E-17	400.
SI+SPEX	2.08E-20	67.8	2.40E-18	75.1	4.43E-17	81.2	5.02E-17	89.4	7.05E-17	93.7	7.98E-17	104.
SI+DPEX	4.17E-21	140.	3.98E-19	170.	1.47E-17	187.	1.59E-17	196.	2.13E-17	205.	2.77E-17	218.
SI SUM	9.33E-20		6.22E-18		5.32E-16		7.83E-16		9.53E-16		8.42E-16	
DI	1.00E-24	33.7	1.00E-21	56.4	7.74E-18	105.	3.52E-17	138.	5.81E-17	162.	5.95E-17	228.
DI+SS	3.68E-24	126.	4.10E-20	148.	6.63E-18	210.	1.81E-17	252.	2.91E-17	285.	3.91E-17	382.
DI+DS	8.18E-25	235.	1.36E-20	278.	3.04E-18	368.	7.23E-18	413.	1.13E-17	453.	1.97E-17	580.
DI+SPEX	3.68E-24	81.5	4.52E-20	109.	7.04E-18	162.	1.83E-17	195.	3.09E-17	219.	4.13E-17	284.
DI+DPEX	8.18E-25	154.	1.02E-20	203.	4.06E-18	267.	1.00E-17	302.	1.66E-17	330.	2.44E-17	398.
DI SUM	1.00E-23		1.11E-19		2.85E-17		8.88E-17		1.46E-16		1.84E-16	
TI	1.73E-20	11.7	1.81E-18	21.6	6.64E-17	87.1	8.01E-17	101.	5.16E-17	132.	4.94E-18	235.
TI+SS	3.00E-20	104.	3.56E-18	113.	3.82E-17	192.	4.33E-17	215.	3.60E-17	255.	8.84E-18	389.
TI+DS	5.62E-21	213.	1.15E-18	243.	1.44E-17	350.	1.60E-17	376.	1.45E-17	423.	5.29E-18	587.
TI+SPEX	3.00E-20	59.5	4.93E-18	73.9	4.16E-17	144.	4.38E-17	158.	3.80E-17	189.	9.15E-18	291.
TI+DPEX	3.74E-21	132.	1.04E-18	169.	2.04E-17	249.	2.28E-17	265.	2.10E-17	300.	6.27E-18	405.
TI SUM	8.67E-20		1.25E-17		1.81E-16		2.06E-16		1.61E-16		3.45E-17	
DCAI	1.72E-16	7.71	1.45E-16	32.9	9.16E-17	99.9	3.15E-17	128.	7.87E-18	152.	7.14E-20	235.
DCAI+SS	7.72E-18	99.9	2.90E-17	125.	3.08E-17	205.	1.40E-17	242.	5.71E-18	275.	2.00E-19	389.
DCAI+DS	4.53E-18	209.	1.22E-17	254.	9.26E-18	363.	4.43E-18	403.	2.16E-18	443.	1.22E-19	587.
DCAI+SPEX	1.19E-17	55.5	4.87E-17	85.0	3.46E-17	157.	1.42E-17	185.	6.09E-18	209.	2.05E-19	291.
DCAI+DPEX	1.81E-18	128.	7.00E-18	180.	1.38E-17	262.	6.54E-18	292.	3.17E-18	320.	1.43E-19	405.
DCAI SUM	1.98E-16		2.42E-16		1.80E-16		7.07E-17		2.50E-17		7.41E-19	
SC	1.36E-15	-7.92	1.04E-15	-3.02	5.51E-16	18.8	2.74E-16	32.4	1.16E-16	46.0	6.91E-18	101.
SC+SS	8.71E-18	84.3	3.51E-17	88.6	3.69E-17	124.	2.59E-17	147.	1.74E-17	169.	3.85E-18	255.
SC+DS	3.58E-18	193.	7.74E-18	218.	4.87E-18	281.	3.02E-18	308.	2.43E-18	337.	1.26E-18	453.
SC+SPEX	1.54E-17	39.9	9.11E-17	49.3	4.62E-17	75.5	2.67E-17	89.7	2.00E-17	103.	4.22E-18	157.
SC+DPEX	2.15E-18	112.	5.04E-18	144.	9.18E-18	181.	6.05E-18	196.	5.14E-18	214.	1.76E-18	271.
SC SUM	1.39E-15		1.18E-15		6.48E-16		3.36E-16		1.61E-16		1.80E-17	
DC	6.41E-16	-3.60	1.67E-16	6.21	2.45E-17	49.8	8.04E-18	77.0	2.09E-18	104.	2.89E-20	213.
DC+SS	1.66E-17	88.6	3.03E-17	97.8	2.15E-17	155.	1.08E-17	191.	5.05E-18	227.	3.29E-19	367.
DC+DS	1.59E-17	198.	1.63E-17	228.	7.20E-18	312.	4.33E-18	352.	2.46E-18	395.	2.39E-19	565.
DC+SPEX	3.02E-17	44.2	6.77E-17	58.5	2.36E-17	107.	1.09E-17	134.	5.23E-18	161.	3.33E-19	269.
DC+DPEX	4.76E-18	116.	4.93E-18	153.	1.05E-17	212.	6.02E-18	241.	3.36E-18	272.	2.71E-19	383.
DC SUM	7.08E-16		2.86E-16		8.73E-17		4.01E-17		1.82E-17		1.20E-18	
TEX	4.25E-19	7.70	1.97E-17	7.70	1.60E-16	7.70	2.25E-16	7.70	2.91E-16	7.70	3.73E-16	7.70
TEX+SS	6.69E-19	99.9	1.06E-17	99.3	7.80E-18	113.	9.40E-18	122.	1.15E-17	131.	1.64E-17	162.
TEX+DS	1.05E-20	209.	3.18E-19	229.	1.04E-18	270.	9.95E-19	283.	1.31E-18	299.	3.95E-18	360.
TEX+SPEX	8.24E-19	55.5	1.99E-17	60.0	1.01E-17	64.4	9.67E-18	65.0	1.34E-17	64.7	1.93E-17	64.1
TEX+DPEX	4.20E-20	128.	2.10E-18	155.	1.95E-18	170.	1.96E-18	172.	2.78E-18	176.	5.55E-18	178.
TEX SUM	1.97E-18		5.26E-17		1.81E-16		2.47E-16		3.20E-16		4.18E-16	

Channel	Energy 500 keV/u		1000		2000		5000		10000		25000	
	cross section cm ²	Eloss eV										
SI	3.33E-16	67.5	1.76E-16	84.3	7.84E-17	99.5	3.88E-17	113.	1.36E-17	154.	5.75E-18	150.
SI+SS	6.22E-17	267.	5.30E-17	316.	3.76E-17	359.	2.79E-17	399.	1.33E-17	475.	8.64E-18	496.
SI+DS	2.38E-17	530.	2.39E-17	634.	1.87E-17	717.	1.34E-17	699.	6.09E-18	889.	2.71E-18	1014.
SI+SPEX	7.49E-17	123.	6.25E-17	140.	4.16E-17	155.	2.82E-17	168.	1.34E-17	209.	8.70E-18	205.
SI+DPEX	3.07E-17	237.	2.59E-17	254.	1.66E-17	269.	9.70E-18	280.	6.21E-18	323.	2.71E-18	321.
SI SUM	5.25E-16		3.41E-16		1.93E-16		1.18E-16		5.26E-17		2.85E-17	
DI	2.11E-17	309.	7.76E-18	345.	1.10E-18	357.	6.60E-19	350.	2.16E-19	331.	3.99E-20	302.
DI+SS	2.17E-17	508.	1.18E-17	576.	6.33E-18	616.	2.30E-18	636.	9.78E-19	652.	3.38E-19	648.
DI+DS	1.25E-17	771.	7.24E-18	894.	4.08E-18	974.	1.44E-18	936.	5.88E-19	1066.	1.51E-19	1166.
DI+SPEX	2.36E-17	365.	1.28E-17	401.	7.15E-18	413.	2.31E-18	405.	9.81E-19	386.	3.39E-19	357.
DI+DPEX	1.47E-17	478.	7.67E-18	515.	3.73E-18	526.	1.11E-18	517.	5.98E-19	500.	1.51E-19	473.
DI SUM	9.36E-17		4.73E-17		2.24E-17		7.82E-18		3.36E-18		1.02E-18	
TI	6.16E-20	428.	3.55E-21	717.	2.49E-22	1799.	5.83E-24	2915.	3.50E-25	5673.	9.00E-27	13842.
TI+SS	4.10E-19	627.	2.76E-20	948.	1.66E-21	2058.	3.34E-23	3201.	1.40E-24	5994.	1.75E-26	14188.
TI+DS	3.15E-19	890.	2.42E-20	1266.	1.56E-21	2416.	3.09E-23	3501.	9.30E-25	6408.	1.75E-26	14706.
TI+SPEX	4.16E-19	484.	2.78E-20	773.	1.67E-21	1855.	3.34E-23	2970.	1.40E-24	5728.	1.75E-26	13897.
TI+DPEX	3.48E-19	597.	2.49E-20	887.	1.51E-21	1968.	3.04E-23	3082.	9.30E-25	5842.	1.75E-26	14013.
TI SUM	1.55E-18		1.08E-19		6.65E-21		1.34E-22		5.01E-24		7.90E-26	
DCAI	5.00E-25	450.	1.00E-28	785.	1.00E-32	1200.	9.00E-38	1900.	1.10E-41	3000.	9.00E-47	5000.
DCAI+SS	4.28E-22	649.	1.53E-24	1016.	2.50E-27	1459.	3.75E-31	2186.	6.24E-34	3321.	1.13E-37	5346.
DCAI+DS	3.57E-22	912.	1.53E-24	1334.	2.50E-27	1817.	3.75E-31	2486.	6.24E-34	3735.	1.13E-37	5864.
DCAI+SPEX	4.36E-22	506.	1.53E-24	841.	2.50E-27	1256.	3.75E-31	1955.	6.24E-34	3055.	1.13E-37	5055.
DCAI+DPEX	3.90E-22	619.	1.53E-24	955.	2.50E-27	1369.	3.75E-31	2067.	6.24E-34	3169.	1.13E-37	5171.
DCAI SUM	1.61E-21		6.12E-24		1.00E-26		1.50E-30		2.50E-33		4.52E-37	
SC	1.61E-20	234.	5.15E-23	506.	1.00E-26	1051.	1.00E-30	2685.	3.00E-34	5408.	1.50E-38	13547.
SC+SS	2.45E-19	433.	2.36E-20	737.	2.22E-21	1310.	7.68E-23	2971.	3.35E-24	5729.	8.63E-26	13893.
SC+DS	1.54E-19	696.	1.99E-20	1055.	2.16E-21	1668.	7.62E-23	3271.	3.35E-24	6143.	8.63E-26	14411.
SC+SPEX	2.54E-19	290.	2.36E-20	562.	2.22E-21	1107.	7.68E-23	2740.	3.35E-24	5463.	8.63E-26	13602.
SC+DPEX	1.80E-19	403.	2.05E-20	676.	2.08E-21	1220.	7.11E-23	2852.	3.35E-24	5577.	8.63E-26	13718.
SC SUM	8.49E-19		8.77E-20		8.68E-21		3.01E-22		1.34E-23		3.45E-25	
DC	5.00E-24	494.	1.00E-26	1039.	1.00E-29	2128.	1.50E-33	5396.	2.00E-30	10842.	2.00E-40	27181.
DC+SS	2.02E-21	693.	2.29E-23	1270.	2.50E-26	2387.	3.75E-30	5682.	5.00E-33	11163.	5.00E-37	27527.
DC+DS	1.77E-21	956.	2.29E-23	1588.	2.50E-26	2745.	3.75E-30	5982.	5.00E-33	11577.	5.00E-37	28045.
DC+SPEX	2.02E-21	550.	2.29E-23	1095.	2.50E-26	2184.	3.75E-30	5451.	5.00E-33	10897.	5.00E-37	27236.
DC+DPEX	1.91E-21	663.	2.29E-23	1209.	2.50E-26	2297.	3.75E-30	5563.	5.00E-33	11011.	5.00E-37	27352.
DC SUM	7.73E-21		9.16E-23		1.00E-25		1.50E-29		2.02E-30		2.00E-36	
TEX	3.08E-16	7.70	2.03E-16	7.70	1.12E-16	7.70	4.54E-17	7.70	2.07E-17	7.70	6.18E-18	7.70
TEX+SS	1.92E-17	207.	1.83E-17	239.	1.62E-17	267.	1.44E-17	294.	1.06E-17	329.	7.98E-18	354.
TEX+DS	6.98E-18	470.	7.75E-18	557.	8.09E-18	625.	6.28E-18	594.	4.27E-18	743.	2.14E-18	872.
TEX+SPEX	2.34E-17	63.6	2.20E-17	63.3	1.99E-17	63.2	1.46E-17	62.8	1.07E-17	62.7	8.05E-18	62.6
TEX+DPEX	9.16E-18	177.	8.43E-18	178.	7.17E-18	177.	4.50E-18	175.	4.36E-18	177.	2.14E-18	179.
TEX SUM	3.67E-16		2.59E-16		1.63E-16		8.52E-17		5.06E-17		2.65E-17	

Table A.7: The integral cross section and associated average energy loss for NSIM and SIM processes in $O^{4+} + H_2$ collisions with impact energies between 1 and 25000 keV/u. (From Schultz et al. (2019))

Channel	Energy 1 keV/u		10		50		75		100		200	
	cross section cm ²	Eloss eV										
SI	2.73E-21	27.5	2.33E-18	13.4	6.87E-16	20.9	1.05E-15	27.0	1.34E-15	31.9	1.23E-15	38.9
SI+SS	9.63E-22	161.	6.70E-19	144.	1.36E-17	166.	2.01E-17	180.	2.91E-17	191.	3.38E-17	232.
SI+DS	5.78E-23	295.	5.12E-20	305.	5.25E-18	355.	6.93E-18	369.	1.02E-17	384.	1.74E-17	452.
SI+SPEX	1.44E-21	90.6	1.24E-18	83.7	1.76E-17	99.1	2.19E-17	108.	3.31E-17	113.	2.10E-17	120.
SI+DPEX	2.60E-22	168.	2.29E-19	181.	9.83E-18	202.	1.12E-17	211.	1.39E-17	218.	2.10E-17	227.
SI SUM	5.45E-21		4.52E-18		7.33E-16		1.11E-15		1.43E-15		1.32E-15	
DI	5.00E-25	35.7	1.75E-21	59.8	5.81E-18	93.1	4.35E-17	119.	9.85E-17	141.	1.49E-16	194.
DI+SS	1.29E-24	169.	1.74E-20	191.	1.52E-18	238.	7.19E-18	272.	1.57E-17	300.	3.07E-17	387.
DI+DS	3.86E-25	303.	5.46E-21	352.	7.85E-19	427.	3.56E-18	461.	7.97E-18	493.	2.08E-17	607.
DI+SPEX	2.31E-24	98.8	2.65E-20	130.	1.74E-18	171.	7.56E-18	200.	1.69E-17	223.	3.49E-17	275.
DI+DPEX	5.14E-25	176.	6.62E-21	228.	1.24E-18	274.	4.98E-18	303.	9.96E-18	327.	2.32E-17	382.
DI SUM	5.00E-24		5.77E-20		1.11E-17		6.68E-17		1.49E-16		2.59E-16	
TI	2.77E-24	4.48	3.65E-18	13.1	1.04E-16	52.2	1.77E-16	83.4	1.48E-16	113.	1.74E-17	211.
TI+SS	1.22E-20	138.	1.93E-18	144.	1.81E-17	197.	3.03E-17	236.	3.26E-17	272.	1.28E-17	404.
TI+DS	3.57E-21	271.	6.10E-19	305.	8.21E-18	386.	1.41E-17	425.	1.65E-17	465.	9.36E-18	624.
TI+SPEX	2.84E-20	67.6	3.26E-18	83.4	2.18E-17	130.	3.21E-17	164.	3.51E-17	195.	1.41E-17	292.
TI+DPEX	4.46E-21	144.	7.42E-19	181.	1.40E-17	233.	2.02E-17	267.	2.06E-17	299.	1.03E-17	399.
TI SUM	7.63E-20		1.02E-17		1.66E-16		2.74E-16		2.53E-16		6.40E-17	
DCAI	6.44E-16	10.0	4.89E-16	35.9	3.21E-16	105.	1.39E-16	138.	4.49E-17	163.	7.38E-19	246.
DCAI+SS	6.56E-18	143.	2.92E-17	167.	3.42E-17	250.	2.03E-17	291.	1.04E-17	322.	5.26E-19	439.
DCAI+DS	7.39E-18	277.	1.65E-17	328.	1.32E-17	439.	8.41E-18	480.	5.02E-18	515.	4.00E-19	659.
DCAI+SPEX	2.09E-17	73.1	6.49E-17	106.	4.37E-17	183.	2.18E-17	219.	1.13E-17	245.	5.74E-19	327.
DCAI+DPEX	3.69E-18	150.	9.13E-18	204.	2.47E-17	286.	1.26E-17	322.	6.34E-18	349.	4.33E-19	434.
DCAI SUM	6.83E-16		6.09E-16		4.37E-16		2.02E-16		7.80E-17		2.67E-18	
SC	1.69E-15	-16.8	1.43E-15	-11.8	9.15E-16	10.0	5.31E-16	23.6	2.52E-16	37.2	2.06E-17	91.7
SC+SS	2.23E-18	117.	8.62E-18	119.	1.03E-17	155.	9.83E-18	176.	8.80E-18	196.	2.62E-18	284.
SC+DS	1.20E-18	250.	2.04E-18	280.	2.22E-18	344.	1.98E-18	365.	2.09E-18	389.	1.38E-18	505.
SC+SPEX	1.08E-17	46.3	2.88E-17	58.5	1.59E-17	88.2	1.12E-17	104.	1.04E-17	119.	3.26E-18	173.
SC+DPEX	1.20E-18	123.	2.11E-18	156.	5.96E-18	191.	4.04E-18	208.	3.30E-18	223.	1.65E-18	280.
SC SUM	1.71E-15		1.47E-15		9.49E-16		5.58E-16		2.77E-16		2.95E-17	
DC	6.62E-16	-16.7	1.96E-16	-6.88	4.47E-17	36.7	2.20E-17	63.9	8.01E-18	91.2	2.16E-19	200.
DC+SS	4.56E-18	117.	1.32E-17	124.	1.36E-17	182.	1.07E-17	217.	6.13E-18	250.	5.30E-19	393.
DC+DS	1.25E-17	250.	1.12E-17	285.	5.75E-18	371.	5.17E-18	406.	3.47E-18	443.	4.36E-19	613.
DC+SPEX	1.75E-17	46.4	3.34E-17	63.4	1.69E-17	115.	1.13E-17	144.	6.47E-18	173.	5.57E-19	281.
DC+DPEX	4.69E-18	123.	3.70E-18	161.	1.01E-17	218.	7.30E-18	248.	4.22E-18	277.	4.63E-19	388.
DC SUM	7.01E-16		2.58E-16		9.11E-17		5.65E-01		2.83E-17		2.20E-18	
TEX	5.43E-19	7.70	2.44E-17	7.70	1.68E-16	7.70	2.68E-16	7.70	3.60E-16	7.70	5.26E-16	7.70
TEX+SS	1.80E-19	141.	2.12E-18	139.	1.48E-18	153.	2.62E-18	160.	3.55E-18	167.	5.19E-18	200.
TEX+DS	2.43E-21	275.	6.31E-20	300.	2.84E-19	342.	4.53E-19	349.	8.40E-19	360.	2.45E-18	421.
TEX+SPEX	4.40E-19	70.8	5.22E-18	78.0	2.18E-18	85.9	1.11E-18	88.2	4.12E-18	89.2	7.23E-18	88.5
TEX+DPEX	2.43E-20	148.	6.60E-19	176.	7.65E-19	189.	8.45E-19	192.	1.24E-18	194.	2.95E-18	196.
TEX SUM	1.19E-18		3.25E-17		1.73E-16		2.73E-16		3.70E-16		5.44E-16	

Channel	Energy 500 keV/u		1000		2000		5000		10000		25000	
	cross section cm ²	Eloss eV										
SI	6.85E-16	48.9	3.95E-16	60.6	2.05E-16	73.3	8.30E-17	87.8	4.21E-17	94.5	1.77E-17	99.4
SI+SS	3.93E-17	306.	3.54E-17	363.	3.23E-17	423.	2.61E-17	487.	1.85E-17	539.	1.06E-17	630.
SI+DS	2.14E-17	592.	2.34E-17	698.	2.23E-17	793.	1.12E-17	911.	7.39E-18	1007.	4.40E-18	1379.
SI+SPEX	4.43E-17	129.	3.96E-17	140.	3.53E-17	152.	2.78E-17	166.	1.94E-17	173.	1.09E-17	177.
SI+DPEX	2.61E-17	235.	2.34E-17	246.	2.23E-17	257.	1.30E-17	271.	8.61E-18	278.	4.05E-18	277.
SI SUM	8.16E-16		5.17E-16		3.17E-01		1.61E-16		9.61E-17		4.77E-17	
DI	6.72E-17	256.	2.85E-17	289.	9.82E-18	305.	2.27E-18	310.	7.05E-19	304.	1.50E-19	283.
DI+SS	2.22E-17	513.	1.17E-17	592.	6.12E-18	655.	2.54E-18	709.	1.12E-18	748.	3.42E-19	814.
DI+DS	1.55E-17	799.	8.92E-18	926.	4.75E-18	1025.	1.33E-18	1133.	5.51E-19	1216.	1.77E-19	1564.
DI+SPEX	2.37E-17	336.	1.26E-17	368.	6.46E-18	384.	2.65E-18	388.	1.15E-18	382.	3.46E-19	361.
DI+DPEX	1.75E-17	442.	8.92E-18	474.	4.75E-18	489.	1.51E-18	493.	6.30E-19	487.	1.65E-19	461.
DI SUM	1.46E-16		7.06E-17		3.19E-17		1.03E-17		4.16E-18		1.18E-18	
TI	3.37E-19	384.	1.43E-20	674.	1.05E-21	1235.	6.00E-24	2824.	1.40E-25	5513.	9.00E-28	13662.
TI+SS	6.09E-19	641.	3.75E-20	977.	2.09E-21	1585.	2.23E-23	3223.	3.43E-24	5957.	4.40E-27	14193.
TI+DS	5.01E-19	927.	3.41E-20	1311.	2.03E-21	1955.	2.23E-23	3647.	3.43E-24	6425.	4.40E-27	14942.
TI+SPEX	6.25E-19	464.	3.80E-20	753.	2.10E-21	1314.	2.37E-23	2902.	3.43E-24	5591.	4.40E-27	13740.
TI+DPEX	5.39E-19	570.	3.41E-20	859.	2.03E-21	1419.	2.12E-23	3007.	3.32E-24	5696.	4.40E-27	13840.
TI SUM	2.61E-18		1.58E-19		9.30E-21		9.45E-23		1.38E-23		1.85E-26	
DCAI	1.76E-22	459.	1.00E-26	779.	1.00E-30	1200.	7.00E-36	1950.	6.00E-40	3100.	2.50E-45	5200.
DCAI+SS	1.21E-21	716.	3.85E-24	1082.	1.25E-26	1550.	6.25E-30	2349.	1.75E-32	3544.	7.50E-36	5731.
DCAI+DS	1.07E-21	1002.	3.85E-24	1416.	1.25E-26	1920.	6.25E-30	2773.	1.75E-32	4012.	7.50E-36	6480.
DCAI+SPEX	1.24E-21	539.	3.85E-24	858.	1.25E-26	1279.	6.25E-30	2028.	1.75E-32	3178.	7.50E-36	5278.
DCAI+DPEX	1.12E-21	645.	3.85E-24	964.	1.25E-26	1384.	6.25E-30	2133.	1.75E-32	3283.	7.50E-36	5378.
DCAI SUM	4.82E-21		1.54E-23		5.00E-26		2.50E-29		7.00E-32		3.00E-35	
SC	1.92E-19	214.	2.07E-21	487.	1.00E-24	1031.	1.00E-28	2665.	8.00E-32	5388.	7.00E-36	13557.
SC+SS	2.56E-19	471.	2.68E-20	790.	2.33E-21	1381.	6.89E-23	3064.	4.88E-24	5832.	1.00E-25	14088.
SC+DS	1.79E-19	757.	2.34E-20	1124.	2.28E-21	1751.	6.00E-23	3488.	4.12E-24	6300.	1.00E-25	14837.
SC+SPEX	2.70E-19	294.	2.73E-20	566.	2.33E-21	1110.	6.89E-23	2743.	4.88E-24	5466.	1.00E-25	13635.
SC+DPEX	2.04E-19	400.	2.34E-20	672.	2.28E-21	1215.	6.62E-23	2848.	4.73E-24	5571.	1.00E-25	13735.
SC SUM	1.10E-18		1.03E-19		9.22E-21		2.64E-22		1.86E-23		4.00E-25	
DC	2.18E-22	465.	1.00E-25	1010.	5.00E-29	2099.	7.00E-33	5466.	7.00E-36	10813.	6.00E-40	27104.
DC+SS	4.74E-21	722.	5.31E-23	1313.	2.50E-25	2449.	2.50E-28	5865.	1.75E-30	11257.	2.25E-33	27635.
DC+DS	4.36E-21	1008.	5.24E-23	1647.	2.50E-25	2819.	2.50E-28	6289.	1.75E-30	11725.	2.25E-33	28384.
DC+SPEX	4.77E-21	545.	5.31E-23	1089.	2.50E-25	2178.	2.50E-28	5544.	1.75E-30	10891.	2.25E-33	27182.
DC+DPEX	4.51E-21	651.	5.24E-23	1195.	2.50E-25	2283.	2.50E-28	5649.	1.75E-30	10996.	2.25E-33	27282.
DC SUM	1.86E-20		2.11E-22		1.00E-24		1.00E-27		7.00E-30		9.00E-33	
TEX	5.33E-16	7.70	3.69E-16	7.70	2.22E-16	7.70	9.65E-17	7.70	4.48E-17	7.70	1.51E-17	7.70
TEX+SS	9.26E-18	265.	1.13E-17	311.	1.10E-17	358.	1.16E-17	407.	9.52E-18	452.	6.69E-18	539.
TEX+DS	4.79E-18	551.	7.12E-18	645.	7.70E-18	728.	4.79E-18	831.	3.59E-18	920.	2.51E-18	1288.
TEX+SPEX	1.05E-17	87.6	1.26E-17	86.9	1.22E-17	86.6	1.25E-17	86.0	1.01E-17	85.8	6.88E-18	85.6
TEX+DPEX	6.13E-18	194.	7.12E-18	193.	7.70E-18	192.	5.59E-18	191.	4.19E-18	191.	2.30E-18	186.
TEX SUM	5.64E-16		4.07E-16		2.61E-16		1.31E-16		7.22E-17		3.35E-17	

Table A.8: The integral cross section and associated average energy loss for NSIM and SIM processes in $O^{5+} + H_2$ collisions with impact energies between 1 and 25000 keV/u. (From Schultz et al. (2019))

Channel	Energy 1 keV/u	10		50		75		100		200		
		cross section cm ²	Eloss eV									
SI	2.35E-20	28.9	1.67E-18	23.0	3.44E-16	22.0	9.24E-16	27.3	1.37E-15	32.7	1.78E-15	35.5
SI+SS	2.24E-21	178.	3.27E-19	183.	5.06E-18	194.	1.45E-17	206.	2.35E-17	218.	4.45E-17	253.
SI+DS	2.24E-25	926.	5.82E-23	965.	8.33E-21	1049.	3.20E-20	1105.	5.98E-20	1144.	1.95E-19	1250.
SI+SPEX	5.59E-21	92.2	1.54E-18	94.1	7.23E-18	105.	1.84E-17	114.	2.93E-17	121.	5.36E-17	124.
SI+DPEX	1.12E-24	579.	2.91E-22	643.	4.64E-20	683.	1.45E-19	689.	2.13E-19	688.	9.34E-19	721.
SI SUM	3.13E-20		3.54E-18		3.56E-16		9.57E-16		1.42E-15		1.88E-15	
DI	1.00E-25	35.7	1.00E-23	51.7	3.17E-18	79.3	3.56E-17	103.	1.09E-16	126.	2.34E-16	174.
DI+SS	1.96E-25	185.	9.97E-21	212.	6.28E-19	251.	5.17E-18	282.	1.51E-17	311.	4.76E-17	392.
DI+DS	3.91E-29	933.	2.66E-24	994.	5.07E-22	1107.	1.25E-20	1180.	6.02E-20	1237.	4.97E-19	1388.
DI+SPEX	7.04E-25	99.0	2.66E-20	123.	7.85E-19	162.	6.03E-18	189.	1.75E-17	215.	5.33E-17	263.
DI+DPEX	3.91E-28	586.	2.66E-23	672.	9.38E-21	740.	7.94E-20	765.	2.21E-19	781.	2.11E-18	859.
DI SUM	1.00E-24		3.66E-20		4.59E-18		4.69E-17		1.42E-16		3.38E-16	
TI	1.66E-20	-5.30	2.83E-18	1.89	1.01E-16	37.0	2.29E-16	66.6	2.40E-16	95.6	5.18E-17	191.
TI+SS	2.31E-21	144.	9.39E-19	162.	1.51E-17	209.	3.73E-17	245.	4.87E-17	281.	2.55E-17	409.
TI+DS	4.62E-25	892.	6.96E-22	944.	1.56E-20	1064.	8.39E-20	1144.	1.92E-19	1207.	3.37E-19	1405.
TI+SPEX	3.08E-20	58.0	4.62E-18	73.0	2.03E-17	120.	4.45E-17	153.	5.64E-17	184.	2.79E-17	280.
TI+DPEX	2.31E-23	545.	6.96E-21	622.	1.70E-19	698.	5.50E-19	729.	7.22E-19	751.	1.41E-18	876.
TI SUM	4.97E-20		8.40E-18		1.37E-16		3.11E-16		3.46E-16		1.07E-16	
DCAI	1.78E-15	31.1	1.06E-15	60.9	6.17E-16	138.	3.10E-16	178.	1.18E-16	208.	2.77E-18	300.
DCAI+SS	2.85E-18	181.	2.39E-17	221.	6.71E-17	310.	4.87E-17	357.	2.74E-17	393.	2.15E-18	518.
DCAI+DS	8.83E-20	929.	1.12E-19	1003.	9.40E-20	1165.	1.15E-19	1255.	1.04E-19	1319.	3.45E-20	1514.
DCAI+SPEX	7.25E-17	94.4	1.90E-16	132.	1.01E-16	222.	5.97E-17	264.	3.20E-17	297.	2.33E-18	389.
DCAI+DPEX	8.83E-19	581.	1.12E-18	681.	6.13E-19	799.	5.73E-19	840.	3.90E-19	863.	1.36E-19	985.
DCAI SUM	1.86E-15		1.28E-15		7.86E-16		4.19E-16		1.78E-16		7.42E-18	
SC	2.04E-15	-8.14	1.70E-15	-3.24	1.20E-15	18.5	7.76E-16	32.2	4.04E-16	45.8	3.68E-17	81.5
SC+SS	3.19E-19	141.	2.67E-18	157.	6.45E-18	190.	7.76E-18	211.	7.62E-18	231.	3.69E-18	299.
SC+DS	9.81E-22	889.	1.58E-21	939.	1.65E-21	1046.	2.39E-21	1110.	3.41E-21	1157.	7.09E-21	1296.
SC+SPEX	7.17E-18	55.2	2.80E-17	67.9	1.34E-17	101.	1.17E-17	118.	1.06E-17	134.	4.47E-18	170.
SC+DPEX	3.92E-21	542.	7.89E-21	617.	9.54E-21	680.	2.26E-20	694.	1.11E-20	701.	3.77E-20	767.
SC SUM	2.05E-15		1.73E-15		1.22E-15		7.95E-16		4.22E-16		4.50E-17	
DC	4.37E-17	-6.68	4.67E-17	3.12	2.66E-17	46.7	1.19E-17	73.9	3.12E-18	101.	1.67E-19	179.
DC+SS	2.42E-19	143.	3.98E-18	163.	1.35E-17	219.	9.55E-18	253.	3.60E-18	286.	4.99E-19	397.
DC+DS	7.24E-21	891.	2.89E-20	946.	2.59E-20	1074.	2.61E-20	1151.	1.85E-20	1212.	1.03E-20	1393.
DC+SPEX	7.75E-18	56.6	3.52E-17	74.2	1.90E-17	130.	1.11E-17	160.	3.99E-18	190.	5.23E-19	268.
DC+DPEX	3.62E-19	543.	1.15E-19	623.	1.06E-19	708.	1.51E-19	736.	6.88E-20	756.	4.15E-20	864.
DC SUM	5.21E-17		8.60E-17		5.92E-17		3.27E-17		1.08E-17		1.24E-18	
TEX	5.67E-19	7.70	1.77E-17	7.70	1.73E-16	7.70	2.84E-16	7.70	3.86E-16	7.70	6.09E-16	7.70
TEX+SS	9.08E-21	157.	3.41E-19	168.	4.92E-19	180.	1.13E-18	186.	2.04E-18	193.	4.17E-18	225.
TEX+DS	3.65E-25	905.	1.88E-23	950.	2.50E-22	1035.	9.09E-22	1085.	2.33E-21	1119.	8.00E-21	1222.
TEX+SPEX	1.95E-19	71.0	2.92E-18	78.8	1.24E-18	90.5	1.95E-18	93.9	3.03E-18	96.2	5.68E-18	96.2
TEX+DPEX	7.37E-25	558.	3.76E-23	628.	6.26E-22	669.	1.82E-21	670.	4.66E-21	663.	2.40E-20	693.
TEX SUM	7.71E-19		2.10E-17		1.75E-16		2.87E-16		3.91E-16		6.19E-16	

Channel	Energy 500 keV/u		1000		2000		5000		10000		25000	
	cross section cm ²	Eloss eV										
SI	1.06E-15	39.6	6.19E-16	46.9	3.32E-16	56.4	1.30E-16	69.1	6.29E-17	76.8	2.47E-17	83.1
SI+SS	5.46E-17	333.	5.84E-17	401.	5.51E-17	465.	4.20E-17	539.	3.01E-17	580.	1.68E-17	635.
SI+DS	1.75E-18	1304.	1.89E-18	1553.	1.82E-18	1940.	1.65E-18	2509.	1.16E-18	2914.	7.24E-19	3427.
SI+SPEX	6.46E-17	126.	6.46E-17	132.	5.77E-17	141.	4.44E-17	153.	3.05E-17	160.	1.68E-17	166.
SI+DPEX	2.12E-18	798.	2.58E-18	836.	3.17E-18	850.	2.47E-18	848.	1.38E-18	867.	8.65E-19	871.
SI SUM	1.18E-15		7.46E-16		4.50E-16		2.21E-16		1.26E-16		5.99E-17	
DI	1.20E-16	219.	5.11E-17	243.	1.87E-17	261.	3.89E-18	273.	1.14E-18	277.	2.10E-19	267.
DI+SS	4.34E-17	512.	2.52E-17	597.	1.29E-17	669.	4.62E-18	743.	1.96E-18	780.	5.49E-19	819.
DI+DS	3.49E-18	1483.	1.46E-18	1749.	6.25E-19	2144.	2.44E-19	2713.	1.40E-19	3115.	3.23E-20	3611.
DI+SPEX	4.77E-17	306.	2.68E-17	328.	1.33E-17	346.	4.79E-18	357.	1.97E-18	360.	5.49E-19	350.
DI+DPEX	4.12E-18	977.	2.36E-18	1032.	1.07E-18	1055.	3.47E-19	1052.	1.23E-19	1067.	3.86E-20	1055.
DI SUM	2.19E-16		1.07E-16		4.66E-17		1.39E-17		5.30E-18		1.38E-18	
TI	7.76E-19	398.	3.42E-20	809.	2.24E-21	1166.	5.28E-23	2802.	3.00E-24	5431.	6.50E-26	13544.
TI+SS	1.60E-18	691.	9.37E-20	1163.	4.97E-21	1574.	1.09E-22	3272.	5.02E-24	5934.	1.04E-25	14096.
TI+DS	1.86E-19	1662.	8.49E-21	2315.	3.82E-22	3049.	6.79E-24	5242.	2.64E-25	8269.	2.08E-26	16888.
TI+SPEX	1.67E-18	485.	9.51E-20	894.	5.00E-21	1251.	1.15E-22	2886.	5.02E-24	5514.	1.04E-25	13627.
TI+DPEX	2.21E-19	1156.	1.35E-20	1598.	6.08E-22	1960.	8.48E-24	3581.	7.93E-25	6221.	2.08E-26	14332.
TI SUM	4.45E-18		2.45E-19		1.32E-20		2.92E-22		1.41E-23		3.15E-25	
DCAI	9.08E-22	523.	1.00E-25	872.	1.00E-29	1500.	1.00E-34	2300.	1.50E-38	3500.	1.50E-43	6400.
DCAI+SS	5.80E-21	816.	2.45E-23	1226.	4.95E-26	1908.	1.25E-29	2770.	2.50E-32	4003.	5.00E-36	6952.
DCAI+DS	8.35E-22	1787.	5.33E-25	2378.	4.95E-28	3383.	1.25E-32	4740.	2.50E-36	6338.	5.00E-41	9744.
DCAI+SPEX	5.95E-21	610.	2.45E-23	957.	4.95E-26	1585.	1.25E-29	2384.	2.50E-32	3583.	5.00E-36	6483.
DCAI+DPEX	1.01E-21	1281.	1.07E-24	1661.	4.95E-28	2294.	1.25E-32	3079.	2.50E-36	4290.	5.00E-41	7188.
DCAI SUM	1.45E-20		5.07E-23		1.00E-25		2.50E-29		5.00E-32		1.00E-35	
SC	3.64E-19	245.	3.24E-21	464.	1.00E-23	1008.	1.00E-28	2642.	8.00E-32	5365.	7.00E-36	13534.
SC+SS	4.80E-19	538.	4.72E-20	818.	4.78E-21	1416.	1.47E-22	3112.	1.05E-23	5868.	2.56E-25	14086.
SC+DS	2.23E-20	1509.	2.80E-21	1970.	1.76E-22	2891.	6.02E-24	5802.	2.83E-25	8203.	2.56E-27	16878.
SC+SPEX	5.27E-19	332.	4.81E-20	549.	4.78E-21	1093.	1.47E-22	2726.	1.05E-23	5448.	2.56E-25	13617.
SC+DPEX	2.70E-20	1003.	4.69E-21	1253.	3.60E-22	1802.	9.04E-24	3421.	2.83E-25	6155.	2.56E-27	14322.
SC SUM	1.42E-18		1.06E-19		1.01E-20		3.09E-22		2.16E-23		5.17E-25	
DC	1.99E-22	506.	1.00E-25	963.	5.00E-29	2052.	2.00E-33	5320.	1.00E-36	10766.	5.00E-41	27104.
DC+SS	3.79E-21	799.	4.66E-23	1317.	4.22E-25	2460.	2.50E-28	5790.	1.00E-30	11269.	7.50E-34	27656.
DC+DS	6.59E-22	1770.	6.57E-24	2469.	6.33E-26	3935.	2.50E-31	7760.	1.00E-34	13604.	7.50E-39	30448.
DC+SPEX	3.85E-21	593.	4.66E-23	1048.	4.22E-25	2137.	2.50E-28	5404.	1.00E-30	10849.	7.50E-34	27187.
DC+DPEX	7.59E-22	1264.	1.03E-23	1752.	9.28E-26	2846.	2.50E-31	6099.	1.00E-34	11556.	7.50E-39	27892.
DC SUM	9.26E-21		1.10E-22		1.00E-24		5.01E-28		2.00E-30		1.50E-33	
TEX	6.97E-16	7.70	5.52E-16	7.70	3.40E-16	7.70	1.58E-16	7.70	7.39E-17	7.70	2.41E-17	7.70
TEX+SS	1.17E-17	301.	1.60E-17	362.	1.78E-17	416.	1.70E-17	478.	1.42E-17	511.	9.45E-18	560.
TEX+DS	3.65E-19	1272.	8.30E-19	1514.	1.15E-18	1891.	1.04E-18	2448.	6.95E-19	2846.	4.52E-19	3351.
TEX+SPEX	1.39E-17	94.2	1.78E-17	93.0	1.87E-17	92.6	1.82E-17	91.8	1.44E-17	91.0	9.45E-18	91.0
TEX+DPEX	4.04E-19	766.	1.06E-18	797.	1.51E-18	802.	1.27E-18	787.	7.61E-19	798.	4.95E-19	796.
TEX SUM	7.23E-16		5.88E-16		3.79E-16		1.96E-16		1.04E-16		4.40E-17	

Table A.9: The integral cross section and associated average energy loss for NSIM and SIM processes in $O^{6+} + H_2$ collisions with impact energies between 1 and 25000 keV/u. (From Schultz et al. (2019))

Channel	Energy 1 keV/u		10		50		75		100		200	
	cross section cm ²	Eloss eV										
SI	3.27E-20	17.1	2.67E-18	23.0	4.16E-16	20.5	8.95E-16	27.9	1.51E-15	33.6	2.45E-15	34.4
SI+SS	1.67E-24	846.	1.36E-22	862.	1.93E-20	879.	4.74E-20	892.	1.72E-19	931.	9.07E-19	950.
SI+DS	2.67E-26	1708.	5.45E-23	1834.	3.19E-21	2031.	1.21E-20	2089.	2.88E-20	2142.	1.10E-19	2194.
SI+SPEX	6.66E-22	437.	5.91E-20	492.	1.35E-19	500.	5.88E-19	518.	8.73E-19	531.	1.73E-18	549.
SI+DPEX	3.33E-28	817.	2.72E-25	923.	7.08E-22	1021.	6.27E-21	1330.	7.76E-20	1149.	4.11E-19	1217.
SI SUM	3.34E-20		2.73E-18		4.16E-16		8.96E-16		1.51E-15		2.45E-15	
DI	5.00E-23	37.7	7.42E-19	55.7	2.30E-18	66.3	3.16E-17	91.4	1.28E-16	117.	4.12E-16	166.
DI+SS	1.66E-28	867.	5.30E-23	895.	8.43E-22	925.	1.96E-20	956.	1.17E-19	1014.	1.54E-18	1081.
DI+DS	1.66E-28	1728.	1.06E-23	1866.	1.06E-22	2077.	2.78E-21	2152.	2.09E-20	2226.	1.88E-19	2326.
DI+SPEX	1.66E-30	458.	5.26E-25	525.	1.18E-20	545.	1.74E-19	581.	5.45E-19	614.	2.88E-18	681.
DI+DPEX	1.66E-28	838.	1.06E-23	956.	1.06E-20	1066.	2.64E-21	1393.	5.54E-20	1232.	7.13E-19	1349.
DI SUM	5.00E-23		7.42E-19		2.32E-18		3.18E-17		1.29E-16		4.17E-16	
TI	2.21E-20	1.90	6.51E-18	12.7	1.10E-16	44.2	3.19E-16	72.8	4.24E-16	102.	1.55E-16	172.
TI+SS	2.20E-24	831.	1.31E-21	852.	4.40E-20	903.	1.89E-19	937.	5.55E-19	999.	1.35E-18	1087.
TI+DS	2.20E-25	1693.	1.31E-22	1823.	4.88E-21	2055.	2.86E-20	2134.	7.98E-20	2211.	1.75E-19	3247.
TI+SPEX	2.20E-22	422.	1.30E-19	482.	4.26E-19	523.	2.03E-18	563.	2.75E-18	599.	2.49E-18	1602.
TI+DPEX	2.20E-25	802.	1.31E-22	913.	4.88E-21	1044.	3.37E-20	1375.	2.41E-19	1217.	6.31E-19	2270.
TI SUM	2.23E-20		6.64E-18		1.10E-16		3.21E-16		4.28E-16		1.60E-16	
DCAI	2.35E-15	47.4	1.78E-15	74.2	1.14E-15	152.	6.83E-16	197.	3.19E-16	228.	1.50E-17	320.
DCAI+SS	1.10E-19	877.	1.67E-19	914.	3.12E-19	1010.	4.23E-19	1061.	5.07E-19	1125.	1.93E-19	1235.
DCAI+DS	2.20E-20	1738.	3.34E-20	1885.	5.01E-20	2163.	6.10E-20	2258.	7.42E-20	2337.	2.15E-20	2480.
DCAI+SPEX	2.20E-18	467.	3.54E-18	543.	2.97E-18	631.	4.26E-18	687.	2.49E-18	725.	3.68E-19	835.
DCAI+DPEX	2.20E-20	847.	3.34E-20	974.	5.01E-20	1152.	6.16E-20	1499.	2.31E-19	1343.	8.69E-20	1503.
DCAI SUM	2.35E-15		1.78E-15		1.14E-15		6.88E-16		3.22E-16		1.57E-17	
SC	2.33E-15	-16.2	1.95E-15	-11.3	1.48E-15	10.5	1.04E-15	35.7	5.82E-16	49.3	6.27E-17	104.
SC+SS	2.26E-21	813.	3.77E-21	828.	5.64E-21	869.	7.25E-21	900.	7.50E-21	947.	2.32E-20	1019.
SC+DS	1.13E-21	1675.	1.89E-21	1799.	2.25E-21	2021.	3.63E-21	2096.	4.06E-21	2158.	3.02E-21	2264.
SC+SPEX	1.13E-19	404.	1.79E-19	458.	2.70E-20	490.	2.67E-20	526.	3.00E-20	546.	4.69E-20	619.
SC+DPEX	2.26E-22	784.	3.77E-22	889.	5.64E-22	1011.	7.25E-22	1338.	1.50E-21	1164.	1.06E-20	1287.
SC SUM	2.33E-15		1.95E-15		1.48E-15		1.04E-15		5.82E-16		6.28E-17	
DC	1.38E-17	-21.4	4.38E-17	-11.6	5.48E-17	32.0	3.47E-17	78.8	1.79E-17	106.	2.53E-18	215.
DC+SS	9.86E-22	808.	1.26E-20	828.	3.28E-20	890.	6.60E-20	943.	1.03E-19	1003.	7.33E-20	1130.
DC+DS	4.93E-22	1669.	4.19E-21	1799.	1.01E-20	2047.	1.93E-20	2140.	1.76E-20	2215.	9.80E-21	2375.
DC+SPEX	4.93E-21	399.	3.74E-19	457.	5.78E-19	511.	8.84E-19	569.	5.31E-19	603.	1.31E-19	730.
DC+DPEX	4.93E-22	779.	4.19E-21	888.	1.01E-20	1032.	1.32E-20	1381.	3.84E-20	1221.	3.82E-20	1398.
DC SUM	1.38E-17		4.42E-17		5.54E-17		3.57E-17		1.86E-17		2.78E-18	
TEX	1.04E-18	7.70	1.17E-17	7.70	1.69E-16	7.70	2.92E-16	7.70	4.07E-16	7.70	6.85E-16	7.70
TEX+SS	5.20E-25	837.	1.17E-23	847.	7.90E-22	866.	9.73E-22	872.	8.48E-21	905.	2.28E-20	923.
TEX+DS	1.04E-25	1698.	5.85E-24	1818.	1.58E-22	2018.	4.87E-22	2068.	1.70E-21	2116.	1.14E-20	2167.
TEX+SPEX	2.08E-21	428.	3.16E-20	477.	1.58E-20	487.	9.73E-22	498.	8.48E-21	505.	2.28E-20	523.
TEX+DPEX	5.20E-25	808.	5.85E-24	908.	1.58E-22	1008.	4.87E-22	1310.	1.70E-21	1123.	1.14E-20	1191.
TEX SUM	1.04E-18		1.17E-17		1.69E-16		2.92E-16		4.07E-16		6.85E-16	

Channel	Energy 500 keV/u		1000		2000		5000		10000		25000	
	cross section cm ²	Eloss eV										
SI	1.69E-15	35.4	1.02E-15	39.2	6.11E-16	45.9	2.94E-16	55.6	1.63E-16	62.2	7.39E-17	69.6
SI+SS	1.35E-18	991.	2.22E-18	1124.	2.14E-18	1385.	1.83E-18	1836.	1.43E-18	2197.	9.77E-19	2566.
SI+DS	3.98E-19	2169.	8.24E-19	2357.	1.44E-18	2940.	1.11E-18	3537.	6.17E-19	4034.	3.89E-19	5468.
SI+SPEX	1.44E-18	578.	2.35E-18	589.	2.21E-18	592.	1.97E-18	600.	1.55E-18	604.	1.05E-18	610.
SI+DPEX	5.77E-19	1246.	1.09E-18	1269.	1.44E-18	1288.	1.11E-18	1270.	9.38E-19	1299.	4.38E-19	1319.
SI SUM	1.69E-15		1.03E-15		6.18E-16		3.00E-16		1.68E-16		7.68E-17	
DI	3.25E-16	198.	1.52E-16	211.	6.68E-17	222.	1.96E-17	232.	7.05E-18	242.	1.66E-18	246.
DI+SS	2.83E-18	1153.	2.52E-18	1295.	9.83E-19	1561.	3.24E-19	2012.	1.42E-19	2377.	5.62E-20	2642.
DI+DS	1.25E-18	2332.	1.01E-18	2529.	6.65E-19	3116.	2.00E-19	3713.	6.17E-20	4214.	1.85E-20	5644.
DI+SPEX	4.03E-18	741.	2.66E-18	761.	1.02E-18	768.	3.47E-19	776.	1.53E-19	784.	4.99E-20	786.
DI+DPEX	1.76E-18	1409.	1.30E-18	1441.	6.65E-19	1464.	2.00E-19	1446.	9.38E-20	1479.	2.08E-20	1495.
DI SUM	3.35E-16		1.59E-16		7.01E-17		2.07E-17		7.50E-18		1.81E-18	
TI	6.48E-18	305.	3.36E-19	576.	1.95E-20	1124.	4.26E-22	2752.	1.48E-23	5451.	4.31E-25	13544.
TI+SS	2.57E-19	1260.	1.93E-20	1660.	6.50E-22	2463.	4.00E-24	4532.	3.73E-26	7586.	1.08E-28	15940.
TI+DS	8.28E-20	2439.	7.90E-21	2894.	3.85E-22	4018.	2.00E-24	6233.	3.73E-26	9423.	1.08E-28	18942.
TI+SPEX	2.70E-19	848.	2.04E-20	1126.	6.50E-22	1670.	4.00E-24	3296.	3.73E-26	5993.	1.08E-28	14084.
TI+DPEX	1.17E-19	1516.	9.95E-21	1806.	3.85E-22	2366.	2.00E-24	3966.	3.73E-26	6688.	1.08E-28	14793.
TI SUM	7.21E-18		3.94E-19		2.16E-20		4.38E-22		1.49E-23		4.31E-25	
DCAI	3.20E-20	547.	9.53E-23	902.	8.00E-26	1700.	9.00E-30	3000.	8.91E-33	4500.	7.99E-37	7000.
DCAI+SS	2.25E-21	1502.	6.70E-24	1986.	6.77E-27	3039.	4.55E-31	4780.	4.09E-35	6635.	3.64E-40	9396.
DCAI+DS	7.58E-22	2681.	2.79E-24	3220.	3.33E-27	4594.	4.55E-31	6481.	4.09E-36	8472.	3.64E-41	12398.
DCAI+SPEX	2.34E-21	1090.	7.26E-24	1452.	6.67E-27	2246.	4.55E-31	3544.	4.09E-35	5042.	3.64E-40	7540.
DCAI+DPEX	1.07E-21	1758.	3.91E-24	2132.	3.33E-27	2942.	4.55E-31	4214.	4.09E-36	5737.	3.64E-41	8249.
DCAI SUM	3.84E-20		1.16E-22		1.00E-25		1.08E-29		9.00E-33		8.00E-37	
SC	1.74E-18	231.	1.09E-19	431.	1.49E-20	976.	2.67E-22	2610.	1.70E-23	5333.	8.62E-25	13502.
SC+SS	1.70E-20	1186.	3.85E-21	1515.	4.75E-22	2315.	6.09E-24	4390.	6.06E-25	7468.	2.16E-30	15898.
SC+DS	4.35E-21	2365.	1.48E-21	2749.	2.83E-22	3870.	3.65E-24	6091.	4.55E-25	9305.	2.16E-30	18900.
SC+SPEX	1.80E-20	774.	4.10E-21	981.	5.01E-22	1522.	7.30E-24	3154.	6.06E-25	5875.	2.16E-30	14042.
SC+DPEX	6.72E-21	1442.	1.90E-21	1661.	2.83E-22	2218.	3.65E-24	3824.	4.55E-25	6570.	2.16E-30	14751.
SC SUM	1.79E-18		1.20E-19		1.64E-20		2.88E-22		1.91E-23		8.62E-25	
DC	2.40E-20	480.	3.09E-22	904.	2.76E-24	1993.	3.00E-27	5261.	2.00E-29	10630.	2.00E-32	26969.
DC+SS	2.37E-21	1435.	3.28E-23	1988.	2.30E-25	3332.	7.50E-31	7041.	5.00E-34	12765.	5.00E-38	29365.
DC+DS	8.40E-22	2614.	1.46E-23	3222.	1.15E-25	4887.	7.50E-31	8742.	5.00E-34	14602.	5.00E-38	32367.
DC+SPEX	2.46E-21	1023.	3.46E-23	1454.	2.30E-25	2539.	7.50E-31	5805.	5.00E-34	11172.	5.00E-38	27509.
DC+DPEX	1.17E-21	1691.	1.73E-23	2134.	1.15E-25	3245.	7.50E-31	6475.	5.00E-34	11867.	5.00E-38	28218.
DC SUM	3.08E-20		4.08E-22		3.45E-24		3.00E-27		2.00E-29		2.00E-32	
TEX	8.96E-16	7.70	7.65E-16	7.70	5.18E-16	7.70	2.76E-16	7.70	1.49E-16	7.70	6.09E-17	7.70
TEX+SS	7.43E-20	963.	4.93E-19	1092.	9.65E-19	1347.	8.93E-19	1788.	6.89E-19	2142.	3.77E-19	2404.
TEX+DS	4.09E-20	2141.	3.10E-19	2325.	7.91E-19	2901.	6.95E-19	3489.	4.50E-19	3978.	2.68E-19	5406.
TEX+SPEX	7.43E-20	551.	5.08E-19	558.	9.82E-19	554.	9.27E-19	552.	7.15E-19	550.	4.44E-19	548.
TEX+DPEX	4.83E-20	1219.	3.51E-19	1238.	7.91E-19	1250.	6.95E-19	1222.	5.56E-19	1245.	2.85E-19	1257.
TEX SUM	8.96E-16		7.67E-16		5.22E-16		2.79E-16		1.51E-16		6.23E-17	

Table A.10: The integral cross section and associated average energy loss for NSIM and SIM processes in $O^{7+} + H_2$ collisions with impact energies between 1 and 25000 keV/u. (From Schultz et al. (2019))

Channel	Energy 1 keV/u		10		50		75		100		200	
	cross section cm ²	Eloss eV										
SI	1.09E-19	16.6	1.99E-18	23.8	4.89E-16	19.4	1.04E-15	26.2	1.80E-15	32.2	3.28E-15	34.2
SI+SS	2.29E-24	988.	6.08E-23	1015.	1.18E-20	1031.	2.40E-20	1046.	1.27E-19	1078.	8.04E-19	1115.
SI+SPEX	1.10E-21	603.	3.70E-20	532.	9.45E-20	545.	2.10E-19	559.	8.23E-19	570.	2.66E-18	600.
SI SUM	1.10E-19		2.03E-18		4.89E-16		1.04E-15		1.80E-15		3.28E-15	
DI	1.00E-24	37.7	4.22E-21	39.8	1.17E-18	58.2	2.21E-17	82.9	1.13E-16	112.	4.44E-16	167.
DI+SS	5.00E-32	1009.	4.22E-28	1031.	1.00E-24	1070.	3.70E-21	1102.	5.11E-20	1157.	9.10E-19	1247.
DI+SPEX	5.00E-32	624.	1.00E-25	548.	1.91E-21	584.	2.89E-20	616.	3.19E-19	650.	2.98E-18	733.
DI SUM	1.00E-24		4.22E-21		1.17E-18		2.21E-17		1.13E-16		4.44E-16	
TI	1.98E-20	-11.2	4.50E-18	3.05	8.99E-17	46.5	3.12E-16	59.3	4.90E-16	89.4	2.18E-16	186.
TI+SS	9.95E-25	960.	4.53E-22	994.	1.46E-20	1058.	6.97E-20	1079.	3.56E-19	1135.	1.03E-18	1266.
TI+SPEX	1.99E-22	575.	6.41E-20	511.	1.59E-19	573.	6.31E-19	592.	2.32E-18	627.	3.29E-18	752.
TI SUM	2.00E-20		4.56E-18		9.01E-17		3.13E-16		4.93E-16		2.22E-16	
DCAI	2.85E-15	611.	2.29E-15	689.	1.52E-15	860.	1.01E-15	943.	5.12E-16	1007.	2.89E-17	1202.
DCAI+SS	1.37E-19	1582.	2.15E-19	1680.	2.45E-19	1871.	3.24E-19	1962.	5.11E-19	2052.	2.02E-19	2282.
DCAI+SPEX	3.19E-18	1197.	3.47E-18	1197.	3.00E-18	1386.	2.79E-18	1476.	3.24E-18	1545.	6.79E-19	1768.
DCAI SUM	2.85E-15		2.29E-15		1.52E-15		1.01E-15		5.16E-16		2.98E-17	
SC	2.61E-15	-26.6	2.22E-15	-21.7	1.74E-15	15.4	1.28E-15	29.0	7.59E-16	42.6	8.44E-17	97.1
SC+SS	2.60E-22	945.	4.42E-22	970.	8.56E-22	1027.	2.40E-21	1048.	4.96E-21	1088.	8.49E-21	1178.
SC+SPEX	7.80E-20	559.	9.57E-20	486.	5.13E-20	541.	3.60E-20	562.	1.73E-20	581.	3.52E-20	663.
SC SUM	2.61E-15		2.22E-15		1.74E-15		1.28E-15		7.59E-16		8.44E-17	
DC	6.94E-18	-40.6	6.44E-18	-30.8	1.29E-17	39.2	1.47E-17	66.5	1.03E-17	93.7	1.74E-18	203.
DC+SS	3.34E-21	931.	6.17E-21	961.	2.03E-20	1051.	3.26E-20	1086.	4.16E-20	1139.	3.39E-20	1283.
DC+SPEX	6.68E-20	545.	1.00E-19	477.	2.13E-19	565.	2.17E-19	600.	2.96E-19	632.	1.11E-19	769.
DC SUM	7.01E-18		6.55E-18		1.31E-17		1.49E-17		1.06E-17		1.88E-18	
TEX	1.25E-18	7.70	7.88E-18	7.70	1.59E-16	7.70	2.96E-16	7.70	4.09E-16	7.70	7.45E-16	7.70
TEX+SS	1.24E-22	979.	3.85E-22	999.	1.57E-21	1019.	1.47E-21	1027.	4.01E-21	1053.	3.19E-20	1088.
TEX+SPEX	9.02E-21	594.	1.51E-20	516.	1.57E-19	534.	2.06E-19	541.	2.00E-19	546.	1.92E-19	574.
TEX SUM	1.26E-18		7.90E-18		1.59E-16		2.96E-16		4.09E-16		7.45E-16	

Channel	Energy 500 keV/u		1000		2000		5000		10000		25000	
	cross section cm ²	Eloss eV										
SI	2.13E-15	33.7	1.35E-15	35.6	8.12E-16	40.0	3.92E-16	47.3	2.18E-16	49.2	9.79E-17	58.6
SI+SS	1.43E-18	1137.	2.15E-18	1263.	3.17E-18	1530.	2.81E-18	2066.	2.43E-18	2427.	1.51E-18	2757.
SI+SPEX	1.72E-18	635.	2.15E-18	656.	3.54E-18	657.	3.15E-18	655.	2.34E-18	655.	1.63E-18	662.
SI SUM	2.13E-15		1.35E-15		8.19E-16		3.98E-16		2.23E-16		1.01E-16	
DI	3.83E-16	193.	2.11E-16	198.	9.77E-17	202.	3.00E-17	203.	1.10E-17	205.	2.56E-18	205.
DI+SS	4.04E-18	1296.	3.81E-18	1425.	2.03E-18	1692.	6.47E-19	2221.	2.96E-19	2582.	8.29E-20	2903.
DI+SPEX	4.80E-18	794.	3.81E-18	818.	2.25E-18	819.	7.23E-19	811.	2.85E-19	811.	8.96E-20	808.
DI SUM	3.92E-16		2.19E-16		1.02E-16		3.14E-17		1.16E-17		2.73E-18	
TI	1.01E-17	360.	5.67E-19	540.	3.09E-20	1077.	7.35E-22	2680.	2.68E-23	4836.	5.99E-25	12980.
TI+SS	3.90E-19	1463.	3.89E-20	1767.	1.51E-21	2567.	1.41E-23	4698.	1.36E-25	7213.	5.45E-29	15678.
TI+SPEX	4.64E-19	961.	3.89E-20	1160.	1.69E-21	1694.	2.26E-23	3288.	1.36E-25	5442.	5.45E-28	13583.
TI SUM	1.10E-17		6.45E-19		3.41E-20		7.72E-22		2.71E-23		6.00E-25	
DCAI	8.21E-20	1634.	2.73E-22	2204.	3.75E-25	2800.	6.75E-29	3600.	1.26E-31	4500.	2.97E-35	6000.
DCAI+SS	5.00E-21	2737.	4.50E-23	3431.	6.25E-26	4290.	6.43E-30	5618.	1.27E-33	6877.	2.73E-38	8698.
DCAI+SPEX	5.22E-21	2235.	4.50E-23	2824.	6.25E-26	3417.	1.61E-29	4208.	1.27E-32	5106.	2.73E-37	6603.
DCAI SUM	9.23E-20		3.63E-22		5.00E-25		9.00E-29		1.40E-31		3.00E-35	
SC	2.21E-18	212.	1.36E-19	484.	1.49E-20	1029.	2.66E-22	2568.	1.86E-23	4781.	4.00E-25	12950.
SC+SS	1.21E-20	1315.	5.13E-21	1711.	7.08E-22	2519.	1.08E-23	4586.	1.06E-24	7158.	2.00E-30	15648.
SC+SPEX	1.50E-20	813.	5.13E-21	1104.	8.15E-22	1646.	1.15E-23	3176.	1.06E-24	5387.	2.00E-30	13553.
SC SUM	2.24E-18		1.46E-19		1.64E-20		2.88E-22		2.07E-23		4.00E-25	
DC	2.31E-20	446.	3.74E-22	990.	4.00E-24	2080.	6.99E-27	5347.	9.00E-29	10630.	1.50E-31	26969.
DC+SS	2.18E-21	1549.	4.17E-23	2217.	5.00E-25	3570.	3.50E-30	7365.	4.50E-33	13007.	7.50E-37	29667.
DC+SPEX	2.72E-21	1047.	4.17E-23	1610.	5.00E-25	2697.	3.50E-30	5955.	4.50E-33	11236.	7.50E-37	27572.
DC SUM	2.80E-20		4.57E-22		5.00E-24		7.00E-27		9.00E-29		1.50E-31	
TEX	1.03E-15	7.70	9.34E-16	7.70	6.79E-16	7.70	3.58E-16	7.70	1.98E-16	7.70	8.22E-17	7.70
TEX+SS	5.60E-20	1111.	3.85E-19	1235.	1.47E-18	1498.	1.73E-18	2026.	1.53E-18	2385.	1.02E-18	2706.
TEX+SPEX	5.60E-20	609.	3.85E-19	628.	1.55E-18	625.	1.83E-18	616.	1.50E-18	614.	1.07E-18	611.
TEX SUM	1.03E-15		9.35E-16		6.82E-16		3.62E-16		2.01E-16		8.43E-17	

Table A.11: The integral cross section and associated average energy loss for NSIM and SIM processes in $O^{8+} + H_2$ collisions with impact energies between 1 and 25000 keV/u. (From Schultz et al. (2019))

Channel	Energy 1 keV/u		10		50		75		100		200	
	cross section cm ²	Eloss eV										
SI	1.00E-22	15.4	1.58E-18	24.1	2.27E-16	22.8	1.17E-15	24.9	2.10E-15	30.9	3.06E-15	38.9
DI	1.00E-33	35.7	1.00E-24	35.7	7.60E-19	53.6	1.60E-17	77.8	9.57E-17	109.	5.32E-16	170.
TI	3.24E-20	-22.3	3.41E-18	-8.87	7.62E-17	49.0	3.01E-16	75.7	5.41E-16	121.	2.88E-16	176.
DCAI	3.39E-15	723.	2.75E-15	805.	1.87E-15	988.	1.33E-15	1076.	7.44E-16	1146.	4.91E-17	1343.
SC	2.90E-15	-18.9	2.45E-15	-14.0	2.00E-15	18.5	1.53E-15	32.1	9.55E-16	45.7	1.08E-16	89.5
DC	1.51E-17	-28.3	1.48E-17	-18.5	1.45E-17	43.8	1.40E-17	71.0	1.23E-17	98.2	1.24E-18	188.
TEX	8.29E-19	7.70	5.48E-18	7.70	1.51E-16	7.70	2.88E-16	7.70	4.07E-16	7.70	7.76E-16	7.70
Channel	Energy 500 keV/u		1000		2000		5000		10000		25000	
	cross section cm ²	Eloss eV										
SI	2.67E-15	33.2	1.70E-15	33.7	1.04E-15	37.3	5.07E-16	43.0	2.86E-16	47.2	1.30E-16	51.8
DI	5.05E-16	196.	2.94E-16	198.	1.42E-16	197.	4.53E-17	195.	1.72E-17	192.	4.19E-18	189.
TI	1.60E-17	345.	9.84E-19	610.	5.59E-20	1125.	1.01E-21	2632.	8.44E-23	4664.	2.20E-24	12790.
DCAI	2.37E-19	1726.	1.67E-21	2153.	1.00E-24	2800.	8.00E-29	3600.	5.00E-32	4500.	3.00E-36	6000.
SC	2.64E-18	233.	1.71E-19	463.	2.10E-20	1008.	3.35E-21	2520.	1.41E-23	4591.	1.72E-25	12760.
DC	1.24E-19	481.	1.81E-22	951.	1.00E-25	2040.	7.00E-30	5095.	5.00E-33	9394.	3.00E-37	25732.
TEX	1.14E-15	7.70	1.12E-15	7.70	8.33E-16	7.70	4.60E-16	7.70	2.59E-16	7.70	1.10E-16	7.70

Appendix B

Tables of Sulfur NSIM and SIM Cross-Sections and Average Energy Loss Values

Table B.1: The integral cross section and associated average energy loss for SIM and NSIM processes in S + H₂ collisions with impact energies between 1 and 2000 keV/u. (From Gharibnejad et al. (2019))

Channel	Energy	Eloss	10		50		75		100	
	1 keV/u		cross section cm ²	cross section cm ²	Eloss eV	cross section cm ²	Eloss eV	cross section cm ²	Eloss eV	cross section cm ²
SI	2.63E-17	5.5	8.11E-19	25.5	4.64E-18	38.5	3.73E-18	52.4	2.49E-18	66.2
SI+SS	7.19E-18	10.8	3.38E-17	36.2	1.22E-16	68.4	1.26E-16	86.6	1.26E-16	103.0
SI+DS	2.54E-18	18.4	1.77E-17	48.7	4.83E-17	97.6	5.92E-17	125.4	6.61E-17	149.2
SI+SPEX	8.09E-18	15.2	3.56E-17	35.3	1.23E-16	48.3	1.28E-16	62.2	1.29E-16	76.0
SI+DPEX	6.04E-19	43.7	1.03E-17	68.5	1.83E-17	82.7	2.03E-17	97.3	8.69E-18	111.9
SI SUM	4.47E-17		9.82E-17		3.16E-16		3.37E-16		3.32E-16	
DI	2.75E-19	268.0	5.45E-18	98.8	5.15E-17	97.0	7.20E-17	141.6	7.80E-17	191.7
DI+SS	8.79E-20	273.3	1.57E-18	109.5	1.52E-17	126.9	2.07E-17	175.8	2.35E-17	228.5
DI+DS	7.71E-20	281.0	1.29E-18	122.0	1.27E-17	156.1	1.82E-17	214.6	2.13E-17	274.6
DI+SPEX	8.79E-20	277.8	1.58E-18	108.7	1.52E-17	106.8	2.07E-17	151.4	2.35E-17	201.5
DI+DPEX	2.16E-20	306.3	1.01E-18	141.8	8.39E-18	141.2	1.23E-17	186.5	9.68E-18	237.3
DI SUM	5.50E-19		1.09E-17		1.03E-16		1.44E-16		1.56E-16	
TEX	5.92E-21	6.9	1.76E-19	8.0	3.24E-18	7.6	3.16E-18	7.4	2.83E-18	7.3
TEX+SS	6.97E-18	12.2	3.66E-17	18.7	7.16E-17	37.5	7.00E-17	41.6	6.88E-17	44.1
TEX+DS	6.37E-18	19.9	2.66E-17	31.2	2.62E-17	66.7	2.74E-17	80.4	2.98E-17	90.2
TEX+SPEX	6.97E-18	16.6	3.72E-17	17.8	7.21E-17	17.4	7.22E-17	17.2	7.28E-17	17.1
TEX+DPEX	1.88E-18	45.2	1.64E-17	50.9	9.78E-18	51.8	8.21E-18	52.2	2.77E-18	53.0
TEX SUM	2.22E-17		1.17E-16		1.83E-16		1.81E-16		1.77E-16	
Channel	Energy	Eloss	500		1000		2000			
200 keV/u	cross section cm ²		cross section cm ²	Eloss eV	cross section cm ²	Eloss eV	cross section cm ²	Eloss eV		
SI	9.80E-19	121.4	3.10E-19	202.2	4.23E-20	246.1	1.00E-24	279.9		
SI+SS	1.03E-16	161.9	8.19E-17	243.2	6.80E-17	286.4	5.07E-17	315.6		
SI+DS	6.14E-17	231.4	5.67E-17	334.2	3.53E-17	385.8	3.21E-17	415.1		
SI+SPEX	1.04E-16	131.2	8.23E-17	211.9	6.83E-17	255.9	5.09E-17	289.7		
SI+DPEX	2.65E-17	167.5	1.38E-17	247.7	1.73E-17	293.0	1.33E-17	323.5		
SI SUM	2.96E-16		2.35E-16		1.89E-16		1.47E-16			
DI	6.95E-17	357.4	4.15E-17	580.4	2.54E-17	685.8	1.49E-17	700.0		
DI+SS	1.91E-17	397.9	1.20E-17	621.4	7.37E-18	726.1	4.29E-18	735.7		
DI+DS	1.79E-17	467.4	1.14E-17	712.4	6.28E-18	825.5	3.89E-18	835.2		
DI+SPEX	1.91E-17	367.1	1.20E-17	590.2	7.37E-18	695.6	4.29E-18	709.8		
DI+DPEX	1.35E-17	403.4	6.10E-18	625.9	4.33E-18	732.7	2.38E-18	743.6		
DI SUM	1.39E-16		8.30E-17		5.07E-17		2.98E-17			
TEX	1.71E-18	7.2	3.06E-19	7.1	1.00E-24	7.1	1.00E-24	7.1		
TEX+SS	6.11E-17	47.7	5.15E-17	48.1	4.41E-17	47.4	3.33E-17	42.8		
TEX+DS	2.76E-17	117.2	2.64E-17	139.1	1.56E-17	146.8	1.57E-17	142.3		
TEX+SPEX	6.20E-17	17.0	5.24E-17	16.9	4.43E-17	16.9	3.34E-17	16.9		
TEX+DPEX	1.06E-17	53.2	5.43E-18	52.6	7.02E-18	54.0	5.88E-18	50.6		
TEX SUM	1.63E-16		1.36E-16		1.11E-16		8.83E-17			

Table B.2: The integral cross section and associated average energy loss for SIM and NSIM processes in $S^+ + H_2$ collisions with impact energies between 1 and 2000 keV/u. (From Gharibnejad et al. (2019))

Channel	Energy 1 keV/u	10		50		75		100		
		cross section cm ²	Eloss eV	cross section cm ²	Eloss eV	cross section cm ²	Eloss eV	cross section cm ²	Eloss eV	
SI	4.53E-19	3.3	1.44E-18	8.2	6.05E-17	28.6	8.33E-17	42.6	6.75E-17	56.0
SI+SS	4.71E-20	15.6	5.40E-18	17.5	8.13E-17	59.4	1.00E-16	81.9	1.01E-16	100.5
SI+DS	4.71E-20	44.4	4.09E-18	33.2	3.56E-17	93.5	4.28E-17	120.6	5.40E-17	148.4
SI+SPEX	4.71E-20	23.8	5.69E-18	29.2	9.60E-17	49.6	1.07E-16	63.6	1.17E-16	77.0
SI+DPEX	4.71E-20	61.9	4.18E-18	67.4	2.15E-17	90.7	3.27E-17	105.0	3.68E-17	118.1
SI SUM	6.41E-19		2.08E-17		2.95E-16		3.66E-16		3.76E-16	
DI	8.61E-20	0.0	8.55E-19	27.1	4.50E-17	81.6	7.67E-17	126.8	8.84E-17	173.3
DI+SS	1.00E-24	12.3	2.16E-19	36.4	1.27E-17	112.4	2.09E-17	166.1	2.38E-17	217.8
DI+DS	1.00E-24	41.1	2.10E-19	52.1	1.01E-17	146.5	1.69E-17	204.7	2.05E-17	265.7
DI+SPEX	1.00E-24	20.4	2.16E-19	48.1	1.29E-17	102.6	2.11E-17	147.7	2.42E-17	194.3
DI+DPEX	1.00E-24	58.6	2.12E-19	86.3	8.16E-18	143.6	1.54E-17	189.1	1.82E-17	235.4
DI SUM	8.61E-20		1.71E-18		8.89E-17		1.51E-16		1.75E-16	
SC	5.31E-16	11.3	5.94E-17	16.2	3.97E-17	38.0	1.18E-17	51.6	2.14E-18	65.3
SC+SS	5.32E-17	23.6	3.99E-17	25.5	6.44E-17	68.8	2.89E-17	90.9	1.43E-17	109.8
SC+DS	2.82E-17	52.5	1.53E-17	41.2	2.59E-17	102.9	1.32E-17	129.6	8.61E-18	157.6
SC+SPEX	4.86E-17	31.8	5.94E-17	37.3	7.66E-17	59.0	3.04E-17	72.6	1.55E-17	86.2
SC+DPEX	3.56E-17	69.9	1.60E-17	75.5	1.45E-17	100.1	1.02E-17	114.0	6.14E-18	127.3
SC SUM	6.97E-16		1.90E-16		2.21E-16		9.45E-17		4.67E-17	
TEX	3.45E-20	6.2	4.47E-18	7.7	4.48E-17	7.5	6.19E-17	7.4	6.30E-17	7.3
TEX+SS	2.93E-18	18.5	2.63E-17	17.0	5.08E-17	38.3	5.04E-17	46.7	4.90E-17	51.8
TEX+DS	2.83E-18	47.3	1.88E-17	32.7	2.07E-17	72.4	1.89E-17	85.4	2.29E-17	99.7
TEX+SPEX	2.92E-18	26.6	2.81E-17	28.7	6.06E-17	28.5	5.49E-17	28.4	5.97E-17	28.2
TEX+DPEX	2.89E-18	64.8	1.92E-17	66.9	1.22E-17	69.5	1.38E-17	69.8	1.45E-17	69.3
TEX SUM	1.16E-17		9.69E-17		1.89E-16		2.00E-16		2.09E-16	
Channel	Energy 200 keV/u	500		1000		2000				
	cross section cm ²	Eloss eV								
SI	5.66E-17	103.2	2.43E-17	173.8	6.06E-18	231.1	3.55E-18	260.2		
SI+SS	9.41E-17	159.2	7.85E-17	240.6	6.20E-17	301.5	5.10E-17	329.7		
SI+DS	4.86E-17	232.2	3.72E-17	360.5	3.31E-17	456.8	2.42E-17	434.4		
SI+SPEX	9.72E-17	124.1	8.03E-17	194.8	6.51E-17	252.0	5.21E-17	281.1		
SI+DPEX	3.35E-17	164.5	3.68E-17	236.8	3.67E-17	293.2	2.71E-17	322.3		
SI SUM	3.30E-16		2.57E-16		2.03E-16		1.58E-16			
DI	8.17E-17	331.5	4.70E-17	540.3	2.83E-17	663.8	1.62E-17	649.7		
DI+SS	2.22E-17	387.5	1.28E-17	607.0	7.63E-18	734.2	4.47E-18	719.2		
DI+DS	1.91E-17	460.6	1.05E-17	726.9	6.38E-18	889.5	3.50E-18	823.9		
DI+SPEX	2.22E-17	352.5	1.28E-17	561.2	7.64E-18	684.7	4.48E-18	670.6		
DI+DPEX	1.68E-17	392.9	1.05E-17	603.2	6.64E-18	725.9	3.70E-18	711.8		
DI SUM	1.62E-16		9.36E-17		5.66E-17		3.23E-17			
SC	1.37E-20	119.7	1.00E-24	283.1	1.00E-24	555.4	1.00E-24	0.0		
SC+SS	2.24E-18	175.7	1.78E-19	349.9	2.75E-20	625.8	3.57E-21	69.6		
SC+DS	1.76E-18	248.8	1.71E-19	469.7	2.75E-20	781.1	3.57E-21	174.2		
SC+SPEX	2.24E-18	140.7	1.78E-19	304.1	2.75E-20	576.3	3.57E-21	20.9		
SC+DPEX	1.36E-18	181.1	1.70E-19	346.0	2.75E-20	617.5	3.57E-21	62.1		
SC SUM	7.61E-18		6.97E-19		1.10E-19		1.43E-20			
TEX	7.19E-17	7.1	4.56E-17	6.9	1.59E-17	6.9	7.65E-18	6.8		
TEX+SS	5.05E-17	63.1	4.69E-17	73.7	4.06E-17	77.3	3.44E-17	76.4		
TEX+DS	2.15E-17	136.2	1.67E-17	193.5	1.59E-17	232.6	1.15E-17	181.1		
TEX+SPEX	5.30E-17	28.0	4.93E-17	27.9	4.65E-17	27.8	3.63E-17	27.7		
TEX+DPEX	1.41E-17	68.5	1.64E-17	69.8	1.81E-17	69.0	1.31E-17	68.9		
TEX SUM	2.11E-16		1.75E-16		1.37E-16		1.03E-16			

Table B.3: The integral cross section and associated average energy loss for SIM and NSIM processes in $S^{2+} + H_2$ collisions with impact energies between 1 and 2000 keV/u. (From Gharibnejad et al. (2019))

Channel	Energy 1 keV/u		10		50		75		100	
	cross section cm ²	Eloss eV								
SI	4.84E-19	1.5	9.34E-19	8.0	1.26E-16	18.6	2.07E-16	27.6	2.28E-16	36.1
SI+SS	1.33E-20	15.1	2.11E-18	17.9	6.81E-17	48.5	1.08E-16	67.6	1.19E-16	83.6
SI+DS	1.90E-21	31.8	1.38E-18	38.9	3.83E-17	85.3	5.15E-17	107.0	5.06E-17	132.1
SI+SPEX	1.33E-20	29.1	2.38E-18	37.2	8.77E-17	48.1	1.36E-16	57.0	1.48E-16	65.5
SI+DPEX	1.14E-20	72.2	1.81E-18	78.8	3.43E-17	90.0	3.97E-17	98.8	4.78E-17	107.2
SI SUM	5.24E-19		8.61E-18		3.54E-16		5.42E-16		5.93E-16	
DI	1.44E-20	0.0	1.42E-19	19.3	3.27E-17	73.4	7.30E-17	113.8	9.63E-17	155.0
DI+SS	1.00E-24	13.7	3.61E-20	29.2	8.16E-18	103.3	1.85E-17	153.8	2.44E-17	202.5
DI+DS	1.00E-24	30.4	3.41E-20	50.2	6.83E-18	140.1	1.47E-17	193.2	1.86E-17	251.0
DI+SPEX	1.00E-24	27.6	3.61E-20	48.5	8.58E-18	102.9	1.94E-17	143.2	2.56E-17	184.4
DI+DPEX	1.00E-24	70.7	3.61E-20	90.1	6.53E-18	144.7	1.34E-17	185.0	1.81E-17	226.1
DI SUM	1.44E-20		2.84E-19		6.28E-17		1.39E-16		1.83E-16	
TI	1.71E-19	5.6	1.74E-19	9.6	9.03E-18	34.3	6.30E-18	57.2	3.23E-18	83.3
TI+SS	9.45E-20	19.3	4.79E-18	19.5	4.49E-17	64.2	4.08E-17	97.2	2.81E-17	130.8
TI+DS	4.56E-20	36.0	3.23E-18	40.5	3.58E-17	101.0	3.25E-17	136.6	2.25E-17	179.4
TI+SPEX	9.79E-20	33.2	4.96E-18	38.8	4.81E-17	63.8	4.29E-17	86.5	2.91E-17	112.7
TI+DPEX	9.28E-20	76.3	4.34E-18	80.4	3.41E-17	105.6	2.94E-17	128.4	2.21E-17	154.4
TI SUM	5.02E-19		1.75E-17		1.72E-16		1.52E-16		1.05E-16	
DCAI	1.69E-20	10.5	1.00E-24	23.9	3.87E-19	62.8	4.48E-19	83.2	1.33E-19	102.1
DCAI+SS	8.45E-21	24.2	1.76E-19	33.7	8.20E-19	92.6	1.18E-18	123.3	9.12E-19	149.6
DCAI+DS	8.45E-21	40.9	1.44E-19	54.7	5.96E-19	129.4	8.41E-19	162.7	6.22E-19	198.1
DCAI+SPEX	8.45E-21	38.1	1.95E-19	53.1	9.54E-19	92.2	1.26E-18	112.6	9.53E-19	131.4
DCAI+DPEX	8.45E-21	81.2	1.63E-19	94.7	5.62E-19	134.1	7.57E-19	154.4	5.80E-19	173.2
DCAI SUM	5.07E-20		6.78E-19		3.32E-18		4.49E-18		3.20E-18	
SC	1.23E-15	-41.2	7.04E-16	-36.3	2.78E-16	-14.5	9.27E-17	-0.9	3.14E-17	12.7
SC+SS	6.59E-17	-27.5	1.73E-16	-26.4	1.41E-16	15.3	7.79E-17	39.1	4.93E-17	60.2
SC+DS	6.06E-18	-10.9	5.25E-17	-5.4	7.01E-17	52.1	3.61E-17	78.5	3.01E-17	108.8
SC+SPEX	1.04E-16	-13.6	3.87E-16	-7.1	1.91E-16	14.9	9.65E-17	28.5	5.61E-17	42.1
SC+DPEX	5.81E-17	29.5	1.04E-16	34.5	6.14E-17	56.8	2.78E-17	70.3	2.92E-17	83.8
SC SUM	1.46E-15		1.42E-15		7.41E-16		3.31E-16		1.96E-16	
DC	7.50E-16	-81.4	1.13E-16	-71.6	1.01E-17	-28.1	1.38E-18	-0.8	2.17E-19	26.4
DC+SS	2.08E-16	-67.8	2.37E-16	-61.8	5.21E-17	1.8	1.84E-17	39.2	1.27E-17	73.9
DC+DS	2.14E-17	-51.1	8.06E-17	-40.8	3.98E-17	38.6	1.49E-17	78.6	1.16E-17	122.4
DC+SPEX	2.95E-16	-53.8	3.55E-16	-42.4	5.65E-17	1.4	1.91E-17	28.5	1.28E-17	55.8
DC+DPEX	1.86E-16	-10.7	1.56E-16	-0.8	3.76E-17	43.3	1.36E-17	70.3	1.15E-17	97.5
DC SUM	1.46E-15		9.42E-16		1.96E-16		6.74E-17		4.88E-17	
TEX	1.32E-20	5.6	5.06E-18	7.1	7.51E-17	7.4	1.15E-16	7.3	1.36E-16	7.2
TEX+SS	1.23E-18	19.3	1.80E-17	17.0	3.55E-17	37.3	3.83E-17	47.3	3.91E-17	54.7
TEX+DS	4.98E-19	36.0	9.71E-18	38.0	1.89E-17	74.0	1.59E-17	86.8	1.36E-17	103.2
TEX+SPEX	1.24E-18	33.2	2.09E-17	36.3	4.67E-17	36.9	5.10E-17	36.7	5.18E-17	36.6
TEX+DPEX	1.22E-18	76.3	1.48E-17	77.9	1.68E-17	78.7	1.21E-17	78.5	1.27E-17	78.3
TEX SUM	4.20E-18		6.85E-17		1.93E-16		2.32E-16		2.53E-16	

Channel	Energy 200 keV/u		500		1000		2000			
	cross section cm ²	Eloss eV								
SI	1.40E-16	64.8	7.67E-17	123.0	2.87E-17	169.6	1.09E-17	203.6		
SI+SS	1.11E-16	128.3	8.86E-17	205.8	8.42E-17	258.0	6.80E-17	300.6		
SI+DS	5.89E-17	200.4	6.00E-17	319.2	5.46E-17	396.6	2.82E-17	449.9		
SI+SPEX	1.48E-16	94.1	1.00E-16	152.2	9.05E-17	198.8	7.14E-17	232.8		
SI+DPEX	6.13E-17	135.9	4.52E-17	194.1	2.60E-17	240.5	2.16E-17	274.1		
SI SUM	5.19E-16		3.71E-16		2.84E-16		2.00E-16			
DI	9.69E-17	297.0	5.57E-17	489.3	3.28E-17	594.5	1.77E-17	639.7		
DI+SS	2.47E-17	360.6	1.43E-17	572.1	9.18E-18	682.9	5.34E-18	736.7		
DI+DS	2.05E-17	432.7	1.28E-17	685.6	8.15E-18	821.5	3.74E-18	886.1		
DI+SPEX	2.61E-17	326.3	1.47E-17	518.6	9.26E-18	623.7	5.36E-18	668.9		
DI+DPEX	2.08E-17	368.2	1.15E-17	560.5	5.76E-18	665.4	3.18E-18	710.3		
DI SUM	1.89E-16		1.09E-16		6.52E-17		3.53E-17			
TI	5.32E-20	165.6	1.00E-24	330.8	1.00E-24	372.1	1.00E-24	305.6		
TI+SS	6.47E-18	229.1	5.14E-19	413.6	4.75E-20	460.5	5.30E-21	402.6		
TI+DS	5.86E-18	301.2	5.14E-19	527.0	4.75E-20	599.1	5.23E-21	552.0		
TI+SPEX	6.53E-18	194.9	5.14E-19	360.0	4.75E-20	401.3	5.31E-21	334.8		
TI+DPEX	5.90E-18	236.8	4.99E-19	402.0	4.45E-20	443.0	5.16E-21	376.2		
TI SUM	2.48E-17		2.04E-18		1.87E-19		2.10E-20			
DCAI	4.75E-21	165.1	6.21E-22	0.0	3.91E-24	0.0	3.91E-26	0.0		
DCAI+SS	9.16E-21	228.6	1.00E-24	82.8	1.00E-24	88.4	1.00E-24	97.0		
DCAI+DS	8.42E-21	300.7	1.00E-24	196.2	1.00E-24	227.0	1.00E-24	246.3		
DCAI+SPEX	9.16E-21	194.4	1.00E-24	29.2	1.00E-24	29.2	1.00E-24	29.2		
DCAI+DPEX	8.42E-21	236.2	1.00E-24	71.2	1.00E-24	70.9	1.00E-24	70.6		
DCAI SUM	3.99E-20		6.25E-22		7.91E-24		4.04E-24			
SC	2.26E-19	67.2	1.00E-24	230.6	1.00E-24	502.9	1.00E-24	1047.5		
SC+SS	6.14E-18	130.7	4.05E-19	313.4	2.31E-20	591.3	6.44E-21	1144.5		
SC+DS	4.24E-18	202.8	4.00E-19	426.8	2.31E-20	729.9	6.42E-21	1293.8		
SC+SPEX	6.63E-18	96.5	4.05E-19	259.8	2.31E-20	532.0	6.44E-21	1076.7		
SC+DPEX	4.36E-18	138.4	3.79E-19	301.8	2.10E-20	573.8	6.21E-21	1118.0		
SC SUM	2.16E-17		1.59E-18		9.03E-20		2.55E-20			
DC	1.00E-24	135.3	1.00E-24	462.1	5.64E-22	0.0	1.00E-24	0.0		
DC+SS	4.40E-19	198.9	5.86E-21	544.9	1.00E-24	88.4	5.97E-24	97.0		
DC+DS	4.24E-19	271.0	5.86E-21	658.3	1.00E-24	227.0	5.97E-24	246.3		
DC+SPEX	4.41E-19	164.6	5.86E-21	491.3	1.00E-24	29.2	5.97E-24	29.2		
DC+DPEX	4.25E-19	206.5	5.81E-21	533.3	1.00E-24	70.9	5.97E-24	70.6		
DC SUM	1.73E-18		2.34E-20		5.68E-22		2.49E-23			
TEX	1.56E-16	7.1	1.20E-16	6.8	6.24E-17	6.6	2.74E-17	6.5		
TEX+SS	4.20E-17	70.7	3.92E-17	89.6	4.25E-17	95.0	3.43E-17	103.5		
TEX+DS	1.93E-17	142.8	2.34E-17	203.0	2.24E-17	233.6	1.26E-17	252.8		
TEX+SPEX	6.33E-17	36.4	4.77E-17	36.0	4.92E-17	35.8	4.72E-17	35.7		
TEX+DPEX	2.03E-17	78.3	1.66E-17	78.0	9.49E-18	77.5	9.40E-18	77.1		
TEX SUM	3.01E-16		2.47E-16		1.86E-16		1.31E-16			

Table B.4: The integral cross section and associated average energy loss for SIM and NSIM processes in $S^{3+} + H_2$ collisions with impact energies between 1 and 2000 keV/u. (From Gharibnejad et al. (2019))

Channel	Energy 1 keV/u		10		50		75		100	
	cross section cm ²	Eloss eV								
SI	3.24E-19	3.0	9.48E-19	8.9	2.46E-16	15.5	4.47E-16	19.3	5.58E-16	25.8
SI+SS	1.44E-20	16.9	1.08E-18	20.8	6.09E-17	43.8	1.03E-16	58.2	1.17E-16	74.0
SI+DS	8.66E-21	3.0	5.13E-19	39.7	2.52E-17	79.0	4.14E-17	97.1	4.68E-17	116.2
SI+SPEX	1.44E-20	38.2	1.17E-18	45.0	7.95E-17	52.9	1.48E-16	56.5	1.39E-16	62.9
SI+DPEX	1.15E-20	105.9	6.39E-19	113.4	1.82E-17	127.4	2.69E-17	131.9	2.91E-17	139.2
SI SUM	3.73E-19		4.35E-18		4.30E-16		7.66E-16		8.90E-16	
DI	3.25E-21	0.0	3.23E-20	32.3	2.00E-17	63.6	6.60E-17	100.7	1.07E-16	138.3
DI+SS	1.00E-24	13.9	8.81E-21	44.2	4.82E-18	91.8	1.53E-17	139.6	2.31E-17	186.5
DI+DS	1.00E-24	0.0	5.87E-21	63.1	3.31E-18	127.1	1.04E-17	178.6	1.59E-17	228.6
DI+SPEX	1.00E-24	35.2	8.81E-21	68.4	5.20E-18	101.0	1.70E-17	137.9	2.45E-17	175.4
DI+DPEX	1.00E-24	102.9	8.81E-21	136.8	2.69E-18	175.4	8.33E-18	213.4	1.24E-17	251.6
DI SUM	3.25E-21		6.46E-20		3.60E-17		1.17E-16		1.83E-16	
TI	1.14E-19	3.6	3.66E-19	9.9	3.12E-17	28.9	2.80E-17	49.7	2.15E-17	73.0
TI+SS	4.11E-20	17.4	2.87E-18	21.9	5.17E-17	57.2	5.74E-17	88.6	4.39E-17	121.2
TI+DS	1.44E-20	3.6	1.48E-18	40.8	3.22E-17	92.4	3.77E-17	127.6	3.13E-17	163.3
TI+SPEX	4.52E-20	38.8	3.04E-18	46.0	5.76E-17	66.3	6.40E-17	87.0	4.62E-17	110.1
TI+DPEX	3.90E-20	106.5	1.76E-18	114.5	2.62E-17	140.8	2.98E-17	162.4	2.50E-17	186.4
TI SUM	2.54E-19		9.52E-18		1.99E-16		2.17E-16		1.68E-16	
DCAI	8.26E-20	8.8	5.38E-19	20.6	1.29E-17	61.0	3.98E-18	83.6	9.84E-19	100.8
DCAI+SS	1.20E-20	22.6	1.49E-18	32.5	8.58E-18	89.3	4.75E-18	122.5	1.36E-18	149.0
DCAI+DS	8.55E-21	8.8	6.25E-19	51.4	4.69E-18	124.5	2.79E-18	161.5	9.63E-19	191.2
DCAI+SPEX	1.20E-20	44.0	1.54E-18	56.7	1.02E-17	98.4	5.58E-18	120.8	1.42E-18	138.0
DCAI+DPEX	1.20E-20	111.7	8.53E-19	125.1	3.77E-18	172.9	2.19E-18	196.2	7.40E-19	214.2
DCAI SUM	1.27E-19		5.05E-18		4.01E-17		1.93E-17		5.47E-18	
SC	1.58E-15	-47.9	1.25E-15	-43.0	7.47E-16	-21.2	3.18E-16	-7.6	1.31E-16	6.0
SC+SS	4.56E-17	-34.0	1.23E-16	-31.1	1.54E-16	7.1	9.68E-17	31.3	5.35E-17	54.2
SC+DS	3.84E-18	-47.9	2.35E-17	-12.2	5.06E-17	42.3	3.39E-17	70.3	2.11E-17	96.4
SC+SPEX	5.46E-17	-12.7	2.19E-16	-6.9	2.14E-16	16.2	1.40E-16	29.6	6.40E-17	43.2
SC+DPEX	1.59E-17	55.0	3.16E-17	61.6	3.41E-17	90.7	2.04E-17	105.1	1.26E-17	119.4
SC SUM	1.70E-15		1.65E-15		1.20E-15		6.09E-16		2.82E-16	
DC	1.53E-15	-94.8	4.55E-16	-85.0	4.82E-17	-41.5	7.71E-18	-14.2	2.03E-18	13.0
DC+SS	2.55E-16	-81.0	3.22E-16	-73.1	9.09E-17	-13.2	3.59E-17	24.7	1.38E-17	61.2
DC+DS	2.01E-17	-94.8	6.62E-17	-54.2	5.32E-17	22.1	2.43E-17	63.6	1.07E-17	103.4
DC+SPEX	2.98E-16	-59.6	4.66E-16	-48.9	1.02E-16	-4.1	3.91E-17	23.0	1.42E-17	50.2
DC+DPEX	9.12E-17	8.1	9.04E-17	19.5	4.23E-17	70.4	1.90E-17	98.4	8.75E-18	126.4
DC SUM	2.19E-15		1.40E-15		3.37E-16		1.26E-16		4.95E-17	
TEX	9.30E-21	5.5	7.31E-18	6.7	1.27E-16	7.3	1.77E-16	7.2	2.48E-16	7.2
TEX+SS	4.77E-19	19.4	1.28E-17	18.6	2.67E-17	35.6	2.75E-17	46.1	2.70E-17	55.4
TEX+DS	1.63E-19	5.5	4.63E-18	37.5	9.83E-18	70.8	8.81E-18	85.1	8.51E-18	97.6
TEX+SPEX	4.82E-19	40.7	1.45E-17	42.8	3.65E-17	44.7	4.19E-17	44.4	3.37E-17	44.4
TEX+DPEX	3.88E-19	108.4	6.09E-18	111.3	6.71E-18	119.2	5.10E-18	119.9	4.24E-18	120.6
TEX SUM	1.52E-18		4.53E-17		2.07E-16		2.60E-16		3.21E-16	

Channel	Energy 200 keV/u		500		1000		2000			
	cross section cm ²	Eloss eV								
SI	3.89E-16	42.6	1.62E-16	80.9	8.47E-17	134.2	3.00E-17	157.6		
SI+SS	1.42E-16	113.2	1.26E-16	179.3	1.07E-16	244.9	7.88E-17	272.3		
SI+DS	5.67E-17	182.8	5.46E-17	283.2	4.28E-17	381.9	3.39E-17	632.3		
SI+SPEX	1.96E-16	79.5	1.53E-16	117.8	1.07E-16	171.0	8.74E-17	194.4		
SI+DPEX	2.95E-17	155.8	3.78E-17	193.6	2.94E-17	246.9	2.49E-17	269.7		
SI SUM	8.13E-16		5.33E-16		3.71E-16		2.55E-16			
DI	1.26E-16	258.1	6.83E-17	440.8	3.85E-17	550.2	2.03E-17	604.2		
DI+SS	3.15E-17	328.8	1.84E-17	539.2	1.11E-17	660.9	6.00E-18	718.9		
DI+DS	2.25E-17	398.4	1.36E-17	643.0	7.89E-18	797.8	4.21E-18	1078.8		
DI+SPEX	3.46E-17	295.1	1.93E-17	477.6	1.11E-17	587.0	6.11E-18	640.9		
DI+DPEX	1.69E-17	371.4	1.14E-17	553.5	6.45E-18	662.9	3.48E-18	716.2		
DI SUM	2.31E-16		1.31E-16		7.50E-17		4.01E-17			
TI	7.76E-19	159.2	3.30E-20	259.2	8.24E-22	361.1	2.46E-22	273.8		
TI+SS	1.12E-17	229.9	5.85E-19	357.6	5.47E-20	471.8	6.74E-21	388.5		
TI+DS	9.19E-18	299.4	5.62E-19	461.4	5.38E-20	608.8	6.55E-21	748.4		
TI+SPEX	1.15E-17	196.2	5.88E-19	296.0	5.47E-20	397.9	6.74E-21	310.5		
TI+DPEX	7.35E-18	272.4	5.31E-19	371.9	5.10E-20	473.8	6.32E-21	385.8		
TI SUM	4.00E-17		2.30E-18		2.15E-19		2.66E-20			
DCAI	1.00E-24	170.4	2.46E-21	0.0	1.55E-23	0.0	1.55E-25	0.0		
DCAI+SS	4.44E-20	241.1	1.00E-24	98.4	1.00E-24	110.6	1.00E-24	114.7		
DCAI+DS	3.46E-20	310.7	1.00E-24	202.2	1.00E-24	247.6	1.00E-24	474.6		
DCAI+SPEX	4.94E-20	207.4	1.00E-24	36.8	1.00E-24	36.8	1.00E-24	36.8		
DCAI+DPEX	2.96E-20	283.7	1.00E-24	112.7	1.00E-24	112.7	1.00E-24	112.0		
DCAI SUM	1.58E-19		2.46E-21		1.95E-23		4.15E-24			
SC	2.30E-18	60.5	1.00E-24	223.9	1.00E-24	496.2	1.00E-24	1040.8		
SC+SS	1.02E-17	131.2	4.99E-19	322.2	6.08E-20	606.8	6.94E-21	1155.5		
SC+DS	5.24E-18	200.7	4.32E-19	426.1	5.96E-20	743.8	6.94E-21	1515.4		
SC+SPEX	1.19E-17	97.4	4.99E-19	260.7	6.08E-20	533.0	6.94E-21	1077.5		
SC+DPEX	2.99E-18	173.7	3.59E-19	336.6	5.38E-20	608.9	6.69E-21	1152.8		
SC SUM	3.26E-17		1.79E-18		2.35E-19		2.75E-20			
DC	1.98E-21	121.9	1.00E-24	448.7	1.00E-24	993.3	1.18E-23	0.0		
DC+SS	8.35E-19	192.6	6.95E-21	547.1	1.66E-22	1104.0	1.00E-24	114.7		
DC+DS	7.57E-19	262.2	6.80E-21	651.0	1.66E-22	1240.9	1.00E-24	474.6		
DC+SPEX	8.40E-19	158.9	6.95E-21	485.5	1.66E-22	1030.1	1.00E-24	36.8		
DC+DPEX	6.56E-19	235.2	6.50E-21	561.4	1.58E-22	1106.0	1.00E-24	112.0		
DC SUM	3.09E-18		2.72E-20		6.57E-22		1.58E-23			
TEX	3.04E-16	7.2	2.40E-16	6.7	1.57E-16	6.5	7.58E-17	6.2		
TEX+SS	3.90E-17	77.9	4.80E-17	105.1	4.74E-17	117.1	3.80E-17	120.9		
TEX+DS	1.29E-17	147.4	1.74E-17	208.9	1.43E-17	254.1	1.33E-17	480.8		
TEX+SPEX	5.97E-17	44.2	6.33E-17	43.5	4.78E-17	43.3	4.63E-17	43.0		
TEX+DPEX	6.29E-18	120.5	1.18E-17	119.4	9.43E-18	119.2	9.65E-18	118.2		
TEX SUM	4.22E-16		3.81E-16		2.76E-16		1.83E-16			

Table B.5: The integral cross section and associated average energy loss for SIM and NSIM processes in $S^{4+} + H_2$ collisions with impact energies between 1 and 2000 keV/u. (From Gharibnejad et al. (2019))

Channel	Energy 1 keV/u		10		50		75		100	
	cross section cm ²	Eloss eV								
SI	2.89E-19	1.5	2.49E-18	8.8	3.21E-16	7.3	5.72E-16	13.9	1.05E-15	19.6
SI+SS	7.05E-21	15.6	7.57E-20	23.8	2.29E-17	34.5	3.32E-17	50.9	6.23E-17	66.5
SI+DS	1.00E-24	1.5	3.95E-20	67.7	1.13E-17	72.9	1.61E-17	88.1	2.94E-17	115.2
SI+SPEX	7.05E-21	56.4	1.23E-19	62.8	3.87E-17	64.2	5.20E-17	70.9	1.03E-16	76.5
SI+DPEX	7.05E-21	125.7	6.27E-20	133.8	1.17E-17	135.6	1.35E-17	143.6	2.50E-17	149.2
SI SUM	3.10E-19		2.79E-18		4.06E-16		6.87E-16		1.27E-15	
DI	9.07E-22	0.0	1.71E-20	33.6	1.20E-17	54.4	6.15E-17	87.6	1.23E-16	120.6
DI+SS	1.00E-24	14.1	2.25E-22	48.6	1.82E-18	81.5	7.49E-18	124.7	1.46E-17	167.5
DI+DS	1.00E-24	0.0	1.13E-22	92.5	1.15E-18	120.0	4.83E-18	161.9	9.98E-18	216.3
DI+SPEX	1.00E-24	54.9	3.37E-22	87.6	2.36E-18	111.2	9.42E-18	144.6	1.86E-17	177.5
DI+DPEX	1.00E-24	124.3	2.25E-22	158.6	1.18E-18	182.7	4.37E-18	217.3	9.01E-18	250.3
DI SUM	9.11E-22		1.80E-20		1.85E-17		8.76E-17		1.75E-16	
TI	1.69E-19	4.0	4.99E-18	18.0	7.39E-17	24.6	1.12E-16	43.6	8.39E-17	63.8
TI+SS	2.14E-20	18.2	2.30E-19	33.0	3.45E-17	51.8	5.07E-17	80.7	4.72E-17	110.8
TI+DS	1.00E-24	4.0	1.17E-19	76.9	2.08E-17	90.3	3.18E-17	117.9	3.17E-17	159.5
TI+SPEX	3.06E-20	59.0	3.44E-19	72.0	4.62E-17	81.5	6.47E-17	100.6	5.96E-17	120.7
TI+DPEX	1.83E-20	128.3	1.86E-19	143.0	2.15E-17	153.0	2.81E-17	173.4	2.86E-17	193.5
TI SUM	2.39E-19		5.87E-18		1.97E-16		2.87E-16		2.51E-16	
DCAI	2.32E-19	8.9	5.51E-18	22.0	5.24E-17	66.5	3.04E-17	92.5	7.77E-18	107.7
DCAI+SS	3.51E-21	23.1	1.88E-19	37.0	1.14E-17	93.6	8.94E-18	129.5	3.08E-18	154.7
DCAI+DS	1.00E-24	8.9	8.75E-20	80.9	6.41E-18	132.1	5.31E-18	166.7	2.02E-18	203.4
DCAI+SPEX	7.03E-21	63.9	3.39E-19	76.0	1.63E-17	123.3	1.21E-17	149.4	3.91E-18	164.6
DCAI+DPEX	3.51E-21	133.2	1.48E-19	147.0	6.69E-18	194.8	4.59E-18	222.2	1.82E-18	237.4
DCAI SUM	2.46E-19		6.27E-18		9.32E-17		6.13E-17		1.86E-17	
SC	1.91E-15	-47.9	1.73E-15	-43.0	1.47E-15	26.9	8.53E-16	40.5	3.70E-16	6.0
SC+SS	1.52E-17	-33.8	2.84E-17	-28.0	7.16E-17	54.1	5.13E-17	77.6	3.56E-17	53.0
SC+DS	1.45E-19	-47.9	9.68E-18	15.9	2.76E-17	92.6	1.95E-17	114.8	1.47E-17	101.7
SC+SPEX	4.09E-17	7.0	1.03E-16	11.1	1.40E-16	83.8	9.12E-17	97.5	6.35E-17	62.9
SC+DPEX	1.02E-17	76.4	1.96E-17	82.0	2.91E-17	155.2	1.54E-17	170.3	1.21E-17	135.7
SC SUM	1.98E-15		1.89E-15		1.74E-15		1.03E-15		4.96E-16	
DC	2.53E-15	-94.8	1.21E-15	-85.0	1.85E-16	54.8	5.64E-17	82.1	1.51E-17	13.0
DC+SS	1.54E-16	-80.7	1.45E-16	-70.0	1.00E-16	82.0	4.75E-17	119.1	2.17E-17	59.9
DC+DS	1.15E-18	-94.8	5.10E-17	-26.1	5.71E-17	120.5	2.99E-17	156.3	1.53E-17	108.7
DC+SPEX	3.99E-16	-39.9	4.93E-16	-31.0	1.38E-16	111.7	5.89E-17	139.0	2.60E-17	69.9
DC+DPEX	1.01E-16	29.4	1.00E-16	40.0	5.90E-17	183.2	2.63E-17	211.8	1.40E-17	142.7
DC SUM	3.19E-15		2.00E-15		5.39E-16		2.19E-16		9.21E-17	
TEX	6.61E-21	5.0	9.45E-18	6.4	1.68E-16	7.2	2.56E-16	7.2	3.39E-16	7.3
TEX+SS	1.94E-19	19.1	4.59E-18	21.4	8.86E-18	34.4	8.54E-18	44.2	9.33E-18	54.2
TEX+DS	7.64E-21	5.0	1.56E-18	65.3	3.81E-18	72.8	3.19E-18	81.4	3.50E-18	103.0
TEX+SPEX	2.32E-19	59.9	9.87E-18	60.5	1.67E-17	64.0	1.58E-17	64.2	1.80E-17	64.2
TEX+DPEX	1.68E-19	129.3	3.23E-18	131.4	4.00E-18	135.5	2.46E-18	136.9	2.74E-18	137.0
TEX SUM	6.08E-19		2.87E-17		2.01E-16		2.86E-16		3.73E-16	

Channel	Energy 200 keV/u		500		1000		2000			
	cross section cm ²	Eloss eV								
SI	8.00E-16	30.2	4.65E-16	53.2	2.43E-16	78.8	1.06E-16	117.4		
SI+SS	7.06E-17	107.9	7.74E-17	172.4	7.55E-17	228.6	7.66E-17	280.9		
SI+DS	3.69E-17	189.3	5.20E-17	291.0	4.22E-17	506.2	3.28E-17	308.2		
SI+SPEX	1.09E-16	86.9	1.10E-16	109.5	9.63E-17	134.9	9.12E-17	173.2		
SI+DPEX	2.31E-17	159.2	4.43E-17	181.9	4.14E-17	207.3	2.76E-17	245.7		
SI SUM	1.04E-15		7.49E-16		4.98E-16		3.34E-16			
DI	1.86E-16	218.0	1.03E-16	374.3	5.28E-17	474.7	2.32E-17	547.1		
DI+SS	2.77E-17	295.7	1.86E-17	493.5	1.12E-17	624.5	6.30E-18	710.7		
DI+DS	2.04E-17	377.1	1.55E-17	612.0	8.53E-18	902.0	3.99E-18	737.9		
DI+SPEX	3.31E-17	274.7	2.16E-17	430.6	1.23E-17	530.7	6.70E-18	602.9		
DI+DPEX	1.58E-17	347.0	1.44E-17	503.0	8.43E-18	603.1	3.55E-18	675.5		
DI SUM	2.83E-16		1.73E-16		9.33E-17		4.37E-17			
TI	8.96E-18	136.6	6.34E-20	271.9	5.54E-21	333.1	3.74E-22	228.3		
TI+SS	1.60E-17	214.2	7.82E-19	391.1	6.89E-20	482.9	5.83E-21	391.9		
TI+DS	1.27E-17	295.6	7.45E-19	509.7	6.70E-20	760.4	5.58E-21	419.1		
TI+SPEX	1.81E-17	193.2	7.94E-19	328.2	6.97E-20	389.1	5.86E-21	284.1		
TI+DPEX	1.01E-17	265.6	7.36E-19	400.6	6.68E-20	461.5	5.46E-21	356.6		
TI SUM	6.59E-17		3.12E-18		2.78E-19		2.31E-20			
DCAI	1.08E-19	190.8	9.06E-21	0.0	5.70E-23	0.0	5.70E-25	0.0		
DCAI+SS	1.23E-19	268.4	1.00E-24	119.2	1.00E-24	149.8	1.00E-24	163.5		
DCAI+DS	1.10E-19	349.8	1.00E-24	237.7	1.00E-24	427.3	1.00E-24	190.8		
DCAI+SPEX	1.43E-19	247.4	1.00E-24	56.3	1.00E-24	56.0	1.00E-24	55.8		
DCAI+DPEX	9.74E-20	319.8	1.00E-24	128.7	1.00E-24	128.4	1.00E-24	128.3		
DCAI SUM	5.81E-19		9.06E-21		6.10E-23		4.57E-24			
SC	1.99E-17	60.5	1.33E-20	223.9	1.00E-24	496.2	1.00E-24	1040.8		
SC+SS	9.34E-18	138.2	5.39E-19	343.0	6.04E-20	646.0	7.04E-21	1204.3		
SC+DS	5.19E-18	219.5	4.65E-19	461.6	5.77E-20	923.5	6.88E-21	1231.6		
SC+SPEX	1.33E-17	117.2	5.71E-19	280.1	6.05E-20	552.2	7.04E-21	1096.6		
SC+DPEX	3.18E-18	189.5	4.31E-19	352.5	5.75E-20	624.6	6.55E-21	1169.1		
SC SUM	5.09E-17		2.02E-18		2.36E-19		2.75E-20			
DC	1.29E-19	121.9	1.00E-24	448.7	1.00E-24	0.0	1.00E-24	0.0		
DC+SS	1.51E-18	199.6	1.16E-20	567.9	2.45E-22	149.8	4.40E-24	163.5		
DC+DS	1.33E-18	281.0	1.14E-20	686.4	2.45E-22	427.3	4.40E-24	190.8		
DC+SPEX	1.58E-18	178.6	1.16E-20	505.0	2.45E-22	56.0	4.40E-24	55.8		
DC+DPEX	1.14E-18	250.9	1.12E-20	577.4	2.45E-22	128.4	4.40E-24	128.3		
DC SUM	5.69E-18		4.58E-20		9.81E-22		1.86E-23			
TEX	5.06E-16	7.2	5.00E-16	6.9	3.32E-16	6.5	1.84E-16	6.2		
TEX+SS	1.49E-17	84.9	2.19E-17	126.1	2.63E-17	156.3	2.97E-17	169.7		
TEX+DS	6.90E-18	166.2	1.41E-17	244.6	1.38E-17	433.8	1.13E-17	197.0		
TEX+SPEX	2.46E-17	63.9	3.49E-17	63.2	3.60E-17	62.5	3.86E-17	62.0		
TEX+DPEX	3.32E-18	136.2	1.15E-17	135.6	1.36E-17	134.9	9.40E-18	134.5		
TEX SUM	5.56E-16		5.82E-16		4.22E-16		2.73E-16			

Table B.6: The integral cross section and associated average energy loss for SIM and NSIM processes in $S^{5+} + H_2$ collisions with impact energies between 1 and 2000 keV/u. (From Gharibnejad et al. (2019))

Channel	Energy 1 keV/u		10		50		75		100	
	cross section cm ²	Eloss eV								
SI	1.81E-19	1.6	7.67E-19	9.3	3.37E-16	7.5	9.56E-16	12.6	1.32E-15	18.3
SI+SS	5.69E-21	17.6	3.55E-19	27.9	1.75E-17	35.3	4.34E-17	48.1	6.31E-17	64.6
SI+DS	1.00E-24	1.6	1.62E-20	9.3	5.44E-19	138.2	1.56E-18	108.5	2.59E-18	143.0
SI+SPEX	6.83E-21	59.0	7.59E-19	68.2	2.54E-17	71.4	6.65E-17	77.4	9.77E-17	83.1
SI+DPEX	1.00E-24	322.6	3.23E-20	332.5	1.31E-18	340.2	2.18E-18	351.3	4.42E-18	370.9
SI SUM	1.94E-19		1.93E-18		3.82E-16		1.07E-15		1.49E-15	
DI	1.24E-21	0.0	2.47E-20	36.6	6.13E-18	43.8	4.48E-17	77.2	1.25E-16	145.5
DI+SS	1.00E-24	16.0	1.00E-24	55.2	8.10E-19	71.6	5.56E-18	112.7	1.54E-17	191.7
DI+DS	1.00E-24	0.0	1.00E-24	36.6	3.41E-20	174.5	4.19E-19	173.1	1.39E-18	270.2
DI+SPEX	1.00E-24	57.4	1.00E-24	95.5	1.05E-18	107.7	7.06E-18	141.9	1.96E-17	210.3
DI+DPEX	1.00E-24	321.1	1.00E-24	359.8	5.97E-20	376.5	5.95E-19	415.8	2.09E-18	498.1
DI SUM	1.24E-21		2.47E-20		8.08E-18		5.84E-17		1.63E-16	
TI	1.49E-19	2.7	7.17E-19	10.5	9.16E-17	21.5	1.73E-16	38.9	1.62E-16	58.1
TI+SS	1.74E-20	18.7	1.07E-18	29.1	3.40E-17	49.3	6.57E-17	74.4	7.76E-17	104.4
TI+DS	2.18E-21	2.7	8.26E-20	10.5	1.53E-18	152.2	4.47E-18	134.8	6.96E-18	182.9
TI+SPEX	1.89E-20	60.1	1.82E-18	69.4	4.39E-17	85.4	8.47E-17	103.7	9.85E-17	123.0
TI+DPEX	6.54E-21	323.8	2.89E-19	333.7	2.99E-18	354.2	6.38E-18	377.6	1.09E-17	410.7
TI SUM	1.94E-19		3.98E-18		1.74E-16		3.34E-16		3.56E-16	
DCAI	4.07E-18	12.2	1.22E-17	25.1	1.59E-16	76.9	1.02E-16	109.5	3.29E-17	139.2
DCAI+SS	3.67E-19	28.2	3.16E-18	43.7	2.92E-17	104.7	2.60E-17	145.1	1.22E-17	185.4
DCAI+DS	4.53E-20	12.2	1.80E-19	25.1	1.10E-18	207.6	1.66E-18	205.4	6.73E-19	263.9
DCAI+SPEX	5.65E-19	69.6	7.48E-18	84.0	4.12E-17	140.8	3.46E-17	174.3	1.65E-17	204.0
DCAI+DPEX	1.12E-19	333.3	5.07E-19	348.3	1.87E-18	409.6	2.30E-18	448.2	1.05E-18	491.7
DCAI SUM	5.16E-18		2.35E-17		2.32E-16		1.67E-16		6.33E-17	
SC	2.21E-15	-47.9	2.02E-15	-43.0	2.07E-15	-21.2	1.35E-15	-7.6	6.55E-16	6.0
SC+SS	8.74E-18	-31.9	1.87E-17	-24.4	6.25E-17	6.6	5.25E-17	27.9	4.35E-17	52.3
SC+DS	6.13E-19	-47.9	9.64E-19	-43.0	8.39E-19	109.5	7.75E-19	88.3	4.85E-19	130.7
SC+SPEX	2.93E-17	9.5	7.59E-17	15.9	1.11E-16	42.7	9.31E-17	57.2	7.62E-17	70.8
SC+DPEX	1.76E-18	273.2	2.93E-18	280.2	1.71E-18	311.5	1.12E-18	331.1	9.48E-19	358.6
SC SUM	2.25E-15		2.12E-15		2.25E-15		1.50E-15		7.76E-16	
DC	3.28E-15	-47.9	1.56E-15	-43.0	2.35E-16	-21.2	8.18E-17	-7.6	2.41E-17	6.0
DC+SS	1.19E-16	-31.9	1.42E-16	-24.4	1.50E-16	6.6	8.14E-17	27.9	4.32E-17	52.3
DC+DS	7.48E-18	-47.9	8.29E-18	-43.0	6.23E-18	109.5	5.15E-18	88.3	3.62E-18	130.7
DC+SPEX	3.95E-16	9.5	5.29E-16	15.9	1.97E-16	42.7	1.02E-16	57.2	5.21E-17	70.8
DC+DPEX	2.23E-17	273.2	2.24E-17	280.2	1.15E-17	311.5	7.04E-18	331.1	5.89E-18	358.6
DC SUM	3.82E-15		2.26E-15		6.00E-16		2.77E-16		1.29E-16	
TEX	7.67E-21	5.0	9.06E-18	5.8	1.79E-16	7.1	2.78E-16	7.2	3.80E-16	7.2
TEX+SS	8.71E-20	21.0	2.46E-18	24.4	5.44E-18	34.9	5.64E-18	42.7	6.99E-18	53.5
TEX+DS	7.91E-21	5.0	1.60E-19	5.8	1.29E-19	137.8	1.00E-24	103.1	1.00E-24	131.9
TEX+SPEX	1.27E-19	62.4	7.61E-18	64.7	9.58E-18	71.0	1.11E-17	72.0	1.42E-17	72.0
TEX+DPEX	2.37E-20	326.1	3.04E-19	329.0	2.07E-19	339.8	5.73E-20	345.9	8.70E-20	359.8
TEX SUM	2.53E-19		1.96E-17		1.94E-16		2.95E-16		4.01E-16	

Channel	Energy 200 keV/u		500		1000		2000				
	cross section cm ²	Eloss eV									
SI	1.39E-15	26.2	8.77E-16	33.7	4.83E-16	57.3	1.93E-16	82.5			
SI+SS	9.20E-17	105.4	1.13E-16	165.6	1.19E-16	222.9	1.17E-16	292.6			
SI+DS	6.51E-18	218.1	1.09E-17	325.1	1.01E-17	520.0	1.23E-17	597.6			
SI+SPEX	1.29E-16	90.5	1.60E-16	97.4	1.29E-16	120.8	1.34E-16	145.7			
SI+DPEX	5.41E-18	417.2	8.80E-18	518.5	1.01E-17	564.3	1.06E-17	582.2			
SI SUM	1.62E-15		1.17E-15		7.51E-16		4.67E-16				
DI	2.64E-16	183.6	1.54E-16	311.7	7.42E-17	391.2	3.01E-17	481.5			
DI+SS	3.78E-17	262.8	3.11E-17	443.5	1.90E-17	556.9	1.00E-17	691.6			
DI+DS	6.83E-18	375.5	7.89E-18	603.0	4.04E-18	853.9	2.12E-18	996.6			
DI+SPEX	4.47E-17	247.8	3.65E-17	375.3	1.97E-17	454.7	1.06E-17	544.7			
DI+DPEX	5.81E-18	574.6	6.71E-18	796.4	4.04E-18	898.3	1.86E-18	981.2			
DI SUM	3.59E-16		2.36E-16		1.21E-16		5.47E-17				
TI	2.68E-17	123.7	2.78E-19	242.4	2.27E-20	240.4	1.05E-21	392.9			
TI+SS	3.06E-17	202.9	1.60E-18	374.3	1.13E-19	406.0	7.46E-21	603.0			
TI+DS	6.51E-18	315.6	6.92E-19	533.8	4.86E-20	703.1	3.35E-21	908.0			
TI+SPEX	3.45E-17	187.9	1.67E-18	306.1	1.13E-19	303.9	7.53E-21	456.1			
TI+DPEX	5.61E-18	514.7	5.49E-19	727.2	4.86E-20	747.4	2.91E-21	892.6			
TI SUM	1.04E-16		4.79E-18		3.46E-19		2.23E-20				
DCAI	3.66E-19	227.6	1.00E-24	453.7	2.34E-22	0.0	2.34E-24	0.0			
DCAI+SS	8.24E-19	306.8	1.86E-20	585.5	1.00E-24	165.7	1.00E-24	210.0			
DCAI+DS	1.82E-19	419.5	1.00E-24	745.0	1.00E-24	462.7	1.00E-24	515.1			
DCAI+SPEX	8.73E-19	291.8	1.86E-20	517.3	1.00E-24	63.5	1.00E-24	63.1			
DCAI+DPEX	1.45E-19	618.6	1.00E-24	938.4	1.00E-24	507.1	1.00E-24	499.7			
DCAI SUM	2.39E-18		3.72E-20		2.38E-22		6.34E-24				
SC	4.68E-17	60.5	5.85E-20	223.9	1.00E-24	496.2	1.00E-24	1040.8			
SC+SS	1.38E-17	139.7	9.02E-19	355.7	9.12E-20	661.8	1.01E-20	1250.8			
SC+DS	4.93E-19	252.4	1.57E-19	515.2	2.63E-20	958.9	3.74E-21	1555.8			
SC+SPEX	1.87E-17	124.7	9.86E-19	287.5	9.12E-20	559.7	1.01E-20	1103.9			
SC+DPEX	3.65E-19	451.5	1.26E-19	708.6	2.63E-20	1003.2	3.18E-21	1540.5			
SC SUM	8.02E-17		2.23E-18		2.35E-19		2.71E-20				
DC	4.50E-19	60.5	1.00E-24	223.9	1.00E-24	496.2	1.00E-24	0.0			
DC+SS	3.47E-18	139.7	1.97E-20	355.7	3.27E-22	661.8	1.32E-23	210.0			
DC+DS	1.06E-18	252.4	1.20E-20	515.2	1.88E-22	958.9	1.00E-24	515.1			
DC+SPEX	3.65E-18	124.7	2.01E-20	287.5	3.27E-22	559.7	1.32E-23	63.1			
DC+DPEX	9.13E-19	451.5	1.08E-20	708.6	1.88E-22	1003.2	1.00E-24	499.7			
DC SUM	9.54E-18		6.26E-20		1.03E-21		2.94E-23				
TEX	6.05E-16	7.3	6.96E-16	7.0	5.33E-16	6.7	3.04E-16	6.3			
TEX+SS	4.87E-18	86.5	2.58E-17	138.9	3.37E-17	172.4	4.05E-17	216.3			
TEX+DS	3.75E-19	199.2	1.84E-18	298.3	2.66E-18	469.4	3.95E-18	521.4			
TEX+SPEX	2.74E-17	71.5	3.76E-17	70.6	3.70E-17	70.2	4.89E-17	69.5			
TEX+DPEX	2.81E-19	398.3	1.46E-18	491.7	2.66E-18	513.8	3.33E-18	506.0			
TEX SUM	6.38E-16		7.63E-16		6.09E-16		4.01E-16				

Table B.7: The integral cross section and associated average energy loss for SIM and NSIM processes in $S^{6+} + H_2$ collisions with impact energies between 1 and 2000 keV/u. (From Gharibnejad et al. (2019))

Channel	Energy 1 keV/u		10		50		75		100	
	cross section cm ²	Eloss eV								
SI	1.21E-19	1.1	1.61E-18	9.2	2.02E-16	12.4	9.10E-16	13.4	1.51E-15	19.1
SI+SS	1.00E-24	1.1	1.76E-20	43.5	2.96E-19	78.6	2.20E-18	84.9	3.82E-18	94.4
SI+DS	2.03E-21	1.1	2.73E-20	9.2	1.36E-19	12.4	5.34E-19	13.4	9.48E-19	225.9
SI+SPEX	3.38E-21	205.6	1.27E-19	200.7	1.11E-18	214.2	3.30E-18	219.5	5.95E-18	227.8
SI+DPEX	2.03E-21	508.4	5.37E-20	518.6	2.84E-19	531.3	1.19E-18	535.0	1.95E-18	560.4
SI SUM	1.28E-19		1.84E-18		2.04E-16		9.17E-16		1.52E-15	
DI	2.15E-22	0.0	4.27E-21	24.9	3.32E-18	41.7	3.98E-17	480.9	1.40E-16	96.7
DI+SS	1.00E-24	0.0	1.00E-24	59.3	3.29E-20	107.8	4.46E-19	552.4	1.26E-18	172.0
DI+DS	1.00E-24	0.0	1.00E-24	24.9	1.83E-20	41.7	1.26E-19	480.9	3.38E-19	303.4
DI+SPEX	1.00E-24	204.5	1.00E-24	216.5	5.48E-20	243.5	6.16E-19	687.0	1.82E-18	305.3
DI+DPEX	1.00E-24	507.3	1.00E-24	534.4	3.29E-20	560.6	2.53E-19	1002.5	7.07E-19	637.9
DI SUM	2.19E-22		4.27E-21		3.46E-18		4.12E-17		1.44E-16	
TI	1.49E-19	2.0	2.98E-18	10.9	1.38E-16	19.4	3.30E-16	35.6	4.15E-16	53.3
TI+SS	1.00E-24	2.0	3.87E-20	45.3	1.51E-18	85.6	6.76E-18	107.1	9.44E-18	128.6
TI+DS	1.00E-24	2.0	6.01E-20	10.9	7.27E-19	19.4	1.63E-18	35.6	2.59E-18	260.0
TI+SPEX	4.78E-21	206.5	2.74E-19	202.4	4.14E-18	221.2	1.02E-17	241.8	1.39E-17	261.9
TI+DPEX	1.59E-21	509.3	1.22E-19	520.3	1.40E-18	538.3	3.71E-18	557.2	5.11E-18	594.5
TI SUM	1.55E-19		3.47E-18		1.46E-16		3.52E-16		4.46E-16	
DCAI	1.17E-16	11.5	2.12E-16	26.4	5.45E-16	89.7	3.81E-16	128.1	1.58E-16	141.2
DCAI+SS	1.72E-19	11.5	3.71E-19	60.7	3.08E-18	155.9	5.31E-18	199.7	2.49E-18	216.5
DCAI+DS	3.29E-19	11.5	5.66E-19	26.4	1.57E-18	89.7	1.25E-18	128.1	8.41E-19	347.9
DCAI+SPEX	1.15E-18	216.0	2.44E-18	217.9	8.96E-18	291.6	8.01E-18	334.3	3.86E-18	349.8
DCAI+DPEX	5.65E-19	518.8	1.09E-18	535.8	2.85E-18	608.7	2.99E-18	649.7	1.46E-18	682.5
DCAI SUM	1.19E-16		2.16E-16		5.61E-16		3.99E-16		1.67E-16	
SC	2.51E-15	-14.6	2.38E-15	-9.7	2.71E-15	12.0	1.96E-15	36.7	1.09E-15	50.3
SC+SS	1.62E-19	-14.6	3.63E-19	24.6	6.34E-19	78.2	9.15E-19	108.2	7.11E-19	125.6
SC+DS	2.86E-19	-14.6	5.26E-19	-9.7	2.48E-19	12.0	1.62E-19	36.7	1.15E-19	257.1
SC+SPEX	1.19E-18	189.9	2.33E-18	181.8	2.27E-18	213.9	1.74E-18	242.8	1.29E-18	258.9
SC+DPEX	5.16E-19	492.6	9.70E-19	499.7	5.51E-19	531.0	3.83E-19	558.3	3.08E-19	591.6
SC SUM	2.51E-15		2.38E-15		2.71E-15		1.96E-15		1.09E-15	
DC	4.07E-15	-123.8	2.38E-15	-114.0	6.28E-16	-70.5	2.91E-16	-43.2	1.39E-16	-16.0
DC+SS	2.88E-18	-123.8	3.17E-18	-79.7	8.69E-18	-4.3	1.13E-17	28.3	7.07E-18	59.3
DC+DS	4.97E-18	-123.8	4.56E-18	-114.0	4.47E-18	-70.5	2.63E-18	-43.2	1.93E-18	190.8
DC+SPEX	2.01E-17	80.7	1.99E-17	77.5	2.57E-17	131.4	1.68E-17	162.9	1.05E-17	192.6
DC+DPEX	9.09E-18	383.5	8.95E-18	395.4	7.97E-18	448.5	5.96E-18	478.4	3.92E-18	525.3
DC SUM	4.11E-15		2.42E-15		6.75E-16		3.28E-16		1.62E-16	
TEX	1.07E-19	5.0	1.52E-17	5.8	1.80E-16	6.9	2.96E-16	7.1	4.12E-16	7.2
TEX+SS	1.00E-24	5.0	5.90E-20	40.2	3.04E-20	73.1	6.49E-20	78.6	8.15E-20	82.5
TEX+DS	4.29E-21	5.0	7.38E-20	5.8	3.04E-20	6.9	1.00E-24	7.1	1.00E-24	214.0
TEX+SPEX	2.57E-20	209.5	2.21E-19	197.3	1.82E-19	208.8	1.30E-19	213.2	1.36E-19	215.8
TEX+DPEX	1.29E-20	512.3	1.03E-19	515.2	3.04E-20	525.8	1.00E-24	528.7	1.00E-24	548.5
TEX SUM	1.50E-19		1.57E-17		1.80E-16		2.96E-16		4.12E-16	

Channel	Energy 200 keV/u		500		1000		2000			
	cross section cm ²	Eloss eV								
SI	1.93E-15	25.0	1.58E-15	25.7	9.88E-16	40.5	5.92E-16	59.1		
SI+SS	4.95E-18	125.9	7.80E-18	202.0	1.02E-17	329.0	1.28E-17	447.1		
SI+DS	2.39E-18	324.6	5.57E-18	417.8	5.31E-18	650.8	6.71E-18	1048.9		
SI+SPEX	7.39E-18	240.3	1.06E-17	243.7	1.08E-17	256.9	1.16E-17	274.1		
SI+DPEX	3.35E-18	592.8	3.77E-18	645.4	5.83E-18	674.6	5.67E-18	704.1		
SI SUM	1.95E-15		1.61E-15		1.02E-15		6.29E-16			
DI	4.08E-16	165.5	2.83E-16	266.9	1.51E-16	336.0	6.53E-17	405.2		
DI+SS	4.93E-18	266.4	7.15E-18	443.2	4.32E-18	624.5	2.65E-18	793.3		
DI+DS	2.52E-18	465.0	5.49E-18	659.0	2.73E-18	946.3	1.52E-18	1395.1		
DI+SPEX	6.69E-18	380.8	8.74E-18	484.9	4.56E-18	552.4	2.45E-18	620.3		
DI+DPEX	3.38E-18	733.2	3.91E-18	886.6	2.94E-18	970.1	1.30E-18	1050.3		
DI SUM	4.26E-16		3.08E-16		1.66E-16		7.32E-17			
TI	1.35E-16	110.3	3.86E-18	213.1	2.50E-19	254.8	1.55E-20	325.0		
TI+SS	6.70E-18	211.2	9.28E-19	389.4	6.72E-20	543.3	4.42E-21	713.0		
TI+DS	3.75E-18	409.9	7.42E-19	605.1	4.46E-20	865.0	2.18E-21	1314.8		
TI+SPEX	9.33E-18	325.6	1.04E-18	431.0	7.05E-20	471.2	3.94E-21	540.0		
TI+DPEX	4.70E-18	678.0	4.98E-19	832.8	4.70E-20	888.9	2.00E-21	970.0		
TI SUM	1.59E-16		7.07E-18		4.79E-19		2.80E-20			
DCAI	6.32E-18	227.4	1.00E-24	427.4	8.37E-23	0.0	8.37E-25	0.0		
DCAI+SS	4.42E-19	328.3	4.43E-21	603.7	1.00E-24	288.6	1.00E-24	388.1		
DCAI+DS	1.74E-19	526.9	4.43E-21	819.4	1.00E-24	610.3	1.00E-24	989.9		
DCAI+SPEX	6.16E-19	442.7	4.43E-21	645.3	1.00E-24	216.4	1.00E-24	215.1		
DCAI+DPEX	2.28E-19	795.1	1.00E-24	1047.1	1.00E-24	634.1	1.00E-24	645.0		
DCAI SUM	7.78E-18		1.33E-20		8.77E-23		4.84E-24			
SC	1.15E-16	93.7	2.15E-18	209.4	1.44E-19	481.7	1.23E-20	1026.3		
SC+SS	3.94E-19	194.6	1.36E-19	385.7	2.81E-20	770.2	5.34E-21	1414.4		
SC+DS	1.40E-19	393.3	8.99E-20	601.4	1.60E-20	1091.9	2.57E-21	2016.1		
SC+SPEX	7.13E-19	309.0	1.81E-19	427.3	2.96E-20	698.1	4.63E-21	1241.4		
SC+DPEX	2.11E-19	661.5	5.36E-20	829.1	1.74E-20	1115.8	2.06E-21	1671.3		
SC SUM	1.16E-16		2.61E-18		2.35E-19		2.69E-20			
DC	9.83E-18	92.9	3.48E-20	419.7	2.18E-22	964.3	2.08E-23	0.0		
DC+SS	1.26E-18	193.8	1.72E-20	596.0	2.34E-22	1252.9	1.00E-24	388.1		
DC+DS	6.71E-19	392.5	1.41E-20	811.7	1.78E-22	1574.6	1.00E-24	989.9		
DC+SPEX	1.67E-18	308.2	1.96E-20	637.6	2.53E-22	1180.7	1.00E-24	215.1		
DC+DPEX	8.72E-19	660.6	1.05E-20	1039.4	1.78E-22	1598.5	1.00E-24	645.0		
DC SUM	1.43E-17		9.62E-20		1.06E-21		2.48E-23			
TEX	7.09E-16	7.3	9.38E-16	7.1	7.97E-16	6.8	5.45E-16	6.4		
TEX+SS	1.97E-19	108.2	9.28E-19	183.4	2.38E-18	295.4	3.80E-18	394.5		
TEX+DS	1.00E-24	306.9	5.67E-19	399.1	1.01E-18	617.1	1.79E-18	996.2		
TEX+SPEX	3.20E-19	222.6	1.22E-18	225.0	2.56E-18	223.2	3.44E-18	221.5		
TEX+DPEX	7.38E-20	575.0	2.23E-19	626.8	1.17E-18	640.9	1.66E-18	651.4		
TEX SUM	7.10E-16		9.41E-16		8.04E-16		5.56E-16			

Table B.8: The integral cross section and associated average energy loss for SIM and NSIM processes in $S^{7+} + H_2$ collisions with impact energies between 1 and 2000 keV/u. (From Gharibnejad et al. (2019))

Channel	Energy 1 keV/u		10		50		75		100	
	cross section cm ²	Eloss eV								
SI	1.91E-19	3.5	1.48E-18	9.7	1.85E-16	13.7	1.03E-15	11.3	1.80E-15	17.3
SI+SS	1.00E-24	3.5	6.31E-20	32.6	3.14E-19	96.2	1.19E-18	93.9	4.63E-18	106.6
SI+DS	1.00E-24	3.5	2.31E-20	9.7	1.46E-19	13.7	5.15E-19	11.3	1.05E-18	178.0
SI+SPEX	1.00E-24	229.1	6.62E-20	216.4	5.85E-19	234.5	3.83E-18	237.1	4.89E-18	247.8
SI+DPEX	1.00E-24	543.0	1.56E-20	551.3	1.36E-19	564.9	1.03E-18	580.4	1.35E-18	607.5
SI SUM	1.91E-19		1.65E-18		1.86E-16		1.04E-15		1.81E-15	
DI	1.60E-22	0.0	3.18E-21	27.2	1.67E-18	35.2	2.63E-17	63.0	1.22E-16	89.6
DI+SS	1.00E-24	0.0	1.00E-24	50.1	7.97E-21	117.7	1.87E-19	145.6	1.21E-18	178.8
DI+DS	1.00E-24	0.0	1.00E-24	27.2	1.00E-24	35.2	8.57E-20	63.0	1.98E-19	250.3
DI+SPEX	1.00E-24	225.6	1.00E-24	233.9	2.39E-20	255.9	4.34E-19	288.8	1.28E-18	320.1
DI+DPEX	1.00E-24	539.5	1.00E-24	568.8	1.00E-24	586.4	1.55E-19	632.1	2.52E-19	679.7
DI SUM	1.64E-22		3.18E-21		1.70E-18		2.72E-17		1.25E-16	
TI	1.21E-19	1.9	2.91E-18	10.3	1.17E-16	17.7	3.27E-16	33.3	4.84E-16	50.6
TI+SS	1.16E-21	1.9	1.31E-19	33.3	1.55E-18	100.2	3.41E-18	115.9	1.09E-17	139.9
TI+DS	1.00E-24	1.9	4.42E-20	10.3	5.33E-19	17.7	1.52E-18	33.3	2.37E-18	211.4
TI+SPEX	1.16E-21	227.5	1.44E-19	217.1	3.38E-18	238.5	9.24E-18	259.2	1.16E-17	281.1
TI+DPEX	1.00E-24	541.4	3.78E-20	552.0	4.72E-19	568.9	3.06E-18	602.4	3.16E-18	640.8
TI SUM	1.23E-19		3.27E-18		1.23E-16		3.44E-16		5.12E-16	
DCAI	1.90E-15	14.2	1.75E-15	210.7	1.17E-15	330.2	7.70E-16	388.6	3.83E-16	434.5
DCAI+SS	5.02E-18	14.2	6.17E-18	233.6	1.01E-17	412.7	6.86E-18	471.2	8.21E-18	523.8
DCAI+DS	6.99E-19	14.2	1.78E-18	210.7	3.63E-18	330.2	3.15E-18	388.6	1.68E-18	595.2
DCAI+SPEX	4.48E-18	239.8	6.62E-18	417.4	2.48E-17	550.9	1.93E-17	614.5	8.86E-18	665.0
DCAI+DPEX	1.08E-18	553.7	1.42E-18	752.3	3.18E-18	881.4	5.85E-18	957.8	2.18E-18	1024.7
DCAI SUM	1.91E-15		1.77E-15		1.21E-15		8.05E-16		4.04E-16	
SC	2.44E-15	-10.7	2.67E-15	-5.8	3.15E-15	16.0	2.41E-15	29.6	1.42E-15	43.2
SC+SS	5.98E-19	-10.7	9.58E-19	17.2	4.24E-19	98.5	3.08E-19	112.2	6.16E-19	132.5
SC+DS	8.47E-20	-10.7	2.98E-19	-5.8	1.39E-19	16.0	1.15E-19	29.6	5.57E-20	203.9
SC+SPEX	5.38E-19	214.9	9.98E-19	201.0	1.47E-18	236.7	1.39E-18	255.5	6.57E-19	273.7
SC+DPEX	1.30E-19	528.8	2.67E-19	535.9	1.16E-19	567.2	2.61E-19	598.7	8.79E-20	633.4
SC SUM	2.44E-15		2.67E-15		3.15E-15		2.41E-15		1.42E-15	
DC	5.46E-17	-20.4	3.32E-16	-10.6	2.29E-16	33.0	1.58E-16	60.2	9.52E-17	87.4
DC+SS	1.64E-18	-20.4	4.71E-18	12.3	6.48E-18	115.4	5.00E-18	142.8	7.06E-18	176.7
DC+DS	2.46E-19	-20.4	1.40E-18	-10.6	2.35E-18	33.0	2.28E-18	60.2	1.40E-18	248.1
DC+SPEX	1.49E-18	205.2	5.00E-18	196.1	1.62E-17	253.7	1.39E-17	286.0	7.51E-18	317.9
DC+DPEX	3.78E-19	519.1	1.14E-18	531.0	2.05E-18	584.1	4.34E-18	629.3	1.84E-18	677.6
DC SUM	5.84E-17		3.44E-16		2.56E-16		1.84E-16		1.13E-16	
TEX	9.77E-20	4.8	1.21E-17	5.7	1.63E-16	6.8	2.92E-16	7.1	4.14E-16	7.2
TEX+SS	8.14E-21	4.8	1.00E-24	28.7	1.00E-24	89.3	1.00E-24	89.7	2.98E-20	96.5
TEX+DS	1.00E-24	4.8	3.97E-20	5.7	1.00E-24	6.8	1.00E-24	7.1	1.00E-24	167.9
TEX+SPEX	8.14E-21	230.4	7.94E-20	212.5	5.21E-20	227.5	5.42E-20	233.0	2.98E-20	237.7
TEX+DPEX	1.00E-24	544.3	1.99E-20	547.4	1.00E-24	558.0	1.00E-24	576.2	1.00E-24	597.4
TEX SUM	1.14E-19		1.22E-17		1.63E-16		2.92E-16		4.14E-16	

Channel	Energy 200 keV/u		500		1000		2000			
	cross section cm ²	Eloss eV								
SI	2.46E-15	24.7	2.08E-15	21.7	1.32E-15	30.6	7.85E-16	43.7		
SI+SS	7.17E-18	131.2	6.74E-18	197.5	8.19E-18	324.2	1.29E-17	486.1		
SI+DS	2.57E-18	264.0	3.72E-18	391.1	4.48E-18	592.5	6.16E-18	949.1		
SI+SPEX	7.95E-18	264.0	9.76E-18	266.1	1.02E-17	273.2	1.42E-17	285.3		
SI+DPEX	3.26E-18	635.6	3.19E-18	688.3	4.23E-18	708.6	4.88E-18	717.0		
SI SUM	2.48E-15		2.10E-15		1.35E-15		8.23E-16			
DI	4.62E-16	154.7	3.86E-16	225.8	2.05E-16	277.7	9.08E-17	342.3		
DI+SS	5.16E-18	261.2	7.00E-18	401.6	5.31E-18	571.3	3.35E-18	784.7		
DI+DS	2.03E-18	394.0	4.31E-18	595.2	3.36E-18	839.6	1.78E-18	1247.6		
DI+SPEX	5.80E-18	394.1	9.42E-18	470.2	6.03E-18	520.3	3.61E-18	583.9		
DI+DPEX	2.68E-18	765.7	4.00E-18	892.4	3.12E-18	955.7	1.45E-18	1015.5		
DI SUM	4.78E-16		4.11E-16		2.23E-16		1.01E-16			
TI	1.97E-16	102.5	7.35E-18	200.7	3.52E-19	242.7	2.34E-20	262.3		
TI+SS	8.47E-18	209.1	1.04E-18	376.5	9.23E-20	536.2	8.45E-21	704.7		
TI+DS	3.28E-18	341.8	6.58E-19	570.1	6.18E-20	804.6	4.61E-21	1167.6		
TI+SPEX	9.35E-18	341.9	1.33E-18	445.2	1.05E-19	485.3	9.15E-21	503.9		
TI+DPEX	4.25E-18	713.5	6.23E-19	867.3	5.78E-20	920.7	4.05E-21	935.5		
TI SUM	2.22E-16		1.10E-17		6.69E-19		4.97E-20			
DCAI	1.64E-17	290.4	3.18E-20	409.4	3.99E-22	0.0	3.99E-24	0.0		
DCAI+SS	6.50E-19	397.0	1.59E-20	585.2	1.00E-24	293.6	1.00E-24	442.4		
DCAI+DS	2.57E-19	529.7	1.00E-24	778.8	1.00E-24	561.9	1.00E-24	905.3		
DCAI+SPEX	7.71E-19	529.8	1.59E-20	653.8	1.00E-24	242.6	1.00E-24	241.6		
DCAI+DPEX	3.48E-19	901.4	1.00E-24	1076.0	1.00E-24	678.0	1.00E-24	673.3		
DCAI SUM	1.84E-17		6.36E-20		4.03E-22		7.99E-24			
SC	1.60E-16	97.7	2.80E-18	189.8	1.38E-19	462.1	1.06E-20	1006.7		
SC+SS	3.24E-19	204.2	1.08E-19	365.6	2.29E-20	755.6	4.11E-21	1449.1		
SC+DS	8.11E-20	337.0	5.00E-20	559.1	1.36E-20	1024.0	2.28E-21	1912.0		
SC+SPEX	3.67E-19	337.0	1.61E-19	434.2	2.72E-20	704.7	4.43E-21	1248.3		
SC+DPEX	9.54E-20	708.6	4.59E-20	856.4	1.29E-20	1140.1	1.52E-21	1680.0		
SC SUM	1.61E-16		3.16E-18		2.15E-19		2.29E-20			
DC	1.04E-17	196.3	5.42E-20	380.5	6.27E-22	0.0	3.69E-23	0.0		
DC+SS	1.30E-18	302.9	1.96E-20	556.3	3.42E-22	293.6	1.00E-24	442.4		
DC+DS	5.12E-19	435.6	1.41E-20	749.9	2.28E-22	561.9	1.00E-24	905.3		
DC+SPEX	1.46E-18	435.7	2.47E-20	624.9	4.56E-22	242.6	1.00E-24	241.6		
DC+DPEX	6.51E-19	807.3	1.33E-20	1047.1	2.28E-22	678.0	1.00E-24	673.3		
DC SUM	1.43E-17		1.26E-19		1.88E-21		4.09E-23			
TEX	7.73E-16	7.3	1.09E-15	7.2	9.90E-16	6.9	7.10E-16	6.5		
TEX+SS	1.17E-19	113.8	6.33E-19	183.0	1.83E-18	300.4	3.45E-18	448.9		
TEX+DS	1.00E-24	246.6	1.00E-24	376.6	7.51E-19	568.8	1.56E-18	911.8		
TEX+SPEX	1.17E-19	246.6	1.07E-18	251.6	2.38E-18	249.5	3.83E-18	248.1		
TEX+DPEX	1.00E-24	618.3	1.00E-24	673.8	7.18E-19	684.9	1.38E-18	679.8		
TEX SUM	7.73E-16		1.09E-15		9.96E-16		7.20E-16			

Table B.9: The integral cross section and associated average energy loss for SIM and NSIM processes in $S^{8+} + H_2$ collisions with impact energies between 1 and 2000 keV/u. (From Gharibnejad et al. (2019))

Channel	Energy 1 keV/u		10		50		75		100	
	cross section cm ²	Eloss eV								
SI	1.98E-19	1.4	1.41E-18	10.1	1.69E-16	10.6	5.78E-16	15.5	2.10E-15	20.9
SI+SS	1.00E-24	1.4	5.75E-21	51.3	1.86E-19	94.7	4.73E-19	110.9	2.06E-18	116.3
SI+DS	1.00E-24	1.4	2.88E-20	10.1	1.33E-19	10.6	2.72E-19	15.5	1.03E-18	375.8
SI+SPEX	1.00E-24	243.0	8.06E-20	231.6	5.98E-19	247.4	1.48E-18	259.6	4.70E-18	270.4
SI+DPEX	1.00E-24	597.7	2.07E-20	608.5	1.06E-19	618.5	3.15E-19	631.1	2.51E-18	654.1
SI SUM	1.98E-19		1.55E-18		1.70E-16		5.81E-16		2.11E-15	
DI	1.95E-22	0.0	3.88E-21	31.6	6.28E-19	31.5	1.76E-17	52.9	1.00E-16	86.1
DI+SS	1.00E-24	0.0	1.00E-24	72.8	1.00E-24	115.6	7.91E-20	148.3	3.23E-19	181.5
DI+DS	1.00E-24	0.0	1.00E-24	31.6	1.00E-24	31.5	3.65E-20	52.9	1.55E-19	441.0
DI+SPEX	1.00E-24	241.6	1.00E-24	253.1	1.00E-24	268.4	1.58E-19	297.0	1.01E-18	335.6
DI+DPEX	1.00E-24	596.3	1.00E-24	630.0	1.00E-24	639.5	4.26E-20	668.5	4.13E-19	719.3
DI SUM	1.99E-22		3.88E-21		6.28E-19		1.79E-17		1.02E-16	
TI	1.42E-19	1.4	2.53E-18	11.5	9.52E-17	16.9	3.16E-16	31.5	5.36E-16	48.2
TI+SS	1.00E-24	1.4	1.79E-20	52.7	5.11E-19	101.0	2.13E-18	126.9	4.28E-18	143.5
TI+DS	1.00E-24	1.4	6.49E-20	11.5	3.87E-19	16.9	1.18E-18	31.5	2.08E-18	403.0
TI+SPEX	1.00E-24	242.9	1.68E-19	233.0	2.37E-18	253.7	6.92E-18	275.6	9.59E-18	297.6
TI+DPEX	1.00E-24	597.6	4.03E-20	609.9	2.94E-19	624.8	1.41E-18	647.2	5.70E-18	681.3
TI SUM	1.42E-19		2.82E-18		9.88E-17		3.28E-16		5.58E-16	
DCAI	3.79E-15	62.0	2.60E-15	240.7	1.75E-15	359.5	1.24E-15	419.6	6.34E-16	274.2
DCAI+SS	5.86E-19	62.0	9.66E-19	281.9	7.96E-18	443.6	9.39E-18	515.0	4.72E-18	369.6
DCAI+DS	2.94E-18	62.0	4.37E-18	240.7	6.01E-18	359.5	5.11E-18	419.6	2.22E-18	629.0
DCAI+SPEX	1.09E-17	303.6	1.28E-17	462.2	3.69E-17	596.3	2.92E-17	663.6	1.05E-17	523.7
DCAI+DPEX	2.94E-18	658.2	3.29E-18	839.1	5.14E-18	967.4	6.36E-18	1035.2	6.23E-18	907.4
DCAI SUM	3.81E-15		2.62E-15		1.81E-15		1.29E-15		6.58E-16	
SC	2.99E-15	-18.9	2.91E-15	-14.0	3.56E-15	18.5	2.84E-15	32.1	1.77E-15	45.7
SC+SS	2.75E-20	-18.9	5.82E-20	27.2	1.22E-19	102.6	9.26E-20	127.5	7.05E-20	141.1
SC+DS	1.56E-19	-18.9	2.33E-19	-14.0	6.99E-20	18.5	7.58E-20	32.1	2.35E-20	400.6
SC+SPEX	6.14E-19	222.7	6.52E-19	207.5	6.38E-19	255.3	7.24E-19	276.2	3.76E-19	295.2
SC+DPEX	1.56E-19	577.4	1.65E-19	584.4	6.12E-20	626.4	7.58E-20	647.7	1.35E-19	678.9
SC SUM	2.99E-15		2.91E-15		3.56E-15		2.84E-15		1.77E-15	
DC	1.42E-20	-36.8	5.15E-20	-26.9	4.28E-19	37.9	6.09E-19	65.1	5.97E-19	92.4
DC+SS	1.00E-24	-36.8	1.00E-24	14.2	2.62E-20	122.0	8.88E-20	160.5	9.56E-20	187.7
DC+DS	1.00E-24	-36.8	5.94E-21	-26.9	2.62E-20	37.9	3.42E-20	65.1	3.04E-20	447.2
DC+SPEX	1.00E-24	204.8	9.90E-21	194.5	1.75E-19	274.7	2.73E-19	309.2	2.17E-19	341.9
DC+DPEX	1.00E-24	559.5	3.96E-21	571.5	1.75E-20	645.8	5.47E-20	680.8	1.30E-19	725.5
DC SUM	1.42E-20		7.13E-20		6.73E-19		1.06E-18		1.07E-18	
TEX	1.01E-19	4.9	8.79E-18	5.5	1.56E-16	6.7	2.87E-16	7.0	4.16E-16	7.2
TEX+SS	1.00E-24	4.9	1.00E-24	46.7	1.00E-24	90.8	1.00E-24	102.4	1.00E-24	102.6
TEX+DS	1.00E-24	4.9	1.00E-24	5.5	1.00E-24	6.7	1.00E-24	7.0	1.00E-24	362.1
TEX+SPEX	1.00E-24	246.5	1.00E-24	227.0	1.00E-24	243.5	1.00E-24	251.1	1.00E-24	256.7
TEX+DPEX	1.00E-24	601.2	1.00E-24	603.9	1.00E-24	614.6	1.00E-24	622.6	1.00E-24	640.4
TEX SUM	1.01E-19		8.79E-18		1.56E-16		2.87E-16		4.16E-16	

Channel	Energy 200 keV/u		500		1000		2000			
	cross section cm ²	Eloss eV								
SI	3.04E-15	24.4	2.64E-15	20.1	1.68E-15	25.0	1.01E-15	34.1		
SI+SS	7.50E-18	139.2	7.78E-18	204.2	6.60E-18	333.3	1.01E-17	493.1		
SI+DS	1.85E-18	247.0	4.29E-18	406.0	3.85E-18	629.6	4.48E-18	1033.1		
SI+SPEX	1.10E-17	286.2	9.78E-18	291.1	8.09E-18	293.4	1.33E-17	300.7		
SI+DPEX	3.01E-18	686.2	3.40E-18	709.9	2.53E-18	731.8	4.26E-18	738.9		
SI SUM	3.06E-15		2.67E-15		1.70E-15		1.04E-15			
DI	5.21E-16	153.3	4.87E-16	214.5	2.79E-16	256.4	1.26E-16	298.6		
DI+SS	4.49E-18	268.1	7.38E-18	398.5	5.56E-18	564.7	3.58E-18	757.6		
DI+DS	1.35E-18	375.9	4.33E-18	600.3	3.43E-18	861.0	1.78E-18	1297.6		
DI+SPEX	6.23E-18	415.1	9.22E-18	485.4	6.54E-18	524.9	4.47E-18	565.1		
DI+DPEX	1.87E-18	815.1	3.25E-18	904.3	2.45E-18	963.3	1.70E-18	1003.4		
DI SUM	5.35E-16		5.11E-16		2.97E-16		1.38E-16			
TI	2.55E-16	101.7	1.13E-17	187.7	5.94E-19	226.3	4.09E-20	215.8		
TI+SS	7.53E-18	216.4	1.04E-18	371.8	1.24E-19	534.5	9.59E-21	674.8		
TI+DS	2.38E-18	324.3	6.50E-19	573.6	8.65E-20	830.8	4.67E-21	1214.8		
TI+SPEX	1.15E-17	363.5	1.31E-18	458.7	1.42E-19	494.7	1.18E-20	482.3		
TI+DPEX	3.53E-18	763.5	5.38E-19	877.5	6.34E-20	933.1	4.41E-21	920.6		
TI SUM	2.80E-16		1.48E-17		1.01E-18		7.14E-20			
DCAI	3.45E-17	379.7	1.01E-19	827.1	1.06E-21	0.0	1.06E-23	0.0		
DCAI+SS	1.08E-18	494.4	1.92E-20	1011.2	1.00E-24	308.2	1.00E-24	459.0		
DCAI+DS	4.30E-19	602.2	1.92E-20	1213.0	1.00E-24	604.5	1.00E-24	999.0		
DCAI+SPEX	1.47E-18	641.5	1.92E-20	1098.1	1.00E-24	268.4	1.00E-24	266.6		
DCAI+DPEX	6.27E-19	1041.5	9.60E-21	1516.9	1.00E-24	706.8	1.00E-24	704.8		
DCAI SUM	3.81E-17		1.68E-19		1.06E-21		1.46E-23			
SC	2.03E-16	89.5	3.36E-18	233.3	1.60E-19	505.6	1.15E-20	984.9		
SC+SS	1.83E-19	204.3	8.24E-20	417.3	1.86E-20	813.9	4.22E-21	1443.9		
SC+DS	1.62E-20	312.1	3.67E-20	619.2	1.09E-20	1110.2	1.61E-21	1983.9		
SC+SPEX	3.54E-19	351.3	1.13E-19	504.2	2.29E-20	774.0	5.39E-21	1251.5		
SC+DPEX	3.95E-20	751.4	2.14E-20	923.1	6.91E-21	1212.5	1.55E-21	1689.7		
SC SUM	2.04E-16		3.61E-18		2.19E-19		2.43E-20			
DC	2.49E-19	180.0	1.31E-20	467.6	1.00E-24	1012.2	1.00E-23	1970.8		
DC+SS	8.57E-20	294.8	9.55E-21	651.6	1.28E-22	1320.5	1.00E-24	2429.8		
DC+DS	2.76E-20	402.6	6.79E-21	853.5	1.28E-22	1616.8	1.00E-24	2969.8		
DC+SPEX	1.30E-19	441.8	1.10E-20	738.5	1.28E-22	1280.6	1.00E-24	2237.3		
DC+DPEX	3.87E-20	841.8	5.10E-21	1157.4	1.28E-22	1719.0	1.00E-24	2675.6		
DC SUM	5.31E-19		4.55E-20		5.13E-22		1.40E-23			
TEX	8.01E-16	7.4	1.22E-15	7.2	1.19E-15	6.9	8.91E-16	6.5		
TEX+SS	6.35E-20	122.2	3.06E-19	191.2	9.46E-19	315.1	1.84E-18	465.5		
TEX+DS	1.00E-24	230.0	1.00E-24	393.1	3.70E-19	611.4	1.25E-18	1005.5		
TEX+SPEX	1.27E-19	269.2	6.12E-19	278.1	1.44E-18	275.3	2.09E-18	273.1		
TEX+DPEX	1.00E-24	669.2	1.00E-24	697.0	3.29E-19	713.7	1.22E-18	711.3		
TEX SUM	8.01E-16		1.22E-15		1.19E-15		8.97E-16			

Table B.10: The integral cross section and associated average energy loss for SIM and NSIM processes in $S^{9+} + H_2$ collisions with impact energies between 1 and 2000 keV/u. (From Gharibnejad et al. (2019))

Channel	Energy 1 keV/u		10		50		75		100	
	cross section cm ²	Eloss eV								
SI	2.61E-19	1.2	1.30E-18	11.7	1.57E-16	10.7	5.73E-16	18.3	1.25E-15	26.4
SI+SS	1.00E-24	1.2	9.36E-21	11.7	3.86E-20	98.0	3.49E-19	122.5	6.73E-19	137.9
SI+DS	1.32E-21	1.2	9.77E-21	11.7	1.93E-20	10.7	1.48E-19	18.3	2.07E-19	26.4
SI+SPEX	1.00E-24	251.5	1.55E-20	264.7	3.09E-19	276.0	9.53E-19	292.5	1.58E-18	307.5
SI+DPEX	1.32E-21	632.0	1.99E-20	644.6	5.79E-20	653.2	5.10E-19	685.4	1.24E-18	703.2
SI SUM	2.64E-19		1.35E-18		1.57E-16		5.75E-16		1.25E-15	
DI	1.12E-22	0.0	1.12E-21	12.5	6.60E-19	30.7	1.13E-17	47.8	8.25E-17	78.5
DI+SS	1.00E-24	0.0	2.23E-22	12.5	1.00E-24	118.0	1.65E-20	151.9	1.59E-19	190.0
DI+DS	1.00E-24	0.0	2.23E-22	12.5	1.00E-24	30.7	1.65E-20	47.8	7.36E-20	78.5
DI+SPEX	1.00E-24	250.3	2.23E-22	265.4	2.64E-20	296.0	3.30E-20	322.0	3.31E-19	359.6
DI+DPEX	1.00E-24	630.8	4.46E-22	645.4	1.00E-24	673.2	1.65E-20	714.9	2.21E-19	755.3
DI SUM	1.16E-22		2.24E-21		6.86E-19		1.14E-17		8.33E-17	
TI	2.17E-19	1.5	2.78E-18	11.6	8.11E-17	15.1	2.96E-16	29.4	5.70E-16	46.7
TI+SS	1.00E-24	1.5	2.76E-20	11.6	2.93E-19	102.4	1.30E-18	133.6	2.86E-18	158.2
TI+DS	1.00E-24	1.5	3.22E-20	11.6	2.16E-19	15.1	6.71E-19	29.4	1.12E-18	46.7
TI+SPEX	1.00E-24	251.8	4.06E-20	264.6	8.52E-19	280.4	3.76E-18	303.6	7.59E-18	327.8
TI+DPEX	1.00E-24	632.3	5.24E-20	644.5	4.07E-19	657.6	1.96E-18	696.5	4.95E-18	723.5
TI SUM	2.17E-19		2.93E-18		8.29E-17		3.04E-16		5.87E-16	
DCAI	4.24E-15	115.8	3.07E-15	282.5	2.11E-15	405.4	1.56E-15	469.7	9.17E-16	351.0
DCAI+SS	1.81E-18	115.8	2.01E-18	282.5	6.37E-18	492.7	8.11E-18	573.9	5.54E-18	462.5
DCAI+DS	2.47E-18	115.8	2.35E-18	282.5	4.19E-18	405.4	3.27E-18	469.7	1.88E-18	351.0
DCAI+SPEX	2.13E-18	366.1	3.07E-18	535.5	2.51E-17	670.7	2.48E-17	743.9	1.47E-17	632.0
DCAI+DPEX	3.80E-18	746.6	4.08E-18	915.4	8.65E-18	1047.9	1.24E-17	1136.9	1.06E-17	1027.7
DCAI SUM	4.25E-15		3.08E-15		2.15E-15		1.61E-15		9.50E-16	
SC	3.28E-15	-28.1	3.17E-15	-23.2	3.96E-15	12.0	3.26E-15	25.7	2.13E-15	39.3
SC+SS	1.01E-19	-28.1	3.86E-20	-23.2	1.53E-20	99.3	2.06E-20	129.9	2.13E-20	150.8
SC+DS	1.37E-19	-28.1	4.83E-20	-23.2	1.53E-20	12.0	1.00E-24	25.7	1.07E-20	39.3
SC+SPEX	1.23E-19	222.2	4.83E-20	229.8	9.20E-20	277.3	1.13E-19	299.9	1.28E-19	320.3
SC+DPEX	1.95E-19	602.7	8.69E-20	609.7	1.53E-20	654.5	5.15E-20	692.8	4.26E-20	716.0
SC SUM	3.28E-15		3.17E-15		3.96E-15		3.26E-15		2.13E-15	
DC	2.06E-20	-55.2	9.86E-20	-45.5	5.51E-19	25.1	5.74E-19	52.3	5.76E-19	79.5
DC+SS	1.00E-24	-55.2	1.00E-24	-45.5	5.27E-20	112.4	7.25E-20	156.5	1.03E-19	191.0
DC+DS	1.00E-24	-55.2	1.00E-24	-45.5	5.27E-20	25.1	2.42E-20	52.3	4.12E-20	79.5
DC+SPEX	1.00E-24	195.1	1.00E-24	207.5	1.14E-19	290.3	1.69E-19	326.5	1.92E-19	360.6
DC+DPEX	1.00E-24	575.5	1.00E-24	587.5	7.91E-20	667.5	8.86E-20	719.5	1.37E-19	756.3
DC SUM	2.06E-20		9.86E-20		8.50E-19		9.28E-19		1.05E-18	
TEX	1.11E-19	4.9	6.32E-18	5.4	1.44E-16	6.6	2.80E-16	6.8	4.07E-16	7.1
TEX+SS	1.00E-24	4.9	1.00E-24	5.4	1.00E-24	93.9	1.00E-24	111.0	7.56E-20	118.6
TEX+DS	1.00E-24	4.9	1.00E-24	5.4	1.00E-24	6.6	1.00E-24	6.8	7.56E-20	7.1
TEX+SPEX	1.00E-24	255.2	1.00E-24	258.4	1.00E-24	271.9	1.00E-24	281.0	7.56E-20	288.2
TEX+DPEX	1.00E-24	635.7	1.00E-24	638.3	1.00E-24	649.1	1.00E-24	674.0	7.56E-20	683.9
TEX SUM	1.11E-19		6.32E-18		1.44E-16		2.80E-16		4.07E-16	

Channel	Energy 200 keV/u	500		1000		2000			
	cross section cm ²	Eloss eV							
SI	3.16E-15	27.8	3.07E-15	20.0	2.08E-15	21.6	1.26E-15	27.8	
SI+SS	4.97E-18	156.0	6.04E-18	212.1	5.73E-18	342.3	8.10E-18	532.9	
SI+DS	1.47E-18	352.7	2.53E-18	482.2	3.04E-18	672.8	4.64E-18	1003.7	
SI+SPEX	8.85E-18	323.7	7.58E-18	330.7	6.08E-18	331.1	9.11E-18	335.2	
SI+DPEX	2.90E-18	719.0	3.51E-18	746.3	2.03E-18	756.6	3.82E-18	755.4	
SI SUM	3.18E-15		3.09E-15		2.10E-15		1.29E-15		
DI	5.72E-16	154.1	5.89E-16	205.4	3.55E-16	233.7	1.68E-16	268.9	
DI+SS	2.74E-18	282.3	5.85E-18	397.5	5.68E-18	554.3	3.54E-18	774.0	
DI+DS	8.58E-19	478.9	3.12E-18	667.7	3.54E-18	884.9	2.32E-18	1244.8	
DI+SPEX	4.44E-18	449.9	7.24E-18	516.2	5.99E-18	543.1	3.85E-18	576.4	
DI+DPEX	1.34E-18	845.2	3.97E-18	931.8	2.71E-18	968.7	2.06E-18	996.5	
DI SUM	5.81E-16		6.09E-16		3.73E-16		1.80E-16		
TI	3.42E-16	101.8	1.55E-17	187.9	1.37E-18	200.7	6.12E-20	157.7	
TI+SS	6.50E-18	230.0	1.28E-18	380.0	1.00E-24	521.4	1.36E-20	662.8	
TI+DS	2.17E-18	426.7	7.58E-19	650.2	1.00E-24	851.9	6.80E-21	1133.6	
TI+SPEX	1.11E-17	397.6	1.64E-18	498.7	2.80E-20	510.2	1.36E-20	465.1	
TI+DPEX	3.34E-18	793.0	9.58E-19	914.3	1.52E-20	935.8	6.80E-21	885.3	
TI SUM	3.65E-16		2.01E-17		1.41E-18		1.02E-19		
DCAI	6.06E-17	646.8	3.38E-19	925.5	2.36E-21	0.0	2.36E-23	0.0	
DCAI+SS	2.03E-18	775.0	9.40E-21	1117.7	1.00E-24	320.7	1.00E-24	505.1	
DCAI+DS	5.79E-19	971.7	9.40E-21	1387.8	1.00E-24	651.2	1.00E-24	975.9	
DCAI+SPEX	3.50E-18	942.6	9.40E-21	1236.3	1.00E-24	309.5	1.00E-24	307.4	
DCAI+DPEX	9.74E-19	1338.0	9.40E-21	1651.9	1.00E-24	735.0	1.00E-24	727.6	
DCAI SUM	6.77E-17		3.76E-19		2.36E-21		2.76E-23		
SC	2.53E-16	55.5	4.08E-18	218.8	1.96E-19	416.3	1.27E-20	961.0	
SC+SS	6.17E-20	183.7	4.98E-20	411.0	1.85E-20	737.0	3.09E-21	1466.1	
SC+DS	1.42E-20	380.3	1.31E-20	681.1	9.03E-21	1067.5	1.68E-21	1936.9	
SC+SPEX	1.04E-19	351.3	7.73E-20	529.6	2.00E-20	725.8	3.40E-21	1268.4	
SC+DPEX	2.85E-20	746.6	1.57E-20	945.2	6.28E-21	1151.4	1.47E-21	1688.6	
SC SUM	2.53E-16		4.24E-18		2.50E-19		2.23E-20		
DC	4.27E-19	111.9	1.59E-20	438.7	1.00E-24	833.6	4.14E-23	0.0	
DC+SS	1.05E-19	240.1	6.68E-21	630.8	5.28E-22	1154.3	1.00E-24	505.1	
DC+DS	2.63E-20	436.8	2.23E-21	900.9	5.28E-22	1484.9	1.00E-24	975.9	
DC+SPEX	1.58E-19	407.7	8.90E-21	749.5	5.28E-22	1143.1	1.00E-24	307.4	
DC+DPEX	5.26E-20	803.1	3.34E-21	1165.0	5.28E-22	1568.7	1.00E-24	727.6	
DC SUM	7.69E-19		3.71E-20		2.11E-21		4.54E-23		
TEX	8.34E-16	7.4	1.36E-15	7.3	1.39E-15	7.0	1.07E-15	6.7	
TEX+SS	1.77E-19	135.6	3.56E-19	199.4	4.58E-19	327.7	1.33E-18	511.8	
TEX+DS	1.77E-19	332.3	3.56E-19	469.6	2.11E-19	658.2	8.90E-19	982.6	
TEX+SPEX	1.77E-19	303.2	4.45E-19	318.1	5.63E-19	316.5	1.64E-18	314.1	
TEX+DPEX	1.77E-19	698.6	3.56E-19	733.7	1.76E-19	742.0	8.34E-19	734.3	
TEX SUM	8.35E-16		1.36E-15		1.39E-15		1.07E-15		

Table B.11: The integral cross section and associated average energy loss for SIM and NSIM processes in $S^{10+} + H_2$ collisions with impact energies between 1 and 2000 keV/u. (From Gharibnejad et al. (2019))

Channel	Energy 1 keV/u		10		50		75		100	
	cross section cm ²	Eloss eV								
SI	3.69E-19	1.5	1.29E-18	10.7	1.45E-16	10.3	5.65E-16	17.8	1.28E-15	25.1
SI+SS	1.00E-24	1.5	1.05E-20	10.7	1.03E-19	114.8	1.60E-19	191.9	6.76E-19	227.4
SI+DS	1.00E-24	1.5	7.86E-21	10.7	3.44E-20	10.3	4.81E-20	17.8	1.99E-19	720.1
SI+SPEX	1.00E-24	230.3	4.72E-20	269.1	3.61E-19	291.2	7.22E-19	306.6	2.31E-18	321.6
SI+DPEX	1.00E-24	629.0	1.83E-20	640.3	1.03E-19	649.4	4.17E-19	665.9	7.96E-19	690.6
SI SUM	3.69E-19		1.37E-18		1.46E-16		5.66E-16		1.28E-15	
DI	1.17E-22	0.0	1.17E-21	5.2	2.57E-19	16.9	9.41E-18	43.0	6.75E-17	74.0
DI+SS	1.00E-24	0.0	1.00E-24	5.2	1.00E-24	121.4	1.00E-24	217.1	9.62E-20	276.3
DI+DS	1.00E-24	0.0	1.00E-24	5.2	1.00E-24	16.9	1.00E-24	43.0	1.00E-24	769.0
DI+SPEX	1.00E-24	228.8	1.17E-21	263.6	1.00E-24	297.8	7.43E-21	331.8	5.05E-19	370.5
DI+DPEX	1.00E-24	627.5	1.00E-24	634.8	1.00E-24	656.0	7.43E-21	691.1	1.20E-19	739.5
DI SUM	1.21E-22		2.34E-21		2.57E-19		9.42E-18		6.82E-17	
TI	1.78E-19	1.9	2.48E-18	11.5	6.75E-17	14.2	2.71E-16	27.3	5.88E-16	44.4
TI+SS	1.00E-24	1.9	2.66E-20	11.5	2.03E-19	118.7	9.39E-19	201.4	2.01E-18	246.7
TI+DS	1.00E-24	1.9	1.20E-20	11.5	1.29E-19	14.2	4.49E-19	27.3	6.45E-19	739.4
TI+SPEX	1.00E-24	230.7	9.56E-20	269.9	1.09E-18	295.1	2.59E-18	316.1	7.06E-18	340.9
TI+DPEX	1.00E-24	629.4	3.32E-20	641.1	2.58E-19	653.3	1.67E-18	675.4	2.39E-18	709.9
TI SUM	1.78E-19		2.65E-18		6.92E-17		2.77E-16		6.00E-16	
DCAI	4.68E-15	154.6	3.51E-15	338.9	2.50E-15	468.5	1.91E-15	358.4	1.21E-15	593.2
DCAI+SS	1.91E-18	154.6	2.49E-18	338.9	5.87E-18	573.0	6.14E-18	532.5	6.30E-18	795.5
DCAI+DS	1.09E-18	154.6	1.55E-18	338.9	2.12E-18	468.5	1.91E-18	358.4	1.77E-18	1288.2
DCAI+SPEX	6.88E-18	383.4	8.92E-18	597.3	3.12E-17	749.4	2.29E-17	647.2	1.93E-17	889.7
DCAI+DPEX	2.95E-18	782.1	3.70E-18	968.5	6.77E-18	1107.6	1.29E-17	1006.5	7.26E-18	1258.8
DCAI SUM	4.69E-15		3.53E-15		2.55E-15		1.95E-15		1.24E-15	
SC	3.58E-15	-21.8	5.85E-15	-16.9	4.58E-15	4.9	3.91E-15	28.5	2.65E-15	42.1
SC+SS	1.00E-24	-21.8	1.00E-24	-16.9	2.18E-20	109.4	1.37E-20	202.6	7.30E-21	244.4
SC+DS	1.00E-24	-21.8	1.00E-24	-16.9	7.28E-21	4.9	1.00E-24	28.5	1.00E-24	737.1
SC+SPEX	1.00E-24	206.9	7.91E-19	241.5	7.28E-20	285.8	6.87E-20	317.3	6.57E-20	338.6
SC+DPEX	1.00E-24	605.7	1.00E-24	612.7	2.18E-20	644.0	4.12E-20	676.6	2.19E-20	707.7
SC SUM	3.58E-15		5.85E-15		4.58E-15		3.91E-15		2.65E-15	
DC	1.80E-21	-42.7	8.62E-21	-32.9	2.48E-20	10.7	1.36E-19	58.0	1.95E-19	85.2
DC+SS	1.00E-24	-42.7	1.00E-24	-32.9	1.00E-24	115.2	1.24E-20	232.1	2.44E-20	287.5
DC+DS	1.00E-24	-42.7	1.00E-24	-32.9	1.00E-24	10.7	6.19E-21	58.0	1.00E-24	780.2
DC+SPEX	1.00E-24	186.1	1.00E-24	225.6	4.95E-20	291.6	6.19E-20	346.8	1.15E-19	381.7
DC+DPEX	1.00E-24	584.8	1.00E-24	596.8	1.00E-24	649.8	4.33E-20	706.1	3.48E-20	750.8
DC SUM	1.80E-21		8.62E-21		7.43E-20		2.60E-19		3.69E-19	
TEX	1.08E-19	4.7	4.29E-18	5.2	1.32E-16	6.6	2.72E-16	6.9	4.07E-16	7.1
TEX+SS	1.00E-24	4.7	1.00E-24	5.2	3.26E-19	111.1	1.00E-24	181.0	1.00E-24	209.4
TEX+DS	1.00E-24	4.7	1.00E-24	5.2	3.26E-19	6.6	1.00E-24	6.9	1.00E-24	702.1
TEX+SPEX	1.00E-24	233.5	1.00E-24	263.6	3.26E-19	287.5	1.59E-19	295.7	1.00E-24	303.6
TEX+DPEX	1.00E-24	632.2	1.00E-24	634.8	3.26E-19	645.7	1.59E-19	655.0	1.00E-24	672.6
TEX SUM	1.08E-19		4.29E-18		1.33E-16		2.72E-16		4.07E-16	

Channel	Energy 200 keV/u	500		1000		2000			
	cross section cm ²	Eloss eV							
SI	3.03E-15	27.9	3.46E-15	20.3	2.54E-15	19.4	1.54E-15	23.6	
SI+SS	4.90E-18	339.0	6.39E-18	710.6	4.51E-18	1338.3	7.03E-18	2383.3	
SI+DS	1.34E-18	653.3	2.15E-18	1473.6	2.59E-18	2776.5	3.79E-18	4676.4	
SI+SPEX	6.47E-18	342.0	8.58E-18	355.2	6.05E-18	353.3	8.20E-18	353.8	
SI+DPEX	4.53E-18	734.1	3.36E-18	748.0	2.59E-18	745.2	2.18E-18	770.3	
SI SUM	3.05E-15		3.48E-15		2.56E-15		1.56E-15		
DI	6.03E-16	151.4	6.86E-16	198.3	4.30E-16	225.3	2.16E-16	244.0	
DI+SS	2.36E-18	462.5	5.04E-18	888.6	5.12E-18	1544.2	4.15E-18	2603.7	
DI+DS	6.67E-19	776.8	2.26E-18	1651.6	2.89E-18	2982.4	2.51E-18	4896.8	
DI+SPEX	3.03E-18	465.5	6.74E-18	533.2	6.26E-18	559.2	4.67E-18	574.2	
DI+DPEX	2.14E-18	857.6	3.37E-18	926.0	2.89E-18	951.1	1.57E-18	990.7	
DI SUM	6.11E-16		7.03E-16		4.47E-16		2.29E-16		
TI	4.14E-16	100.1	2.58E-17	175.4	1.91E-18	198.1	1.06E-19	95.5	
TI+SS	5.65E-18	411.2	1.00E-24	865.7	1.00E-24	1517.0	1.39E-20	2455.2	
TI+DS	1.80E-18	725.5	1.00E-24	1628.7	1.00E-24	2955.2	9.12E-21	4748.3	
TI+SPEX	7.72E-18	414.2	1.00E-24	510.3	1.00E-24	532.0	1.56E-20	425.7	
TI+DPEX	5.36E-18	806.3	1.00E-24	903.1	1.00E-24	923.9	5.28E-21	842.2	
TI SUM	4.35E-16		2.58E-17		1.91E-18		1.50E-19		
DCAI	9.47E-17	733.2	2.64E-19	919.4	2.21E-21	0.0	2.21E-23	0.0	
DCAI+SS	2.06E-18	1044.3	2.20E-20	1609.7	1.00E-24	1318.9	1.00E-24	2359.7	
DCAI+DS	5.90E-19	1358.6	2.20E-20	2372.7	1.00E-24	2757.1	1.00E-24	4652.8	
DCAI+SPEX	2.76E-18	1047.3	2.20E-20	1254.3	1.00E-24	333.9	1.00E-24	330.2	
DCAI+DPEX	1.95E-18	1439.4	2.20E-20	1647.1	1.00E-24	725.8	1.00E-24	746.7	
DCAI SUM	1.02E-16		3.52E-19		2.21E-21		2.61E-23		
SC	3.05E-16	96.6	5.11E-18	233.3	2.23E-19	390.2	1.42E-20	934.8	
SC+SS	4.37E-20	407.7	3.75E-20	923.6	1.12E-20	1709.1	3.10E-21	3294.5	
SC+DS	1.00E-24	722.0	9.36E-21	1686.6	4.97E-21	3147.3	1.63E-21	5587.6	
SC+SPEX	6.79E-20	410.7	5.91E-20	568.2	1.55E-20	724.1	3.62E-21	1265.0	
SC+DPEX	3.64E-20	802.8	1.58E-20	961.0	4.97E-21	1116.0	8.35E-22	1681.5	
SC SUM	3.05E-16		5.23E-18		2.60E-19		2.34E-20		
DC	1.75E-19	194.1	2.97E-20	467.6	2.93E-21	781.3	1.00E-24	0.0	
DC+SS	5.00E-20	505.2	1.18E-20	1157.9	1.83E-22	2100.2	3.59E-23	2359.7	
DC+DS	1.80E-20	819.5	4.33E-21	1920.9	1.83E-22	3538.4	1.00E-24	4652.8	
DC+SPEX	6.81E-20	508.3	1.55E-20	802.5	1.83E-22	1115.3	3.59E-23	330.2	
DC+DPEX	4.40E-20	900.3	5.57E-21	1195.3	1.83E-22	1507.1	1.00E-24	746.7	
DC SUM	3.55E-19		6.69E-20		3.66E-21		7.48E-23		
TEX	8.68E-16	7.3	1.45E-15	7.3	1.54E-15	7.1	1.24E-15	6.8	
TEX+SS	1.00E-24	318.4	1.00E-24	697.6	1.27E-18	1326.0	8.42E-19	2366.5	
TEX+DS	1.00E-24	632.7	1.00E-24	1460.6	1.27E-18	2764.2	6.68E-19	4659.6	
TEX+SPEX	1.00E-24	321.4	3.43E-19	342.2	1.32E-18	341.1	1.02E-18	337.0	
TEX+DPEX	1.00E-24	713.5	1.00E-24	735.0	1.27E-18	732.9	5.52E-19	753.5	
TEX SUM	8.68E-16		1.45E-15		1.55E-15		1.24E-15		

Table B.12: The integral cross section and associated average energy loss for SIM and NSIM processes in $S^{11+} + H_2$ collisions with impact energies between 1 and 2000 keV/u. (From Gharibnejad et al. (2019))

Channel	Energy 1 keV/u		10		50		75		100	
	cross section cm ²	Eloss eV								
SI	5.39E-19	1.3	1.10E-18	11.6	1.35E-16	10.0	5.52E-16	17.4	1.31E-15	24.7
SI+SS	1.00E-24	1.3	2.61E-20	11.6	4.96E-20	110.4	8.69E-20	136.8	3.47E-19	156.7
SI+DS	1.00E-24	1.3	1.56E-20	11.6	2.48E-20	10.0	8.69E-20	17.4	2.48E-19	24.7
SI+SPEX	1.00E-24	1.3	9.81E-20	283.8	3.97E-19	302.7	5.65E-19	318.6	1.78E-18	335.0
SI+DPEX	1.00E-24	723.8	1.91E-20	736.3	4.96E-20	744.2	1.09E-19	757.6	3.47E-19	782.7
SI SUM	5.39E-19		1.26E-18		1.36E-16		5.53E-16		1.31E-15	
DI	7.00E-23	0.0	1.39E-21	17.6	3.53E-19	29.3	6.62E-18	41.4	5.27E-17	70.6
DI+SS	1.00E-24	0.0	1.00E-24	17.6	1.00E-24	129.7	6.87E-21	160.8	2.14E-20	202.6
DI+DS	1.00E-24	0.0	1.00E-24	17.6	1.00E-24	29.3	1.00E-24	41.4	1.00E-24	70.6
DI+SPEX	1.00E-24	0.0	1.00E-24	289.8	3.21E-20	322.1	2.06E-20	342.5	6.43E-20	381.0
DI+DPEX	1.00E-24	722.5	1.00E-24	742.3	1.00E-24	763.5	2.06E-20	781.5	2.14E-20	828.6
DI SUM	7.40E-23		1.39E-21		3.85E-19		6.67E-18		5.28E-17	
TI	2.44E-19	1.7	2.69E-18	12.2	5.87E-17	13.2	2.53E-16	25.6	5.79E-16	42.5
TI+SS	1.00E-24	1.7	1.00E-24	12.2	1.28E-19	113.7	3.06E-19	144.9	1.62E-18	174.4
TI+DS	1.00E-24	1.7	1.00E-24	12.2	1.07E-19	13.2	3.06E-19	25.6	6.39E-19	42.5
TI+SPEX	1.00E-24	1.7	1.00E-24	284.3	8.12E-19	306.0	1.92E-18	326.7	5.54E-18	352.8
TI+DPEX	1.00E-24	724.2	1.00E-24	736.8	1.71E-19	747.4	4.89E-19	765.7	1.49E-18	800.5
TI SUM	2.44E-19		2.69E-18		5.99E-17		2.56E-16		5.88E-16	
DCAI	5.17E-15	177.2	3.98E-15	383.0	2.83E-15	517.5	2.24E-15	386.8	1.51E-15	440.0
DCAI+SS	5.04E-18	177.2	4.89E-18	383.0	4.79E-18	617.9	4.36E-18	506.2	6.19E-18	572.0
DCAI+DS	2.96E-18	177.2	3.36E-18	383.0	3.93E-18	517.5	4.01E-18	386.8	3.39E-18	440.0
DCAI+SPEX	1.98E-17	177.2	2.21E-17	655.2	2.58E-17	810.2	2.69E-17	688.0	2.24E-17	750.3
DCAI+DPEX	3.52E-18	899.7	3.93E-18	1107.7	5.88E-18	1251.7	6.51E-18	1127.0	5.81E-18	1198.0
DCAI SUM	5.20E-15		4.01E-15		2.87E-15		2.28E-15		1.55E-15	
SC	6.94E-15	-29.8	6.31E-15	-24.9	5.35E-15	9.1	4.38E-15	30.6	3.08E-15	44.2
SC+SS	1.00E-24	-29.8	4.59E-20	-24.9	1.00E-24	109.5	1.15E-20	149.9	8.89E-21	176.1
SC+DS	1.00E-24	-29.8	2.76E-20	-24.9	1.00E-24	9.1	1.15E-20	30.6	1.00E-24	44.2
SC+SPEX	1.00E-24	-29.8	1.10E-19	247.3	3.47E-20	301.8	2.30E-20	331.7	3.56E-20	354.5
SC+DPEX	1.00E-24	692.8	2.76E-20	699.8	1.16E-20	743.3	1.15E-20	770.7	8.89E-21	802.2
SC SUM	6.94E-15		6.31E-15		5.35E-15		4.38E-15		3.08E-15	
DC	7.46E-22	-58.5	3.57E-21	-48.7	1.54E-20	19.1	1.00E-24	62.1	1.34E-20	89.3
DC+SS	1.00E-24	-58.5	1.00E-24	-48.7	1.00E-24	119.5	1.00E-24	181.4	8.34E-21	221.3
DC+DS	1.00E-24	-58.5	1.00E-24	-48.7	1.00E-24	19.1	1.00E-24	62.1	8.34E-21	89.3
DC+SPEX	1.00E-24	-58.5	1.00E-24	223.4	1.54E-20	311.9	2.87E-20	363.2	4.17E-20	399.6
DC+DPEX	1.00E-24	664.0	1.00E-24	675.9	1.00E-24	753.3	1.00E-24	802.2	8.34E-21	847.3
DC SUM	7.50E-22		3.57E-21		3.08E-20		2.87E-20		8.01E-20	
TEX	1.03E-19	4.7	3.05E-18	5.3	1.26E-16	6.5	2.57E-16	6.8	3.91E-16	7.1
TEX+SS	1.00E-24	4.7	1.00E-24	5.3	1.00E-24	107.0	1.00E-24	126.2	2.79E-18	139.1
TEX+DS	1.00E-24	4.7	1.00E-24	5.3	1.00E-24	6.5	1.00E-24	6.8	2.79E-18	7.1
TEX+SPEX	1.00E-24	4.7	1.00E-24	277.5	1.36E-18	299.3	2.80E-18	307.9	2.79E-18	317.4
TEX+DPEX	1.00E-24	727.2	1.00E-24	730.0	1.36E-18	740.7	1.00E-24	746.9	2.79E-18	765.1
TEX SUM	1.03E-19		3.05E-18		1.29E-16		2.60E-16		4.02E-16	

Channel	Energy 200 keV/u		500		1000		2000			
	cross section cm ²	Eloss eV								
SI	3.50E-15	33.6	4.11E-15	20.1	3.02E-15	17.9	1.83E-15	20.6		
SI+SS	2.99E-18	183.6	6.56E-18	226.7	4.66E-18	348.5	6.11E-18	558.6		
SI+DS	1.95E-18	404.7	3.86E-18	396.1	2.36E-18	670.1	2.93E-18	1263.9		
SI+SPEX	7.53E-18	363.7	8.24E-18	376.9	4.43E-18	374.2	6.93E-18	373.5		
SI+DPEX	2.38E-18	845.7	3.86E-18	873.7	1.79E-18	875.2	2.63E-18	889.9		
SI SUM	3.51E-15		4.13E-15		3.03E-15		1.85E-15			
DI	6.31E-16	151.4	7.69E-16	202.2	5.12E-16	215.0	2.70E-16	228.0		
DI+SS	1.50E-18	301.4	5.06E-18	408.8	5.38E-18	545.6	4.08E-18	766.0		
DI+DS	9.19E-19	522.6	2.84E-18	578.1	3.25E-18	867.1	2.20E-18	1471.4		
DI+SPEX	3.84E-18	481.6	5.98E-18	559.0	5.18E-18	571.2	4.45E-18	580.9		
DI+DPEX	1.27E-18	963.6	2.84E-18	1055.7	2.68E-18	1072.3	2.01E-18	1097.4		
DI SUM	6.39E-16		7.86E-16		5.28E-16		2.83E-16			
TI	4.90E-16	101.1	2.99E-17	185.7	2.03E-18	212.2	1.64E-19	133.9		
TI+SS	4.73E-18	251.1	1.49E-18	392.3	2.03E-19	542.8	6.20E-21	671.9		
TI+DS	3.02E-18	472.2	8.52E-19	561.7	1.23E-19	864.4	2.48E-21	1377.2		
TI+SPEX	1.14E-17	431.2	1.76E-18	542.5	2.01E-19	568.5	7.44E-21	486.8		
TI+DPEX	4.08E-18	913.3	8.52E-19	1039.3	1.02E-19	1069.5	2.48E-21	1003.2		
TI SUM	5.13E-16		3.49E-17		2.66E-18		1.83E-19			
DCAI	1.18E-16	565.0	7.24E-19	1031.1	5.25E-21	0.0	5.25E-23	0.0		
DCAI+SS	1.70E-18	715.0	5.57E-20	1237.7	1.00E-24	330.6	1.00E-24	538.0		
DCAI+DS	9.42E-19	936.1	1.00E-24	1407.1	1.00E-24	652.2	1.00E-24	1243.3		
DCAI+SPEX	3.86E-18	895.1	5.57E-20	1387.9	1.00E-24	356.3	1.00E-24	352.9		
DCAI+DPEX	1.29E-18	1377.1	1.00E-24	1884.7	1.00E-24	857.3	1.00E-24	869.3		
DCAI SUM	1.26E-16		8.35E-19		5.25E-21		5.65E-23			
SC	3.65E-16	98.6	5.94E-18	242.0	2.15E-19	457.1	1.61E-20	1001.8		
SC+SS	1.40E-20	248.7	2.66E-20	448.6	9.94E-21	787.8	1.97E-21	1539.8		
SC+DS	9.32E-21	469.8	5.15E-21	617.9	4.22E-21	1109.3	9.00E-22	2245.1		
SC+SPEX	6.52E-20	428.8	3.26E-20	598.8	9.69E-21	813.4	2.29E-21	1354.7		
SC+DPEX	1.40E-20	910.8	5.15E-21	1095.5	2.48E-21	1314.5	7.55E-22	1871.1		
SC SUM	3.65E-16		6.01E-18		2.41E-19		2.20E-20			
DC	3.66E-20	198.2	1.28E-20	485.0	1.00E-24	915.3	1.00E-24	0.0		
DC+SS	5.49E-21	348.3	4.11E-21	691.6	3.30E-22	1245.9	2.49E-23	538.0		
DC+DS	2.75E-21	569.4	2.93E-21	860.9	3.30E-22	1567.4	1.25E-23	1243.3		
DC+SPEX	8.24E-21	528.4	4.69E-21	841.8	3.30E-22	1271.5	2.49E-23	352.9		
DC+DPEX	5.49E-21	1010.4	2.93E-21	1338.5	3.30E-22	1772.6	1.25E-23	869.3		
DC SUM	5.86E-20		2.75E-20		1.32E-21		7.58E-23			
TEX	8.64E-16	7.3	1.52E-15	7.4	1.73E-15	7.1	1.45E-15	6.8		
TEX+SS	3.91E-18	157.3	6.31E-18	214.0	2.58E-18	337.7	1.01E-18	544.8		
TEX+DS	3.91E-18	378.5	6.22E-18	383.3	2.58E-18	659.3	8.96E-19	1250.1		
TEX+SPEX	3.93E-18	337.4	6.34E-18	364.2	2.58E-18	363.4	1.04E-18	359.7		
TEX+DPEX	3.91E-18	819.5	6.22E-18	860.9	1.00E-24	864.4	8.96E-19	876.1		
TEX SUM	8.80E-16		1.55E-15		1.74E-15		1.45E-15			

Table B.13: The integral cross section and associated average energy loss for SIM and NSIM processes in $S^{12+} + H_2$ collisions with impact energies between 1 and 2000 keV/u. (From Gharibnejad et al. (2019))

Channel	Energy 1 keV/u		10		50		75		100	
	cross section cm ²	Eloss eV								
SI	7.97E-19	1.6	1.05E-18	11.8	1.27E-16	9.7	5.39E-16	17.3	1.33E-15	24.1
SI+SS	1.00E-24	1.6	1.00E-24	11.8	1.00E-24	132.6	7.51E-20	143.3	2.33E-19	168.6
SI+DS	1.00E-24	1.6	6.44E-21	11.8	1.00E-24	9.7	3.75E-20	17.3	5.83E-20	373.9
SI+SPEX	3.93E-21	292.8	4.72E-20	325.8	1.07E-19	340.4	2.07E-19	354.3	1.46E-18	371.8
SI+DPEX	1.00E-24	709.3	7.52E-21	721.7	1.00E-24	729.2	5.63E-20	742.7	2.33E-19	798.9
SI SUM	8.01E-19		1.11E-18		1.27E-16		5.39E-16		1.33E-15	
DI	7.50E-23	0.0	1.49E-21	10.4	2.07E-19	20.6	4.83E-18	39.0	4.07E-17	64.1
DI+SS	1.00E-24	0.0	1.00E-24	10.4	1.00E-24	143.5	1.00E-24	165.0	1.00E-24	208.6
DI+DS	1.00E-24	0.0	1.00E-24	10.4	1.00E-24	20.6	1.00E-24	39.0	1.00E-24	413.9
DI+SPEX	1.00E-24	291.2	1.00E-24	324.4	1.00E-24	351.2	1.00E-24	376.0	7.43E-20	411.8
DI+DPEX	1.00E-24	707.8	1.00E-24	720.3	1.00E-24	740.0	1.00E-24	764.4	1.00E-24	838.8
DI SUM	7.90E-23		1.49E-21		2.07E-19		4.83E-18		4.08E-17	
TI	2.72E-19	1.7	2.32E-18	12.0	5.43E-17	12.3	2.34E-16	24.0	5.79E-16	41.0
TI+SS	1.00E-24	1.7	1.28E-21	12.0	1.00E-24	135.2	3.50E-19	150.1	1.38E-18	185.4
TI+DS	1.00E-24	1.7	1.02E-20	12.0	1.00E-24	12.3	6.57E-20	24.0	4.77E-19	390.7
TI+SPEX	1.00E-24	292.9	1.48E-19	326.0	4.85E-19	342.9	1.03E-18	361.1	5.49E-18	388.6
TI+DPEX	1.00E-24	709.5	1.28E-20	721.9	3.23E-20	731.7	1.75E-19	749.4	1.19E-18	815.7
TI SUM	2.72E-19		2.49E-18		5.48E-17		2.36E-16		5.88E-16	
DCAI	5.72E-15	206.6	4.45E-15	247.8	3.20E-15	585.7	2.59E-15	425.4	1.84E-15	481.9
DCAI+SS	9.80E-20	206.6	1.60E-19	247.8	1.65E-18	708.5	6.87E-18	551.5	6.63E-18	626.3
DCAI+DS	1.34E-18	206.6	1.78E-18	247.8	1.96E-18	585.7	2.11E-18	425.4	1.87E-18	831.6
DCAI+SPEX	8.88E-18	497.9	1.68E-17	561.9	1.99E-17	916.3	1.85E-17	762.5	2.11E-17	829.5
DCAI+DPEX	1.54E-18	914.4	2.00E-18	957.8	3.39E-18	1305.1	3.61E-18	1150.8	5.66E-18	1256.6
DCAI SUM	5.73E-15		4.47E-15		3.23E-15		2.62E-15		1.88E-15	
SC	1.22E-15	-24.0	6.72E-15	-19.1	5.82E-15	12.0	4.86E-15	25.7	3.53E-15	39.3
SC+SS	1.00E-24	-24.0	1.00E-24	-19.1	1.00E-24	134.9	5.14E-21	151.7	1.00E-24	183.7
SC+DS	1.00E-24	-24.0	1.00E-24	-19.1	1.00E-24	12.0	1.00E-24	25.7	1.00E-24	389.0
SC+SPEX	1.00E-24	267.2	1.54E-19	294.9	1.00E-24	342.7	5.14E-21	362.7	1.34E-20	386.9
SC+DPEX	1.00E-24	683.7	1.00E-24	690.8	1.00E-24	731.5	5.14E-21	751.0	1.00E-24	814.0
SC SUM	1.22E-15		6.72E-15		5.82E-15		4.86E-15		3.53E-15	
DC	4.01E-22	-47.0	1.92E-21	-37.2	1.65E-20	25.1	1.54E-20	52.3	1.34E-20	79.5
DC+SS	1.00E-24	-47.0	1.00E-24	-37.2	1.00E-24	147.9	1.00E-24	178.3	1.00E-24	224.0
DC+DS	1.00E-24	-47.0	1.00E-24	-37.2	1.00E-24	25.1	1.00E-24	52.3	1.00E-24	429.3
DC+SPEX	1.00E-24	244.2	1.00E-24	276.8	1.00E-24	355.7	1.00E-24	389.3	1.00E-24	427.2
DC+DPEX	1.00E-24	660.7	1.00E-24	672.6	1.00E-24	744.5	1.00E-24	777.7	1.00E-24	854.2
DC SUM	4.05E-22		1.92E-21		1.65E-20		1.54E-20		1.34E-20	
TEX	9.57E-20	4.9	2.07E-18	5.1	1.10E-16	6.3	2.42E-16	6.8	3.72E-16	7.0
TEX+SS	1.00E-24	4.9	1.00E-24	5.1	2.43E-18	129.2	1.00E-24	132.8	7.89E-18	151.5
TEX+DS	1.00E-24	4.9	1.00E-24	5.1	2.43E-18	6.3	1.00E-24	6.8	1.00E-24	356.8
TEX+SPEX	1.00E-24	296.1	1.00E-24	319.1	2.68E-18	336.9	8.75E-18	343.8	8.40E-18	354.6
TEX+DPEX	1.00E-24	712.7	1.00E-24	715.0	2.47E-18	725.7	1.00E-24	732.2	7.85E-18	781.7
TEX SUM	9.57E-20		2.07E-18		1.20E-16		2.51E-16		3.96E-16	

Channel	Energy 200 keV/u		500		1000		2000			
	cross section cm ²	Eloss eV								
SI	3.97E-15	33.9	4.79E-15	20.5	3.51E-15	17.0	2.15E-15	18.4		
SI+SS	2.34E-18	198.3	5.71E-18	240.1	5.01E-18	371.4	3.40E-18	594.1		
SI+DS	7.25E-19	336.3	1.84E-18	459.1	2.77E-18	815.7	2.04E-18	1128.9		
SI+SPEX	5.88E-18	404.9	7.74E-18	424.4	5.50E-18	423.3	3.86E-18	422.9		
SI+DPEX	4.83E-18	843.1	4.11E-18	870.8	2.35E-18	894.2	1.67E-18	878.4		
SI SUM	3.98E-15		4.81E-15		3.53E-15		2.16E-15			
DI	6.62E-16	153.0	8.82E-16	196.4	5.99E-16	207.0	3.32E-16	216.5		
DI+SS	8.51E-19	317.4	3.42E-18	416.0	4.04E-18	561.4	3.29E-18	792.2		
DI+DS	2.48E-19	455.4	9.75E-19	635.0	2.56E-18	1005.8	2.19E-18	1327.0		
DI+SPEX	2.37E-18	524.0	4.42E-18	600.4	4.34E-18	613.4	3.65E-18	621.0		
DI+DPEX	1.79E-18	962.1	2.54E-18	1046.7	2.12E-18	1084.3	1.93E-18	1076.5		
DI SUM	6.67E-16		8.93E-16		6.12E-16		3.43E-16			
TI	5.92E-16	100.4	3.60E-17	184.8	2.91E-18	255.4	1.76E-19	175.7		
TI+SS	2.31E-18	264.8	1.37E-18	404.4	1.06E-19	609.8	1.43E-20	751.3		
TI+DS	5.30E-19	402.8	4.77E-19	623.5	6.79E-20	1054.2	8.47E-21	1286.1		
TI+SPEX	6.73E-18	471.4	1.76E-18	588.8	1.13E-19	661.7	1.57E-20	580.1		
TI+DPEX	5.27E-18	909.5	1.12E-18	1035.1	6.03E-20	1132.7	7.13E-21	1035.6		
TI SUM	6.07E-16		4.07E-17		3.26E-18		2.22E-19			
DCAI	1.51E-16	609.6	7.79E-19	1286.0	5.95E-21	971.6	5.95E-23	0.0		
DCAI+SS	1.18E-18	774.1	4.17E-20	1505.6	1.00E-24	1326.0	1.00E-24	575.7		
DCAI+DS	4.03E-19	912.0	1.00E-24	1724.6	1.00E-24	1770.4	1.00E-24	1110.4		
DCAI+SPEX	2.91E-18	980.6	1.25E-19	1689.9	1.00E-24	1377.9	1.00E-24	404.4		
DCAI+DPEX	2.44E-18	1418.8	1.00E-24	2136.2	1.00E-24	1848.9	1.00E-24	860.0		
DCAI SUM	1.58E-16		9.46E-19		5.95E-21		6.35E-23			
SC	4.32E-16	93.7	6.85E-18	233.3	2.56E-19	437.6	1.70E-20	982.2		
SC+SS	1.00E-24	258.2	1.11E-20	452.9	5.27E-21	792.0	1.25E-21	1557.9		
SC+DS	1.00E-24	396.2	2.46E-21	672.0	1.86E-21	1236.3	8.79E-22	2092.7		
SC+SPEX	6.19E-21	464.8	1.72E-20	637.3	6.08E-21	843.9	1.53E-21	1386.6		
SC+DPEX	6.19E-21	902.9	6.15E-21	1083.6	1.62E-21	1314.9	7.87E-22	1842.2		
SC SUM	4.32E-16		6.89E-18		2.71E-19		2.14E-20			
DC	8.67E-20	188.4	2.37E-20	467.6	7.90E-22	876.2	6.75E-23	0.0		
DC+SS	1.14E-20	352.9	2.64E-21	687.2	1.97E-22	1230.6	1.69E-23	575.7		
DC+DS	5.72E-21	490.9	1.76E-21	906.3	1.97E-22	1674.9	1.69E-23	1110.4		
DC+SPEX	3.43E-20	559.5	3.52E-21	871.6	1.97E-22	1282.5	1.69E-23	404.4		
DC+DPEX	2.29E-20	997.6	2.64E-21	1317.9	1.97E-22	1753.4	1.69E-23	860.0		
DC SUM	1.61E-19		3.43E-20		1.58E-21		1.35E-22			
TEX	8.45E-16	7.3	1.60E-15	7.4	1.86E-15	7.1	1.63E-15	6.8		
TEX+SS	1.27E-17	171.7	1.20E-17	227.0	1.06E-17	361.5	3.48E-18	582.5		
TEX+DS	1.23E-17	309.7	1.00E-24	446.1	1.02E-17	805.9	3.39E-18	1117.2		
TEX+SPEX	1.34E-17	378.3	1.21E-17	411.4	1.06E-17	413.4	3.51E-18	411.2		
TEX+DPEX	1.32E-17	816.5	1.19E-17	857.7	1.02E-17	884.4	3.36E-18	866.8		
TEX SUM	8.97E-16		1.64E-15		1.90E-15		1.64E-15			

Table B.14: The integral cross section and associated average energy loss for SIM and NSIM processes in $S^{13+} + H_2$ collisions with impact energies between 1 and 2000 keV/u. (From Gharibnejad et al. (2019))

Channel	Energy 1 keV/u		10		50		75		100	
	cross section cm ²	Eloss eV								
SI	8.44E-19	1.5	9.81E-19	12.3	1.20E-16	10.1	5.22E-16	16.7	1.36E-15	23.1
SI+SS	1.00E-24	1.5	6.27E-21	12.3	2.92E-20	131.7	3.46E-20	148.5	2.71E-19	167.5
SI+DS	1.00E-24	1.5	4.48E-22	12.3	1.00E-24	10.1	1.00E-24	16.7	6.78E-20	23.1
SI+SPEX	1.00E-24	300.5	5.10E-20	327.5	1.17E-19	336.8	4.15E-19	353.2	1.42E-18	370.2
SI+DPEX	1.00E-24	2696.0	8.95E-22	2709.0	1.00E-24	2716.3	1.00E-24	2728.8	6.78E-20	2741.1
SI SUM	8.44E-19		1.04E-18		1.20E-16		5.22E-16		1.36E-15	
DI	2.59E-23	0.0	5.15E-22	25.5	1.11E-19	14.4	3.57E-18	34.3	3.66E-17	60.0
DI+SS	1.00E-24	0.0	1.00E-24	25.5	1.00E-24	136.0	1.00E-24	166.1	1.00E-24	204.5
DI+DS	1.00E-24	0.0	1.00E-24	25.5	1.00E-24	14.4	1.00E-24	34.3	1.00E-24	60.0
DI+SPEX	1.00E-24	299.1	1.00E-24	340.7	1.00E-24	341.1	1.85E-20	370.8	8.01E-20	407.1
DI+DPEX	1.00E-24	2694.5	1.00E-24	2722.2	1.00E-24	2720.6	1.00E-24	2746.4	1.00E-24	2778.1
DI SUM	2.99E-23		5.19E-22		1.11E-19		3.59E-18		3.67E-17	
TI	2.11E-19	1.8	1.89E-18	12.5	4.74E-17	11.6	2.10E-16	22.3	5.39E-16	39.3
TI+SS	1.00E-24	1.8	1.68E-20	12.5	6.05E-20	133.2	1.28E-19	154.1	1.03E-18	183.7
TI+DS	1.00E-24	1.8	4.41E-22	12.5	1.00E-24	11.6	1.00E-24	22.3	1.72E-19	39.3
TI+SPEX	3.71E-21	300.8	1.09E-19	327.7	2.72E-19	338.3	7.98E-19	358.8	3.43E-18	386.4
TI+DPEX	1.00E-24	2696.3	8.83E-22	2709.2	1.00E-24	2717.8	1.00E-24	2734.4	1.72E-19	2757.3
TI SUM	2.15E-19		2.02E-18		4.77E-17		2.11E-16		5.44E-16	
DCAI	6.29E-15	262.0	4.93E-15	307.1	3.55E-15	428.4	2.94E-15	498.1	2.15E-15	558.0
DCAI+SS	2.02E-18	262.0	2.40E-18	307.1	4.07E-18	549.9	4.07E-18	629.9	4.26E-18	702.4
DCAI+DS	7.04E-20	262.0	7.47E-20	307.1	9.38E-20	428.4	1.61E-19	498.1	6.99E-20	558.0
DCAI+SPEX	1.46E-17	561.1	1.56E-17	622.2	2.40E-17	755.0	3.11E-17	834.6	3.02E-17	905.1
DCAI+DPEX	1.79E-19	2956.5	2.02E-19	3003.7	2.50E-19	3134.5	2.58E-19	3210.2	6.99E-20	3276.0
DCAI SUM	6.31E-15		4.95E-15		3.58E-15		2.98E-15		2.18E-15	
SC	7.69E-15	-31.0	7.33E-15	-26.1	6.28E-15	6.7	5.35E-15	27.9	3.96E-15	41.5
SC+SS	1.00E-24	-31.0	1.00E-24	-26.1	1.00E-24	128.3	1.00E-24	159.7	1.00E-24	185.9
SC+DS	1.00E-24	-31.0	1.00E-24	-26.1	1.00E-24	6.7	1.00E-24	27.9	1.00E-24	41.5
SC+SPEX	1.00E-24	268.1	1.00E-24	289.1	1.00E-24	333.4	1.76E-20	364.4	1.00E-24	388.6
SC+DPEX	1.00E-24	2663.6	1.00E-24	2670.6	1.00E-24	2712.9	1.00E-24	2740.0	1.00E-24	2759.6
SC SUM	7.69E-15		7.33E-15		6.28E-15		5.35E-15		3.96E-15	
DC	4.58E-22	-60.9	2.19E-21	-51.1	1.89E-20	14.4	1.00E-24	56.7	1.00E-24	84.0
DC+SS	1.00E-24	-60.9	1.00E-24	-51.1	1.00E-24	136.0	8.80E-21	188.5	1.00E-24	228.4
DC+DS	1.00E-24	-60.9	1.00E-24	-51.1	1.00E-24	14.4	1.00E-24	56.7	1.00E-24	84.0
DC+SPEX	1.00E-24	238.1	1.00E-24	264.0	1.00E-24	341.1	8.80E-21	393.2	1.39E-20	431.1
DC+DPEX	1.00E-24	2633.6	1.00E-24	2645.5	1.00E-24	2720.6	1.00E-24	2768.9	1.00E-24	2802.0
DC SUM	4.62E-22		2.19E-21		1.89E-20		1.76E-20		1.39E-20	
TEX	1.24E-19	4.7	1.54E-18	5.3	1.06E-16	6.4	2.28E-16	6.6	3.69E-16	7.0
TEX+SS	1.00E-24	4.7	3.08E-20	5.3	1.00E-24	128.0	1.00E-24	138.4	1.00E-24	151.4
TEX+DS	1.00E-24	4.7	1.00E-24	5.3	1.00E-24	6.4	1.00E-24	6.6	1.00E-24	7.0
TEX+SPEX	1.00E-24	303.8	3.08E-20	320.5	7.95E-18	333.1	1.73E-17	343.1	2.11E-17	354.1
TEX+DPEX	1.00E-24	2699.2	1.00E-24	2702.0	1.00E-24	2712.6	1.00E-24	2718.7	1.00E-24	2725.1
TEX SUM	1.24E-19		1.60E-18		1.14E-16		2.45E-16		3.90E-16	

Channel	Energy 200 keV/u		500		1000		2000			
	cross section cm ²	Eloss eV								
SI	4.45E-15	34.7	5.48E-15	20.2	4.05E-15	16.3	2.49E-15	16.9		
SI+SS	4.50E-18	200.3	8.53E-18	255.3	5.91E-18	381.9	4.23E-18	631.8		
SI+DS	7.14E-20	34.7	1.00E-24	20.2	4.92E-19	1265.8	2.26E-19	619.2		
SI+SPEX	9.99E-18	406.8	1.29E-17	427.4	7.57E-18	432.8	5.65E-18	426.3		
SI+DPEX	1.00E-24	2776.6	1.00E-24	2833.5	2.46E-19	2937.9	3.53E-19	3143.9		
SI SUM	4.46E-15		5.50E-15		4.06E-15		2.50E-15			
DI	6.68E-16	155.7	9.95E-16	199.9	6.99E-16	203.1	3.95E-16	208.2		
DI+SS	1.59E-18	321.2	5.94E-18	435.0	5.98E-18	568.7	5.16E-18	823.1		
DI+DS	2.53E-20	155.7	9.36E-20	199.9	4.52E-19	1452.6	2.10E-19	810.5		
DI+SPEX	3.49E-18	527.8	8.80E-18	607.0	7.40E-18	619.6	6.40E-18	617.6		
DI+DPEX	2.53E-20	2897.5	9.36E-20	3013.2	2.45E-19	3124.7	4.34E-19	3335.2		
DI SUM	6.73E-16		1.01E-15		7.13E-16		4.07E-16			
TI	6.75E-16	99.8	4.54E-17	185.4	3.05E-18	206.6	2.19E-19	146.5		
TI+SS	5.27E-18	265.3	2.26E-18	420.5	2.82E-19	572.2	2.33E-20	761.4		
TI+DS	5.11E-20	99.8	7.07E-20	185.4	1.00E-24	1456.2	2.11E-21	748.8		
TI+SPEX	1.18E-17	471.9	3.01E-18	592.5	3.24E-19	623.1	2.95E-20	559.2		
TI+DPEX	5.11E-20	2841.7	7.07E-20	2998.7	1.53E-20	3128.2	2.59E-21	3273.5		
TI SUM	6.92E-16		5.08E-17		3.67E-18		2.77E-19			
DCAI	2.00E-16	704.8	1.02E-18	977.4	6.90E-21	1296.5	6.90E-23	0.0		
DCAI+SS	1.83E-18	870.3	5.65E-20	1212.5	1.00E-24	1662.2	1.00E-24	614.9		
DCAI+DS	1.00E-24	704.8	1.00E-24	977.4	1.00E-24	2546.1	1.00E-24	602.3		
DCAI+SPEX	4.85E-18	1076.9	5.65E-20	1384.5	1.00E-24	1713.0	1.00E-24	409.4		
DCAI+DPEX	1.00E-24	3446.7	1.00E-24	3790.7	1.00E-24	4218.1	1.00E-24	3127.0		
DCAI SUM	2.07E-16		1.13E-18		6.90E-21		7.30E-23			
SC	5.08E-16	88.4	7.90E-18	223.9	2.48E-19	416.3	1.60E-20	961.0		
SC+SS	1.00E-24	254.0	7.31E-21	459.0	3.69E-21	782.0	1.50E-21	1575.8		
SC+DS	1.00E-24	88.4	1.00E-24	223.9	1.84E-22	1665.9	1.00E-24	1563.2		
SC+SPEX	3.31E-20	460.6	1.64E-20	631.0	5.16E-21	832.8	2.09E-21	1370.4		
SC+DPEX	1.00E-24	2830.3	1.00E-24	3037.1	1.84E-22	3337.9	2.59E-23	4088.0		
SC SUM	5.08E-16		7.92E-18		2.57E-19		1.96E-20			
DC	1.98E-20	177.8	1.00E-24	448.7	1.32E-21	833.6	1.00E-24	0.0		
DC+SS	1.00E-24	343.4	4.50E-21	683.8	1.00E-24	1199.3	1.12E-23	614.9		
DC+DS	1.00E-24	177.8	1.00E-24	448.7	1.00E-24	2083.2	1.00E-24	602.3		
DC+SPEX	1.98E-20	550.0	6.00E-21	855.9	1.00E-24	1250.1	1.12E-23	409.4		
DC+DPEX	1.00E-24	2919.7	1.00E-24	3262.0	1.00E-24	3755.2	1.00E-24	3127.0		
DC SUM	3.96E-20		1.05E-20		1.32E-21		2.54E-23			
TEX	8.29E-16	7.3	1.61E-15	7.4	2.01E-15	7.2	1.81E-15	6.9		
TEX+SS	4.07E-17	172.9	5.32E-17	242.5	2.64E-17	372.8	1.01E-17	621.8		
TEX+DS	1.00E-24	7.3	1.00E-24	7.4	1.00E-24	1256.8	1.00E-24	609.2		
TEX+SPEX	4.35E-17	379.4	5.51E-17	414.6	2.70E-17	423.7	1.03E-17	416.3		
TEX+DPEX	1.00E-24	2749.2	1.00E-24	2820.7	1.00E-24	2928.8	1.00E-24	3133.9		
TEX SUM	9.13E-16		1.72E-15		2.06E-15		1.83E-15			

Table B.15: The integral cross section and associated average energy loss for SIM and NSIM processes in $S^{14+} + H_2$ collisions with impact energies between 1 and 2000 keV/u. (From Gharibnejad et al. (2019))

Channel	Energy 1 keV/u		10		50		75		100	
	cross section cm ²	Eloss eV								
SI	7.52E-19	1.4	7.53E-19	11.9	2.47E-16	9.5	1.06E-15	16.5	1.37E-15	22.9
SI+SS	1.00E-24	1.4	1.00E-24	11.9	1.00E-24	9.5	1.00E-24	16.5	1.00E-24	22.9
SI+DS	1.00E-24	1.4	1.00E-24	11.9	1.00E-24	9.5	1.00E-24	16.5	1.00E-24	22.9
SI+SPEX	1.00E-24	1.4	6.89E-21	2133.3	1.00E-24	1937.1	8.39E-20	1905.6	1.00E-24	1958.7
SI+DPEX	1.00E-24	1.4	1.00E-24	11.9	1.00E-24	9.5	1.00E-24	16.5	1.00E-24	22.9
SI SUM	7.52E-19		7.60E-19		2.47E-16		1.06E-15		1.37E-15	
DI	2.90E-23	0.0	5.75E-22	15.2	1.98E-19	10.0	3.29E-18	36.1	3.04E-17	57.5
DI+SS	1.00E-24	0.0	1.00E-24	15.2	1.00E-24	10.0	1.00E-24	36.1	1.00E-24	57.5
DI+DS	1.00E-24	0.0	1.00E-24	15.2	1.00E-24	10.0	1.00E-24	36.1	1.00E-24	57.5
DI+SPEX	1.00E-24	0.0	1.00E-24	2136.7	1.00E-24	1937.7	1.00E-24	1925.3	1.00E-24	1993.3
DI+DPEX	1.00E-24	0.0	1.00E-24	15.2	1.00E-24	10.0	1.00E-24	36.1	1.00E-24	57.5
DI SUM	3.30E-23		5.79E-22		1.98E-19		3.29E-18		3.04E-17	
TI	2.30E-19	1.6	1.55E-18	12.2	4.24E-17	11.8	1.92E-16	20.4	5.44E-16	37.5
TI+SS	1.00E-24	1.6	1.00E-24	12.2	1.00E-24	11.8	1.00E-24	20.4	1.00E-24	37.5
TI+DS	1.00E-24	1.6	1.00E-24	12.2	1.00E-24	11.8	1.00E-24	20.4	1.00E-24	37.5
TI+SPEX	1.00E-24	1.6	2.13E-20	2133.7	1.00E-24	1939.5	3.97E-20	1909.6	1.00E-24	1973.3
TI+DPEX	1.00E-24	1.6	1.00E-24	12.2	1.00E-24	11.8	1.00E-24	20.4	1.00E-24	37.5
TI SUM	2.30E-19		1.57E-18		4.24E-17		1.92E-16		5.44E-16	
DCAI	6.88E-15	289.7	5.42E-15	335.5	3.90E-15	460.1	3.32E-15	533.1	2.51E-15	596.4
DCAI+SS	1.00E-24	289.7	1.00E-24	335.5	1.00E-24	460.1	1.00E-24	533.1	1.00E-24	596.4
DCAI+DS	5.85E-20	289.7	7.36E-20	335.5	3.89E-20	460.1	1.45E-19	533.1	3.33E-19	596.4
DCAI+SPEX	3.73E-18	289.7	3.38E-18	2457.0	2.06E-18	2387.7	1.56E-18	2422.2	1.00E-24	2532.2
DCAI+DPEX	1.00E-24	289.7	1.00E-24	335.5	1.00E-24	460.1	1.00E-24	533.1	1.00E-24	596.4
DCAI SUM	6.88E-15		5.42E-15		3.90E-15		3.32E-15		2.51E-15	
SC	8.24E-15	-25.7	7.58E-15	-20.8	6.73E-15	1.0	5.83E-15	23.4	6.65E-16	37.0
SC+SS	1.00E-24	-25.7	1.00E-24	-20.8	1.00E-24	1.0	1.00E-24	23.4	1.00E-24	37.0
SC+DS	1.00E-24	-25.7	1.00E-24	-20.8	1.00E-24	1.0	1.00E-24	23.4	1.00E-24	37.0
SC+SPEX	1.00E-24	-25.7	1.00E-24	2100.7	1.00E-24	1928.7	1.00E-24	1912.5	1.00E-24	1972.8
SC+DPEX	1.00E-24	-25.7	1.00E-24	-20.8	1.00E-24	1.0	1.00E-24	23.4	1.00E-24	37.0
SC SUM	8.24E-15		7.58E-15		6.73E-15		5.83E-15		6.65E-16	
DC	4.89E-22	-50.4	2.34E-21	-40.6	2.02E-20	3.0	1.88E-20	47.7	7.70E-21	74.9
DC+SS	1.00E-24	-50.4	1.00E-24	-40.6	1.00E-24	3.0	1.00E-24	47.7	1.00E-24	74.9
DC+DS	1.00E-24	-50.4	1.00E-24	-40.6	1.00E-24	3.0	1.00E-24	47.7	1.00E-24	74.9
DC+SPEX	1.00E-24	-50.4	1.00E-24	2080.8	1.00E-24	1930.6	1.00E-24	1936.8	1.00E-24	2010.7
DC+DPEX	1.00E-24	-50.4	1.00E-24	-40.6	1.00E-24	3.0	1.00E-24	47.7	1.00E-24	74.9
DC SUM	4.93E-22		2.34E-21		2.02E-20		1.88E-20		7.70E-21	
TEX	2.65E-19	4.9	1.22E-18	5.0	1.08E-16	6.3	2.35E-16	6.6	3.80E-16	6.9
TEX+SS	1.00E-24	4.9	1.00E-24	5.0	1.00E-24	6.3	1.00E-24	6.6	1.00E-24	6.9
TEX+DS	1.00E-24	4.9	1.00E-24	5.0	1.00E-24	6.3	1.00E-24	6.6	1.00E-24	6.9
TEX+SPEX	1.00E-24	4.9	1.00E-24	2126.5	1.00E-24	1934.0	1.00E-24	1895.7	1.00E-24	1942.7
TEX+DPEX	1.00E-24	4.9	1.00E-24	5.0	1.00E-24	6.3	1.00E-24	6.6	1.00E-24	6.9
TEX SUM	2.65E-19		1.22E-18		1.08E-16		2.35E-16		3.80E-16	

Channel	Energy 200 keV/u		500		1000		2000			
	cross section cm ²	Eloss eV								
SI	4.95E-15	35.0	6.23E-15	20.1	4.63E-15	15.8	2.85E-15	15.8		
SI+SS	1.00E-24	521.5	1.87E-19	1145.8	1.45E-19	1789.0	2.28E-19	3058.5		
SI+DS	5.70E-20	35.0	1.87E-19	20.1	2.91E-19	15.8	1.19E-19	15.8		
SI+SPEX	5.70E-20	2100.7	6.55E-19	2133.7	2.91E-19	2198.1	2.56E-19	2278.7		
SI+DPEX	1.00E-24	35.0	1.00E-24	20.1	1.00E-24	15.8	1.00E-24	15.8		
SI SUM	4.95E-15		6.23E-15		4.63E-15		2.85E-15			
DI	6.79E-16	155.1	1.13E-15	202.1	8.19E-16	201.9	4.75E-16	203.3		
DI+SS	1.00E-24	641.6	4.98E-20	1327.8	1.22E-19	1975.2	3.81E-19	3246.0		
DI+DS	4.01E-20	155.1	1.74E-19	202.1	2.76E-19	201.9	2.04E-19	203.3		
DI+SPEX	4.01E-20	2220.8	5.23E-19	2315.8	2.76E-19	2384.2	4.93E-19	2466.2		
DI+DPEX	1.00E-24	155.1	1.00E-24	202.1	1.00E-24	201.9	1.00E-24	203.3		
DI SUM	6.79E-16		1.13E-15		8.20E-16		4.76E-16			
TI	7.71E-16	100.1	5.86E-17	191.7	4.47E-18	202.7	3.15E-19	147.7		
TI+SS	1.00E-24	586.6	4.40E-20	1317.4	1.47E-20	1976.0	2.71E-21	3190.3		
TI+DS	1.44E-19	100.1	4.40E-20	191.7	1.47E-20	202.7	1.00E-24	147.7		
TI+SPEX	9.62E-20	2165.8	1.76E-19	2305.4	1.47E-20	2385.0	3.48E-21	2410.6		
TI+DPEX	1.00E-24	100.1	1.00E-24	191.7	1.00E-24	202.7	1.00E-24	147.7		
TI SUM	7.71E-16		5.89E-17		4.51E-18		3.21E-19			
DCAI	2.58E-16	750.4	1.58E-18	1030.4	1.83E-20	1312.2	2.03E-22	0.0		
DCAI+SS	1.00E-24	1236.9	1.00E-24	2156.1	1.02E-21	3085.4	1.00E-24	3042.7		
DCAI+DS	1.07E-19	750.4	1.00E-24	1030.4	1.00E-24	1312.2	1.00E-24	0.0		
DCAI+SPEX	5.34E-20	2816.1	1.00E-24	3144.1	1.02E-21	3494.5	1.00E-24	2262.9		
DCAI+DPEX	1.00E-24	750.4	1.00E-24	1030.4	1.00E-24	1312.2	1.00E-24	0.0		
DCAI SUM	2.58E-16		1.58E-18		2.03E-20		2.07E-22			
SC	2.38E-16	91.4	8.29E-18	233.3	4.20E-20	453.4	3.02E-21	998.0		
SC+SS	1.00E-24	577.9	1.00E-24	1359.0	1.00E-24	2226.6	1.00E-24	4040.6		
SC+DS	1.00E-24	91.4	1.00E-24	233.3	1.00E-24	453.4	1.00E-24	998.0		
SC+SPEX	1.00E-24	2157.1	1.00E-24	2347.0	1.00E-24	2635.6	1.00E-24	3260.9		
SC+DPEX	1.00E-24	91.4	1.00E-24	233.3	1.00E-24	453.4	1.00E-24	998.0		
SC SUM	2.38E-16		8.29E-18		4.20E-20		3.02E-21			
DC	2.20E-20	183.8	2.00E-20	467.6	8.95E-23	907.7	2.24E-23	0.0		
DC+SS	1.00E-24	670.3	1.00E-24	1593.3	1.00E-24	2681.0	1.00E-24	3042.7		
DC+DS	1.00E-24	183.8	1.00E-24	467.6	4.47E-23	907.7	1.00E-24	0.0		
DC+SPEX	1.00E-24	2249.5	1.00E-24	2581.3	4.47E-23	3090.0	1.00E-24	2262.9		
DC+DPEX	1.00E-24	183.8	1.00E-24	467.6	1.00E-24	907.7	1.00E-24	0.0		
DC SUM	2.20E-20		2.00E-20		1.81E-22		2.64E-23			
TEX	9.15E-16	7.3	1.80E-15	7.4	2.21E-15	7.2	2.02E-15	6.9		
TEX+SS	1.00E-24	493.8	1.00E-24	1133.1	1.00E-24	1780.5	1.00E-24	3049.6		
TEX+DS	1.00E-24	7.3	1.00E-24	7.4	1.00E-24	7.2	1.00E-24	6.9		
TEX+SPEX	1.00E-24	2073.0	1.00E-24	2121.1	1.00E-24	2189.5	1.00E-24	2269.8		
TEX+DPEX	1.00E-24	7.3	1.00E-24	7.4	1.00E-24	7.2	1.00E-24	6.9		
TEX SUM	9.15E-16		1.80E-15		2.21E-15		2.02E-15			

Table B.16: The integral cross section and associated average energy loss for SIM and NSIM processes in $S^{15+} + H_2$ collisions with impact energies between 1 and 2000 keV/u. (From Gharibnejad et al. (2019))

Channel	Energy 1 keV/u		10		50		75		100	
	cross section cm ²	Eloss eV								
SI	1.61E-19	1.4	8.14E-19	12.3	1.06E-16	10.0	4.74E-16	17.6	1.23E-15	22.1
SI+SPEX	1.00E-24	1.4	7.91E-21	2290.8	2.11E-21	2071.7	1.00E-24	1981.9	8.90E-20	2079.6
SI+DPEX	1.00E-24	1.4	1.00E-24	12.3	1.00E-24	10.0	1.00E-24	17.6	1.00E-24	22.1
SI SUM	1.61E-19		8.22E-19		1.06E-16		4.74E-16		1.23E-15	
DI	7.96E-24	0.0	1.58E-22	36.1	9.09E-20	21.6	3.06E-18	33.9	2.47E-17	58.1
DI+SPEX	1.00E-24	0.0	1.00E-24	2314.7	1.00E-24	2083.2	1.00E-24	1998.2	1.00E-24	2115.6
DI+DPEX	1.00E-24	0.0	1.00E-24	36.1	1.00E-24	21.6	1.00E-24	33.9	1.00E-24	58.1
DI SUM	9.96E-24		1.60E-22		9.09E-20		3.06E-18		2.47E-17	
TI	1.61E-19	2.1	1.25E-18	12.3	4.08E-17	11.1	1.76E-16	19.0	5.19E-16	35.8
TI+SPEX	1.00E-24	2.1	1.48E-20	2290.9	1.27E-20	2072.7	1.00E-24	1983.2	1.00E-24	2093.3
TI+DPEX	1.00E-24	2.1	1.00E-24	12.3	1.00E-24	11.1	1.00E-24	19.0	1.00E-24	35.8
TI SUM	1.61E-19		1.26E-18		4.08E-17		1.76E-16		5.19E-16	
DCAI	7.47E-15	2799.3	5.89E-15	2959.6	4.29E-15	3291.6	3.67E-15	3444.6	2.84E-15	3575.7
DCAI+SPEX	4.41E-18	2799.3	1.00E-24	5238.2	1.24E-18	5353.2	1.27E-18	5408.9	8.94E-19	5633.2
DCAI+DPEX	1.00E-24	2799.3	1.00E-24	2959.6	1.00E-24	3291.6	1.00E-24	3444.6	1.00E-24	3575.7
DCAI SUM	7.47E-15		5.89E-15		4.29E-15		3.67E-15		2.84E-15	
SC	8.93E-15	-31.9	8.01E-15	-27.0	7.21E-15	4.9	6.31E-15	25.7	4.88E-15	39.3
SC+SPEX	1.99E-19	-31.9	1.00E-24	2251.6	1.00E-24	2066.5	1.00E-24	1989.9	1.00E-24	2096.8
SC+DPEX	1.00E-24	-31.9	1.00E-24	-27.0	1.00E-24	4.9	1.00E-24	25.7	1.00E-24	39.3
SC SUM	8.93E-15		8.01E-15		7.21E-15		6.31E-15		4.88E-15	
DC	2.71E-22	-62.8	1.30E-21	-53.0	1.12E-20	10.7	1.04E-20	52.3	4.28E-21	79.5
DC+SPEX	1.00E-24	-62.8	1.00E-24	2225.6	1.00E-24	2072.3	1.00E-24	2016.5	1.00E-24	2137.0
DC+DPEX	1.00E-24	-62.8	1.00E-24	-53.0	1.00E-24	10.7	1.00E-24	52.3	1.00E-24	79.5
DC SUM	2.73E-22		1.30E-21		1.12E-20		1.04E-20		4.28E-21	
TEX	2.00E-19	4.6	9.29E-19	4.9	1.01E-16	6.1	2.29E-16	6.7	3.70E-16	6.9
TEX+SPEX	1.00E-24	4.6	1.00E-24	2283.4	1.00E-24	2067.7	1.00E-24	1970.9	1.00E-24	2064.4
TEX+DPEX	1.00E-24	4.6	1.00E-24	4.9	1.00E-24	6.1	1.00E-24	6.7	1.00E-24	6.9
TEX SUM	2.00E-19		9.29E-19		1.01E-16		2.29E-16		3.70E-16	

Channel	Energy 200 keV/u		500		1000		2000			
	cross section cm ²	Eloss eV								
SI	3.79E-15	35.3	2.96E-15	20.0	2.07E-15	15.5	1.35E-15	15.0		
SI+SPEX	3.45E-19	2149.7	2.64E-19	2223.0	2.97E-19	2311.9	1.95E-19	2380.7		
SI+DPEX	1.00E-24	35.3	1.00E-24	20.0	1.00E-24	15.5	1.00E-24	15.0		
SI SUM	3.79E-15		2.96E-15		2.07E-15		1.35E-15			
DI	6.74E-16	155.3	1.26E-15	205.8	9.30E-16	203.7	5.49E-16	202.4		
DI+SPEX	4.31E-20	2269.7	5.01E-19	2408.8	6.77E-19	2500.1	6.13E-19	2568.0		
DI+DPEX	1.00E-24	155.3	1.00E-24	205.8	1.00E-24	203.7	1.00E-24	202.4		
DI SUM	6.74E-16		1.26E-15		9.31E-16		5.50E-16			
TI	8.60E-16	99.6	6.80E-17	194.5	5.26E-18	213.9	4.21E-19	146.7		
TI+SPEX	4.31E-19	2213.9	2.06E-19	2397.5	1.00E-24	2510.3	2.99E-21	2512.4		
TI+DPEX	1.00E-24	99.6	1.00E-24	194.5	1.00E-24	213.9	1.00E-24	146.7		
TI SUM	8.60E-16		6.82E-17		5.26E-18		4.24E-19			
DCAI	3.16E-16	3948.2	2.20E-18	4667.9	2.43E-21	5619.6	2.43E-23	0.0		
DCAI+SPEX	2.58E-19	6062.6	1.00E-24	6870.9	1.00E-24	7916.1	1.00E-24	2365.7		
DCAI+DPEX	1.00E-24	3948.2	1.00E-24	4667.9	1.00E-24	5619.6	1.00E-24	0.0		
DCAI SUM	3.16E-16		2.20E-18		2.43E-21		2.63E-23			
SC	6.70E-16	93.7	1.02E-17	225.3	3.07E-19	437.6	1.87E-20	982.2		
SC+SPEX	1.00E-24	2208.1	1.00E-24	2428.2	1.00E-24	2734.1	3.37E-23	3347.9		
SC+DPEX	1.00E-24	93.7	1.00E-24	225.3	1.00E-24	437.6	1.00E-24	982.2		
SC SUM	6.70E-16		1.02E-17		3.07E-19		1.88E-20			
DC	1.22E-20	188.4	1.11E-20	451.5	8.97E-22	876.2	8.96E-23	0.0		
DC+SPEX	1.00E-24	2302.8	1.00E-24	2654.5	1.00E-24	3172.6	2.24E-23	2365.7		
DC+DPEX	1.00E-24	188.4	1.00E-24	451.5	1.00E-24	876.2	1.00E-24	0.0		
DC SUM	1.22E-20		1.11E-20		8.99E-22		1.13E-22			
TEX	9.24E-16	7.3	1.66E-15	7.4	2.16E-15	7.2	2.10E-15	6.9		
TEX+SPEX	1.00E-24	2121.7	2.14E-16	2210.4	2.03E-16	2303.7	1.07E-16	2372.6		
TEX+DPEX	1.00E-24	7.3	1.00E-24	7.4	1.00E-24	7.2	1.00E-24	6.9		
TEX SUM	9.24E-16		1.87E-15		2.36E-15		2.21E-15			

Table B.17: The integral cross section and associated average energy loss for SIM and NSIM processes in $S^{16+} + H_2$ collisions with impact energies between 1 and 2000 keV/u. (From Gharibnejad et al. (2019))

Channel	Energy 1 keV/u		10		50		75		100	
	cross section cm ²	Eloss eV								
SI	1.80E-20	0.3	4.84E-19	13.4	1.01E-16	9.6	4.69E-16	15.9	1.39E-15	21.5
DI	7.69E-24	0.0	1.53E-22	0.0	8.78E-20	18.5	1.93E-18	32.1	2.12E-17	57.6
TI	2.25E-20	1.0	1.05E-18	13.2	3.76E-17	11.1	1.62E-16	17.9	5.11E-16	35.5
DCAI	8.08E-15	3028.9	6.35E-15	3195.6	4.62E-15	3539.9	4.05E-15	3697.8	3.21E-15	3833.9
SC	9.30E-15	-27.0	8.48E-15	-22.1	7.63E-15	-0.3	6.79E-15	27.5	5.34E-15	41.1
DC	1.27E-22	-53.1	6.08E-22	-43.3	5.24E-21	0.3	4.88E-21	56.0	2.00E-21	83.2
TEX	9.62E-20	4.6	6.33E-19	5.0	9.65E-17	6.3	2.23E-16	6.6	3.57E-16	6.8
Channel	Energy 200 keV/u		500		1000		2000			
	cross section cm ²	Eloss eV								
SI	6.01E-15	35.9	7.81E-15	20.0	5.85E-15	15.3	3.64E-15	14.5		
DI	6.67E-16	155.8	1.40E-15	210.1	1.05E-15	206.8	5.86E-16	198.3		
TI	9.55E-16	100.8	8.38E-17	193.8	6.21E-18	232.8	4.29E-19	189.9		
DCAI	3.74E-16	4221.8	2.39E-18	4979.6	2.03E-20	5959.0	2.03E-22	0.0		
SC	7.63E-16	89.5	1.08E-17	233.3	3.14E-19	420.7	1.86E-20	965.3		
DC	5.71E-21	180.0	5.19E-21	467.6	4.20E-22	842.4	5.24E-23	0.0		
TEX	9.35E-16	7.3	1.93E-15	7.4	2.49E-15	7.2	2.40E-15	6.9		

Appendix C

Tables of Chemical Reactions

Table C.1: Electron Recombination for the Selected Reactions

Reaction	Rate Coefficient cm^3s^{-1}	Reference
$\text{H}^+ + \text{e}^- \rightarrow \text{H} + h\nu$	$4.00 \times 10^{-12}(300/T_e)^{0.64}$	Yelle & Miller (2004)
$\text{He}^+ + \text{e}^- \rightarrow \text{He} + h\nu$	$4.60 \times 10^{-12}(300/T_e)^{0.64}$	Yelle & Miller (2004)
$\text{H}_2^+ + \text{e}^- \rightarrow \text{H} + \text{H}$	$2.30 \times 10^{-7}(300/T_e)^{0.4}$	Yelle & Miller (2004)
$\text{H}_3^+ + \text{e}^- \rightarrow \text{H}_2 + \text{H}$	$4.4 \times 10^{-8}(300/T_e)^{0.5}$	Woodall et al. (2007)
$\text{H}_3^+ + \text{e}^- \rightarrow \text{H} + \text{H} + \text{H}$	$5.6 \times 10^{-8}(300/T_e)^{0.5}$	Kim & Fox (1994)
$\text{HeH}^+ + \text{e}^- \rightarrow \text{He} + \text{H}$	$1.00 \times 10^{-8}(300/T_e)^{0.6}$	Yelle & Miller (2004)
$\text{CH}^+ + \text{e}^- \rightarrow \text{C} + \text{H}$	$1.50 \times 10^{-7}(300/T_e)^{0.42}$	Woodall et al. (2007)
$\text{CH}_2^+ + \text{e}^- \rightarrow \text{C} + \text{H}_2$	$7.68 \times 10^{-8}(300/T_e)^{0.6}$	Woodall et al. (2007)
$\text{CH}_2^+ + \text{e}^- \rightarrow \text{C} + \text{H} + \text{H}$	$4.03 \times 10^{-7}(300/T_e)^{0.6}$	Woodall et al. (2007)
$\text{CH}_2^+ + \text{e}^- \rightarrow \text{CH} + \text{H}$	$1.60 \times 10^{-7}(300/T_e)^{0.6}$	Woodall et al. (2007)
$\text{CH}_3^+ + \text{e}^- \rightarrow \text{CH} + \text{H}_2$	$8.00 \times 10^{-7}(300/T_e)^{0.5}$	Perry et al. (1999)
$\text{CH}_4^+ + \text{e}^- \rightarrow \text{CH}_3 + \text{H}$	$1.75 \times 10^{-7}(300/T_e)^{0.5}$	Woodall et al. (2007)
$\text{CH}_4^+ + \text{e}^- \rightarrow \text{CH}_2 + \text{H} + \text{H}$	$1.75 \times 10^{-7}(300/T_e)^{0.5}$	Woodall et al. (2007)
$\text{CH}_5^+ + \text{e}^- \rightarrow \text{CH}_3 + \text{H} + \text{H}$	$1.96 \times 10^{-7}(300/T_e)^{0.52}$	Woodall et al. (2007)
$\text{CH}_5^+ + \text{e}^- \rightarrow \text{CH} + \text{H}_2 + \text{H}_2$	$8.40 \times 10^{-9}(300/T_e)^{0.52}$	Woodall et al. (2007)
$\text{CH}_5^+ + \text{e}^- \rightarrow \text{CH}_4 + \text{H}$	$1.40 \times 10^{-8}(300/T_e)^{0.52}$	Woodall et al. (2007)
$\text{CH}_5^+ + \text{e}^- \rightarrow \text{CH}_2 + \text{H}_2 + \text{H}$	$4.76 \times 10^{-8}(300/T_e)^{0.52}$	Woodall et al. (2007)

Table C.1: Electron Dissociative Recombination (continued)

Reaction	Rate Coefficient cm^3s^{-1}	Reference
$\text{CH}_5^+ + e^- \rightarrow \text{CH}_3 + \text{H}_2$	$1.40 \times 10^{-8} (300/T_e)^{0.52}$	Woodall et al. (2007)
$\text{C}_2\text{H}^+ + e^- \rightarrow \text{C}_2 + \text{H}$	$1.16 \times 10^{-7} (300/T_e)^{0.76}$	Woodall et al. (2007)
$\text{C}_2\text{H}^+ + e^- \rightarrow \text{CH} + \text{C}$	$1.53 \times 10^{-7} (300/T_e)^{0.76}$	Woodall et al. (2007)
$\text{C}_2\text{H}_3^+ + e^- \rightarrow \text{C}_2\text{H}_2 + \text{H}$	$5.00 \times 10^{-7} (300/T_e)^{0.84}$	Robertson et al. (2009)
$\text{C}_2\text{H}_4^+ + e^- \rightarrow \text{C}_2\text{H}_3 + \text{H}$	$5.60 \times 10^{-7} (300/T_e)^{0.78}$	Robertson et al. (2009)
$\text{C}_2\text{H}_5^+ + e^- \rightarrow \text{C}_2\text{H}_4 + \text{H}$	$1.20 \times 10^{-6} (300/T_e)^{0.8}$	Robertson et al. (2009)
$\text{C}_2\text{H}_6^+ + e^- \rightarrow \text{C}_3\text{H}_3 + \text{H}_2 + \text{H}$	$1.00 \times 10^{-6} (300/T_e)^{0.7}$	Robertson et al. (2009)
$\text{C}_2\text{H}_7^+ + e^- \rightarrow \text{C}_3\text{H}_3 + \text{H}_2 + \text{H}_2$	$3.00 \times 10^{-7} (300/T_e)^{0.5}$	Woodall et al. (2007)
$\text{C}_3\text{H}^+ + e^- \rightarrow \text{C}_3 + \text{H}$	$2.00 \times 10^{-7} (300/T_e)^{0.7}$	Robertson et al. (2009)
$\text{C}_3\text{H}^+ + e^- \rightarrow \text{C}_2\text{H} + \text{C}$	$2.00 \times 10^{-7} (300/T_e)^{0.7}$	Robertson et al. (2009)
$\text{C}_3\text{H}_2^+ + e^- \rightarrow \text{C}_3\text{H} + \text{H}$	$4.00 \times 10^{-7} (300/T_e)^{0.7}$	Robertson et al. (2009)
$\text{C}_3\text{H}_3^+ + e^- \rightarrow \text{C}_3\text{H}_2 + \text{H}$	$7.00 \times 10^{-7} (300/T_e)^{0.5}$	Woodall et al. (2007)
$\text{C}_3\text{H}_4^+ + e^- \rightarrow \text{C}_3\text{H}_3 + \text{H}$	$2.95 \times 10^{-6} (300/T_e)^{0.67}$	Robertson et al. (2009)
$\text{C}_3\text{H}_5^+ + e^- \rightarrow \text{C}_3\text{H}_3 + \text{H}_2$	$2.00 \times 10^{-6} (300/T_e)^{0.7}$	Robertson et al. (2009)
$\text{C}_3\text{H}_6^+ + e^- \rightarrow \text{C}_3\text{H}_3 + \text{H}_2 + \text{H}$	$1.00 \times 10^{-6} (300/T_e)^{0.7}$	Robertson et al. (2009)
$\text{C}_3\text{H}_7^+ + e^- \rightarrow \text{C}_3\text{H}_3 + \text{H}_2 + \text{H}_2$	$1.90 \times 10^{-6} (300/T_e)^{0.67}$	Robertson et al. (2009)
$\text{C}_n\text{H}_m^+ + e^- \rightarrow \text{C}_n\text{H}_m$	$3.50 \times 10^{-7} (300/T_e)^{0.5}$	Robertson et al. (2009)
$\text{H}_2\text{C}_3\text{H}^+ + e^- \rightarrow \text{C}_2\text{H}_2 + \text{CH}$	$8.00 \times 10^{-7} (300/T_e)^{1.0}$	Robertson et al. (2009)

Table C.2: Selected Ion-Molecule Reactions in the Jovian Ionosphere

Reaction	Rate Coefficient [cm^3s^{-1}]	Reference
$\text{H}_2 + \text{He}^+ \rightarrow \text{H}^+ + \text{HeH}$	1.00×10^{-10}	Kim & Fox (1994)
$\text{H}_2 + \text{He}^+ \rightarrow \text{H}_2^+ + \text{He}$	9.35×10^{-15}	Kim & Fox (1994)
$\text{H}_2 + \text{He}^+ \rightarrow \text{HeH}^+ + \text{H}$	4.21×10^{-13}	Perry et al. (1999)
$\text{H}_2 + \text{H}_2^+ \rightarrow \text{H}_3^+ + \text{H}$	2.08×10^{-9}	Yelle & Miller (2004); Perry et al. (1999)
$\text{H}_2 + \text{HeH}^+ \rightarrow \text{H}_3^+ + \text{He}$	1.05×10^{-9}	Yelle & Miller (2004)
$\text{H}_2 + \text{CH}_4^+ \rightarrow \text{CH}_5^+ + \text{H}$	3.30×10^{-11}	Woodall et al. (2007)
$\text{H}_2 + \text{CH}_3^+ \rightarrow \text{CH}_4^+ + \text{H}$	1.30×10^{-14}	Woodall et al. (2007)
$\text{H}_2 + \text{CH}_2^+ \rightarrow \text{CH}_3^+ + \text{H}$	1.60×10^{-9}	Woodall et al. (2007)
$\text{H}_2 + \text{CH}^+ \rightarrow \text{CH}_2^+ + \text{H}$	1.20×10^{-9}	Woodall et al. (2007)
$\text{H}_2 + \text{C}^+ \rightarrow \text{CH}^+ + \text{H}$	1.00×10^{-10}	Woodall et al. (2007)
$\text{H}_2 + \text{C}_2\text{H}_2^+ \rightarrow \text{C}_2\text{H}_3^+ + \text{H}$	1.00×10^{-11}	Woodall et al. (2007)
$\text{H}_2 + \text{C}_2\text{H}^+ \rightarrow \text{C}_2\text{H}_2^+ + \text{H}$	1.70×10^{-9}	Woodall et al. (2007)
$\text{He} + \text{H}_2^+ \rightarrow \text{HeH}^+ + \text{H}$	1.40×10^{-10}	Kim & Fox (1994)
$\text{H} + \text{H}_2^+ \rightarrow \text{H}^+ + \text{H}_2$	6.40×10^{-10}	Yelle & Miller (2004); Perry et al. (1999)
$\text{H} + \text{H}_3^+ \rightarrow \text{H}_2^+ + \text{H}_2$	1.00×10^{-20}	estimate
$\text{H} + \text{HeH}^+ \rightarrow \text{H}_2^+ + \text{He}$	9.10×10^{-10}	Yelle & Miller (2004); Perry et al. (1999)
$\text{H} + \text{CH}_5^+ \rightarrow \text{CH}_4^+ + \text{H}_2$	1.50×10^{-10}	Woodall et al. (2007)
$\text{H} + \text{CH}^+ \rightarrow \text{C}^+ + \text{H}_2$	7.50×10^{-10}	Woodall et al. (2007)
$\text{H} + \text{C}_2\text{H}_6^+ \rightarrow \text{C}_2\text{H}_5^+ + \text{H}_2$	1.00×10^{-10}	Kim & Fox (1994)
$\text{H} + \text{C}_2\text{H}_5^+ \rightarrow \text{C}_2\text{H}_4^+ + \text{H}_2$	1.00×10^{-11}	Woodall et al. (2007)
$\text{H} + \text{C}_2\text{H}_4^+ \rightarrow \text{C}_2\text{H}_3^+ + \text{H}_2$	3.00×10^{-10}	Woodall et al. (2007)

Table C.2: Ion-Molecule Reactions (continued)

Reaction	Rate Coefficient [cm^3s^{-1}]	Reference
$\text{H} + \text{C}_2\text{H}_3^+ \rightarrow \text{C}_2\text{H}_2^+ + \text{H}_2$	6.80×10^{-11}	Woodall et al. (2007)
$\text{H} + \text{C}_3\text{H}_5^+ \rightarrow \text{C}_2\text{H}_3^+ + \text{CH}_3$	9.50×10^{-12}	Robertson et al. (2009)
$\text{H} + \text{C}_3\text{H}_5^+ \rightarrow \text{C}_2\text{H}_2^+ + \text{CH}_4$	5.00×10^{-13}	Robertson et al. (2009)
$\text{H} + \text{C}_3\text{H}_2^+ \rightarrow \text{C}_3\text{H}^+ + \text{H}_2$	6.00×10^{-11}	Robertson et al. (2009)
$\text{H} + \text{C}_2\text{H}_6^+ \rightarrow \text{C}_2\text{H}_5^+ + \text{H}_2$	1.00×10^{-10}	Kim & Fox (1994)
$\text{CH}_4 + \text{H}^+ \rightarrow \text{CH}_4^+ + \text{H}$	2.30×10^{-9}	Woodall et al. (2007)
$\text{CH}_4 + \text{H}^+ \rightarrow \text{CH}_3^+ + \text{H}_2$	1.50×10^{-9}	Woodall et al. (2007)
$\text{CH}_4 + \text{He}^+ \rightarrow \text{H}^+ + \text{CH}_3 + \text{He}$	4.80×10^{-10}	Woodall et al. (2007)
$\text{CH}_4 + \text{He}^+ \rightarrow \text{CH}_4^+ + \text{He}$	5.10×10^{-11}	Woodall et al. (2007)
$\text{CH}_4 + \text{He}^+ \rightarrow \text{CH}_3^+ + \text{He} + \text{H}$	8.50×10^{-11}	Woodall et al. (2007)
$\text{CH}_4 + \text{He}^+ \rightarrow \text{CH}_2^+ + \text{He} + \text{H}_2$	9.50×10^{-10}	Woodall et al. (2007)
$\text{CH}_4 + \text{He}^+ \rightarrow \text{CH}^+ + \text{He} + \text{H}_2 + \text{H}$	2.40×10^{-10}	Woodall et al. (2007)
$\text{CH}_4 + \text{H}_2^+ \rightarrow \text{CH}_5^+ + \text{H}$	1.14×10^{-10}	Woodall et al. (2007)
$\text{CH}_4 + \text{H}_2^+ \rightarrow \text{CH}_4^+ + \text{H}_2$	1.40×10^{-9}	Woodall et al. (2007)
$\text{CH}_4 + \text{H}_2^+ \rightarrow \text{CH}_3^+ + \text{H}_2 + \text{H}$	2.30×10^{-9}	Woodall et al. (2007)
$\text{CH}_4 + \text{H}_3^+ \rightarrow \text{CH}_5^+ + \text{H}_2$	2.40×10^{-9}	Robertson et al. (2009)
$\text{CH}_4 + \text{CH}_4^+ \rightarrow \text{CH}_5^+ + \text{CH}_3$	1.50×10^{-9}	Woodall et al. (2007)
$\text{CH}_4 + \text{CH}_3^+ \rightarrow \text{C}_2\text{H}_5^+ + \text{H}_2$	1.20×10^{-9}	Woodall et al. (2007)
$\text{CH}_4 + \text{CH}_2^+ \rightarrow \text{C}_2\text{H}_5^+ + \text{H}$	3.60×10^{-10}	Woodall et al. (2007)
$\text{CH}_4 + \text{CH}_2^+ \rightarrow \text{C}_2\text{H}_4^+ + \text{H}_2$	8.40×10^{-10}	Woodall et al. (2007)
$\text{CH}_4 + \text{CH}^+ \rightarrow \text{C}_2\text{H}_4^+ + \text{H}$	6.50×10^{-11}	Woodall et al. (2007)
$\text{CH}_4 + \text{CH}^+ \rightarrow \text{C}_2\text{H}_3^+ + \text{H}_2$	1.09×10^{-9}	Woodall et al. (2007)
$\text{CH}_4 + \text{CH}^+ \rightarrow \text{C}_2\text{H}_2^+ + \text{H}_2 + \text{H}$	1.43×10^{-10}	Woodall et al. (2007)
$\text{CH}_4 + \text{C}^+ \rightarrow \text{C}_2\text{H}_3^+ + \text{H}$	1.10×10^{-9}	Woodall et al. (2007)

Table C.2: Ion-Molecule Reactions (continued)

Reaction	Rate Coefficient [cm^3s^{-1}]	Reference
$\text{CH}_4 + \text{C}^+ \rightarrow \text{C}_2\text{H}_2^+ + \text{H}_2$	4.00×10^{-10}	Woodall et al. (2007)
$\text{CH}_4 + \text{C}_2\text{H}_5^+ \rightarrow \text{C}_3\text{H}_7^+ + \text{H}_2$	9.00×10^{-14}	Woodall et al. (2007)
$\text{CH}_4 + \text{C}_2\text{H}_3^+ \rightarrow \text{C}_3\text{H}_5^+ + \text{H}_2$	2.00×10^{-10}	Woodall et al. (2007)
$\text{CH}_4 + \text{C}_2\text{H}_2^+ \rightarrow \text{C}_3\text{H}_5^+ + \text{H}$	6.64×10^{-10}	Woodall et al. (2007)
$\text{CH}_4 + \text{C}_2\text{H}_2^+ \rightarrow \text{C}_3\text{H}_4^+ + \text{H}_2$	1.76×10^{-10}	Woodall et al. (2007)
$\text{CH}_4 + \text{C}_2\text{H}^+ \rightarrow \text{C}_2\text{H}_2^+ + \text{CH}_3$	3.74×10^{-10}	Woodall et al. (2007)
$\text{CH}_4 + \text{C}_2\text{H}^+ \rightarrow \text{C}_3\text{H}_4^+ + \text{H}$	1.32×10^{-10}	Woodall et al. (2007)
$\text{CH}_4 + \text{C}_2\text{H}^+ \rightarrow \text{H}_2\text{C}_3\text{H}^+ + \text{H}_2$	3.74×10^{-10}	Woodall et al. (2007)
$\text{C}_2\text{H}_2 + \text{He}^+ \rightarrow \text{CH}^+ + \text{CH} + \text{He}$	7.70×10^{-10}	Woodall et al. (2007)
$\text{C}_2\text{H}_2 + \text{He}^+ \rightarrow \text{C}_2\text{H}^+ + \text{H} + \text{He}$	8.75×10^{-10}	Kim & Fox (1994)
$\text{C}_2\text{H}_2 + \text{He}^+ \rightarrow \text{C}_2\text{H}_2^+ + \text{He}$	2.54×10^{-10}	Woodall et al. (2007)
$\text{C}_2\text{H}_2 + \text{H}_2^+ \rightarrow \text{C}_2\text{H}_3^+ + \text{H}$	4.80×10^{-10}	Woodall et al. (2007)
$\text{C}_2\text{H}_2 + \text{H}_2^+ \rightarrow \text{C}_2\text{H}_2^+ + \text{H}_2$	4.82×10^{-9}	Woodall et al. (2007)
$\text{C}_2\text{H}_2 + \text{H}_3^+ \rightarrow \text{C}_2\text{H}_3^+ + \text{H}_2$	3.50×10^{-9}	Woodall et al. (2007)
$\text{C}_2\text{H}_2 + \text{CH}_5^+ \rightarrow \text{C}_2\text{H}_3^+ + \text{CH}_4$	1.60×10^{-9}	Woodall et al. (2007)
$\text{C}_2\text{H}_2 + \text{CH}_4^+ \rightarrow \text{C}_2\text{H}_3^+ + \text{CH}_3$	1.23×10^{-9}	Woodall et al. (2007)
$\text{C}_2\text{H}_2 + \text{CH}_4^+ \rightarrow \text{C}_2\text{H}_2^+ + \text{CH}_4$	1.13×10^{-9}	Woodall et al. (2007)
$\text{C}_2\text{H}_2 + \text{CH}_4^+ \rightarrow \text{H}_2\text{C}_3\text{H}^+ + \text{H}_2 + \text{H}$	1.51×10^{-10}	Woodall et al. (2007)
$\text{C}_2\text{H}_2 + \text{CH}_3^+ \rightarrow \text{H}_2\text{C}_3\text{H}^+ + \text{H}_2$	1.20×10^{-9}	Woodall et al. (2007)
$\text{C}_2\text{H}_2 + \text{CH}_2^+ \rightarrow \text{H}_2\text{C}_3\text{H}^+ + \text{H}$	2.50×10^{-9}	Woodall et al. (2007)
$\text{C}_2\text{H}_2 + \text{CH}^+ \rightarrow \text{C}_3\text{H}_2^+ + \text{H}$	2.40×10^{-9}	Woodall et al. (2007)
$\text{C}_2\text{H}_2 + \text{C}^+ \rightarrow \text{C}_3\text{H}^+ + \text{H}$	2.80×10^{-9}	Woodall et al. (2007)
$\text{C}_2\text{H}_2 + \text{C}_2\text{H}_5^+ \rightarrow \text{C}_3\text{H}_3^+ + \text{CH}_4$	6.84×10^{-11}	Woodall et al. (2007)
$\text{C}_2\text{H}_2 + \text{C}_2\text{H}_4^+ \rightarrow \text{C}_3\text{H}_3^+ + \text{CH}_3$	6.45×10^{-10}	Woodall et al. (2007)

Table C.2: Ion-Molecule Reactions (continued)

Reaction	Rate Coefficient [cm^3s^{-1}]	Reference
$\text{C}_2\text{H}_2 + \text{C}_2\text{H}_4^+ \rightarrow \text{C}_4\text{H}_5^+ + \text{H}$	1.93×10^{-10}	Woodall et al. (2007)
$\text{C}_2\text{H}_2 + \text{C}_2\text{H}_3^+ \rightarrow \text{C}_4\text{H}_3^+ + \text{H}_2$	7.20×10^{-10}	Woodall et al. (2007)
$\text{C}_2\text{H}_2 + \text{C}_2\text{H}_2^+ \rightarrow \text{C}_4\text{H}_3^+ + \text{H}$	9.10×10^{-10}	Woodall et al. (2007)
$\text{C}_2\text{H}_2 + \text{C}_3\text{H}_5^+ \rightarrow \text{C}_5\text{H}_5^+ + \text{H}_2$	3.80×10^{-10}	Woodall et al. (2007)
$\text{C}_2\text{H}_2 + \text{C}_3\text{H}_3^+ \rightarrow \text{C}_5\text{H}_3^+ + \text{H}_2$	1.10×10^{-9}	Woodall et al. (2007)
$\text{C}_2\text{H}_2 + \text{C}_2\text{H}_6^+ \rightarrow \text{C}_2\text{H}_5^+ + \text{C}_3\text{H}_3$	2.20×10^{-10}	Kim & Fox (1994)
$\text{C}_2\text{H}_2 + \text{C}_2\text{H}_6^+ \rightarrow \text{C}_3\text{H}_5^+ + \text{CH}_3$	8.19×10^{-10}	Kim & Fox (1994)
$\text{C}_2\text{H}_2 + \text{C}_2\text{H}_6^+ \rightarrow \text{C}_4\text{H}_7^+ + \text{H}_3$	1.29×10^{-10}	Kim & Fox (1994)
$\text{C}_2\text{H}_2 + \text{C}_2\text{H}_7^+ \rightarrow \text{C}_2\text{H}_3^+ + \text{C}_2\text{H}_6$	1.00×10^{-9}	Kim & Fox (1994)
$\text{C}_2\text{H}_2 + \text{H}_2\text{C}_3\text{H}^+ \rightarrow \text{C}_3\text{H}_3^+ + \text{C}_2\text{H}_2$	2.50×10^{-10}	Kim & Fox (1994)
$\text{C}_2\text{H}_2 + \text{C}_2\text{H}^+ \rightarrow \text{C}_4\text{H}_2^+ + \text{H}$	1.20×10^{-9}	Kim & Fox (1994)
$\text{C}_2\text{H}_4 + \text{He}^+ \rightarrow \text{CH}_2^+ + \text{CH}_2 + \text{He}$	4.80×10^{-10}	Woodall et al. (2007)
$\text{C}_2\text{H}_4 + \text{He}^+ \rightarrow \text{CH}_2\text{H}_4^+ + \text{He}$	2.40×10^{-10}	Woodall et al. (2007)
$\text{C}_2\text{H}_4 + \text{He}^+ \rightarrow \text{C}_2\text{H}_3^+ + \text{He} + \text{H}$	1.70×10^{-10}	Woodall et al. (2007)
$\text{C}_2\text{H}_4 + \text{He}^+ \rightarrow \text{C}_2\text{H}_2^+ + \text{He} + \text{H}_2$	2.20×10^{-9}	Woodall et al. (2007)
$\text{C}_2\text{H}_4 + \text{He}^+ \rightarrow \text{C}_2\text{H}^+ + \text{He} + \text{H}_2 + \text{H}$	4.42×10^{-10}	Kim & Fox (1994)
$\text{C}_2\text{H}_4 + \text{H}_2^+ \rightarrow \text{C}_2\text{H}_4^+ + \text{H}_2$	2.21×10^{-9}	Woodall et al. (2007)
$\text{C}_2\text{H}_4 + \text{H}_2^+ \rightarrow \text{C}_2\text{H}_3^+ + \text{H}_2 + \text{H}$	1.81×10^{-9}	Woodall et al. (2007)
$\text{C}_2\text{H}_4 + \text{H}_2^+ \rightarrow \text{C}_2\text{H}_2^+ + \text{H}_2 + \text{H}_2$	8.82×10^{-10}	Woodall et al. (2007)
$\text{C}_2\text{H}_4 + \text{H}_3^+ \rightarrow \text{C}_2\text{H}_5^+ + \text{H}_2$	6.90×10^{-10}	Kim & Fox (1994)
$\text{C}_2\text{H}_4 + \text{H}_3^+ \rightarrow \text{C}_2\text{H}_3^+ + \text{H}_2 + \text{H}_2$	1.15×10^{-9}	Woodall et al. (2007)
$\text{C}_2\text{H}_4 + \text{HeH}^+ \rightarrow \text{C}_2\text{H}_4^+ + \text{H} + \text{He}$	7.00×10^{-10}	Kim & Fox (1994)
$\text{C}_2\text{H}_4 + \text{HeH}^+ \rightarrow \text{C}_2\text{H}_3^+ + \text{H}_2 + \text{He}$	2.10×10^{-9}	Kim & Fox (1994)
$\text{C}_2\text{H}_4 + \text{CH}_5^+ \rightarrow \text{C}_2\text{H}_5^+ + \text{CH}_4$	1.50×10^{-9}	Woodall et al. (2007)

Table C.2: Ion-Molecule Reactions (continued)

Reaction	Rate Coefficient [cm^3s^{-1}]	Reference
$\text{C}_2\text{H}_4 + \text{CH}_4^+ \rightarrow \text{C}_2\text{H}_5^+ + \text{CH}_3$	4.23×10^{-10}	Woodall et al. (2007)
$\text{C}_2\text{H}_4 + \text{CH}_4^+ \rightarrow \text{C}_2\text{H}_4^+ + \text{CH}_4$	1.38×10^{-9}	Woodall et al. (2007)
$\text{C}_2\text{H}_4 + \text{CH}_3^+ \rightarrow \text{C}_2\text{H}_3^+ + \text{CH}_4$	3.50×10^{-10}	Woodall et al. (2007)
$\text{C}_2\text{H}_4 + \text{CH}_3^+ \rightarrow \text{C}_3\text{H}_5^+ + \text{H}_2$	5.24×10^{-10}	Woodall et al. (2007)
$\text{C}_2\text{H}_4 + \text{CH}_3^+ \rightarrow \text{H}_2\text{C}_3\text{H}^+ + \text{H}_2 + \text{H}_2$	4.60×10^{-11}	Woodall et al. (2007)
$\text{C}_2\text{H}_4 + \text{C}^+ \rightarrow \text{C}_2\text{H}_4^+ + \text{C}$	1.70×10^{-10}	Woodall et al. (2007)
$\text{C}_2\text{H}_4 + \text{C}^+ \rightarrow \text{C}_2\text{H}_3^+ + \text{CH}$	8.50×10^{-11}	Woodall et al. (2007)
$\text{C}_2\text{H}_4 + \text{C}^+ \rightarrow \text{C}_3\text{H}_2^+ + \text{H}_2$	3.40×10^{-10}	Woodall et al. (2007)
$\text{C}_2\text{H}_4 + \text{C}^+ \rightarrow \text{C}_3\text{H}^+ + \text{H} + \text{H}_2$	8.50×10^{-11}	Woodall et al. (2007)
$\text{C}_2\text{H}_4 + \text{C}^+ \rightarrow \text{H}_2\text{C}_3\text{H}^+ + \text{H}$	1.02×10^{-9}	Woodall et al. (2007)
$\text{C}_2\text{H}_4 + \text{C}_2\text{H}_5^+ \rightarrow \text{C}_3\text{H}_5^+ + \text{CH}_4$	3.90×10^{-10}	Woodall et al. (2007)
$\text{C}_2\text{H}_4 + \text{C}_2\text{H}_4^+ \rightarrow \text{C}_3\text{H}_5^+ + \text{CH}_3$	7.11×10^{-10}	Woodall et al. (2007)
$\text{C}_2\text{H}_4 + \text{C}_2\text{H}_4^+ \rightarrow \text{C}_4\text{H}_7^+ + \text{H}$	7.90×10^{-11}	Woodall et al. (2007)
$\text{C}_2\text{H}_4 + \text{C}_2\text{H}_3^+ \rightarrow \text{C}_2\text{H}_5^+ + \text{C}_2\text{H}_2$	8.90×10^{-10}	Woodall et al. (2007)
$\text{C}_2\text{H}_4 + \text{C}_2\text{H}_2^+ \rightarrow \text{C}_2\text{H}_4^+ + \text{C}_2\text{H}_2$	4.14×10^{-10}	Woodall et al. (2007)
$\text{C}_2\text{H}_4 + \text{C}_2\text{H}_2^+ \rightarrow \text{C}_4\text{H}_5^+ + \text{H}$	3.17×10^{-10}	Woodall et al. (2007)
$\text{C}_2\text{H}_4 + \text{C}_2\text{H}_2^+ \rightarrow \text{H}_2\text{C}_3\text{H}^+ + \text{CH}_3$	6.62×10^{-10}	Woodall et al. (2007)
$\text{C}_2\text{H}_4 + \text{C}_2\text{H}_6^+ \rightarrow \text{C}_2\text{H}_4^+ + \text{C}_2\text{H}_6$	1.15×10^{-9}	Woodall et al. (2007)
$\text{C}_2\text{H}_4 + \text{C}_2\text{H}_7^+ \rightarrow \text{C}_2\text{H}_5^+ + \text{C}_2\text{H}_6$	1.00×10^{-9}	Kim & Fox (1994)
$\text{C}_2\text{H}_4 + \text{C}_2\text{H}^+ \rightarrow \text{C}_n\text{H}_m^+$ products	1.71×10^{-9}	Kim & Fox (1994)
$\text{C}_2\text{H}_6 + \text{H}^+ \rightarrow \text{C}_2\text{H}_5^+ + \text{H}_2$	1.30×10^{-9}	Woodall et al. (2007)
$\text{C}_2\text{H}_6 + \text{H}^+ \rightarrow \text{C}_2\text{H}_4^+ + \text{H}_2 + \text{H}$	1.40×10^{-9}	Woodall et al. (2007)
$\text{C}_2\text{H}_6 + \text{H}^+ \rightarrow \text{C}_2\text{H}_3^+ + \text{H}_2 + \text{H}_2$	2.80×10^{-9}	Woodall et al. (2007)
$\text{C}_2\text{H}_6 + \text{He}^+ \rightarrow \text{C}_2\text{H}_4^+ + \text{He} + \text{H}_2$	4.20×10^{-10}	Woodall et al. (2007)

Table C.2: Ion-Molecule Reactions (continued)

Reaction	Rate Coefficient [cm^3s^{-1}]	Reference
$\text{C}_2\text{H}_6 + \text{He}^+ \rightarrow \text{C}_2\text{H}_3^+ + \text{He} + \text{H}_2 + \text{H}$	1.80×10^{-9}	Woodall et al. (2007)
$\text{C}_2\text{H}_6 + \text{He}^+ \rightarrow \text{C}_2\text{H}_2^+ + \text{He} + \text{H}_2 + \text{H}_2$	8.40×10^{-10}	Woodall et al. (2007)
$\text{C}_2\text{H}_6 + \text{H}_2^+ \rightarrow \text{C}_2\text{H}_6^+ + \text{H}_2$	2.94×10^{-10}	Woodall et al. (2007)
$\text{C}_2\text{H}_6 + \text{H}_2^+ \rightarrow \text{C}_2\text{H}_5^+ + \text{H}_2 + \text{H}$	1.37×10^{-9}	Woodall et al. (2007)
$\text{C}_2\text{H}_6 + \text{H}_2^+ \rightarrow \text{C}_2\text{H}_4^+ + \text{H}_2 + \text{H}_2$	2.35×10^{-9}	Woodall et al. (2007)
$\text{C}_2\text{H}_6 + \text{H}_2^+ \rightarrow \text{C}_2\text{H}_3^+ + \text{H}_2 + \text{H}_2 + \text{H}$	6.86×10^{-10}	Kim & Fox (1994)
$\text{C}_2\text{H}_6 + \text{H}_2^+ \rightarrow \text{C}_2\text{H}_2^+ + \text{H}_2 + \text{H}_2 + \text{H}_2$	1.96×10^{-10}	Kim & Fox (1994)
$\text{C}_2\text{H}_6 + \text{H}_3^+ \rightarrow \text{C}_2\text{H}_7^+ + \text{H}_2$	2.90×10^{-11}	Perry et al. (1999)
$\text{C}_2\text{H}_6 + \text{H}_3^+ \rightarrow \text{C}_2\text{H}_5^+ + \text{H}_2 + \text{H}_2$	2.40×10^{-9}	Woodall et al. (2007)
$\text{C}_2\text{H}_6 + \text{HeH}^+ \rightarrow \text{C}_2\text{H}_5^+ + \text{He} + \text{H}_2$	1.05×10^{-9}	Kim & Fox (1994)
$\text{C}_2\text{H}_6 + \text{HeH}^+ \rightarrow \text{C}_2\text{H}_3^+ + \text{He} + \text{H}_2 + \text{H}_2$	1.05×10^{-9}	Kim & Fox (1994)
$\text{C}_2\text{H}_6 + \text{CH}_5^+ \rightarrow \text{C}_2\text{H}_7^+ + \text{CH}_4$	1.15×10^{-9}	Perry et al. (1999)
$\text{C}_2\text{H}_6 + \text{CH}_5^+ \rightarrow \text{C}_2\text{H}_5^+ + \text{CH}_4 + \text{H}_2$	2.03×10^{-10}	Perry et al. (1999)
$\text{C}_2\text{H}_6 + \text{CH}_4^+ \rightarrow \text{C}_2\text{H}_4^+ + \text{CH}_4 + \text{H}_2$	1.91×10^{-9}	Kim & Fox (1994)
$\text{C}_2\text{H}_6 + \text{CH}_3^+ \rightarrow \text{C}_2\text{H}_5^+ + \text{CH}_4$	1.48×10^{-9}	Woodall et al. (2007)
$\text{C}_2\text{H}_6 + \text{CH}_3^+ \rightarrow \text{C}_3\text{H}_7^+ + \text{H}_2$	1.00×10^{-10}	Kim & Fox (1994)
$\text{C}_2\text{H}_6 + \text{CH}_3^+ \rightarrow \text{C}_3\text{H}_5^+ + \text{H}_2 + \text{H}_2$	1.57×10^{-10}	Woodall et al. (2007)
$\text{C}_2\text{H}_6 + \text{C}^+ \rightarrow \text{C}_2\text{H}_5^+ + \text{CH}$	2.31×10^{-10}	Woodall et al. (2007)
$\text{C}_2\text{H}_6 + \text{C}^+ \rightarrow \text{C}_2\text{H}_4^+ + \text{CH}_2$	1.16×10^{-10}	Woodall et al. (2007)
$\text{C}_2\text{H}_6 + \text{C}^+ \rightarrow \text{C}_2\text{H}_3^+ + \text{CH}_3$	4.95×10^{-10}	Woodall et al. (2007)
$\text{C}_2\text{H}_6 + \text{C}^+ \rightarrow \text{C}_2\text{H}_2^+ + \text{CH}_4$	8.25×10^{-11}	Woodall et al. (2007)
$\text{C}_2\text{H}_6 + \text{C}^+ \rightarrow \text{C}_3\text{H}_2^+ + \text{H}_2 + \text{H}_2$	1.65×10^{-11}	Woodall et al. (2007)
$\text{C}_2\text{H}_6 + \text{C}^+ \rightarrow \text{C}_3\text{H}_3^+ + \text{H}_2 + \text{H}$	7.10×10^{-10}	Woodall et al. (2007)
$\text{C}_2\text{H}_6 + \text{C}_2\text{H}_6^+ \rightarrow \text{C}_3\text{H}_8^+ + \text{CH}_4$	7.98×10^{-12}	Kim & Fox (1994)

Table C.2: Ion-Molecule Reactions (continued)

Reaction	Rate Coefficient [cm^3s^{-1}]	Reference
$\text{C}_2\text{H}_6 + \text{C}_2\text{H}_6^+ \rightarrow \text{C}_3\text{H}_9^+ + \text{CH}_3$	1.10×10^{-11}	Kim & Fox (1994)
$\text{C}_2\text{H}_6 + \text{C}_2\text{H}_5^+ \rightarrow \text{C}_3\text{H}_7^+ + \text{CH}_4$	5.46×10^{-12}	Robertson et al. (2009)
$\text{C}_2\text{H}_6 + \text{C}_2\text{H}_5^+ \rightarrow \text{C}_4\text{H}_9^+ + \text{H}_2$	4.00×10^{-11}	Kim & Fox (1994)
$\text{C}_2\text{H}_6 + \text{C}_2\text{H}_4^+ \rightarrow \text{C}_3\text{H}_7^+ + \text{CH}_3$	4.62×10^{-12}	Woodall et al. (2007)
$\text{C}_2\text{H}_6 + \text{C}_2\text{H}_4^+ \rightarrow \text{C}_3\text{H}_6^+ + \text{CH}_4$	5.15×10^{-13}	Woodall et al. (2007)
$\text{C}_2\text{H}_6 + \text{C}_2\text{H}_3^+ \rightarrow \text{C}_2\text{H}_5^+ + \text{C}_2\text{H}_4$	2.91×10^{-10}	Woodall et al. (2007)
$\text{C}_2\text{H}_6 + \text{C}_2\text{H}_3^+ \rightarrow \text{C}_3\text{H}_5^+ + \text{CH}_4$	2.48×10^{-10}	Woodall et al. (2007)
$\text{C}_2\text{H}_6 + \text{C}_2\text{H}_3^+ \rightarrow \text{C}_4\text{H}_7^+ + \text{H}_2$	8.06×10^{-11}	Kim & Fox (1994)
$\text{C}_2\text{H}_6 + \text{C}_2\text{H}_2^+ \rightarrow \text{C}_2\text{H}_5^+ + \text{C}_2\text{H}_3$	1.31×10^{-10}	Kim & Fox (1994)
$\text{C}_2\text{H}_6 + \text{C}_2\text{H}_2^+ \rightarrow \text{C}_2\text{H}_4^+ + \text{C}_2\text{H}_4$	2.48×10^{-10}	Woodall et al. (2007)
$\text{C}_2\text{H}_6 + \text{C}_2\text{H}_2^+ \rightarrow \text{C}_3\text{H}_5^+ + \text{CH}_3$	7.45×10^{-10}	Woodall et al. (2007)
$\text{C}_4\text{H}_2 + \text{H}^+ \rightarrow \text{C}_4\text{H}_2^+ + \text{H}$	2.00×10^{-9}	Woodall et al. (2007)
$\text{C}_4\text{H}_2 + \text{H}_3^+ \rightarrow \text{C}_4\text{H}_3^+ + \text{H}_2$	2.60×10^{-9}	Woodall et al. (2007)
$\text{C}_4\text{H}_2 + \text{CH}_3^+ \rightarrow \text{C}_5\text{H}_3^+ + \text{H}_2$	1.30×10^{-10}	Woodall et al. (2007)
$\text{C}_4\text{H}_2 + \text{CH}_3^+ \rightarrow \text{H}_2\text{C}_3\text{H}^+ + \text{C}_2\text{H}_2$	1.27×10^{-9}	Woodall et al. (2007)
$\text{C}_4\text{H}_2 + \text{C}^+ \rightarrow \text{C}_3\text{H}^+ + \text{C}_2\text{H}$	1.45×10^{-10}	Woodall et al. (2007)
$\text{C}_4\text{H}_2 + \text{C}^+ \rightarrow \text{C}_5\text{H}^+ + \text{H}$	1.45×10^{-9}	Woodall et al. (2007)
$\text{C}_4\text{H}_2 + \text{C}^+ \rightarrow \text{C}_4\text{H}_2^+ + \text{C}$	1.31×10^{-9}	Woodall et al. (2007)
$\text{C}_4\text{H}_2 + \text{C}_2\text{H}_5^+ \rightarrow \text{C}_4\text{H}_3^+ + \text{C}_2\text{H}_4$	3.00×10^{-10}	Robertson et al. (2009)
$\text{C}_4\text{H}_2 + \text{C}_2\text{H}_2^+ \rightarrow \text{C}_4\text{H}_2^+ + \text{C}_2\text{H}_2$	1.26×10^{-9}	Woodall et al. (2007)
$\text{C}_4\text{H}_2 + \text{C}_2\text{H}_2^+ \rightarrow \text{C}_6\text{H}_3^+ + \text{H}$	1.40×10^{-10}	Woodall et al. (2007)
$\text{C}_4\text{H}_2 + \text{C}_3\text{H}_2^+ \rightarrow \text{C}_7\text{H}_3^+ + \text{H}$	3.00×10^{-10}	Woodall et al. (2007)
$\text{C}_4\text{H}_2 + \text{C}_3\text{H}_2^+ \rightarrow \text{C}_7\text{H}_2^+ + \text{H}_2$	3.00×10^{-10}	Woodall et al. (2007)
$\text{H}_{2vib} + \text{H}^+ \rightarrow \text{H}_2^+ + \text{H}$	1.00×10^{-9}	Yelle & Miller (2004) est.

Appendix D

Additional Oxygen Tables

Table D.1: Altitude integrated ion production [$\text{cm}^{-2} \text{s}^{-1}$] from charge exchange collisions (i.e. TI, SC, SC+SS) for oxygen with incident ion energies between 10 and 25000 keV/u with no opacity effects considered. Everything has been normalized to a single incident ion/ cm^2/s .

Ion Charge State	Energy					
	10 keV/u	50	75	100	200	300
O	2.27E+02	7.67E+02	8.12E+02	8.21E+02	8.26E+02	8.24E+02
O ⁺	1.34E+02	9.43E+02	1.16E+03	1.24E+03	1.28E+03	1.27E+03
O ⁺⁺	1.25E+01	2.24E+02	3.99E+02	5.54E+02	7.11E+02	7.12E+02
O ³⁺	3.57E-01	2.73E+01	8.23E+01	1.78E+02	4.79E+02	5.03E+02
O ⁴⁺	3.06E-03	1.28E+00	7.01E+00	2.65E+01	2.67E+02	3.66E+02
O ⁵⁺	————	4.16E-02	4.18E-01	2.90E+00	1.55E+02	4.79E+02
O ⁶⁺	————	————	1.04E-04	2.08E-03	1.33E+00	1.79E+01
O ⁷⁺	————	————	————	1.04E-04	9.14E-02	2.33E+00

Ion Charge state	Energy					
	500 keV/u	1000	2000	5000	10000	25000
O	8.24E+02	8.23E+02	8.22E+02	8.22E+02	8.21E+02	8.28E+02
O ⁺	1.27E+03	1.27E+03	1.27E+03	1.27E+03	1.27E+03	1.28E+03
O ⁺⁺	1.25E+01	2.24E+02	3.99E+02	5.54E+02	7.11E+02	7.12E+02
O ³⁺	5.03E+02	5.02E+02	5.03E+02	5.02E+02	5.01E+02	5.05E+02
O ⁴⁺	3.75E+02	3.74E+02	3.74E+02	3.74E+02	3.73E+02	3.77E+02
O ⁵⁺	6.73E+02	7.00E+02	7.00E+02	6.99E+02	6.98E+02	7.04E+02
O ⁶⁺	7.01E+01	1.17E+02	1.19E+02	1.19E+02	1.18E+02	1.19E+02
O ⁷⁺	2.35E+01	1.10E+02	1.49E+02	1.61E+02	1.63E+02	1.64E+02

Table D.2: Altitude integrated ion production [$\text{cm}^{-2} \text{s}^{-1}$] from direct excitation collisions (i.e. SI+SPEX, DI+SPEX, TEX+SPEX) for oxygen with incident ion energies between 10 and 25000 keV/u with no opacity effects considered. Everything has been normalized to a single incident ion/ cm^2/s .

Ion Charge State	Energy					
	10 keV/u	50	75	100	200	300
O	2.53E+02	1.02E+03	1.13E+03	1.17E+03	1.18E+03	1.18E+03
O ⁺	1.94E+01	3.48E+02	5.33E+02	6.30E+02	6.86E+02	6.86E+02
O ⁺⁺	3.21E+00	8.89E+01	1.95E+02	3.23E+02	5.17E+02	5.21E+02
O ³⁺	7.55E-02	7.28E+00	2.91E+01	8.40E+01	3.72E+02	4.10E+02
O ⁴⁺	7.14E-04	3.04E-01	1.67E+00	8.88E+00	1.43E+02	2.25E+02
O ⁵⁺	————	5.31E-03	9.45E-02	1.04E+00	1.15E+02	4.43E+02
O ⁶⁺	————	————	1.04E-04	2.29E-03	1.63E+00	1.97E+01
O ⁷⁺	————	————	————	————	1.59E-02	9.38E-01
Ion Charge state	Energy					
	500 keV/u	1000	2000	5000	10000	25000
O	1.18E+03	1.18E+03	1.18E+03	1.18E+03	1.17E+03	1.18E+03
O ⁺	6.85E+02	6.84E+02	6.83E+02	6.85E+02	6.83E+02	6.89E+02
O ⁺⁺	5.21E+02	5.20E+02	5.20E+02	5.20E+02	5.19E+02	5.23E+02
O ³⁺	4.11E+02	4.10E+02	4.10E+02	4.10E+02	4.09E+02	4.13E+02
O ⁴⁺	2.39E+02	2.38E+02	2.38E+02	2.38E+02	2.38E+02	2.40E+02
O ⁵⁺	6.60E+02	6.91E+02	6.91E+02	6.90E+02	6.89E+02	6.96E+02
O ⁶⁺	7.00E+01	1.09E+02	1.11E+02	1.11E+02	1.11E+02	1.12E+02
O ⁷⁺	1.47E+01	9.39E+01	1.34E+02	1.48E+02	1.49E+02	1.51E+02

Table D.3: The X-ray efficiency ($[\text{cm}^2\text{sec}]^{-1}[\text{keV/u}]^{-1}$) of outgoing photons as a function of initial ion energy including opacity effects from a single incident ion/cm²/s with an isotropic downward distribution of pitch angles. No opacity effects and the viewing angles of 0°, 80°, and 90° are displayed for atmosphere 1. The efficiency shown here is that solely from charge exchange collisions for oxygen. I also include the X-ray efficiencies that correspond to the JEDI energy bins at the time of writing.

Atmosphere 1 (Original atmosphere)								
Energy [keV/u]	No Opacity		0°		80°		90°	
	O ⁶⁺	O ⁷⁺						
100	0.00002	————	0.00002	————	0.00002	————	0.00002	————
121	0.00013	————	0.00013	————	0.00013	————	0.00013	————
125	0.00017	0.00001	0.00017	0.00001	0.00017	0.00001	0.00017	0.00001
150	0.00084	0.00004	0.00084	0.00004	0.00084	0.00004	0.00083	0.00004
175	0.00281	0.00017	0.00280	0.00017	0.00280	0.00017	0.00279	0.00017
200	0.00676	0.00045	0.00676	0.00045	0.00675	0.00045	0.00670	0.00045
218	0.01122	0.00083	0.01121	0.00083	0.01120	0.00083	0.01110	0.00082
250	0.02283	0.00201	0.02282	0.00201	0.02278	0.00201	0.02251	0.00199
300	0.04796	0.00569	0.04793	0.00569	0.04780	0.00567	0.04690	0.00560
350	0.07630	0.01209	0.07623	0.01208	0.07591	0.01204	0.07364	0.01182
400	0.10308	0.02163	0.10294	0.02161	0.10232	0.02151	0.09755	0.02098
450	0.12439	0.03339	0.12417	0.03335	0.12311	0.03316	0.11448	0.03205
456	0.12697	0.03509	0.12673	0.03504	0.12560	0.03483	0.11634	0.03363
500	0.13987	0.04676	0.13952	0.04668	0.13787	0.04634	0.12372	0.04429
600	0.15391	0.07349	0.15318	0.07328	0.14981	0.07241	0.11957	0.06671
700	0.15051	0.09296	0.14925	0.09254	0.14353	0.09083	0.09536	0.07866
800	0.14038	0.10470	0.13850	0.10395	0.13006	0.10107	0.06782	0.07982
900	0.12843	0.10958	0.12589	0.10844	0.11476	0.10415	0.04539	0.07304
1000	0.11703	0.11002	0.11385	0.10843	0.10024	0.10258	0.03000	0.06267
1250	0.09460	0.10269	0.08997	0.09985	0.07150	0.09008	0.01143	0.03800
1500	0.07939	0.09270	0.07349	0.08865	0.05176	0.07529	0.00491	0.02157
1750	0.06784	0.08262	0.06095	0.07756	0.03774	0.06155	0.00251	0.01233
2000	0.05952	0.07455	0.05169	0.06854	0.02774	0.05030	0.00138	0.00715
5000	0.02374	0.03229	0.01087	0.02029	0.00113	0.00440	0.00004	0.00018
10000	0.01182	0.01628	0.00121	0.00373	0.00007	0.00026	————	0.00001
25000	0.00477	0.00657	0.00003	0.00009	————	0.00001	————	————

Table D.4: The X-ray efficiency ($[\text{cm}^2\text{sec}]^{-1}[\text{keV/u}]^{-1}$) of outgoing photons as a function of initial ion energy including opacity effects from a single incident ion/cm²/s with an isotropic downward distribution of pitch angles. No opacity effects and the viewing angles of 0°, 80°, and 90° are displayed for atmosphere 2. The efficiency shown here is that solely from charge exchange collisions for oxygen. I also include the X-ray efficiencies that correspond to the JEDI energy bins at the time of writing.

Atmosphere 2 (Well-mixed atmosphere)								
Energy [keV/u]	No Opacity		0°		80°		90°	
	O ⁶⁺	O ⁷⁺						
100	0.00002	————	0.00002	————	0.00002	————	0.00002	————
121	0.00013	————	0.00013	————	0.00013	————	0.00013	————
125	0.00017	0.00001	0.00017	0.00001	0.00017	0.00001	0.00017	0.00001
150	0.00084	0.00004	0.00084	0.00004	0.00083	0.00004	0.00081	0.00004
175	0.00281	0.00017	0.00280	0.00017	0.00279	0.00017	0.00270	0.00017
200	0.00676	0.00045	0.00675	0.00045	0.00670	0.00045	0.00646	0.00044
218	0.01122	0.00083	0.01120	0.00083	0.01112	0.00082	0.01065	0.00080
250	0.02283	0.00201	0.02278	0.00201	0.02257	0.00200	0.02135	0.00193
300	0.04796	0.00569	0.04783	0.00568	0.04719	0.00563	0.04346	0.00536
350	0.07630	0.01209	0.07601	0.01206	0.07462	0.01192	0.06620	0.01119
400	0.10308	0.02163	0.10255	0.02156	0.10008	0.02125	0.08452	0.01957
450	0.12439	0.03339	0.12357	0.03326	0.11976	0.03267	0.09518	0.02940
456	0.12697	0.03509	0.12610	0.03494	0.12210	0.03431	0.09618	0.03079
500	0.13987	0.04676	0.13871	0.04653	0.13337	0.04554	0.09835	0.03988
600	0.15391	0.07349	0.15199	0.07296	0.14328	0.07076	0.08631	0.05738
700	0.15051	0.09296	0.14783	0.09204	0.13597	0.08829	0.06296	0.06434
800	0.14038	0.10470	0.13701	0.10330	0.12234	0.09779	0.04145	0.06216
900	0.12843	0.10958	0.12444	0.10768	0.10746	0.10042	0.02621	0.05453
1000	0.11703	0.11002	0.11248	0.10761	0.09361	0.09867	0.01673	0.04529
1250	0.09460	0.10269	0.08885	0.09904	0.06658	0.08638	0.00626	0.02641
1500	0.07939	0.09270	0.07256	0.08792	0.04817	0.07213	0.00270	0.01487
1750	0.06784	0.08262	0.06018	0.07692	0.03512	0.05895	0.00140	0.00850
2000	0.05952	0.07455	0.05103	0.06798	0.02581	0.04817	0.00077	0.00493
5000	0.02374	0.03229	0.01072	0.02013	0.00105	0.00423	0.00003	0.00012
10000	0.01182	0.01628	0.00119	0.00369	0.00007	0.00025	————	0.00001
25000	0.00477	0.00657	0.00003	0.00009	————	0.00001	————	————

Table D.5: The X-ray efficiency ($[\text{cm}^2\text{sec}]^{-1}[\text{keV/u}]^{-1}$) of outgoing photons as a function of initial ion energy including opacity effects from a single incident ion/cm²/s with an isotropic downward distribution of pitch angles. No opacity effects and the viewing angles of 0°, 80°, and 90° are displayed for atmosphere 1. The efficiency shown here is that solely from direct excitation collisions for oxygen. I also include the X-ray efficiencies that correspond to the JEDI energy bins at the time of writing.

Atmosphere 1 (Original atmosphere)								
Energy [keV/u]	No Opacity		0°		80°		90°	
	O ⁶⁺	O ⁷⁺						
100	0.00003	-----	0.00003	-----	0.00003	-----	0.00003	-----
121	0.00014	-----	0.00014	-----	0.00014	-----		
125	0.00020	-----	0.00020	-----	0.00020	-----	0.00020	-----
150	0.00098	-----	0.00098	-----	0.00098	-----	0.00097	-----
175	0.00313	0.00002	0.00313	0.00002	0.00313	0.00002	0.00311	0.00002
200	0.00747	0.00007	0.00746	0.00007	0.00745	0.00007	0.00740	0.00007
218	0.01242	0.00017	0.01242	0.00017	0.01240	0.00017	0.01230	0.00017
250	0.02443	0.00054	0.02442	0.00054	0.02437	0.00054	0.02408	0.00054
300	0.04852	0.00194	0.04849	0.00194	0.04835	0.00193	0.04741	0.00192
350	0.07465	0.00498	0.07458	0.00498	0.07426	0.00497	0.07195	0.00492
400	0.09801	0.01013	0.09788	0.01012	0.09726	0.01010	0.09252	0.00994
450	0.11545	0.01736	0.11523	0.01735	0.11421	0.01729	0.10580	0.01690
456	0.11761	0.01849	0.11738	0.01848	0.11629	0.01842	0.10727	0.01798
500	0.12752	0.02654	0.12719	0.02652	0.12562	0.02641	0.11202	0.02556
600	0.13589	0.04735	0.13522	0.04728	0.13209	0.04696	0.10395	0.04400
700	0.13063	0.06541	0.12949	0.06525	0.12430	0.06448	0.08060	0.05705
800	0.12044	0.07738	0.11876	0.07706	0.11125	0.07557	0.05622	0.06109
900	0.10968	0.08317	0.10744	0.08263	0.09765	0.08012	0.03734	0.05722
1000	0.09991	0.08502	0.09713	0.08419	0.08527	0.08044	0.02481	0.04944
1250	0.08049	0.08112	0.07653	0.07945	0.06070	0.07217	0.00968	0.02952
1500	0.06746	0.07423	0.06245	0.07164	0.04397	0.06090	0.00434	0.01657
1750	0.05762	0.06658	0.05179	0.06316	0.03211	0.04975	0.00233	0.00939
2000	0.05053	0.06048	0.04391	0.05623	0.02363	0.04057	0.00138	0.00550
5000	0.02016	0.02673	0.00932	0.01641	0.00104	0.00311	0.00015	0.00025
10000	0.01006	0.01347	0.00107	0.00266	0.00012	0.00022	0.00006	0.00007
25000	0.00406	0.00544	0.00005	0.00009	0.00003	0.00003	0.00003	0.00003

Table D.6: The X-ray efficiency ($[\text{cm}^2\text{sec}]^{-1}[\text{keV/u}]^{-1}$) of outgoing photons as a function of initial ion energy including opacity effects from a single incident ion/cm²/s with an isotropic downward distribution of pitch angles. No opacity effects and the viewing angles of 0°, 80°, and 90° are displayed for atmosphere 2. The efficiency shown here is that solely from direct excitation collisions for oxygen. I also include the X-ray efficiencies that correspond to the JEDI energy bins at the time of writing.

Atmosphere 2 (Well-mixed atmosphere)								
Energy [keV/u]	No Opacity		0°		80°		90°	
	O ⁶⁺	O ⁷⁺						
100	0.00003	-----	0.00003	-----	0.00003	-----	0.00003	-----
121	0.00014	-----	0.00014	-----	0.00014	-----	0.00013	-----
125	0.00020	-----	0.00020	-----	0.00020	-----	0.00019	-----
150	0.00098	-----	0.00098	-----	0.00097	-----	0.00095	-----
175	0.00313	0.00002	0.00313	0.00002	0.00311	0.00002	0.00302	0.00002
200	0.00747	0.00007	0.00745	0.00007	0.00741	0.00007	0.00714	0.00007
218	0.01242	0.00017	0.01240	0.00017	0.01231	0.00017	0.01179	0.00017
250	0.02443	0.00054	0.02438	0.00054	0.02414	0.00054	0.02280	0.00053
300	0.04852	0.00194	0.04838	0.00193	0.04772	0.00192	0.04382	0.00185
350	0.07465	0.00498	0.07435	0.00497	0.07297	0.00493	0.06447	0.00469
400	0.09801	0.01013	0.09749	0.01010	0.09508	0.01000	0.07979	0.00933
450	0.11545	0.01736	0.11466	0.01731	0.11103	0.01708	0.08743	0.01561
456	0.11761	0.01849	0.11678	0.01844	0.11297	0.01819	0.08812	0.01656
500	0.12752	0.02654	0.12643	0.02645	0.12143	0.02603	0.08837	0.02315
600	0.13589	0.04735	0.13414	0.04711	0.12623	0.04602	0.07426	0.03805
700	0.13063	0.06541	0.12825	0.06495	0.11769	0.06282	0.05266	0.04678
800	0.12044	0.07738	0.11749	0.07664	0.10464	0.07322	0.03415	0.04740
900	0.10968	0.08317	0.10621	0.08210	0.09147	0.07727	0.02157	0.04220
1000	0.09991	0.08502	0.09598	0.08361	0.07968	0.07730	0.01396	0.03501
1250	0.08049	0.08112	0.07559	0.07883	0.05658	0.06902	0.00546	0.01989
1500	0.06746	0.07423	0.06167	0.07105	0.04095	0.05812	0.00254	0.01105
1750	0.05762	0.06658	0.05114	0.06264	0.02990	0.04744	0.00142	0.00628
2000	0.05053	0.06048	0.04336	0.05576	0.02200	0.03866	0.00088	0.00369
5000	0.02016	0.02673	0.00919	0.01626	0.00098	0.00297	0.00013	0.00021
10000	0.01006	0.01347	0.00106	0.00264	0.00012	0.00022	0.00006	0.00006
25000	0.00406	0.00544	0.00005	0.00008	0.00003	0.00003	0.00003	0.00003

Appendix E

Additional Sulfur Tables

Table E.1: Altitude integrated ion production [$\text{cm}^{-2} \text{s}^{-1}$] from charge exchange collisions (i.e. TI, SC, SC+SS) for sulfur with incident ion energies between 10 and 2000 keV/u with no opacity effects considered. Everything has been normalized to a single incident ion/ cm^2/s .

Ion Charge State	Energy				
	10 keV/u	50	75	100	200
S	2.33E+02	9.94E+02	1.07E+03	1.08E+03	1.08E+03
S ⁺	2.07E+02	2.24E+03	2.66E+03	2.78E+03	2.81E+03
S ⁺⁺	3.88E+01	9.92E+02	1.51E+03	1.85E+03	2.09E+03
S ³⁺	2.16E+00	1.79E+02	4.61E+02	8.23E+02	1.42E+03
S ⁴⁺	3.01E-02	1.39E+01	6.23E+01	1.79E+02	8.22E+02
S ⁵⁺	3.57E-04	7.27E-01	5.21E+00	2.77E+01	6.14E+02
S ⁶⁺	————	1.89E-03	3.04E-02	3.29E-01	4.12E+01
S ⁷⁺	————	1.02E-04	6.12E-04	1.00E-02	4.99E+00
S ⁸⁺	————	————	————	1.53E-04	3.35E-01
S ⁹⁺	————	————	————	————	2.23E-02
S ¹⁰⁺	————	————	————	————	7.14E-04
S ¹¹⁺	————	————	————	————	5.10E-05
S ¹²⁺	————	————	————	————	————
S ¹³⁺	————	————	————	————	————
S ¹⁴⁺	————	————	————	————	————
S ¹⁵⁺	————	————	————	————	————

Ion Charge State	Energy			
	300 keV/u	500	1000	2000
S	1.08E+03	1.08E+03	1.08E+03	1.08E+03
S ⁺	2.81E+03	2.81E+03	2.81E+03	2.81E+03
S ⁺⁺	2.09E+03	2.09E+03	2.09E+03	2.09E+03
S ³⁺	1.45E+03	1.45E+03	1.45E+03	1.45E+03
S ⁴⁺	9.50E+02	9.56E+02	9.56E+02	9.56E+02
S ⁵⁺	1.18E+03	1.33E+03	1.33E+03	1.33E+03
S ⁶⁺	1.87E+02	3.28E+02	3.29E+02	3.30E+02
S ⁷⁺	5.56E+01	1.86E+02	1.92E+02	1.92E+02
S ⁸⁺	1.03E+01	9.98E+01	1.16E+02	1.16E+02
S ⁹⁺	1.87E+00	6.18E+01	8.92E+01	8.92E+01
S ¹⁰⁺	2.31E-01	2.60E+01	5.34E+01	5.34E+01
S ¹¹⁺	3.42E-02	1.66E+01	6.12E+01	6.13E+01
S ¹²⁺	7.96E-03	1.11E+01	7.91E+01	8.15E+01
S ¹³⁺	1.12E-03	1.03E+01	2.27E+02	2.78E+02
S ¹⁴⁺	————	7.41E-02	1.19E+01	3.81E+01
S ¹⁵⁺	————	4.14E-02	6.96E+00	2.39E+01

Table E.2: Altitude integrated ion production [$\text{cm}^{-2} \text{s}^{-1}$] from direct excitation collisions (i.e. SI+SPEX, DI+SPEX, TEX+SPEX) for sulfur with incident ion energies between 10 and 2000 keV/u with no opacity effects considered. Everything has been normalized to a single incident ion/ cm^2/s .

Ion Charge State	Energy	50	75	100	200
	10 keV/u				
S	3.33E+02	2.58E+03	2.95E+03	3.05E+03	3.08E+03
S ⁺	4.71E+01	1.22E+03	1.72E+03	1.98E+03	2.12E+03
S ⁺⁺	2.07E+00	1.78E+02	4.77E+02	7.89E+02	1.15E+03
S ³⁺	1.57E-01	3.13E+01	1.50E+02	3.73E+02	1.01E+03
S ⁴⁺	2.26E-03	2.27E+00	1.34E+01	6.17E+01	7.08E+02
S ⁵⁺	————	1.07E-01	1.52E+00	1.20E+01	5.16E+02
S ⁶⁺	————	1.51E-04	3.92E-03	7.59E-02	1.50E+01
S ⁷⁺	————	————	————	6.53E-04	9.02E-01
S ⁸⁺	————	————	————	————	1.16E-01
S ⁹⁺	————	————	————	————	4.12E-03
S ¹⁰⁺	————	————	————	————	5.02E-04
S ¹¹⁺	————	————	————	————	5.02E-05
S ¹²⁺	————	————	————	————	————
S ¹³⁺	————	————	————	————	————
S ¹⁴⁺	————	————	————	————	————
S ¹⁵⁺	————	————	————	————	————

Ion Charge State	Energy	500	1000	2000
	300 keV/u			
S	3.08E+03	3.07E+03	3.08E+03	3.08E+03
S ⁺	2.12E+03	2.12E+03	2.12E+03	2.12E+03
S ⁺⁺	1.16E+03	1.16E+03	1.16E+03	1.16E+03
S ³⁺	1.08E+03	1.08E+03	1.08E+03	1.08E+03
S ⁴⁺	9.24E+02	9.41E+02	9.41E+02	9.42E+02
S ⁵⁺	1.20E+03	1.42E+03	1.42E+03	1.42E+03
S ⁶⁺	9.54E+01	2.01E+02	2.03E+02	2.03E+02
S ⁷⁺	1.72E+01	9.47E+01	1.00E+02	1.00E+02
S ⁸⁺	5.32E+00	6.71E+01	7.97E+01	7.96E+01
S ⁹⁺	6.79E-01	3.37E+01	5.15E+01	5.15E+01
S ¹⁰⁺	8.24E-02	1.65E+01	3.83E+01	3.80E+01
S ¹¹⁺	1.30E-02	9.15E+00	3.52E+01	3.54E+01
S ¹²⁺	2.15E-03	6.59E+00	5.89E+01	6.06E+01
S ¹³⁺	6.50E-04	1.15E+01	2.46E+02	3.00E+02
S ¹⁴⁺	————	1.25E-01	1.05E+01	2.97E+01
S ¹⁵⁺	————	7.21E-02	2.08E+02	2.88E+03

Table E.3: The X-ray efficiency ($[\text{cm}^2\text{sec}]^{-1}[\text{keV/u}]^{-1}$) of outgoing photons as a function of initial ion energy excluding opacity effects from a single incident ion/cm²/s with an isotropic downward distribution of pitch angles. No opacity effects is displayed for atmosphere 1. The efficiency shown here is that solely from charge exchange collisions for sulfur.

Atmosphere 1 (Original atmosphere)							
Energy [keV/u]	No Opacity						
	S ⁸⁺	S ⁹⁺	S ¹⁰⁺	S ¹¹⁺	S ¹²⁺	S ¹³⁺	S ¹⁴⁺
125	0.00002						
150	0.00010						
175	0.00048	0.00002					
200	0.00168	0.00011					
250	0.01033	0.00119	0.00009	0.00001			
300	0.03435	0.00622	0.00077	0.00011	0.00003		
350	0.07751	0.02099	0.00377	0.00086	0.00026	0.00007	
400	0.13211	0.05073	0.01291	0.00427	0.00181	0.00076	
450	0.17796	0.09057	0.03048	0.01437	0.00774	0.00495	0.00002
500	0.19957	0.12365	0.05208	0.03326	0.02226	0.02065	0.00015
600	0.19061	0.14001	0.07467	0.06741	0.06023	0.08874	0.00122
700	0.16565	0.12694	0.07368	0.07715	0.08247	0.15869	0.00334
800	0.14505	0.11168	0.06641	0.07405	0.08766	0.20345	0.00609
900	0.12878	0.09920	0.05931	0.06757	0.08488	0.22342	0.00907
1000	0.11593	0.08921	0.05339	0.06117	0.07910	0.22688	0.01191
1250	0.09275	0.07149	0.04272	0.04902	0.06474	0.20672	0.01681
1500	0.07726	0.05951	0.03565	0.04084	0.05431	0.18070	0.01895
1750	0.06618	0.05094	0.03055	0.03507	0.04660	0.15759	0.01950
2000	0.05796	0.04462	0.02672	0.03063	0.04077	0.13882	0.01907

Table E.4: The X-ray efficiency ($[\text{cm}^2\text{sec}]^{-1}[\text{keV/u}]^{-1}$) of outgoing photons as a function of initial ion energy including opacity effects from a single incident ion/cm²/s with an isotropic downward distribution of pitch angles. The viewing angle of 0° is displayed for atmosphere 1. The efficiency shown here is that solely from charge exchange collisions for sulfur.

Atmosphere 1 (Original atmosphere)							
Energy [keV/u]	0°						
	S ⁸⁺	S ⁹⁺	S ¹⁰⁺	S ¹¹⁺	S ¹²⁺	S ¹³⁺	S ¹⁴⁺
125	0.00002						
150	0.00010						
175	0.00047	0.00002					
200	0.00167	0.00011					
250	0.01024	0.00119	0.00009	0.00001			
300	0.03391	0.00619	0.00077	0.00011	0.00003		
350	0.07618	0.02083	0.00375	0.00086	0.00026	0.00007	
400	0.12911	0.05025	0.01284	0.00426	0.00181	0.00075	
450	0.17269	0.08948	0.03027	0.01433	0.00773	0.00494	0.00002
500	0.19194	0.12176	0.05162	0.03314	0.02221	0.02061	0.00015
600	0.17921	0.13648	0.07358	0.06701	0.05998	0.08846	0.00121
700	0.15150	0.12194	0.07190	0.07635	0.08191	0.15785	0.00334
800	0.12849	0.10528	0.06388	0.07278	0.08666	0.20172	0.00607
900	0.11009	0.09141	0.05598	0.06572	0.08331	0.22044	0.00904
1000	0.09534	0.08011	0.04923	0.05867	0.07686	0.22232	0.01185
1250	0.06888	0.05982	0.03679	0.04496	0.06068	0.19741	0.01664
1500	0.05167	0.04624	0.02854	0.03564	0.04878	0.16689	0.01860
1750	0.03981	0.03672	0.02272	0.02910	0.04003	0.14030	0.01896
2000	0.03125	0.02976	0.01839	0.02411	0.03343	0.11879	0.01834

Table E.5: The X-ray efficiency ($[\text{cm}^2\text{sec}]^{-1}[\text{keV/u}]^{-1}$) of outgoing photons as a function of initial ion energy including opacity effects from a single incident ion/cm²/s with an isotropic downward distribution of pitch angles. The viewing angle of 80° is displayed for atmosphere 1. The efficiency shown here is that solely from charge exchange collisions for sulfur.

Energy [keV/u]	Atmosphere 1 (Original atmosphere)						
	80°						
	S ⁸⁺	S ⁹⁺	S ¹⁰⁺	S ¹¹⁺	S ¹²⁺	S ¹³⁺	S ¹⁴⁺
125	0.00002						
150	0.00010						
175	0.00046	0.00002					
200	0.00162	0.00011					
250	0.00984	0.00116	0.00009	0.00001			
300	0.03200	0.00603	0.00076	0.00011	0.00003		
350	0.07051	0.02013	0.00367	0.00085	0.00026	0.00007	
400	0.11672	0.04811	0.01250	0.00421	0.00179	0.00075	
450	0.15163	0.08471	0.02930	0.01413	0.00765	0.00490	0.00002
500	0.16248	0.11359	0.04957	0.03258	0.02194	0.02041	0.00015
600	0.13816	0.12174	0.06880	0.06515	0.05884	0.08713	0.00121
700	0.10425	0.10197	0.06436	0.07277	0.07931	0.15406	0.00331
800	0.07775	0.08107	0.05370	0.06721	0.08217	0.19411	0.00601
900	0.05797	0.06380	0.04334	0.05798	0.07651	0.20778	0.00890
1000	0.04345	0.05016	0.03452	0.04872	0.06752	0.20369	0.01161
1250	0.02220	0.02817	0.01954	0.03095	0.04572	0.16341	0.01597
1500	0.01231	0.01657	0.01152	0.02018	0.03088	0.12204	0.01739
1750	0.00735	0.01025	0.00715	0.01371	0.02135	0.09018	0.01724
2000	0.00466	0.00662	0.00459	0.00952	0.01510	0.06700	0.01618

Table E.6: The X-ray efficiency ($[\text{cm}^2\text{sec}]^{-1}[\text{keV/u}]^{-1}$) of outgoing photons as a function of initial ion energy including opacity effects from a single incident ion/cm²/s with an isotropic downward distribution of pitch angles. The viewing angle of 90° is displayed for atmosphere 1. The efficiency shown here is that solely from charge exchange collisions for sulfur.

Energy [keV/u]	Atmosphere 1 (Original atmosphere)						
	90°						
	S ⁸⁺	S ⁹⁺	S ¹⁰⁺	S ¹¹⁺	S ¹²⁺	S ¹³⁺	S ¹⁴⁺
125	0.00001						
150	0.00009						
175	0.00041	0.00002					
200	0.00140	0.00010					
250	0.00796	0.00105	0.00008	0.00001			
300	0.02387	0.00519	0.00068	0.00011	0.00003		
350	0.04837	0.01656	0.00324	0.00080	0.00025	0.00006	
400	0.07273	0.03760	0.01071	0.00391	0.00170	0.00072	
450	0.08421	0.06225	0.02418	0.01292	0.00718	0.00468	0.00002
500	0.07789	0.07701	0.03900	0.02926	0.02035	0.01935	0.00015
600	0.04480	0.06372	0.04579	0.05407	0.05178	0.07970	0.00118
700	0.02137	0.03639	0.03238	0.05213	0.06319	0.13267	0.00318
800	0.01059	0.01843	0.01833	0.03799	0.05554	0.15203	0.00566
900	0.00599	0.00957	0.00963	0.02374	0.04068	0.14184	0.00817
1000	0.00379	0.00562	0.00534	0.01387	0.02666	0.11634	0.01033
1250	0.00163	0.00220	0.00186	0.00432	0.00872	0.05583	0.01299
1500	0.00088	0.00113	0.00092	0.00196	0.00368	0.02668	0.01312
1750	0.00053	0.00066	0.00053	0.00110	0.00192	0.01381	0.01241
2000	0.00035	0.00043	0.00034	0.00068	0.00114	0.00763	0.01131

Table E.7: The X-ray efficiency ($[\text{cm}^2\text{sec}]^{-1}[\text{keV/u}]^{-1}$) of outgoing photons as a function of initial ion energy excluding opacity effects from a single incident ion/cm²/s with an isotropic downward distribution of pitch angles. No opacity effects is displayed for atmosphere 2. The efficiency shown here is that solely from charge exchange collisions for sulfur.

Atmosphere 2 (Well-mixed atmosphere)							
Energy [keV/u]	No Opacity						
	S ⁸⁺	S ⁹⁺	S ¹⁰⁺	S ¹¹⁺	S ¹²⁺	S ¹³⁺	S ¹⁴⁺
125	0.00002						
150	0.00010						
175	0.00048	0.00002					
200	0.00168	0.00011					
250	0.01033	0.00119	0.00009	0.00001			
300	0.03435	0.00622	0.00077	0.00011	0.00003		
350	0.07751	0.02099	0.00377	0.00086	0.00026	0.00007	
400	0.13211	0.05073	0.01291	0.00427	0.00181	0.00076	
450	0.17796	0.09057	0.03048	0.01437	0.00774	0.00495	0.00002
500	0.19957	0.12365	0.05208	0.03326	0.02226	0.02065	0.00015
600	0.19061	0.14001	0.07467	0.06741	0.06023	0.08874	0.00122
700	0.16565	0.12694	0.07368	0.07715	0.08247	0.15869	0.00334
800	0.14505	0.11168	0.06641	0.07405	0.08766	0.20345	0.00609
900	0.12878	0.09920	0.05931	0.06757	0.08488	0.22342	0.00907
1000	0.11593	0.08921	0.05339	0.06117	0.07910	0.22688	0.01191
1250	0.09275	0.07149	0.04272	0.04902	0.06474	0.20672	0.01681
1500	0.07726	0.05951	0.03565	0.04084	0.05431	0.18070	0.01895
1750	0.06618	0.05094	0.03055	0.03507	0.04660	0.15759	0.01950
2000	0.05796	0.04462	0.02672	0.03063	0.04077	0.13882	0.01907

Table E.8: The X-ray efficiency ($[\text{cm}^2\text{sec}]^{-1}[\text{keV/u}]^{-1}$) of outgoing photons as a function of initial ion energy including opacity effects from a single incident ion/cm²/s with an isotropic downward distribution of pitch angles. The viewing angle of 0° is displayed for atmosphere 2. The efficiency shown here is that solely from charge exchange collisions for sulfur.

Atmosphere 2 (Well-mixed atmosphere)							
Energy [keV/u]	0°						
	S ⁸⁺	S ⁹⁺	S ¹⁰⁺	S ¹¹⁺	S ¹²⁺	S ¹³⁺	S ¹⁴⁺
125	0.00002						
150	0.00010						
175	0.00047	0.00002					
200	0.00165	0.00011					
250	0.01012	0.00118	0.00009	0.00001			
300	0.03339	0.00613	0.00076	0.00011	0.00003		
350	0.07476	0.02060	0.00371	0.00086	0.00026	0.00007	
400	0.12624	0.04958	0.01268	0.00422	0.00180	0.00075	
450	0.16819	0.08807	0.02984	0.01421	0.00768	0.00492	0.00002
500	0.18611	0.11951	0.05076	0.03283	0.02204	0.02050	0.00015
600	0.17222	0.13299	0.07182	0.06607	0.05935	0.08780	0.00121
700	0.14454	0.11795	0.06954	0.07481	0.08066	0.15619	0.00333
800	0.12201	0.10123	0.06124	0.07081	0.08486	0.19885	0.00604
900	0.10425	0.08755	0.05331	0.06354	0.08112	0.21643	0.00899
1000	0.09015	0.07658	0.04670	0.05649	0.07450	0.21748	0.01177
1250	0.06503	0.05707	0.03477	0.04311	0.05850	0.19203	0.01650
1500	0.04875	0.04409	0.02694	0.03414	0.04696	0.16200	0.01842
1750	0.03754	0.03500	0.02144	0.02786	0.03851	0.13607	0.01877
2000	0.02947	0.02836	0.01735	0.02308	0.03216	0.11517	0.01814

Table E.9: The X-ray efficiency ($[\text{cm}^2\text{sec}]^{-1}[\text{keV/u}]^{-1}$) of outgoing photons as a function of initial ion energy including opacity effects from a single incident ion/cm²/s with an isotropic downward distribution of pitch angles. The viewing angle of 80° is displayed for atmosphere 2. The efficiency shown here is that solely from charge exchange collisions for sulfur.

Atmosphere 2 (Well-mixed atmosphere)							
Energy [keV/u]	80°						
	S ⁸⁺	S ⁹⁺	S ¹⁰⁺	S ¹¹⁺	S ¹²⁺	S ¹³⁺	S ¹⁴⁺
125	0.00002						
150	0.00009						
175	0.00044	0.00002					
200	0.00154	0.00011					
250	0.00922	0.00112	0.00008	0.00001			
300	0.02947	0.00572	0.00072	0.00011	0.00003		
350	0.06386	0.01891	0.00347	0.00082	0.00025	0.00007	
400	0.10384	0.04470	0.01169	0.00404	0.00173	0.00073	
450	0.13230	0.07776	0.02711	0.01348	0.00738	0.00478	0.00002
500	0.13862	0.10275	0.04526	0.03089	0.02106	0.01984	0.00015
600	0.11235	0.10593	0.06038	0.06028	0.05546	0.08362	0.00119
700	0.08137	0.08516	0.05375	0.06509	0.07285	0.14540	0.00325
800	0.05905	0.06551	0.04272	0.05787	0.07320	0.17956	0.00587
900	0.04337	0.05047	0.03323	0.04827	0.06613	0.18824	0.00866
1000	0.03227	0.03926	0.02591	0.03964	0.05694	0.18111	0.01123
1250	0.01640	0.02188	0.01442	0.02471	0.03752	0.14143	0.01531
1500	0.00909	0.01286	0.00847	0.01609	0.02521	0.10477	0.01662
1750	0.00543	0.00796	0.00526	0.01096	0.01743	0.07731	0.01647
2000	0.00345	0.00514	0.00338	0.00764	0.01236	0.05754	0.01547

Table E.10: The X-ray efficiency ($[\text{cm}^2\text{sec}]^{-1}[\text{keV/u}]^{-1}$) of outgoing photons as a function of initial ion energy including opacity effects from a single incident ion/cm²/s with an isotropic downward distribution of pitch angles. The viewing angle of 90° is displayed for atmosphere 2. The efficiency shown here is that solely from charge exchange collisions for sulfur.

Atmosphere 2 (Well-mixed atmosphere)							
Energy [keV/u]	90°						
	S ⁸⁺	S ⁹⁺	S ¹⁰⁺	S ¹¹⁺	S ¹²⁺	S ¹³⁺	S ¹⁴⁺
125	0.00001						
150	0.00007						
175	0.00034	0.00002					
200	0.00113	0.00009					
250	0.00609	0.00086	0.00007	0.00001			
300	0.01732	0.00410	0.00055	0.00009	0.00002		
350	0.03359	0.01259	0.00249	0.00067	0.00022	0.00006	
400	0.04824	0.02752	0.00793	0.00320	0.00144	0.00064	
450	0.05301	0.04366	0.01719	0.01029	0.00597	0.00411	0.00002
500	0.04589	0.05121	0.02633	0.02257	0.01652	0.01678	0.00014
600	0.02259	0.03628	0.02626	0.03697	0.03823	0.06468	0.00111
700	0.00948	0.01756	0.01518	0.03026	0.04100	0.09898	0.00293
800	0.00450	0.00803	0.00724	0.01850	0.03111	0.10298	0.00510
900	0.00257	0.00410	0.00349	0.01006	0.01997	0.08746	0.00724
1000	0.00164	0.00244	0.00194	0.00542	0.01186	0.06631	0.00905
1250	0.00071	0.00097	0.00070	0.00168	0.00362	0.02883	0.01131
1500	0.00038	0.00050	0.00035	0.00078	0.00153	0.01334	0.01163
1750	0.00023	0.00029	0.00020	0.00044	0.00080	0.00680	0.01122
2000	0.00015	0.00019	0.00013	0.00028	0.00048	0.00373	0.01044

Table E.11: The X-ray efficiency ($[\text{cm}^2\text{sec}]^{-1}[\text{keV/u}]^{-1}$) of outgoing photons as a function of initial ion energy excluding opacity effects from a single incident ion/cm²/s with an isotropic downward distribution of pitch angles. No opacity effects is displayed for atmosphere 1. The efficiency shown here is that solely from direct excitation collisions for sulfur.

Atmosphere 1 (Original atmosphere)							
Energy [keV/u]	No Opacity						
	S ⁸⁺	S ⁹⁺	S ¹⁰⁺	S ¹¹⁺	S ¹²⁺	S ¹³⁺	S ¹⁴⁺
125							
150	0.00003						
175	0.00013						
200	0.00060	0.00002					
250	0.00455	0.00035	0.00003				
300	0.01774	0.00231	0.00027	0.00004	0.00001	0.00001	
350	0.04474	0.00900	0.00164	0.00039	0.00010	0.00008	
400	0.08190	0.02446	0.00655	0.00210	0.00079	0.00081	
450	0.11585	0.04698	0.01763	0.00764	0.00404	0.00548	
500	0.13365	0.06738	0.03289	0.01821	0.01317	0.02286	
600	0.13013	0.07984	0.05156	0.03814	0.04072	0.09703	
700	0.11346	0.07309	0.05221	0.04407	0.05900	0.17309	
800	0.09936	0.06444	0.04732	0.04241	0.06448	0.22100	0.00001
900	0.08822	0.05710	0.04235	0.03873	0.06317	0.24218	0.00001
1000	0.07929	0.05126	0.03798	0.03508	0.05871	0.24513	0.00001
1250	0.06358	0.04104	0.03041	0.02820	0.04796	0.22260	0.00001
1500	0.05286	0.03429	0.02530	0.02351	0.04016	0.19461	0.00002
1750	0.04544	0.02937	0.02172	0.02016	0.03447	0.16986	0.00002
2000	0.03967	0.02567	0.01898	0.01767	0.03015	0.14960	0.00002

Table E.12: The X-ray efficiency ($[\text{cm}^2\text{sec}]^{-1}[\text{keV/u}]^{-1}$) of outgoing photons as a function of initial ion energy including opacity effects from a single incident ion/cm²/s with an isotropic downward distribution of pitch angles. The viewing angle of 0° is displayed for atmosphere 1. The efficiency shown here is that solely from direct excitation collisions for sulfur.

Atmosphere 1 (Original atmosphere)							
Energy [keV/u]	0°						
	S ⁸⁺	S ⁹⁺	S ¹⁰⁺	S ¹¹⁺	S ¹²⁺	S ¹³⁺	S ¹⁴⁺
125							
150	0.00003						
175	0.00013						
200	0.00059	0.00002					
250	0.00451	0.00035	0.00003				
300	0.01753	0.00230	0.00027	0.00004	0.00001	0.00001	
350	0.04404	0.00894	0.00163	0.00039	0.00010	0.00008	
400	0.08018	0.02425	0.00651	0.00209	0.00079	0.00081	
450	0.11267	0.04648	0.01751	0.00761	0.00404	0.00547	
500	0.12890	0.06645	0.03262	0.01813	0.01314	0.02282	
600	0.12277	0.07801	0.05083	0.03786	0.04054	0.09677	
700	0.10418	0.07044	0.05097	0.04351	0.05857	0.17232	
800	0.08836	0.06100	0.04553	0.04151	0.06369	0.21940	0.00001
900	0.07571	0.05290	0.03995	0.03742	0.06190	0.23937	0.00001
1000	0.06546	0.04635	0.03495	0.03332	0.05688	0.24074	0.00001
1250	0.04740	0.03475	0.02604	0.02534	0.04458	0.21312	0.00001
1500	0.03547	0.02711	0.02007	0.01987	0.03553	0.18011	0.00001
1750	0.02743	0.02166	0.01593	0.01601	0.02897	0.15135	0.00002
2000	0.02147	0.01760	0.01283	0.01314	0.02400	0.12789	0.00002

Table E.13: The X-ray efficiency ($[\text{cm}^2\text{sec}]^{-1}[\text{keV/u}]^{-1}$) of outgoing photons as a function of initial ion energy including opacity effects from a single incident ion/cm²/s with an isotropic downward distribution of pitch angles. The viewing angle of 80° is displayed for atmosphere 1. The efficiency shown here is that solely from direct excitation collisions for sulfur.

Energy [keV/u]	Atmosphere 1 (Original atmosphere)						
	80°						
	S ⁸⁺	S ⁹⁺	S ¹⁰⁺	S ¹¹⁺	S ¹²⁺	S ¹³⁺	S ¹⁴⁺
125							
150	0.00003						
175	0.00013						
200	0.00058	0.00002					
250	0.00435	0.00034	0.00003				
300	0.01663	0.00225	0.00027	0.00004	0.00001	0.00001	
350	0.04099	0.00867	0.00160	0.00039	0.00010	0.00008	
400	0.07301	0.02332	0.00635	0.00206	0.00079	0.00080	
450	0.09983	0.04424	0.01696	0.00748	0.00399	0.00544	
500	0.11030	0.06238	0.03137	0.01776	0.01297	0.02265	
600	0.09587	0.07025	0.04762	0.03657	0.03972	0.09554	
700	0.07267	0.05965	0.04568	0.04103	0.05659	0.16875	
800	0.05414	0.04776	0.03827	0.03764	0.06014	0.21207	0.00001
900	0.04034	0.03773	0.03083	0.03206	0.05643	0.22680	0.00001
1000	0.03017	0.02981	0.02433	0.02647	0.04928	0.22159	0.00001
1250	0.01547	0.01713	0.01358	0.01595	0.03228	0.17560	0.00001
1500	0.00859	0.01035	0.00794	0.00980	0.02095	0.12857	0.00001
1750	0.00523	0.00655	0.00491	0.00630	0.01393	0.09243	0.00001
2000	0.00338	0.00430	0.00317	0.00419	0.00944	0.06624	0.00001

Table E.14: The X-ray efficiency ($[\text{cm}^2\text{sec}]^{-1}[\text{keV/u}]^{-1}$) of outgoing photons as a function of initial ion energy including opacity effects from a single incident ion/cm²/s with an isotropic downward distribution of pitch angles. The viewing angle of 90° is displayed for atmosphere 1. The efficiency shown here is that solely from direct excitation collisions for sulfur.

Atmosphere 1 (Original atmosphere)							
Energy [keV/u]	90°						
	S ⁸⁺	S ⁹⁺	S ¹⁰⁺	S ¹¹⁺	S ¹²⁺	S ¹³⁺	S ¹⁴⁺
125							
150	0.00002						
175	0.00012						
200	0.00050	0.00002					
250	0.00358	0.00031	0.00002				
300	0.01267	0.00196	0.00024	0.00004	0.00001	0.00001	
350	0.02877	0.00727	0.00141	0.00036	0.00009	0.00007	
400	0.04675	0.01867	0.00546	0.00189	0.00074	0.00077	
450	0.05721	0.03341	0.01411	0.00674	0.00373	0.00521	
500	0.05483	0.04355	0.02498	0.01562	0.01200	0.02156	
600	0.03238	0.03846	0.03223	0.02923	0.03473	0.08782	
700	0.01558	0.02249	0.02341	0.02754	0.04456	0.14553	
800	0.00787	0.01159	0.01337	0.01911	0.03965	0.16435	0.00001
900	0.00463	0.00614	0.00715	0.01129	0.02864	0.14966	0.00001
1000	0.00307	0.00371	0.00406	0.00634	0.01796	0.11821	0.00001
1250	0.00156	0.00164	0.00160	0.00214	0.00546	0.05164	0.00001
1500	0.00097	0.00097	0.00095	0.00112	0.00240	0.02350	0.00001
1750	0.00070	0.00067	0.00063	0.00074	0.00137	0.01180	0.00001
2000	0.00055	0.00050	0.00047	0.00055	0.00088	0.00649	0.00001

Table E.15: The X-ray efficiency ($[\text{cm}^2\text{sec}]^{-1}[\text{keV/u}]^{-1}$) of outgoing photons as a function of initial ion energy excluding opacity effects from a single incident ion/cm²/s with an isotropic downward distribution of pitch angles. No opacity effects is displayed for atmosphere 2. The efficiency shown here is that solely from direct excitation collisions for sulfur.

Atmosphere 2 (Well-mixed atmosphere)							
Energy [keV/u]	No Opacity						
	S ⁸⁺	S ⁹⁺	S ¹⁰⁺	S ¹¹⁺	S ¹²⁺	S ¹³⁺	S ¹⁴⁺
125							
150	0.00003						
175	0.00013						
200	0.00060	0.00002					
250	0.00455	0.00035	0.00003				
300	0.01774	0.00231	0.00027	0.00004	0.00001	0.00001	
350	0.04474	0.00900	0.00164	0.00039	0.00010	0.00008	
400	0.08190	0.02446	0.00655	0.00210	0.00079	0.00081	
450	0.11585	0.04698	0.01763	0.00764	0.00404	0.00548	
500	0.13365	0.06738	0.03289	0.01821	0.01317	0.02286	
600	0.13013	0.07984	0.05156	0.03814	0.04072	0.09703	
700	0.11346	0.07309	0.05221	0.04407	0.05900	0.17309	
800	0.09936	0.06444	0.04732	0.04241	0.06448	0.22100	0.00001
900	0.08822	0.05710	0.04235	0.03873	0.06317	0.24218	0.00001
1000	0.07929	0.05126	0.03798	0.03508	0.05871	0.24513	0.00001
1250	0.06358	0.04104	0.03041	0.02820	0.04796	0.22260	0.00001
1500	0.05286	0.03429	0.02530	0.02351	0.04016	0.19461	0.00002
1750	0.04544	0.02937	0.02172	0.02016	0.03447	0.16986	0.00002
2000	0.03967	0.02567	0.01898	0.01767	0.03015	0.14960	0.00002

Table E.16: The X-ray efficiency ($[\text{cm}^2\text{sec}]^{-1}[\text{keV/u}]^{-1}$) of outgoing photons as a function of initial ion energy including opacity effects from a single incident ion/cm²/s with an isotropic downward distribution of pitch angles. The viewing angle of 0° is displayed for atmosphere 2. The efficiency shown here is that solely from direct excitation collisions for sulfur.

Atmosphere 2 (Well-mixed atmosphere)							
Energy [keV/u]	0°						
	S ⁸⁺	S ⁹⁺	S ¹⁰⁺	S ¹¹⁺	S ¹²⁺	S ¹³⁺	S ¹⁴⁺
125							
150	0.00003						
175	0.00013						
200	0.00059	0.00002					
250	0.00446	0.00034	0.00003				
300	0.01729	0.00228	0.00027	0.00004	0.00001	0.00001	
350	0.04327	0.00885	0.00161	0.00039	0.00010	0.00008	
400	0.07851	0.02398	0.00643	0.00208	0.00079	0.00080	
450	0.10991	0.04587	0.01727	0.00754	0.00401	0.00545	
500	0.12520	0.06542	0.03209	0.01792	0.01303	0.02270	
600	0.11818	0.07634	0.04964	0.03722	0.04008	0.09601	
700	0.09954	0.06848	0.04930	0.04246	0.05760	0.17038	
800	0.08401	0.05901	0.04362	0.04015	0.06224	0.21602	0.00001
900	0.07178	0.05101	0.03800	0.03592	0.06010	0.23461	0.00001
1000	0.06198	0.04462	0.03310	0.03181	0.05491	0.23493	0.00001
1250	0.04481	0.03340	0.02456	0.02407	0.04274	0.20662	0.00001
1500	0.03351	0.02604	0.01891	0.01884	0.03400	0.17416	0.00001
1750	0.02591	0.02080	0.01500	0.01517	0.02770	0.14617	0.00002
2000	0.02028	0.01690	0.01208	0.01245	0.02294	0.12343	0.00001

Table E.17: The X-ray efficiency ($[\text{cm}^2\text{sec}]^{-1}[\text{keV/u}]^{-1}$) of outgoing photons as a function of initial ion energy including opacity effects from a single incident ion/cm²/s with an isotropic downward distribution of pitch angles. The viewing angle of 80° is displayed for atmosphere 2. The efficiency shown here is that solely from direct excitation collisions for sulfur.

Atmosphere 2 (Well-mixed atmosphere)							
Energy [keV/u]	80°						
	S ⁸⁺	S ⁹⁺	S ¹⁰⁺	S ¹¹⁺	S ¹²⁺	S ¹³⁺	S ¹⁴⁺
125							
150	0.00003						
175	0.00012						
200	0.00055	0.00002					
250	0.00409	0.00033	0.00003				
300	0.01540	0.00215	0.00026	0.00004	0.00001	0.00001	
350	0.03736	0.00823	0.00151	0.00037	0.00009	0.00008	
400	0.06542	0.02194	0.00594	0.00197	0.00076	0.00078	
450	0.08778	0.04118	0.01573	0.00708	0.00384	0.00529	
500	0.09491	0.05733	0.02874	0.01666	0.01242	0.02197	
600	0.07866	0.06250	0.04193	0.03330	0.03726	0.09138	
700	0.05722	0.05122	0.03823	0.03585	0.05161	0.15840	
800	0.04149	0.03987	0.03044	0.03138	0.05297	0.19449	0.00001
900	0.03047	0.03094	0.02359	0.02560	0.04793	0.20287	0.00001
1000	0.02265	0.02424	0.01820	0.02051	0.04058	0.19366	0.00001
1250	0.01161	0.01385	0.01001	0.01203	0.02560	0.14807	0.00001
1500	0.00648	0.00838	0.00588	0.00736	0.01646	0.10687	0.00001
1750	0.00398	0.00532	0.00366	0.00475	0.01092	0.07632	0.00001
2000	0.00260	0.00351	0.00238	0.00317	0.00740	0.05453	0.00001

Table E.18: The X-ray efficiency ($[\text{cm}^2\text{sec}]^{-1}[\text{keV/u}]^{-1}$) of outgoing photons as a function of initial ion energy including opacity effects from a single incident ion/cm²/s with an isotropic downward distribution of pitch angles. The viewing angle of 90° is displayed for atmosphere 2. The efficiency shown here is that solely from direct excitation collisions for sulfur.

Atmosphere 2 (Well-mixed atmosphere)							
Energy [keV/u]	90°						
	S ⁸⁺	S ⁹⁺	S ¹⁰⁺	S ¹¹⁺	S ¹²⁺	S ¹³⁺	S ¹⁴⁺
125							
150	0.00002						
175	0.00010						
200	0.00041	0.00002					
250	0.00278	0.00026	0.00002				
300	0.00938	0.00160	0.00020	0.00003	0.00001		
350	0.02037	0.00575	0.00109	0.00029	0.00008	0.00007	
400	0.03168	0.01429	0.00409	0.00150	0.00063	0.00068	
450	0.03694	0.02459	0.01017	0.00518	0.00306	0.00452	
500	0.03333	0.03053	0.01721	0.01155	0.00963	0.01838	
600	0.01713	0.02370	0.01902	0.01879	0.02510	0.06918	
700	0.00752	0.01209	0.01157	0.01476	0.02803	0.10348	
800	0.00386	0.00581	0.00583	0.00853	0.02127	0.10372	0.00001
900	0.00240	0.00313	0.00308	0.00447	0.01331	0.08419	0.00001
1000	0.00168	0.00199	0.00184	0.00243	0.00747	0.06045	0.00001
1250	0.00096	0.00099	0.00086	0.00098	0.00226	0.02403	0.00001
1500	0.00066	0.00064	0.00058	0.00060	0.00108	0.01076	0.00001
1750	0.00051	0.00047	0.00042	0.00045	0.00068	0.00539	0.00001
2000	0.00042	0.00037	0.00033	0.00037	0.00047	0.00302	0.00001